

The University of Nottingham

UNITED KINGDOM · CHINA · MALAYSIA

Centre for Doctoral Training – Advanced Therapeutics and Nanomedicines

Amphiphilic polymers: structure-activity relationship between their properties and interactions with cell membranes

Lorenzo Schiazza, MSc, MSc

Thesis submitted to the University of Nottingham for the degree of Doctor of Philosophy

30/03/2022

CDT in Advanced Therapeutics and Nanomedicines



Abstract

Polymers are extensively employed in drug delivery for a wide variety of purposes; specifically, the use of drug delivery systems which include bioadhesive polymers has been investigated for decades. Whilst there have been recent examples of phospholipid and cholesterol-based amphiphilic polymers for drug delivery and cell membrane modification purposes, no drug formulation based on membrane-inserting polymers has proven successful when applied *in vivo* to more complex systems.

An important aspect of this PhD work is that, although its overall aim was to design membrane-inserting polymers for drug encapsulation and release, it allowed for a thorough investigation of the interactions between membrane-inserting polymers and lipid bilayers. This aspect is critical for further progress in the membrane-binding polymers field, as no previous study has conducted a systematic investigation on the effect that polymers with membrane inserting chain-ends have when they associate with lipid bilayer membrane. Accordingly, this PhD work describes the design, synthesis and characterisation of polymers presenting different membrane components such as cholesterol, a 1,2-dioleoyl-sn-glycero-3-phosphoethanolamine (DOPE) phospholipid, at their alpha chain end, or multiple units of long fatty acid chains. These polymers were synthesised by reversible addition−fragmentation chain-transfer (RAFT) polymerisation with different chain lengths and by employing hydrophilic and functional monomers, to produce tools to explore polymer-membrane interaction.

We demonstrated that amphiphilic polymers containing cell membrane lipids at their polymer chain-end readily interacted with lipid bilayer membranes, as confirmed by a range of *in vitro* experiments. Conversely, analogous hydrophilic control polymers missing those functional chain-ends showed a negligible degree of interaction with these membranes. Further elucidation of the mechanisms,

kinetics and thermodynamics of these processes was achieved by investigating the interaction of the described polymers with synthetic model membranes. This thesis work further expanded on this aspect by also including an initial *in silico* modelling of these phenomena, providing an initial understanding of these polymer-membrane interactions. These also provide a structure-function relationship for the membrane-inserting materials synthesised in terms of their effect on membrane fluidity, kinetics and thermodynamics of membrane association and dissociation.

As membrane-binding polymers could help retention of formulations *in vivo* following oral administration, we worked on two potential delivery systems. We first focused on nitrofurantoin, an antibiotic used to treat infections in the urinary tract with a fast intestinal absorption and fast elimination. The encapsulation experiments for this drug were based on the formation of an ionic interaction between the acid-bearing polymers and the drug, which contains a basic nitrogen atom. This approach yielded promising initial results, but inconsistencies in terms of reproducibility prompted the adoption of covalent drug encapsulation. For this purpose, we used mesalazine, an immunomodulatory drug employed in the treatment of inflammatory bowel diseases. We synthesised a mesalazine-bearing *N*-alkyl acrylamide monomer and employed this novel monomer to produce drug-conjugated polymers. The membrane-interacting polymers loaded with mesalazine were still able to interact with membranes and showed a pH-dependent drug release.

Acknowledgements

Firstly, I would like to deeply thank my University of Nottingham supervisors Beppe, Snow and Pavel. I would never have made through this journey without your push to improve, your encouragement and the thought-provoking meetings that always lasted longer than planned. I would also like to thank my industrial supervisors, Alexander, Christian and Marcel for the continued support and enthusiasm through these years.

My thoughts go to my family, my mother Lucia Anna, my sister Alessandra, my niece Cecilia and my brother-in-law Cristiano. Thank you for supporting me throughout my long studies. Giovanni, our bond has grown so much during the years we spent abroad, thank you for being here.

Nicoletta, thank you for being there for me through all these years, before and after. We moved to the UK and grew so much together; I would not be the person that I am now was it not for you.

Thank you to all my friends dotted around Europe, I wish I could have seen you more often in these years. Pierpaolo, Davide and Pietro, every time we meet back home it feels like we left yesterday. Thank you to the "pirates", especially Simone, Alberto, Bobbi and Palermo; keeping in touch with you always brings me back to the old days.

All the thanks in the world to the friends I have made here in the UK. Pratik (you would deserve an entire page on this thesis), George, Josh, Shaun and Matteo, you have made me feel at home here and you made the PhD journey into an unforgettable one.

Thank you to everybody that I worked with in B15, A03 and D13: "I don't know half of you half as well as I should like; and I like less than half of you half as well

as you deserve”. An immense thanks goes to the collaborators that made this work so much stronger: Rosa, Gokhan, Vivien, Boyan and Charlie.

Finally, I would like to thank my new colleagues of the Lucideon Pharma team: Aia, Ikra and Stephen, thank you for welcoming me with open arms in this new and exciting adventure within Industry.

List of abbreviations

° C	Celsius degrees
λ_{em}	Emission Wavelength
λ_{ex}	Excitation Wavelength
µg	Microgram
µL	Microlitre
µM	Micromolar
nM	Nanomolar
3-AAPA	3-acrylamido propanoic acid
AA	Acrylic acid
ADME	Absorption, Distribution, Metabolism, Excretion
aMFI	Adjusted Mean Fluorescence Intensity
CAC	Critical aggregation Concentration
Caco-2	Carcinomal Colon cell lines
CRP	Controlled Radical Polymerisation
CTA	Chain Transfer Agent
Đ	Dispersity
DCM	Dichloromethane
DMF	*N,N*-Dimethylformammide
DLS	Dynamic Light Scattering
DMEM	Dulbecco's modified Eagle medium
DMPC	Dimyristoyl Phosphatidylcholine
DMSO	Dimethylsulfoxide
DOPC	Dioleyl Phosphatidylcholine
DOPE	1,2-dioleyl-*sn*-glycero-3-phosphoethanolamine
DP	Degree of Polymerisation
DPPTE	1,2-dipalmitoyl-sn-glycero-3- phosphothioethanol

DSPC	Distearoyl Phosphatidylcholine
EDTA	Ethylenediaminotetraacetic acid
EMEM	Eagle's Minimal Essential Medium
FBS	Foetal bovine serum
GP	Generalised Polarisation
GPI	GlycosylPhosphatidylInositol
GPC	Gel Permeation Chromatography
HEA	2-hydroxyethyl acrylamide
HBSS	Hank's balanced salt solution
HPLC	High Performance Liquid Chromatography
LDH	Lactate Dehydrogenase
MAES	N-methacryloylaminoethyl 5-amino salicylamide
MFI	Mean Fluorescence Intensity
M_n	Number-Average Molecular Weight
MOES	Methacryloyloxyethyl 5-amino salicylate
M_w	Weight-Average Molecular Weight
MWCO	Molecular weight cut-off
NMR	Nuclear Magnetic Resonance
PABTC	Propanoic acid-2-[[(butylthio)thiomethyl]thio]-carbonate
PC	Phosphatidylcholine
PDI	Polydispersity Index
RAFT	Reversible Addition Fragmentation Chain Transfer
RDRP	Reversible Deactivation Radical Polymerisation
RiU	Response index Units
r_p	Rate of propagation
r_t	Rate of termination
SEC	Size Exclusion Chromatography
SPR	Surface Plasmon Resonance

SSNMR	Solid-State Nuclear Magnetic Resonance
THF	Tetrahydrofuran

Table of Contents

Abstract ii

Acknowledgements iv

List of abbreviations vi

List of Figures xvi

List of Equations xxv

List of Tables xxvi

List of Schemes xxviii

Chapter 1 Literature review and scope of the research 1

1 Introduction 2

1.1 Oral administration 3

1.1.1 Floatation devices 4

1.1.2 Janus mucoadhesive devices 5

1.1.3 Swellable matrix tablets 6

1.1.4 Osmotic pumps 7

1.1.5 Polymeric nanofibers 8

1.2 Project hypothesis – use of glycosylphosphatidylinositol anchors mimics to achieve prolonged formulation residence times 10

1.3 Polymers 13

1.3.2 Free radical polymerisation 16

1.3.3 Controlled radical polymerisation (CRP) 17

1.3.4 RAFT polymerisation 18

1.4 Encapsulation of drugs in polymeric formulations 19

1.4.1 Ionomeric encapsulation 19

1.4.2 Covalent encapsulation 21

1.5 Supramolecular aggregation and mucus 22

1.6 Project aims and objectives 22

1.7 Bibliography 24

Chapter 2 Synthesis and characterisation of membrane-binding amphiphilic polymers 31

2.1 Introduction 32

2.2 Materials and Methods 33

2.2.1 Materials 33

2.2.2 Polymer purification 33

2.2.3 ^{1}H NMR analysis of polymers 34

2.2.4 SEC analysis 34

2.2.5 Critical aggregation concentration determination 35

2.2.6 Synthesis of DOPE RAFT agent **(2)** 36

2.2.7 Polymerysations mediated by cholesterol RAFT **(1)** (Ultrafast) 38

2.2.8 Single-phase polymerisations mediated by Cholesterol RAFT **(1)** 40

2.2.9 Polymerisations mediated by DOPE RAFT **(2)** 42

2.2.10 Polymerisations mediated by PABTC RAFT **(3)** 44

2.2.11 Synthesis of 3- acrylamido propanoic acid (3-AAPA, **4**) monomer [5]. 47

2.2.12 Synthesis of 2-acrylamido palmitate (2-AP, **5**) 48

2.2.13 RAFT polymerisation of 2-AP 49

2.2.14 Polymerisations mediated by 2-AP MacroCTA 50

2.2.15 Synthesis of MalPyr Blue 52

2.2.16 One-pot end-capping of trithiocarbonate polymers with MalPyr Blue 54

2.2.17 One-pot end-capping of trithiocarbonate polymers with Rhodamine Red 56

2.2.18 Trithiocarbonate group substitution with an -H group 57

2.2.19 First synthesis of a phospholipid RAFT agent (**13**) 58

2.2.20 Hydrophilic-lipophilic balance (HLB) calculation (Griffin) 62

2.3 Results and Discussion 63

2.3.1 Synthesis of 1,2-dioleoyl-sn-glycero-3-phosphoethanolamine (DOPE)-based RAFT agent **(2)** and 3-acrylamido propanoic acid monomer (3-AAPA) 66

2.3.2 Synthesis of membrane inserting (co)polymers employed in this study 72

2.3.3 Synthesis of non-membrane-inserting control (co)polymers. 78

2.3.4 Membrane-inserting polymers with alternative structures: membrane-inserting repeating units. 80

2.3.5 Synthesis of fluorescently labelled membrane-inserting (co)polymers 86

2.3.6 "One-Pot" aminolysis-fluorescent tagging of polymers investigated in this study 89

2.3.7 Replacement of trithiocarbonate groups at polymer chain-ends with hydrogen -H atoms 95

2.3.8 Critical Aggregation Concentration (CAC) of the polymers synthesised in this work 98

2.4 Concluding remarks 102

2.5 Bibliography 103

Chapter 3 Structural based assessment of polymer-cell interaction 108

3.1 Introduction 109

3.2 Materials and Methods 113

3.2.1 Materials 113

3.2.2 Routine cell culture conditions 113

3.2.3 PrestoBlue™ cell viability and Lactate Dehydrogenase (LDH) joint assays protocol 114

3.2.4 Laurdan assay 115

3.2.5 Preparation of the staining DiL solution 116

3.2.6 Fluorescence microscopy 116

3.2.7 Quantitation of interaction by exposure to fluorescent polymers 117

3.2.8 Cell fixing and confocal microscopy 117

3.2.9 Statistical testing 118

3.2.10 Haemolysis assay 118

3.3.11 Flow Cytometry 119

3.3 Results and Discussion 121

3.3.1 Cell toxicity of the membrane-inserting polymers synthesised in this work 121

3.3.2 Haemolysis assay 132

3.3.3 Cell membrane fluidity evaluation 134

3.3.4 Kinetics of polymer interaction with cell membrane: effect on membrane fluidity *vs.* time 145

3.3.5 24-hour membrane fluidity evaluation 148

3.3.5 Interaction of membrane-inserting polymers with Laurdan fluorescent probe 149

3.3.6 Polymer-Laurdan interaction on cells 152

3.3.7 Cell interaction for trithiocarbonate-cleaved polymers..... 157

3.3.8 Localisation of polymers in cell membranes: fluorescence microscopy studies..... 159

3.3.9 Characterisation of polymer-cell association by Flow Cytometry Imaging 161

3.4 Concluding remarks 172

3.5 Bibliography 174

Chapter 4 Effect of polymers on model lipid bilayer membranes 180

4.1 Introduction..... 181

4.2 Materials and Methods 183

4.2.1 Materials..... 183

4.2.2 Liposome preparation 183

4.2.3 Laurdan assay 183

4.2.4 Gold sputtering on glass coverslips 184

4.2.5 Phosphatidylcholine/1,2-dipalmitoyl-sn-glycero-3- phosphothioethanol liposomes preparation and adhesion 184

4.2.6 AFM analysis of lipid bilayers on gold..... 185

4.2.7 Surface plasmon resonance (SPR) – immobilisation of liposomes on chips on L1 chips 185

4.2.9 Solid-state NMR analysis of multilamellar lipid vesicles 187

4.2.11 Molecular Modelling of Cholesterol-HEA homopolymer interactions with a simulated DPPC bilayer membrane 188

4.3 Results and Discussion 192

4.3.1 Suitability of liposomes as bilayer membrane models for cell membrane-polymer interaction 192

4.3.2 Surface Plasmon Resonance (SPR) 195

4.3.3 Solid-state NMR (SSNMR) 208

4.3.4 Molecular Modelling 219

4.4 Concluding Remarks 226

4.5 Bibliography 227

Chapter 5 Drug encapsulation 232

5.1 Introduction 233

5.2 Materials and Methods 235

5.2.1 Materials 235

5.2.2 Nanoprecipitation 235

5.2.3 Solid drug encapsulation 235

5.2.3 Dialysis of formulations 236

5.2.4 PD10 on formulations 236

5.2.5 Synthesis of mesalazine monomer 236

5.2.6 Synthesis of mesalazine-containing polymers 239

5.2.7 Dynamic Light Scattering 241

5.2.8 RP-HPLC quantitation of drugs 241

5.2.9 Encapsulation efficiency of nitrofurantoin 244

5.2.10 Mesalazine release from polymers 245

5.3 Results and Discussion 246

5.3.1 Nitrofurantoin ionotropic encapsulation 246

5.3.2 Polymer-drug conjugates – drug selection 252

5.3.3 Mesalazine-based polymer-drug conjugates 255

5.4 Concluding Remarks 272

5.5 Bibliography 274

Chapter 6 Conclusions and future directions 279

6.1 Conclusions 280

6.2 Future Directions 283

6.3 Bibliography 285

Appendix 288

A1 Supporting information for Chapter 2 289

A1 Supporting information for Chapter 2 – NMR spectra 289

A1 Supporting information for Chapter 2 – Mass spectra 335

A1 Supporting information for Chapter 2 – FT-IR spectra 337

A1 Supporting information for Chapter 2 – GPC Chromatograms 339

A2 Supporting information for Chapter 3 343

A2 Supporting information for Chapter 3 - Toxicity graphs 343

A3 Supporting information for Chapter 5 350

A3 Supporting information for Chapter 5 – NMR spectra 350

A3 Supporting Information for Chapter 5 – Mass spectra 355

A3 Supporting information for Chapter 5 – GPC Chromatograms 356

List of Figures

Figure 1.1 Graph showing the different plasmatic concentration profiles achieved by repeated administration of a drug (red curve) versus controlled release single unit administration (blue curve). 3

Figure 1.2 Representation of a floating drug delivery device (Ichikawa *et al.*) .. 5

Figure 1.3 Schematic of a Janus adhesive-omniphobic device, (Lee *et al.*)..... 6

Figure 1.4 Representation of drug release from a swellable matrix solid dosage form, Timmins *et al.* 7

Figure 1.5 Schematic representation of a simple osmotic pump system..... 8

Figure 1.6 Schematic representation of drug-loaded polymeric nanofibres with different encapsulation procedures and release mechanisms (Torres-Martinez *et al.*). 9

Figure 1.7 Schematic representation of a GPI-anchored protein (not to scale), highlighting the defining structural elements for a GPI anchor. 10

Figure 1.8 Schematic representation of cell membrane organisation 11

Figure 1.9 Ringsdorf design model for pharmacologically active polymers, adapted from Ringsdorf, 1975. 15

Figure 1.10 Schematic of the acid-base interaction between nitrofurantoin and the acidic side chain of a polymer. 20

Figure 1.11 Structures of Flucloxacillin and acyclovir. 21

Figure 1.12 Structure of Mesalazine and the Mesalazine-based monomers previously employed in literature. 21

Figure 2.1 Main RAFT agents and monomers employed in this study..... 65

Figure 2.2 Detail of the diagnostic peaks for the formation of **11**..... 67

Figure 2.3 ^{1}H NMR showing the reaction progression for the synthesis of **2**. .. 70

Figure 2.4 Representation of a RAFT polymerisation conducted in a two-phase system. 73

Figure 2.5 ^{1}H NMR peaks monitored to confirm polymer composition in synthesised polymers. 76

Figure 2.6 Schematic of the lipid monomer approach to producing amphiphilic polymers with tunable lipid content. 81

Figure 2.7 ^{1}H NMR spectra of the main macro RAFT agents isolated by SiO_2 flash chromatography 84

Figure 2.8 SEC-HPLC chromatograms for MalPyr Blue **(9)**-tagged polymers .. 91

Figure 2.9 SEC-HPLC-chromatograms for Rhodamine Red tagged polymers ... 94

Figure 2.10 Structures of the polymers synthesised in this study, showing the difference in the chemical structure of the trithiocarbonate (ω-chain ends). 95

Figure 2.11 UV-visible spectra of the same polymer, before and after the trithiocarbonate replacement reaction.. 97

Figure 2.12 Pyrene fluorescence emission profile (λ_{ex} = 340 nm) at different concentrations of amphiphilic polymer. 99

Figure 2.13 CAC for the homo and copolymers synthesised in this study as determined using pyrene as the fluorescence probe (μM). 100

Figure 2.14 CAC for the homo and copolymers synthesised in this study as determined using pyrene as the fluorescence probe (mg/mL). 101

Figure 3.1 Modalities of interaction between amphiphilic molecules and cell membranes..... 111

Figure 3.2 Cell toxicity results for select cholesterol-based polymers.. 122

Figure 3.3 Cell toxicity results for selected control polymers. 125

Figure 3.4 Cell toxicity of selected DOPE-containing polymers. 128

Figure 3.5 Cell toxicity results for selected cholesterol-containing polymers with targeted DP ~ 50. 130

Figure 3.6 Cell toxicity results for select cholesterol-based polymers. The assays were performed on Caco2 cells, after 30 minutes incubation with polymer solutions at the same molar concentration (0.1 μM)..... 131

Figure 3.7 Haemolytic activity of Chol and PABTC control polyHEA polymers 132

Figure 3.8 Representation of the emission shift for the Laurdan dye when the cell membrane fluidity changes. Representation of the Laurdan dye intercalating with phospholipids, and of water molecules..... 134

Figure 3.9 Membrane fluidity assays (Laurdan on Caco-2 cells, polymer concentration: 0.1 μM; incubation time: 30 minutes), employing cholesterol-based polymers. 136

Figure 3.10 Membrane fluidity assays (Laurdan on Caco-2 cells, polymer concentration: 0.1 μM; incubation time: 30 minutes) for the non membrane-inserting PABTC-terminated control polymers. 137

Figure 3.11 Membrane fluidity assays (Laurdan on Caco2 cells, polymer concentration: 0.1 μM; incubation time: 30 minutes) for the DOPE-based polymers and the low molecular weight RAFT agents. 138

Figure 3.12 Membrane fluidity assays (Laurdan on Caco2 cells, polymer concentration: 0.1 μM; incubation time: 30 minutes) for copolymers containing phobic lipid-like repeating units. 139

Figure 3.13 Membrane fluidity assays (Laurdan on Caco2 cells, polymer concentration: 0.1 μM; incubation time: 30 minutes) for the additional polymers, shown in the figure 3.16 and tested here for comparative purposes.. 141

Figure 3.14 Correlation analysis between Griffin HLB and average ΔGP obtained for Caco-2 cells treated with all polymers tested within this chapter at the same molar concentration (0.1 μM). 142

Figure 3.15 Membrane fluidity assays (Laurdan on Caco2 cells, polymer concentration: 0.1 μM; incubation time: 30 minutes) polymers for targeted DP below and above the DP 50-100 tested for the majority of the materials investigated in this work. 143

Figure 3.16 Membrane fluidity kinetic assay (Laurdan on Caco2 cells, polymer concentration: 0.1 μM; incubation time: 60 minutes) for the cholesterol-HEA_{52} polymer. 145

Figure 3.17 Membrane fluidity kinetic assay (Laurdan on Caco2 cells, polymer concentration: 0.1 μM; incubation time: 60 minutes) for the DOPE-based HEA_{47} polymer. 146

Figure 3.18 Membrane fluidity kinetic assay (Laurdan on Caco2 cells, polymer concentration: 0.1 μM; incubation time: 60 minutes) for the non membrane-inserting PABTC-terminated HEA_{50} control polymer. 147

Figure 3. 19 Membrane fluidity assays (Laurdan on Caco2 cells) carried out following 24 hour incubation with polyHEAs with cholesterol (Chol), DOPE and PATBC (control) chain units and DP ~ 50. 148

Figure 3.20 GP values for Laurdan in a solution of selected polymers in HBSS, at different concentrations, to evaluate the direct interaction between the polymers and the Laurdan probe in the absence of cell membranes 150

Figure 3.21 GP values for Laurdan in HBSS solution with a series of Chol-$[(HEA)_{100\%}]$ polymers at different concentrations. 151

Figure 3.22 Schematic of the experimental setup for the elucidation of the interactions between polymers, cells and the Laurdan dye. 152

Figure 3.23 Membrane fluidity results for the different solutions and cells analysed to identify the polymer-Laurdan interaction involving Caco2 cells, with results expressed as ΔGP. 153

Figure 3.24 Fluorescence intensity (%) of Laurdan dye (λ_{em} = 440 and 490 nm) for supernatant and cells with fresh medium, after incubation of Caco2 cells with polymers at different concentrations. 155

Figure 3.25 Structures of the Cholesterol Chol-$[(HEA)_{100\%}]_{58}$ and control PATCB-$[(HEA)_{100\%}]_{63}$ polymers after removal of the trithiocarbonate ω-chain end 157

Figure 3.26 Membrane fluidity assays (Laurdan on Caco-2 cells, 0.1 μM incubation for 30 minutes), employing cleaved and non-cleaved polymers. ... 158

Figure 3.27 TRITC channel Confocal Microscopy images of cells treated with Rhodamine Red tagged polymers and untreated cells. 160

Figure 3.28 Chemical structure of the MalPyr Blue fluorescently-tagged polymers: MalPyr Blue Chol-[(HEA)$_{100\%}$]$_{52}$, MalPyr Blue Chol-[(HEA)$_{100\%}$]$_{70}$, MalPyr Blue Chol-[(HEA)$_{100\%}$]$_{108}$, MalPyr Blue DOPE-[(HEA)$_{100\%}$]$_{47}$, MalPyr Blue PABTC-[(HEA)$_{100\%}$]$_{50}$..... 162

Figure 3.29 aMFI graph for cells treated with 0.1 μM HBSS solutions of MalPyr Blue fluorscently-tagged polymers. 163

Figure 3.30 Flow cytometry images for Caco-2 cells treated with MalPyr Blue Chol-[(HEA)$_{100\%}$]$_{50}$, showing channel 03 (λ_{ex} = 377 nm and λ_{em} = 420 nm) and brightfield images. 165

Figure 3.31 Flow cytometry images for Caco-2 cells treated with MalPyr Blue Chol-[(HEA)$_{100\%}$]$_{70}$, showing channel 03 (λ_{exc} = 377 nm and λ_{em} = 420 nm) and brightfield images. 166

Figure 3.32 Flow cytometry images for Caco-2 cells treated with MalPyr Blue Chol-[(HEA)$_{100\%}$]$_{108}$, showing channel 03 (λ_{ex} = 377 nm and λ_{em} = 420 nm) and brightfield images. 167

Figure 3.33 Flow cytometry images for Caco-2 cells treated with MalPyr Blue DOPE-[(HEA)$_{100\%}$]$_{47}$, showing channel 03 (λ_{ex} = 377 nm and λ_{em} = 420 nm) and brightfield images. 168

Figure 3.34 Flow cytometry images for Caco-2 cells treated with MalPyr Blue PABTC-[(HEA)$_{100\%}$]$_{50}$, showing channel 03 (λ_{ex} = 377 nm and λ_{em} = 420 nm) and brightfield images. 170

Figure 4.1 Division of Chol-[(HEA)]$_n$ (top) into fragments for modelling..... 188

Figure 4.2 Coarse graining scheme for [(HEA)]$_n$ and details of polymer backbone dihedral distributions inferred from atomistic simulations..... 189

Figure 4.3 DLS particle size analysis of the Laurdan-loaded liposomes employed for membrane fluidity studies. 193

Figure 4.4 Kinetic Laurdan fluorescence measurement for Laurdan-loaded liposomes interacting with different types of polymers. 194

Figure 4.5 Representation of an SPR system. 195

Figure 4.6 Example sensorgram highlighting the main phases in an SPR analysis: 1) baseline, 2) association, 3) dissociation and 4) regeneration. 196

Figure 4.7 Example sensorgram, highlighting the parameters influencing each phase. 197

Figure 4.8 Glass coverslips functionalisation procedure to prepare surfaces for SPR 199

Figure 4.9 AFM images in peak force tapping mode showing the ITO + gold deposition layer and the surface after deposition of liposomes. 200

Figure 4.10 AFM image in tapping mode showing a dishomogeneous distribution of lipid bilayers deposited following incubation of gold surface with liposomes 200

Figure 4.11 Diagrams depicting the two types of SPR sensor chips considered for this study. 201

Figure 4.12 Immobilisation of phosholipid lipid bilayer on an SPR L1 sensor chip. 202

Figure 4.13 Dynamic light scattering (DLS) particle size analysis of of liposomes employed to form immobilisied bilayers for the SPR studies. 203

Figure 4.14 SPR sensorgrams for the cholesterol-and DOPE-containing polymers, and control PABTC polymer 204

Figure 4.15 ^{31}P SSNMR spectrum of 1,2-dimyristoyl-sn-glycero-3-phosphocholine (DMPC) MLVs. 209

Figure 4.16 ^{31}P MAS wideline spectra of DMPC MLVs treated with polymers. 210

Figure 4.17 Solid state NMR pulse sequence of (A) cross polarisation and (B) direct excitation. 211

Figure 4. 18 ^{13}C MAS NMR spectra with direct excitation of DMPC lipid bilayer, DMPC with cholesterol, PABTC-$[(HEA)_{100\%}]_{63}$, DOPE-$[(HEA)_{100\%}]_{47}$, Chol-$[(HEA)_{100\%}]_{13}$ and Chol-$[(HEA)_{100\%}]_{58}$ prepared with DMPC and cholesterol membrane.. 212

Figure 4.19 Assignments for the key peaks observed by SSNMR for the analysed HEA homopolymers and for DMPC. 213

Figure 4.20 ^{13}C MAS NMR spectra, zoomed in between 5 to 75 ppm, with direct excitation of DMPC lipid bilayer, DMPC with cholesterol, PABTC-$[(HEA)_{100\%}]_{63}$, (red) DOPE-$[(HEA)_{100\%}]_{47}$, Chol-$[(HEA)_{100\%}]_{13}$ and Chol-$[(HEA)_{100\%}]_{58}$ prepared with DMPC and cholesterol membrane. 214

Figure 4.21 ^{13}C CP MAS NMR of DMPC lipid bilayer, DMPC with cholesterol, PABTC-$[(HEA)_{100\%}]_{63}$, DOPE-$[(HEA)_{100\%}]_{47}$, Chol-$[(HEA)_{100\%}]_{13}$ and Chol-$[(HEA)_{100\%}]_{58}$ prepared with DMPC and cholesterol membrane. 215

Figure 4.22 ^{13}C CP MAS NMR of DMPC lipid bilayer, DMPC with cholesterol , PABTC-$[(HEA)_{100\%}]_{63}$, DOPE-$[(HEA)_{100\%}]_{47}$, Chol-$[(HEA)_{100\%}]_{13}$ and Chol-$[(HEA)_{100\%}]_{58}$ prepared with DMPC and cholesterol membrane. 216

Figure 4.23 ^{13}C MAS NMR of DMPC lipid bilayer, DMPC with cholesterol, PABTC-$[(HEA)_{100\%}]_{63}$, DOPE-$[(HEA)_{100\%}]_{47}$, Chol-$[(HEA)_{100\%}]_{13}$ and Chol-$[(HEA)_{100\%}]_{58}$ prepared with DMPC and cholesterol membrane, comparing CP and direct excitation. 217

Figure 4.24 Coarse graining scheme for $[(HEA)]_n$ and details of polymer backbone dihedral distributions inferred from atomistic simulations 219

Figure 4.25 Analysis of 300 ns CG simulations of atactic $[(HEA)]_{58}$ in water. 221

Figure 4.26 Snapshots from the 500 ns atomistic simulation of Chol-$[(HEA)]_{50}$ in a DPPC bilayer 222

Figure 4.27 Deuterium order parameters calculated along lipid chains within radial shells. 223

Figure 4.28 Aggregation simulations for Chol-$[(HEA)]_n$ (blue) on a plasma membrane surface 224

Figure 5.1 Chemical structure of the model drugs chosen for encapsulation, nitrofurantoin and mesalazine 234

Figure 5. 2 Nitrofurantoin HPLC-UV calibration curve. 242

Figure 5.3 UV-vis spectrum of mesalazine in water. 243

Figure 5.4 Mesalazine HPLC-UV calibration curve. 244

Figure 5.5 Schematic for the block copolymer approach to Nitrofurantoin ionomeric encapsulation. 248

Figure 5.6 Encapsulation efficiency and dose loading for different approaches of nitrofurantoin encapsulation. 251

Figure 5.7 Chemical structures of mesalazine, and sulfasalazine. 253

Figure 5.8 Comparison of critical aggregation concentration in aqueous solution between the HEA-based polymers and the mesalazine-based copolymers. 259

Figure 5.9 Particle size results obtained by DLS for the mesalazine-based polymers comparing intensity, volume and number particle size distribution. 260

Figure 5.10 Metabolic activity of Caco2 cells incubated with mesalazine-containing polymers using PrestoBlue™ assay. 262

Figure 5.11 Change of membrane fluidity results for the different polymer solutions (Chol-[(HEA)$_{80\%}$-*r*-(MES)$_{20\%}$]$_{80}$ and Chol-[(HEA)$_{75\%}$-*r*-(MES)$_{25\%}$]$_{46}$) and Caco-2 cells. 264

Figure 5.12 Change of membrane fluidity results for the different polymer solutions (Chol-[(HEA)$_{90\%}$-*r*-(MES)$_{10\%}$]$_{44}$, PABTC-[(HEA)$_{90\%}$-*r*-(MES)$_{10\%}$]$_{38}$ and DOPE-[(HEA)$_{90\%}$-*r*-(MES)$_{10\%}$]$_{44}$) and Caco-2 cells analysed to identify the polymer-Laurdan interaction involving cells, with results expressed as ΔGP. 266

Figure 5.13 Membrane fluidity kinetic assay (Laurdan on Caco2 cells) for the Chol-[(HEA)$_{80\%}$-*r*-(MES)$_{20\%}$]$_{80}$. 267

Figure 5.14 Mesalazine release over 3 days, from Chol-[(HEA)$_{80\%}$-*r*-(MES)$_{20\%}$]$_{80}$ polymer, with and without the presence of porcine esterase enzyme 269

Figure 5.15 Release of Mesalazine from Chol-[(HEA)$_{75\%}$-*r*-(MES)$_{25\%}$]$_{46}$ comparing different pH conditions, focusing on the first 8 hours of release. 270

Figure 5.16 Release of mesalazine from Chol-[(HEA)$_{75\%}$-*r*-(MES)$_{25\%}$]$_{46}$, Chol-[(HEA)$_{90\%}$-*r*-(MES)$_{10\%}$]$_{44}$, PABTC-[(HEA)$_{90\%}$-*r*-(MES)$_{10\%}$]$_{38}$ and DOPE-[(HEA)$_{90\%}$-*r*-(MES)$_{10\%}$]$_{44}$ in FaSSIF over the course of 24 hours. 271

Figure 6.1 General structure of polymers employed in this study: cholesterol-, DOPE- and PABTC-containing control polymers (from top to bottom, respectively). 281

Figure 6.2 Correlation analysis between Griffin hydrophilic-lipophilic balance (HLB) of the polymers and average cell fluidity measurement (ΔGP) obtained for Caco-2 cells treated with a range of polymers at the same molar concentration (0.1 μM). 282

List of Equations

Equation 1.1 Dependence of the ratio between r_p and r_t on the monomer/active polymer concentrations. 17

Equation 3.1 Calculation of relative LDH release, for the purpose of membrane damage evaluation..... 114

Equation 3.2 Calculation of relative metabolic activity, PrestoBlue™ assay. . 115

Equation 3.3 Calculation of Generalised Polarisation (GP) of Laurdan..... 116

Equation 3.4 Calculation of relative fluorescence (%) of cells following incubation with MalPyr Blue-tagged fluorescent polymers 117

Equation 3.5 Griffin HLB calculation..... 62

Equation 3.6 Calculation of relative haemolysis, for the purpose of cell damage evaluation..... 119

Equation 3.7 Calculation of adjusted median fluorescence intensity (MFI).. . 120

Equation 5.1 Encapsulation efficiency calculation, employed to estimate the percentage of starting drug that is encapsulated in the formulation..... 244

Equation 5.2 Dose loading calculation, employed to quantify the amount of drug contained in the formulation. 245

List of Tables

Table 1.1 Examples of membrane-interacting polymers in recent literature, employed for a variety of purposes 14

Table 2.1 Polymerisation table for ultrafast RAFT polymerisations..... 39

Table 2.2 Polymerisation table for single-phase RAFT polymerisations mediated by **1** 41

Table 2.3 Polymerisation table for single-phase RAFT polymerisations mediated by **2** 43

Table 2.4 Polymerisation table for single-phase RAFT polymerisations mediated by **3**, 50 DP polymers 45

Table 2.5 Polymerisation table for single-phase polymerisations mediated by **3**, 100 DP polymers 46

Table 2.6 Polymerisation table for single-phase RAFT polymerisations mediated by **6** 51

Table 2.7 Cholesterol-based (co)polymers produced in this study. 75

Table 2.8 DOPE-based (co)polymers produced in this study. 77

Table 2.9 PABTC-based polymers produced in this study. 79

Table 2.10 DDMAT-$[(HEA)_{100\%}]_{42}$: composition and characterisation. 80

Table 2.11 Fractions of the **(5)**-HEA macro RAFT agent purified by SiO_2 flash chromatography 83

Table 2.12 Lipid monomer-based polymers produced in this study. 85

Table 2.13 MalPyr Blue fluorescently tagged polymers. 92

Table 2.14 Rhodamine Red maleimide-tagged polymers investigated in this study. 94

Table 2.15 Trithiocarbonate removal from polymers, estimated from the decrease of absorbance at λ = 320 nm. 97

Table 2.16 SEC analysis of cleaved and non-cleaved polymers. 98

Table 3.1 PrestoBlue and LDH IC_{50} values for Caco-2 cells exposed for 24 hours to solutions of the amphiphilic cholesterol polymers…… …… 124

Table 3.2 PrestoBlue and LDH IC_{50} values for Caco-2 cells incubated for 24 hours with solutions of the PABTC control polymers. 127

Table 3.3 PrestoBlue and LDH IC_{50} values for Caco-2 cells exposed for 24 hours to solutions of the amphiphilic DOPE polymers. 128

Table 3.4 Toxicity comparison between the polymers described within this study and examples of amphiphilic polymers in the literature, expressed as IC_{50} (μM) and showing the toxicity assay(s) used. 129

Table 3.5 IC_{50} values for cleaved and non-cleaved polymers on Caco-2 cells (24 hours incubation)..... 157

Table 4.1 Polymers selected for the surface plasmon resonance evaluation of polymer-bilayer interactions…… …… 186

Table 4.2 Polymers selected for the solid-state NMR evaluation of polymer-bilayer interactions..... 187

Table 4.3 Composition of the liposomes employed as a model membrane for fluidity studies..... 192

Table 4.4 Kinetic parameters obtained from SPR analysis for the interaction between the tested polymers and L1-immobilised bilayers. 206

Table 5.1 Synthesis of mesalazine monomer (16)-containing copolymers: reaction conditions and targeted composition of final polymers…… 240

Table 5.2 Cholesterol HEA-AAPA block copolymers..... 249

Table 5.3 Mesalazine **(16)**-HEA copolymers synthesised in this work 258

Table 5.4 Particle size measurement results for aggregates of the mesalazine-based polymers, reporting the Z-average diameter (nm) and Pdi values. 259

Table 5.5 Cell metabolic activity - IC_{50} values for mesalazine-based polymers 263

List of Schemes

Scheme 1.1 Conventional free radical polymerisation reaction steps, from initiation to propagation to termination. 16

Scheme 1.2 Equilibrium between dormant (P-X) and active (P·) species in CRP reactions. 17

Scheme 1.3 RAFT polymerisation initiation and equilibrium. 18

Scheme 2.1 Synthesis of cholesterol-based CTA **(1)** (R. Catania *et al.*)..... 63

Scheme 2.2 Synthetic scheme of the DOPE-based RAFT agent **(2)**. 64

Scheme 2.3 First successful synthetic scheme of DOPE-based RAFT agent..... 68

Scheme 2.4 Synthesis of DOPE-based RAFT agent **(2)**. 69

Scheme 2.5 Synthesis of 3-acrylamido propanoic acid **(4)** monomer from β-alanine. 70

Scheme 2.6 Synthesis of cholesterol-terminated polymers by biphasic ultrafast RAFT polymerisation, starting from cholesterol-containing RAFT agent **(1)** and N-hydroxyethyl acrylamide (HEA), 3-acrylamido propanoic acid (3-AAPA, **4**) and acrylic acid (AA). 72

Scheme 2.7 Synthesis of membrane-inserting cholesterol-terminated polymers by single-phase RAFT polymerisation, starting from cholesterol-containing RAFT agent **(1)** and N-hydroxyethyl acrylamide (HEA), 3-acrylamido propanoic acid (3-AAPA, **4**) and acrylic acid (AA)..... 74

Scheme 2.8 Synthesis of DOPE-terminated polymers by single-phase RAFT polymerisation, starting from DOPE-containing RAFT agent **(2)** and N-hydroxyethyl acrylamide (HEA), 3-acrylamido propanoic acid (3-AAPA, **4**) and acrylic acid (AA). 76

Scheme 2.9 Synthesis of control polymers by single-phase RAFT polymerisation, starting from PABTC RAFT agent **(3)** and N-hydroxyethyl acrylamide (HEA), 3-acrylamido propanoic acid (3-AAPA, **4**) and acrylic acid (AA). 78

Scheme 2.10 Synthesis of DDMAT-[$(HEA)_{100\%}]_{42}$, starting from DDMAT and N-hydroxyethyl acrylamide (HEA) 79

Scheme 2.11 Synthesis of hydrophilic 2-acrylamido palmitate monomer **(5)**. 81

Scheme 2.12 Single-phase, polymerisation of the lipophilic macroCTA based on the lipid monomer **5**. 82

Scheme 2.13 Fluorescent tagging of the polymers utilised in this study, requiring aminolysis of trithiocarbonate groups to obtain thiol-terminated polymers, and subsequent thiol-ene Michael addition with a maleimide-functionalised fluorescent dye. 86

Scheme 2.14 Synthesis of maleimide fluorescent dye, MalPyr Blue **(9)**. 87

Scheme 2.15 One-pot fluorescent tagging of (co)polymers utilized in this study with fluorescent MalPyr blue **(9)** dye. 89

Scheme 2.16 One-pot fluorescent tagging of (co)polymers utilized in this study with fluorescent rhodamine Red™ C 2 Maleimide. 93

Scheme 2.17 Removal of trithiocarbonate polymer chain-ends using N-ethylpiperidine hypophosphite (EPHP), under radical conditions. 96

Scheme 2.18 Mechanism of trithiocarbonate group substitution with H atom. 96

Scheme 5.2 Block copolymerisation for AAPA-HEA based polymers…… ……249

Scheme 5.2 Examples of synthesis of two different mesalazine-based monomers, methacryloyloxyethyl 5-amino salicylate (MOES) and N-methacryloylaminoethyl 5-amino salicylamide (MAES). 254

Scheme 5.3 Synthesis of mesalazine-based acrylamide monomer **(16)**. 255

Scheme 5.4 Scheme for the single-phase RAFT copolymerisation of HEA and 16 with the different RAFT agents - cholesterol, DOPE and PABTC (control). 257

Scheme 5.5 Mechanism of acid-catalysed hydrolysis for mesalazine release from the polymers. 271

Chapter 1

Literature review and scope of the research

This chapter will provide insight into the research question behind the research, and our approach to tackle current challenges in sustained oral drug delivery. Despite many efforts, currently there are no true long-acting (more than 48h sustained drug delivery) oral drug delivery systems. Therefore, a novel cell membrane binding approach, which conceptually mimics the mechanism by which in nature glycosylphosphatidylinositol anchors link proteins to biological barriers, was adopted for this study. In this study, membrane-binding polymers were designed and synthesised by RAFT polymerisation, which allows for precise control over the polymeric structure.

1 Introduction

One of the most prominent issues for modern healthcare is the lack of patients' adherence to prescribed dosing regimens. This is crucial for effective therapy[1], particularly for the treatment of bacterial infections and chronic diseases. These therapies generally tend to be characterised by repeated administrations per day, often spanning weeks (antibiotics) up to years for chronic conditions management. The classic approach of repeated administrations often results in reduced patient compliance and thus efficacy of the treatment. In addition, improper dosing throughout a therapy leads to poor healthcare outcomes, and ultimately increase the rates of hospitalization. These factors account for an increase in healthcare spending, which could be avoidable if adherence to medications could be improved[2]. Long-acting formulations have therefore been extensively investigated for a wide variety of drugs, especially for the oral drug delivery route.

Patient compliance would improve with the achievement of a controlled drug release platform, capable of delivering a treatment over the course of one day, or multiple days with one single administration[3]. Therefore, this would naturally increase the adherence to therapy (particularly for multi-dose drugs) and would benefit healthcare, especially in countries where no easy access to medication is available[4]. A single unit dosage form would allow the patients to receive the full treatment without the necessity for multiple interactions with the medication provider. Additionally, multiple unit dosage forms require repeated administrations before reaching a "steady-state" plasmatic level concentrations[5], thus delaying the onset of beneficial effects for the patient.

As it can be observed in the illustration in **Figure 1.1**, repeated administration of a multi-dose drug (red curve) causes fluctuations in the plasmatic concentration of the active. This approach to therapy can cause the plasmatic concentration to reach levels below the minimum effective concentration (MEC) to above the

minimum toxic concentration (MTC). These fluctuations in plasmatic concentration are influenced by ADME (Absorption, Distribution, Metabolism, Excretion), that can change intra- and inter-patient[6–8]. Controlled single unit dosage form (blue curve) ideally could help maintain the plasmatic concentration in the therapeutic window for a prolonged period of time[9].

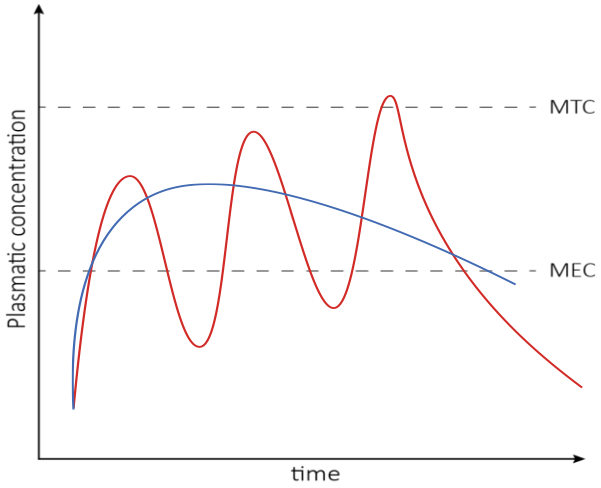


Figure 1.1 Graph showing the different plasmatic concentration profiles achieved by repeated administration of a drug (red curve) versus controlled release single unit administration (blue curve), in relation to minimum effective concentration (MEC) and minimum toxic concentration (MTC)

Thanks to these advantages, there has been extensive research over the years in the field of extended drug release platforms. This is especially true for the treatment of difficult to manage conditions such as psychiatric disorders[10] and epilepsy[11]. Over time, a wide variety of successful and unsuccessful approaches have been implemented: from solid implants[12] to floatation stomach devices[13], to mucoadhesive formulations[14,15].

1.1 Oral administration

Oral administration represents the most widespread route for drug delivery, given its low invasiveness and high patient compliance[16]. Low sterility requirements and ease of production make oral administration also an industry-favourite, since it is the cheapest to manufacture[17]. However, it presents very well-known challenges,

from variations in bioavailability[18] (inter- and intra-patient) to rapid physiological transit time in the gastrointestinal (GI) tract[19]. Since the digestive system is subject to peristaltic movements that are physiologically used for the bolus transit, any formulation is transported downstream and excreted. This limits the residence time of oral formulations in the small intestine (where optimal drug absorption occurs) to 2-6 hours[20], thus challenging the development of a long-acting oral drug delivery formulation. The total transit time for a formulation in the GI tract highly varies between individuals, and depends on the fed/fasted state of the subject (29.81 ± 14.52 h)[20]. The transit time of a formulation can highly influence the biodistribution of a drug, as different areas of the intestine offer different drug absorption characteristics[21]; as an example, shorter transit times in areas where absorption is high (such as the small intestine) can decrease the bioavailability for a drug[22]. Additionally, the mucus barrier present in the intestine is a significant hurdle for long-release formulations. This barrier is designed to protect the intestinal epithelium and –effectively- the body from exogenous particulate, such as pathogens and nanoparticles, while enabling the absorption of nutrients.

To address these challenges and produce a long-lasting oral drug delivery formulation, different approaches have been explored. Some of these have shown promising results *in vitro*, but most did not produce the expected results when translated *in vivo*[23]. These are a prime example of the principle postulated by Tom Connors, where an elegant working hypothesis is only sometimes successful in the clinic[24,25].

1.1.1 Floatation devices

These systems (**Figure 1.2**) have exploited floatation in order to achieve permanence in the stomach[26], using gelling-effervescent polymers such as Eudragit E® and Carrageenan[27]. However, these systems could not achieve gastric

residence over 12 hours, and are heavily influenced by the variability in gastric content and the position assumed by the patient (supine or standing)[28].

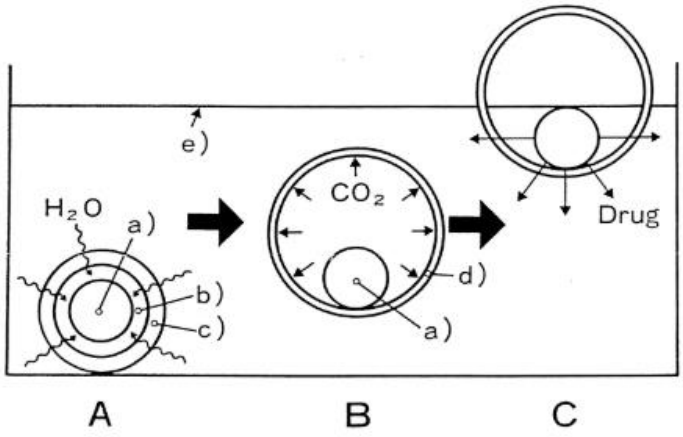


Figure 1.2 Representation of a floating drug delivery device, showing the different phases of the process (A) penetration of the water through the external layers; (B) CO_2 generation and floating; (C) dissolution and release of the drug. The representation also highlights the different structures: a) standard release solid formulation; b) effervescent layer; c) swellable layer and d) expanded swellable membrane layer and e) medium surface (Ichikawa *et al.*[29])

1.1.2 Janus mucoadhesive devices

Another system – a mucoadhesive-omniphobic double-faced Janus device, with one side adhering to the mucus layer and the opposite side with non-interacting antifouling properties – was designed to possess mucus adhesive properties to achieve prolonged gastric retention[30] (**Figure 1.3**). This should have been achieved by mimicking natural bioadhesion mechanisms, through which bacteria accomplish residence in the GI tract[31]. However, this type of formulation failed to achieve the predicted long-acting drug delivery *in vivo*, despite the promising *in vitro* results. This could be explained by the rapid turnover rate of the enteric mucus (2 hours)[32], as mucus adhering formulation tend to be removed by this physiological mechanism.

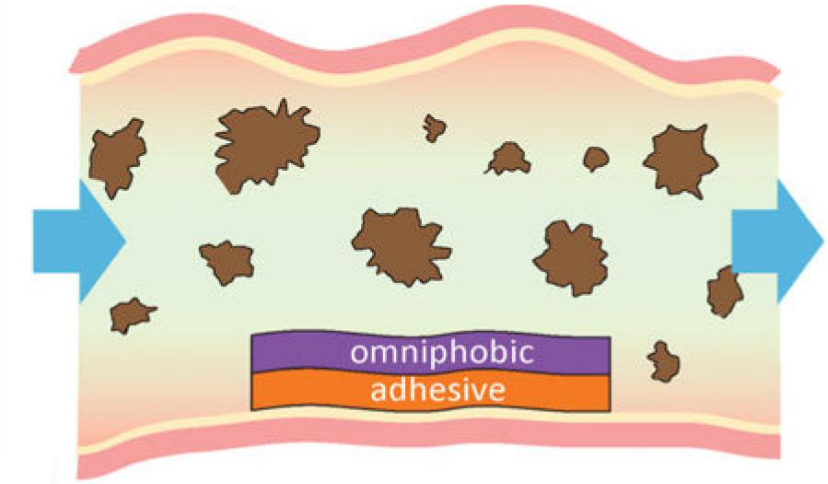


Figure 1.3 Schematic of a Janus adhesive-omniphobic device, (Lee *et al.*[30]). The omniphobic layer minimises interaction with particulate in the digestive tract, therefore minimising dislodgement.

1.1.3 Swellable matrix tablets

Swellable matrix tablets (**Figure 1.4**) are capable of achieving prolonged residence in the stomach by increasing in size when in contact with liquid[33], and provide a steady drug release (zero order kinetics) from the resulting swollen matrix. These systems are usually formed by hydrophilic polymers[34] or a combination of hydrophilic/hydrophobic polymers[35]. However, residence beyond 24 hours is hindered by the physiological GI tract movements, which disrupt the settlement of these materials.

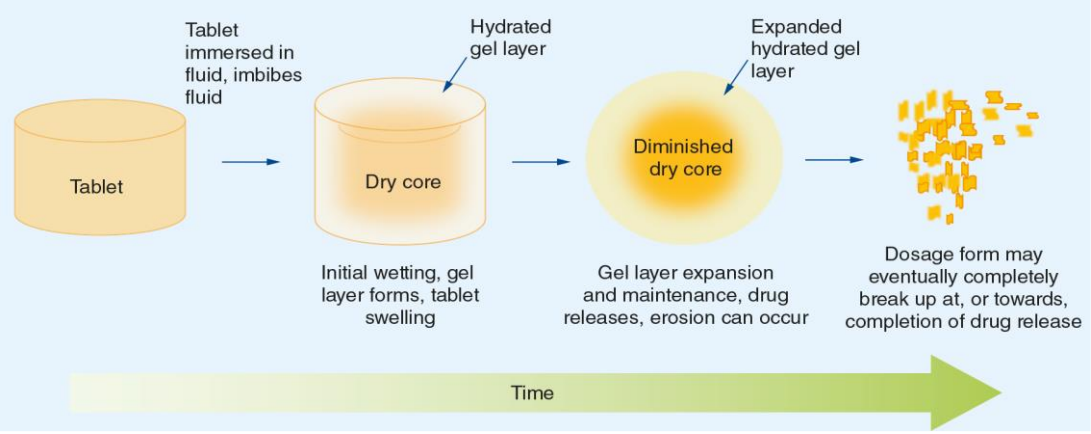


Figure 1.4 Representation of drug release from a swellable matrix solid dosage form, Timmins *et al.*[36] .

1.1.4 Osmotic pumps

Another oral formulation used to achieve prolonged drug release is represented by osmotic pumps (**Figure 1.5**): due to their large size, these formulations are eliminated slowly by the digestive system and gradually release the contained drug[37]. Though many designs exist, their structure can be described as a hard shell (semi-permeable membrane) with a laser-drilled orifice and two internal layers. The upper layer, adjacent to the delivery orifice, consists of a formulation of the active pharmaceutical ingredient of choice, and a bottom polymeric push layer. Following oral administration the formulation gets in contact with bodily fluids, water gradually enters the osmotic pump formulation through the semipermeable membrane, and swelling of the bottom polymeric push layer slowly induces drug release through the delivery orifice. However, these systems cannot achieve residence beyond 24 hours and the release can be influenced by the composition of the gastric content[28]. This could result in potential toxicity if the system releases its contents too quickly, on in lack of efficacy if the system releases the drug too slowly.

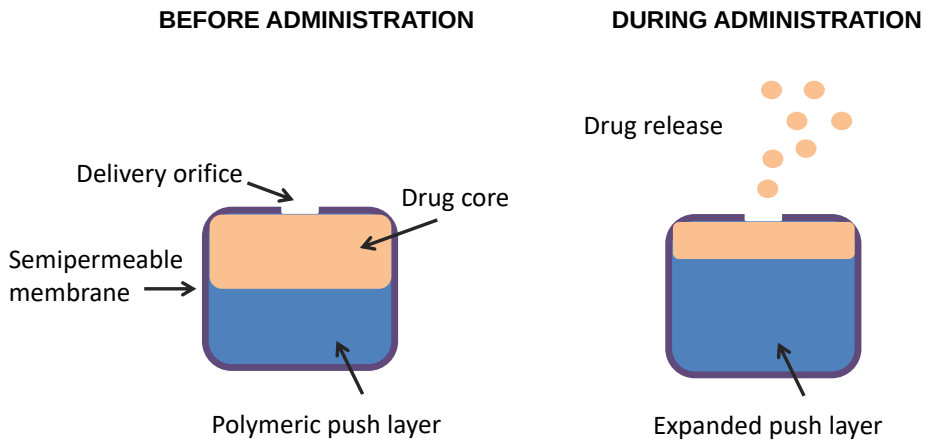


Figure 1.5 Schematic representation of a simple osmotic pump system.

1.1.5 Polymeric nanofibers

Specific polymer solutions can be subject to electrospinning, which uses an electrical field to produce filaments of polymeric fibres[38]. This process can be tweaked to obtain nanofibers with specific architectures (**Figure 1.6**). Given the tuneable nature of polymers, these systems can be used to achieve longer permanence in the GI tract (through swelling and anchoring[39]) and to incorporate slowly-releasing drugs. However, the scaling up of these systems is problematic[38] and crystalline drugs might cause instability/heterogeneity in the filaments produced[40].

The aforementioned systems exemplify the abundant and ingenious approaches that have been implemented in the past for achievement of extended oral drug delivery. Recent approaches are focusing on the production of mucus penetrating formulations[41] to elude the sweeping and protective functions performed by the mucus.

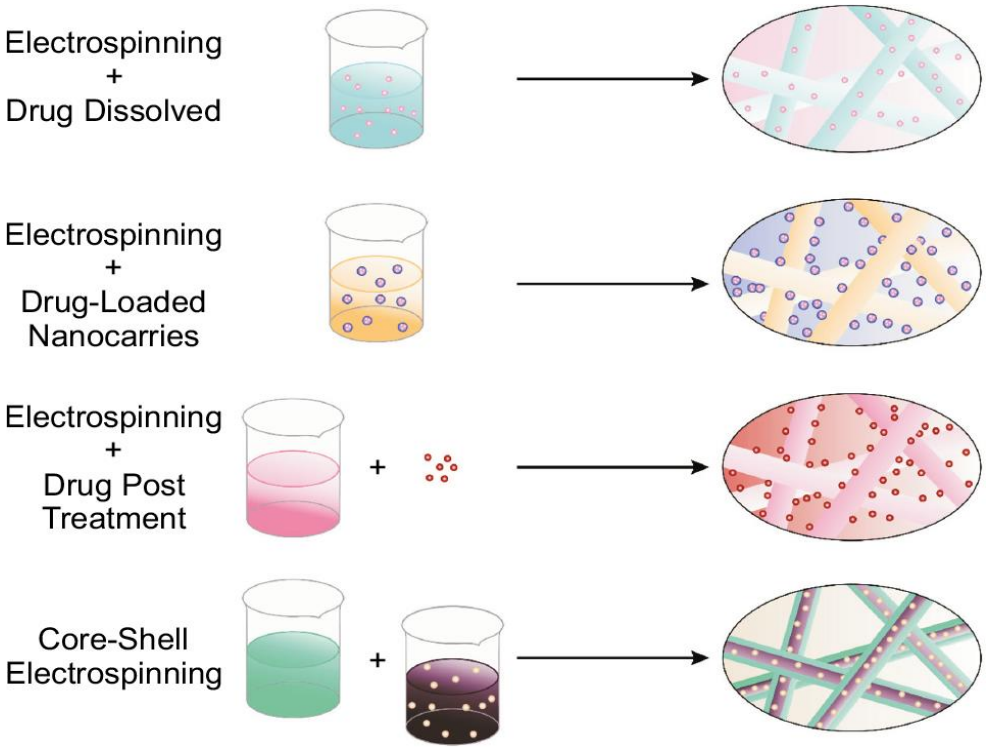


Figure 1.6 Schematic representation of drug-loaded polymeric nanofibres with different encapsulation procedures and release mechanisms (Torres-Martinez *et al.*[42]).

1.2 Project hypothesis – use of glycosylphosphatidylinositol anchors mimics to achieve prolonged formulation residence times

The inspiration for this PhD work stems from a cell adhesion mechanism present in nature. In eukaryotic cells, a number of proteins are bound to membranes via glycosylphosphatidylinositol (GPI) anchors[43,44]. These structures (**Figure 1.7**) contain a phosphatidylinositol moiety (linked through the phosphate group to two or three long lipid chains), bound to a glucose/mannose oligosaccharide linker, which in turn is connected to the surface protein[45]. The types of known protein anchored to cell through GPI anchors are very diverse in nature and function, ranging from enzymes (alkaline phosphatase, acetylcholinesterase[46]) to mediators of cell-cell interaction (neural cell adhesion molecule[47]), and antigens (CD52[48],

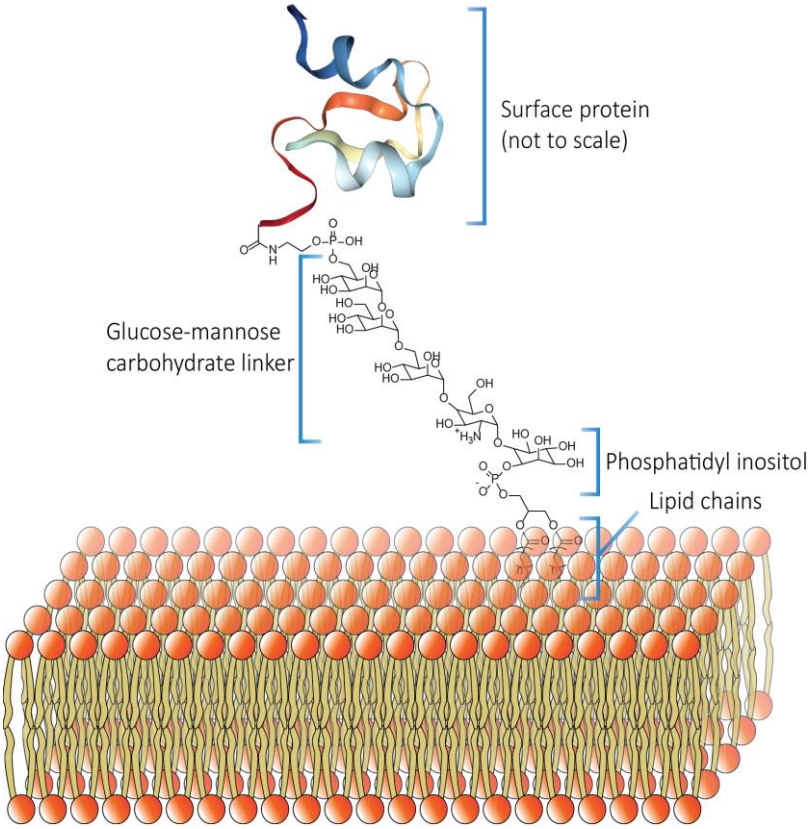


Figure 1.7 Schematic representation of a GPI-anchored protein (not to scale), highlighting the defining structural elements for a GPI anchor.

Thy-1[49]). The glycan linker of the anchor is highly conserved throughout the different GPI anchor classes, and except for the core glucosamine has a high degree of complex variations in carbohydrate composition[45]. However, when designing synthetic analogues of GPIs, the glycan may not be critical for membrane-binding[50], as it appears to merely provide a means to covalently link the membrane-inserting lipid chains of GPIs to the protein, as well as to control the protein mobility on the membrane bilayer[51]. The anchoring moieties (lipid chains) can be highly varied in length, unsaturation and number of lipids (2 to 3)[45].

The GPI anchor is added post-translationally to the proteins in the endoplasmic reticulum and the resulting GPI-anchored protein is transferred via vesicles to the plasmatic membrane[52]. These anchors are often located in more ordered domains of the cell plasma membrane[53], and studies postulated that these are a fundamental component of lipid rafts[54] (**Figure 1.8**). Recent studies have also shown that these glycosylphosphatidylinositol structures possess properties beyond simple anchoring of proteins to cell surface, and may be involved in cell signalling[55] and even development of prionic diseases[56].

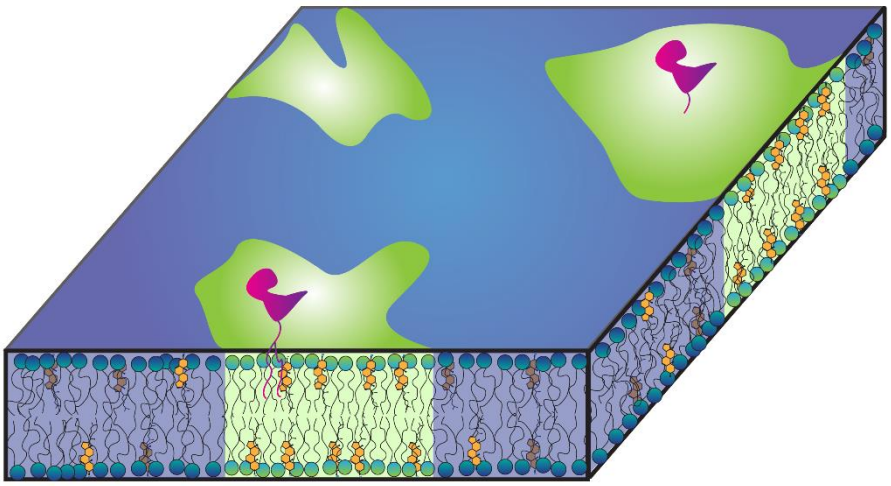


Figure 1.8 Schematic representation of cell membrane organisation highlighting lipid ordered domains (rafts, in green), with GPI-anchored proteins (in purple)

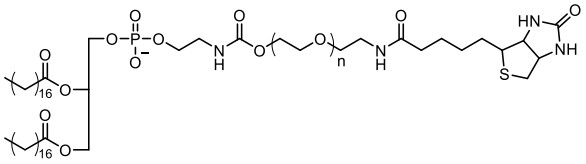
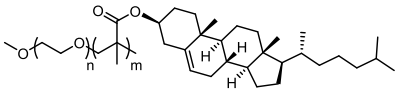
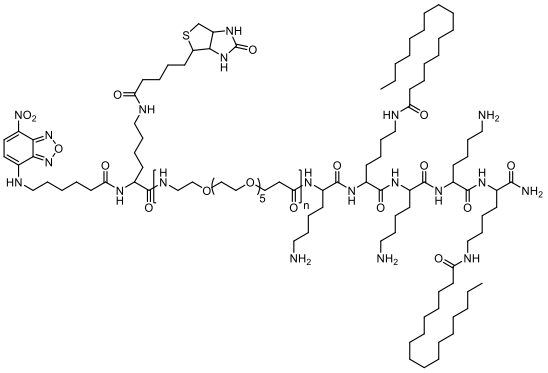
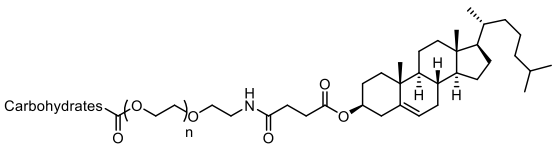
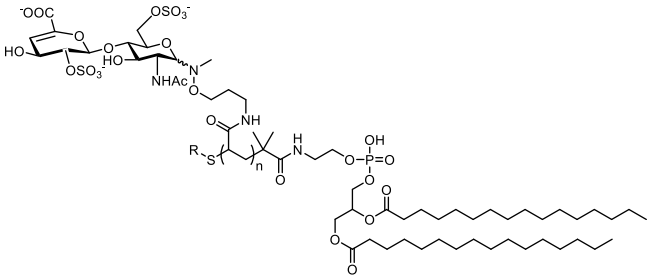
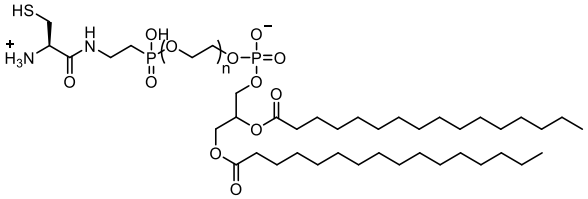
GPI anchors insert only partially in cell lipid bilayers of cells, as the lipid chains do not extend through the full membrane length and thus only interact with it relatively weakly, the anchored proteins associate with cell membranes in a reversible manner, and over time they can move from cell to cell[45]. This type of functionality has not been explored yet for drug delivery purposes and may represent a new approach in tackling the issue of producing an oral controlled drug release platform. Studies have demonstrated that externally-introduced GPI-anchored proteins readily interact with cells.[55,57] Therefore, an exogenous polymer equipped with GPI anchor mimicking moieties may be able to interact directly with the cell membrane and reside on it for extended periods of time.

1.3 Polymers

This study aimed at producing formulations which, by mimicking the GPI membrane-anchoring mechanism, could prolong their residence time in the GI tract by adhering to intestinal epithelial cells. This will allow controlled drug release over an extended period of time. To achieve these goals, the choice of materials naturally fell on polymers. These materials are extensively used for drug delivery purposes, as their functionalities and physico-chemical properties can be tailored to grant the specifics required by each application. The extreme adaptability and tuneability of polymers is particularly suited for drug delivery application[58]: pH sensitive[59], redox-responsive[60], controlled targeted delivery[61] and thermoresponsive[62] polymers are few amongst the countless other examples.

In previous literature, polymers equipped with membrane-interacting moieties have been investigated for a broad range of applications, from membrane functionalisation[63] to drug delivery purposes[64] (**Table 1.1**). Membrane-interacting polymers are usually designed with one or more lipophilic membrane anchors such as distearoyl phosphatidylethanolamine (DSPE) or cholesterol. These moieties can be placed at the polymer chain end[65–67] or as part of the polymer repeating units[68]. Usually, these lipophilic groups are natural components of the cell membrane, such as cholesterol or phospholipids, and ideally enable rapid polymer interaction with target cell membranes. Dipalmitoyl phosphatidylethanolamine (DPPE) anchors have been used for the design of membrane-anchoring glycomaterials to understand the glycocalyx role in neural differentiation of cells[69].

Table 1.1 Examples of membrane-interacting polymers in recent literature, employed for a variety of purposes

Polymer	Membrane-binding moiety	Purpose	Ref
	DSPE	Protein delivery	65
	Cholesterol	Drug delivery	64
	Palmitoyl Lysine	Cell surface modification	70
	Cholesterol	Imaging	66
	DPPE	Glycocalyx remodelling	69
	DPPE	GPI investigation	50

Finally, work in the Bertozzi's group extensively focussed on understanding the function of the GPI anchor[45], and for this purpose have produced GPI-mimicking polymers[51]. Their efforts unveiled that the glycan core was not important for membrane interaction, and that the synthesised GPI-mimicking polymers were involved in cell lipid recycling[50].

The membrane-interacting moieties are lipophilic by nature, therefore the polymer backbone needs to be relatively hydrophilic to avoid poor solubility in physiological media and to decrease macrophage uptake[71]. As highlighted in the examples in **Table 1.1**, this is usually achieved by introducing a hydrophilic polymer such as polyethylene glycol (PEG, which is widely employed for its stealth properties[72].

For this study, we designed the polymers based on the concepts proposed by Ringsdorf[73] (**Figure 1.9**), with the following characteristics: i)GPI-mimicking membrane-inserting moieties, to enable intestinal epithelial cell membrane binding, ii) ionisable groups (ionomers), to bind the drug molecules in a reversible manner through ionic interactions, and iii) hydrophilic repeating units, which improve the colloidal stability of the formulations in aqueous environments. The principles guiding the selection of monomers for this PhD work are in **Chapter 2.**

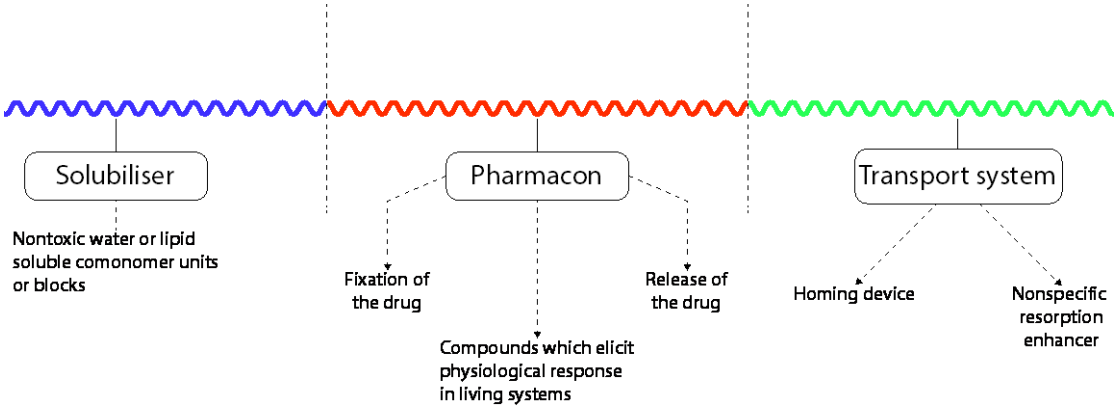
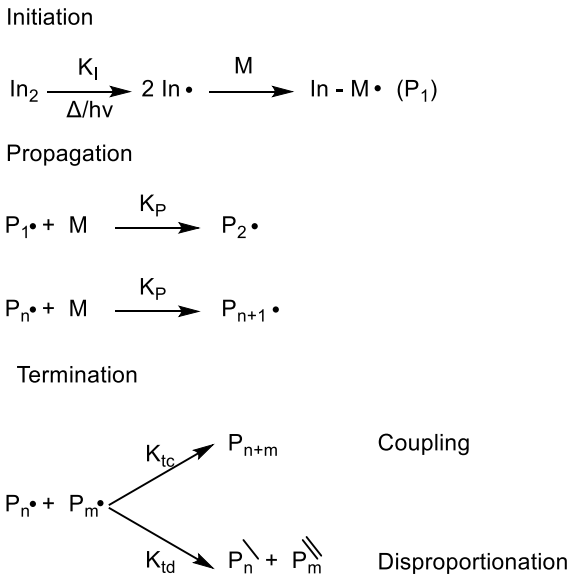


Figure 1.9 Ringsdorf design model for pharmacologically active polymers, adapted from Ringsdorf, 1975[73].

1.3.2 Free radical polymerisation

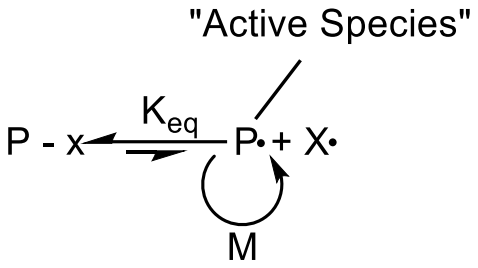
The materials synthesised in this work were prepared by controlled radical polymerisation (CRP). To better understand this class of polymerisation techniques, the mechanism of free radical polymerisation (**Scheme 1.1**) must be briefly discussed first. Free radical polymerisation utilises a source (homolitical initiator, light) that produces a radical (*initiation*), which in turn reacts with a C=C double bond in a vinyl monomer. This results in the formation of a new radical species, which in turn continues to react with other monomers in the same fashion in a process known as *chain growth,* or *propagation*[74]. The polymerisation ends when the growing chain reacts with another growing chain, resulting in either *coupling* when a new sigma bond is generated between these two chains to generate a new macromolecule with molecular weight equal to the sum of the reacting chains, or *disproportionation* when one of the two chains extract a hydrogen radical H· from the other, resulting in the oxidation of one chain ends and in the reduction of the other. This irreversible termination reactions lead to broadening of molecular weight distributions resulting in dispersity values Đ typically > 1.6.



Scheme 1.1 Conventional free radical polymerisation reaction steps, from initiation to propagation to termination.

1.3.3 Controlled radical polymerisation (CRP)

CRPs, also known as "living" radical polymerisations, and reversible-deactivation radical polymerisation, allow for good control of polymer molar mass and low dispersity Đ by minimsing irreversible termination processes. This is achieved by establishing an equilibrium between the "active" and the "dormant" species in the growing polymer (**Scheme 1.2**).



Scheme 1.3 Equilibrium between dormant (P-X) and active (P·) species in CRP reactions.

The equilibrium established proceeds in cycles, increasing the length of the growing polymer each time, resulting in a slow and controlled chain growth. The active species reacts with monomers, but the equilibrium is shifted towards dormant P-X species. Therefore, as illustrated in **Equation 1.1**, the ratio between rate of propagation (r_p) and rate of termination (r_t) depends on the concentration of monomer [M] and concentration of the active polymer [P·].

$$\frac{r_p}{r_t} = \frac{k_p[P\cdot][M]}{k_t[P\cdot]^2} \cong k\frac{[M]}{[P\cdot]}$$

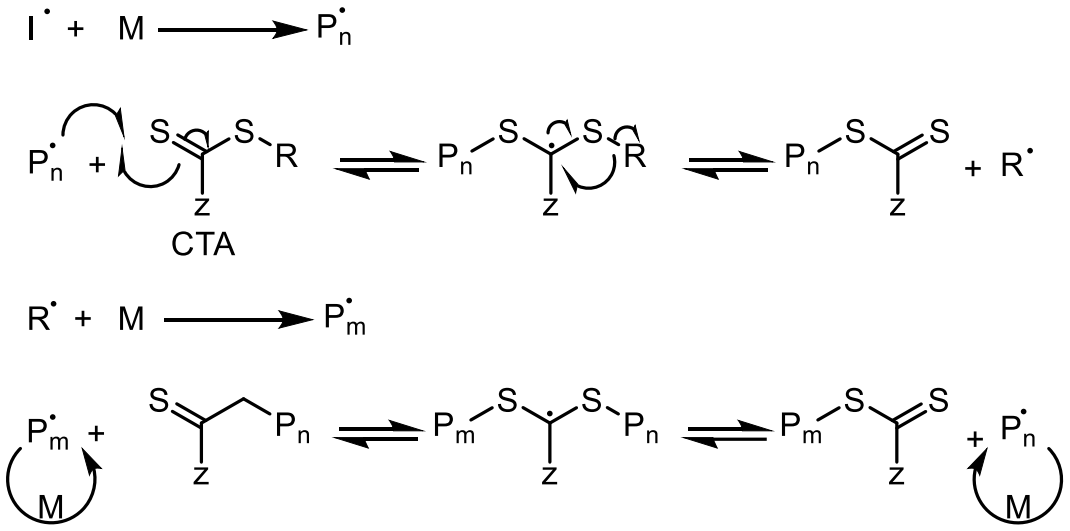
Equation 1.1 Dependence of the ratio between r_p and r_t on the monomer/active polymer concentrations.

If the concentration of active radical species [P·] is low, the rate of termination is kept low; when the monomer starts to deplete, termination increases. Therefore, the equilibrium between active and dormant species helps preventing termination, which will start increasing the closer to 100% is the conversion rate. Additionally, when the reaction is complete and P_n-X is formed, the active P_n· species can be generated again by restarting the reaction with addition of more radical source for

RAFT polymerisation, or additional monomer for NMP, ATRP and SET. This ability to resume the reaction from polymers made by CRP and elongate them allows for easy synthesis of block co-polymers[75].

1.3.4 RAFT polymerisation

In this study, the synthesis of bespoke polymers was carried out by reverse addition-fragmentation chain transfer (RAFT) polymerisation[76], a type of CRP[77]. The main difference that RAFT has over other reversible deactivation radical polymerisation (RDRP) processes is that this equilibrium involves a reversible fragmentation of a chain transfer agent (CTA), which acts here as the dormant species (**Scheme 1.3**). The CTA is a compound presenting a dithiocarbonyl moiety, which mediates the polymerisation process and is conserved through the process, allowing for design of polymers with discrete groups at the alpha and omega chain ends of the polymers.



Scheme 1.5 RAFT polymerisation initiation and equilibrium, showing the initiator I after activation transferring the radical to a monomer M, that propagates the reaction to form an initial P_n, which then reacts with the chain transfer agent (CTA) to start the equilibrium between active and dormant species.

In RAFT polymerisation, the propagation process is dominant over irreversible termination, so it is possible to achieve very narrow distributions in molar mass of the polymers. Additionally, RAFT is a controlled radical polymerisation and therefore it creates chains that can be elongated by adding further monomer.

Recent development of this technique reported by the Perrier group[78] now allows, for highly reactive hydrophilic monomers, to reach conversions very close to 100% whilst maintaining high chain-end fidelity. This in turn allows for the synthesis of block copolymers by sequentially adding monomers once full conversion of the previous monomer has been achieved, avoiding lengthy purification – e.g. by precipitation and/or dialysis – of block copolymer intermediates. Unlike other RDRP processes, RAFT polymerisation uses radical initiators as a source of radicals. This allows fine control over the number of living chains generated by the initiation mechanism, and the number of "dead" chains can be limited by controlling the CTA/initiator ratio[79].

1.4 Encapsulation of drugs in polymeric formulations

In order to encapsulate the drug and achieve a controlled release from the formulation, in this PhD work two different approaches were investigated: ionomeric coupling and covalent binding.

1.4.1 Ionomeric encapsulation

This type of encapsulation employs the formation of an acid-base pair between the drug and the polymer. This approach avoids the strategy of covalently binding the drug to the polymer chain[80], which might alter the profile of the drug[81] and requires additional testing to prove the efficacy and safety of the released drug. Ionomeric encapsulation can potentially be applied to a wide variety of drugs, as long as these possess suitable ionisable groups. Within our group it has been previously shown[82] that by using 2-(methacryloyloxy)ethyl-3-chloro-4-hydroxybenzoate monomers this approach can achieve sustained release of a drug from a formulation.

Due to its uniquely suitable characteristics, nitrofurantoin was chosen for the initial encapsulation tests with the polymers. This drug is an antibiotic which, despite having been in use for the treatment of urinary infections since 1953[83] has had "virtually no development of resistance"[84]. Additionally, it was chosen as model due to its currently quite unfavourable dosing regimen (4 administrations per day[5]) and the presence of a mildly basic nitrogen (pKa 7.2[85]). **Figure 1.10** illustrates the interaction between nitrofurantoin and a polymer acid side chain.

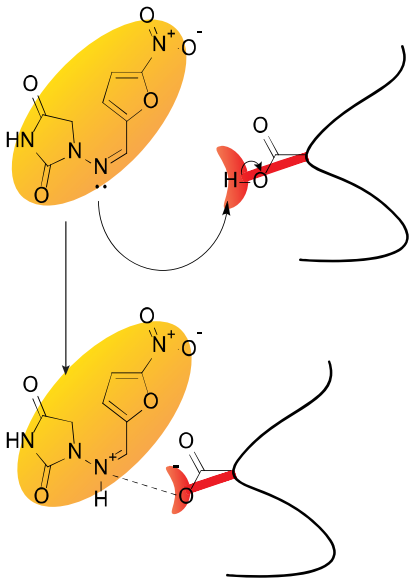


Figure 1.10 Schematic of the acid-base interaction between nitrofurantoin (in yellow) and the acidic side chain (red) of a polymer.

Additional drugs that were initially considered for the system for a future implementation were flucloxacillin and acyclovir (Structures in **Figure 1.11**). Both drugs have characteristics similar to nitrofurantoin (demanding dosing regimen and ionisation capacity). Acyclovir has a basic functionality and needs to be administered 3–5 times per day[5]. Flucloxacillin possesses an acid moiety, which would be able to form ionic bonds with basic side chains present in a potentially developed polymer, and its dosing regimen is 4 times per day[5].

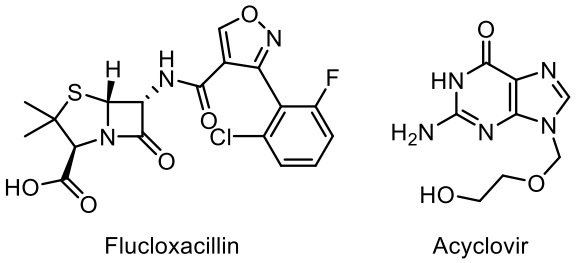


Figure 1.11 Structures of Flucloxacillin (left) and acyclovir (right), two potential candidates for ionotropic encapsulation

1.4.2 Covalent encapsulation

During the later stages of this study, we decided to also investigate covalent encapsulation of drugs within the polymers. This approach can potentially modify the activity of the encapsulated drug due to the introduction of a novel covalent polymer-drug bond. However, as stated previously, this approach might cause an alteration in the toxicological and activity profiles of the drug[81] and requires additional testing to prove the efficacy and safety of the released drug.

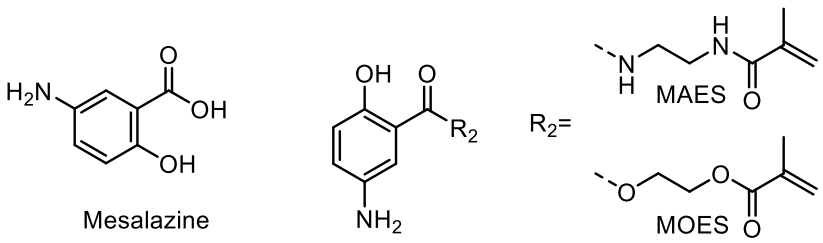


Figure 1.12 Structure of Mesalazine (left) and the Mesalazine-based monomers previously employed in literature, methacryloyloxyethyl 5-amino salicylate (MOES) and N-methacryloylaminoethyl 5-amino salicylamide (MAES)

The drug chosen for covalent encapsulation is mesalazine (**Figure 1.12**), an immunomodulator salicylate[5] that has been previously employed to produce mesalazine-based monomers (MAES and MOES, **Figure 1.12**) and successfully polymerised[86,87].

1.5 Supramolecular aggregation and mucus

Due to the amphiphilic properties of these membrane-inserting polymers, in water it is expected that above their critical aggregation concentration (CAC) they will tend to self-assemble into supramolecular aggregates.

To interact with the membrane of intestinal epithelial cells, these supramolecular assemblies must cross the mucus. This physiological barrier has a three-dimensional structure with pores roughly 100 nm diameter in size, hence mucus-penetrating supramolecular aggregates need to be produced with smaller size. However, particle net charge is also important for effective diffusion through mucus pores. The presence of sialic acid and sulfonic acid moieties confers the mucus a net negative charge[88]. Therefore, mucus-penetrating aggregates with a positive charge tend to be immobilised in the mucus layer, while negatively charged aggregates are more capable of crossing this layer and interacting with the underlying epithelium[89].

1.6 Project aims and objectives

This PhD project has two main aims:

1) Utilise membrane-binding polymers as a novel approach to extended oral drug delivery and
2) provide a better understanding on the effect that insertion of polymers has on the physico-chemical properties of lipid bilayers in both artificial and cell plasma membranes.

To this aim, in this work novel membrane-inserting polymers have been designed to possess different membrane-interacting moieties (cholesterol, phospholipid and long chain hydrocarbons), as well as a control polymer devoid of membrane-interacting fragments. The polymers were also designed to possess a hydrophilic

backbone with different functionalities (acid, hydrophilic) and different chain lengths.

These polymers were employed in the characterisation of their interaction with cell membranes (Caco-2 cells) and synthetic bilayer membrane models. To the best of our knowledge studies focussing on the systematic characterisation of how the structure of membrane-inserting polymers affect their interaction with cells and cell membrane models are scarce, hence this PhD work addresses a current lack of information in this field.

Finally, these membrane-inserting polymers were tested for their potential in drug delivery. These initial studies were carried out by ionomerically binding a nitrofurantoin to membrane-interacting polymers possessing multiple acid functionalities, and with the synthesis of membrane-interacting drug-polymer conjugates.

Accordingly, these aims were achieved through the delivery of the following objectives:

I. Design and synthesis of (co)polymers with different degrees of polymerisation, monomer composition and membrane-inserting anchor (or lack thereof)
II. Testing these materials with Caco-2 cells to assess their effect on cell membrane fluidity, cell toxicity and polymer uptake
III. Characterisation of the polymer-synthetic bilayer membrane interaction and proposal of a mechanistic model for the polymer-membrane interaction
IV. Proof-of-concept synthesis of polymer-drug conjugates and confirmation of membrane interaction capabilities for these novel polymers.

1.7 Bibliography

(1) Burkholder, R.; Linn, E. So Simple, so Hard: Taking Medication as Directed. *Res. Soc. Adm. Pharm.* **2017**, *13* (1), 233–249. https://doi.org/10.1016/j.sapharm.2016.02.002.

(2) Cutler, R. L.; Fernandez-Llimos, F.; Frommer, M.; Benrimoj, C.; Garcia-Cardenas, V. Economic Impact of Medication Non-Adherence by Disease Groups: A Systematic Review. *BMJ Open* **2018**, *8* (1), e016982. https://doi.org/10.1136/bmjopen-2017-016982.

(3) Kardas, P. Comparison of Patient Compliance with Once-Daily and Twice-Daily Antibiotic Regimens in Respiratory Tract Infections: Results of a Randomized Trial. *J. Antimicrob. Chemother.* **2007**, *59* (3), 531–536. https://doi.org/10.1093/jac/dkl528.

(4) Nachega, J. B.; Mills, E. J.; Schechter, M. Antiretroviral Therapy Adherence and Retention in Care in Middle-Income and Low-Income Countries: Current Status of Knowledge and Research Priorities. *Curr. Opin. HIV AIDS* **2010**, *5* (1), 70–77. https://doi.org/10.1097/COH.0b013e328333ad61.

(5) Brunton, L.; Chabner, B.; Knollman, B. *Goodman & Gilman's The Pharmacological Basis of Therapeutics*; 2013; Vol. 53. https://doi.org/10.1017/CBO9781107415324.004.

(6) Hovelson, D. H.; Xue, Z.; Zawistowski, M.; Ehm, M. G.; Harris, E. C.; Stocker, S. L.; Gross, A. S.; Jang, I. J.; Ieiri, I.; Lee, J. E.; Cardon, L. R.; Chissoe, S. L.; Abecasis, G.; Nelson, M. R. Characterization of ADME Gene Variation in 21 Populations by Exome Sequencing. *Pharmacogenet. Genomics* **2017**, *27* (3), 89–100. https://doi.org/10.1097/FPC.0000000000000260.

(7) Siccardi, M.; D'Avolio, A.; Rodriguez-Novoa, S.; Cuenca, L.; Simiele, M.; Baietto, L.; Calcagno, A.; Moss, D.; Bonora, S.; Soriano, V.; Back, D. J.; Owen, A.; Perri, G. Di. Intrapatient and Interpatient Pharmacokinetic Variability of Raltegravir in the Clinical Setting. *Ther. Drug Monit.* **2012**, *34* (2), 232–235. https://doi.org/10.1097/FTD.0b013e31824aa50a.

(8) Siccardi, M.; Olagunju, A.; Simiele, M.; D'Avolio, A.; Calcagno, A.; Di Perri, G.; Bonora, S.; Owen, A. Class-Specific Relative Genetic Contribution for Key Antiretroviral Drugs. *J. Antimicrob. Chemother.* **2015**, *70* (11), 3074–3079. https://doi.org/10.1093/jac/dkv207.

(9) Ummadi, S.; B, S.; N. G, R. R.; M, S. R.; B, S.; Nayak. Overview on Controlled Release Dosage Form. *Int. J. Pharma Sci.* **2013**, *3* (4), 13.

(10) Andrade, C. Sustained-Release, Extended-Release, and Other Time-Release Formulations in Neuropsychiatry. *J. Clin. Psychiatry* **2015**, *76* (8), e995–e999. https://doi.org/10.4088/JCP.15f10219.

(11) Brandt, C.; May, T. W. Extended-Release Drug Formulations for the Treatment of Epilepsy. *Expert Opin. Pharmacother.* **2018**, *19* (8), 843–850. https://doi.org/10.1080/14656566.2018.1465561.

(12) Udipi, K.; Chen, M.; Cheng, P.; Jiang, K.; Judd, D.; Caceres, A.; Melder, R. J.; Wilcox, J. N. Development of a Novel Biocompatible Polymer System for Extended Drug Release in a Next-Generation Drug-Eluting Stent. *J. Biomed. Mater. Res. - Part A* **2008**, *85* (4), 1064–1071. https://doi.org/10.1002/jbm.a.31664.

(13) Awasthi, R.; Kulkarni, G. T. Decades of Research in Drug Targeting to the Upper Gastrointestinal Tract Using Gastroretention Technologies: Where Do We Stand? *Drug Deliv.* **2016**, *23* (2), 378–394. https://doi.org/10.3109/10717544.2014.936535.

(14) Kumar, K.; Dhawan, N.; Sharma, H.; Vaidya, S.; Vaidya, B. Bioadhesive Polymers: Novel Tool for Drug Delivery. *Artif. Cells, Nanomedicine Biotechnol.* **2014**, *42* (4), 274–283. https://doi.org/10.3109/21691401.2013.815194.

(15) Lele, B. S.; Hoffman, A. S. Mucoadhesive Drug Carriers Based on Complexes of Poly(Acrylic Acid) and PEGylated Drugs Having Hydrolysable PEG-Anhydride-Drug Linkages. *J. Control. Release* **2000**, *69* (2), 237–248. https://doi.org/10.1016/S0168-3659(00)00303-5.

(16) Alqahtani, M. S.; Kazi, M.; Alsenaidy, M. A.; Ahmad, M. Z. Advances in Oral Drug Delivery. *Front. Pharmacol.* **2021**, *12* (February). https://doi.org/10.3389/fphar.2021.618411.

(17) Wang, J.; Levi, J.; Ellis, L.; Hill, A. Minimum Manufacturing Costs, National Prices and Estimated Global Availability of New Repurposed Therapies for COVID-19. *medRxiv* **2021**, *3432* (3498), 2021.06.01.21258147.

(18) Sugihara, M.; Takeuchi, S.; Sugita, M.; Higaki, K.; Kataoka, M.; Yamashita, S. Analysis of Intra- and Intersubject Variability in Oral Drug Absorption in Human Bioequivalence Studies of 113 Generic Products. *Mol. Pharm.* **2015**, *12* (12), 4405–4413. https://doi.org/10.1021/acs.molpharmaceut.5b00602.

(19) Bellinger, A. M.; Jafari, M.; Grant, T. M.; Zhang, S.; Hannah, C.; Wenger, E. A.; Mo, S.; Lee, Y. L.; Mazdiyasni, H.; Kogan, L.; Barman, R.; Cleveland, C.; Booth, L.; Bensel, T.; Hurowitz, H. M.; Tai, T.; Daily, J.; Nikolic, B.; Wood, L. Oral, Ultra–Long-Lasting Drug Delivery: Application toward Malaria Elimination Goals. *Sci Transl Med.* **2017**, *8* (365). https://doi.org/10.1126/scitranslmed.aag2374.Oral.

(20) Abuhelwa, A. Y.; Foster, D. J. R.; Upton, R. N. A Quantitative Review and Meta-Models of the Variability and Factors Affecting Oral Drug Absorption—Part II: Gastrointestinal Transit Time. *AAPS J.* **2016**, *18* (5), 1322–1333. https://doi.org/10.1208/s12248-016-9953-7.

(21) Rouge, N.; Buri, P.; Doelker, E. Drug Absorption Sites in the Gastrointestinal Tract and Dosage Forms for Site-Specific Delivery. *Int. J. Pharm.* **1996**, *136* (1–2), 117–139. https://doi.org/10.1016/0378-5173(96)85200-8.

(22) Yuen, K. H. The Transit of Dosage Forms through the Small Intestine. *Int. J. Pharm.* **2010**, *395* (1–2), 9–16. https://doi.org/10.1016/j.ijpharm.2010.04.045.

(23) Kirtane, A. R.; Abouzid, O.; Minahan, D.; Bensel, T.; Hill, A. L.; Selinger, C.; Bershteyn, A.; Craig, M.; Mo, S. S.; Mazdiyasni, H.; Cleveland, C.; Rogner, J.; Lee, Y. A. L.; Booth, L.; Javid, F.; Wu, S. J.; Grant, T.; Bellinger, A. M.; Nikolic, B.; Hayward, A.; Wood, L.; Eckhoff, P. A.; Nowak, M. A.; Langer, R.; Traverso, G. Development of an Oral Once-Weekly Drug Delivery System for HIV Antiretroviral Therapy. *Nat. Commun.* **2018**, *9* (1). https://doi.org/10.1038/s41467-017-02294-6.

(24) Newell, D. R.; Searle, K. M.; Westwood, N. B.; Burtles, S. S. Professor Tom Connors and the Development of Novel Cancer Therapies by the Phase I/II Clinical Trials Committee of Cancer Research UK. *Br. J. Cancer* **2003**, *89* (3), 437–454. https://doi.org/10.1038/sj.bjc.6601106.

(25) Duncan, R. The Dawning Era of Polymer Therapeutics. *Nat. Rev. Drug Discov.* **2003**, *2* (5), 347–360. https://doi.org/10.1038/nrd1088.

(26) Singh, B. N.; Kim, K. H. Floating Drug Delivery Systems: An Approach to Oral Controlled Drug Delivery via Gastric Retention. *Journal of Controlled Release*. 2000. https://doi.org/10.1016/S0168-3659(99)00204-7.

(27) Bani-Jaber, A.; Al-Aani, L.; Alkhatib, H.; Al-Khalidi, B. Prolonged Intragastric Drug Delivery Mediated by Eudragit® E-Carrageenan Polyelectrolyte Matrix Tablets. *AAPS PharmSciTech* **2011**, *12* (1), 354–361. https://doi.org/10.1208/s12249-011-9595-0.

(28) Xiaoling, L.; Bhaskara, J. *Design of Controlled Release Drug Delivery Systems*; 2006.

(29) Ichikawa, M.; Watanabe, S.; Miyake, Y. A New Multiple-unit Oral Floating Dosage System. I: Preparation and in Vitro Evaluation of Floating and Sustained-release Characteristics. *J. Pharm. Sci.* **1991**, *80* (11), 1062–1066. https://doi.org/10.1002/jps.2600801113.

(30) Lee YA, Zhang S, Lin J, Langer R, T. G. A Janus Mucoadhesive and Omniphobic Device for Gastrointestinal Retention. *Adv Heal. Mater.* **2016**, *5* (10), 1141–1146. https://doi.org/10.1021/jacs.5b07154.Total.

(31) Mercier-Bonin, M.; Chapot-Chartier, M. P. Surface Proteins of Lactococcus Lactis: Bacterial Resources for Muco-Adhesion in the Gastrointestinal Tract. *Front. Microbiol.* **2017**, *8* (NOV), 1–7. https://doi.org/10.3389/fmicb.2017.02247.

(32) Pelaseyed, T.; Bergström, J. H.; Jenny K. Gustafsson, Anna Ermund, George M. H. Birchenough, André Schütte, Sjoerd van der Post, Frida Svensson, Ana M. Rodríguez- Piñeiro, Elisabeth E.L. Nyström, Catharina Wising, Malin E.V. Johansson, and G. C. H. The Mucus and Mucins of the Goblet Cells and Enterocytes Provide the First Defense Line of the Gastrointestinal Tract and Interact with the Immune System. *Immunol Rev.* **2014**, *260* (1), 8–20. https://doi.org/10.1111/imr.12182.The.

(33) Antovska, P.; Ugarkovic, S.; Petruševski, G.; Stefanova, B.; Manchevska, B.; Petkovska, R.; Makreski, P. Development and Experimental Design of a Novel Controlled-Release Matrix Tablet Formulation for Indapamide Hemihydrate. *Pharm. Dev. Technol.* **2017**, *22* (7), 851–859. https://doi.org/10.3109/10837450.2015.1089898.

(34) Borgquist, P.; Körner, A.; Piculell, L.; Larsson, A.; Axelsson, A. A Model for the Drug Release from a Polymer Matrix Tablet-Effects of Swelling and Dissolution. *J. Control. Release* **2006**, *113* (3), 216–225. https://doi.org/10.1016/j.jconrel.2006.05.004.

(35) Boyapally, H.; Nukala, R. K.; Douroumis, D. Development and Release Mechanism of Diltiazem HCl Prolonged Release Matrix Tablets. *Drug Deliv.* **2009**, *16* (2), 67–74. https://doi.org/10.1080/10717540802586220.

(36) Timmins, P.; Desai, D.; Chen, W.; Wray, P.; Brown, J.; Hanley, S. Advances in Mechanistic Understanding of Release Rate Control Mechanisms of Extended-Release Hydrophilic Matrix Tablets. *Ther. Deliv.* **2016**, *7* (8), 553–572. https://doi.org/10.4155/tde-2016-0026.

(37) Patel, A.; Mehta, T.; Patel, M.; Patel, K.; Patel, N. Recent Patent in Controlled Porosity Osmotic Pump. *Recent Pat. Drug Deliv. Formul.* **2013**, *7* (1), 66–72. https://doi.org/10.2174/187221113804805810.

(38) Williams, G. R.; Raimi-Abraham, B. T.; Luo, C. J. *Nanofibres in Drug Delivery*; 2018. https://doi.org/10.1017/CBO9781107415324.004.

(39) Akhgari, A.; Shakib, Z.; Sanati, S. A Review on Electrospun Nanofibers for Oral Drug Delivery. *Nanomedicine J.* **2017**, *4* (4), 197–207. https://doi.org/10.22038/NMJ.2017.04.001.

(40) Thakkar, S.; Misra, M. Electrospun Polymeric Nanofibers: New Horizons in Drug Delivery. *Eur. J. Pharm. Sci.* **2017**, *107* (June), 148–167. https://doi.org/10.1016/j.ejps.2017.07.001.

(41) Taipaleenmäki, E. M.; Mouritzen, S. A.; Schattling, P. S.; Zhang, Y.; Städler, B. Mucopenetrating Micelles with a PEG Corona. *Nanoscale* **2017**, *9* (46), 18438–18448. https://doi.org/10.1039/c7nr06821b.

(42) Torres-Martinez, E. J.; Cornejo Bravo, J. M.; Serrano Medina, A.; Pérez González, G. L.; Villarreal Gómez, L. J. A Summary of Electrospun Nanofibers as Drug Delivery System: Drugs Loaded and Biopolymers Used as Matrices. *Curr. Drug Deliv.* **2018**, *15* (10), 1360–1374. https://doi.org/10.2174/1567201815666180723114326.

(43) Saha, S.; Anilkumar, A. A.; Mayor, S. GPI-Anchored Protein Organization and Dynamics at the Cell Surface. *J. Lipid Res.* **2015**, *57* (2), 159–175. https://doi.org/10.1194/jlr.r062885.

(44) Low, M. G. The Glycosyl-Phosphatidylinositol Anchor of Membrane Proteins. *BBA - Rev. Biomembr.* **1989**, *988* (3), 427–454. https://doi.org/10.1016/0304-4157(89)90014-2.

(45) Paulick, M. G.; Bertozzi, C. R. The Glycosylphosphatidylinositol Anchor: A Complex Membrane-Anchoring Structure for Proteins. *Biochemistry* **2008**, *47* (27), 6991–7000. https://doi.org/10.1021/bi8006324.

(46) Hooper, N. M. Glycosyl-Phosphatidylinositol Anchored Membrane Enzymes. *Clin. Chim. Acta* **1997**, *266* (1), 3–12. https://doi.org/10.1016/S0009-8981(97)00161-7.

(47) Olive, S.; Dubois, C.; Schachner, M.; Rougon, G. The F3 Neuronal Glycosylphosphatidylinositol-Linked Molecule Is Localized to Glycolipid-Enriched Membrane Subdomains and Interacts with L1 and Fyn Kinase in Cerebellum. *J. Neurochem.* **1995**, *65* (5), 2307–2317. https://doi.org/10.1046/j.1471-4159.1995.65052307.x.

(48) Treumann, A.; Lifely, R.; Schneider, P.; Ferguson, M. Primary Structure of CD52. *J. Biol. Chem.* **1995**, *271* (11), 6088–6099.

(49) Nemoto, Y. L.; Morris, R. J.; Hijikata, H.; Tsunoyama, T. A.; Shibata, A. C. E.; Kasai, R. S.; Kusumi, A.; Fujiwara, T. K. Dynamic Meso-Scale Anchorage of GPI-Anchored Receptors in the Plasma Membrane: Prion Protein vs. Thy1. *Cell Biochem. Biophys.* **2017**, *75* (3–4), 399–412. https://doi.org/10.1007/s12013-017-0808-3.

(50) Paulick, M. G.; Forstner, M. B.; Groves, J. T.; Bertozzi, C. R. A Chemical Approach to Unraveling the Biological Function of the Glycosylphosphatidylinositol Anchor. *Proc. Natl. Acad. Sci.* **2007**, *104* (51), 20332–20337. https://doi.org/10.1073/pnas.0710139104.

(51) Paulick, M. G.; Wise, A. R.; Forstner, M. B.; Groves, J. T.; Bertozzi, C. R. Synthetic Analogues of Glycosylphosphatidylinositol-Anchored Proteins and Their Behavior in Supported Lipid Bilayers. *J. Am. Chem. Soc.* **2007**, *129* (37), 11543–11550. https://doi.org/10.1021/ja073271j.

(52) Eisenhaber, B.; Maurer-Stroh, S.; Novatchkova, M.; Schneider, G.; Eisenhaber, F. Enzymes and Auxiliary Factors for GPI Lipid Anchor Biosynthesis and Post-Translational Transfer to Proteins. *BioEssays* **2003**, *25* (4), 367–385. https://doi.org/10.1002/bies.10254.

(53) Baumgart, T.; Hammond, A. T.; Sengupta, P.; Hess, S. T.; Holowka, D. A.; Baird, B. A.; Webb, W. W. Large-Scale Fluid/Fluid Phase Separation of Proteins and Lipids in Giant Plasma Membrane Vesicles. *Proc. Natl. Acad. Sci. U. S. A.* **2007**, *104* (9), 3165–3170. https://doi.org/10.1073/pnas.0611357104.

(54) Levental, I.; Levental, K. R.; Heberle, F. A. Lipid Rafts: Controversies Resolved, Mysteries Remain. *Trends Cell Biol.* **2020**, 1–13. https://doi.org/10.1016/j.tcb.2020.01.009.

(55) Premkumar, D. R. D.; Fukuoka, Y.; Sevlever, D.; Brunschwig, E.; Rosenberry, T. L.; Tykocinski, M. L.; Edward Medof, M. Properties of Exogenously Added GPI-Anchored Proteins Following Their Incorporation into Cells. *J. Cell. Biochem.* **2001**, *82* (2), 234–245. https://doi.org/10.1002/jcb.1154.

(56) Bate, C.; Nolan, W.; Williams, A. Glycosylphosphatidylinositols: More than Just an Anchor? *Commun. Integr. Biol.* **2016**, *9* (2), 1–3. https://doi.org/10.1080/19420889.2016.1149671.

(57) Van den Berg, C. W.; Cinek, T.; Hallett, M. B.; Horejsi, V.; Morgan, B. P. Exogenous Glycosyl Phosphatidylinositol-Anchored CD59 Associates with Kinases in Membrane Clusters on U937 Cells and Becomes Ca2+-Signaling Competent. *J. Cell Biol.* **1995**, *131* (3), 669–677. https://doi.org/10.1083/jcb.131.3.669.

(58) Pillai, O.; Panchagnula, R. Polymers in Drug Delivery. *Curr. Opin. Chem. Biol.* **2001**, *5*, 447–451.

(59) Yoshida, T.; Lai, T. C.; Kwon, G. S.; Sako, K.; Takayuki Yoshida, PhD†, 1, Tsz Chung Lai2, Glen S Kwon2, and K. S. PH- and Ion-Sensitive Polymers for Drug Delivery. *Expert Opin Drug Deliv* **2013**, *10* (11), 1497–1513. https://doi.org/10.1007/s10439-011-0452-9.Engineering.

(60) Huo, M.; Yuan, J.; Tao, L.; Wei, Y. Redox-Responsive Polymers for Drug Delivery: From Molecular Design to Applications. *Polym. Chem.* **2014**, *5* (5), 1519–1528. https://doi.org/10.1039/c3py01192e.

(61) Ulbrich, K.; Holá, K.; Šubr, V.; Bakandritsos, A.; Tuček, J.; Zbořil, R. Targeted Drug Delivery with Polymers and Magnetic Nanoparticles: Covalent and Noncovalent Approaches, Release Control, and Clinical Studies. *Chem. Rev.* **2016**, *116* (9), 5338–5431. https://doi.org/10.1021/acs.chemrev.5b00589.

(62) Gandhi, A.; Paul, A.; Sen, S. O.; Sen, K. K. Studies on Thermoresponsive Polymers: Phase Behaviour, Drug Delivery and Biomedical Applications. *Asian J. Pharm. Sci.* **2015**, *10* (2), 99–107. https://doi.org/10.1016/j.ajps.2014.08.010.

(63) Li, C.; Takeo, M.; Matsuda, M.; Nagai, H.; Xizheng, S.; Hatanaka, W.; Kishimura, A.; Inoue, H.; Tani, K.; Mori, T.; Katayama, Y. Facilitating the Presentation of Antigen Peptides on Dendritic Cells for Cancer Immunotherapy Using a Polymer-Based Synthetic Receptor. *Medchemcomm* **2017**, *8* (6), 1207–1212. https://doi.org/10.1039/c7md00188f.

(64) Essi Taipaleenmäki, A.; Gustav Christensen, a# Edit Brodszkij, A.; Sidsel A. Mouritzen, A.; Noga Gal, A.; Sidsel; Madsen, B.; Mette Skou Hedemann, b Tine Ahrendt Knudsen, C.; Henrik Max Jensen, C.; Laage, S.; Christiansen, c Flemming Vang Sparsø, c and B. S. Mucopenetrating Polymer – Lipid Hybrid Nanovesicles as Subunits in Alginate Beads as an Oral Formulation. *J. Control. Release* **2020**. https://doi.org/10.1016/j.aquaculture.2020.734967.

(65) Tobinaga, K.; Li, C.; Takeo, M.; Matsuda, M.; Nagai, H.; Niidome, T.; Yamamoto, T.; Kishimura, A.; Mori, T.; Katayama, Y. Rapid and Serum-Insensitive Endocytotic Delivery of Proteins Using Biotinylated Polymers Attached via Multivalent Hydrophobic Anchors. *J. Control. Release* **2014**, *177* (1), 27–33. https://doi.org/10.1016/j.jconrel.2013.12.024.

(66) Wang, H. Y.; Jia, H. R.; Lu, X.; Chen, B.; Zhou, G.; He, N.; Chen, Z.; Wu, F. G. Imaging Plasma Membranes without Cellular Internalization: Multisite Membrane Anchoring Reagents Based on Glycol Chitosan Derivatives. *J. Mater. Chem. B* **2015**, *3* (30), 6165–6173. https://doi.org/10.1039/c5tb00930h.

(67) Woods, E.; Yee, N.; Shen, J.; Bertozzi, C. R. Glycocalyx Engineering with a Recycling Glycopolymer That Increases Cell Survival in Vivo. *Angew Chem Int Ed Engl.* **2015**, *54* (52), 15782–15788. https://doi.org/10.1586/14737175.2015.1028369.Focused.

(68) Li, D.; Wu, L.; Qu, F.; Ribadeneyra, M. C.; Tu, G.; Gautrot, J. Core-Independent Approach for Polymer Brush-Functionalised Nanomaterials with a Fluorescent Tag for RNA Delivery. *Chem. Commun.* **2019**, *55* (94), 14166–14169. https://doi.org/10.1039/c9cc05790k.

(69) Huang, M. L.; Godula, K. Priming the Cellular Glycocalyx for Neural Development. *ACS Chem. Neurosci.* **2014**, *5* (10), 873–875. https://doi.org/10.1021/cn500194b.

(70) Matsuda, M.; Hatanaka, W.; Takeo, M.; Kim, C. W.; Niidome, T.; Yamamoto, T.; Kishimura, A.; Mori, T.; Katayama, Y. Short Peptide Motifs for Long-Lasting Anchoring to the Cell Surface. *Bioconjug. Chem.* **2014**, *25* (12), 2134–2143. https://doi.org/10.1021/bc500465j.

(71) Kenry; Yeo, T.; Manghnani, P. N.; Middha, E.; Pan, Y.; Chen, H.; Lim, C. T.; Liu, B. Mechanistic Understanding of the Biological Responses to Polymeric Nanoparticles. *ACS Nano* **2020**, *14* (4), 4509–4522. https://doi.org/10.1021/acsnano.9b10195.

(72) Butcher, N. J.; Mortimer, G. M.; Minchin, R. F. Drug Delivery: Unravelling the Stealth Effect. *Nat. Nanotechnol.* **2016**, *11* (4), 310–311. https://doi.org/10.1038/nnano.2016.6.

(73) Ringsdorf, H. Structure and Properties of Pharmacologically Active Polymers. *J Polym Sci Polym Symp* **1975**, *153* (51), 135–153. https://doi.org/10.1002/polc.5070510111.

(74) Koltzenburg, S.; Maskos, M.; Nuyken, O. *Polymer Chemistry*; Springer, 2015. https://doi.org/10.007/9783662492796.

(75) Barner-Kowollik, C. *Handbook of RAFT Polymerization*; Wiley-vch, 2008.

(76) Matyjaszewski, K.; Janzen, E.; He, Y. Z.; Cui, J. P.; Mallard, W. G.; Tsang, W.; Chiefari, J.; Chong, Y. K. B.; Ercole, F.; Krstina, J.; Jeffery, J.; Le, T. P. T.; Mayadunne, R. T. A.; Meijs, G. F.; Moad, C. L.; Moad, G.; Rizzardo, E.; Thang, S. H.; South, C. Living Free-Radical Polymerization by Reversible

Addition - Fragmentation Chain Transfer : The RAFT Process. *Macromolecules* **1998**. https://doi.org/10.1017/CBO9781107415324.004.

(77) Moad, G. RAFT Polymerization – Then and Now. **2015**, 211–246. https://doi.org/10.1021/bk-2015-1187.ch012.

(78) Gody, G.; Barbey, R.; Danial, M.; Perrier, S. Ultrafast RAFT Polymerization: Multiblock Copolymers within Minutes. *Polym. Chem.* **2015**, *6* (9), 1502–1511. https://doi.org/10.1039/c4py01251h.

(79) Perrier, S. 50th Anniversary Perspective: RAFT Polymerization - A User Guide. *Macromolecules* **2017**, *50* (19), 7433–7447. https://doi.org/10.1021/acs.macromol.7b00767.

(80) Elvira, C.; Gallardo, A.; San Roman, J.; Cifuentes, A. Covalent Polymer-Drug Conjugates. *Molecules* **2005**, *10* (1), 114–125. https://doi.org/10.3390/10010114.

(81) Torchilin, V. P. Structure and Design of Polymeric Surfactant-Based Drug Delivery Systems. *J. Control. Release* **2001**, *73* (2–3), 137–172. https://doi.org/10.1016/S0168-3659(01)00299-1.

(82) Mastrotto, F.; Salmaso, S.; Alexander, C.; Mantovani, G.; Caliceti, P. Novel PH-Responsive Nanovectors for Controlled Release of Ionisable Drugs. *J. Mater. Chem. B* **2013**, *1* (39), 5335. https://doi.org/10.1039/c3tb20360c.

(83) Blass, B. E. *Case Studies in Drug Discovery*; 2015. https://doi.org/10.1016/b978-0-12-411508-8.00013-x.

(84) Cunha, B. A.; Schoch, P. E.; Hage, J. R. Nitrofurantoin: Preferred Empiric Therapy for Community-Acquired Lower Urinary Tract Infections. *Mayo Clin. Proc.* **2011**, *86* (12), 1243–1244. https://doi.org/10.4065/mcp.2011.0411.

(85) Bates, T. R.; Young, J. M.; Wu, C. M.; Rosenberg, H. A. PH-dependent Dissolution Rate of Nitrofurantoin from Commercial Suspensions, Tablets, and Capsules. *J. Pharm. Sci.* **1974**, *63* (4), 643–645. https://doi.org/10.1002/jps.2600630441.

(86) Babazadeh, M.; Edjlali, L.; Rashidian, L. Application of 2-Hydroxyethyl Methacrylate Polymers in Controlled Release of 5-Aminosalicylic Acid as a Colon-Specific Drug. *J. Polym. Res.* **2007**, *14* (3), 207–213. https://doi.org/10.1007/s10965-007-9099-5.

(87) Davaran, S.; Hanaee, J.; Khosravi, A. Release of 5-Amino Salicylic Acid from Acrylic Type Polymeric Prodrugs Designed for Colon-Specific Drug Delivery. *J. Control. Release* **1999**, *58* (3), 279–287. https://doi.org/10.1016/S0168-3659(98)00167-9.

(88) Miller, C. R.; Bondurant, B.; McLean, S. D.; McGovern, K. A.; O'Brien, D. F. Liposome-Cell Interactions in Vitro: Effect of Liposome Surface Charge on the Binding and Endocytosis of Conventional and Sterically Stabilized Liposomes. *Biochemistry* **1998**, *37* (37), 12875–12883. https://doi.org/10.1021/bi980096y.

(89) Netsomboon, K.; Bernkop-Schnürch, A. Mucoadhesive vs. Mucopenetrating Particulate Drug Delivery. *Eur. J. Pharm. Biopharm.* **2016**, *98*, 76–89. https://doi.org/10.1016/j.ejpb.2015.11.003.

Chapter 2

Synthesis and characterisation of membrane-binding amphiphilic polymers

This chapter will describe the synthesis and characterisation of the functional materials that have been used throughout the study: amphiphilic cholesterol-based polymers, amphiphilic DOPE-based polymers, lipid monomer-based amphiphilic polymers and PABTC-based hydrophilic control polymers. These materials were chosen due to their potential for inserting in lipid bilayer membranes, with the PABTC-based polymers, devoid of membrane binding capabilities, used as a control materials. This chapter describes the synthesis and the characterisation of these (co)polymers, as well as their low molecular weight precursors, namely RAFT agents, monomers and a novel maleimide-based fluorescent dye used to fluorescently tag these materials.

2.1 Introduction

As discussed in the first chapter, membrane-binding and specifically GPI-mimicking polymers are materials that can be employed in a new approach to drug delivery, or to understand biological phenomena. Therefore, the first part of the project focused on the production and characterisation of these amphiphilic polymers, as well as "control" polymers, devoid of any membrane-interacting capability.

The polymers were synthesised by RAFT polymerisation[1,2], which allowed for the production of polymers with narrow dispersity and finely controlled chain length. Most importantly, this type of reversible-deactivation radical polymerisation (RDRP) allowed specific moieties to be placed at the alpha end of polymer chains, while leaving a thiocarbonylthio group at the other (omega) chain end, available for further chemical modification. Specifically, here amphiphilic polymers were produced with a cholesterol or with a 1,2-dioleyl-*sn*-glycero-3-phosphoethanolamine (DOPE) moiety at the alpha end. These specific groups were chosen as both are found in natural and synthetic membranes and offered potential for interaction with cell membranes. Additionally, we produced an additional family of polymers where the percentage of lipophilic content could be tuned by co-polymerising a lipid-based monomer.

This fine control over the polymer characteristics allowed us to synthesise polymers where both the nature and number repeating units per chain, as well as the type of moiety at the alpha chain end were systematically varied, explore the effect that these variations had on the polymer properties, such as supramolecular aggregation and interaction with cell membranes. Thus, in this part of our work we focused on: i) the nature of the membrane-inserting polymer chain end, ii) the chemical composition of the polymer chains, and iii) the degree of polymerisation of the polymer chains.

2.2 Materials and Methods

2.2.1 Materials

Reagents used for synthesis were purchased from Sigma-Aldrich (Dorset, UK), unless otherwise specified. Methanol, isopropanol, dichloromethane, diethyl ether, ethyl acetate, chloroform, tetrahydrofuran, petroleum ether, DMF were purchased from Fischer Scientific (Loughborough, UK). DOPE was purchased from Avanti Polar Lipids (Alabaster, Alabama). VA-044 was purchased from Wako Pure chemical Industries (Neuss, Germany). Propanoic acid-2-[(butylthio)thiomethyl]thio]-carbonate (PABTC)-*O*-succinimide was previously synthesised by Dr Joshua Petch, and the cholesterol-based RAFT agent **(1)** was previously synthesised within our group by Dr Rosa Catania.

2.2.2 Polymer purification

Typically, to purify the polymers from unreacted monomers and reagents, the viscous or semi-solid reaction mixture was solubilised in the minimum amount of CH_2Cl_2:MeOH 6:5 vol:vol, and precipitated (in acetone, or *tert*-butyl methyl ether for DOPE-based polymers) in a falcon tube. The suspension was centrifuged (4500 rpm, 10 min), the supernatant was removed, and the solid residue was dried under reduced pressure, then suspended in water, and purified by dialysis against 4L deionised water for 2-3 days, changing the solvent every 12-24 h. The dialysis was carried out using an appropriately sized MWCO membrane (1, 2, 5 or 7 kDa) and finally the polymer solutions were freeze-dried.

Where we utilised a lipophilic monomer (such as **5**), the purification procedure was carried out with the same protocol, except for the dialysis. The solvent mixture employed for this process was water:acetone 1:1, to allow for removal of monomers with low aqueous solubility.

2.2.3 ^{1}H NMR analysis of polymers

^{1}H NMR Nuclear Magnetic Resonance spectra were recorded on a Bruker-AV 400 at 400.13 MHz. The samples (14-18 mg) were solubilised in 0.7 mL of an appropriate solvent (DMSO-d_6, $CDCl_3$, D_2O), transferred to NMR tubes and analysed. Chemical shifts (δ) were obtained in ppm calibrating the spectrum to the chemical shift of the solvent used. Coupling constants (J) are reported to the nearest 0.1Hz, with peak multiplicities and assignments. Mestrenova 12 was used to process the spectra.

DP Degree of polymerisation (DP) was estimated by ^{1}H NMR, comparing the integrals of specific groups at the polymer chain end to those of the CH_2 and CH peaks in the polymer backbone (1.58 ppm and 2 ppm respectively). For the polymers synthesised with the DOPE RAFT agent (**2**), the three terminal CH_3s at 0.78 ppm were used as internal reference, with their integration set as 9. For polymers synthesised with the cholesterol RAFT agent (**1**), the signal used as reference was a cholesterol CH_3 triplet at 0.64 ppm, with its integration set as 3. For the PABTC RAFT agent (**3**), the signal used as reference was that corresponding to a single CH_3, 0.93 ppm), with integration set as 3.

2.2.4 SEC analysis

Polymer number-average molecular weight (M_n,SEC), weight-average molecular weight (M_w,SEC) and dispersity (*Đ*) were determined by Gel Permeation Chromatography (GPC), and calculated through Cirrus software and Microsoft Excel.

SEC was carried out using and appropriate GPC apparatus, depending on the solubility of the polymer:

i) Shimadzu GPC Prominence, LC-20AD (liquid chromatograph), SIL-20A HT (autosampler), RID 10A (Refractive index detector), CTO-20A (column oven). 2 successive mixed-D columns. 30 degrees, eluent tetrahydrofuran (THF), 2% Et_3N,

0.001% BHT. Software LCsolution (Shimadzu). PMMA standards (Agilent EasyVials) were used for conventional calibration between 500−955,550 g mol^{-1}. Number-average molar mass ($M_{n,SEC}$) and dispersity (*Đ*) values of synthesized polymers were determined by using Cirrus GPC software;

ii) Agilent 1260 Infinity, detector WYATT technology DAWN 8+. Software OpenLAB and Excel. Eluent HPLC water + 0.1 M $NaNO_3$, stationary phase two Aquagel-OH columns. PEO/PEG standards (Agilent EasyVials) were used for conventional calibration between 162−6,035,000 g mol^{-1}. Number-average molar mass ($M_{n,SEC}$) and dispersity (*Đ*) values of synthesized polymers were determined by using Agilent GPC software and Microsoft Excel ;

iii) Polymer Laboratories PL-GPC 50, with PL-AS RT autosampler, Eluent dimethylformamide (DMF) + 0.1% LiBr, stationary phase 2 successive mixed-D columns. PMMA standards (Agilent EasyVials) were used for conventional calibration between 500−955,550 g mol^{-1}. Number-average molar mass ($M_{n,SEC}$) and dispersity (*Đ*) values of synthesized polymers were determined by using Cirrus GPC software; and

iv) SEC-HPLC. Analysis of fluorescently-tagged polymers was performed with a Shimadzu UFLC HPLC with a SPD-M20A Diode array detector (Deuterium and Wolframium) and a RF-10XL fluorescence detector (Xenon lamp). A SEC Aquagel-OH column was used as stationary phase, while the mobile phase was HPLC-grade water. The fluorescence detector was set at λ_{ex} = 377 nm and λ_{em} = 420 nm for MalPyr Blue polymers, and at λ_{ex} = 560 nm and λ_{em} = 580 nm for Rhodamine polymers.

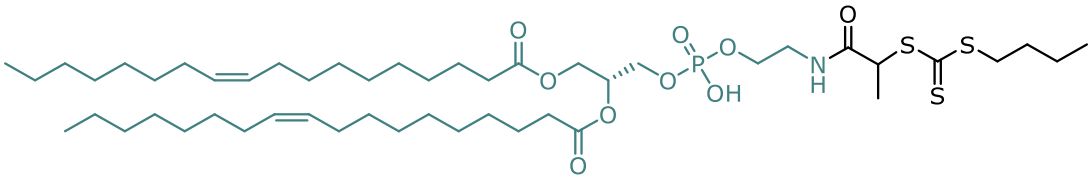
2.2.5 Critical aggregation concentration determination

This CAC determination method uses pyrene[3] to determine whether the concentration level where a species forms supramolecular aggregates. The fluorescence emission spectrum of pyrene changes whether it is in a lipophilic or

hydrophilic solvent, with the ratio between two of its peaks (I_1 and I_3) changing with the solvation status of the molecule[4]. A saturated pyrene solution in HPLC-grade water and 10 mg/mL polymer solutions were prepared. The fluorescence emission at λ_{em} = 373 nm and λ_{em} = 385 nm of the prepared pyrene-polymer solutions was measured, with a λ_{ex} = 340 nm. The solutions were subject to serial dilution, using the saturated pyrene suspension, and subject to further fluorescence emission measurements.

Plotting polymer concentration against I_1/I_3 results in two intersecting lines. By calculating the equations of the two lines, we calculated the intersection point between the two lines, which corresponded to the CAC. If, by plotting polymer concentration against I_1/i_3 against a species produces only one line for concentrations up to saturation, it was assumed that the species was not capable of forming supramolecular aggregates.

2.2.6 Synthesis of DOPE RAFT agent (2)



(2)

1,2-dioleoyl-sn-glycero-3-phosphoethanolamine (DOPE, 257 mg, 1 eq, 0.345 mmol) was solubilised in chloroform (15 mL) in a round-bottom flask and *N*-methylmorpholine was added (209 mg, 228 µL, 6 eq, 2.30 mmol). PABTC-*O*-succinimide (570 mg, 2.2 eq, 0.690 mmol) was solubilised in chloroform (25 mL) and added dropwise under stirring to the first solution, at room temperature. The reaction was left stirring for 7 days, progress was monitored by ^{1}H NMR. At completion the impurities were extracted with acidified (pH 3.9) water (3x40 mL).

The organic phase was dried under reduced pressure to obtain DOPE RAFT agent **(2)** as a bright yellow, sticky oily residue (397 mg, 53% yield).

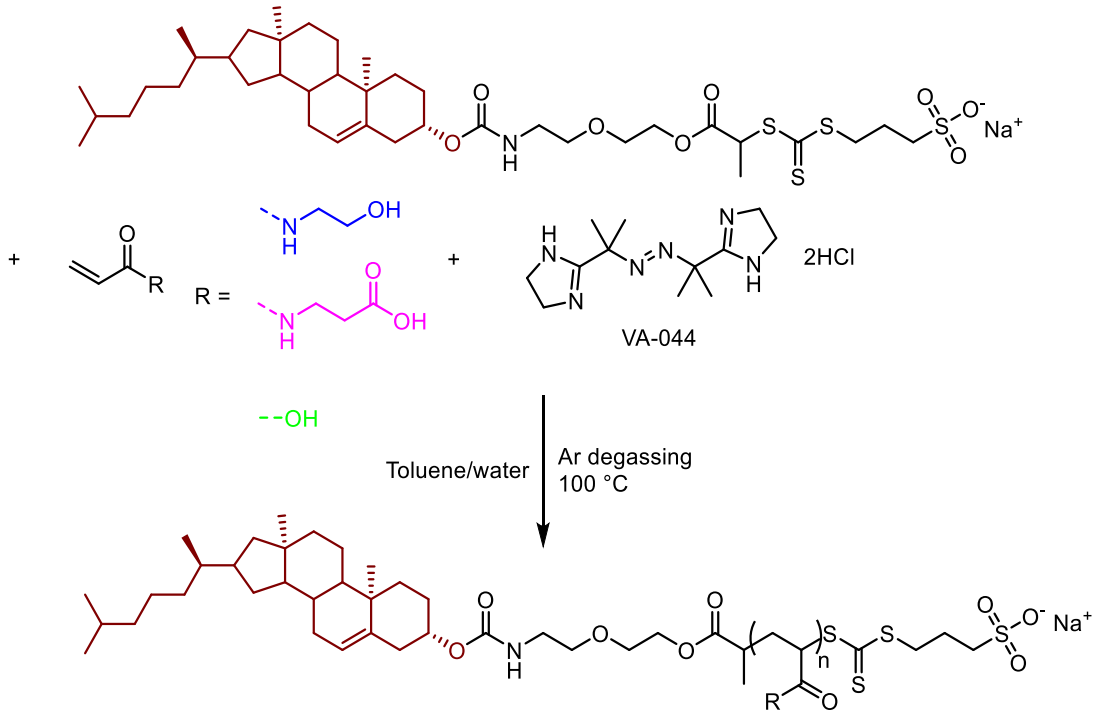
ESI-MS (expected m/z $[M]^-$ 962.55, found 962.54).

^{1}H NMR (400 MHz, DMSO-d6) δ 8.77 (t, J = 5.3 Hz, 1H, NH), 5.31 (t, J = 4.9 Hz, 4H, CH=CH), 5.08 (dq, J = 8.3, 4.8 Hz, 1H, glycerol CH), 4.68 (dq, J = 14.6, 7.1 Hz, 2H, glycerol CH_2-OC=O), 4.27 (dd, J = 12.1, 3.1 Hz, 1H, glycerol CH_2-OPO_3), 4.07 (dd, J = 12.0, 7.1 Hz, 1H, glycerol CH_2-OPO_3), 3.72 (tq, J = 20.1, 6.1 Hz, 8H, CH_2s ethanolamine linker + N-methylmorpholine impurity), 3.21 (q, J = 5.7 Hz, 2H, CH_2-S), 2.90 (d, J = 5.1 Hz, 4H, N-methylmorpholine impurity), 2.57 (s, 4H, N-methylmorpholine impurity), 2.34 – 2.17 (m, 4H, CH_2-COO), 1.97 (q, J = 6.3 Hz, 8H, allylic CH_2s), 1.62 (pd, J = 7.4, 4.3 Hz, 4H, CH_2s β to carbonyl), 1.49 (dd, J = 12.9, 7.2 Hz, 9H, CH_2 alkyl chains + CH_2 β to trithiocarbonate), 1.41 – 1.33 (m, 2H, CH_2 γ to trithiocarbonate), 1.32 – 1.15 (m, 37H, CH_2 alkyl chains), 0.92 – 0.78 (m, 12H, terminal CH_3s).

^{13}C NMR (101 MHz, DMSO) δ 223.30 (CS_3), 172.94, 172.70 (COO), 172.03 (COO), 169.67 (CONH), 130.07 (CH=CH), 130.01 (CH=CH), 70.81+ 70.74 (glycerol CH), 64.54 (glycerol CH_2OP), 53.56 (ethanolamine CH_2OP), 50.48 (glycerol CH_2OCO), 48.87 (CH-S), 43.92 (CH_2NH), 36.52 (CH_2COO), 34.03 (CH_2COO), 33.86 (CH_2 alkyl chain), 31.77 (CH_2S), 30.07 (CH_2 β to trithiocarbonate), [29.61, 29.59, 29.33, 29.18, 29.13, 29.08, 29.02, 28.99, 28.93, 28.91, 27.09 (CH_2s alkyl chain)], 27.05 (allylic CH_2s), 24.94 (CH_2 β to carbonyl), 24.87 (CH_2 β to carbonyl), 22.58 (CH_2s alkyl chain), 21.91 (CH_2 β to trithiocarbonate), 17.38 (CH_3 β to trithiocarbonate), 14.39 (terminal CH_3), 13.89 (terminal CH_3), 13.87 (terminal CH_3 δ to trithiocarbonate)

FT-IR: 1750 cm^{-1} ester C=O stretching, 1680 cm^{-1} secondary amide C=O stretching,1150 cm^{-1} trithiocarbonate, 1050 cm^{-1} phosphate P=O stretching.

2.2.7 Polymerysations mediated by cholesterol RAFT **(1)** (Ultrafast)



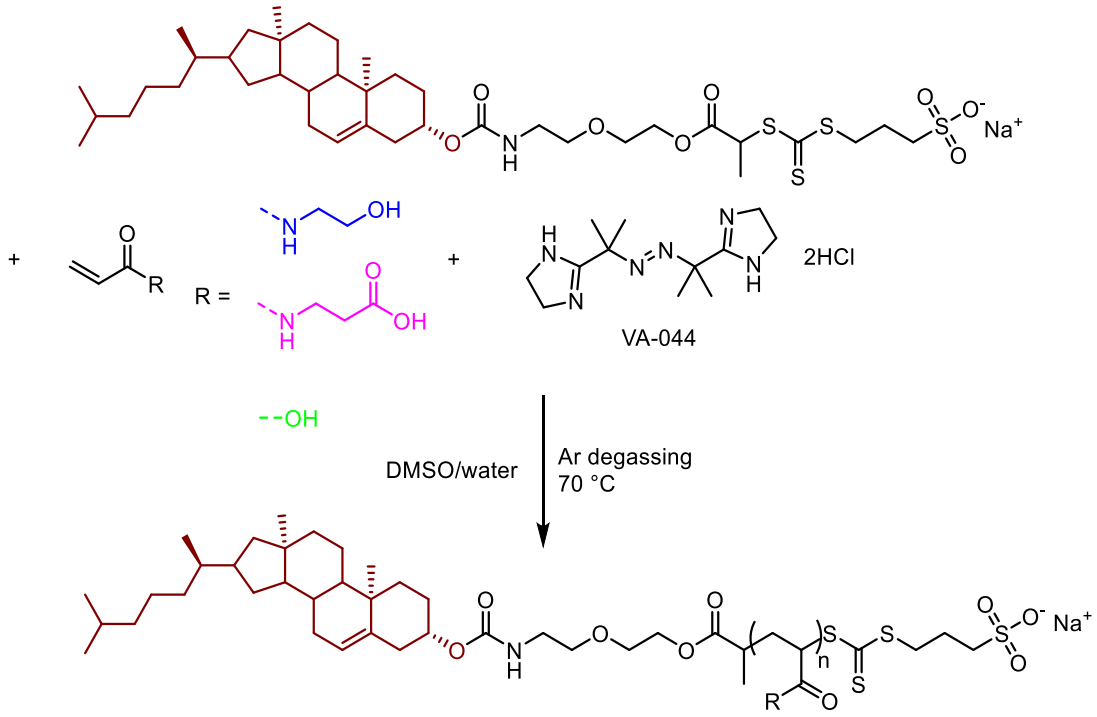
In a typical polymerisation reaction, cholesterol-RAFT agent **(1)** was solubilised in toluene in the reaction vessel (Schlenk tube), then the chosen monomer(s) was solubilised in deionised water (2M monomer concentration) and added to the toluene solution (toluene:water 1:1 vol:vol). The exact initial co-monomer ratios were determined at this stage by ^{1}H NMR analysis of an aliquot taken from the reaction mixture. An appropriate volume of a 2.0 mg/mL aqueous stock solution of VA-044 radical initiator (1:0.01 RAFT agent:initiator mol:mol) was added. The exact reagents ratio for all polymerisation reactions is shown in **Table 2.1**. The vessel was then closed with a rubber seal, cooled to 0 °C, and degassed by N_2 bubbling for 15 minutes. The Schlenk tube was then heated up to 100 °C, under vigorous stirring. After 15 minutes, the reaction was stopped by rapid cooling (ice bath) and exposure to air. Finally, the reaction solution was analysed by ^{1}H NMR to determine the final monomer conversion. If the target conversion was not reached, the reaction mixture was subject to degassing, addition of fresh initiator and heating to 100 °C.

Table 2.1 Polymerisation table for ultrafast RAFT polymerisations

Code	Chol-$[(HEA)_{100\%}]_{108}$	Chol-$[(HEA)_{90\%}$-*r*-$(AAPA)_{10\%}]_{140}$	Chol-$[(AA)_{100\%}]_{123}$	Chol-$[(HEA)_{90\%}$-*r*-$(AA)_{10\%}]_{51}$	Chol-$[(HEA)_{70\%}$-*r*-$(AA)_{30\%}]_{52}$	Chol-$[(HEA)_{50\%}$-*r*-$(AA)_{50\%}]_{70}$
$DP_{targeted}$ [a]	100	100	100	50	50	50
Monomers (mg)	HEA (2.53 g)	HEA (805) AAPA (111)	AA (286)	HEA (244) AA (17.0)	HEA (164) AA (44.1)	HEA (117) AA (73.5)
CTA **1** (mg)	230	81.3	41.6	49.3	42.7	42.7
VA-044 (mg)	0.711	0.251	0.129	0.152	0.132	0.132
Toluene (mL)	10.9	3.88	1.99	1.18	1.02	1.02
H_2O (mL)	8.36	3.76	1.64	1.08	0.911	0.882
CTA:monomers:initiator (targeted m/r ratios) [b]	1:100:0.01	1:100:0.01	1:100:0.01	1:50:0.01	1:50:0.01	1:50:0.01

[a] Degree of polymerisation (DP) chosen for the polymer. [b] Targeted m/r ratios for the key components of a RAFT polymerisation (CTA, monomers and initiator)

2.2.8 Single-phase polymerisations mediated by Cholesterol RAFT (1)



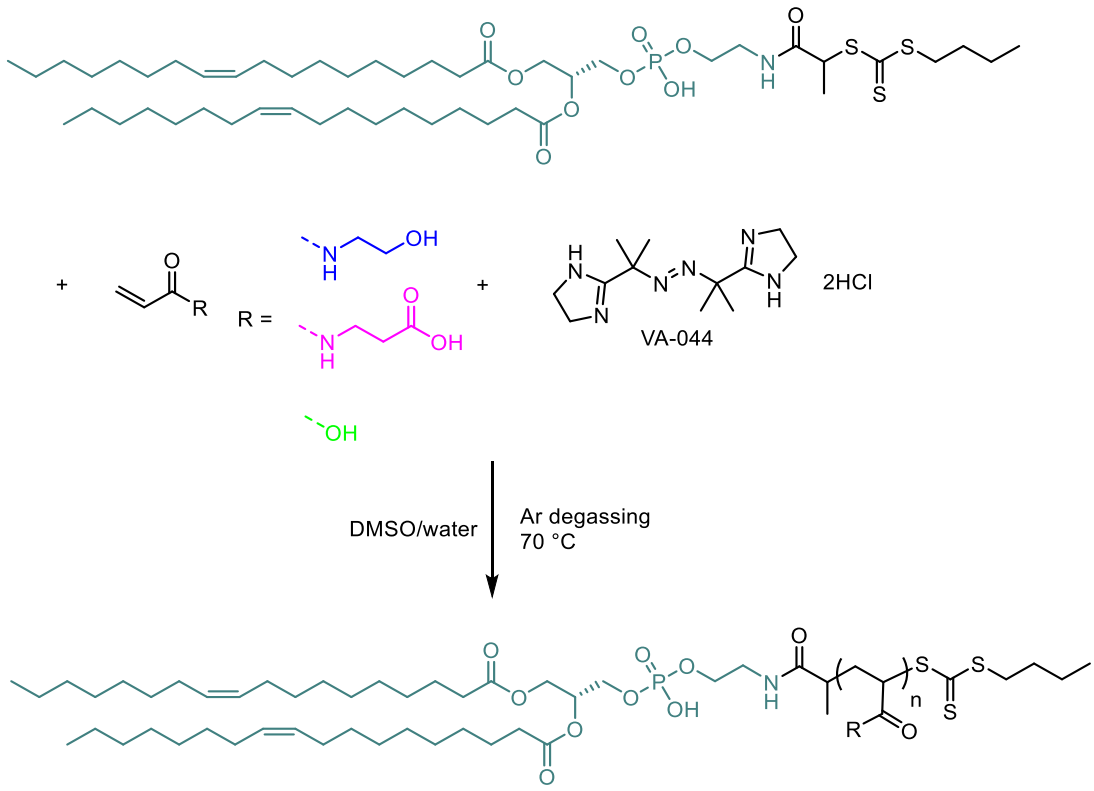
In a typical polymerisation reaction, cholesterol-RAFT agent **(1)** was solubilised in DMSO in the reaction vessel (Schlenk tube, or scintillation vial), then the chosen monomer(s) was solubilised in deionised water (2M monomer concentration) and added to the DMSO solution (DMSO:water 4:1 vol:vol). The exact initial co-monomer ratios were determined by ^{1}H NMR analysis of al aliquot withdrawn from the reaction mixture. An appropriate volume of a 2.0 mg/mL aqueous stock solution of VA-044 radical initiator the initiator (VA-044, 1:0.025 CTA:initiator ratio mol:mol) was added. The exact ratio for all polymerisation reactions is shown in **Table 2.2**. The vessel was then closed with a rubber seal, cooled to 0 °C, and degassed by N_2 bubbling for 15 minutes. The Schlenk tube was then heated up to 70 °C, under vigorous stirring. After 2 hours, the reaction was stopped by rapid cooling (ice bath) and exposure to air. Finally, the reaction solution was analysed by ^{1}H NMR to determine the final monomer conversion. If the target conversion was not reached, the reaction mixture was subject to degassing, addition of fresh initiator and heating to 70 °C.

Table 2.2 Polymerisation table for single-phase RAFT polymerisations mediated by **1**

Code	Chol-[(HEA)$_{90\%}$-*r*-(AA)$_{10\%}$]$_{105}$	Chol-[(HEA)$_{70\%}$-*r*-(AA)$_{30\%}$]$_{94}$	Chol-[(HEA)$_{100\%}$]$_{52}$	Chol-[(HEA)$_{90\%}$-*r*-(AAPA)$_{10\%}$]$_{50}$	Chol-[(AA)$_{100\%}$]$_{54}$
$DP_{targeted}$ [a]	100	100	50	50	50
Monomers (mg)	HEA (397) AA (27.6)	HEA (422) AA (113)	HEA (206)	HEA (196) AAPA (27.1)	AA (185)
CTA **1** (mg)	40.1	54.8	37.4	39.6	53.6
VA-044 (mg)	0.310	0.423	0.289	0.306	0.414
H_2O (mL)	0.383	0.524	0.179	0.189	0.256
DMSO (mL)	1.533	2.095	0.715	0.757	1.02
CTA:monomers:initiator (targeted m/r ratios) [b]	1:100:0.025	1:100:0.025	1:50:0.025	1:50:0.025	1:50:0.025

[a] Degree of polymerisation (DP) chosen for the polymer. [b] Targeted m/r ratios for the key components of a RAFT polymerisation (CTA, monomers and initiator)

2.2.9 Polymerisations mediated by DOPE RAFT **(2)**



In a typical polymerisation reaction, DOPE-RAFT agent **(2)** was solubilised in DMSO in the reaction vessel (Schlenk tube, or scintillation vial), then the chosen monomer(s) was solubilised in deionised water (2M monomer concentration) and added to the DMSO solution (DMSO:water 4:1 vol:vol). The exact initial co-monomer ratios were determined by ^{1}H NMR analysis of al aliquot withdrawn from the reaction mixture. An appropriate volume of a 2.0 mg/mL aqueous stock solution of VA-044 radical initiator the initiator (VA-044, 1:0.025 CTA:initiator ratio mol:mol) was added. The exact ratio for all polymerisation reactions is shown in **Table 2.3**. The vessel was then closed with a rubber seal, cooled to 0 °C, and degassed by N_2 bubbling for 15 minutes. The Schlenk tube was then heated up to 70 °C, under vigorous stirring. After 2 hours, the reaction was stopped by rapid cooling (ice bath) and exposure to air. Finally, the reaction solution was analysed by ^{1}H NMR to determine the final monomer conversion. If the target conversion

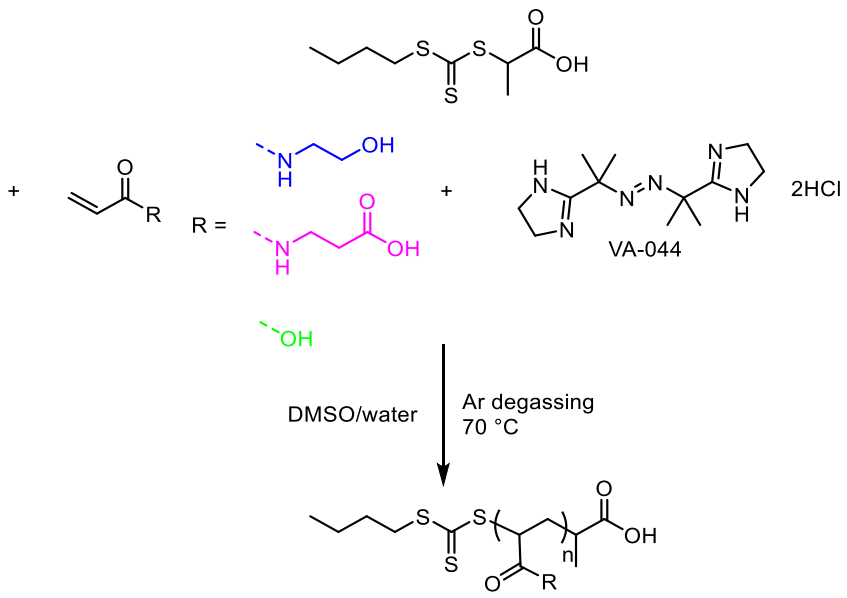
was not reached, the reaction mixture was subject to degassing, addition of fresh initiator and heating to 70 °C.

Table 2.3 Polymerisation table for single-phase RAFT polymerisations mediated by **2**

Code	DOPE-$[(HEA)_{100\%}]_{47}$	DOPE-$[(HEA)_{50\%}$-*r*-$(AA)_{50\%}]_{48}$	DOPE-$[(HEA)_{90\%}$-*r*-$(AA)_{10\%}]_{30}$	DOPE-$[(AA)_{100\%}]_{42}$
$DP_{targeted}$ [a]	50	50	50	50
Monomers (mg)	HEA (312)	HEA (145) AA (90.7)	HEA (186) AA (46.4)	AA (168)
CTA **2** (mg)	52.3	48.5	62.4	45.0
VA-044 (mg)	0.439	0.407	0.523	0.377
H_2O (mL)	0.271	0.126	0.162	0.234
DMSO (mL)	1.09	0.503	0.648	0.934
CTA:monomers:initiator (targeted m/r ratios) [b]	1:50:0.025	1:50:0.025	1:50:0.025	1:50:0.025

[a] Degree of polymerisation (DP) chosen for the polymer. [b] Targeted m/r ratios for the key components of a RAFT polymerisation (CTA, monomers and initiator)

2.2.10 Polymerisations mediated by PABTC RAFT (3)



In a typical polymerisation reaction, PABTC RAFT agent (**3**) was solubilised in DMSO in the reaction vessel (Schlenk tube, or scintillation vial), then the chosen monomer(s) was solubilised in deionised water (2M monomer concentration) and added to the DMSO solution (DMSO:water 4:1 vol:vol). The exact initial co-monomer ratios were determined by ^{1}H NMR analysis of an aliquot withdrawn from the reaction mixture. An appropriate volume of a 2.0 mg/mL aqueous stock solution of VA-044 radical initiator the initiator (VA-044, 1:0.025 CTA:initiator ratio mol:mol) was added. The exact ratio for all polymerisation reactions is shown in **Table 2.4** and **Table 2.5**. The vessel was then closed with a rubber seal, cooled to 0 °C, and degassed by N_2 bubbling for 15 minutes. The Schlenk tube was then heated up to 70 °C, under vigorous stirring. After 2 hours, the reaction was stopped by rapid cooling (ice bath) and exposure to air. Finally, the reaction solution was analysed by ^{1}H NMR to determine the final monomer conversion. If the target conversion was not reached, the reaction mixture was subject to degassing, addition of fresh initiator and heating to 70 °C.

Table 2.4 Polymerisation table for single-phase RAFT polymerisations mediated by the PABTC RAFT agent **3**, 50 DP polymers

Code	PABTC-$[(HEA)_{100\%}]_{50}$	PABTC-$[(HEA)_{90\%}$-*r*-$(AAPA)_{10\%}]_{46}$	PABTC-$[(AA)_{100\%}]_{37}$	PABTC-$[(HEA)_{90\%}$-*r*-$(AA)_{10\%}]_{45}$	PABTC-$[(HEA)_{70\%}$-*r*-$(AA)_{30\%}]_{44}$	PABTC-[$(HEA)_{50\%}$-*r*-$(AA)_{50\%}]_{49}$
$DP_{targeted}$ [a]	50	50	50	50	50	50
Monomers (mg)	HEA (665)	AA (425)	HEA (464) AAPA (64.0)	HEA (731) AA (99.5)	HEA (472) AA (248)	HEA (389) AA (477)
CTA **3** (mg)	27.5	28.1	21.3	33.6	27.9	32.2
VA-044 (mg)	0.934	0.954	0.723	0.456	0.379	0.437
H_2O (mL)	0.578	0.590	0.403	0.635	0.410	0.338
DMSO (mL)	2.31	2.36	1.61	2.54	1.64	1.35
CTA:monomers:initiator (targeted m/r ratios) [b]	1:50:0.025	1:50:0.025	1:50:0.025	1:50:0.01	1:50:0.01	1:50:0.01

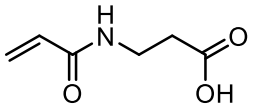
[a] Degree of polymerisation (DP) chosen for the polymer. [b] Targeted m/r ratios for the key components of a RAFT polymerisation (CTA, monomers and initiator)

Table 2.5 Polymerisation table for single-phase polymerisations mediated by **3**, 100 DP polymers

Code	PABTC-$[(HEA)_{100\%}]_{80}$	PABTC-$[(HEA)_{90\%}$-*r*-$(AAPA)_{10\%}]_{81}$	PABTC-$[(HEA)_{90\%}$-*r*-$(AA)_{10\%}]_{75}$	PABTC-$[(HEA)_{70\%}$-*r*-$(AA)_{30\%}]_{80}$
$DP_{targeted}$ [a]	100	100	100	100
Monomers (mg)	HEA (929)	HEA (888) AAPA (123)	HEA (1.39 g) AA (96.6)	HEA (863) AA (232)
CTA **3** (mg)	19.2	20.4	31.9	25.5
VA-044 (mg)	0.261	0.277	1.08	0.866
H_2O (mL)	0.807	0.771	1.21	0.750
DMSO (mL)	3.23	3.08	4.82	3.00
CTA:monomers:initiator (targeted m/r ratios) [b]	1:100:0.01	1:100:0.01	1:100:0.025	1:100:0.025

[a] Degree of polymerisation (DP) chosen for the polymer. [b] Targeted m/r ratios for the key components of a RAFT polymerisation (CTA, monomers and initiator)

2.2.11 Synthesis of 3- acrylamido propanoic acid (3-AAPA, **4**) monomer [5]



(4)

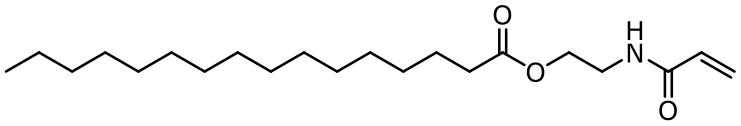
Beta alanine (6.00g, 1 eq, 0.0678 mol) and NaOH (2.98 g, 1.1 eq, 0.0746 mol) were solubilised in water (54 mL) in a round-bottom flask, and the resulting solution was cooled with an ice bath. Acryloyl chloride (6.75 g, 1.1 eq, 0.0746 mol, 6.06 mL) was diluted in THF (10 mL) and the resulting solution was added dropwise to the reaction vessel. The reaction completion was monitored by ^{1}H NMR for appearance of the amide peak at 8.27 ppm. The reaction mixture was acidified to pH 2 using 0.1 N HCl) and extracted with ethyl acetate (3 x 80 mL). The organic layers were combined and dried over $MgSO_4$. Petroleum ether was added to the solution until a white precipitate was formed, to be then collected by filtration. The white-solid that formed was dried in a desiccator under vacuum overnight to obtain white transparent crystals (4.71 g, 48% yield).

ESI-MS: expected m/z $[M+H]^+$ 144.065, found 144.065.

^{1}H NMR (400 MHz, DMSO-d_6, ppm): 11.47 (s, 1H, COOH), 7.35 (t, *J* = 5.7 Hz, 1H, NH), 5.48 – 5.32 (m, 1H, CH2=CH), 5.30 – 5.20 (m, 1H, CH_2=CH), 4.74 (dd, *J* = 10.1, 2.3 Hz, 1H, CH=CH_2), 1.59 (t, *J* = 6.8 Hz, 2H, CH_2 α to COOH).

^{13} C NMR (400 MHz, DMSO-d_6, ppm): 173.33 (COOH), 165.10 (CONH), 131.17 (CH=CH_2), 125.54 (CH_2=CH), 35.30 (CH_2NH), 34.22 (CH_2COOH).

2.2.12 Synthesis of 2-acrylamido palmitate (2-AP, **5**)



(5)

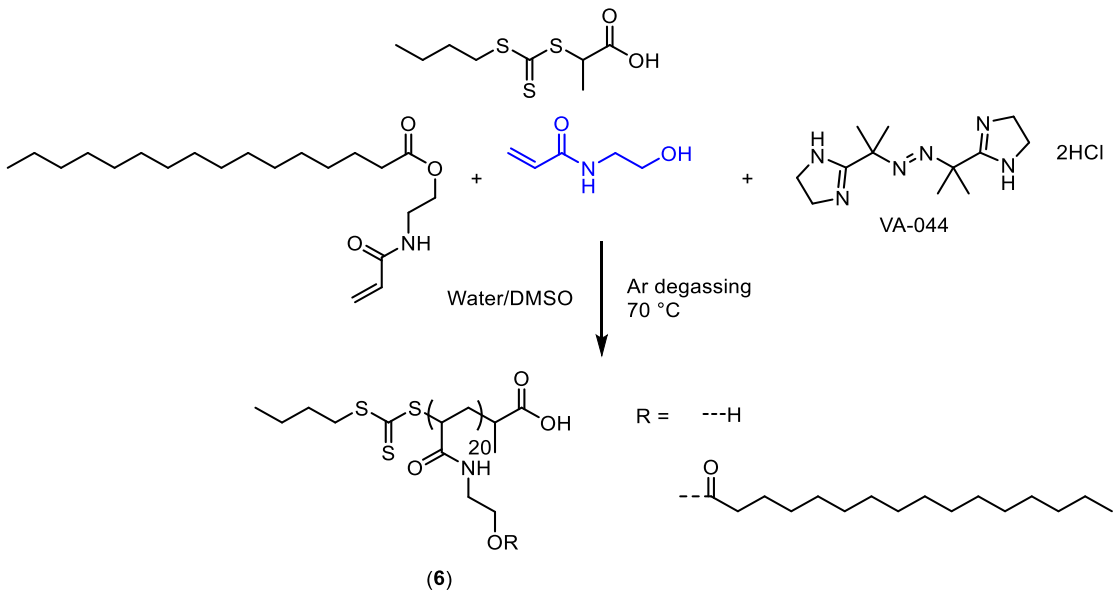
Hydroxyethyl acrylamide (12.9 g, 1 eq, 0.112 mol) was solubilised in dichloromethane (30 mL) in a round-bottom flask. DMAP (6.58 g, 0.5 eq, 0.0560 mol) and triethylamine (22.7 g, 2 eq, 0.224 mol, 31.2 mL) were added dropwise to the stirring solution and the reaction mixture was brought to 0 °C with an ice bath. A solution of the palmitoyl chloride (15.4 g, 0.5 eq, 0.0560 mol, 17.0 mL) in dichloromethane (20 mL) was added dropwise to the stirring solution, and left to react overnight. The reaction mixture was extracted with acidified brine (HCl to acidify, pH 2) and DCM (3x50 mL). The organic fractions were collected, and the solvent was removed under reduced pressure (max 30°C) until half of the solvent was removed. The resulting flution was then kept at 4°C without stirring overnight. The resulting white precipitate was collected by filtration (25.2 g, 63% yield).

ESI-MS: expected m/z $[M+Na]^+$ 376.28, found 376.282.

^{1}H NMR (400 MHz, Chloroform-*d*): 6.27 (dd, *J* = 17.0, 1.5 Hz, 1H, vinylic CH_2), 6.10 (dd, *J* = 17.0, 10.2 Hz, 1H, vinylic CH_2), 5.64 (dd, *J* = 10.2, 1.5 Hz, 1H, vinylic CH), 4.19 (t, *J* = 5.3 Hz, 2H, ethanolamine linker CH_2-O), 3.59 (q, *J* = 5.5 Hz, 2H, ethanolamine linker CH_2-NH), 2.29 (q, *J* = 6.6, 5.7 Hz, 2H, α CH_2), 1.61 (q, *J* = 7.3 Hz, 2H, β CH_2), 1.24 (s, 25H, alkyl chain), 0.86 (t, *J* = 6.7 Hz, 3H, terminal CH_3).

^{13}C NMR (101 MHz, Chloroform-*d*) δ 174.22 (COO), 165.72 (CONH), 130.71 (vinylic CH), 126.92 (vinylic CH_2), 63.08 (ethanolamine linker CH_2-O), 39.14 (ethanolamine linker CH_2-NH), [34.31, 32.06, 29.82, 29.81, 29.78, 29.74, 29.60, 29.49, 29.40, 29.27, 25.04, 22.82 (CH_2 in the alkyl chain)], 14.25 (terminal CH_3).

2.2.13 RAFT polymerisation of 2-AP



(**6**)

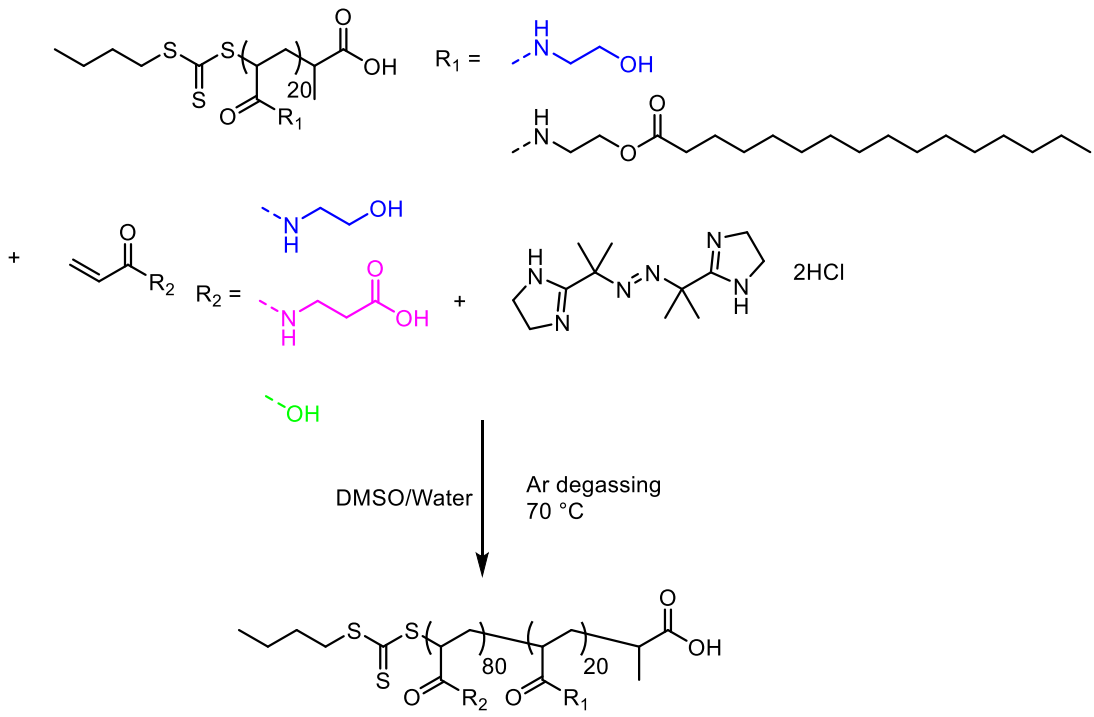
For this polymerisation reaction, the PABTC RAFT (**3**) agent was solubilised in DMSO in the reaction vessel (Schlenk tube, or scintillation vial), then the chosen monomer(s) was solubilised in deionised water (2.0 M monomer concentration) and added to the DMSO solution (DMSO:water 4:1 vol:vol). The exact initial co-monomer ratio was determined by ^{1}H NMR analysis of the reaction mixture, then the initiator (VA-044, 1:0.025 CTA:initiator ratio mol:mol) 2 mg/mL aqueous stock solution was added. The vessel was then closed using a rubber seal and degassed with N_2 for 15 minutes. The Schlenk tube was immersed in a 70 °C oil bath, under stirring. After 2 hours, the reaction was stopped by rapid cooling (ice bath) and exposure to air. Finally, the reaction solution was analysed by ^{1}H NMR to determine the final monomer conversion.

The resulting polymer was subject to a first round of purification as standard (details in 2.2.2, with the exception that a 1:1 water:acetone mixture was used as dialysis solvent), to remove reaction side products and unreacted monomers.

The solid polymer was purified by column chromatography by loading the samples on silica gel (pore size 60Å, 230-440 mesh, 0.040-0.063 mm), using mobile phases with increasing polarity (DCM:MeOH 1:0 → 9:1). Two main products were

isolated: a more lipophilic fraction, composed of polymers containing an average of 2-3 units of **5** (fraction A) a more hydrophilic fraction, composed of polymers containing an average of 1 unit of **5** (fraction B).

2.2.14 Polymerisations mediated by 2-AP MacroCTA



In a typical polymerisation reaction, the macro CTA RAFT agent (**6**) was solubilised in DMSO in the reaction vessel (Schlenk tube, or scintillation vial), then the chosen monomer(s) was solubilised in deionised water (2.0 M monomer concentration) and added to the DMSO solution (DMSO:water 4:1 vol:vol). The exact initial co-monomer ratio was determined by ^{1}H NMR analysis of the reaction mixture, then the initiator (VA-044, 1:0.025 CTA:initiator ratio mol:mol) 2 mg/mL aqueous stock solution was added. Exact ratio for all polymerisation reactions is shown in **Table 2.6**. The vessel was then closed using a rubber seal and degassed with N_2 for 15 minutes. The Schlenk tube was immersed in a 70 °C oil bath, under stirring. After 2 hours, the reaction was stopped by rapid cooling (ice bath) and exposure

to air. Finally, the reaction solution was analysed by ^{1}H NMR to determine the final monomer conversion.

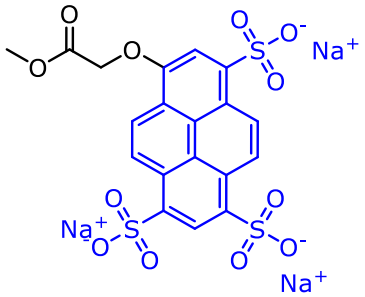
Table 2.6 Polymerisation table for single-phase RAFT polymerisations mediated by **6**

Code	(2-AP)$_1$-[(HEA)$_{100\%}$]$_{95}$	(2-AP)$_1$-[(HEA)$_{90\%}$-*r*-(AAPA)$_{10\%}$]$_{160}$	(2-AP)$_1$-PABTC-[(AA)$_{100\%}$]$_{143}$	(2-AP)$_1$-[(HEA)$_{90\%}$-*r*-(AA)$_{10\%}$]$_{139}$	(2-AP)$_1$-[(HEA)$_{70\%}$-*r*-(AA)$_{30\%}$]$_{130}$	(2-AP)$_1$-[(HEA)$_{50\%}$-*r*-(AA)$_{50\%}$]$_{120}$
$DP_{targeted}$ [a]	100	100	100	100	100	100
Monomers (mg)	HEA (907)	HEA (764) 3-AAPA (119)	AA (578)	HEA (1.05g) AA (82.3)	HEA (646) AA (202)	HEA (455) AA (356)
CTA **6** (mg)	200	190	204	261	214	226
VA-044 (mg)	0.283	0.670	0.720	0.923	0.756	0.799
H_2O (mL)	0.788	0.663	0.802	0.914	0.561	0.791
DMSO (mL)	3.15	2.65	3.21	3.66	2.24	3.16
CTA:monomers:initiator (targeted m/r ratios) [b]	1:100:0.1	1:100:0.025	1:100:0.025	1:100:0.025	1:100:0.025	1:100:0.025

[a] Degree of polymerisation (DP) chosen for the polymer. [b] Targeted m/r ratios for the key components of a RAFT polymerisation (CTA, monomers and initiator)

2.2.15 Synthesis of MalPyr Blue

*2.2.15.1 Pyranine methyl ester **(7)***



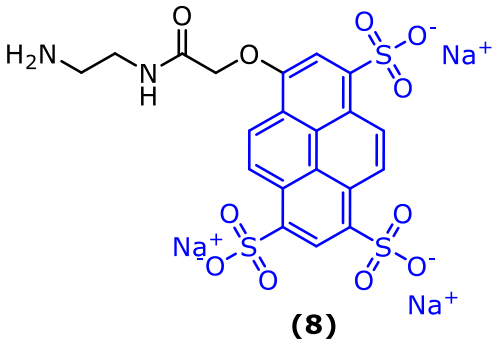
(7)

Pyranine (1 eq, 3.09 g, 5.90 mmol) was solubilised in methanol (150 mL) under stirring in a round-bottom flask, protected from light, and the resulting solution was heated up to reflux. Methyl bromoacetate (3.8 eq, 3.41 g, 22.4 mmol) and N,N-diisopropylethylamine (2.8 eq, 2.14 g, 16.5 mmol, 2.87 mL) were solubilised in methanol (30 mL) and added to the stirring reaction portion-wise (1/3 every 1.5 hours). After adding the last portion, the reaction was left refluxing for 3 additional hours. The solution was then cooled down to room temperature and transferred in a larger vessel, where isopropanol (50 mL) was added to precipitate the product. The precipitate was filtered and dried under reduced pressure, to give **(7)** as a dark yellow solid (1.61 g, 45% yield) which was used for the subsequent step without further purification.

ESI-MS (expected m/z $[M+H]^+$ 597.91 found 597.41

^{1}H NMR (400 MHz, Deuterium Oxide) δ 9.20 (s, 1H, aromatic CH), 9.16 (d, *J* = 9.8 Hz, 1H, aromatic CH), 9.09 (d, *J* = 9.7 Hz, 1H, aromatic CH), 9.02 (d, *J* = 9.8 Hz, 1H, aromatic CH), 8.92 (d, *J* = 9.6 Hz, 1H, aromatic CH), 8.29 (s, 1H, aromatic CH), 5.33 (s, 2H, CH_2), 3.91 (s, 3H, CH_3).

*2.2.15.2 Pyranine ethylenediamine **(8)***



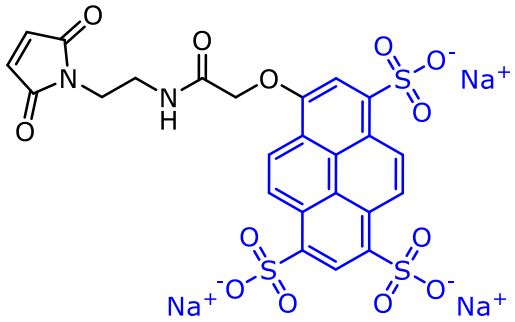
(8)

Pyranine methyl ester **(7)** (1 eq, 1.61 g, 2.68 mmol) was solubilised in methanol (96 mL) in a round-bottom flask, protected from light. Ethylenediamine (2.5 eq, 0.403 g, 6.70 mmol, 0.450 mL) was added to this solution under stirring and the reaction was monitored by ^{1}H NMR by conversion of the 5.33 ppm CH_2 peak to 4.94 ppm. At completion, isopropanol (40 mL) was added to the reaction mixture until formation of a yellow precipitate **(8)**, which was filtered, and dried under reduced pressure, to obtain a bright yellow solid (0.918 g, 57% yield).

ESI-MS (expected m/z [M-3Na+2H] 557.00 found 557.00

^{1}H NMR (400 MHz, Deuterium Oxide) δ 9.17 (s, 1H, aromatic CH), 9.08 (d, *J* = 9.8 Hz, 1H, aromatic CH), 9.02 (d, *J* = 9.7 Hz, 1H, aromatic CH), 8.95 (d, *J* = 9.9 Hz, 1H) , aromatic CH, 8.72 (d, *J* = 9.8 Hz, 1H, aromatic CH), 8.16 (s, 1H, aromatic CH), 4.94 (s, 2H, CH_2O), 3.54 – 3.48 (m, 1H, CH_2NH), 3.18 – 3.12 (m, 1H, CH_2NH), 2.88 (t, *J* = 6.2 Hz, 2H, CH_2NH_2), 2.83 (s, 1H, terminal amine).

*2.2.15.3 MalPyr Blue **(9)***

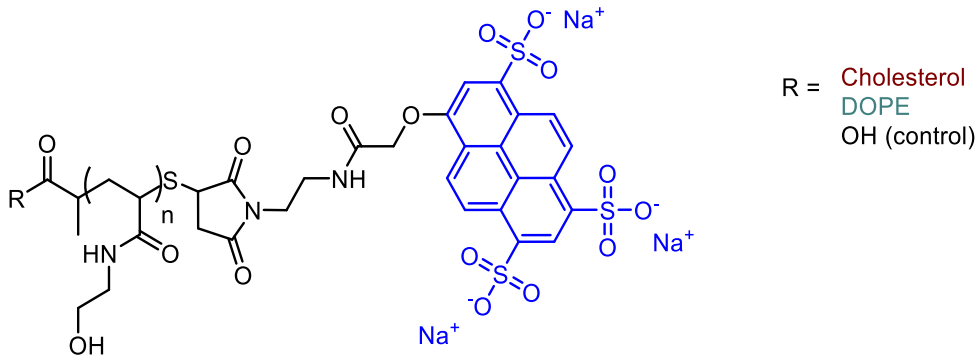


Pyranine ethylenediamine **(8)** (1 eq, 0.800 g, 1.28 mmol) was solubilised in a saturated aqueous solution of $NaHCO_3$ (12.5 mL) in a round-bottom flask and the resulting solution was cooled to 0 °C. N-methoxycarbonylmaleimide (1 eq, 0.198 g, 1.28 mmol) was added and left stirring at 0 °C for 40 minutes, then at room temperature for further 24 hours. The reaction mixture was poured into a separating funnel containing brine:dichloromethane (40:30 mL vol:vol), the organic phase (~ 40 mL) was collected and concentrated to 1/3 of the original volume under reduced pressure. The resulting solution was transferred to a larger vessel, where isopropanol (50 mL) was added to precipitate a yellow solid, that was collected via centrifugation. The precipitate was dried under reduced pressure, to give MalPyr Blue **(9)** as a yellow solid (950 mg, quantitative yield).

ESI-MS (expected m/z $[M-2Na+3H]^+$ 660.98, found 658.78).

^{1}H NMR (400 MHz, Deuterium Oxide) δ 9.10 (s, 1H, aromatic CH), 9.08 – 9.02 (m, 1H, aromatic CH), 8.98 (d, *J* = 9.7 Hz, 1H, aromatic CH), 8.91 (d, *J* = 9.9 Hz, 1H, aromatic CH), 8.80 (d, *J* = 9.6 Hz, 1H, aromatic CH), 8.18 (d, *J* = 3.2 Hz, 1H, aromatic CH), 5.91 (s, 2H, CH=CH), 5.04 (s, 2H, CH_2O), 3.44 (t, *J* = 5.5 Hz, 2H, CH_2N), 3.33 (t, *J* = 5.9 Hz, 2H, CH_2-NH_2).

2.2.16 One-pot end-capping of trithiocarbonate polymers with MalPyr Blue



Typically, the selected polymer (1 eq) was solubilised in water (800 µL per 100 mg of polymer) in a round-bottom flask. The flask was sealed, and the solution

degassed for 15 minutes by Argon bubbling. Benzylamine (10 eq) and tris(2-carboxyethyl)phosphine (TCEP 0.01 eq) were added to the stirring solution. The reaction was left for 1 hour (or until the solution went from yellow to colourless), and MalPyr Blue **(9)** (8 eq) was added and left reacting protected from light for 10 hours. Then, isopropanol (20 mL) was added to precipitate the polymer, and excess of starting materials were removed by dialysis against deionised water (2 days, using a dialysis membrane with a molecular weight cut-off chosen to retain the polymer and to allow removal of smaller molecules, such as unreacted monomers and dye). Following freeze-drying, the polymers were isolated as pale yellow solids.

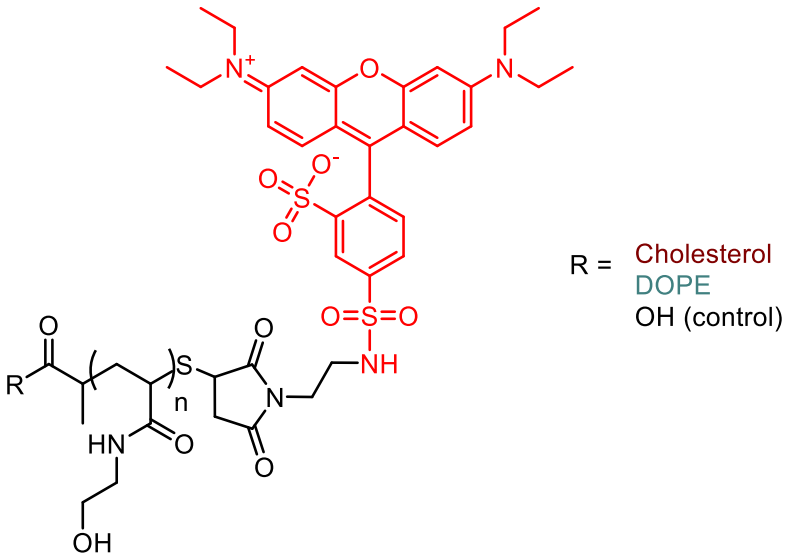
Successful conjugation was confirmed through SEC-HPLC. Analysis of fluorescently-tagged polymers was performed with a Shimadzu UFLC HPLC with a SPD-M20A Diode array detector (Deuterium and Wolframium) and a RF-10XL fluorescence detector (Xenon lamp). A SEC Aquagel-OH column was used as stationary phase, while the mobile phase was HPLC-grade water. The fluorescence detector was set at λ_{ex} = 377 nm and λ_{em} = 420 nm.

Relative fluorescence intensity was determined using 0.1 μM HBSS solutions of the fluorescently tagged polymers and of MalPyr Blue (**9**). The solutions were transferred in a 96-well plate (Costar black bottom), 150 μL per well. The fluorescence intensity measurement was run on a Spark 10M Plate Reader (Tecan). The analysis was performed at 37 °C, with λ_{ex} = 377 nm and λ_{em} = 420 nm.

The relative tagging efficiency was calculated by:

$$Tagging\ efficiency = \frac{fluorescence\ intensity\ for\ x\ polymer}{fluorescence\ intensity\ for\ free\ dye} \times 100$$

2.2.17 One-pot end-capping of trithiocarbonate polymers with Rhodamine Red



Typically, the selected polymer (1 eq) was solubilised in water (800 µL per 100 mg of polymer) in a round-bottom flask. The flask was sealed, and the solution degassed for 15 minutes by Argon bubbling. Benzylamine (10 eq) and tris(2-carboxyethyl)phosphine (TCEP 0.01 eq) were added to the stirring solution. The reaction mixture was left under stirring for 1 hour (or until the solution went from yellow to colourless), and Rhodamine Red™ C_2 maleimide (8 eq) was added and left reacting protected from light for 10 hours. Then, the polymer was precipitated by addition of excess isopropanol, the solid was collected by centrifugation and excess of starting materials were removed by dialysis against deionised water (2 days, using an appropriate dialysis membrane with a molecular weight cut-off chosen to retain the polymer and to allow removal of smaller molecules, such as unreacted monomers and dye). Following freeze-drying the polymers were isolated as bright magenta waxy solids.

Successful conjugation was confirmed through SEC-HPLC. Analysis of fluorescently-tagged polymers was performed with a Shimadzu UFLC HPLC with a SPD-M20A Diode array detector (Deuterium and Wolframium) and a RF-10XL fluorescence detector (Xenon lamp). A SEC Aquagel-OH column was used as

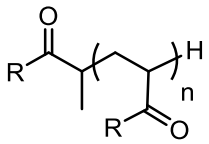
stationary phase, while the mobile phase was HPLC-grade water. The fluorescence detector was set at, and at λ_{ex} = 560 nm and λ_{em} = 580 nm.

For the Rhodamine Red tagged polymers, 0.10 μM Hank's Balanced Salt Solution (HBSS) solutions of the polymers and of the dye starting material were prepared. The solutions (300 μL each) were transferred in plastic disposable UV micro cuvettes and the fluorescence intensity was measured at λ_{ex} = 560 nm and λ_{em} = 580-620 nm.

The relative tagging efficiency was calculated by:

$$Tagging\ efficiency = \frac{fluorescence\ intensity\ for\ x\ polymer}{fluorescence\ intensity\ for\ free\ dye} \times 100$$

2.2.18 Trithiocarbonate group substitution with an -H group

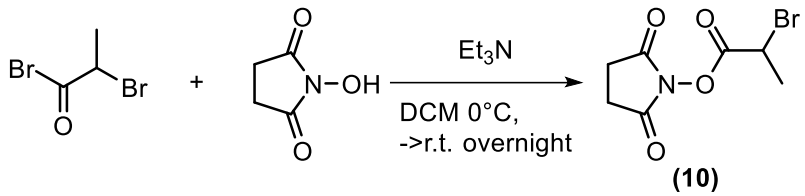


The selected polymer (1 eq) was solubilised in a DMSO:water (4:1 vol:vol) mixture (800 μL per 100 mg of polymer) in a vial. Solid 1-ethylpiperidine hypophosphite (EPHP, 5 eq) was added to the solution, then VA-044 initiator (1:0.025 CTA:initiator ratio mol:mol) 2 mg/mL aqueous stock solution was added. The vessel was then closed using a rubber seal and degassed with N_2 for 15 minutes. The Schlenk tube was immersed in a 70 °C oil bath, under stirring. After 2 hours, the reaction was stopped by rapid cooling (ice bath) and exposure to air. The polymer was then purified as described in 2.2.2, and analysed via UV-visible spectrometry with a Varian Cary 50 Scan UV/Vis Spectrophotometer to confirm complete removal of the trithiocarbonate group. The polymer solutions (0.1 μM in HPLC water) were transferred in quartz cuvettes (Hellma® semi Micro absorption cuvettes, Suprasil® quartz, spectral range 200-2500 nm, pathlength 5 mm,

chamber volume 700 µL) for measurement of UV-Vis absorbance at λ_{abs} = 310 nm.

2.2.19 First synthesis of a phospholipid RAFT agent (**13**)

*2.2.19.1 Synthesis of bromopropyonyl O-succinimide **(10)***

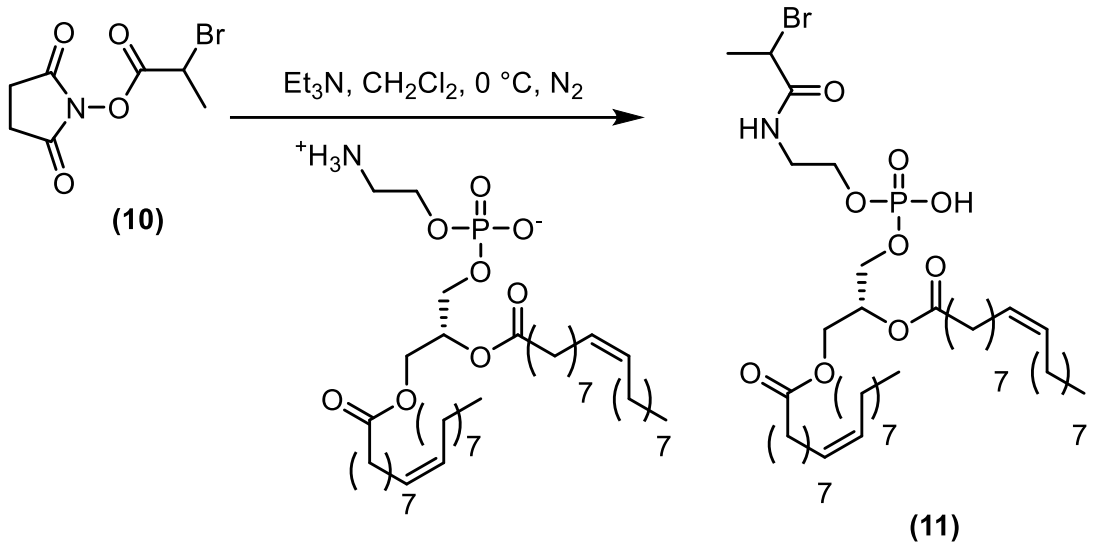


n-hydroxysuccinimide (NHS, 3.93 g, 1 eq, 3.42 mmol) was solubilised in THF (20 mL) in a round-bottom flask, and the resulting solution was cooled with an ice bath. Triethylamine (3.63 g, 1.05 eq, 3.59 mmol, 5.00 mL) was diluted in dichloromethane (10 mL) and the resulting solution was added dropwise to the reaction vessel. 2- bromopropyonyl bromide (7.74 g, 1.05 eq, 3.59 mmol, 3.76 mL) was diluted in dichloromethane (10 mL) and the resulting solution was added dropwise to the reaction vessel, over the course of 1 hour. The reaction completion was monitored by thin layer chromatography. The reaction mixture was extracted with brine (3 x 50 mL). The organic layers were combined and dried over $MgSO_4$. The organic solvents were removed under reduced pressure, resulting in a white solid (13.8 g, 95% yield).

^{1}H NMR (400 MHz, $CDCl_3$, ppm): 4.62 (q, *J* = 7.0 Hz, 1H, CH α to carbonyl), 2.86 (s, 4H, CH_2s on NHS), 1.96 (d, *J* = 7.0 Hz, 3H, CH_3)

^{13}C NMR (101 MHz, $CDCl_3$) δ 168.48 (α-bromo ester CO), 166.06 (succinimide COs), 34.85 (CBr), 25.61 (succinimide CH_2s), 21.54 (CH_3).

*2. 2.19.2 Synthesis of the bromo-phosphatidylethanolamide **(11)***

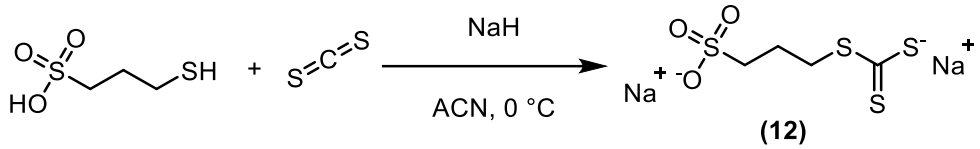


10 (0.129 g, 1.1 eq, 0.517 mmol) was solubilised in dichloromethane (10 mL) in a round-bottom flask, and the resulting solution was cooled with an ice bath. The vessel was then closed with rubber seals and degassed by N_2 bubbling. Triethylamine (0.143 g, 3 eq, 1.41 mmol, 0.196 mL) was added dropwise to the reaction vessel. 1,2-dioleoyl-sn-glycero-3-phosphoethanolamine (DOPE, 350 mg, 1 eq, 0.470 mmol) was solubilised in chloroform (10 mL) and added dropwise to the reaction vessel. The reaction was left stirring overnight, and reaction completion was monitored by ninhydrine staining. The reaction mixture was then diluted with dichloromethane to 50 mL and extracted with a 5% $NaHCO_3$ aqueous solution (1 x 50 mL). The organic layers were combined and dried over $MgSO_4$ and dried under reduced pressure, to yield a clear oil. The oil was purified by column chromatography by loading the samples on silica gel (pore size 60Å, 230-440 mesh, 0.040-0.063 mm), using mobile phases with increasing polarity (DCM:MeOH 1:0 → 9:1). The product **11** was isolated as a clear, transparent oil (630 mg, 152% yield) with residual impurities.

^{1}H NMR (400 MHz, DMSO-d_6, ppm): 9.97 (s, 1H, P-OH), 8.82 (t, J = 5.0 Hz, 1H, NH), 5.47 – 5.18 (m, 4H, vinyl CHs), 5.17 – 4.88 (m, 1H, CH glycerol moiety), 4.47 (q, J = 6.8 Hz, 1H, CH α to carbonyl), 4.27 (dd, J = 12.0, 3.1 Hz, 1H,

impurity), 4.09 (dq, J = 15.5, 7.1, 6.1 Hz, 4H, CH_2 glycerol), 3.72 (td, J = 5.9, 3.1 Hz, 1H, CH_2 phosphatidylethanolamine), 3.64 (dt, J = 8.7, 5.7 Hz, 2H, CH_2 phosphatidylethanolamine), 3.16 (d, J = 4.2 Hz, 11H, residual MeOH), 3.03 (q, J = 7.3 Hz, 4H, αCH_2 in lipid chains), 2.68 – 2.58 (m, 1H, impurity), 2.25 (td, J = 7.4, 2.3 Hz, 4H, βCH_2 in lipid chains), 1.97 (q, J = 6.4 Hz, 8H, allylic CH_2), 1.64 (d, J = 6.7 Hz, 3H, CH_3 β to carbonyl), 1.58 – 1.41 (m, 4H, impurity), 1.32 – 1.20 (m, 36H, alkyl chains), 1.16 (t, J = 7.3 Hz, 6H, impurity), 0.92 – 0.76 (m, 6H, terminal CH_3s)

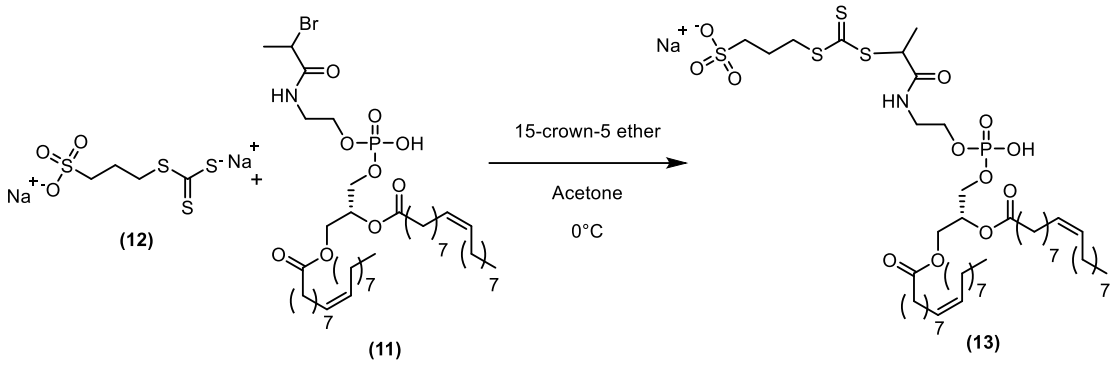
*2.2.19.3 Synthesis of 3-(trithiocarboxyl)propane-1-sulfonate **(12)***



3- mercapto 1- propanesulfonate (4.02 g, 1 eq, 2.26 mmol) was suspended in acetonitrile (40 mL) in a round-bottom flask, and the resulting solution was cooled with an ice bath. The vessel was then closed with rubber seals and degassed by N_2 bubbling. Sodium hydride (0.902 g, 1 eq, 2.26 mmol) was solubilised in acetonitrile (20 mL) and added dropwise to the reaction vessel. The reaction was left stirring for 2 hours and carbon disulfide (6.87 g, 4 eq, 9.02 mmol, 5.43 mL) was added dropwise to the reaction vessel and the reaction was left stirring overnight. The reaction mixture was then transferred to a larger vessel, where diethyl ether (250 mL) was added until a bright yellow precipitate was formed. The precipitate was collected by filtration, yielding a bright yellow solid (4.65 g, 89.5% yield).

^{1}H NMR (400 MHz, D_2O, ppm): 3.65 – 3.49 (m, 1H, residual Et_2O), 3.37 – 3.29 (m, 2H, CH_2 α to trithiocarbonate), 3.09 – 2.98 (m, 3H, CH_2 γ to trithiocarbonate), 2.9-2.5 region (t, <1H, residual unreacted starting material), 2.16 (dp, J = 15.0, 7.3 Hz, 2H, CH_2 β to trithiocarbonate), 2.08 (d, J = 1.0 Hz, 1H, residual Et_2O), 1.19 (td, J = 7.1, 1.0 Hz, 1H, residual ACN).

*2.2.19.4 Synthesis of first DOPE-based RAFT agent **(13)***



12 (0.130 g, 1.2 eq, 0.563 mmol) was suspended in acetone (10 mL) in a round-bottom flask, and the resulting solution was cooled with an ice bath. 15-crown 5-ether (0.248g, 2.4 eq, 1.13 mmol, 0.223 mL) was added dropwise to the suspension. **11** (0.413 g, 1 eq, 0.470 mmol) was solubilised in acetone (10 mL) and added dropwise to the reaction vessel. The reaction was left stirring for 6 hours, progress was monitored by ^{1}H NMR for shift of the triplet peak at 4.4 ppm to 4.2 ppm (CH-Br to CH-trithiocarbonate). Once completion was reached, the organic solvent was removed under reduced pressure, resulting in a yellow amorphous solid. The product was purified by multiple column chromatography separations by loading the samples on silica gel (pore size 60Å, 230-440 mesh, 0.040-0.063 mm), using different mobile phases (DCM:EtOAc 1:0 → 9:1; DCM:MeOH 1:0 → 9:1). The product **13** was isolated as a yellow, sticky solid (40 mg, <10% yield) with residual impurities.

^{1}H NMR (400 MHz, Chloroform-*d*): 7.74 (d, *J* = 53.5 Hz, 2H, NH), 5.36 – 5.31 (m, 5H, vinyl CHs), 5.30 (s, 4H, vinyl CHs, impurity), 4.70 (d, *J* = 7.5 Hz, 1H, CH α to carbonyl and trithiocarbonate), 4.41 (d, *J* = 11.5 Hz, 1H, CH α to carbonyl from impurity), 4.15 (d, *J* = 15.4 Hz, 1H, impurity), 3.91 (s, 7H, CH_2 glycerol product+impurity), 3.74 – 3.52 (m, 2H, CH_2OP ethanolamine), 3.31 (d, *J* = 12.8 Hz, 2H, CH_2N ethanolamine), 2.31 (ddt, *J* = 11.0, 8.1, 5.1 Hz, 7H, impurity), 2.16 (d, *J* = 9.3 Hz, 2H), 2.01 (p, *J* = 6.6 Hz, 16H, allylic CH_2 product+impurity), 1.58 (d, *J* = 10.8 Hz, 10H, impurity), 1.44 (d, *J* = 6.6 Hz, 2H, impurity), 1.28 (d, *J* =

11.9 Hz, 82H, alkyl chains product+impurity), 0.87 (t, J = 6.7 Hz, 11H, terminal CH_3 product+impurity).

2.2.20 Hydrophilic-lipophilic balance (HLB) calculation (Griffin)

HLB of the synthesised polymers was calculated as exemplified by Griffin[30,31]:

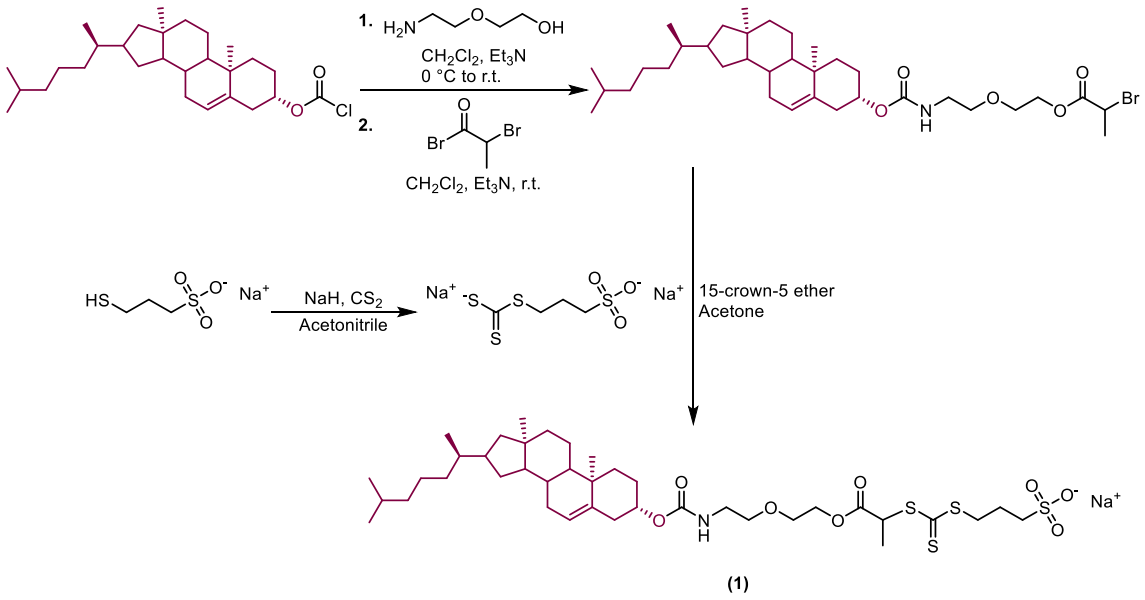
$$HLB = 20 \times \frac{MW_h}{MW}$$

Equation 3.1 Griffin HLB calculation. MWh represents the molecular weight of the hydrophilic portion of the molecule, while MW is the total molecular weight of the species.

Where MW_h is the molecular weight of the hydrophilic portion of the molecule, and MW is the total molecular weight of the molecule.

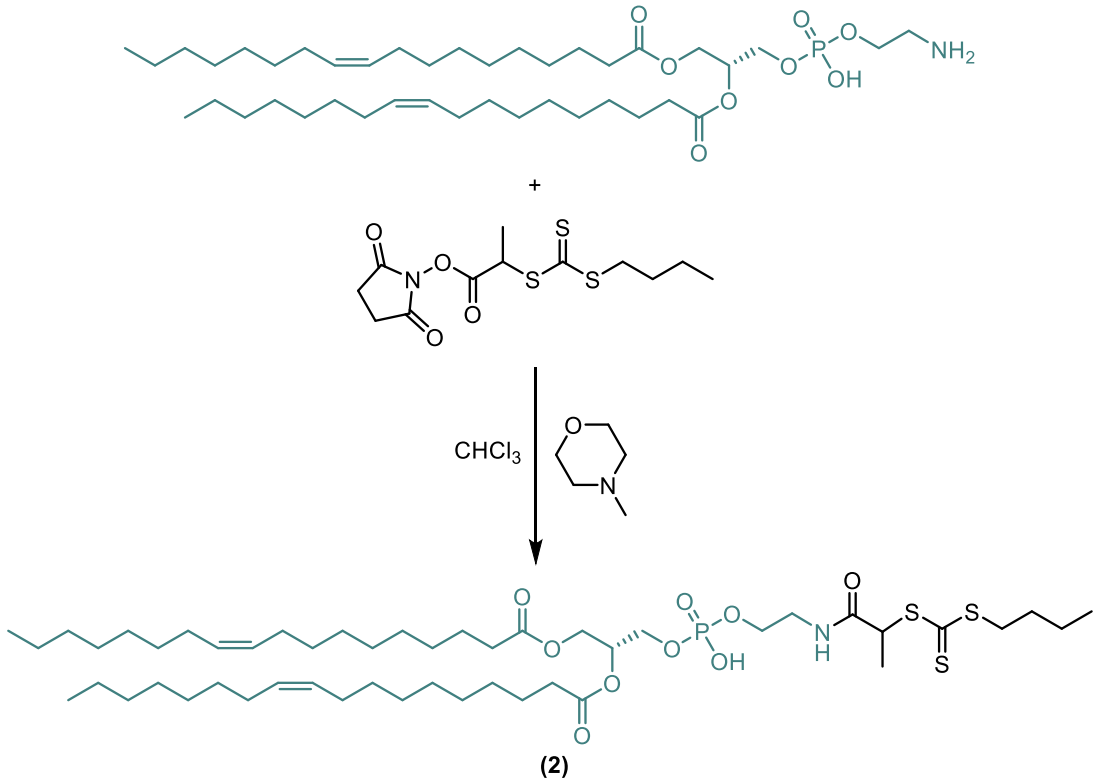
2.3 Results and Discussion

The first part of this work focussed on the synthesis of the RAFT agents required to synthesise the required membrane-inserting polymers. Previous research within our group[6] described the synthesis of a cholesterol-based RAFT agent **(1)**, which was used here to produce a library of polymers possessing a membrane-inserting cholesterol moiety at the α-chain end. The synthesis of **1** is depicted in **Scheme 2.1**.



Scheme 2.1 Synthesis of cholesterol-based RAFT agent (**1**), as described in published work by R. Catania et al.

Additionally, a GPI-mimicking, 1,2-dioleoyl-*sn*-glycero-3-phosphoethanolamine (DOPE)-based RAFT agent was also synthesised **(2)** and this was used to produce a second family of membrane-binding, amphiphilic polymers, bearing a membrane-inserting phospholipid with two monounsaturated hydrocarbon groups at one of the polymer chain-ends (**Scheme 2.2**).



Scheme 2.2 Synthetic scheme of the DOPE-based RAFT agent (**2**).

Finally, propanoic acid-2-[[(butylthio)thioxomethyl]thio]-carbonate (PABTC) RAFT agent **(3)** (structure shown in **Figure 2.1**) was used to synthesise a library of control polymers, identical to those described above except for the absence of membrane–inserting chain-end groups

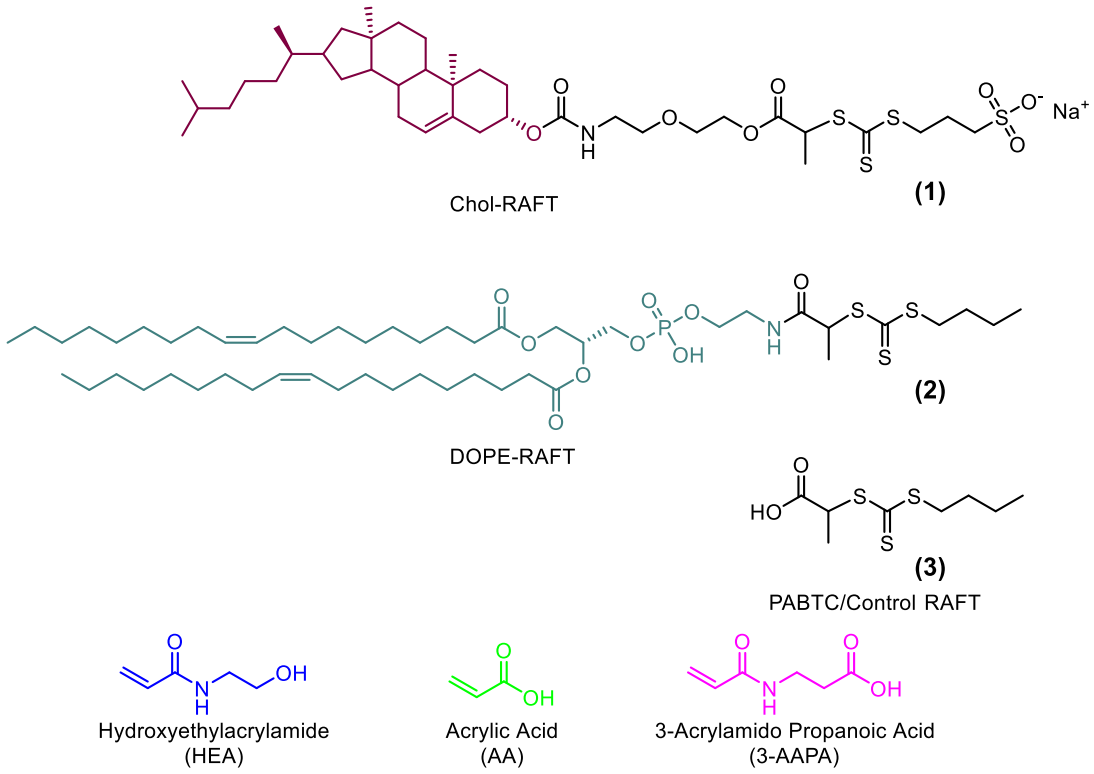


Figure 2.1 Main RAFT agents and monomers employed in this study. Cholesterol-based RAFT agent **(1)**; and DOPE-based RAFT agent **(2)**; non membrane-inserting PABTC RAFT agent **(3)**; monomers used: HEA is a neutral, hydrophilic monomer used to synthesise hydrophilic (co)polymers; AA is monomer containing an acid functionality which potentially allows interaction with basic drugs; 3-AAPA is also an acid monomer, with a spacer between the polymerisable acrylamide moiety and the carboxylic acid group.

The monomers chosen for this study are shown in **Figure 2.1**. Hydroxyethyl acrylamide (HEA) was chosen for its hydrophilicity, often used to synthesise hydrophilic and biocompatible polymers [7]. Being an acrylamide, this monomer is particularly suited for ultrafast, high conversion RAFT polymerisation where control over the molecular weight, molecular weight dispersity Đ and chain-end fidelity can be maintained even at virtually quantitative monomer conversion[2]. This is possible due to acrylamide monomers having a high rate of propagation (k_p) under radical polymerisation conditions especially in water[8], thus allowing for rapid polymerisation[9].

In **Chapter 1**, we discussed the formation of acid-base pairs between acidic polymers and basic drugs as a means for encapsulation and drug release. To introduce the acidic side-chains required to potentially bind basic groups in drug molecules through electrostatic interactions[10], two different acid monomers were

selected: 3-acrylamido propanoic acid (3-AAPA, **4**) and the more hydrophilic acrylic acid (AA). The two different acid monomers have similar reported pK_a (4.2 for AA[11] and 4.4 for 3-AAPA[12]); however, for an AA-based polymers the acid functionality is closer to the polymer backbone. One could hypothesise that the reduced distance between the acid functionalities and the polymer backbone in AA-based polymers could potentially prevent the formation of ionic interactions with drug molecules, while introducing a spacer between the polymer backbone and the acid functionality in polymer synthesised from monomer **4** could make such acid functionalities more accessible and therefore potentially aid complexation of (macro)molecules containing basic functionalities. Although their different reactivity ratios may result in non-fully stochastic distribution of different repeating units along the polymer chains, random radical copolymerisation of acrylamides and acrylic acid yielding polymers with well controlled composition and narrow distribution has been reported previously [13,14], so these monomers were chosen for our study.

2.3.1 Synthesis of 1,2-dioleoyl-sn-glycero-3-phosphoethanolamine (DOPE)-based RAFT agent (2) and 3-acrylamido propanoic acid monomer (3-AAPA)

The initial strategy chosen for the synthesis of DOPE RAFT agent was based on the approach previously employed for the synthesis of **(1)**. This convergent synthetic procedure consisted of building two separate blocks (lipophilic two tailed lipid and hydrophilic trithiocarbonate salt) and joining them together in a final step (**Scheme 2.3**).

The first block was synthesised by converting DOPE into an α-bromo propionamide, obtained by conjugation with the reactive N-hydroxysuccinimide adduct (**10**) of 2- bromopropyonyl bromide. However, whilst ^{1}H NMR spectroscopy confirmed that in the crude product the desired DOPE α-bromo propionamide was

indeed present based on the presence of the characteristic amide peak at 8.8 ppm (**Figure 2.2**), its purification by flash chromatography was found to be particularly challenging, due to the presence of impurities with very similar polarity. Therefore, we were not able to fully purify the product; we decided to employ the partially purified product in the successive step as the unreacted DOPE would not have been capable of forming an adduct with **12**.

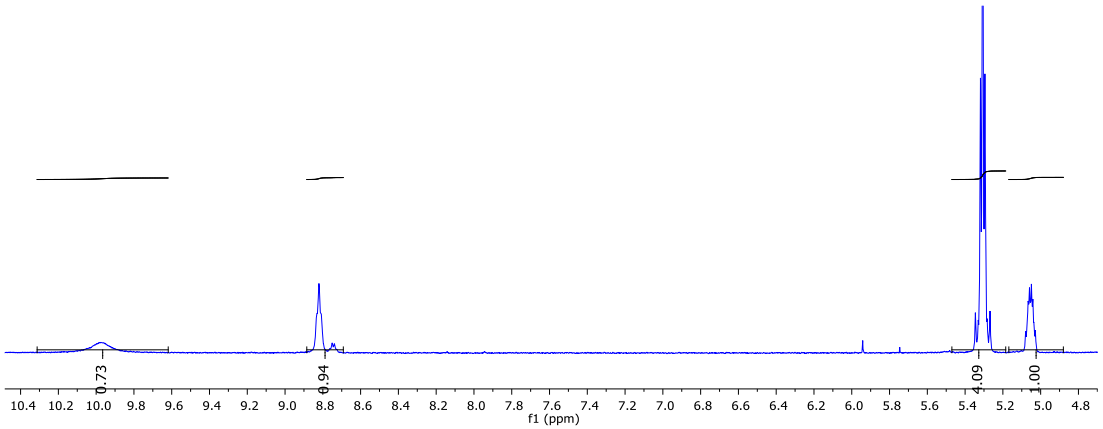
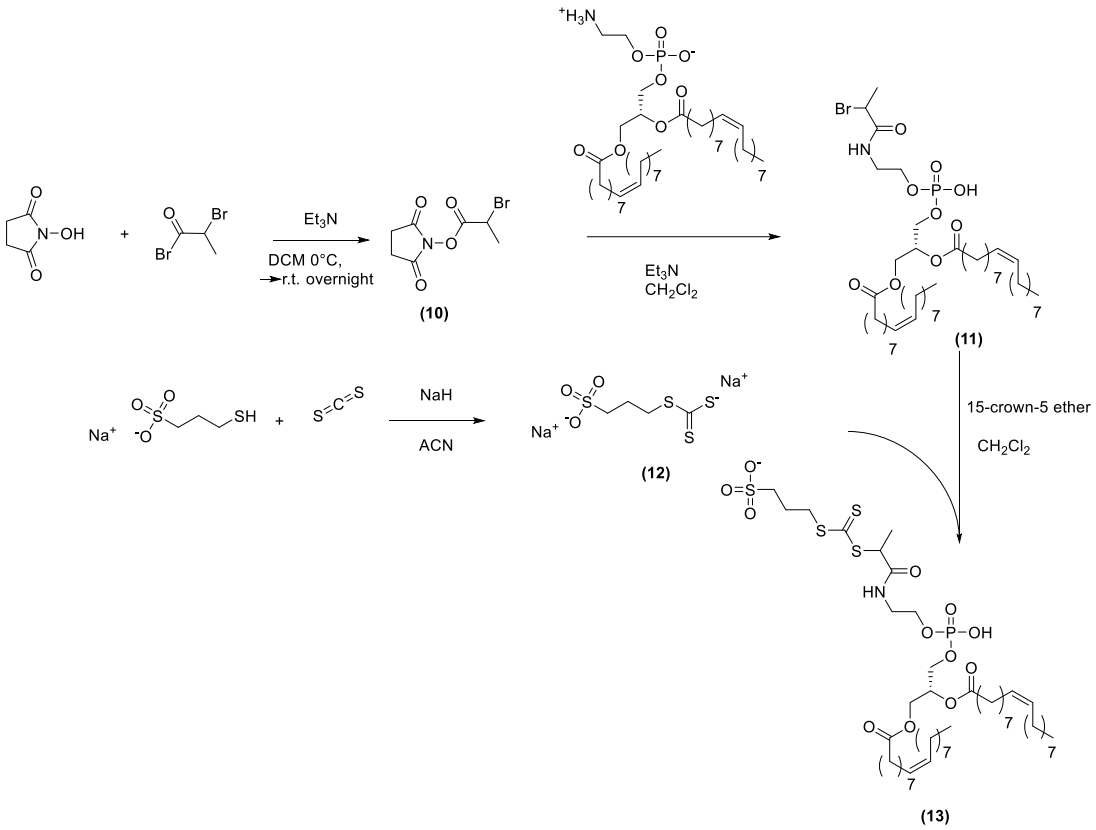


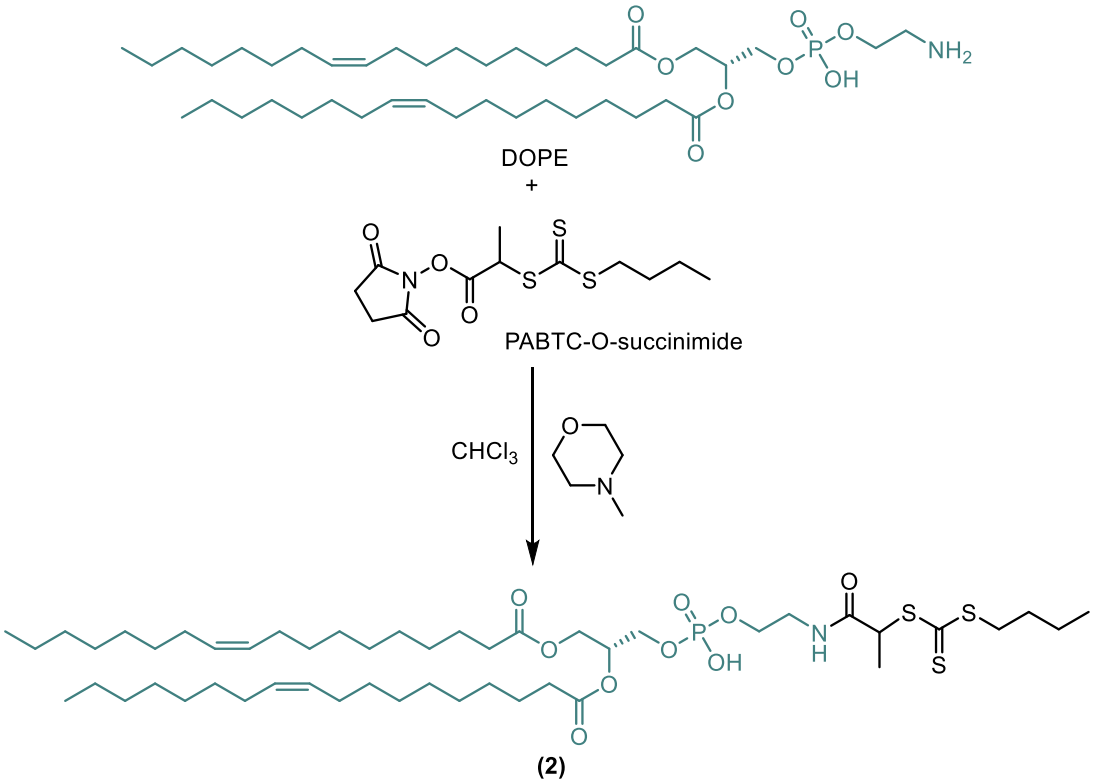
Figure 2.2 Detail of the diagnostic peaks for the formation of **11**: 9.97 (s, 1H, P-OH), 8.82 (t, J = 5.0 Hz, 1H, NH), 5.47 – 5.18 (m, 4H, vinyl CHs), 5.17 – 4.88 (m, 1H, CH glycerol moiety)

In parallel, the required trithiocarbonate salt (**12**) was synthesised by conjugating 3-mercapto 1-propanesulfonate and carbon disulfide in basic conditions, and purified by precipitation of the product in diethyl ether and successive filtration. . The two products (**11** and **12**) were then reacted to form the desired DOPE-based membrane-inserting RAFT agent (**13**). Due to the difference in polarity between relatively hydrophobic **11** and very hydrophilic **12**, a solvent which could dissolve both starting materials could not be identified. Thus 15-crown-5 ether was used to complex the two Na^+ counterions of **12**, and increase its solubility in dichloromethane, which was used as the reaction solvent. However, complete removal of 15-crown-5 ether from the final DOPE RAFT agent **(13)** was proven to be difficult, even after repeated purifications by ion exchange chromatography and flash chromatography on silica .



Scheme 2.3 First successful synthetic scheme of DOPE-based RAFT agent.

Due to the challenging purification of the final DOPE RAFT agent **(13)** and corresponding intermediates through this first synthetic pathway, a different synthetic route was identified, to produce the structurally similar RAFT agent **2**. Accordingly, 1,2-dioleoyl-sn-glycero-3-phosphoethanolamine (DOPE) was then directly coupled with propanoic acid-2-[[(butylthio)thioxomethyl]thio]-carbonate (PABTC-*O*-succinimidyl ester at room temperature for 7 days to give the desired RAFT agent (**2**) in 53% yield (**Scheme 2.4**).



Scheme 2.4 Synthesis of DOPE-based RAFT agent **(2).**

Accordingly, the synthesis of **2** was therefore carried out by conjugating the primary amine of 1,2-dioleoyl-sn-glycero-3-phosphoethanolamine (DOPE) with the activate acyl group of the N-hydroxysuccinimide (NHS) ester of PABTC[15]. NHS esters are routinely used in peptide synthesis to form new amide bonds[16], and we chose this approach to selectively acylate the amine without causing aminolysis of the trithiocarbonate group of PABTC. The presence of a good leaving group, NHS, allows for selectivity for the ester group of PABTC over the trithiocarbonate moiety and improves the reactivity of PABTC, thus increasing the conversion to **2**. This was fundamental for the success of the reaction, as a higher conversion removed the need for column chromatography that would have been otherwise necessary to remove any unreacted DOPE. A non-nucleophilic base (*N*-methyl morpholine) was chosen as an acid scavenger (reported pKa of *N*-hydroxysuccinimide in water is 6.0[17]). Additionally, tertiary amines do not cause aminolysis of the trithiocarbonate group[18–20], which is key to maintain the integrity of the RAFT agent[21].

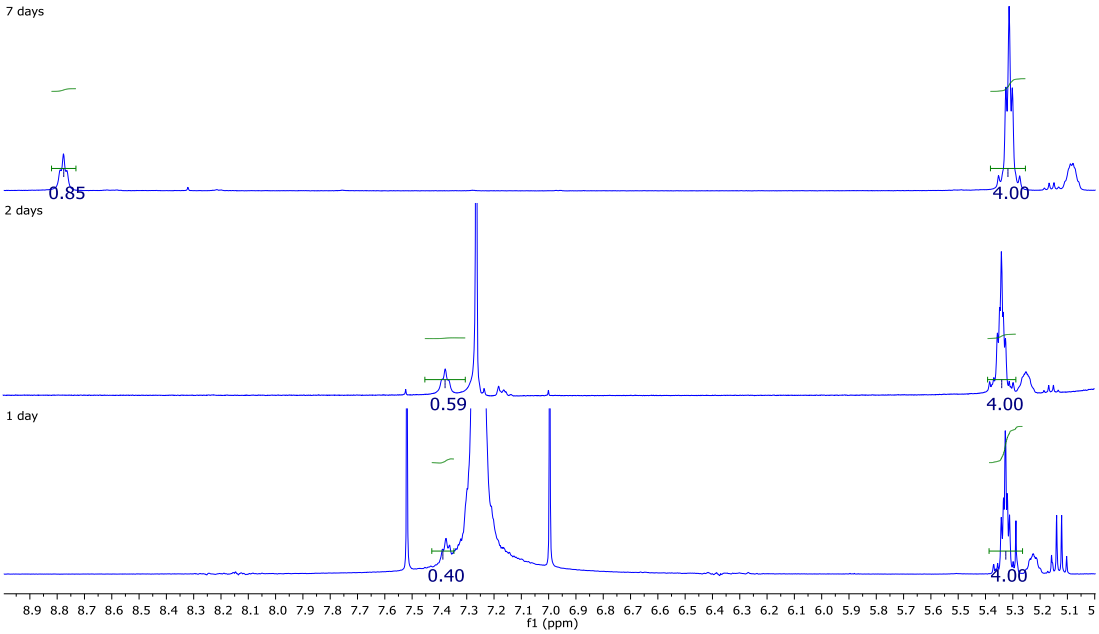
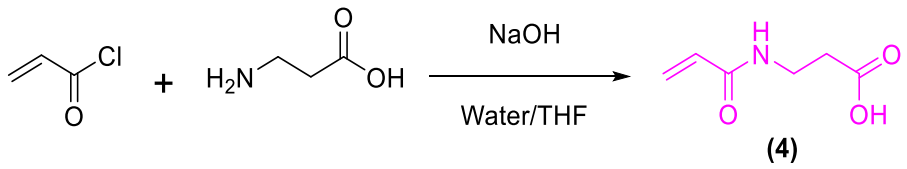


Figure 2.3 ^{1}H NMR showing the reaction progression for the synthesis of **2**. The reaction was monitored through the appearance of the amide signal at 8.77 ppm (or 7.38 ppm in $CDCl_3$), comparing the integration of this peak to the internal reference vinyl CH peak at 5.31 ppm.

The reaction was monitored by ^{1}H NMR, by following the increase of the amide NH signal at 8.77 ppm (or 7.38 ppm in $CDCl_3$), compared the integration of this peak to the vinyl CH peak at 5.31 ppm, which does not change during this reaction and therefore can be used as an internal reference (**Figure 2.3**).

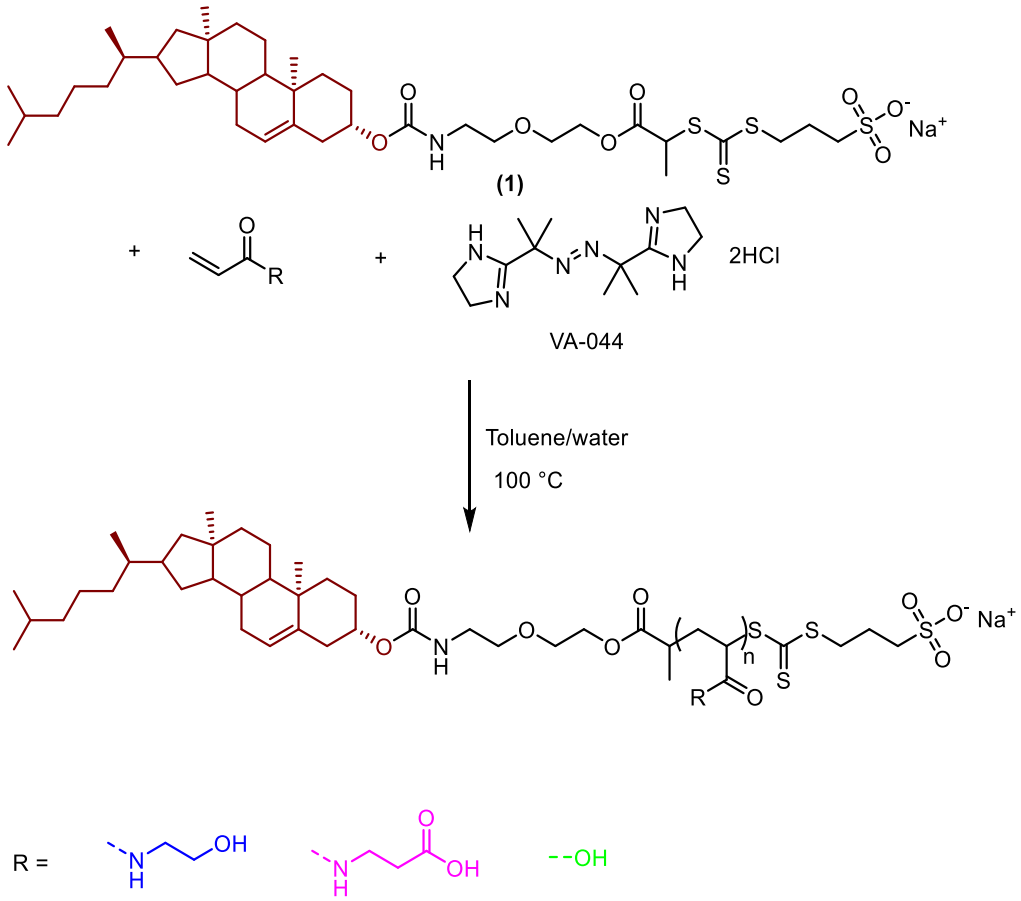


Scheme 2.5 Synthesis of 3-acrylamido propanoic acid **(4)** monomer from β-alanine.

The procedure for the synthesis of the required 3-acrylamido propanoic acid (3-AAPA, **4**, **Scheme 2.5**) monomer was adapted from previous literature[22,23], and was performed by utilising the classical Schotten-Baumann reaction[24,25], where sodium hydroxide is used to neutralise the HCl produced during the reaction[26], which would otherwise protonate the basic primary amine on the β-alanine, decreasing the yield. To avoid reacting OH^- with the acyl halide, a biphasic system is used, H_2O/THF in this example. THF and water are normally miscible with each

other, however two phases can be formed when additional species are dissolved in one or both these two solvents[27,28]. In this process neutralisation of the generated HCl is believed to occur at the interface between the two phases[26].

2.3.2 Synthesis of membrane inserting (co)polymers employed in this study



Scheme 2.6 Synthesis of cholesterol-terminated polymers by biphasic ultrafast RAFT polymerisation, starting from cholesterol-containing RAFT agent **(1)** and N-hydroxyethyl acrylamide (HEA, blue), 3-acrylamido propanoic acid (3-AAPA, **4**, violet) and acrylic acid (AA, green).

In order to produce the first library of membrane-interacting polymers, we first synthesised (co)polymers with cholesterol alpha chain ends (**Scheme 2.6**), based on the cholesterol RAFT agent **1**. Due to the amphiphilic nature of the RAFT agent **1**, mostly dictated by the very hydrophobic nature of cholesterol, the very polar conditions required for ultrafast polymerisation described by Perrier *et al.*[9] could not be directly employed. Therefore, we utilised the polymerisation conditions previously developed by our group[6] which employ a biphasic toluene/water system. The cholesterol RAFT agent **(1)** is designed to include a very polar trithiocarbonate head, and therefore sits at the interface between the two phases, with the hydrophobic cholesterol in toluene and the hydrophilic head in the water phase. As a result, polymerisation will occur in the aqueous phase – monomers

and radical azoinitiator VA044 are water-soluble - as required by the Perrier protocol, while cholesterol moieties will remain fully solvated due to the presence of the hydrophobic toluene phase (**Figure 2.4**). The cholesterol-terminated (co)polymers produced as well as their DP, monomer ratios, dispersity determined via SEC and number-average molecular weight determined by ^{1}H NMR are listed in **Table 2.7**. We synthesised two different classes of cholesterol-based polymers, targeting DP = 50 and 100. The chosen conditions allowed for the production of cholesterol-terminated (co)polymers with narrow dispersity ($Đ$<1.25).

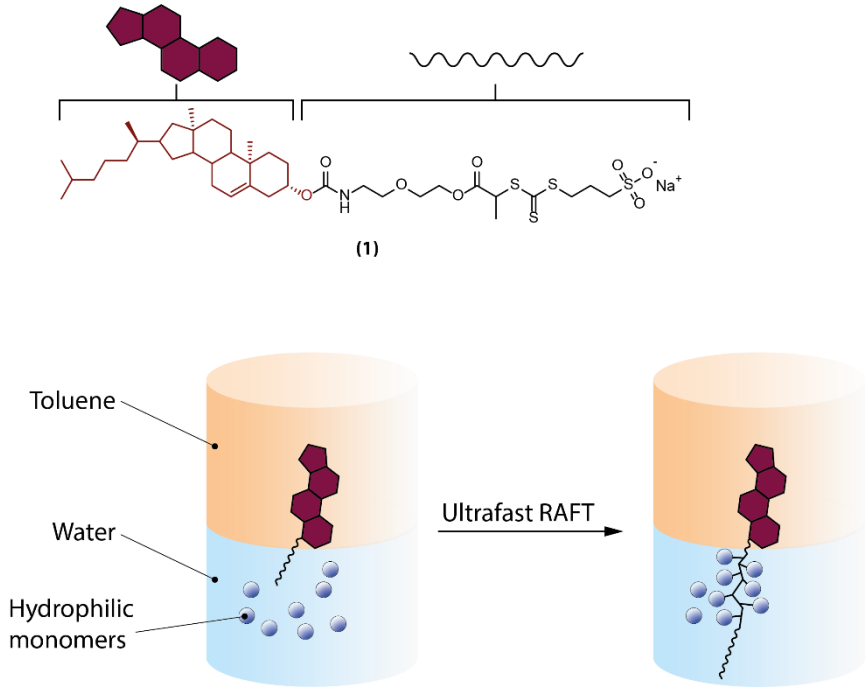
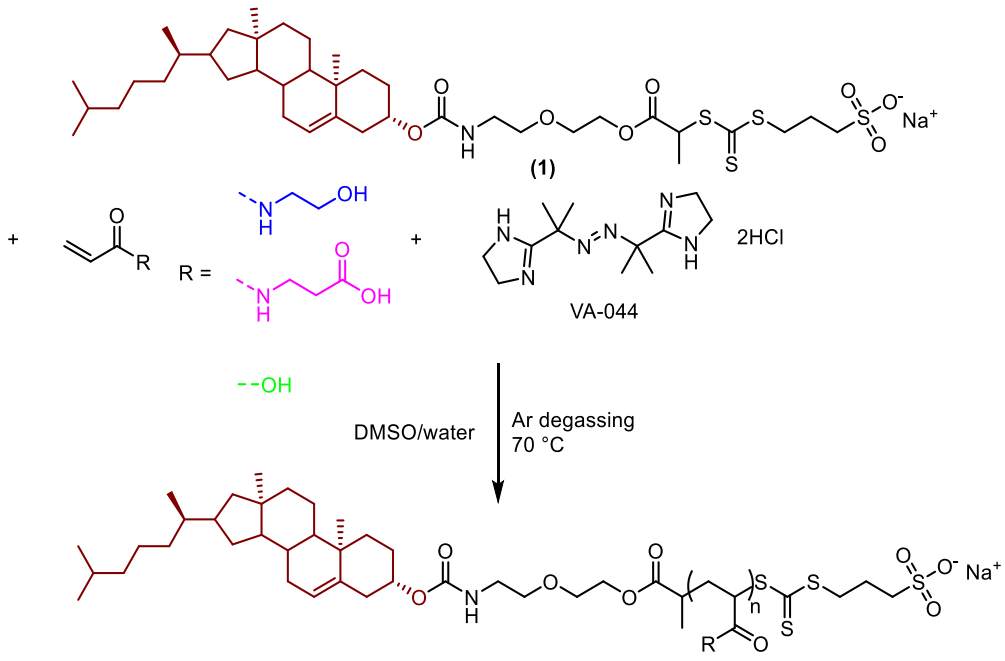


Figure 2.4 Representation of a RAFT polymerisation conducted in a two-phase system, employing the amphiphilic cholesterol RAFT agent **1**, showing the polymer growth occurring at the interface between the two phases.

Interestingly, we observed that whilst these ultrafast biphasic polymerisation conditions allowed for the controlled polymerisation of hydroxyethyl acrylamide (HEA) and 3-acrylamido propanoic acid (AAPA), they were not equally efficient for the synthesis of acrylic acid (AA)-based copolymers and homopolymers. Syntheses of AA-based copolymers required multiple (up to 5) additions of the initiator before the polymerisation started, and the resulting polymers (especially homopolymers) showed a lower degree of control on monomer conversion (targeted DP = 100, final DP = 163). This could be explained in terms of by high concentrations of an acid monomer, which could have hydrolysed the RAFT agent

carbamate and ester groups. Aprotic solvents as DMSO make sure that the AA is not in its ionised form, which negatively impacts the polymerisation reaction[13]. Therefore, for the synthesis of AA-containing polymers we decided to employ an aprotic solvent (DMSO) which is capable of solubilising the differently polar reagents involved. As the VA-044 radical initiator is poorly soluble in DMSO, we selected a 4:1 ratio (DMSO:water) to ensure full solubility of the initiator, while still employing a relatively low proportion of water to ensure sufficient solvation of the RAFT agent **(1)**. These reaction conditions (**Scheme 2.7**) were adapted from the setup designed by Gurnani *et al.*[29] for the synthesis of HEA/N-acryloyl morpholine based polymers in mild environments. To increase monomer conversion, especially with acrylic acid, we increased the reaction time to 2 hours, while setting the temperature at 70 °C to avoid full decomposition of the initiator before reaction completion[30]. This allowed the initiator to produce radicals throughout the whole reaction, thus decreasing the irreversible termination events.



Scheme 2.7 Synthesis of membrane-inserting cholesterol-terminated polymers by single-phase RAFT polymerisation, starting from cholesterol-containing RAFT agent **(1)** and N-hydroxyethyl acrylamide (HEA, blue), 3-acrylamido propanoic acid (3-AAPA, **4**, violet) and acrylic acid (AA, green).

Changing these conditions from the initial biphasic toluene/water RAFT polymerisation conditions still yielded materials with low dispersity ($Đ$ < 1.25) and precise control over the polymer composition, as shown in **Table 2.7**.

Table 2.7 Cholesterol-based (co)polymers produced in this study.

Code	DP[a]	HEA[b]	AAPA[b]	AA[b]	$Đ$[c]	$M_{n\ (NMR)}$ (kDa)
Chol-[(HEA)$_{100\%}$]$_{108}$*	108	108	-	-	1.07	13.5
Chol-[(HEA)$_{90\%}$-*r*-(AAPA)$_{10\%}$]$_{140}$*	140	126	14	-	1.10	17.6
Chol-[(AA)$_{100\%}$]$_{163}$*	163	-	-	163	1.21	12.8
Chol-[(HEA)$_{90\%}$-*r*-(AA)$_{10\%}$]$_{105}$‡	105	94	-	11	1.20	12.7
Chol-[(HEA)$_{70\%}$-*r*-(AA)$_{30\%}$]$_{94}$‡	94	75	-	19	1.18	11.1
Chol-[(HEA)$_{100\%}$]$_{52}$‡	52	52	-	-	1.14	7.0
Chol-[(HEA)$_{90\%}$-*r*-(AAPA)$_{10\%}$]$_{50}$‡	50	45	5	-	1.23	6.9
Chol-[(AA)$_{100\%}$]$_{54}$‡	54	-	-	54	1.13	4.9
Chol-[(HEA)$_{90\%}$-*r*-(AA)$_{10\%}$]$_{51}$*	51	46	-	5	1.19	6.7
Chol-[(HEA)$_{70\%}$-*r*-(AA)$_{30\%}$]$_{52}$*	52	37	-	15	1.18	6.4
Chol-[(HEA)$_{50\%}$-*r*-(AA)$_{50\%}$]$_{70}$*	70	35	-	35	1.14	7.6

[a] Degree of polymerisation (DP), estimated by ^{1}H NMR (see materials and methods). [b] HEA = hydroxyethyl acrylamide, AAPA 3-acrylamido propanoic acid, AA = acrylic acid. [c] Molecular weight dispersity (M_w/M_n, Đ) was estimated by SEC (see materials and methods). * Polymer was synthesised in a two-phase system. ‡ Polymer was synthesised in a single-phase system

Polymer composition was confirmed through ^{1}H NMR by integrating characteristic peaks generated by the different monomers, as highlighted in **Figure 2.5**.

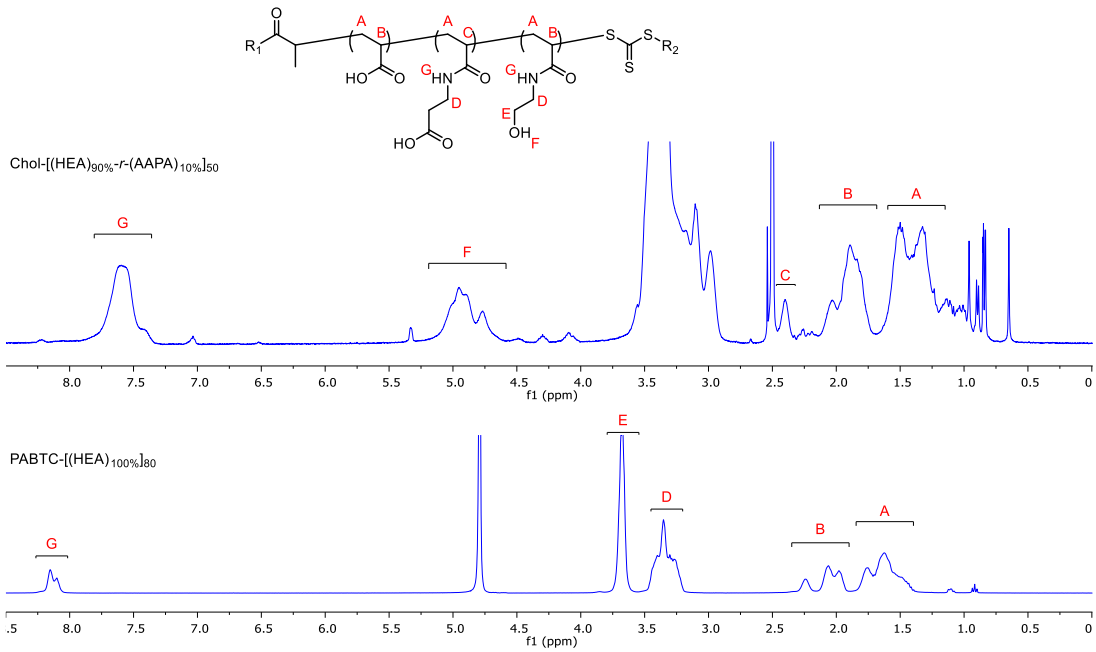
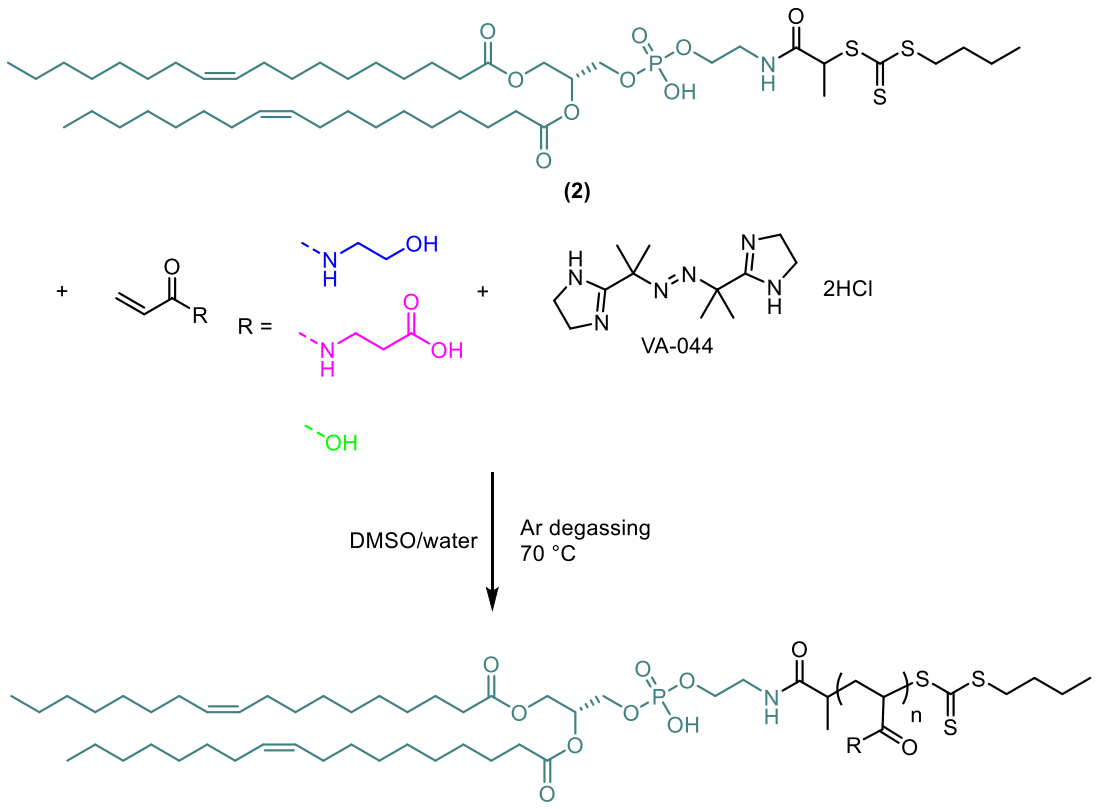


Figure 2.5 ^{1}H NMR peaks monitored to confirm polymer composition in synthesised polymers. Shifts in ppm and appearance of specific peaks (-OH and -NH) dependant on the dispersant selected for the ^{1}H NMR analysis (D_2O and DMSO-d_6)



Scheme 2.8 Synthesis of DOPE-terminated polymers by single-phase RAFT polymerisation, starting from DOPE-containing RAFT agent **(2)** and N-hydroxyethyl acrylamide (HEA, blue), 3-acrylamido propanoic acid (3-AAPA, **4**, violet) and acrylic acid (AA, green).

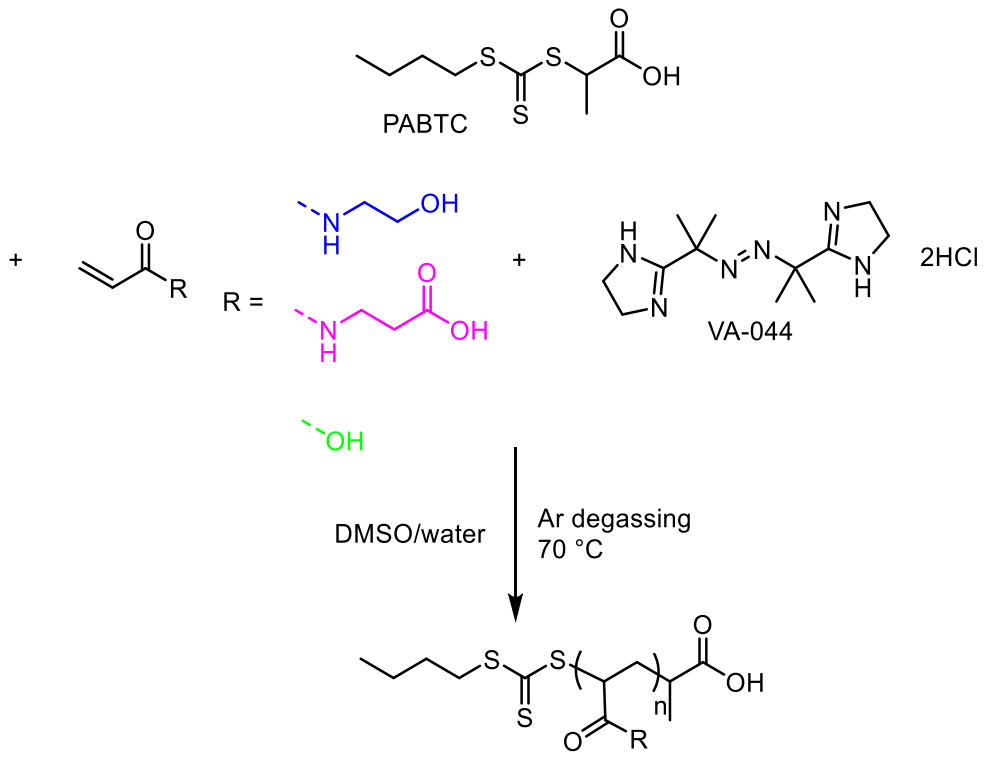
For the synthesis of 1,2-dioleoyl-sn-glycero-3-phosphoethanolamine (DOPE)-containing polymers, we decided to directly employ the reaction conditions analogous to those already developed for the cholesterol-containing materials were utilised (**Scheme 2.8**). As per the cholesterol-terminated (co)polymer, this yielded polymers with low dispersity ($Đ$ < 1.25, except for DOPE-[$(HEA)_{50\%}$-*r*-$(AA)_{50\%}]_{50}$), and precise control over repeating unit composition. Here we focused on a smaller library due to the limited amount of **2** RAFT agent available (~ 400 mg), whose synthesis involved an expensive starting material (1,2-dioleoyl-sn-glycero-3-phosphoethanolamine). Accordingly, DOPE-terminated materials were prepared aiming to DP 50 and 100, with HEA and AA homopolymers, and HEA-AA copolymers (**Table 2.8**).

Table 2.8 DOPE-based (co)polymers produced in this study.

Code	DP[a]	HEA[b]	AAPA[b]	AA[b]	$Đ$[c]	$M_{n\ (NMR)}$ (kDa)
DOPE-$[(HEA)_{100\%}]_{47}$	47	47	-	-	1.20	6.4
DOPE-$[(HEA)_{100\%}]_{80}$	80	80	-	-	1.11	10.2
DOPE-$[(HEA)_{50\%}$-*r*-$(AA)_{50\%}]_{50}$	50	21	-	29	1.43	5.5
DOPE-$[(HEA)_{90\%}$-*r*-$(AA)_{10\%}]_{30}$	30	27	3	-	1.12	4.5
DOPE-$[(AA)_{100\%}]_{42}$	42	-	-	42	1.04	4.0

[a] Degree of polymerisation (DP), calculated by ^{1}H NMR (see materials and methods). [b] HEA = hydroxyethyl acrylamide, AAPA 3-acrylamido propanoic acid, AA = acrylic acid. [c] Molecular weight dispersity (Mw/Mn, Đ) was determined by SEC (see materials and methods).

2.3.3 Synthesis of non-membrane-inserting control (co)polymers.



Scheme 2.9 Synthesis of control polymers by single-phase RAFT polymerisation, starting from PABTC RAFT agent **(3)** and N-hydroxyethyl acrylamide (HEA, blue), 3-acrylamido propanoic acid (3-AAPA, **4**, violet) and acrylic acid (AA, green).

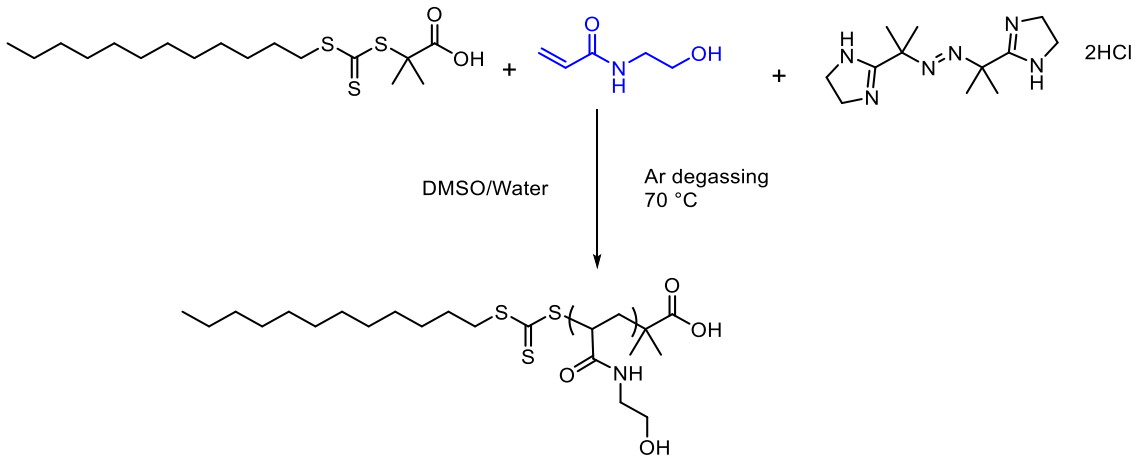
To produce the "control" polymers, unable to insert into bilayer membranes, PABTC was chosen as the RAFT agent. PABTC possesses a short hydrophobic butyl chain, which however was deemed to be too short to enable significant insertion of the corresponding (co)polymers into lipid bilayers. This initial hypothesis was then confirmed in subsequent membrane-inserting experiments (**Chapter 3**). Due to its good solubility in DMSO:water, this single phase polymerisation medium was chosen for the synthesis of the corresponding control (co)polymers, yielding polymers with low dispersity ($Đ$ < 1.30, **Table 2.9**).

Table 2.9 PABTC-based polymers produced in this study.

Code	DP[a]	HEA[b]	AAPA[b]	AA[b]	$Đ$[c]	$M_{n\ (NMR)}$ kDa
PABTC-[(HEA)$_{100\%}$]$_{80}$	80	80	-	-	1.24	9.5
PABTC-[(HEA)$_{90\%}$-*r*-(AAPA)$_{10\%}$]$_{81}$	81	73	8	-	1.16	9.8
PABTC-[(AA)$_{100\%}$]$_{140}$	140	-	-	140	1.23	10.4
PABTC-[(HEA)$_{90\%}$-*r*-(AA)$_{10\%}$]$_{75}$	75	70	-	≈ 5	1.15	8.6
PABTC-[(HEA)$_{70\%}$-*r*-(AA)$_{30\%}$]$_{80}$	80	67	-	13	1.28	8.9
PABTC-[(HEA)$_{100\%}$]$_{50}$	50	50	-	-	1.29	6.0
PABTC-[(HEA)$_{90\%}$-*r*-(AAPA)$_{10\%}$]$_{46}$	46	39	7	-	1.15	5.7
PABTC-[(AA)$_{100\%}$]$_{37}$	37	-	-	37	1.05	2.9
PABTC-[(HEA)$_{90\%}$-*r*-(AA)$_{10\%}$]$_{45}$	45	40	-	5	1.11	5.2
PABTC-[(HEA)$_{70\%}$-*r*-(AA)$_{30\%}$]$_{44}$	44	31	-	13	1.07	4.7
PABTC-[(HEA)$_{50\%}$-*r*-(AA)$_{50\%}$]$_{49}$	49	25	-	24	1.12	4.8

[a] Degree of polymerisation (DP), calculated by ^{1}H NMR (see materials and methods). [b] HEA = hydroxyethyl acrylamide, AAPA 3-acrylamido propanoic acid, AA = acrylic acid. [c] Molecular weight dispersity (M_w/M_n, $Đ$) was determined by SEC (see materials and methods).

An additional "control" polymer based on 2-(dodecylthiocarbonothioylthio)-2-methylpropionic acid (DDMAT) was synthesised (**Scheme 2.10**). This RAFT agent



Scheme 2.10 Synthesis of DDMAT-[(HEA)$_{100\%}$]$_{42}$, starting from DDMAT and N-hydroxyethyl acrylamide (HEA)

is structurally very similar to PABTC, except for a second methyl group α to the carboxylic acid and a longer alkyl chain bound to the trithiocarbonate group (12C instead of 4C).

This polymer was synthesised to further expand the control polymer library with a small increase in lipophilicity on the PABTC-based polymers. Due to the good solubility of DDMAT in DMSO:water, this single-phase polymerisation medium was chosen for the synthesis of the corresponding polymer, resulting in a low dispersity value (*Đ* = 1.05, **Table 2.10**).

Table 2.10 DDMAT-[$(HEA)_{100\%}]_{42}$: composition and characterisation.

Code	DP[a]	HEA[b]	AAPA[b]	AA[b]	*Đ*[c]	$M_{n\ (NMR)}$ kDa
DDMAT-[$(HEA)_{100\%}]_{42}$	42	42	-	-	1.05	5.5

[a] Degree of polymerisation (DP), calculated by ^{1}H NMR (see materials and methods). [b] HEA = hydroxyethyl acrylamide, AAPA 3-acrylamido propanoic acid, AA = acrylic acid. [c] Molecular weight dispersity (M_w/M_n, Đ) was determined by SEC (see materials and methods).

2.3.4 Membrane-inserting polymers with alternative structures: membrane-inserting repeating units.

The polymerisation reactions previously described produced different classes of (co) polymers for *in vitro* testing. However, the lipophilic content in each amphiphilic polymer is strictly defined by the alpha-end of the RAFT agent that mediated the polymerisation reaction. Therefore, a different class of polymers was synthesised, whose lipophilic content could be tuned through the introduction of a lipophilic monomer. For the synthesis of the required membrane-inserting materials, we synthesised diblock copolymers possessing a short block containing potentially membrane-inserting palmitoyl side-chains, and a second, longer,

hydrophilic block. Accordingly, the synthesis of the required block copolymers was carried out in 2 successive steps (**Figure 2.6**).

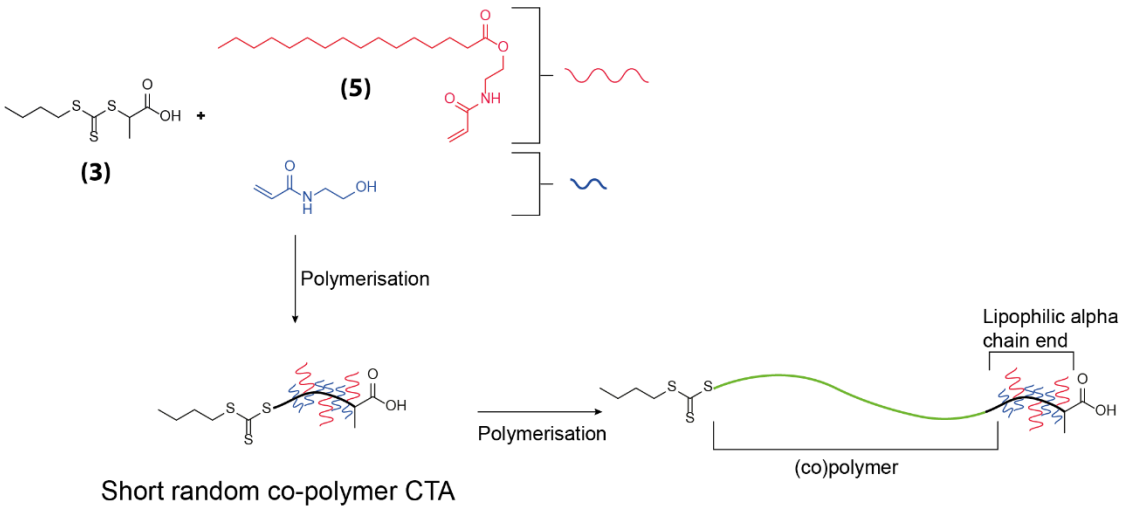
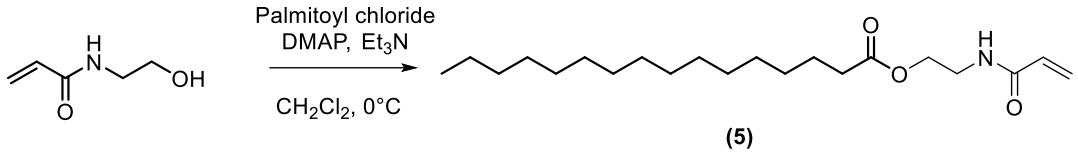


Figure 2.6 Schematic of the lipid monomer approach to producing amphiphilic polymers with tunable lipid content.

For this purpose, we synthesised a lipid monomer based on palmitoyl chloride, 2-AP **(5)** to introduce lipophilic, potentially membrane-inserting, repeating units on the polymer chain.

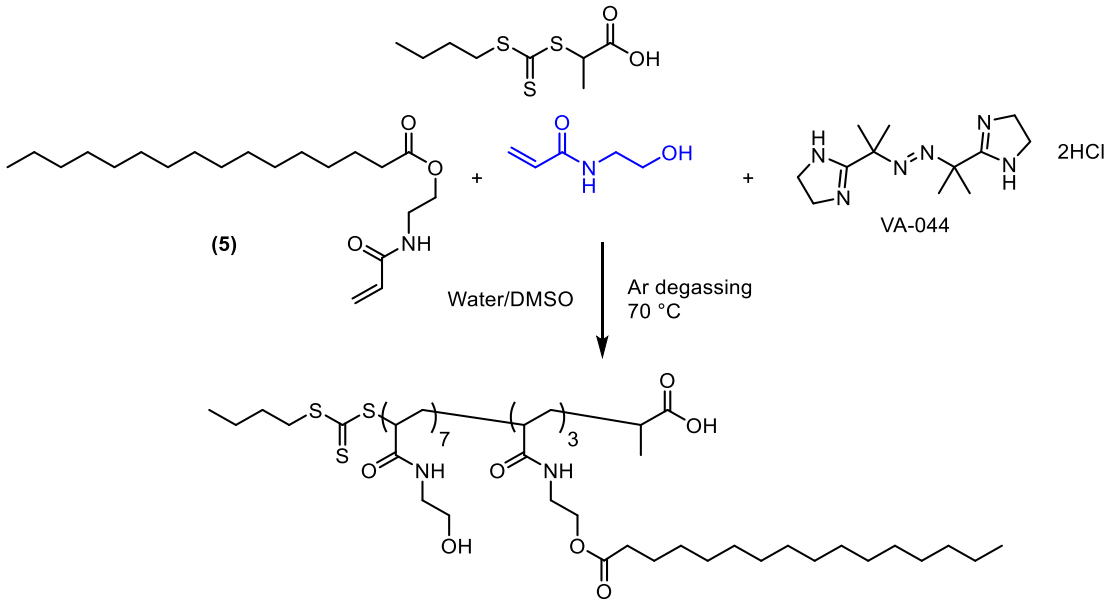


Scheme 2.11 Synthesis of hydrophilic 2-acrylamido palmitate monomer **(5).**

To this aim, the *N*-substituted acrylamide monomer **(5)** – acrylamides typically have high k_p values[2] which makes them suitable for rapid and well-controlled RAFT polymerisation – containing a long fatty acid derived chain, was synthesised. The reaction involved a condensation between 2-hydroxyethyl acrylamide and palmitoyl chloride, using triethylamine as the acid scavenger, and DMAP, an organocatalyst, to increase the reactivity of palmitoyl chloride which could

otherwise be relatively low due to steric hindrance provided by its long alkyl chain (**Scheme 2.11**).

First, a very short (target DP=10) hydrophobic "block" containing the lipophilic monomer 2-acrylamidoethyl palmitate (2-AP) and HEA at a 3:7 mol:mol ratio, respectively, was produced (**Scheme 2.12**), with the aim to use it as a macro RAFT agent which could then be elongated with the hydrophilic/acid monomers, to give block copolymers with general formula [**(5)**$_{30\%}$-*r*-(HEA)$_{70\%}$]$_{10}$-*b*-(M)$_z$.



Scheme 2.12 Single-phase, polymerisation of the lipophilic macroCTA based on the lipid monomer **5.**

Similarly to the cholesterol and DOPE-containing polymers previously described, these polymers would possess a large hydrophobic group close to one of the two polymer chain ends, which could potentially allow for their interaction/insertion into lipid bilayers. The first block included a proportion of HEA due to the large molecular size of 2-acrylamido palmitate monomer **(5)** which would make it difficult to homopolymerize it in a controlled manner. Inclusion of a proportion (70%) of a smaller acrylamide monomer, HEA, allowed to partially address this issue, generating a first [**(5)**$_{30\%}$-*r*-(HEA)$_{70\%}$]$_{10}$ block, with non-ideal control over the average molar mass and molecular weight distribution ($Đ$ = 1.80). PABTC was chosen as the RAFT agent, as it allows to control the polymerisation of both

acrylates and acrylamides, and does not possess large lipid moieties that would interfere with subsequent membrane binding experiments.

Table 2.11 Fractions of the **(5)**-HEA macro RAFT agent purified by SiO_2 flash chromatography

Code	DP[a]	HEA[b]	**(5)**[b]	$Đ$[c]	$M_{n\ (NMR)}$ kDa
Fraction A [**(5)**$_{30\%}$-*r*-(HEA)$_{70\%}$]$_{10}$	10	7	3	1.88	2.10
Fraction B [**(5)**$_{5\%}$-*r*-(HEA)$_{95\%}$]$_{20}$	20	19	1	1.84	2.78

[a] Degree of polymerisation (DP), calculated by ^{1}H NMR (see materials and methods). [b] HEA = hydroxyethyl acrylamide, **(5)** 2-acrylamido palmitate. [c] Molecular weight dispersity (Mw/Mn, $Đ$) was determined by SEC (see materials and methods).

Given the intrinsically random nature of this radical co-polymerisation, the polymer produced in this step consisted on a mixture of oligomers with different relative content in 2-AP. To obtain materials with better defined average content of palmitoyl side-chains, these oligomers were fractionated by SiO_2 flash chromatography using DCM:MeOH 1:0 → 9:1 as the mobile phase. The different fractions (**Table 2.11** and **Figure 2.7** for ^{1}H NMR peak assignments) were then used as macro-RAFT agents to produce a library of bock copolymers with general structure [**(5)**$_x$-*r*-(HEA)$_y$]$_n$-*b*-(M)$_z$.

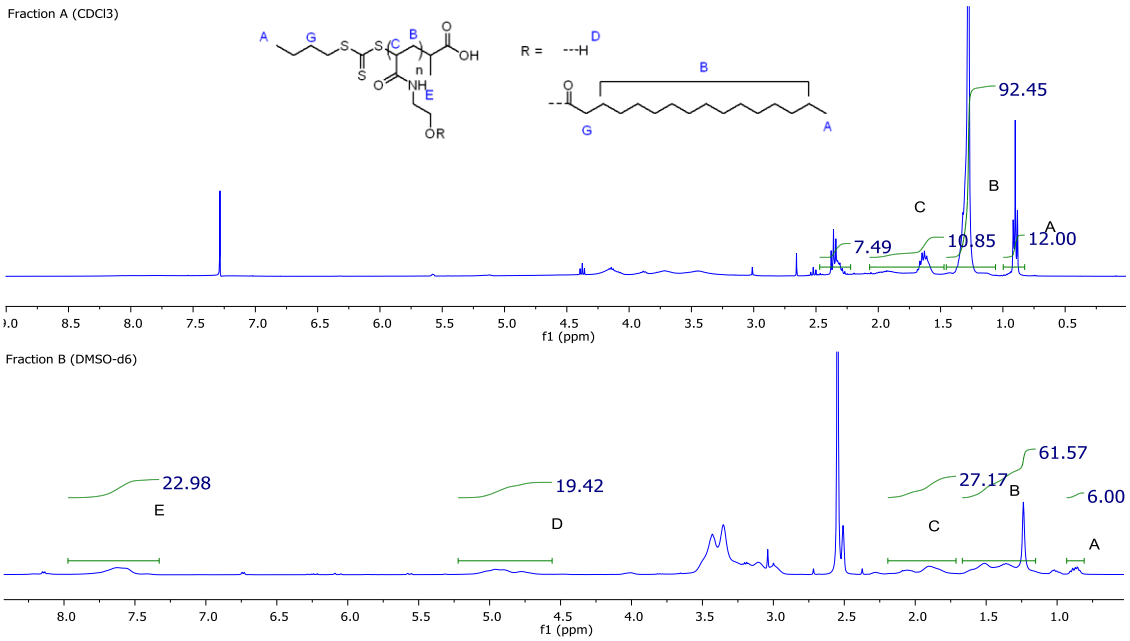
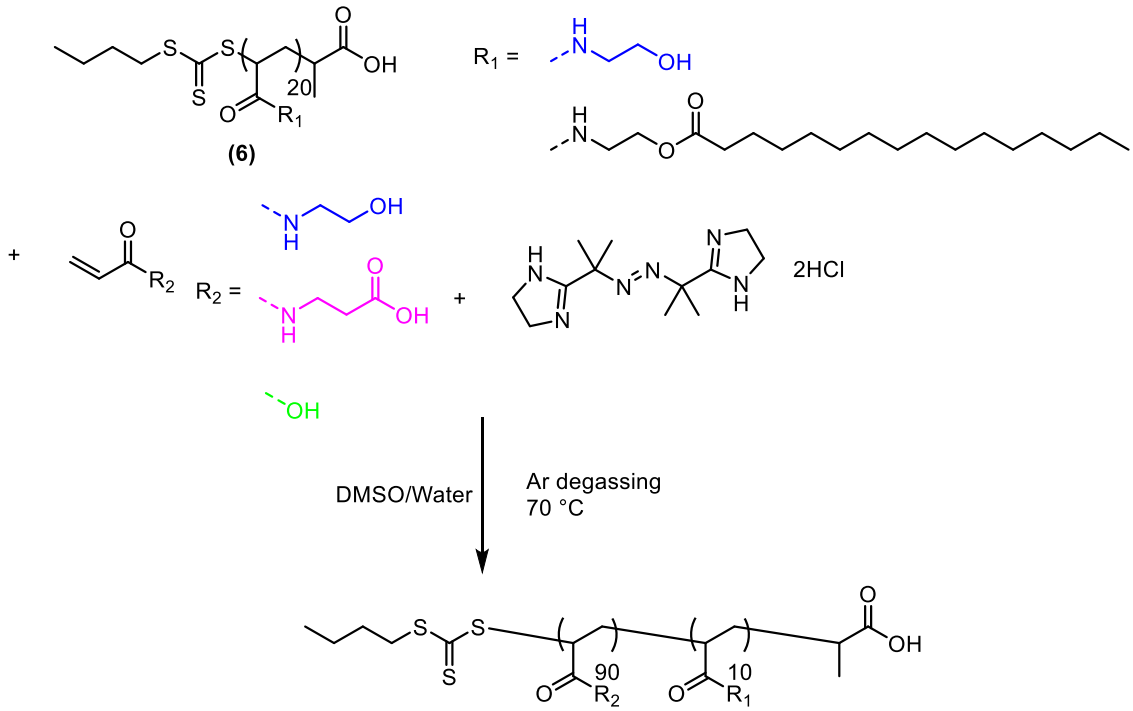


Figure 2.7 ^{1}H NMR spectra of the main macro RAFT agents isolated by SiO_2 flash chromatography, Fraction A [**(5)**$_{30\%}$-r-(HEA)$_{70\%}$]$_{10}$ and Fraction B [**(5)**$_{5\%}$-r-(HEA)$_{95\%}$]$_{20}$



Scheme 2.13 Synthesis of polymers by single-phase RAFT polymerisation, starting from (5)-based macro RAFT agent (6) and N-hydroxyethyl acrylamide (HEA, blue), 3-acrylamido propanoic acid (3-AAPA, 4, violet) and acrylic acid (AA, green).

To chain-extend the [**(5)**$_{20\%}$-*r*-(HEA)$_{30\%}$]$_{10}$ block, the single-phase conditions (**Scheme 2.13**) using DMSO:water (4:1) described in section in 2.3.1, using hydroxyethyl acrylamide (HEA), 3-acrylamido propanoic acid (AAPA), and acrylic acid (AA) as the monomers (**Table 2.12**). For this purpose, fraction B [**(5)**$_{5\%}$-*r*-(HEA)$_{95\%}$]$_{20}$ was designated as compound **(6)** and employed to produce a polymer library analogous to the libraries described for cholesterol, DOPE and PABTC polymers. Fraction A [**(5)**$_{30\%}$-*r*-(HEA)$_{70\%}$]$_{10}$ was employed as macro RAFT agent using HEA as monomer. Importantly, this allowed to systematically vary the number of palmitoyl lipid moieties at one end of the polymer chain (first block), to explore the effect that this variation has on the interaction with lipid bilayer membranes.

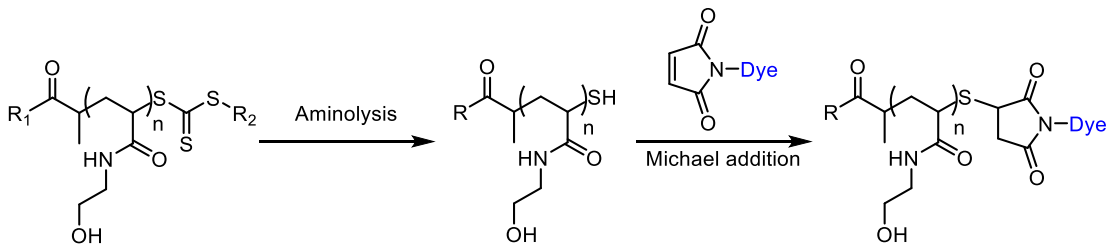
Table 2.12 Lipid monomer-based polymers produced in this study.

Code	DP[a]	HEA[b]	AAPA[b]	AA[b]	*Đ*[c]	$M_{n\ (NMR)}$ kDa
(6)-[(HEA)$_{100\%}$]$_{102}$	95	95	-	-	1.13	12.3
(6)-[(HEA)$_{90\%}$-*r*-(AAPA)$_{10\%}$]$_{167}$	160	141	26	-	1.11	20.5
(6)-[(AA)$_{100\%}$]$_{120}$	120	-	-	120	1.24	10.7
(6)-[(HEA)$_{90\%}$-*r*-(AA)$_{10\%}$]$_{146}$	146	120	-	26	1.11	16.3
(6)-[(HEA)$_{70\%}$-*r*-(AA)$_{30\%}$]$_{130}$	130	100	-	30	1.21	14.3
(6)-[(HEA)$_{50\%}$-*r*-(AA)$_{50\%}$]$_{120}$	120	73	-	47	1.45	12.4
[**(5)**$_{30\%}$-*r*-(HEA)$_{70\%}$]$_{10}$-b-[(HEA)$_{100\%}$]$_{65}$	65	65	-	-	1.05	8.60

[a] Degree of polymerisation (DP), calculated by ^{1}H NMR (see materials and methods). [b] HEA = hydroxyethyl acrylamide, AAPA 3-acrylamido propanoic acid, AA = acrylic acid. [c] Molecular weight dispersity (Mw/Mn, *Đ*) was determined by SEC (see materials and methods).

2.3.5 Synthesis of fluorescently labelled membrane-inserting (co)polymers

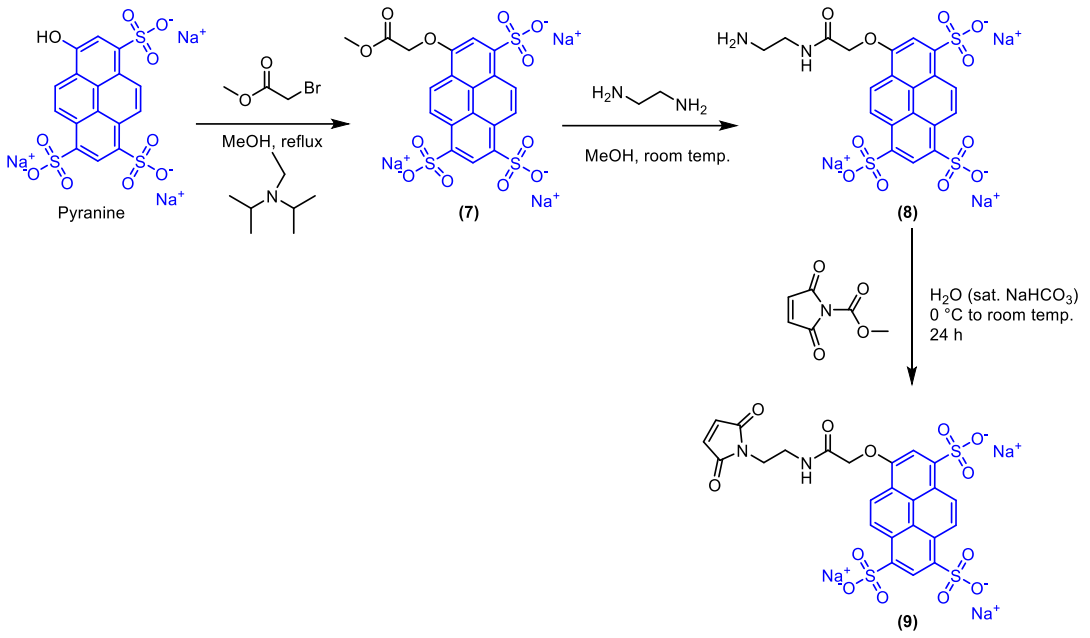
In **Chapter 3**, we will describe the investigation on the interaction between the amphiphilic (and control) polymers prepared in this work and cell plasma membranes. To facilitate tracking of these materials in these cell experiments, selected polymers were fluorescently tagged. To this aim the trithiocarbonate units at the polymer chain ends were converted into sulfhydryl groups by aminolysis using benzylamine, then the resulting macromolecular thiols were conjugated with maleimide-containing fluorescent dyes (**Scheme 2.14**).



Scheme 2.14 Fluorescent tagging of the polymers utilised in this study, requiring aminolysis of trithiocarbonate groups to obtain thiol-terminated polymers, and subsequent thiol-ene Michael addition with a maleimide-functionalised fluorescent dye.

Accordingly, tor the fluorescent tagging of selected (co)polymers two fluorescent dyes, commercially available Rhodamine Red™ C2 maleimide and pyranine maleimide **(9)** prepared in this pH work, were utilised. Under specific reaction conditions, maleimides react efficiently and selectively with thiols, and have been used extensively for "click" Michael additions in bioconjugation reactions[31]. This is due to the electron-withdrawing properties of the two carbonyl groups that cause maleimides to be "soft" electrophiles (good Michael acceptors[32]), combined with the "soft" nucleophilic nature of thiols. This, coupled with the thermodynamically favoured release of ring straining (by reduction of the maleimide double bond), enables efficient and selective reaction with nucleophiles. This high reactivity towards sulfhydryl groups is particularly useful for grafting molecules at one end of RAFT-synthesised polymers, which react slowly (being large molecules) and might present multiple reactive centres.

For the latter, pyranine was chosen because when functionalised with a carboxymethyl group it is highly resistant to photobleaching and it does not exhibit variations of fluorescence at different pH which are typical of unmodified pyranine starting material[33]. As these fluorescent polymers were meant to be utilised in membrane-binding experiments it was important to choose fluorophores that would not interact with lipid bilayer membranes. Although the pyrene core of the dye is lipophilic, its three negatively charged sulfonic acid salts groups would make it sufficiently hydrophilic to prevent any interaction with cell membranes. Additionally, carboxymethyl pyranine dyes have a fluorescence emission profile (λ_{ex} = 377 nm and λ_{em} = 420) that does not overlap with cell autofluorescence of mammalian cells, which is often in the green region of the visible electromagnetic spectrum[33,34].



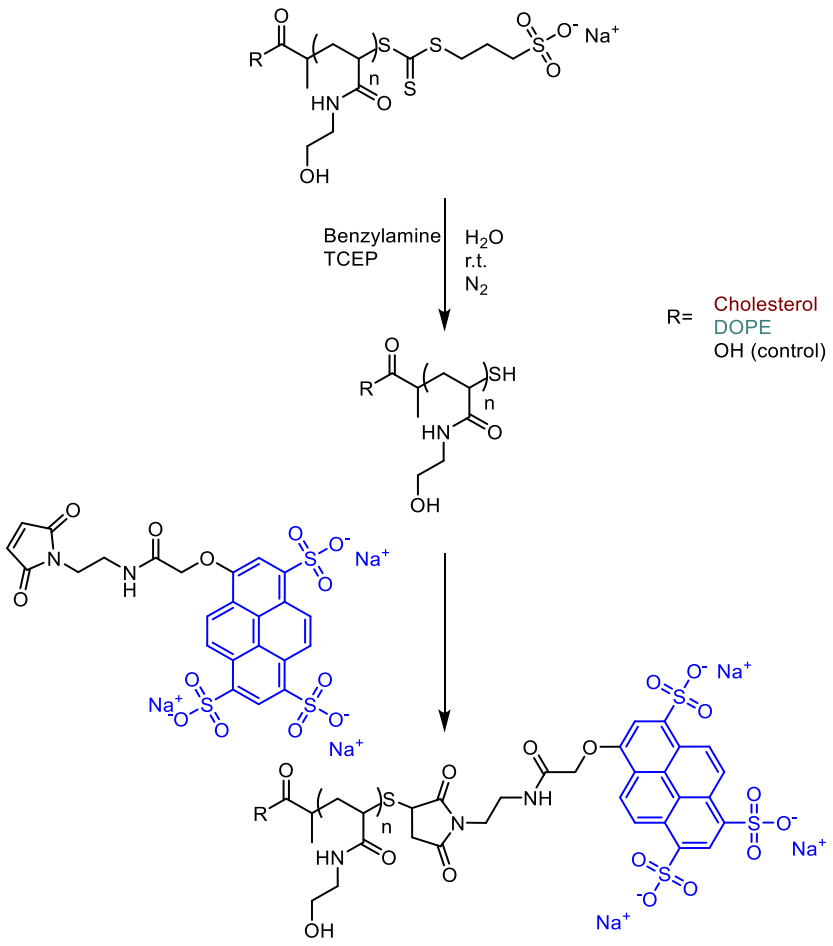
Scheme 2.15 Synthesis of maleimide fluorescent dye, MalPyr Blue (**9**).

Accordingly, the novel maleimide-containing carboxymethyl pyranine dye MalPyr **(9)** was designed (**Scheme 2.16**). This dye contained a short linear spacer between the dye and the maleimide to reduce steric hindrance caused by the bulky fluorophore, which could have prevented reaction with the polymer.

The first step for the synthesis of **(9)** was to functionalise the aromatic hydroxyl group of pyranine. This was achieved by adapting a method from previous literature,[33] by treating pyranine with methyl bromoacetate and *N,N*-diisopropylethylamine, a non-nucleophilic base, in refluxing methanol. In this step, a methyl ester was introduced in the structure of **(7)** to facilitate further functionalisation of this molecule with primary amines the favourable reaction between esters and amines[35].The resulting alkylated intermediate **(7)** was isolated in 57% yield by simple precipitation in 2-propanol.

In the second step a primary amine group was introduced by treatment of **(7)** with ethylenediamine in methanol, at room temperature. To prevent reaction of ethylenediamine with two pyranine molecules, an excess (2.5 equivalents) of the diamine was used. The primary amino group was then converted into an ether maleimide moiety by reaction of **(8)** with *N*-methoxycarbonylmaleimide in saturated $NaHCO_3$. The saturated sodium bicarbonate solution is utilised to maintain a slightly basic pH in the reaction mixture (thus avoiding potential hydrolysis of the product caused by the formation of the acidic *N*-acylcarbamate), with the hydrogen carbonate ion potentially playing a catalytic effect on the coupling reaction[36] This reaction was conducted at 0 °C for the initial 40 min to avoid a potential Michael addition of the primary amine group of starting material **(8)** with maleimide group of *N*-methoxycarbonylmaleimide starting material and MalPyr Blue **(9)**. In this final step **(9)** was isolated in nearly quantitative yield.

2.3.6 "One-Pot" aminolysis-fluorescent tagging of polymers investigated in this study



Scheme 2.16 One-pot fluorescent tagging of (co)polymers utilized in this study with fluorescent MalPyr blue **(9)** dye.

The functionalisation of RAFT polymers with maleimide-containing fluorescent dyes was adapted from previous literature[37]. This process involves *in situ* aminolysis of the trithiocarbonate group of polymers synthesised by RAFT polymerisation to produce a reactive thiol, and their subsequent reaction with maleimide derivatives[37,38]. Fluorescent tagging was carried out on a small subfamily of the polymers synthesised in this work, namely cholesterol-containing Chol-[$(HEA)_{100\%}]_{52}$, Chol-[$(HEA)_{100\%}]_{70}$, and Chol-[$(HEA)_{100\%}]_{108}$, phospholipid DOPE-containing DOPE-[$(HEA)_{100\%}]_{47}$, and non membrane-inserting control polymer PABTC-[$(HEA)_{100\%}]_{50}$. The rationale for this choice is that we aimed at comparing polymers with the same number of repeating units (target DP = 50) but with different membrane-inserting chain ends – cholesterol, phospholipid

DOPE and non membrane-inserting PABTC – as well as polymers with the same membrane-inserting chain end, cholesterol, but different number of repeating units – DP 52, 70 and 100.

The first step of this one-pot tagging strategy the RAFT polymers were treated with benzylamine, visually following the conversion of yellow trithiocarbonate units into colourless sulfhydryl SH groups, at which point MalPyr Blue **(9)** dye was added[39]. Tris(2-carboxyethyl)phosphine (TCEP) was also employed in this step to reduce potential polymer dimers that could form by oxidation of -SH terminated polymer, leading to S-S disulfide bridges, in the presence of air. Furthermore, TCEP acts as a catalyst for the subsequent thiol-ene reaction[40,41] increasing the yield and decreasing the need for extended reaction times[42]. The reaction was carried out using large excess of benzylamine (10 eq) to ensure quantitative cleaving of the trithiocarbonate, and similarly large excess of **(9)** (8 eq), to ensure high tagging efficiency. As the unreacted maleimide dye **(9)** and side products of the reaction are water-soluble, the purification of the fluorescently-tagged polymers was efficiently carried out by dialysis against deionised water.

The fluorescent tagging of the polymer was confirmed by SEC-HPLC using fluorescence detection (see section 2.2.4, iv), which also showed that no residual MalPyr **(9)** dye was left in the polymer samples after purification by dialysis (**Figure 2.8**). (λ_{ex} = 377 nm and λ_{em} = 420)

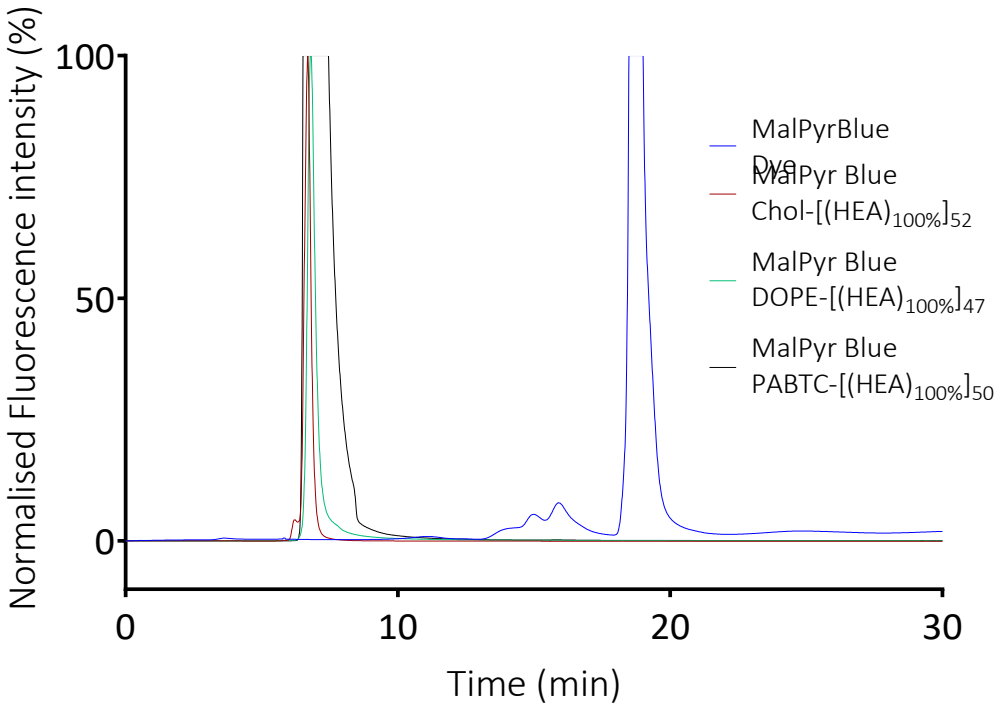


Figure 2.8 SEC-HPLC chromatograms for MalPyr Blue **(9)**-tagged polymers, showing different elution times for the free dye **(9)** and RAFT polymers fluorescently tagged with **(9)**. (λ_{ex} = 377 nm and λ_{em} = 420)

The efficiency of this tagging protocol, that is, the percentage of polymer chains that were conjugated to the dye **(9)** was evaluated by comparing the fluorescence intensity of 0.1 and 0.05 μM HBSS solutions of tagged polymers and MalPyr Blue dye (**9**). The results are shown in **Table 2.13**. Two concentrations were tested, to account for potential concentration-dependent effects of the polymers on the fluorescence emission profile of the dye.

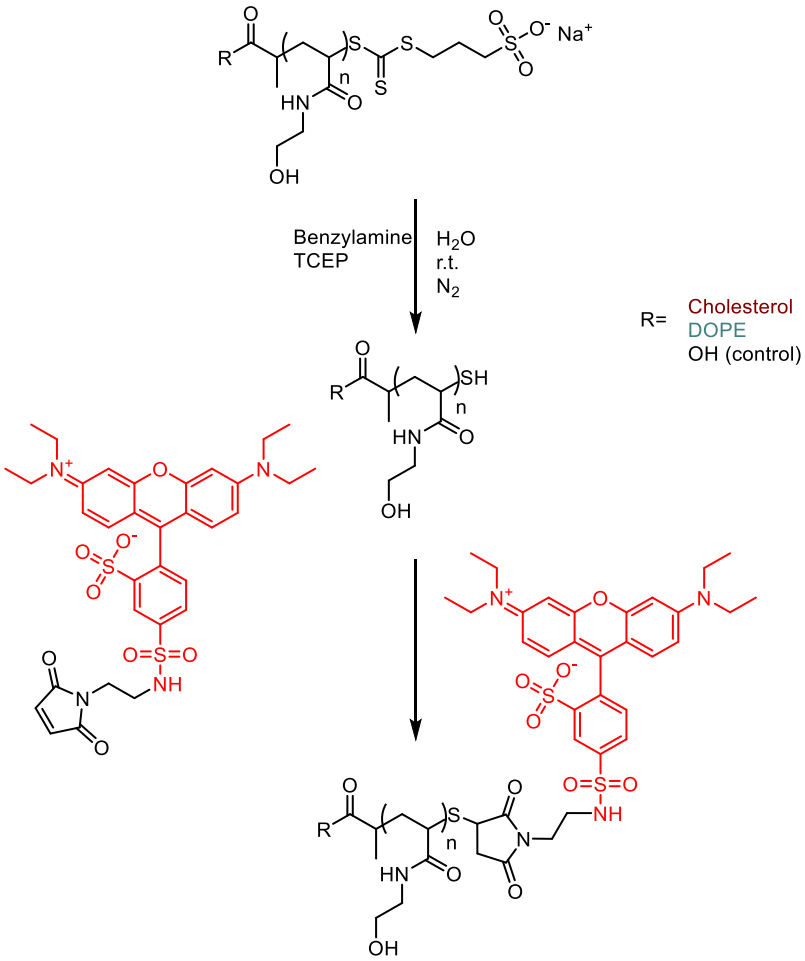
Table 2.13 MalPyr Blue fluorescently tagged polymers.

Code	Tagging efficiency[a]	M_n[b] kDa	$Đ$[c]
MalPyr Blue Chol-$[(HEA)_{100\%}]_{52}$	82.9±7%	7.51	1.07
MalPyr Blue Chol-$[(HEA)_{100\%}]_{70}$	105.2±10%	9.70	1.21
MalPyr Blue Chol-$[(HEA)_{100\%}]_{108}$	113.4±3%	14.0	1.12
MalPyr Blue DOPE-$[(HEA)_{100\%}]_{47}$	90.6±4%	6.96	1.10
MalPyr Blue PABTC-$[(HEA)_{100\%}]_{50}$	102.4±2%	6.58	1.11

[a] Tagging efficiency, calculated by comparing the fluorescence emission spectrum of the dye and the investigated polymer, at the same molar concentration, averaged between the two concentrations (n=12). [b] Number-average molecular weight M_n was calculated by ^{1}NMR as previously described. [c] Molecular weight dispersity (M_w/M_n, $Đ$) was determined by SEC (see materials and methods).

The results confirmed high tagging efficiency for all polymers. Some samples showed slightly higher fluorescence than the dye alone. To rule out that this was due to some potential non-covalent association between polymers and the pyranine dye, the fluorescence intensity of our samples was compared with that of a solution of untagged polymers and **(9),** each at 0.1 μM concentration. This test showed no statistically significant increase in fluorescence for the latter, hence the slightly higher fluorescent tagging efficiency observed for MalPyr Blue Chol-$[(HEA)_{100\%}]_{108}$ could not fully be rationalised, although one could speculate that this could be ascribed to an increase in dye solubility, or to addition of multiple dye molecules to a single polymer[37].

To expand the range of fluorophores in subsequent in vitro cell experiments, three polymers with target DP=50 - Chol-$[(HEA)1_{00\%}]_{52}$ PABTC-$[(HEA)_{100\%}]_{50}$ DOPE-$[(HEA)_{100\%}]_{47}$ - were tagged using Rhodamine Red™ C2 Maleimide, using the same one-pot procedure described for MalPyr Blue (**Scheme 2.17**).



Scheme 2.17 One-pot fluorescent tagging of (co)polymers utilized in this study with fluorescent rhodamine Red™ C 2 Maleimide.

Similarly, efficiency of the tagging reaction was assessed by comparing the fluorescence intensity of 0.1 μM solutions of tagged polymers and Rhodamine Red™ C2 Maleimide. The results are shown in **Table 2.14**.

Table 2.14 Rhodamine Red maleimide-tagged polymers investigated in this study.

Code	Tagging efficiency[a]	Mn[b] kDa	Đ[c]
Rhodamine PABTC-[(HEA)$_{100\%}$]$_{50}$	87.5%	6.57	1.05
Rhodamine Chol-[(HEA)$_{100\%}$]$_{58}$	90.6%	8.17	1.07
Rhodamine DOPE-[(HEA)$_{100\%}$]$_{47}$	99.3%	6.95	1.08

[a] Tagging efficiency, calculated by comparing the fluorescence emission spectrum of the dye and the investigated polymer, at the same molar concentration (n = 1). [b] Number-average molecular weight M_n was calculated by ^{1}NMR as previously described. [c] Molecular weight dispersity (M_w/M_n, Đ) was determined by SEC (see materials and methods).

The results suggested successful tagging of these polymers, with high tagging efficiencies. The complete removal of unreacted rhodamine Red™ C2 maleimide from the polymer samples was confirmed by SEC-HPLC, with fluorescence detection - λ_{ex} = 560 nm and λ_{em} = 580 nm (**Figure 2.9**).

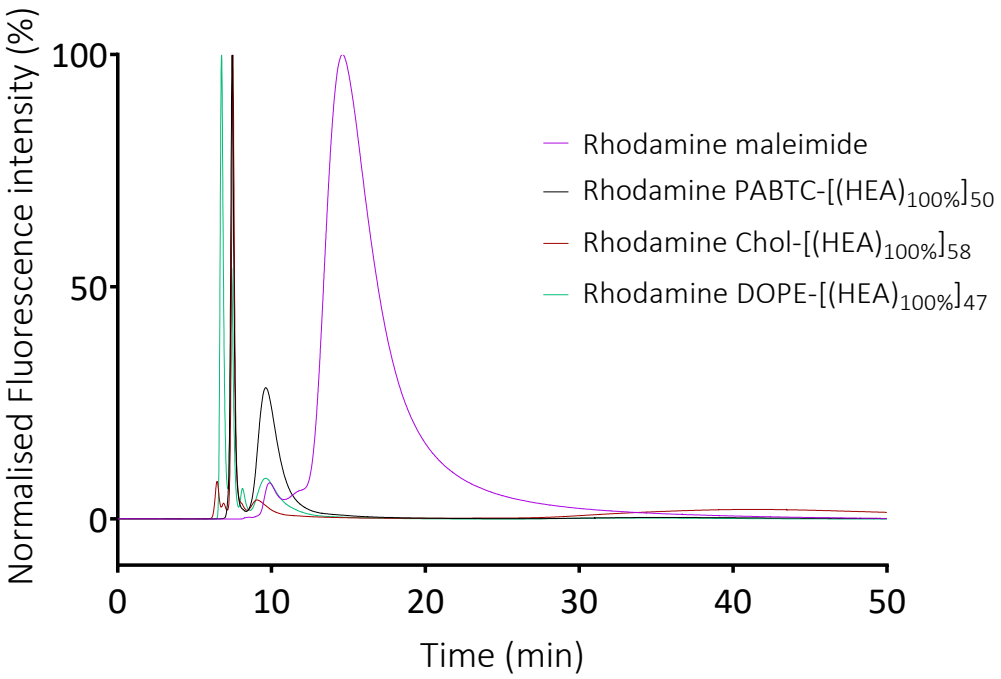


Figure 2.9 SEC-HPLC-chromatograms for Rhodamine Red tagged polymers, showing different elution times for Rhodamine Red C 2 maleimide free dye and Rhodamine Red C 2 maleimide fluorescently-tagged polymers. (λ_{ex} = 560 nm and λ_{em} = 580 nm)

2.3.7 Replacement of trithiocarbonate groups at polymer chain-ends with hydrogen - H atoms

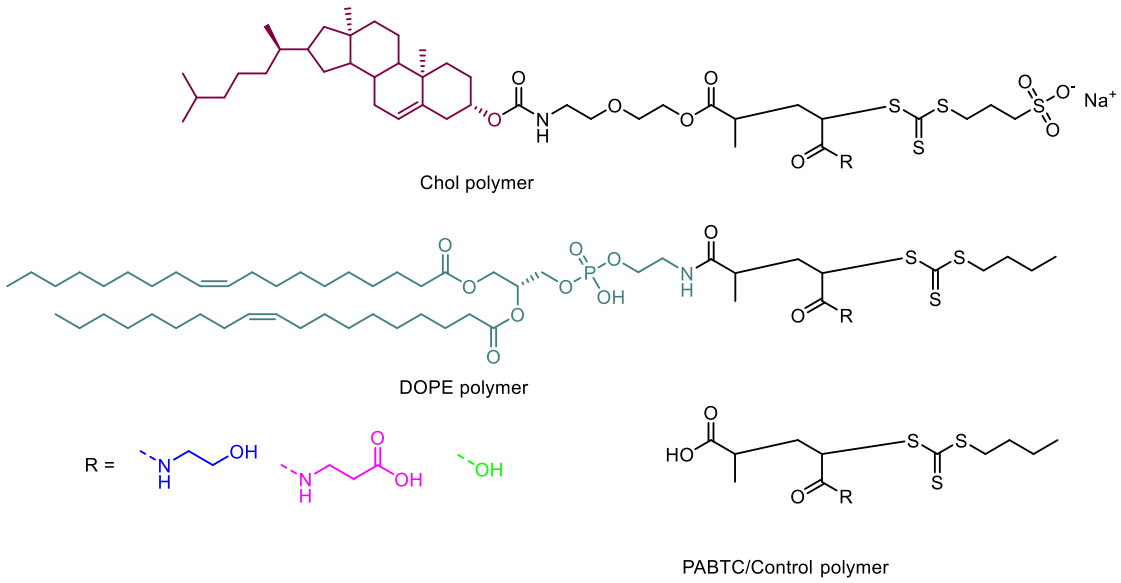
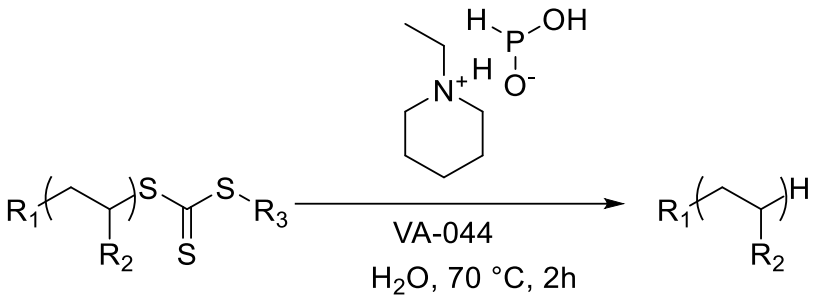


Figure 2.10 Structures of the polymers synthesised in this study, showing the difference in the chemical structure of the trithiocarbonate (ω-chain ends).

Due to different synthetic routes required for their synthesis, the three RAFT agents (**Figure 2.10**) used to synthesise the polymers possess two different trithiocarbonate moieties, a butyl chain (**2**, **3**) and a propanesulfonic acid salt (**1**). For the polymers synthesised from these RAFT agents, we hypothesised that these trithiocarbonate moieties, given their small size compared to the polymer chains and their inability to insert into lipid bilayers, should not have an impact on the overall membrane-inserting properties of these polymers.

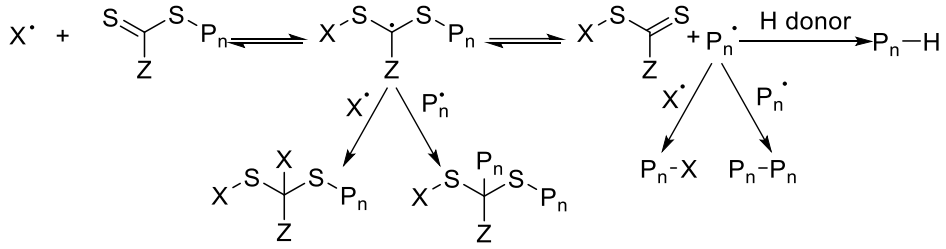
To test this hypothesis, the trithiocarbonate moiety at the polymer chain-ends was substituted it with the simplest group possible – a hydrogen atom. This was achieved by using conditions similar to those used for RAFT polymerisations: a radical initiator (VA-044, 0.25:1 mol:mol ratio with respect to the RAFT agent) and heating at 70 °C for 2 hours. Instead of monomers, a reducing agent, *N*-ethylpiperidine hypophosphite (EPHP) was used (**Scheme 2.18**). Unlike other trithiocarbonate removal procedures, radical-induced trithiocarbonate removal

using hypophosphite salts does not require lengthy purification steps, as all side products are water-soluble and can be efficiently removed through dialysis[19,43].



Scheme 2.18 Removal of trithiocarbonate polymer chain-ends using N-ethylpiperidine hypophosphite (EPHP), under radical conditions.

The reaction was initiated using water-soluble VA-044 radical azoinitiator. This produced the addition-fragmentation equilibrium, which in turn generated the polymeric radical. This radical was irreversibly reduced by the excess of H· donor, resulting in a H-terminated "cleaved" polymer (**Scheme 2.19**). In order to reduce chances of irreversible chain-chain coupling events, leading to larger Pn-Pn polymer chains shown in Scheme 2.20, during the addition-fragmentation step, we selected a low ratio of initiator:CTA (mol:mol), where "CTA" here refers to the trithiocarbonate moieties.



Scheme 2.19 Mechanism of trithiocarbonate group substitution with a H atom.

Trithiocarbonate group removal was monitored by measuring the change of UV absorbance of the trithiocarbonate group at λ = 310 nm[44]. **Figure 2.11** shows the disappearance of the λ = 310 nm band following removal of the trithiocarbonate end-group in PABTC-[(HEA)$_{100\%}$]$_{80}$. The results are expressed as % of removed in **Table 2.15**, and show that the trithiocarbonate group was partially (from 65% to quantitative) removed from the polymers.

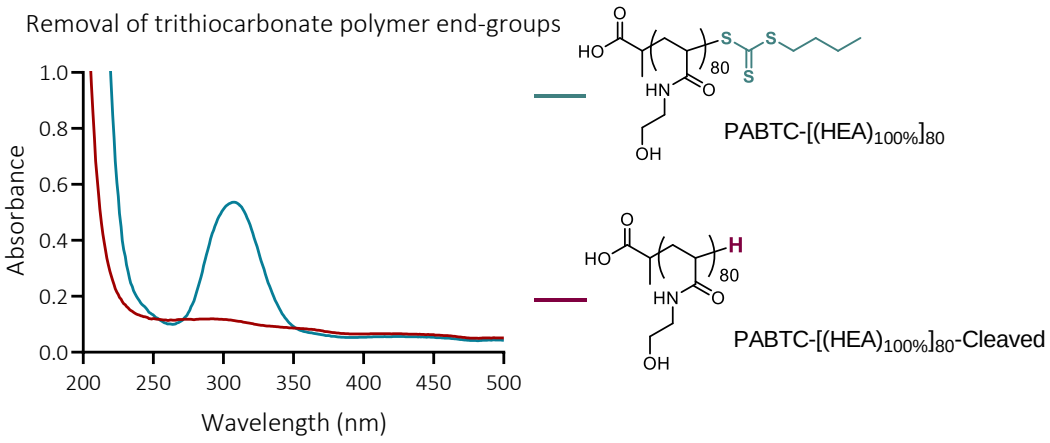


Figure 2.11 UV-visible spectra of the same polymer, before and after the trithiocarbonate replacement reaction. The trithiocarbonate group is characterised by an absorbance peak at λ = 310 nm[44].

Table 2.15 Trithiocarbonate removal from polymers, estimated from the decrease of absorbance at λ = 320 nm.

Code	Trithiocarbonate removal (%)[a]
Chol-[(HEA)$_{100\%}$]$_{70}$ Cleaved	84.1
Chol-[(HEA)$_{100\%}$]$_{58}$ Cleaved	84.8
PABTC-[(HEA)$_{100\%}$]$_{80}$ Cleaved	94.6
PABTC-[(HEA)$_{100\%}$]$_{63}$ Cleaved	68.3

[a] Trithiocarbonate removal, calculated from the ratio of the UV-vis absorbance peak at λ = 310 nm between the "cleaved" and the trithiocarbonate-presenting polymer.

SEC analysis of a polymer before and after trithiocarbonate removal (**Table 2.16**) shows that while the dispersity remained constant, for PABTC-[(HEA)$_{100\%}$]$_{80}$ the $M_{n,SEC}$ was found to increase. The GPC analysis is dependent on the hydrodynamic radius of the polymers, which may be affected by the removal of the polar end-group. For the PABTC-based polymer, the removal of the trithiocarbonate increased the M_n significantly (closer to NMR-calculated values) and the dispersity decreased. Potential explanation for this effect is irreversible termination in the

form of chain-chain coupling between two polymers, which could result in an increase in measured M_n.

Table 2.16 SEC analysis of cleaved and non-cleaved polymers.

Code	M_n (GPC) [a] kDa	M_n (^{1}H NMR)[b] kDa	$Đ$ [c]
Chol-[(HEA)$_{100\%}$]$_{70}$	8.04	9.10	1.05
Chol-[(HEA)$_{100\%}$]$_{70}$ CLEAVED	9.51	8.89*	1.05
PABTC-[(HEA)$_{100\%}$]$_{80}$	2.62	9.45	1.20
PABTC-[(HEA)$_{100\%}$]$_{80}$ CLEAVED	4.75	9.30*	1.16

[a] Mn number average molecular weight, determined by SEC. [b c] Molecular weight dispersity (M_w/M_n, Đ) was determined by SEC (see materials and methods).* Estimated M_n, based on subtraction of the MW of the trithiocarbonate ω-chain end to the M_n of the "non-cleaved" polymer.

2.3.8 Critical Aggregation Concentration (CAC) of the polymers synthesised in this work

The critical aggregation concentration of polymers was determined via evaluation of the pyrene fluorescence in solution with different polymer concentrations. Pyrene is an extremely lipophilic fluorescent compound that shows a different fluorescence emission spectrum based on the chemical microenvironment, lipophilic or hydrophilic, it is surrounded by[4,45].

As it is shown in the example using polymer Chol-[(HEA)$_{100\%}$]$_{58}$ (**Figure 2.12**), at higher polymer concentrations (where it forms supramolecular aggregates) an additional peak (I_3) can be observed in the pyrene fluorescence emission spectrum. This peak (found around λ_{em} = 385 nm) is present only when pyrene is solubilised in a lipophilic environment[46], and the ratio between I_1 and I_3 is employed for CAC determination. The Log_{10} of the concentration of the surfactant, our amphiphilic polymers in this case, is then plotted against their I_1/I_3 ratio. Two

intersecting lines are then extrapolated, fitting the crossing point. This point represents the CAC for the polymers.

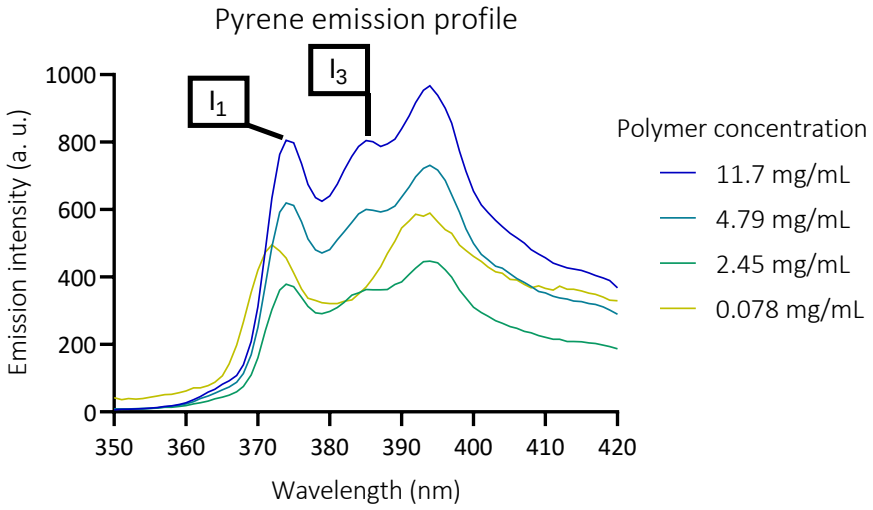


Figure 2.12 Pyrene fluorescence emission profile (λ_{ex} = 340 nm) at different concentrations of amphiphilic polymer Chol-[$(HEA)_{100\%}$]$_{58}$. The ratio between I_1 and I_3 is used to identify the CAC of the polymers.

The CAC for the PABTC-based control polymers did not show any CAC as these are not amphiphilic and therefore did not form supramolecular aggregates at the tested concentrations - i.e. up to 10 mg/mL). For the amphiphilic polymers the results were as expected, where increasing the size of the hydrophilic portion decreased the critical aggregation concentration in agreement with previous literature[47].

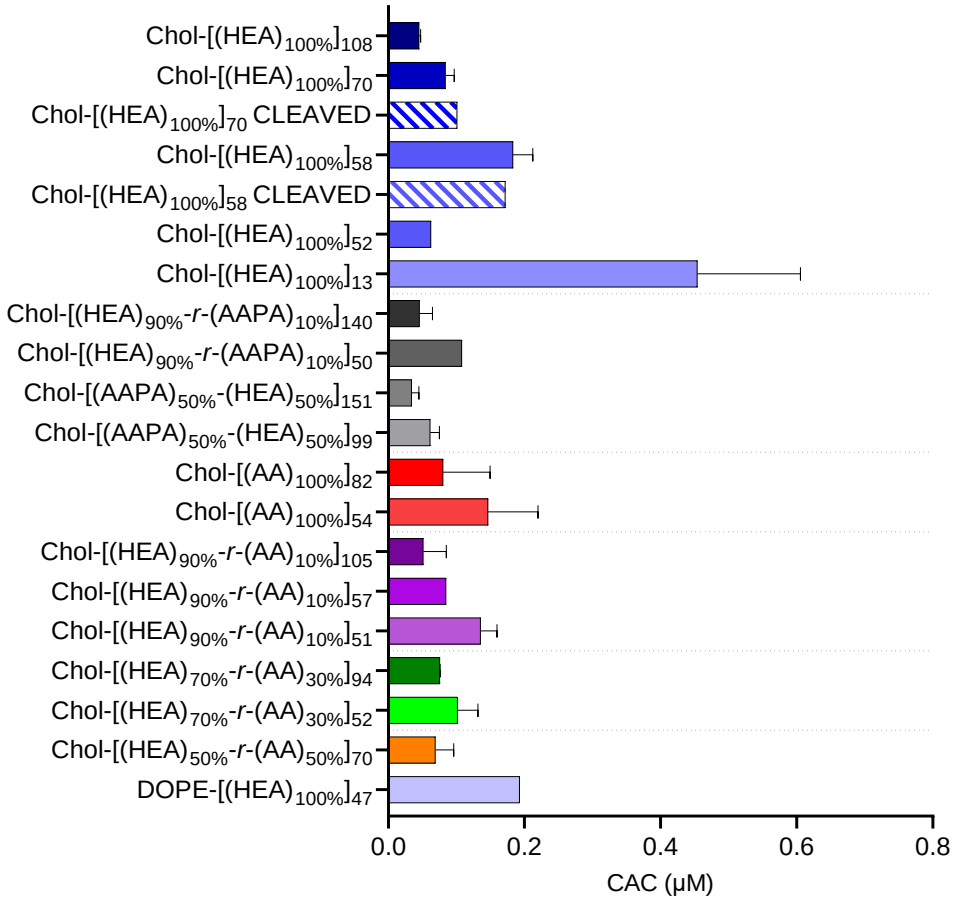


Figure 2.13 CAC for the homo- and copolymers synthesised in this study as determined using pyrene as the fluorescence probe (μM, n = 1-3, SD).

As it can be observed in **Figure 2.13**, most of the polymers have relatively similar CACs (between 0.1 and 0.2 μM), with the exception of the shortest polymer, (Chol-[(HEA)$_{100\%}$]$_{13}$). This polymer aggregated at a significantly higher concentration than any other comparable Cholesterol-HEA homopolymer.

The removal of the trithiocarbonate group did not impact the critical aggregation concentration for HEA homopolymers, as the differences of the observed CMC before and after cleavage of the trithiocarbonate group were found to be non-statistically different (one-way ANOVA).

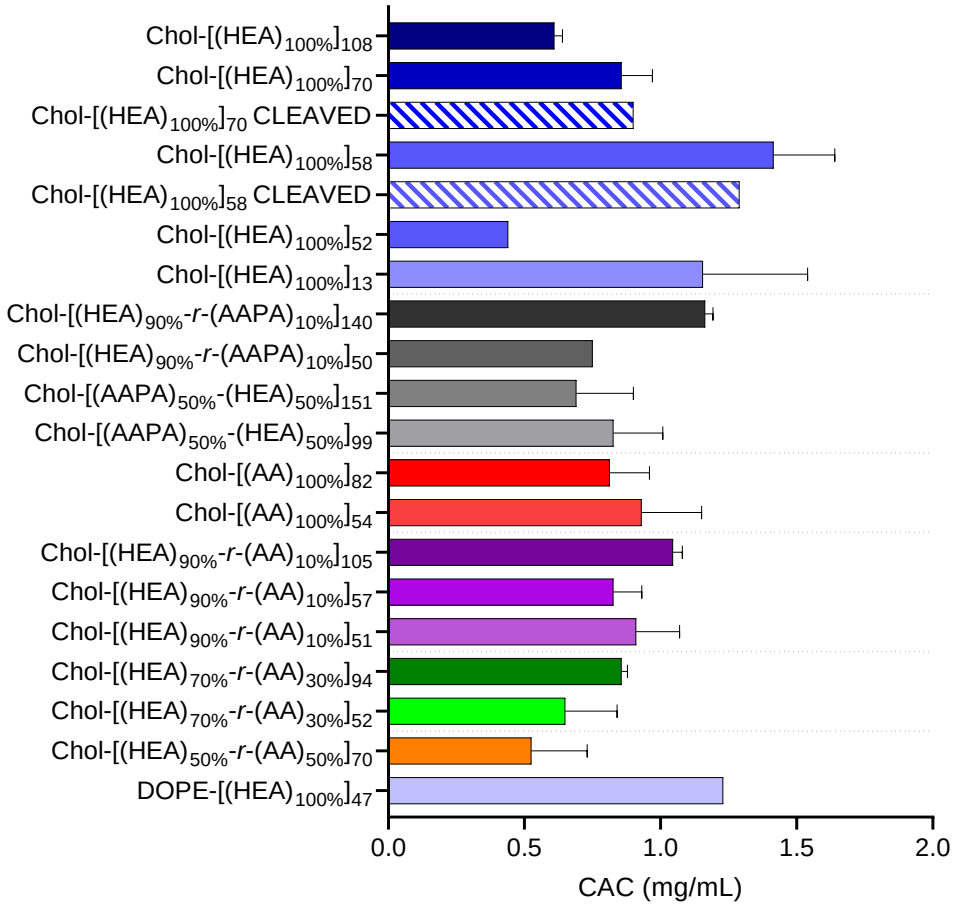


Figure 2.14 CAC for the homo and copolymers synthesised in this study as determined using pyrene as the fluorescence probe (mg/mL, n = 1-3, SD).

The CAC measured (expressed in mg/mL values in **Figure 2.14**) is in line with what described in the literature for many amphiphilic polymers. For example, poloxamers have similar to higher CACs, based on their architecture (0.7 to 45 mg/mL); a structurally more similar A-B polymer, C18-monoalkyl hyperbranched polyglycerol showed a similar CAC (0.08 mg/mL)[48]. Similarly, another A-B block chain copolymer based on poly(N-isopropyl acrylamide) and a tetrohydrapyran-protected poly 2-hydroxyethyl methacrylate showed a CAC comparable to our polymers (0.1 mg/mL)[49]. Another class of polymers based on PEG linked to two polycaprolactone tails showed a slightly lower tendency to aggregate than our polymers (1.33 to 6.46 mg/mL)[50].

2.4 Concluding remarks

In this chapter we described the synthesis and characterisation of four libraries of polymers with different structural and functional characteristics:

i) Nature of the membrane-inserting polymer chain end (or lack of it);

ii) Chemical composition of the polymers, with hydrophilic and acid monomers in different proportions;

iii) Chain length of the polymers.

Furthermore, we described the synthesis of a novel phospholipid RAFT agent, as well as synthesis of a lipid macroCTA, one-pot removal of the trithiocarbonate group and synthesis of a novel maleimide dye and its application for the fluorescent tagging of RAFT polymers.

2.5 Bibliography

(1) Matyjaszewski, K.; Janzen, E.; He, Y. Z.; Cui, J. P.; Mallard, W. G.; Tsang, W.; Chiefari, J.; Chong, Y. K. B.; Ercole, F.; Krstina, J.; Jeffery, J.; Le, T. P. T.; Mayadunne, R. T. A.; Meijs, G. F.; Moad, C. L.; Moad, G.; Rizzardo, E.; Thang, S. H.; South, C. Living Free-Radical Polymerization by Reversible Addition - Fragmentation Chain Transfer : The RAFT Process. *Macromolecules* **1998**. https://doi.org/10.1017/CBO9781107415324.004.

(2) Perrier, S. 50th Anniversary Perspective: RAFT Polymerization - A User Guide. *Macromolecules* **2017**, *50* (19), 7433–7447. https://doi.org/10.1021/acs.macromol.7b00767.

(3) Domínguez, A.; Fernández, A.; González, N.; Iglesias, E.; Montenegro, L.; Dominguez, A.; Fernandez, A.; Gonzalez, N.; Iglesias, E.; Montenegro, L. Determination of Critical Micelle Concentration of Some Surfactants by Three Techniques. *J. Chem. Educ.* **2009**, *74* (10), 1227. https://doi.org/10.1021/ed074p1227.

(4) Piñeiro, L.; Novo, M.; Al-Soufi, W. Fluorescence Emission of Pyrene in Surfactant Solutions. *Adv. Colloid Interface Sci.* **2015**, *215*, 1–12. https://doi.org/10.1016/j.cis.2014.10.010.

(5) Ayala, R.; Zhang, C.; Yang, D.; Hwang, Y.; Aung, A.; Shroff, S. S.; Arce, F. T.; Lal, R.; Arya, G.; Varghese, S. Engineering the Cell-Material Interface for Controlling Stem Cell Adhesion, Migration, and Differentiation. *Biomaterials* **2011**, *32* (15), 3700–3711. https://doi.org/10.1016/j.biomaterials.2011.02.004.

(6) Catania, R.; Mastrotto, F.; Moore, C. J.; Bosquillon, C.; Falcone, F. H.; Huett, A.; Mantovani, G.; Stolnik, S. Study on Significance of Receptor Targeting in Killing of Intracellular Bacteria with Membrane-Impermeable Antibiotics. *Adv. Ther.* **2021**, *4* (12), 1–11. https://doi.org/10.1002/adtp.202100168.

(7) Ringsdorf, H. Structure and Properties of Pharmacologically Active Polymers. *J Polym Sci Polym Symp* **1975**, *153* (51), 135–153. https://doi.org/10.1002/polc.5070510111.

(8) Valdebenito, A.; Encinas, M. V. Effect of Solvent on the Free Radical Polymerization of N,N-Dimethylacrylamide. *Polym. Int.* **2010**, *59* (9), 1246–1251. https://doi.org/10.1002/pi.2856.

(9) Gody, G.; Barbey, R.; Danial, M.; Perrier, S. Ultrafast RAFT Polymerization: Multiblock Copolymers within Minutes. *Polym. Chem.* **2015**, *6* (9), 1502–1511. https://doi.org/10.1039/c4py01251h.

(10) Ramasamy, T.; Kim, J.; Choi, H. G.; Yong, C. S.; Kim, J. O. Novel Dual Drug-Loaded Block Ionomer Complex Micelles for Enhancing the Efficacy of Chemotherapy Treatments. *J. Biomed. Nanotechnol.* **2014**, *10* (7), 1304–1312. https://doi.org/10.1166/jbn.2014.1821.

(11) Swift, T.; Swanson, L.; Geoghegan, M.; Rimmer, S. The PH-Responsive Behaviour of Poly(Acrylic Acid) in Aqueous Solution Is Dependent on Molar Mass. *Soft Matter* **2016**, *12* (9), 2542–2549. https://doi.org/10.1039/c5sm02693h.

(12) Chiari, M.; Casale, E.; Santaniello, E.; Righetti, P. G. Synthesis of Buffers for Generating Immobilized PH Gradients. I: Acidic Acrylamido Buffers.

Appl. Theor. Electrophor. Off. J. Int. Electrophor. Soc. **1989**, *1* (2), 99–102.

(13) Capasso Palmiero, U.; Chovancová, A.; Cuccato, D.; Storti, G.; Lacík, I.; Moscatelli, D. The RAFT Copolymerization of Acrylic Acid and Acrylamide. *Polym. (United Kingdom)* **2016**, *98*, 156–164. https://doi.org/10.1016/j.polymer.2016.06.024.

(14) Jin, T.; Yin, H.; Easton, C. D.; Seeber, A.; Hao, X.; Huang, C.; Zeng, R. New Strategy of Improving the Dispersibility of Acrylamide-Functionalized Graphene Oxide in Aqueous Solution by RAFT Copolymerization of Acrylamide and Acrylic Acid. *Eur. Polym. J.* **2019**, *117* (March), 148–158. https://doi.org/10.1016/j.eurpolymj.2019.05.029.

(15) Larnaudie, S. C.; Brendel, J. C.; Jolliffe, K. A.; Perrier, S. Cyclic Peptide-Polymer Conjugates: Grafting-to vs Grafting-From. *J. Polym. Sci. Part A Polym. Chem.* **2016**, *54* (7), 1003–1011. https://doi.org/10.1002/pola.27937.

(16) Anderson, G. W.; Zimmerman, J. E.; Callahan, F. M. The Use of Esters of N-Hydroxysuccinimide in Peptide Synthesis. *J. Am. Chem. Soc.* **1964**, *86* (9), 1839–1842. https://doi.org/10.1021/ja01063a037.

(17) Ames, D. E.; Grey, T. F. The Synthesis of Some N-Hydroxyimides. *J. Chem. Soc.* **1955**, 631. https://doi.org/10.1039/jr9550000631.

(18) Chong, B. Y. K.; Krstina, J.; Le, T. P. T.; Moad, G.; Postma, A.; Rizzardo, E.; Thang, S. H. Thiocarbonylthio Compounds [S=C(Ph)S-R) in Free Radical Polymerization with Reversible Addition-Fragmentation Chain Transfer (RAFT Polymerization). Role of the Free-Radical Leaving Group (R). *Macromolecules* **2003**, *36* (7), 2256–2272. https://doi.org/10.1021/ma020882h.

(19) Chong, Y. K.; Moad, G.; Rizzardo, E.; Thang, S. H. Thiocarbonylthio End Group Removal from RAFT-Synthesized Polymers by Radical-Induced Reduction. *Macromolecules* **2007**, *40* (13), 4446–4455. https://doi.org/10.1021/ma062919u.

(20) Qiu, X. P.; Winnik, F. M. Facile and Efficient One-Pot Transformation of RAFT Polymer End Groups via a Mild Aminolysis/Michael Addition Sequence. *Macromol. Rapid Commun.* **2006**, *27* (19), 1648–1653. https://doi.org/10.1002/marc.200600436.

(21) Keddie, D. J.; Moad, G.; Rizzardo, E.; Thang, S. H. RAFT Agent Design and Synthesis. *Macromolecules* **2012**, *45* (13), 5321–5342. https://doi.org/10.1021/ma300410v.

(22) Yin, M.; Bucsiova, L.; Habicher, W. D.; Voit, B. Reversible Addition-Fragmentation Chain Transfer (RAFT) Polymerization of Functional Acryl- and Methacryl Derivatives. *J. Nanostructured Polym. Nanocomposites* **2006**, *2* (1).

(23) Contino, C.; Ollier, M.; Maurizis, J. C.; Lacombe, J. M.; Pucci, B. Synthesis of Cotelomers Derived from Tris(Hydroxymethyl)Acrylamidomethane (THAM) Bearing Cytosine Arabinoside Moieties. Preliminary Investigation of Their Biological Activity. *Tetrahedron Lett.* **1996**, *37* (50), 9049–9052. https://doi.org/10.1016/S0040-4039(96)02122-3.

(24) Schotten, C. Ueber Die Oxydation Des Piperidins. *Berichte der Dtsch. Chem. Gesellschaft* **1884**, 2544–2547. https://doi.org/10.1002/ardp.18772100149.

(25) Baumann, E. Ueber Eine Einfache Methode Der Darstellung von Benzoësäureäthern. *Berichte der Dtsch. Chem. Gesellschaft* **1886**, *19* (2), 3218–3222.

(26) Clayden, J.; Greeves, N.; Warren, S. *Organic Chemistry*, 2nd ed.; Oxford University Press, 2012; Vol. 85. https://doi.org/10.1021/ja00892a048.

(27) Hirayama, N.; Higo, T.; Imura, H. Salting-out Phase Separation System of Water-Tetrahydrofuran with Co-Using 1-Butyl-3-Methylimidazolium Chloride and Sodium Chloride for Possible Extraction Separation of Chloro-Complexes. *Solvent Extr. Res. Dev.* **2014**, *21* (1), 71–76. https://doi.org/10.15261/serdj.21.71.

(28) Xie, Y.; Yu, F.; Wang, Y.; He, X.; Zhou, S.; Cui, H. Salt Effect on Liquid–Liquid Equilibria of Tetrahydrofuran/Water/5-Hydroxymethylfurfural Systems. *Fluid Phase Equilib.* **2019**, *493*, 137–143. https://doi.org/10.1016/j.fluid.2019.04.018.

(29) Gurnani, P.; Floyd, T.; Tanaka, J.; Stubbs, C.; Lester, D.; Sanchez-Cano, C.; Perrier, S. PCR-RAFT: Rapid High Throughput Oxygen Tolerant RAFT Polymer Synthesis in a Biology Laboratory. *Polym. Chem.* **2020**, *11* (6), 1230–1236. https://doi.org/10.1039/c9py01521c.

(30) Wako. Azo Polymerization Initiators Comprehensive Catalog. *Wako Cat.* **2016**, 33.

(31) Northrop, B. H.; Frayne, S. H.; Choudhary, U. Thiol-Maleimide "Click" Chemistry: Evaluating the Influence of Solvent, Initiator, and Thiol on the Reaction Mechanism, Kinetics, and Selectivity. *Polym. Chem.* **2015**, *6* (18), 3415–3430. https://doi.org/10.1039/c5py00168d.

(32) Méndez, F.; Galván, M.; Garritz, A.; Vela, A.; Gàzquez, J. Local Softness and Chemical Reactivity of Maleimide: Nucleophilic Addition. *J. Mol. Struct. THEOCHEM* **1992**, *277* (C), 81–86. https://doi.org/10.1016/0166-1280(92)87131-I.

(33) Legenzov, E. A.; Dirda, N. D. A.; Hagen, B. M.; Kao, J. P. Y. Synthesis and Characterization of 8-Ocarboxymethylpyranine (CM-Pyranine) as a Bright, Violet-Emitting, Fluid-Phase Fluorescent Marker in Cell Biology. *PLoS One* **2015**, *10* (7), 1–18. https://doi.org/10.1371/journal.pone.0133518.

(34) Ferreira, D. S.; Henriques, M.; Oliveira, R.; Correia, J. H.; Minas, G. Autofluorescence Spectroscopy of a Human Gastrointestinal Carcinoma Cell Line : Design of Optical Sensors for the Detection of Early Stage Cancer. *BIODEVICES 2009 - Proc. 2nd Int. Conf. Biomed. Electron. Devices* **2009**, No. January, 61–66.

(35) Jencks, W. P.; Carriuolo, J. Reactivity of Nucleophilic Reagents toward Esters. *J. Am. Chem. Soc.* **1960**, *82* (7), 1778–1786. https://doi.org/10.1021/ja01492a058.

(36) Keller, O.; Rudinger, J. Preparation and Some Properties of of Maleimido Acids and Maleoyl Derivatives of Peptides. *Helv. Chim. Acta* **1975**, *58* (62–63), 531–541. https://doi.org/10.1063/1.1662110.

(37) Abel, B. A.; McCormick, C. L. "one-Pot" Aminolysis/Thiol-Maleimide End-Group Functionalization of RAFT Polymers: Identifying and Preventing Michael Addition Side Reactions. *Macromolecules* **2016**, *49* (17), 6193–6202. https://doi.org/10.1021/acs.macromol.6b01512.

(38) Boyer, C.; Granville, A.; Davis, T. P.; Bulmus, V. Modification of RAFT-

Polymers via Thiol-Ene Reactions: A General Route to Functional Polymers and New Architectures. *J. Polym. Sci. Part A Polym. Chem.* **2009**, *47* (15), 3773–3794. https://doi.org/10.1002/pola.23433.

(39) Scales, C. W.; Convertine, A. J.; McCormick, C. L. Fluorescent Labelling of RAFT-Generated Poly(N-Isopropylacrylamide) via a Facile Maleimide-Thiol Coupling Reaction. *Biomacromolecules* **2006**, *7* (5), 1389–1392. https://doi.org/10.1021/bm060192b.

(40) Jones, M. W.; Mantovani, G.; Ryan, S. M.; Wang, X.; Brayden, D. J.; Haddleton, D. M. Phosphine-Mediated One-Pot Thiol-Ene "Click" Approach to Polymer-Protein Conjugates. *Chem. Commun.* **2009**, No. 35, 5272–5274. https://doi.org/10.1039/b906865a.

(41) Chan, J. W.; Yu, B.; Hoyle, C. E.; Lowe, A. B. The Nucleophilic, Phosphine-Catalyzed Thiol-Ene Click Reaction and Convergent Star Synthesis with RAFT-Prepared Homopolymers. *Polymer (Guildf).* **2009**, *50* (14), 3158–3168. https://doi.org/10.1016/j.polymer.2009.04.030.

(42) Li, G. Z.; Randev, R. K.; Soeriyadi, A. H.; Rees, G.; Boyer, C.; Tong, Z.; Davis, T. P.; Becer, C. R.; Haddleton, D. M. Investigation into Thiol-(Meth)Acrylate Michael Addition Reactions Using Amine and Phosphine Catalysts. *Polym. Chem.* **2010**, *1* (8), 1196–1204. https://doi.org/10.1039/c0py00100g.

(43) Willcock, H.; O'Reilly, R. K. End Group Removal and Modification of RAFT Polymers. *Polym. Chem.* **2010**, *1* (2), 149–157. https://doi.org/10.1039/b9py00340a.

(44) Skrabania, K.; Miasnikova, A.; Bivigou-Koumba, A. M.; Zehm, D.; Laschewsky, A. Examining the UV-Vis Absorption of RAFT Chain Transfer Agents and Their Use for Polymer Analysis. *Polym. Chem.* **2011**, *2* (9), 2074–2083. https://doi.org/10.1039/c1py00173f.

(45) Tummino, P. J.; Gafni, A. Determination of the Aggregation Number of Detergent Micelles Using Steady-State Fluorescence Quenching. *Biophys. J.* **1993**, *64* (5), 1580–1587. https://doi.org/10.1016/S0006-3495(93)81528-5.

(46) Wolfbeis, O. S.; Fürlinger, E.; Kroneis, H.; Marsoner, H. Fluorimetric Analysis - 1. A Study on Fluorescent Indicators for Measuring near Neutral ("Physiological") PH-Values. *Fresenius' Zeitschrift für Anal. Chemie* **1983**, *314* (2), 119–124. https://doi.org/10.1007/BF00482235.

(47) Huesmann, D.; Sevenich, A.; Weber, B.; Barz, M. A Head-to-Head Comparison of Poly(Sarcosine) and Poly(Ethylene Glycol) in Peptidic, Amphiphilic Block Copolymers. *Polymer (Guildf).* **2015**, *67*, 240–248. https://doi.org/10.1016/j.polymer.2015.04.070.

(48) Ábrahám, Á.; Katona, M.; Kasza, G.; Kiss, É. Amphiphilic Polymer Layer – Model Cell Membrane Interaction Studied by QCM and AFM. *Eur. Polym. J.* **2017**, *93* (May), 212–221. https://doi.org/10.1016/j.eurpolymj.2017.05.047.

(49) Klaikherd, A.; Nagamani, C.; Thayumanavan, S. Multi-Stimuli Sensitive Amphiphilic Block Copolymer Assemblies. *J. Am. Chem. Soc.* **2009**, *131* (13), 4830–4838. https://doi.org/10.1021/ja809475a.

(50) Saravanakumar, G.; Park, H.; Kim, J.; Park, D.; Pramanick, S.; Kim, D. H.; Kim, W. J. Miktoarm Amphiphilic Block Copolymer with Singlet Oxygen-Labile Stereospecific β-Aminoacrylate Junction: Synthesis, Self-Assembly,

and Photodynamically Triggered Drug Release. *Biomacromolecules* **2018**, *19* (6), 2202–2213. https://doi.org/10.1021/acs.biomac.8b00290.

Chapter 3

Structural based assessment of polymer-cell interaction

The work described in this chapter aimed at characterising the effect that the variations in structure of the synthesised membrane-inserting polymers had on the interaction with an intestinal cell culture model, Caco-2 cells. This investigation was carried out through a variety of experimental methods, comparing these polymeric materials for their effect on cell membrane fluidity (using Laurdan, a fluorescent probe sensitive to local membrane packing/order), cell viability/membrane damage (with PrestoBlue™ and LDH assays. Finally, association with Caco2 cell membranes was assessed by flow cytometry and fluorescence microscopy.

3.1 Introduction

As described in **Chapter 1**, GPI anchors possess a lipophilic phosphatidyl-inositol domain that inserts with weak interactions in cell membranes, and a larger hydrophilic domain consisting of a polysaccharide linker connected to the C-terminus of a protein[1]. The polymers synthesised in **Chapter 2** are designed to mimic some of these characteristics, with lipophilic cholesterol or phospholipid as a membrane-binding chain end-group, connected to a larger hydrophilic domain. Within **Chapter 3**, these amphiphilic polymers were applied to relevant cell models to evaluate the potential for membrane interaction, as well as the effect the polymers had on cell viability and cell membrane damage. Analogous PABTC-based polymers were used as control, as these do not possess membrane-inserting domains.

The polymers were tested on Caco-2 cells, as this cell line is commonly used as a model for intestinal epithelium[2] and with this cell line it is possible to achieve differentiation and formation of a monolayer presenting tight junctions and microvilli[3–5].

We first investigated the toxicity of the previously described polymers on Caco-2 cells, to correlate the effect that the polymer structure had on cell viability and cell membrane damage. After having established safe concentrations to employ on cells, we employed the Laurdan assay to investigate the effect that these polymers had on cell membrane fluidity. The data showed that the amphiphilic polymers increased the cell membrane fluidity, while the hydrophilic control polymers were not having an analogous effect. Therefore, we hypothesised that polymers presenting membrane-derived moieties such as cholesterol and DOPE were inserting in the cell membrane and causing a disruption of the membrane packing.

Finally, by employing the previously described fluorescently tagged polymers, confocal microscopy allowed visualise the tagged polymers interacting with cells. Additionally, flow cytometry was used to quantify the amount of fluorescent polymers interacting with Caco-2 cells. This allowed us to compare the various polymers synthesised in this study in terms of their ability to associate with cells, and to confirm the hypothesis postulated on the basis of the Laurdan assay data. These studies were employed to establish a structure-activity relationship (SAR) model for these materials in terms of their ability to interact with cell membranes.

When amphiphilic molecules interact with cell membranes, they can induce changes in the cell membrane's equilibrium curvature[6], resulting in loss of cell membrane organisation and stability[7]. This is caused by two main drivers: firstly, bilayers exposed to amphiphiles are characterised by endothermic excess of enthalpy due to the disturbance of intra- and inter-molecular interactions in the membrane[8,9]. At the same time, this interaction causes an increase in entropy of the system, due to increased motional and conformational freedom for the membrane components[9,10] The combination of these effects results in an increase in free energy of the system, which causes thinning of the lipophilic membrane and strain disorder[11,12]. Based on the structural characteristics of the amphiphilic species, the interaction may destabilise the lipid bilayer membrane in different ways:

i) Direct insertion of amphiphilic molecules in the cell membrane[13] (**Figure 3.1A**). Depending on the characteristics of the amphiphilic molecule, this insertion could lead to formation of holes[14] or bilayer discs[15,16] within the membrane.

ii) Extraction of membrane phospholipids by amphiphilic molecules in micellar form (**Figure 3.1B**). This is typical for larger amphiphiles, which do not readily insert in the membrane and tend to remain as supramolecular aggregates. The depletion of phospholipids from the

cell membrane causes vesicle reorganisation and migration of phospholipids from the inner leaflet to the outer leaflet[13].

iii) Non-specific interaction of amphiphilic molecules with membranes[17] (**Figure 3.1C**). Typical of antimicrobial peptides and larger molecules, such as polymers. The interaction starts with the amphiphilic molecules sitting transversally on the membrane, which is then destabilised by the formation of pores (barrel-stave model[18]) or by coverage of the surface until a threshold concentration is reached (carpet-like model[19]).

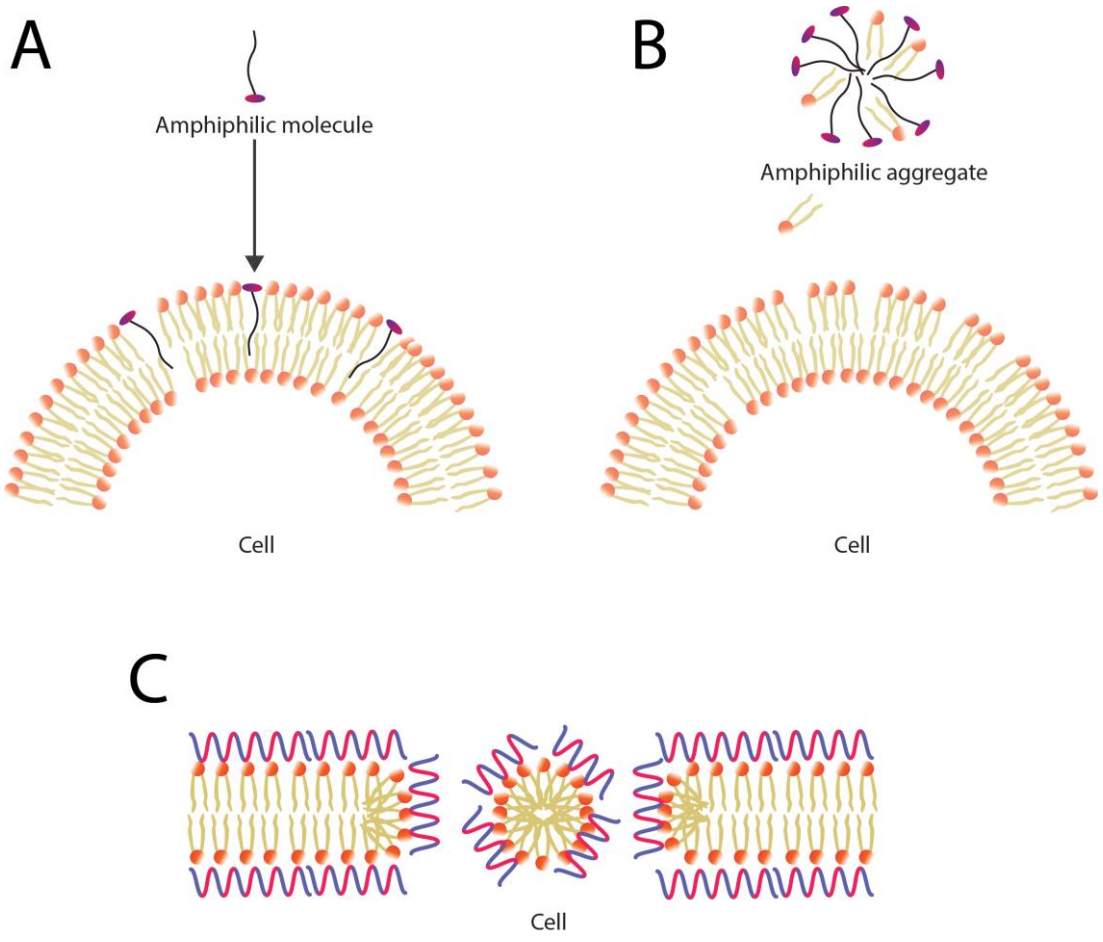


Figure 3.1 Modalities of interaction between amphiphilic molecules and cell membranes : A) direct insertion of detergent-like molecules; B) extraction of phospholipids from the cell membrane by amphiphilic aggregates; C) carpet-like interaction, typical of antimicrobial peptides.

Regarding influence of amphophilic molecules on membrane packing, it is also important to consider that some cholesterol-based cationic amphiphiles can inhibit the activity of Protein Kinase C (PKC)[20].This is especially important since PKC activity regulates the intracellular calcium levels [21,22], which in turn are responsible for cell membrane fluidity regulation[23,24]. Therefore, a potential increase in membrane fluidity could be caused either by direct interaction of the amphiphiles with cell membrane, or by inhibition of PKC.

3.2 Materials and Methods

3.2.1 Materials

Human epithelial colorectal adenocarcinoma cells (Caco-2, American Type Culture Collection ATCC; Manassas, Virginia, passage 45-52) were used for this study. EMEM, HBSS, streptomycin/amphotericin solution, FBS, L-glutamine, PBS and trypsin/EDTA solution were purchased from Sigma (UK).

PrestoBlue™ cell toxicity reagent, LDH cytotoxicity assay kit (Pierce™) and Laurdan dye (6-dodecanoyl-2-dimethylaminonaphthalene) were purchased from ThermoFisher Scientific (USA).

3.2.2 Routine cell culture conditions

Cells were cultured in 75 cm^2 flasks with EMEM supplemented with 10% (v/v) FBS, 0.1 mg/mL of streptomycin, 100 units/mL of penicillin, 0.25 µg/mL of amphotericin, and 2 mM L-glutamine at 37 °C with 5% CO_2. Cells were fed every other day or every three days with pre-warmed (37 °C) media, after having aspired old media. Cells were split after confirming confluence through optical microscopy. First, old medium was removed and cells were washed twice with pre-warmed (37 °C) PBS to remove any debris and remaining FBS, which would inhibit the effect of trypsin. Once washed, PBS was removed and 2.5 mL of a pre-warmed (37 °C) trypsin-EDTA solution were added to the cells, which were incubated for 5 minutes in the standard cell culture conditions. Then, an equal amount (2.5 mL) of pre-warmed media was added to the detached cells, to inhibit further effect of trypsin and to recover as many cells as possible. The combined solution was transferred into a falcon tube for centrifugation (250g for 4 minutes), to obtain a pellet of cells. The supernatant was aspirated, and the cell pellet was suspended in an adequate amount of pre-warmed (37 °C) media. Aliquots from this suspension were transferred to new flasks, based on the desired splitting ratio.

Cells were regularly split with ratios of 1:2, 1:3, 1:6, 1:10 (based on the amount and speed of growth needed). Cells were incubated at 37 °C and in a 5% CO_2 atmosphere.

For multiple compounds and experimental repeats, cells were seeded in 96 and plates. Cells were prepared with the same procedures used for splitting, and the solution for seeding was prepared with a concentration of $6.6*10^5$ cells per mL of media. Using a multi-channel pipette, 150 µL of this suspension were transferred in each well, resulting in a concentration $1*10^4$ per well, a value commonly found in literature for this type of cells and well size[25]. If possible, the outermost wells were avoided from being seeded with cells, in order to avoid variation associated with uneven temperature[26] and adsorption fluctuations[27] (also known as "edge effect"[28]).

3.2.3 PrestoBlue™ cell viability and Lactate Dehydrogenase (LDH) joint assays protocol

Caco-2 cells were seeded at concentration $1*10^4$ per well in 96-well plates (black) and cultured for 24 hours. The medium was removed from cells, and these were exposed to solutions of selected polymers for the chosen amount of time (generally 24 hours) in phenol-free medium. Following exposure, 50 µL of supernatant from each well were transferred to another 96-well plate, LDH solution was added to each well and after 25 min incubation the absorbance was measured at 490 nm. Relative LDH release was calculated through **Equation 3.1**, with the negative control taken as untreated cells, and positive control as total cell lysis (Triton X):

$$Relative\ LDH\ release = \left(\frac{(\mathrm{A}x - \mathrm{A}(Negative\ control))}{(\mathrm{A}(Positive\ control) - \mathrm{A}(Negative\ control))}\right) \times 100$$

Equation 3.2 Calculation of relative LDH release, for the purpose of membrane damage evaluation. A values used represent absorbance at λ = 490 nm. Ax represents sample absorbance.

The solution remaining in the original plate was washed off with PBS, PrestoBlue™ (Thermofisher) 10% solution (in phenol red-free medium) was added, and after 60 min incubation fluorescence was measured at λ_{em} = 600 nm (λ_{ex} =560). The relative metabolic activity was calculated through **Equation 3.2**, with the negative control as untreated cells, and negative control as total cell lysis (triton X):

$$Relative\ metabolic\ activity = \left(\frac{(\mathrm{I}x - \mathrm{I}(Positive\ control))}{(\mathrm{I}(Negative\ control) - \mathrm{I}(Positive\ control))}\right) \times 100$$

Equation 3.3 Calculation of relative metabolic activity, PrestoBlue™ assay. All I values represent fluorescence intensity following excitation at λ_{ex} = 560 nm and emission at λ_{em} = 600 nm. Ex represents sample fluorescent signal.

The 96-well plates were analysed with a Spark 10M Plate Reader (Tecan) and analysed with SparkControl 2.1 software, then further elaborated with Prism 8.4.2 (GraphPad). The measurement was run at 37 °C, with λ_{ex} = 560 nm and λ_{em} = 600 nm for PrestoBlue™ and absorbance 490 nm for LDH.

3.2.4 Laurdan assay

Caco-2 cells were seeded at concentration $1*10^4$ per well in 96-well plates (black) and cultured for 24 hours. The medium was removed from cells and these were incubated with a 2 µM HBSS solution of Laurdan dye (6-dodecanoyl-*N,N*-dimethyl-2-naphthylamine, Thermofisher) for 30 minutes[25]. Following exposure, the dye was washed off twice with PBS, and the chosen treatment in HBSS (150 µL) was added to the wells. After 30 minutes of incubation, fluorescence was measured at 360/460 nm ($\lambda_{ex}/\lambda_{em}$) and at 360/500 nm ($\lambda_{ex}/\lambda_{em}$), at 37 °C.

Generalised Polarisation (GP) of Laurdan was calculated by subtracting the blank (cells + medium, to account for the auto fluorescence) to the values measured in every Laurdan-exposed well, and by using **Equation 3.3**:

$$GP = \frac{(I_{460} - I_{500})}{(I_{460} + I_{500})}$$

Equation 3.4 Calculation of Generalised Polarisation (GP) of Laurdan. I_{460} and I_{500} represent fluorescence intensities at λ_{em} = 460 nm and λ_{em} = 500 nm respectively, following excitation at λ_{ex} = 360 nm.

The 96-well plates were analysed with a Spark 10M Plate Reader (Tecan) and data was recorded using a SparkControl 2.1 software. Data was processed with Prism 8.4.2 (GraphPad).

3.2.5 Preparation of the staining DiL solution

The DiL membrane staining solution was prepared by solubilising solid DiL in EtOH (3 mg/mL). This solution was then diluted in HBSS (1:99) and employed for cell membrane staining (final DiL concentration 30 µg/mL)[29].

3.2.6 Fluorescence microscopy

Caco-2 cells were seeded at concentration $1*10^4$/mL in 12-well plates, and cultured in phenol-red free EMEM. After 24 hours incubation, the medium was removed from cells and these were treated with an appropriate quantity of the DiL staining solution[29] (1 mL for 12-well plates) and were incubated for 20 minutes. The cells were washed twice with PBS to remove excess DiL staining solution, and the fluorescently tagged polymer solutions (0.1 µM in HBSS) were added to the wells and cells were incubated for 20 minutes. The fluorescent polymer solutions were removed, and cells were washed twice with PBS to remove the excess polymer solutions, and HBSS medium was added to the wells.

Cells were imaged on an inverted Nikon Eclipse TE 300 fluorescence microscope on DAPI, FITC, TRITC and Cy5 filters.

3.2.7 Quantitation of interaction by exposure to fluorescent polymers

Caco-2 cells were seeded at concentration $1*10^4$ in 96-well plates (black) and cultured for 24 hours. The medium was removed from cells, and these were exposed to HBSS solutions of fluorescently tagged polymer 30 minutes. After incubation, the fluorescence (λ_{ex} = 377 nm and λ_{em} = 420) was registered to set the starting values for each well (FI_{start}). Following exposure, the unbound polymers were washed off with PBS, and fresh HBSS (150 µL) was added to the wells. Fluorescence (λ_{ex} = 377 nm and λ_{em} = 420) was measured to estimate the amount of polymer still present after washing (FI_w). The percentage of relative fluorescence was calculated per each well by using **Equation 3.4**:

$$\%\, relative\ fluorescence = \frac{FI_w}{FI_{start}} * 100$$

Equation 3.5 Calculation of relative fluorescence (%) of cells following incubation with MalPyr Blue-tagged fluorescent polymers and washing of unbound polymers. Values represent fluorescence intensities measured at λ_{ex} = 377 nm and λ_{em} = 420.

3.2.8 Cell fixing and confocal microscopy

Caco-2 cells were seeded at concentration $1*10^4$/mL in 12-well plates, with glass coverslips (22 mm diameter) on the bottom of each well and cultured in phenol-red free EMEM. The glass coverslips were previously sterilised by immersion in 70% industrial methylated solvent (IMS) and rinsed with PBS. After 24 hours incubation, the medium was removed from cells and these were treated with an appropriate quantity of the DiL staining solution[29] (1 mL for 12-well plates) and were incubated for 20 minutes. The cells were washed twice with PBS to remove excess DiL staining solution, and the fluorescently tagged polymer solutions (0.1 µM in HBSS) were added to the wells and cells were incubated for 20 minutes. The fluorescent polymer solution was removed, and cells were washed twice with PBS to remove the polymer solutions.

Medium was then removed and a 4% paraformaldehyde fixing solution was added to the wells. After 20 minutes incubation, the fixing solution was removed, and the cells were washed twice with PBS. The medium was aspirated, and the coverslips were mounted on glass slides with ProLong™ Gold antifade mounting reagent. The glass slides were stored in the fridge (2-8 °C) for 2 weeks before being imaged.

3.2.9 Statistical testing

Statistical analysis was performed using GraphPad Prism. Statistical significance of data was determined by one-way or two-way ANOVA testing, followed up by multiple comparisons tests (** $P < 0.01$, *** $P < 0.001$, **** $P < 0.0001$). The error bars in the graphs have been calculated as Standard Error of Mean (SEM).

3.2.10 Haemolysis assay

Equal volumes of blood (defibrinated sheep blood, Oxoid) and PBS were added to falcon tubes; after centrifugation (5 min, 5000g, room temperature) the supernatant was removed, and PBS was added to the pellet. This process was repeated twice, and the final solid residue was resuspended in 50 mL PBS. The polymers were solubilised in PBS, and 0.5 mL of each tested concentration were transferred in 1.5 mL Eppendorf vials. The resuspended blood solution was added (0.5 mL each) to the Eppendorf vials containing the polymer solutions, as well as to vials containing positive control (1% Triton X-100) and negative control (PBS).

The solutions were left to interact for 3 hours in a shaking heated water bath (37 °C). The Eppendorf vials were subject to centrifugation (5 min, 5000 g) and 0.100 mL of the supernatant from each vial was transferred in a 96-well plate (Costar clear bottom). After making sure there were no bubbles present in the wells,

absorbance was measured at λ = 540 nm. Percentage of haemolysis was calculated as:

$$\%haemolysis = \left[\frac{(x - negative\ control)}{(positive\ control - negative\ control)}\right] \times 100$$

Equation 3.6 Calculation of relative haemolysis, for the purpose of cell damage evaluation. Values used represent absorbance at λ = 540 nm. X represents sample absorbance.

The blood-containing suspensions were disposed of by using commercial bleach, or a 10% NaClO solution prepared extemporaneously.

3.3.11 Flow Cytometry

Caco-2 cells were seeded at concentration $1*10^4$/mL in 12-well plates in phenol-red free EMEM. After 24 hours incubation, the medium was removed from cells, and these were treated with an appropriate volume (1 mL) of the fluorescently tagged polymer solutions (0.1 μM in HBSS) for a 20 minute incubation. The fluorescent polymer solutions were removed, and cells were washed twice with PBS to remove the polymer solutions. The cells were exposed to an appropriate quantity (0.3 mL per well) of a pre-warmed (37 °C) trypsin-EDTA solution. Cells were incubated for 5 minutes in the standard cell culture conditions. Then, an equal amount (0.3 mL) of pre-warmed phenol red-free medium was added to the detached cells, to inhibit further effect of trypsin and to recover as many cells as possible. The cell suspensions were transferred into 1.5 mL Eppendorf vials for centrifugation (250g for 4 minutes), to obtain a pellet of cells. The supernatant was aspirated, and the cell pellet was suspended in 40 μL of room temperature PBS. Cells were stored on ice and covered from light for 2 hours, and then were analysed on Amnis® Imagestream^{X}® MKII Imaging Flow Cytometer (Luminex).

The images and data were elaborated using the IDEAS® 6.0 software (LuminexCorp). The results are expressed as adjusted Median Fluorescence Intensity (aMFI), calculated as:

$$aMFI = \frac{median\ fluorescence\ intenstity\ (sample)}{median\ fluorescence\ intensity\ (untreated\ cells)} \times Tagging\ efficiency$$

Equation 3.7 Calculation of adjusted median fluorescence intensity (MFI). Values represent median fluorescence intensity measured for cells, measured at λ_{ex} = 377 nm and λ_{em} = 420 nm for MalPyr Blue polymers and λ_{ex} = 560 nm and λ_{em} = 580 nm for Rhodamine Red polymers.

3.3 Results and Discussion

3.3.1 Cell toxicity of the membrane-inserting polymers synthesised in this work

The polymer toxicity was evaluated with two different assays, which assessed the polymer influence on cell metabolic activity and on cell membrane damage. The first assessment was conducted on cell viability after exposure to the synthesised polymers. This was performed using PrestoBlue™, a resazurin-based assay that estimates the viability of cells by measuring their metabolic activity[32]. The second toxicity assay performed (LDH) assesses the cell membrane damage following treatment with a given compound/material by quantifying the LDH enzyme released from the cytoplasm[33].

In these experiments Caco-2 cells were incubated with polymer at different concentrations for 24 hours, to evaluate the effect of the treatment on cell metabolism and membrane integrity. Tests were done to investigate whether the lipophilic groups on the polymer chains induced membrane damage decreasing cell viability at high polymer concentrations. The control polymers on the other hand should have a lesser effect on cells, specifically on cell membrane damage.

The toxicity results for cholesterol-based polymers showed that some polymers, irrespective of their monomer composition, were increasing the cell metabolic activity measured by PrestoBlue™ assay (**Figure 3.2**). This effect could be the result of a cellular response to external stress factors[34,35].

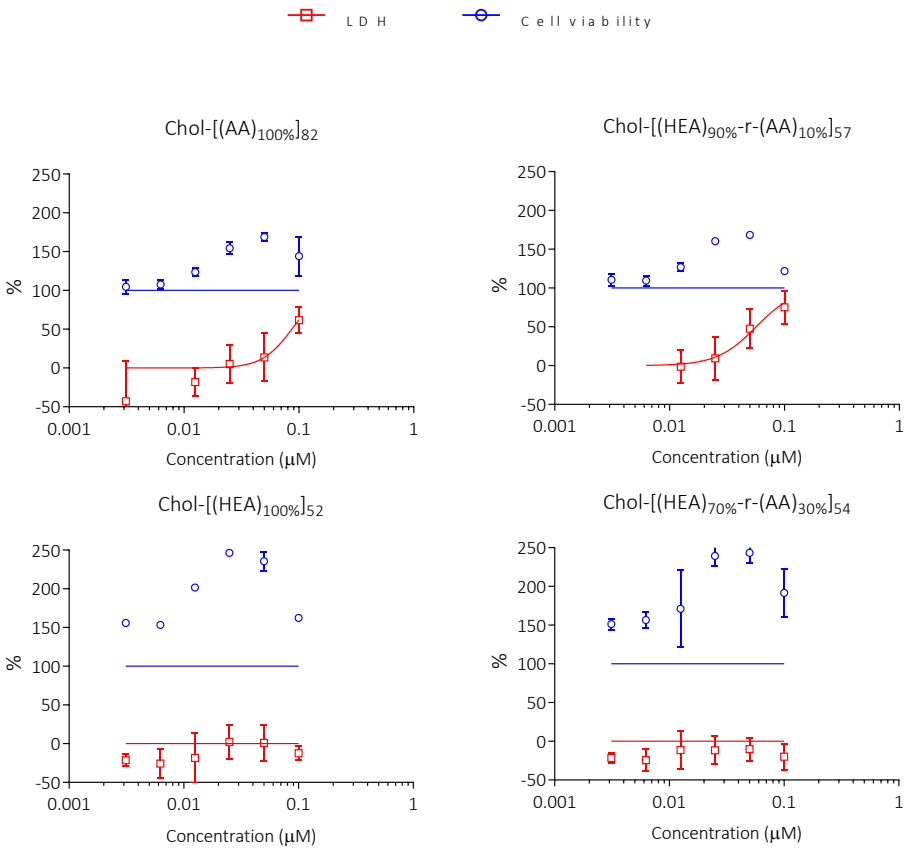


Figure 3.2 Cell toxicity results for select cholesterol-based polymers. The assays were performed on Caco2 cells, after 24 hours exposition to the polymer suspensions at different concentrations. The graph shows LDH release, indicative of membrane damage, in red and PrestoBlue™ results, which indicate cell viability, in blue. IC_{50} values were calculated using an [inhibitor] versus normalised response nonlinear regression curve fitting. 100% membrane damage was assumed for cells treated with a 1% Triton X-100 solution and 0% membrane damage was assumed for untreated cells. 0% metabolic activity was assumed for cells treated with a 1% Triton X-100 solution and 100% metabolic activity was assumed for untreated cells (n = 9, error bars expressed as SD).

As described previously, PrestoBlue™ assay relies on the reduction of Resazurin to Resorufin promoted by NADH-dependent enzymes. Therefore, an increase in NADH concentration would also translate in a metabolic activity increase. As NADH levels are linked to glycolysis[34] and this process is linked to the activation of survival pathways[36,37], it is possible that exposure of Caco2 cells to the tested polymers could activate some of these processes. A recent study[25] showed that exposure to a non-ionic surfactant as Kolliphor HS15 increases the glycolytic processes in cells exposed to stress as a survival mechanism[35,38]. This cascade of

processes could explain the observed increase in metabolic activity for cells exposed to amphiphilic polymers.

The results for the larger library of cholesterol-based polymers are summarised in **Table 3.1**. The trend showed an IC_{50} value for cell metabolic activity between 0.1-0.2 μM polymer concentration, with no evident correlation to monomer composition. The Cholesterol-based polymers showed high potential for cell membrane damage, with the upper IC_{50} values averaging around 0.1-0.2 μM polymer concentration, while more toxic polymers showed an elevated degree of membrane damage between 0.04-0.08 μM. These results showed that, for most cholesterol-based polymers, we observed cell membrane damage at concentrations where the cells were still metabolically viable. As the LDH assay measures extracellular presence of intracellular material, the high level of damage measured could be due to membrane instability caused by the interaction of polymers with the cell membrane while the cells were still metabolically viable, as represented by the higher IC50 values measured with the PrestoBlue™ assay.

Table 3.1 PrestoBlue and LDH IC_{50} values for Caco-2 cells exposed for 24 hours to solutions of the amphiphilic cholesterol polymers. calculated by using an [inhibitor] versus normalised response nonlinear regression curve fitting (n = 9-12).

Polymer	**IC_{50} (μM)**	
	PrestoBlue™	LDH
Chol-[$(HEA)_{100\%}$]$_{108}$	>1	0.17
Chol-[$(HEA)_{100\%}$]$_{70}$	0.11	0.04
Chol-[$(HEA)_{100\%}$]$_{58}$	>1	0.043
Chol-[$(HEA)_{100\%}$]$_{52}$	0.11	>1
Chol-[$(AA)_{100\%}$]$_{82}$	>0.2	0.28
Chol-[$(AA)_{100\%}$]$_{54}$	>0.2	0.1
Chol-[$(HEA)_{90\%}$-*r*-$(AA)_{10\%}$]$_{105}$	>0.2	0.11
Chol-[$(HEA)_{90\%}$-*r*-$(AA)_{10\%}$]$_{57}$	0.12	0.05
Chol-[$(HEA)_{90\%}$-*r*-(AA)10%]$_{51}$	0.21	0.05
Chol-[$(HEA)_{70\%}$-*r*-(AA)30%]$_{94}$	>0.2	0.1134
Chol-[$(HEA)_{70\%}$-*r*-$(AA)_{30\%}$]$_{54}$	>1	>1
Chol-[$(HEA)_{70\%}$-*r*-$(AA)_{30\%}$]$_{52}$	0.21	0.05
Chol-[$(HEA)_{90\%}$-*r*-$(AAPA)_{10\%}$]$_{140}$	>1	0.08
Chol-[$(AAPA)_{50\%}$-$(HEA)_{50\%}$]$_{99}$	0.0911	/
Chol-[$(AAPA)_{50\%}$-$(HEA)_{50\%}$]$_{151}$	0.2	/

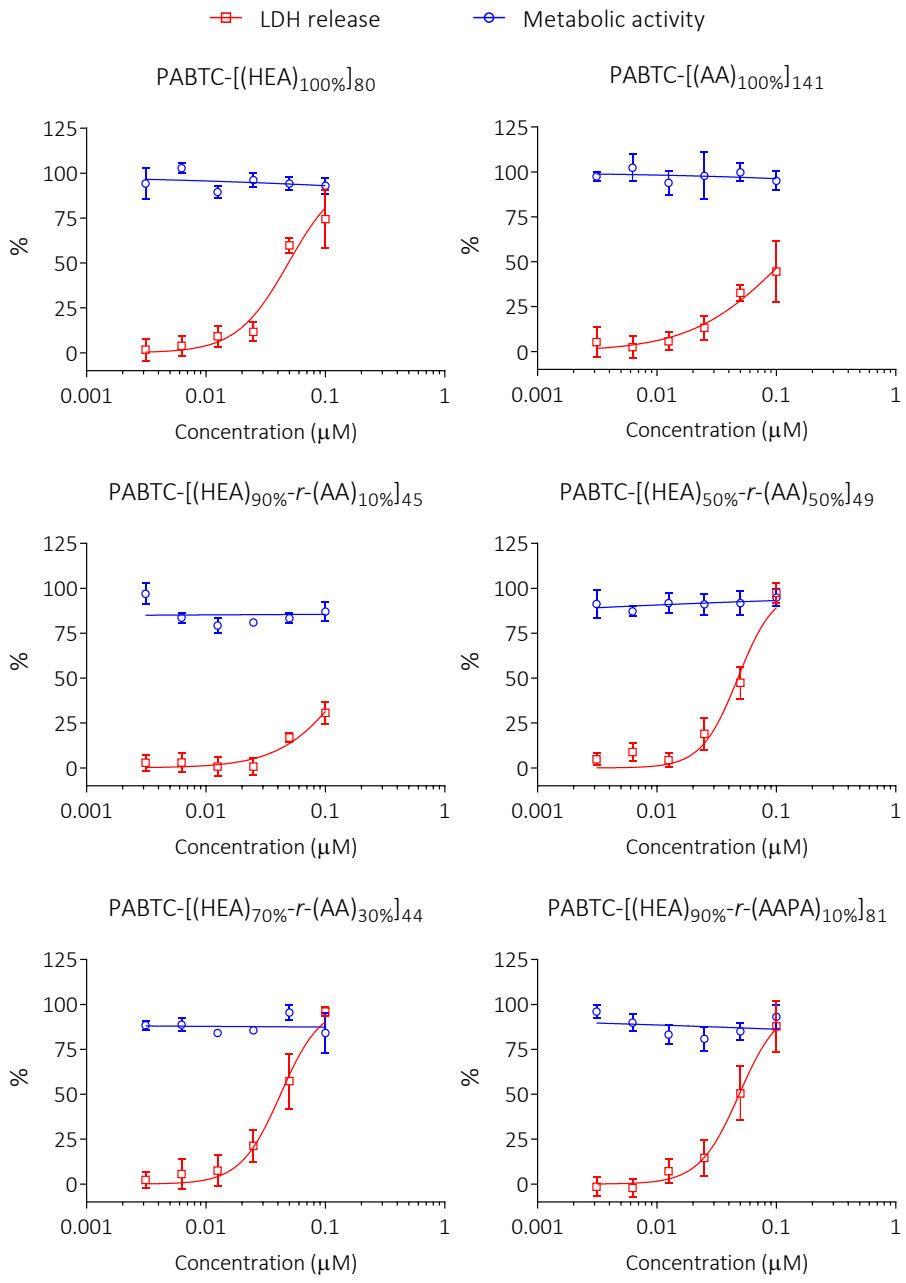


Figure 3.3 Cell toxicity results for selected control polymers. The assays were performed on Caco2 cells, after 24 hours incubation with the polymer solutions at different concentrations. The graph shows LDH release, indicative of membrane damage, in red and PrestoBlue™ results, which indicate cell viability, in blue. IC_{50} values were calculated using an [inhibitor] versus normalised response nonlinear regression curve fitting. 100% membrane damage was assumed for cells treated with a 1% Triton X-100 solution and 0% membrane damage was assumed for untreated cells. 0% metabolic activity was assumed for cells treated with a 1% Triton X-100 solution and 100% metabolic activity was assumed for untreated cells (n = 9, error bars expressed as SD).

PABTC-based control polymers did not impact Caco-2 cell viability at the tested concentrations (**Figure 3.3**). This effect was in accordance with our initial

hypothesis, where control polymers would have a smaller degree of interaction with cells and cell membranes. Exposure to control polymers did not also increase cell metabolic activity, indicating that the presence, or indeed absence like in these control polymers, of membrane-inserting moieties at the polymer chain-ends may be indeed responsible for the observed effect. However, some of the control polymers did appear to cause some degree of cell membrane damage. This could have been caused by a limited degree of membrane interaction, which may be expected with these polymers, as hydrophilic and methacrylate-based polymers are often used as cryoprotectants for cell membranes[39,40].

The IC_{50} results showed an overall less toxic profile for the control polymers when compared with cholesterol-based polymers. Most of the PABTC-based polymers were not impacting cell metabolic activity at the tested concentrations, and only some polymers were showing levels of cell membrane damage similar to that of Chol- and DOPE-polymers (**Table 3.2**).

Table 3.2 PrestoBlue and LDH IC_{50} values for Caco-2 cells incubated for 24 hours with solutions of the PABTC control polymers, calculated by using an [inhibitor] versus normalised response nonlinear regression curve fitting (n = 9-12).

Polymer	**IC_{50} (µM)**	
	PrestoBlue™	LDH
PABTC-$[(AA)_{100\%}]_{141}$	>1	0.11
PABTC-$[(HEA)_{100\%}]_{80}$	>1	0.049
PABTC-$[(HEA)_{90\%}$-*r*-$(AAPA)_{10\%}]_{81}$	>1	0.049
PABTC-$[(HEA)_{90\%}$-*r*-$(AA)_{10\%}]_{45}$	>1	0.16
PABTC-$[(HEA)_{70\%}$-*r*-$(AA)_{30\%}]_{44}$	>1	0.042
PABTC-$[(HEA)_{50\%}$-*r*-$(AA)_{50\%}]_{49}$	>1	0.048
PABTC-$[(HEA)_{100\%}]_{50}$	>1	/
PABTC-$[(AA)_{100\%}]_{37}$	>1	/
PABTC-$[(HEA)_{90\%}$-*r*-$(AAPA)_{10\%}]_{46}$	>1	/
PABTC-$[(HEA)_{90\%}$-*r*-$(AA)_{10\%}]_{75}$	>1	/
PABTC-$[(HEA)_{70\%}$-*r*-$(AA)_{30\%}]_{80}$	>1	/
PABTC-$[(HEA)_{100\%}]_{63}$	0.14	1.85

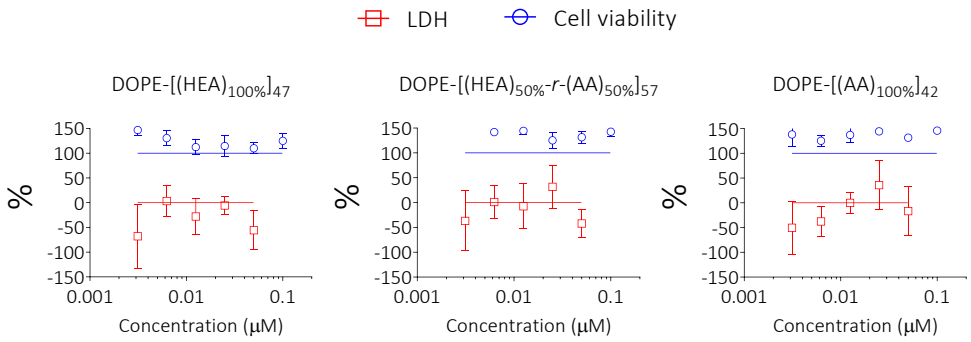


Figure 3.4 Cell toxicity of selected DOPE-containing polymers with targeted DP = 50. The assays were performed on Caco2 cells, after 24 hours exposition to the polymer suspensions at different concentrations. The graph shows LDH release, indicative of membrane damage, in red and PrestoBlue™ results, which indicate cell viability, in blue. IC_{50} values were calculated using an [inhibitor] versus normalised response nonlinear regression curve fitting. 100% membrane damage was assumed for cells treated with a 1% Triton X-100 solution and 0% membrane damage was assumed for untreated cells. 0% metabolic activity was assumed for cells treated with a 1% Triton X-100 solution and 100% metabolic activity was assumed for untreated cells (n = 9, error bars expressed as SD).

Interestingly, DOPE-based polymers (**Figure 3.4**) did not cause significant changes in cell viability and membrane damage at the tested concentrations. The IC_{50} values for the DOPE polymers (**Table 3.3**) showed that only one of the polymers was affecting cell metabolic activity at 0.2 µM polymer concentration, and no polymer was causing cell membrane damage at the tested concentrations.

Table 3.3 PrestoBlue and LDH IC_{50} values for Caco-2 cells exposed for 24 hours to solutions of the amphiphilic DOPE polymers, calculated by using an [inhibitor] versus normalised response nonlinear regression curve fitting (n = 9).

Polymer	**IC_{50} (µM)**	
	PrestoBlue™	LDH
DOPE-$[(HEA)_{100\%}]_{47}$	0.22	>1
DOPE-$[(HEA)_{50\%}$-*r*-$(AA)_{50\%}]_{57}$	>1	>1
DOPE-$[(AA)_{100\%}]_{42}$	>1	>1

When comparing the IC_{50} values obtained for our polymers, we generally found that these were in line or less toxic when compared with similar polymers

described in literature (**Table 2.4**), some of which were tested by (3-(4,5-dimethylthiazol-2-yl)-2,5-diphenyltetrazolium bromide (MTT) cell viability assay[41].

Table 3.4 Toxicity comparison between the polymers described within this study and examples of amphiphilic polymers in the literature, expressed as IC_{50} (μM) and showing the toxicity assay(s) used.

Polymer	Cell line	IC_{50} (μM)	Assay	Ref
PEG-polycaprolactone-linear polyethyleneimine	HeLa	0.0390	MTT	[42]
Chitosan-*g*-polymethyl methacrylate	Caco-2	0.0009	MTT	[43]
Branched polyethyleneimine	HeLa	<0.002	LDH, PrestoBlue	[44]
Chol-$[(HEA)_{100\%}]_{70}$	Caco-2	0.04	LDH, PrestoBlue	/
PABTC-$[(HEA)_{100\%}]_{63}$	Caco-2	0.14	LDH, PrestoBlue	/

Thus, analysis of the relevant literature showed that that the toxicity of our polymers was similar or lower than that of many natural and synthetic polymers tested on the same Caco2 cell line.

In this work, the effect of polymers on cell membrane fluidity (see section 3.3.3 Cell membrane fluidity evaluation) was tested by Laurdan assay which required a 30-minute incubation of Caco2 cells with the selected polymers. Therefore, we also explored the toxicity of the polymers at different concentrations in a 30-minute exposure toxicity assay. We chose to test two Cholesterol-based, AA-based copolymers as these showed the highest potential for toxicity after 24-hour exposure to cells.

The results (**Figure 3.5**) showed that these two cholesterol-based polymers did not impair cell viability or cause membrane damage at the tested concentrations. This showed that, for the short-term incubation employed in the Laurdan assay, these polymers did not cause significant cell membrane damage or impaired cell metabolic activity.

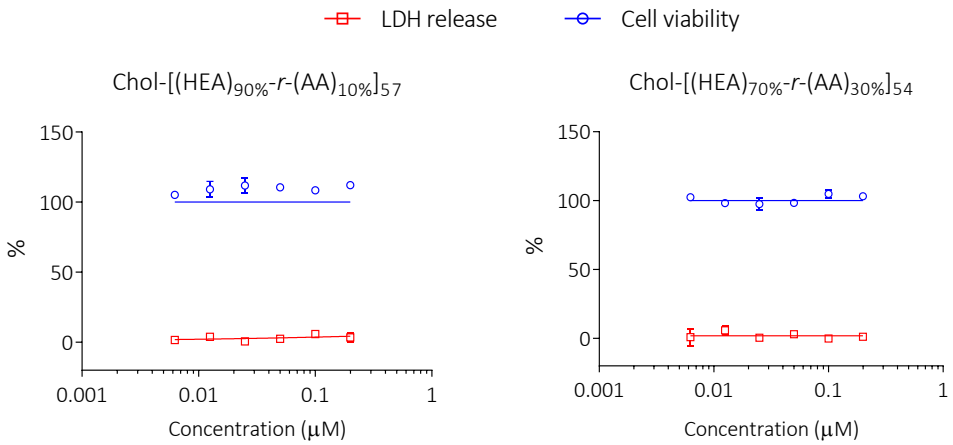


Figure 3.5 Cell toxicity results for selected cholesterol-containing polymers with targeted DP ~ 50. The assays were performed on Caco2 cells, after 30 minutes incubation with polymer solutions at different concentrations. The graph shows LDH release, indicative of membrane damage, in red and PrestoBlue™ results, which indicate cell viability, in blue. IC_{50} values were calculated using an [inhibitor] versus normalised response nonlinear regression curve fitting. 100% membrane damage was assumed for cells treated with a 1% Triton X-100 solution and 0% membrane damage was assumed for untreated cells. 0% metabolic activity was assumed for cells treated with a 1% Triton X-100 solution and 100% metabolic activity was assumed for untreated cells (n = 6, error bars expressed as SD).

Subsequently, we performed a larger set of experiments on cholesterol and control PABTC-containing polymers at the same concentration (0.1 μM in HBSS), with Caco-2 cells. This specific concentration was chosen due to being the highest that did not show significant toxic effects on Caco2 cells after 24-hour incubation time, and it was chosen for the membrane evaluation studies. The results showed a uniformly low degree of cell membrane damage across the variety of polymer compositions, irrespective on the presence of cholesterol at the polymer chain-ends (**Figure 3.6**). These results showed that LDH release caused by cell membrane damage occurred over longer exposure times (24 hours) and was not

significant within a 30-minute exposure to polymer solutions. Conversely, we observed a degree of impact on metabolic activity for both polymer classes, reducing the metabolic activity to 40% of what measured in untreated cells. The effect was higher for shorter polymers and inversely proportional to the percentage of acid monomers present in the polymer. However, we know from the 24-hour polymer exposure that the metabolic activity is reduced at higher concentrations (0.2 μM) or in some cases it is increased. Therefore, we concluded that some polymers can cause an initial decrease in cell metabolic activity, which is then recovered over the course of the following 24 hours.

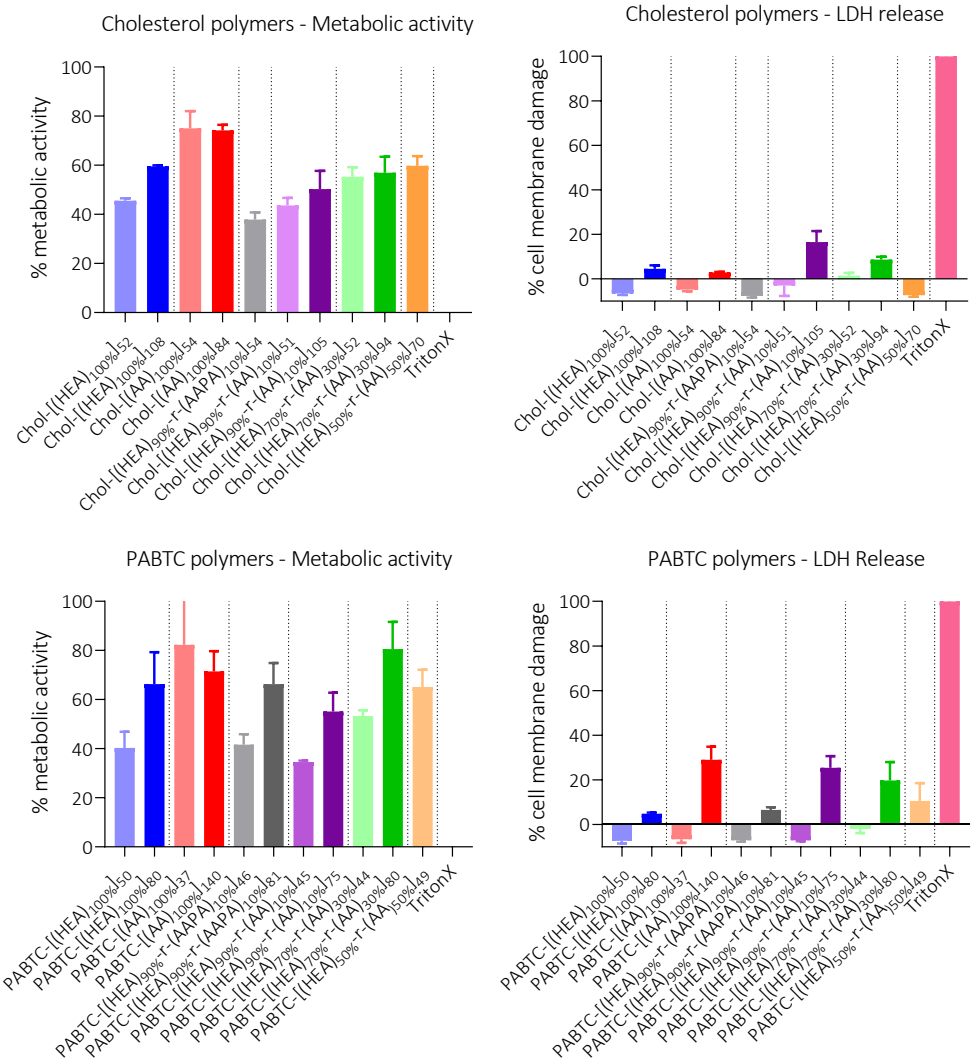


Figure 3.6 Cell toxicity results for select cholesterol-based polymers. The assays were performed on Caco2 cells, after 30 minutes incubation with polymer solutions at the same molar concentration (0.1 μM). The graph shows LDH release, indicative of membrane

damage, on the right and PrestoBlue™ results, which indicate cell viability, on the left. 100% membrane damage was assumed for cells treated with a 1% Triton X-100 solution and 0% membrane damage was assumed for untreated cells. 0% metabolic activity was assumed for cells treated with a 1% Triton X-100 solution and 100% metabolic activity was assumed for untreated cells (n = 6, error bars expressed as SD).

3.3.2 Haemolysis assay

Polymers, especially cationic and amphiphilic, tend to cause rupture of the cell membrane in red blood cells[45]. Therefore, haemolytic activity is commonly used to evaluate the potential for materials to disrupt cell membranes [46]. We employed defibrinated sheep blood as the lack of blood coagulation factors facilitates the washing of erythrocytes[47]. The test carried out following a previously described *in vitro* method where erythrocytes are incubated with test materials at specific concentrations, and their absorbance at λ_{abs} = 540 nm is evaluated against a positive control (Triton X-100) and a negative control (PBS)[48]. The absorbance at λ = 540 nm is directly proportional to the haemoglobin PO_2[49], and is a measure of erythrocyte integrity.

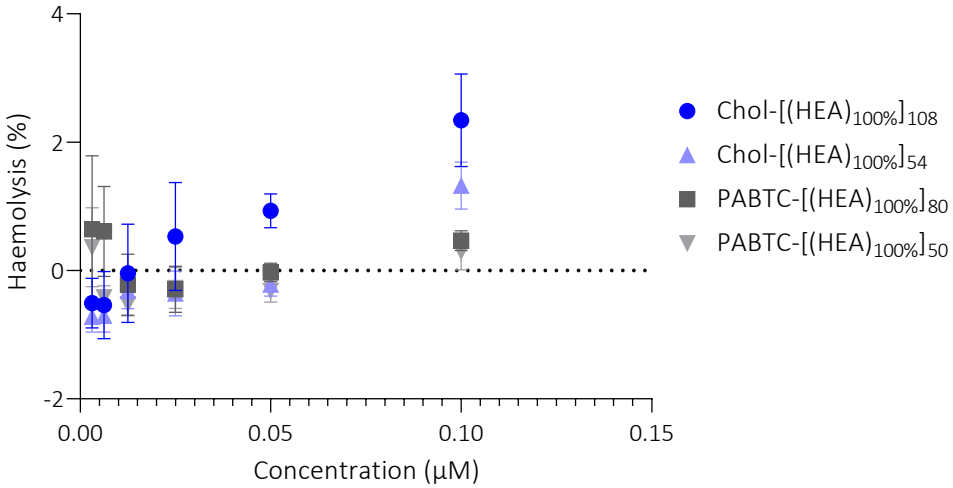


Figure 3.7 Haemolytic activity of (Chol) and PABTC control polyHEA polymers, tested after a 3-hour incubation with erythrocytes. 0% haemolysis is assumed for untreated erythrocytes, while 100% haemolysis is assumed for erythrocytes treated with Triton X-100 (n = 3, error bars expressed as SD).

As it can be observed in **Figure 3.7**, the haemolysis caused by the polymers is very limited when compared with the positive control (Triton-X100). However, we observed a small difference between the cholesterol-bearing polymers and the controls. Therefore, we ran a two-way ANOVA with multiple comparisons between rows (same concentration of different polymers). This test showed statistically significant differences between the two different cholesterol polymers, Chol-$[(HEA)_{100\%}]_{54}$ and Chol-$[(HEA)_{100\%}]_{108}$ as well as statistically significant differences between the cholesterol polymers and the PABTC control polymers lacking membrane-inserting moieties at the polymer chain ends. The results are lower to what was observed for the amphiphilic cholesterol copolymers (10% haemolytic activity at 0.01 mg/mL, equivalent to 0.05 μM)[50] and Pluronic F127 (65% haemolytic activity at 2 μg/mL concentration)[51], showing comparably low haemolytic activity for our polymers.

3.3.3 Cell membrane fluidity evaluation

In the previous sections, we investigated the interaction between cells and amphiphilic polymers, in terms of cell viability and membrane integrity. The LDH assay showed that the phospholipid DOPE and especially the cholesterol-presenting polymers caused cell membrane damage at high concentrations. This trend was not observed for the control PABTC polymers, suggesting that the presence of a membrane-inserting moiety at the end of polymer chains was mostly responsible for the observed phenomena.

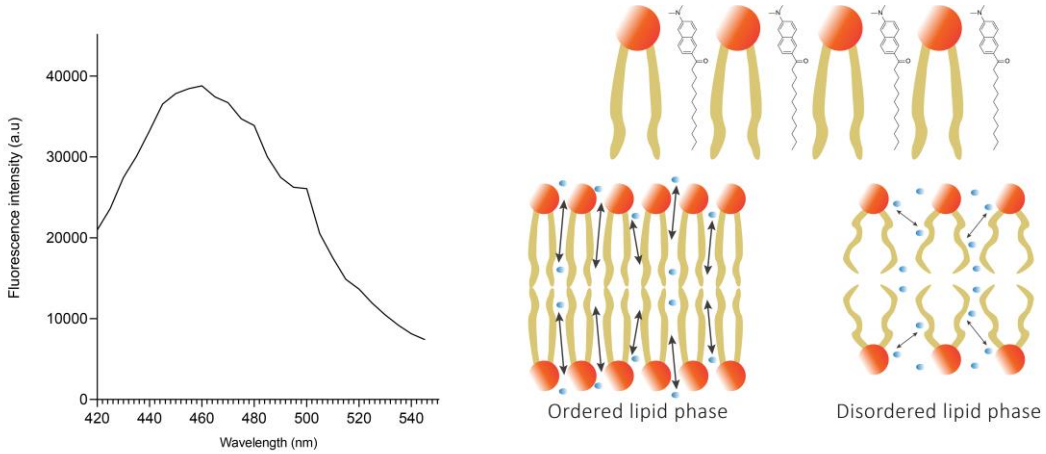


Figure 3.8 Representation of the emission for the Laurdan dye, showing the two main emission peaks (left). Representation of the Laurdan dye intercalating with phospholipids (top right), and of water molecules (small blue spheres) being more able to move in a disordered lipid phase when compared with an ordered lipid phase (bottom right).

In this part of our study, we then decided to further investigate and understand the effect of polymer insertion on the packing and fluidity of the cell membranes, using the Laurdan assay. Laurdan is a lipid bilayer-intercalating dye which when excited at λ_{ex} = 390 nm fluoresces more strongly at λ_{em2} = 490 nm, when in less orderly membranes, or membrane domains.[52,53] Conversely, the dye fluoresces more strongly at λ_{em1} = 440 nm in more packed and ordered membranes. This difference in emission profile is due to the higher concentration of water in more disordered L_d lipid phase. H-bonding with water changes the dipolar moment relaxation for the excited state of Laurdan, affecting its the emission spectrum[54]. Thus, it is possible to correlate the general order of the membrane based on the observed the Laurdan fluorescence emission shift, as illustrated in **Figure 3.8**.

The extent of this effect can be expressed as generalised polarisation (GP), which is calculated by comparing the emission spectrum of the dye at λ_{em1} = 440 nm and at λ_{em2} = 490 nm (eq. 3.3 in Materials and Methods). GP is a value that ranges from -1 to +1, with positive values indicative of a rigid membrane, and negative values indicating that a given membrane is fluid. In this part of this work, results are also expressed as ΔGP, which is the difference between the GP of cells treated with our polymers and that of untreated cells. Expressing results as ΔGP allows for a more straightforward interpretation of the cell membrane fluidity graphs, setting the baseline as the GP of untreated cells. As a general reference, untreated Caco-2 cells yielded a GP of 0.2, in line with what reported in previous literature[25].

To understand the effect of polymer structural variables – i.e. chain length and composition - on membrane fluidity, the materials were tested at the same molar concentration (0.1 μM). When exposed to polymer solutions at these concentrations for 24 hours, Caco-2 cells were still viable, although some degree of membrane damage was present. Low molecular weight RAFT agents containing the same membrane inserting moieties found at the chain ends of our polymers were also tested, to investigate the effect of polymer chains on membrane fluidity. The results are illustrated in the following figures, with statistical significance tested through a one-way ANOVA comparing the fluidity values obtained for polymer-treated cells with the values measured for untreated cells.

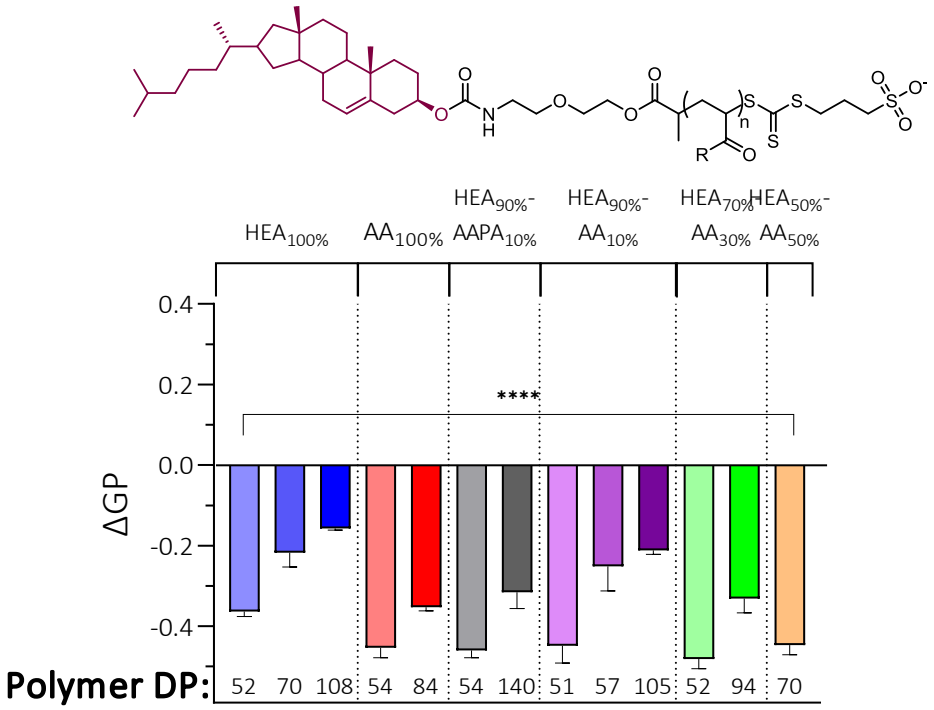


Figure 3.9 Membrane fluidity assays (Laurdan on Caco-2 cells, polymer concentration: 0.1 μM; incubation time: 30 minutes), employing cholesterol-based polymers. Results are expressed as delta generalised polarisation (ΔGP): a positive value represents an increase in membrane rigidity, while a negative value an increase in membrane fluidity, compared to untreated cells. The cholesterol-based polymers caused a statistically significant increase in membrane fluidity, and exhibit a chain length dependent effect on membrane fluidity: at the same molar concentration of polymer chains, independently from monomer composition shorter polymers induced a larger increase in membrane fluidity. Statistical analysis of the results was carried out through a one-way ANOVA test, comparing the fluidity values obtained with the values measured for untreated cells (** P<0.01, *** P<0.001, **** P<0.0001, n = 18, error bars expressed as SEM).

Cholesterol-containing polymers (**Figure 3.9**) showed an increase in cell membrane fluidity, with the effect being more dependent on the chain length rather than on monomer composition. All the tested polymers cause a statistically significant increase in cell membrane fluidity, when compared with the untreated cells.

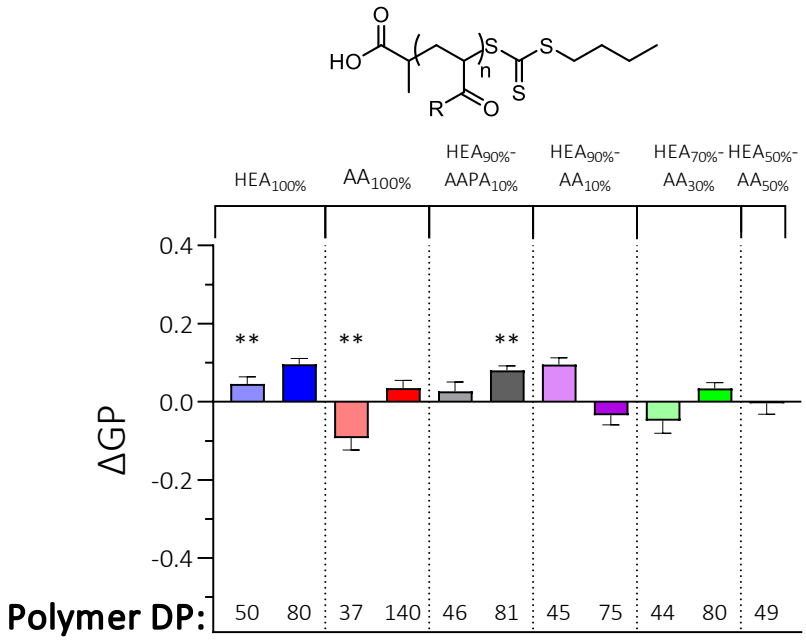


Figure 3.10 Membrane fluidity assays (Laurdan on Caco-2 cells, polymer concentration: 0.1 μM; incubation time: 30 minutes) for the non membrane-inserting PABTC-terminated control polymers. Results are expressed as delta generalised polarisation (ΔGP): a positive value represents an increase in membrane rigidity, while a negative value an increase in membrane fluidity, compared to untreated cells. The control polymers did not significantly change membrane fluidity, save for some which slightly increased the rigidity. Statistical analysis of the results was carried out through a one-way ANOVA test, comparing the fluidity values obtained with the values measured for untreated cells (** P<0.01, *** P<0.001, **** P<0.0001, n = 12, error bars expressed as SEM).

Conversely, PABTC-based control polymers (**Figure 3.10**) had little effect on membrane fluidity, although some of them marginally increased membrane rigidity. The majority of the effects of control polymers on Caco-2 cell membrane fluidity was not statistically significant, indicating that these polymers were not interacting directly with cell membranes, or were not causing significant changes in cell membrane fluidity if any interaction was happening.

The results obtained are in agreement with previous studies, which showed that amphiphilic polymers with sufficiently large lipophilic moieties (such as Poloxamers) insert in cell membranes and increase their fluidity[55–57], while hydrophilic polymers increase membrane rigidity[58]. Regarding the observation that polymers with lower molecular weight polymers increase membrane fluidity more that analogous higher molecular weight ones (i.e. ΔGP Chol-$[(HEA)_{100\%}]_{52}$ <

Chol-[(HEA)$_{100\%}$]$_{70}$ < Chol-[(HEA)$_{100\%}$]$_{108}$), we hypothesised that as shorter polymers are comparatively more hydrophobic, they would also be more prone to interact with cell membranes. Additionally, smaller polymers should offer less steric hindrance around their hydrophobic chain ends when interacting with the cells, allowing easier access to cell membranes.

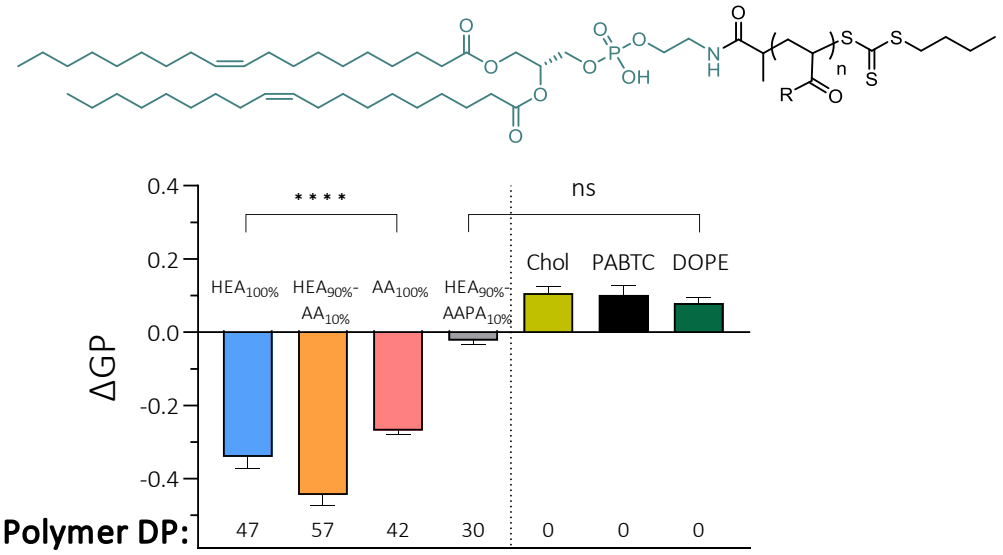


Figure 3.11 Membrane fluidity assays (Laurdan on Caco2 cells, polymer concentration: 0.1 μM; incubation time: 30 minutes) for the DOPE-based polymers and the low molecular weight RAFT agents. Results are expressed as delta generalised polarisation (ΔGP) a positive value represents an increase in membrane rigidity, while a negative value an increase in membrane fluidity, compared to untreated cells. The DOPE polymers increased the membrane fluidity, while low molecular weight RAFT agent increase membrane rigidity. Statistical analysis of the results was carried out through a one-way ANOVA test, comparing the fluidity values obtained with the values measured for untreated cells (** P<0.01, *** P<0.001, **** P<0.0001, n = 12, error bars expressed as SEM).

The DOPE-based polymers (**Figure 3.11**) behaved similarly to the amphiphilic cholesterol analogues, increasing the membrane fluidity, with the only exception being DOPE-[(HEA)$_{90\%}$-*r*-(AAPA)$_{10\%}$]$_{30}$, which did not appear to influence the membrane fluidity. This result was not easy to rationalise at this stage, with one possible explanation being that for this specific polymer, being the shortest amongst these DOPE copolymers, the chain length was not sufficiently large to create perturbation in the membranes when anchored. On the other hand, Chol, PABTC, and DOPE RAFT agents, full structure shown in **Chapter 2**, **Figure 2.1**

which are structurally analogous to the polymer chain-ends but lack the actual polymer chain, slightly increased membrane rigidity. This was in line with what expected, especially for cholesterol, as it is known to cause an increase in packing for cell membranes[59].

Additionally, we also tested the effect of polymers with a limited number of lipid pendant groups at one side of the polymer chain, synthesis discussed in **Chapter 2**, section **2.3.4**, on Caco2 cell plasma membrane fluidity. The results (**Figure 3.12**) show that also these amphiphilic polymers cause an increase in cell membrane fluidity. This effect appears weaker when compared to cholesterol and DOPE-based polymers, but this could be explained by the small size of the anchoring moiety (single lipid group) in comparison with the long hydrophilic backbone of these polymers.

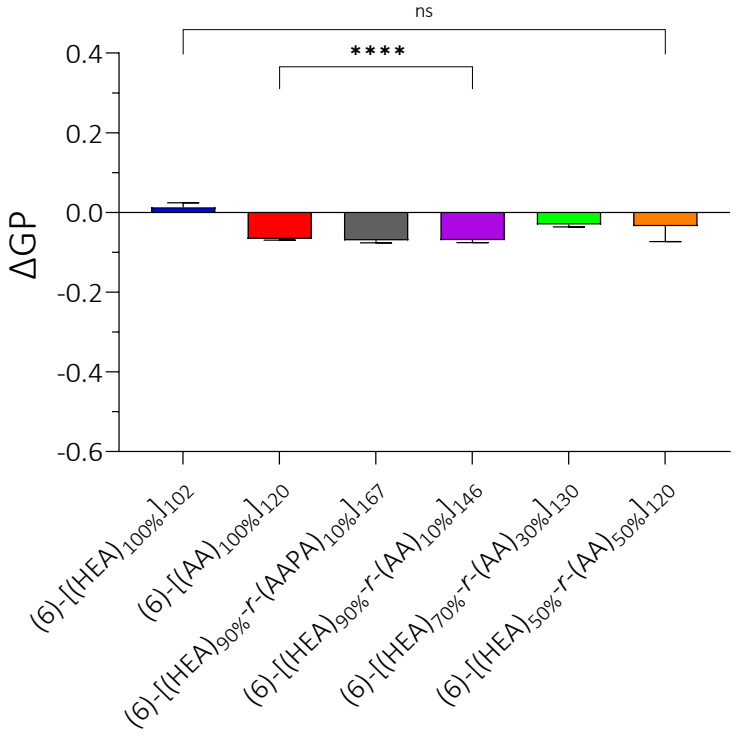


Figure 3.12 Membrane fluidity assays (Laurdan on Caco2 cells, polymer concentration: 0.1 μM; incubation time: 30 minutes) for copolymers containing phobic lipid-like repeating units. Results are expressed as delta generalised polarisation (ΔGP) a positive value represents an increase in membrane rigidity, while a negative value an increase in membrane fluidity, compared to untreated cells. The polymers caused a small increase in membrane fluidity, not as marked as what observed for the cholesterol and DOPE-based polymers. Statistical analysis of the results was carried out through a one-way ANOVA test,

comparing the fluidity values obtained with the values measured for untreated cells (** P<0.01, *** P<0.001, **** P<0.0001, n=9, error bars expressed as SEM).

Next, we tested the effect that polymers with different structural variations had on Caco-2 cell membrane fluidity:

i. A DDMAT-HEA homopolymer, which possessed a short lipid chain (12 carbon atoms).
ii. A lipid monomer-based polymer ([**(5)**$_{30\%}$-*r*-(HEA)$_{70\%}$]$_{10}$-*b*-[(HEA)$_{100\%}$]$_{65}$), with an average number of lipid monomers higher than the previously tested polymers (3 instead of 1).
iii. A commercially available DOPE-functionalised PEG 2000.

These additional polymers were tested in the same conditions as the previously described polymers. The results (**Figure 3.13**) showed that the polymer with the shorter lipid chain, DDMAT-[(HEA)$_{100\%}$]$_{42}$, increased cell membrane fluidity, similarly to what found for control polymers. Conversely, the other two tested polymers, ([**(5)**$_{30\%}$-*r*-(HEA)$_{70\%}$]$_{10}$-*b*-[(HEA)$_{100\%}$]$_{65}$ and 16:0 PEG$_{2000}$ PE behaved similarly to cholesterol and DOPE-containing polymers, increasing the cell membrane fluidity.

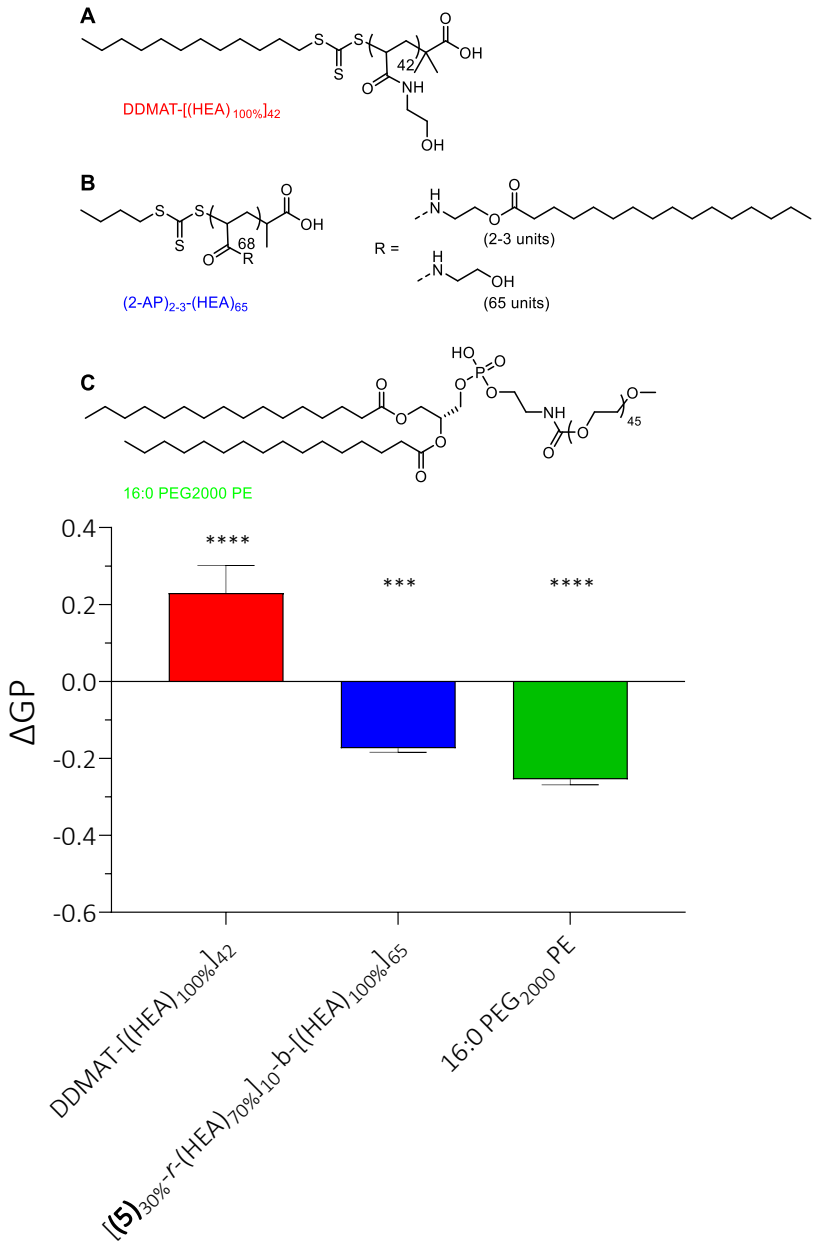


Figure 3.13 Membrane fluidity assays (Laurdan on Caco2 cells, polymer concentration: 0.1 μM; incubation time: 30 minutes) for the additional polymers, shown in the figure and tested here for comparative purposes. Results are expressed as delta generalised polarisation (ΔGP) a positive value represents an increase in membrane rigidity, while a negative value an increase in membrane fluidity, compared to untreated cells. The commercially available PEG-PE and the more lipophilic $(2\text{-AP})_{2\text{-}3}\text{-}(HEA)_{65}$ increased the cell membrane fluidity, similarly to what observed for previously tested amphiphilic polymers. The DDMAT-based polymer behaved similarly to what observed for control polymers, increasing cell membrane rigidity. Statistical analysis of the results was carried out through a one-way ANOVA test, comparing the fluidity values obtained with the values measured for untreated cells (** $P<0.01$, *** $P<0.001$, **** $P<0.0001$, $n=12$, error bars expressed as SEM).

To understand whether there was a correlation between the overall physico-chemical characteristics of these polymers and their ability to interfere with membrane packing, we analysed the correlation between the hydrophilic: lipophilic MW ratio of the polymers and the average ΔGP of cells after 30 minute incubation with 0.1 μM solutions of polymers in HBSS. Amongst the tested parameters, the Griffin hydrophilic-lipophilic balance HLB of polymers was found to increase as the measured ΔGP increased (-0.858 Pearson r, P<0.0001). This means that a more lipophilic polymer will cause a larger increase in membrane fluidity than a hydrophilic polymer. **Figure 3.14** illustrates the relationship between the two values, showing a linear correlation (R^2 = 0.7682, simple linear regression).

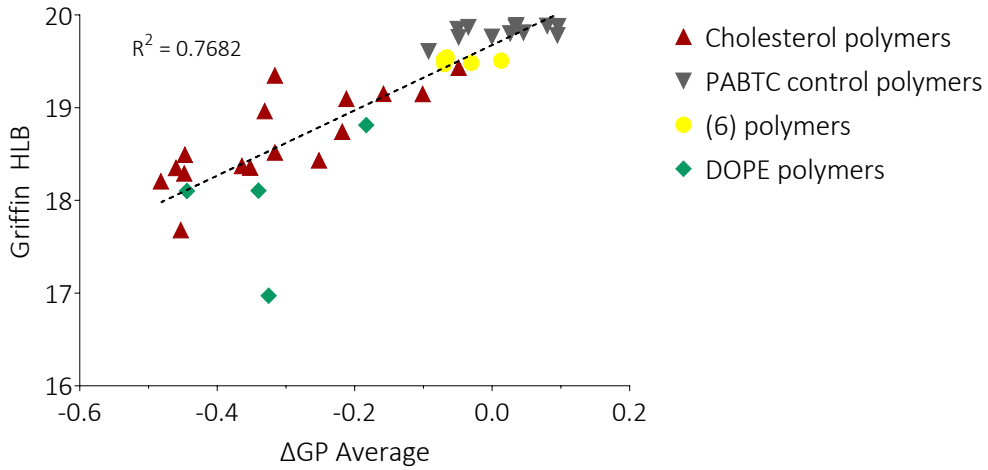


Figure 3.14 Correlation analysis between Griffin HLB and average ΔGP obtained for Caco-2 cells treated with all polymers tested within this chapter at the same molar concentration (0.1 μM), except for Chol-$[(HEA)_{100\%}]_{13}$.

After the initial tests, which focussed mostly on polymers with targeted DP in the 50-100 range, we decided to investigate whether significantly longer or shorter polymers would elicit similar effects on cell membrane fluidity. As observed in **Figure 3.15**, a very short cholesterol-based polymer (Chol-$[(HEA)_{100\%}]_{13}$) did not increase membrane fluidity and behaved in line with the cholesterol RAFT agent.

We hypothesised that this could have been caused lower impact on cell membrane organisation induced by polymers with shorter hydrophilic chain.

Conversely, a longer polymer (Chol-[(AAPA)$_{50\%}$-(HEA)$_{50\%}$]$_{151}$) increased the cell membrane fluidity, although this effect was significantly less pronounced than what observed with cholesterol polymers in the DP 50-100 size range. This was in accordance with the trend observed that correlates ΔGP with HLB: amphiphilic polymers with a larger hydrophilic section tended to increase less the cell membrane fluidity. Similarly to what observed for shorter polymers, the treatment with this longer polymer increases cell membrane fluidity in a concentration-dependent fashion.

We also observed that a longer control polymer (PABTC-[(HEA)$_{73\%}$-*r*-(3-AAPA)$_{27\%}$]$_{331}$) did not cause increase in Caco-2 cell membrane fluidity, similarly to what observed for shorter control polymers.

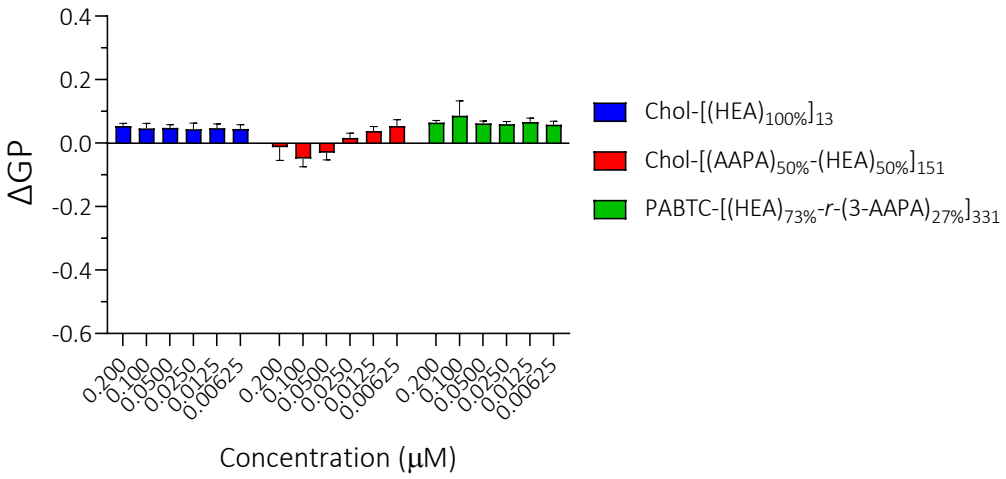


Figure 3.15 Membrane fluidity assays (Laurdan on Caco2 cells, polymer concentration: 0.1 μM; incubation time: 30 minutes) polymers for targeted DP below and above the DP 50-100 tested for the majority of the materials investigated in this work. Results are expressed as delta generalised polarisation (ΔGP) a positive value represents an increase in membrane rigidity, while a negative value an increase in membrane fluidity, compared to untreated cells. Statistical significance of the results was assessed through a one-way ANOVA test, comparing the fluidity values obtained with the values measured for untreated cells (** P<0.01, *** P<0.001, **** P<0.0001, n=6, error bars expressed as SD).

The membrane fluidity results shown in this chapter showed that the amphiphilic polymers caused an increase in cell membrane fluidity not strictly related to the nature of the hydrophilic repeating units. Rather, this effect was mainly dependent on the polymer chain length, and consequently by the polymer HLB. As discussed previously in this chapter, the HLB-ΔGP correlation could have been caused by: i) a higher steric hindrance that larger polymers offer when interacting with the cell membrane, so fewer polymers could interact with it; ii) polymers with a longer hydrophilic chain will have a more hydrophilic character, therefore have a higher tendency to remain in solution rather than interact with cell membranes.

Finally, the results showed that the amphiphilic Cholesterol- and DOPE phospholipid-containing polymers can interact with cell plasma membranes, while the PABTC control polymers did not.

3.3.4 Kinetics of polymer interaction with cell membrane: effect on membrane fluidity *vs.* time

In this part of the PhD work, the timescale of the membrane fluidity increase was investigated through a kinetic Laurdan experiment, to understand how quickly the polymers started modifying the membrane fluidity and to observe any potential fluctuations in fluidity over the course of the analysis. Accordingly, following excitation at λ=390 nm, the emission intensity of the Laurdan probe at λ_{em1} = 440 nm and at λ_{em2} = 490 nm were recorded every 90 seconds for 1 hour. This experiment was performed using polyHEA materials with targeted DP = 50 from each class (Chol-$[(HEA)_{100\%}]_{52}$, DOPE-$[(HEA)_{100\%}]_{47}$, PABTC-$[(HEA)_{100\%}]_{50}$), to evaluate the effect of the membrane-binding moiety on the interaction with membranes over time. The results are expressed as ΔGP, that is, the difference in GP between polymer-treated and untreated cells over the course of the analysis.

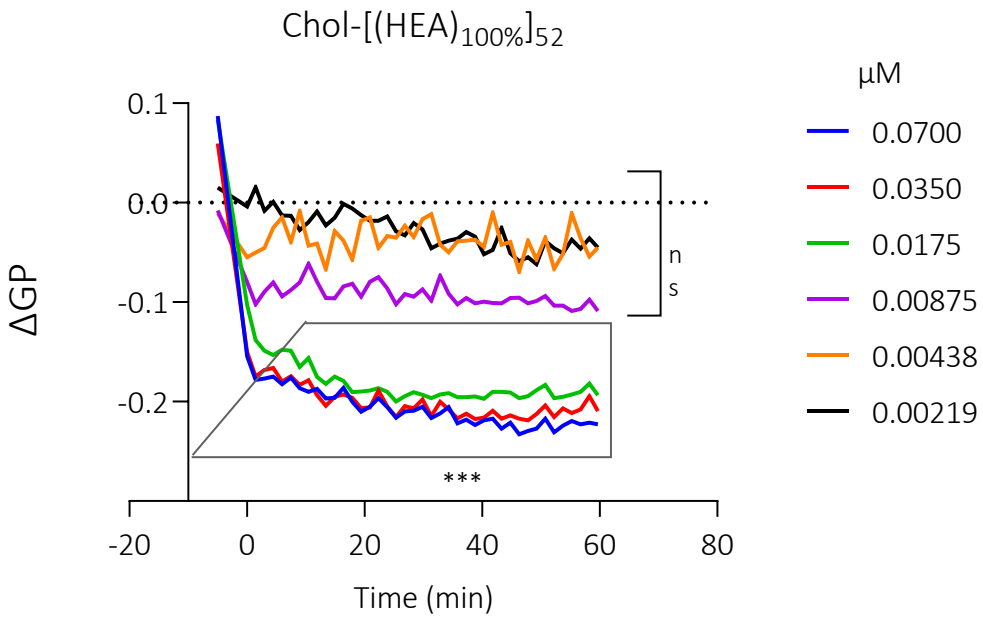


Figure 3.16 Membrane fluidity kinetic assay (Laurdan on Caco2 cells, polymer concentration: 0.1 μM; incubation time: 60 minutes) for the Chol-$[(HEA)_{100\%}]_{52}$ polymer. Results are expressed as delta generalised polarisation (ΔGP) a positive value represents an increase in membrane rigidity, while a negative value an increase in membrane fluidity, compared to untreated cells. This polymer influenced membrane fluidity quickly after treatment (t=0), and the effect was still in place after 1 hour. Statistical significance of the results was investigated through a one-way ANOVA test, comparing the fluidity values

obtained with the values measured for untreated cells (** P<0.01, *** P<0.001, **** P<0.0001, n = 4).

The results showed that for the cholesterol-based polymer Chol-[(HEA)$_{100\%}$]$_{52}$ (**Figure 3.16**) the increase in membrane fluidity took place as soon as the polymer solution was added (t=0) and it did not revert to baseline levels over the course of the analysis. The effect was also concentration-dependent, with the higher concentrations causing a proportionally higher change in the membrane fluidity increase, while the lower concentrations (≤0.00875 μM) not causing a statistically significant change.

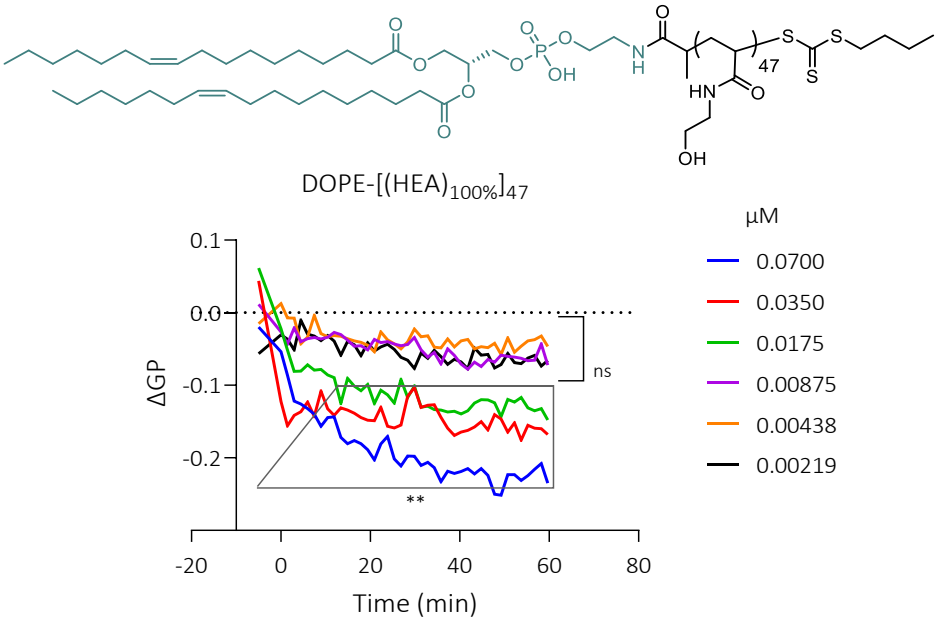


Figure 3.17 Membrane fluidity kinetic assay (Laurdan on Caco2 cells, polymer concentration: 0.1 μM; incubation time: 60 minutes) for the DOPE-[(HEA)$_{100\%}$]$_{47}$ polymer. Results are expressed as delta generalised polarisation (ΔGP) a positive value represents an increase in membrane rigidity, while a negative value an increase in membrane fluidity, compared to untreated cells. The membrane-interacting polymer influenced membrane fluidity quickly after treatment with polymer solutions (t=0), and the effect was still in place after 1 hour. Statistical significance of the results was investigated through a one-way ANOVA test, comparing the fluidity values obtained with the values measured for untreated cells (** P<0.01, *** P<0.001, **** P<0.0001, n = 2).

The phospholipid-terminated DOPE-[(HEA)$_{100\%}$]$_{47}$ behaved similarly to the analogue cholesterol-based polymer, causing a quick cell membrane fluidity

increase that was maintained for 1 hour and was concentration-dependent (**Figure 3.17**). In terms of ΔGP, effect was slightly less pronounced than what observed for the Cholesterol polymer, in line with what observed for previous membrane fluidity experiments (**Figures 3.9** and **3.11**).

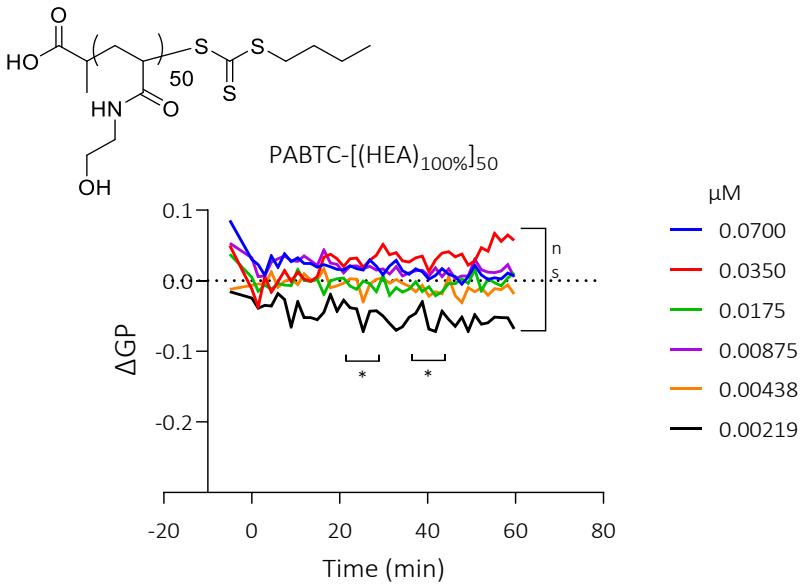


Figure 3.18 Membrane fluidity kinetic assay (Laurdan on Caco2 cells, polymer concentration: 0.1 μM; incubation time: 60 minutes) for the non membrane-inserting PABTC-$[(HEA)_{100\%}]_{50}$ control polymer. Results are expressed as delta generalised polarisation (ΔGP) a positive value represents an increase in membrane rigidity, while a negative value an increase in membrane fluidity, compared to untreated cells. The control polymers did not have significant effects on membrane fluidity. Statistical significance of the results was investigated through a one-way ANOVA test, comparing the fluidity values obtained with the values measured for untreated cells (** P<0.01, *** P<0.001, **** P<0.0001, n = 3).

As expected, control PABTC-terminated polymer did not have any statistically significant effect on membrane fluidity, corroborating the previous results (**Figure 3.18**).

3.3.5 24-hour membrane fluidity evaluation

Next, the effect of long polymer incubation times on the fluidity of the plasma membrane of Caco2 cells was assessed. This was done by first incubating Caco-2 cells for 24 hours with polymers DP 50 cholesterol, DOPE and PABTC polyHEAs, then removing polymer-containing cell media, washing cells twice with PBS and finally applying the Laurdan dye as previously described. Laurdan-containing medium was then removed, HBSS was added to the wells and Laurdan fluorescence was recorded. For these experiments the same polymers used kinetic Laurdan assay, Chol-$[(HEA)_{100\%}]_{52}$, DOPE-$[(HEA)_{100\%}]_{47}$, PABTC-$[(HEA)_{100\%}]_{50}$ were utilised.

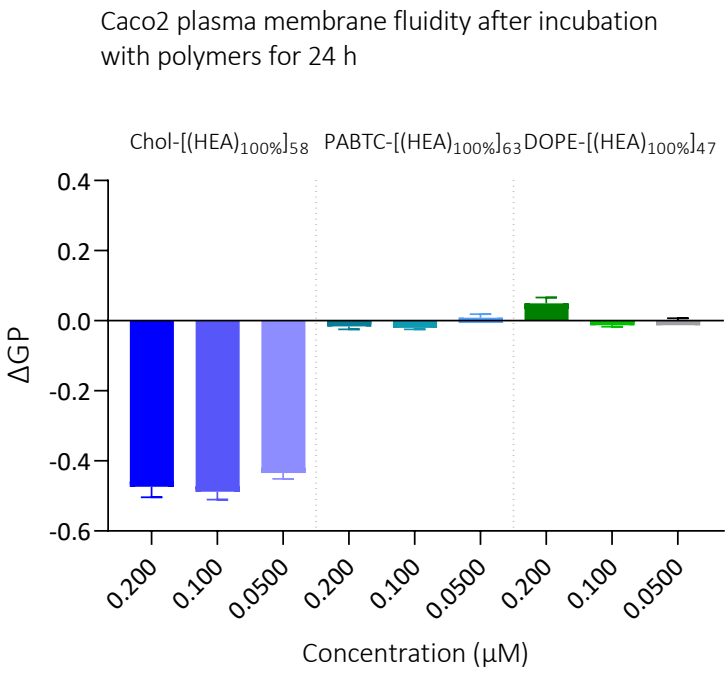


Figure 3. 19 Membrane fluidity assays (Laurdan on Caco2 cells) carried out following 24 hour incubation with polyHEAs with cholesterol (Chol), DOPE and PATBC (control) chain units and DP ~ 50. Results are expressed as delta generalised polarisation (ΔGP) a positive value represents an increase in membrane rigidity, while a negative value an increase in membrane fluidity, compared to untreated cells. In this case, only the cholesterol polymer Chol-$[(HEA)_{100\%}]_{58}$ was found to have an impact on cell membrane fluidity, whilst the DOPE-containing polymer DOPE-$[(HEA)_{100\%}]_{63}$ was not. Statistical significance of the results was investigated through a one-way ANOVA test, comparing the fluidity values obtained with the values measured for untreated cells (** P<0.01, *** P<0.001, **** P<0.0001, n =12, error bars expressed as SD).

As it can be observed from **Figure 3.19**, the cell membrane fluidification effect was observed only for the cholesterol-based polymer Chol-[$(HEA)_{100\%}$]$_{52}$. These results indicated that after 24 hours, the DOPE polymer DOPE-[$(HEA)_{100\%}$]$_{47}$ was either being removed by the washing step or was not increasing the cell membrane fluidity anymore. The control polymer PABTC-[$(HEA)_{100\%}$]$_{50}$ behaved as expected, not influencing the membrane fluidity.

3.3.5 Interaction of membrane-inserting polymers with Laurdan fluorescent probe

Since Laurdan is a hydrophobic molecule that spontaneously tends to localise within bilayers, it can interact with any surfactants[60] and supramolecular aggregates formed by amphiphilic polymers[61]. To confirm whether the measured changes in fluorescence emission spectrum of the Laurdan probe were caused, at least in part, by interactions with the amphiphilic polymers synthesised in this work, Laurdan and polymers were incubated at different concentrations. Thus, polymer solutions in the 0.05-0.2 μM range were prepared in HBSS and the fluorescence emission spectrum for Laurdan (2 μM) was recorded after 30 minutes of incubation to the polymers, at 37 °C. These conditions were used to mimic the experimental conditions used in the cell membrane fluidity assays employed in **Section 3.3.4**. The results are expressed as GP and not the previously used ΔGP,

to highlight the GP registered for the blank sample (2 μM Laurdan dye the in HBSS).

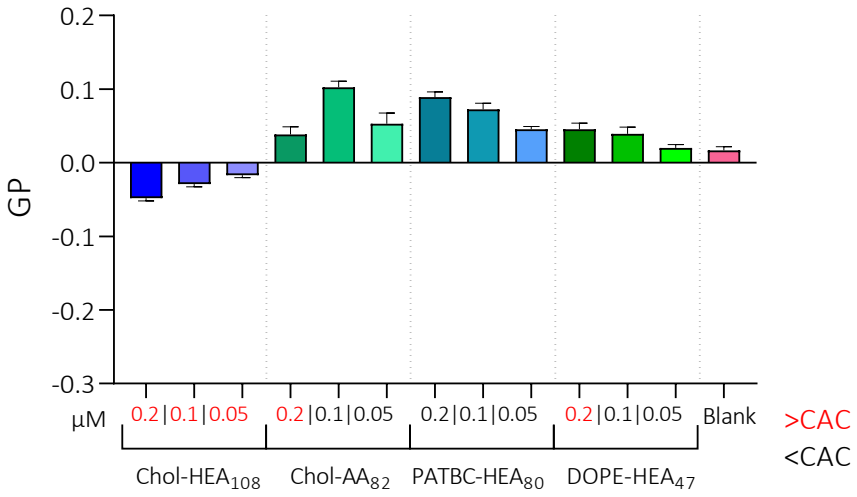


Figure 3.20 *GP* values for Laurdan in a solution of selected polymers in HBSS, at different concentrations (red>CAC, black<CAC), to evaluate the direct interaction between the polymers and the Laurdan probe in the absence of cell membranes. Blank: Laurdan dye the in HBSS in the absence of polymers (n = 8, error bars expressed as SD).

We first investigated this effect with the longest HEA homopolymer available per library (Chol-$[(HEA)_{100\%}]_{108}$, DOPE-$[(HEA)_{100\%}]_{47}$ and PABTC-$[(HEA)_{100\%}]_{80}$) to investigate the potential Laurdan-polymer interaction. Additionally, we selected an AA homopolymer Chol-$[(AA)_{100\%}]_{82}$ to exclude any potential effects caused by an acid homopolymer.

The results indicated that Chol-$[(HEA)_{100\%}]_{108}$ caused a shift in the Laurdan fluorescence emission spectrum similar to what observed when treating cells with

the dye and the polymers (**Figure 3.20**), resulting in negative GP values. Conversely, all the other polymers tested with this assay gave positive GP values.

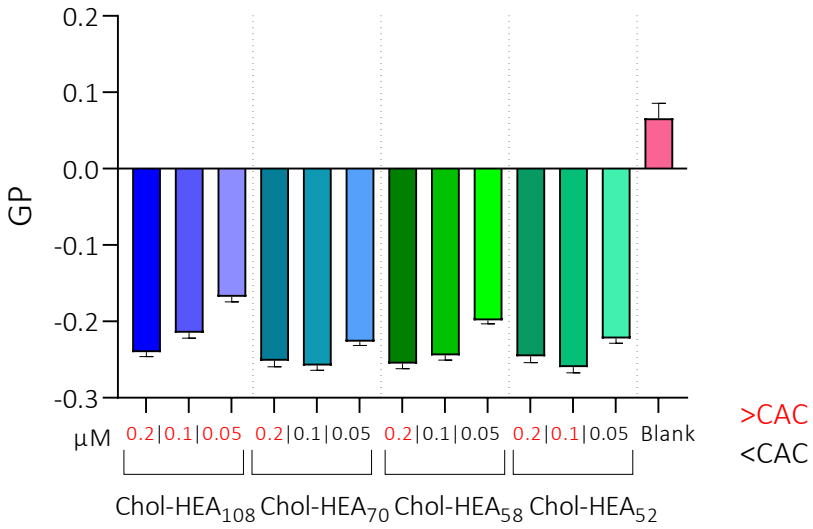


Figure 3.21 GP values for Laurdan in HBSS solution with a series of Chol-[$(HEA)_{100\%}$] polymers at different concentrations (red>CAC, black<CAC), to evaluate the direct interaction between these polymers and the Laurdan dye. We observed that for all the tested polymers there was a shift in Laurdan fluorescence emission towards 490 nm (n=8, error bars expressed as SD).

Next, the effect of the polymer chain length on the interaction between Chol-$HEA_{100\%}$ polymers and Laurdan was tested using polymers with DP in the 52-108 range. The results (**Figure 3.21**) showed that all the polymers gave negative GP values, in a same fashion than what observed in the cell-based assays, regardless of the polymer CAC. It should be noted, however, that most fluorescent probes are π-conjugated molecules that are inherently hydrophobic and at least some of them can promote aggregation of amphiphilic molecules at concentration below their CAC[62]. The concentrations tested in the experiments described in this section are close to the polymers CAC, hence, although this point was not directly assessed at this stage, it is possible that the presence of Laurdan facilitated the formation of polymer aggregates incorporating Laurdan in their hydrophobic core.

The negative GP observed for these cholesterol polymer-laurdan aggregates may indicate that they possess of a disordered/more water exposed hydrophobic core.

Overall, these experiments suggested that the HEA-cholesterol-based polymers influenced the fluorescence emission spectrum of the Laurdan dye in solution. Additionally, the results showed that polymer-Laurdan interaction could contribute, at least in part, to the observed negative ΔGP observed in Caco2 cells. This latter point will be further investigated in the next sections.

3.3.6 Polymer-Laurdan interaction on cells

To better frame the results presented in **Section 3.3.5** in the context of the laurdan assays with Caco2 cells, a modified procedure for this assay was designed. Accordingly, Caco2 cells were initially treated with Laurdan, and the excess unbound dye was removed via successive washing with PBS and replacing with fresh medium (**Figure 3.22**).

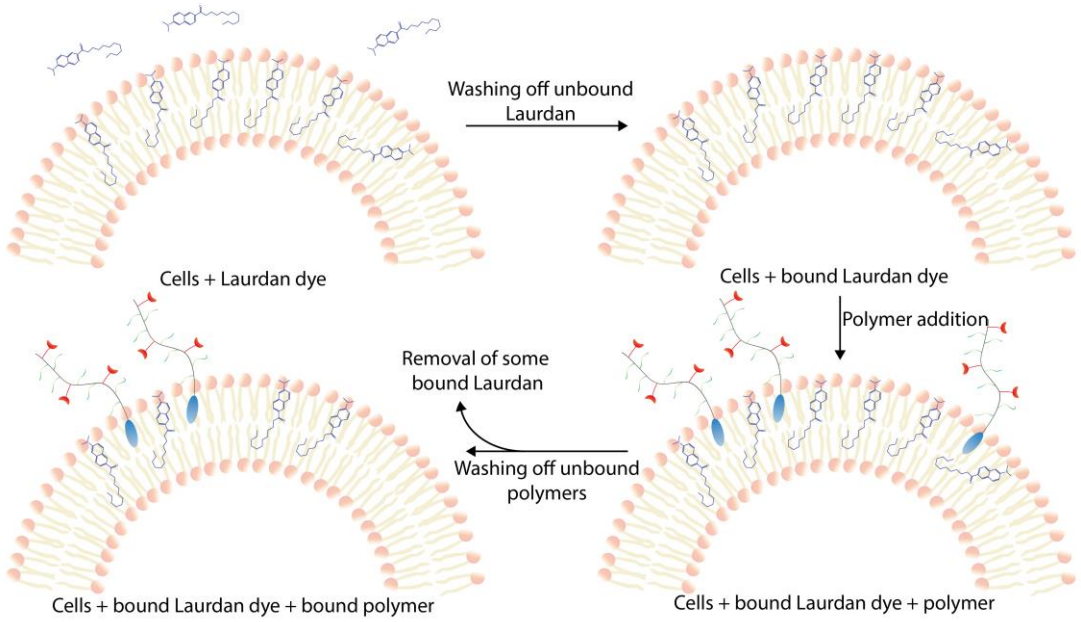


Figure 3.22 Schematic of the experimental setup for the elucidation of the interactions between polymers, cells and the Laurdan dye. The cells were treated with Laurdan first, then the unbound dye was removed. The cells were incubated with solution of polymers,

and the Laurdan fluorescence spectra were recorded. Then, the supernatant suspensions were transferred in a second 96-well plate, and fresh medium was added to the cells. The Laurdan fluorescence spectra were recorded both for the supernatant solutions and for the cells with fresh medium.

This was done so Laurdan was only present in the cell membrane when the polymer solutions were added. Cells were incubated with polymers for 30 minutes, and emission intensity at λ_{em1} = 440 nm and λ_{em2} = 490 nm was recorded to be used as reference. Then, the polymer-containing supernatant was removed and transferred it in a second 96-well plate. Fresh HBSS was then added to the well plates, and the fluorescence emission for both 96-well plates was recorded, and compared it the reference measurement. This allowed to:

i) observe whether any Laurdan was removed when the polymer-containing supernatant was removed;

ii) confirm that the membrane fluidity change, expressed as ΔGP, was still present on cells after removing any potential effect from Laurdan-polymer interactions.

For this experiment, cholesterol-based polymer which caused membrane fluidity increase in the previous assays, Chol-$[(HEA)_{100\%}]_{58}$ was employed, along with a control polymer with very similar chain length (PABTC$[(HEA)_{100\%}]_{63}$).

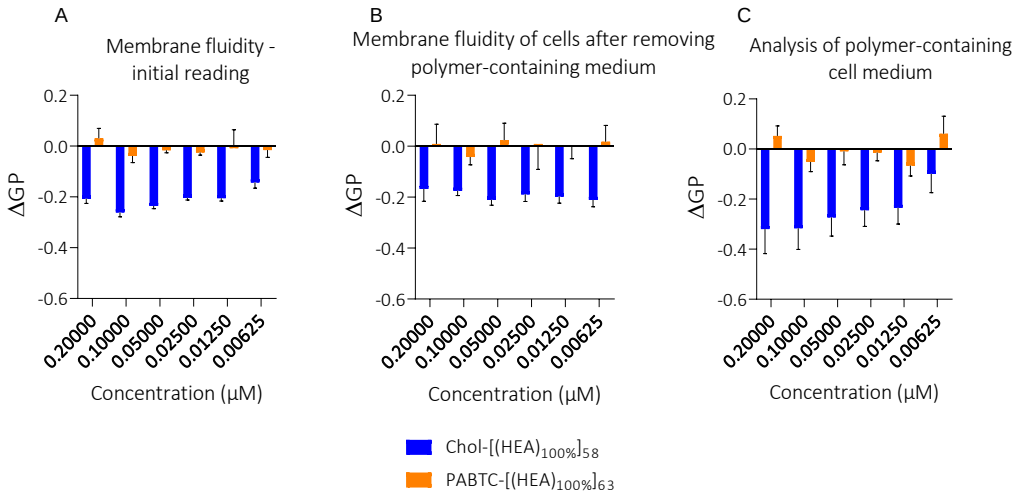


Figure 3.23 Membrane fluidity results for the different solutions and cells analysed to identify the polymer-Laurdan interaction involving Caco2 cells, with results expressed as

ΔGP. **A** ΔGP values obtained for cells with bound Laurdan, in a polymer-containing cell medium. **B** ΔGP values of Caco2 cells after medium at point A was replaced with fresh, polymer-free, cell medium. **C** analysis of the polymer-containing supernatant removed from cells at stage B (n = 6, error bars expressed as SD).

The Laurdan assay showed that a negative ΔGP was still present after removing the unbound cholesterol-based Chol-$[(HEA)_{100\%}]_{58}$ polymer (**Figure 3.23**), although the effect was less pronounced (non statistically significant difference between initial measurement and measurement after removing polymer-containing medium). Importantly, Laurdan was also present on the polymer-containing supernatant removed from the cells after 30 min incubation, confirming the results obtained in **Section 3.3.5**. As expected, the PABTC-based control polymer did not show any statistically significant difference between the different phases of the experiment. These results confirmed that some polymers remained bound to the cell membrane and increased cell membrane fluidity after removal of the polymer-containing supernatant.

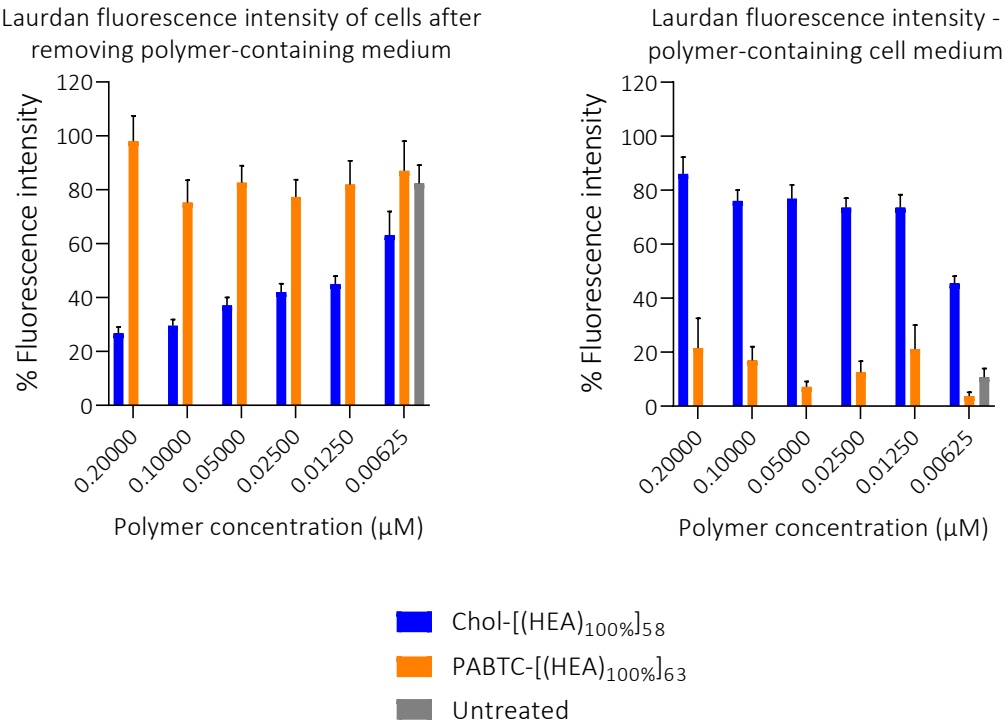


Figure 3.24 Fluorescence intensity (%) of Laurdan dye (λ_{em} = 440 and 490 nm) for supernatant and cells with fresh medium, after incubation of Caco2 cells with polymers at different concentrations. The values are calculated on a well-to-well basis, using the starting fluorescence intensity (cells+bound Laurdan+polymers) as 100% (n = 6, error bars expressed as SD).

It is important to note that GP values are calculated from the *relative* intensity of Laurdan emission at λ_{em1} = 440 nm and λ_{em2} = 490 nm, but do not say much about the *absolute* intensity of emission - which in a first, crude approximation we could assume it is proportional to the concentration of Laurdan in the samples - in the two set of samples analysed – i) Caco2 cells after removal of polymer-containing supernatant and ii) the actual polymer-containing supernatant itself. Data showed that a proportion of the Laurdan fluorescence intensity was found in the supernatant for the cholesterol-based polymer, while approximately 40-60% of the initial fluorescence intensity was left in the samples containing Caco2 cells after removal of polymer-containing supernatant ($p<0.0001$ between any incubated Chol-$[(HEA)_{100\%}]_{58}$ concentration and untreated cells, two-way ANOVA with simple effect between rows comparison) (**Figure 3.24**). This suggested that polymer-containing supernatant was able to remove Laurdan from cells pre-

treated with this fluorescent probe, and that the effect appeared to be concentration dependent, with the higher concentrations removing more of the Laurdan fluorescence intensity. Conversely, the control polymer behaves similarly to the untreated cells: most of the fluorescence intensity remains on the cells, and there little fluorescence was observed in the supernatant ($p>1$ between any incubated PABC-$[(HEA)_{100\%}]_{63}$ concentration and untreated cells, two-way ANOVA with simple effect between rows comparison).

These results seem to suggest that that the cholesterol-based polymer Chol-$[(HEA)_{100\%}]_{58}$ can extract part of the Laurdan dye from the cell membrane. However, these data also shows that negative ΔGP in polymer-treated Caco2 are still observed after removing the supernatant containing unbound polymer, indicating that Chol-$[(HEA)_{100\%}]_{58}$can increase the fluidity of the plasma membrane of Caco2 cells.

3.3.7 Cell interaction for trithiocarbonate-cleaved polymers

As illustrated in **Chapter 2**, to investigate a potential effect of the trithiocarbonate groups at the polymer chain-ends for a selected subfamily of polymers, the trithiocarbonate moiety was replaced with a hydrogen atom. The resulting polymers (**Figure 3.25**) were then tested in the same cell assays run previously with the non-cleaved polymers.

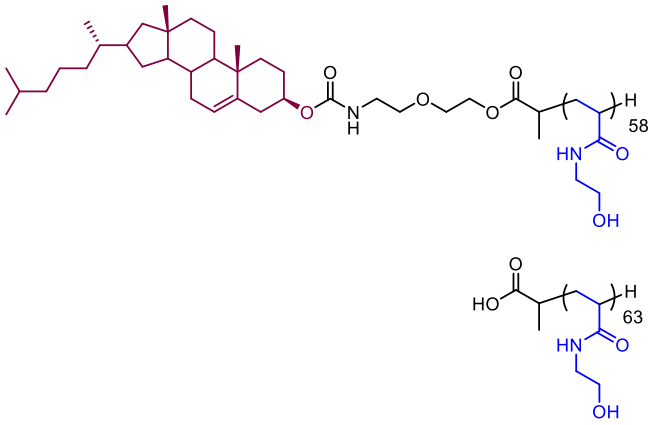


Figure 3.25 Structures of the Cholesterol Chol-$[(HEA)_{100\%}]_{58}$ and control PATCB-$[(HEA)_{100\%}]_{63}$ polymers after removal of the trithiocarbonate ω-chain end.

The IC_{50} values (**Table 3.5**) showed a decrease in toxicity for the cleaved polymers, both in terms of metabolic activity and cell membrane damage. This may be ascribed by the intrinsic reactivity of the trithiocarbonate group, which can potentially be degraded and cause additional cytotoxicity[63].

Table 3.5 IC_{50} values for cleaved and non-cleaved polymers on Caco-2 cells (24 hours incubation). Values are for cell metabolic activity and cell membrane damage (LDH), and were calculated by using an [inhibitor] versus normalised response nonlinear regression curve fitting (n = 6).

Polymer	**IC_{50} value (μM)**	
	Metabolic activity	LDH release
Chol-$[(HEA)_{100\%}]_{58}$	0.213	0.0432
Cleaved-Chol-$[(HEA)_{100\%}]_{58}$	>1	0.163
PABTC-$[(HEA)_{100\%}]_{63}$	0.313	>1
Cleaved-PABTC-$[(HEA)_{100\%}]_{63}$	>1	>1

After proving that the toxicity is partially affected by the removal of the trithiocarbonate group, we proceeded to test the effect of the polymers on cell membrane fluidity. This assay was performed as described previously on Caco-2 cells, incubated with 0.1 μM polymer solutions. The results showed very similar effects on cell membrane fluidity when comparing the same polymer with and without the end-group (**Figure 3.26**).

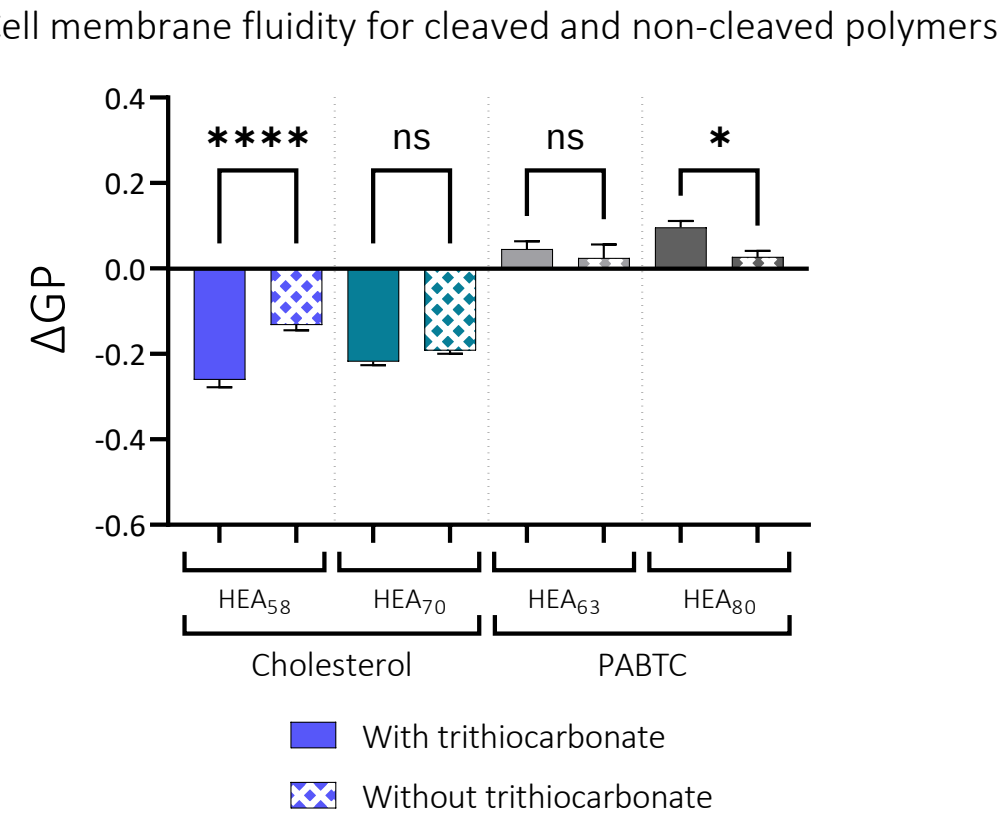


Figure 3.26 Membrane fluidity assays (Laurdan on Caco-2 cells, 0.1 μM incubation for 30 minutes), employing cleaved and non-cleaved polymers. Results are expressed as delta generalised polarisation (ΔGP): a positive value represents an increase in membrane rigidity, while a negative value an increase in membrane fluidity, compared to untreated cells. The results are in line with what observed previously for cholesterol and PABTC polymers, showing little difference between cleaved and non-cleaved polymers. Statistical significance of the results was investigated through a one-way ANOVA test, comparing the fluidity values obtained with the values measured for untreated cells (** P<0.01, *** P<0.001, **** P<0.0001, n = 8, error bars expressed as SD).

Thus, these experiments showed that the removal of the different end groups slightly affect the toxicity of these materials, potentially due to the potential cytotoxicity of the trithiocarbonate group. However, the presence or absence of the trithiocarbonate ω-end group did not change the effect on membrane fluidity for these materials.

As the removal of the trithiocarbonate slightly decreased the toxicity but did not affect the interaction of these polymers with cells, future *in vivo* studies should employ the cleaved polymers.

3.3.8 Localisation of polymers in cell membranes: fluorescence microscopy studies

Next, fluorescently labelled polymers were employed to directly observe polymer-decorated membranes by confocal fluorescence microscopy. To this aim, a smaller library of polymers, (Chol-[$(HEA)_{100\%}]_{52}$ DOPE-[$(HEA)_{100\%}]_{47}$, PABTC-[$(HEA)_{100\%}]_{50}$), were tagged using the Rhodamine Red Maleimide dye, as described in Chapter 2 . Caco-2 cells, treated with the fluorescent polymers were fixed and imaged by fluorescence microscopy (TRITC filter, λ_{ex} = 557 nm and λ_{em} = 576 nm). **Figure 3.27** shows that the Rho-DOPE-[$(HEA)_{100\%}]_{52}$ polymer was located on the cell membrane of the Caco-2 cells. This qualitatively confirmed the presence of membrane-binding polymers on the cell membrane.

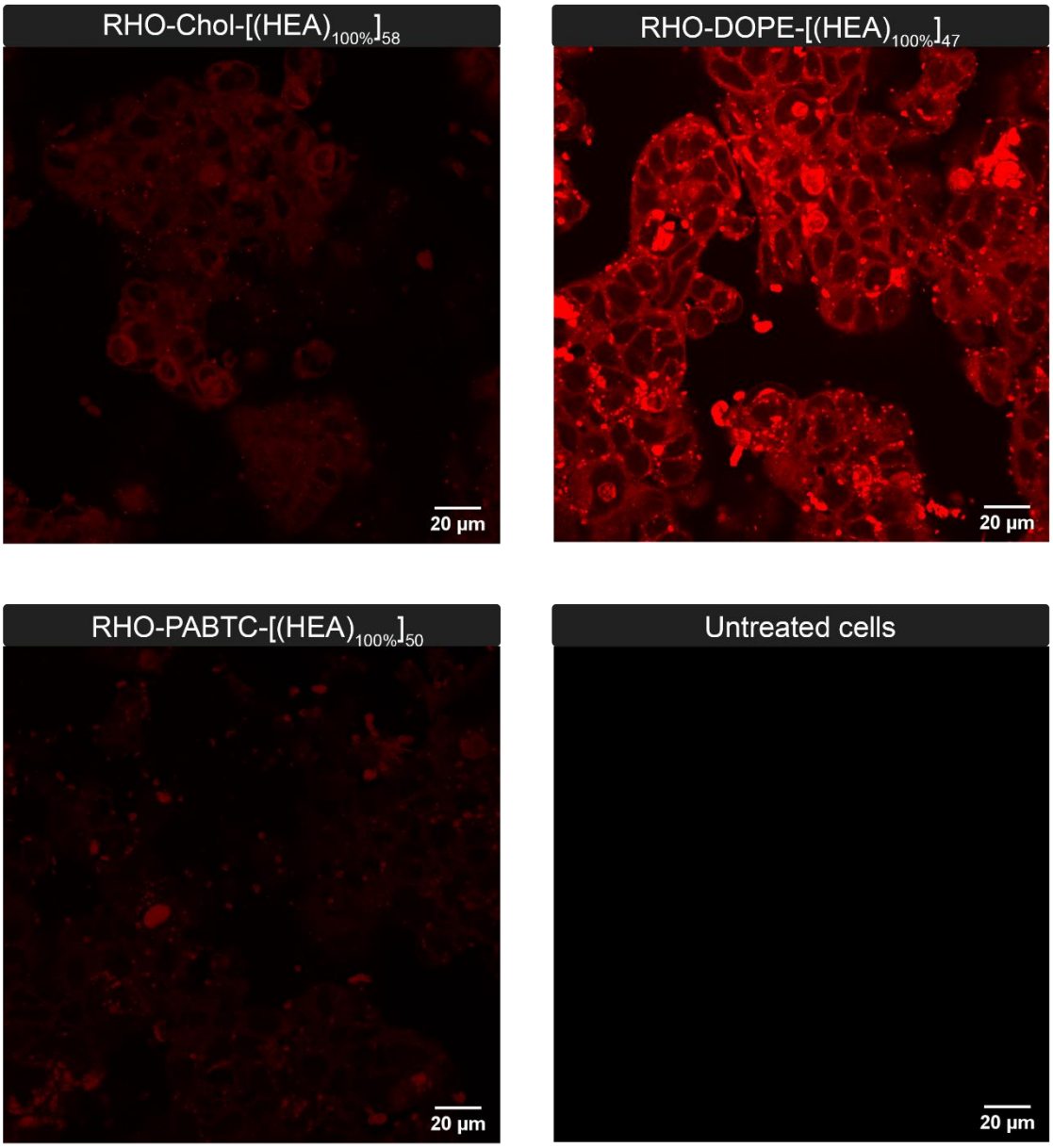


Figure 3.27 TRITC channel (λ_{ex} = 557 nm and λ_{em} = 576 nm) Confocal Microscopy images of cells treated with Rhodamine Red tagged polymers and untreated cells.

3.3.9 Characterisation of polymer-cell association by Flow Cytometry Imaging

A comparison of the ability of different polymers to insert into cell membranes was carried out by flow cytometry. This technique allows for fast analysis of large numbers of cells and measurement of fluorescence intensity of single cells. This allows for the analysis of the distribution in a cell population of specific parameters, such as mean fluorescence intensity. Values derived from this distribution describe the cell population better than the average values obtained by other fluorescence techniques[64]. The instrument we employed (Imagestream^{X}® MKII) also allows for image capture throughout the analysis[65] and also to estimate the proportion of dye internalisation[66]. The internalisation values were calculated using the internalisation tool, eroding 3-6 pixels per cell from the brightfield image (Ch 09) to separate the cytosol from the cell membrane. The values were calculated on focused and single cells, employing the signal of the dye (Ch 03, λ_{ex} = 377 nm and λ_{em} = 420 nm) to calculate the localisation of the polymers. Larger values indicate a species that tends to localise outside of the cell, while negative values indicate a species that tends to localise inside the cell. These values normally range from -3 to +3.

This technique is employed in numerous studies[67–69] to evaluate the interaction of fluorescently tagged polymers with cell membrane. For these experiments Caco-2 cells were incubated with 0.1 μM solutions of the different types of fluorescently tagged polymers synthesised in this work, in HBSS. The results were adjusted to the relative fluorescence of each polymer (with the free dye set as 100%), to account for the slight difference in the extent of fluorescent tagging for the polymers employed in these experiments (see **Chapter 2**).

For this investigation, we employed polyHEA homopolymers with degrees of polymerisation of 52, 70, and 108 for cholesterol polymers, a DOPE polymer (DOPE-[$(HEA)_{100\%}$]$_{47}$) and a control polymer (PABTC-[$(HEA)_{100\%}$]$_{50}$) (**Figure 3.28**). Fluorescent cholesterol-containing polymers with different chain length -

MalPyr Blue Chol-[(HEA)$_{100\%}$]$_{52}$, MalPyr Blue Chol-[(HEA)$_{100\%}$]$_{70}$, MalPyr Blue Chol-[(HEA)$_{100\%}$]$_{108}$ - were investigated here because previous membrane fluidity experiments showed that for polymers in the DP ~ 50-100, shorter polymers have a higher effect on cell membrane fluidification. Here, by measuring the average MalPyr Blue fluorescence intensity per cell, relative number of polymer chains of polymers bound to the cell membrane could be in principle estimated. The experiment was run using polymers at the same molar concentration (0.1 μM) and accounting for relative fluorescence intensity calculated via tagging efficiency (see **Chapter 2**).

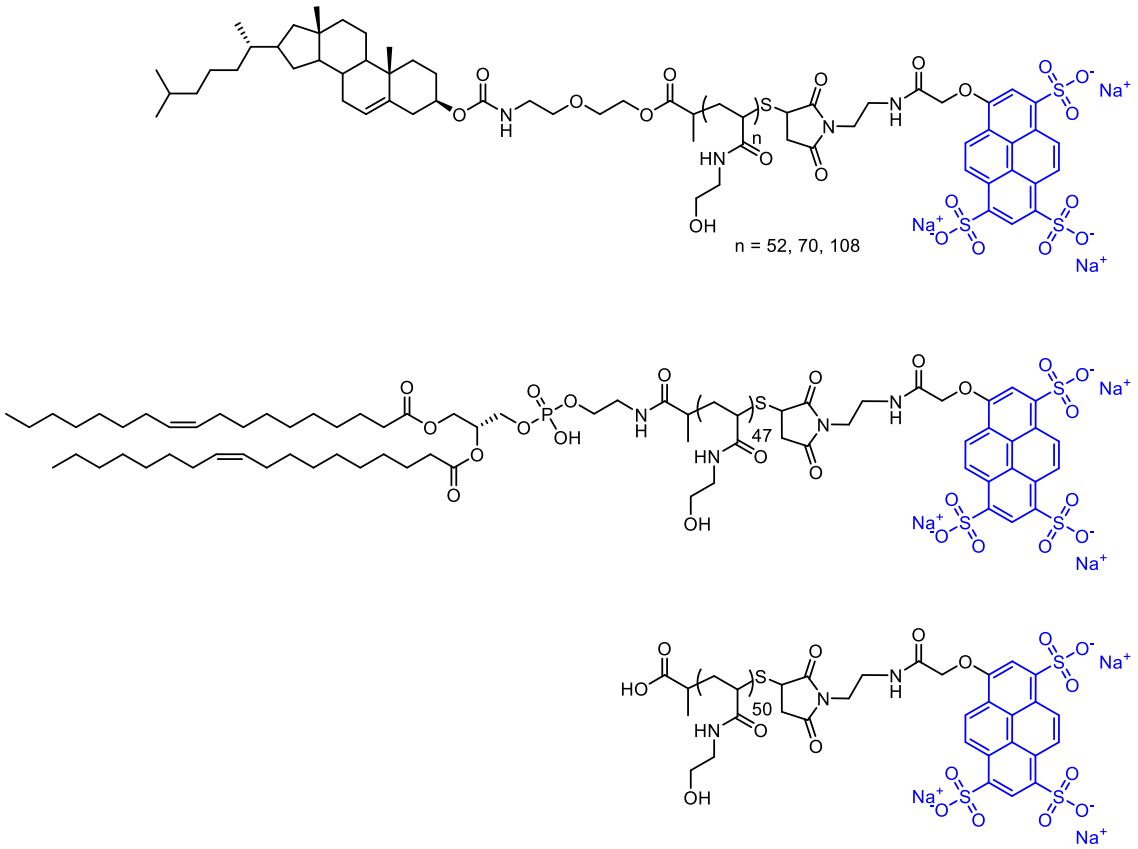
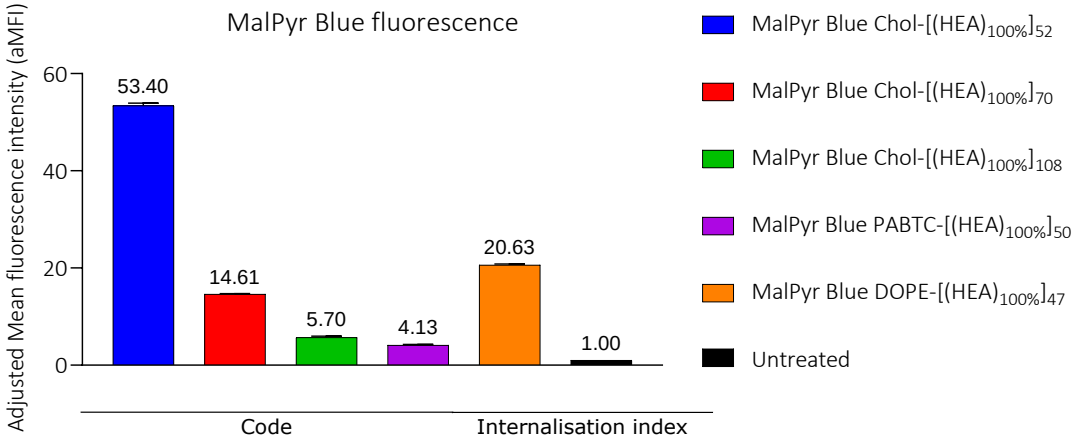


Figure 3.28 Chemical structure of the MalPyr Blue fluorescently-tagged polymers: MalPyr Blue Chol-[(HEA)$_{100\%}$]$_{52}$, MalPyr Blue Chol-[(HEA)$_{100\%}$]$_{70}$, MalPyr Blue Chol-[(HEA)$_{100\%}$]$_{108}$ (top), MalPyr Blue DOPE-[(HEA)$_{100\%}$]$_{47}$ (middle), MalPyr Blue PABTC-[(HEA)$_{100\%}$]$_{50}$ (bottom).

Caco-2 cells were incubated with the fluorescent polymer solutions for 30 minutes, and after washing off unbound polymers cells were detached with Trypsin-EDTA.

The cells were then resuspended in phenol-red free medium and centrifugated to collect the pellet and resuspended in HBSS. The cell suspension was then analysed by Flow Cytometry Imaging with the results expressed as MFI, as described in **Equation 3.7**. This value accounts for the potential autofluorescence[70] at the specific wavelength analysed, as the adjusted median fluorescence intensity (aMFI) for a species is divided by the median fluorescence intensity measured for untreated cells.



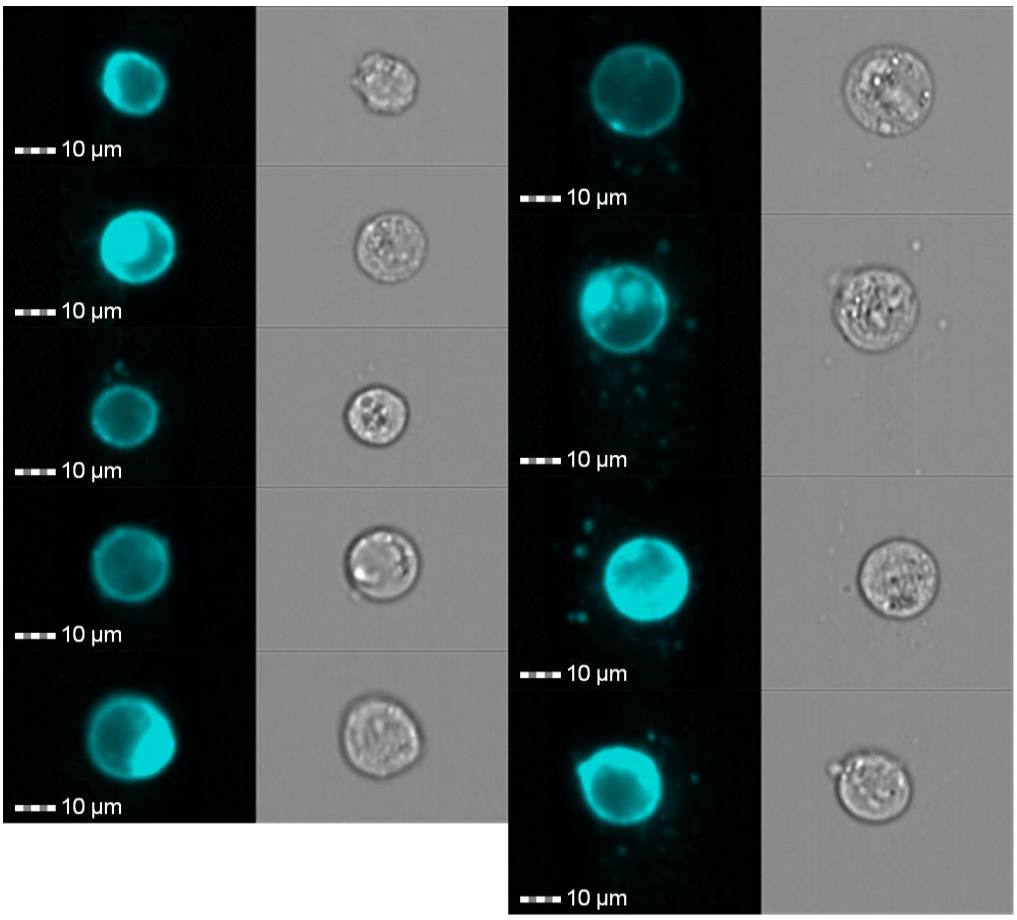
Code	Internalisation index
MalPyr Blue Chol-[(HEA)$_{100\%}$]$_{52}$	1.4257
MalPyr Blue Chol-[(HEA)$_{100\%}$]$_{70}$	1.3507
MalPyr Blue Chol-[(HEA)$_{100\%}$]$_{108}$	3.9055
MalPyr Blue PABTC-[(HEA)$_{100\%}$]$_{50}$	3.9249
MalPyr Blue DOPE-[(HEA)$_{100\%}$]$_{47}$	1.8246

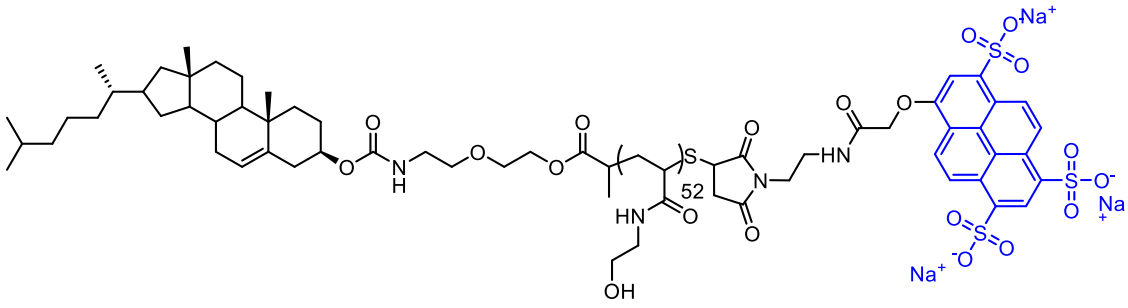
Figure 3.29 aMFI graph for cells treated with 0.1 μM HBSS solutions of MalPyr Blue fluorscently-tagged polymers. The values are adjusted to the relative fluorescent tagging efficiency, calculated in Chapter 2. The table shows the internalisation values, calculated via the internalisation tool in IDEAS® 6.0, (error bars expressed as SEM).

As it can be observed in **Figure 3.29**, the aMFI for Chol-HEA homopolymers was found to decrease with the increase in chain length, in the order MalPyr Blue Chol-[(HEA)$_{100\%}$]$_{52}$ > MalPyr Blue Chol-[(HEA)$_{100\%}$]$_{70}$ > MalPyr Blue Chol-[(HEA)$_{100\%}$]$_{108}$. This trend was in line with that observed on the membrane fluidity experiments,

where, again, shorter cholesterol-containing polymers induced the largest decrease in ΔGP. The control PABTC-[$(HEA)_{100\%}]_{108}$ homopolymer showed a small degree of interaction with the membrane, as the aMFI is greater than untreated cells and similar in value to the Chol-HEA homopolymer with 108 DP. Hydrophilic polymers have been previously shown to have the propensity to adsorb on the surface of cell membrane models, which may explain the observed behaviour[71]. The DOPE-HEA homopolymer MalPyr Blue DOPE-[$(HEA)_{100\%}]_{47}$ showed a lower aMFI when compared with its analogous cholesterol counterpart MalPyr Blue Chol-[$(HEA)_{100\%}]_{52}$. This is in line with what observed in the effect on cell membrane fluidity, as cholesterol-based polymers were shown to have a higher impact on cell membrane fluidity when compared with DOPE-based polymers, although an effect of the intrinsic nature of the membrane inserting moiety on cell membrane fluidity cannot be ruled out. Additionally, these results showed that a higher number of MalPyr Blue Chol-[$(HEA)_{100\%}]_{52}$ polymer chains were present at the cell membrane, when compared with longer polymers. This support a model where MalPyr Blue Chol-[$(HEA)_{100\%}]_{52}$ indce more cell membrane fluidification due to more polymer chains being present on the cell surface.

The internalisation values (Table in **Figure 3.29**) obtained via the internalisation tool showed a difference between the more interacting polymers (short cholesterol-HEA and DOPE-HEA) and the less interacting polymers. The polymers that interacted more with the cells (higher aMFI) showed a lower internalisation index, which is synonymous with the dye being more localised outside of the cells. This can also be qualitatively observed in the images in **Figures 3.30-34**, which are briefly described below.

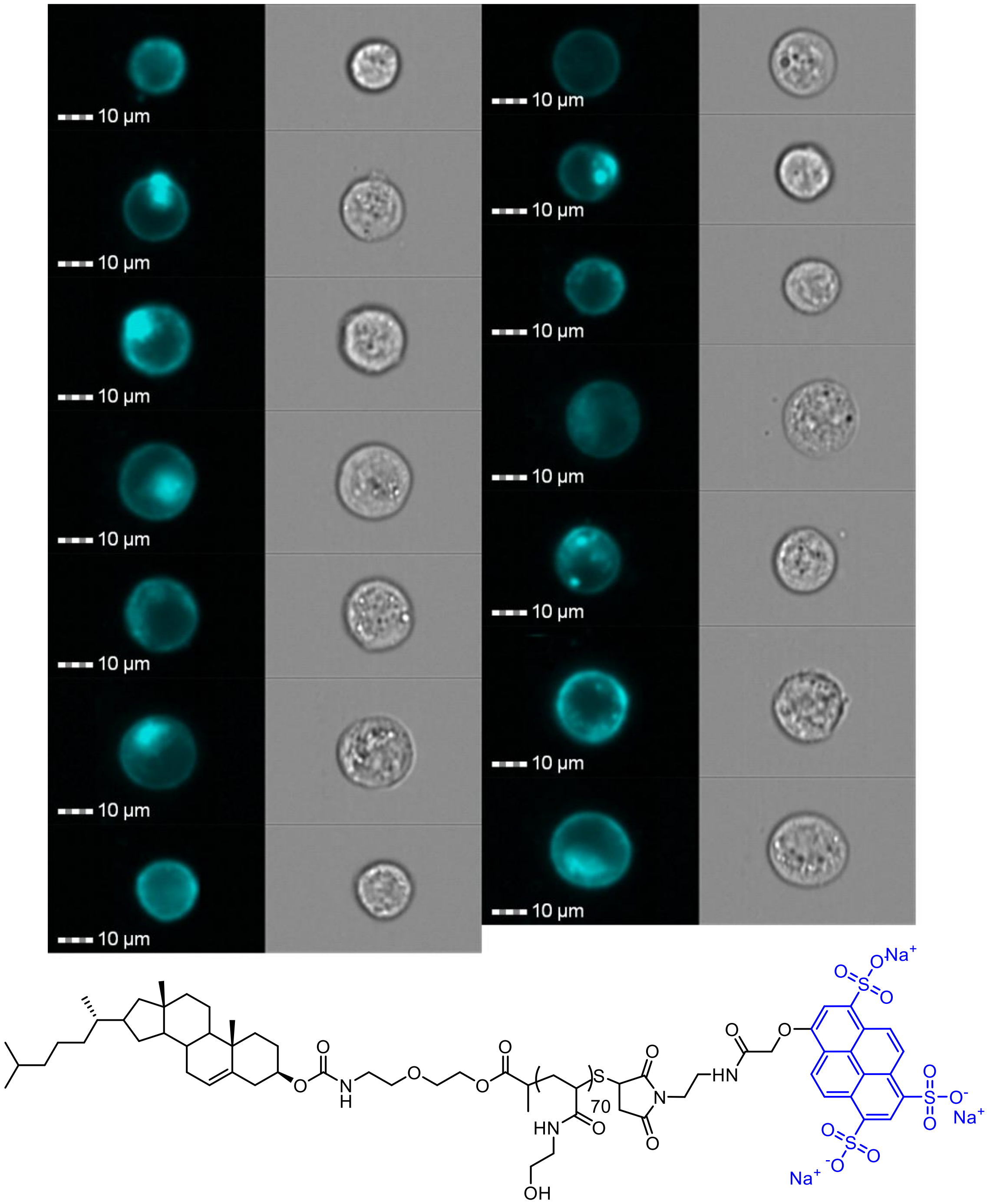




MalPyr Blue Chol-[(HEA)$_{100\%}$]$_{52}$

Figure 3.30 Flow cytometry images for Caco-2 cells treated with MalPyr Blue Chol-[(HEA)$_{100\%}$]$_{50}$, showing channel 03 (λ_{ex} = 377 nm and λ_{em} = 420 nm) and brightfield images.

Figure 3.30 illustrates the fluorescence distribution of MalPyr Blue Chol-[(HEA)$_{100\%}$]$_{52}$ in selected cells analysed by Flow Cytometry. It can be observed that the fluorescence is preferentially located on the cell surface, further confirming the hypothesis of the direct interaction between polymers and cell membranes.



MalPyr Blue Chol-$[(HEA)_{100\%}]_{70}$

Figure 3.31 Flow cytometry images for Caco-2 cells treated with MalPyr Blue Chol-$[(HEA)_{100\%}]_{70}$, showing channel 03 (λ_{exc} = 377 nm and λ_{em} = 420 nm) and brightfield images.

Figure 3.31 illustrates the fluorescence distribution of MalPyr Blue Chol-$[(HEA)_{100\%}]_{70}$ in selected cells analysed by Flow Cytometry. As previously observed for the shorter cholesterol-based polymer, the fluorescence is located mainly on the cell surface. Since fewer polymers were present, the localisation of the tagged

polymers can be observed more clearly than for the shorter MalPyr Blue Chol-[(HEA)$_{100\%}$]$_{52}$ polymer.

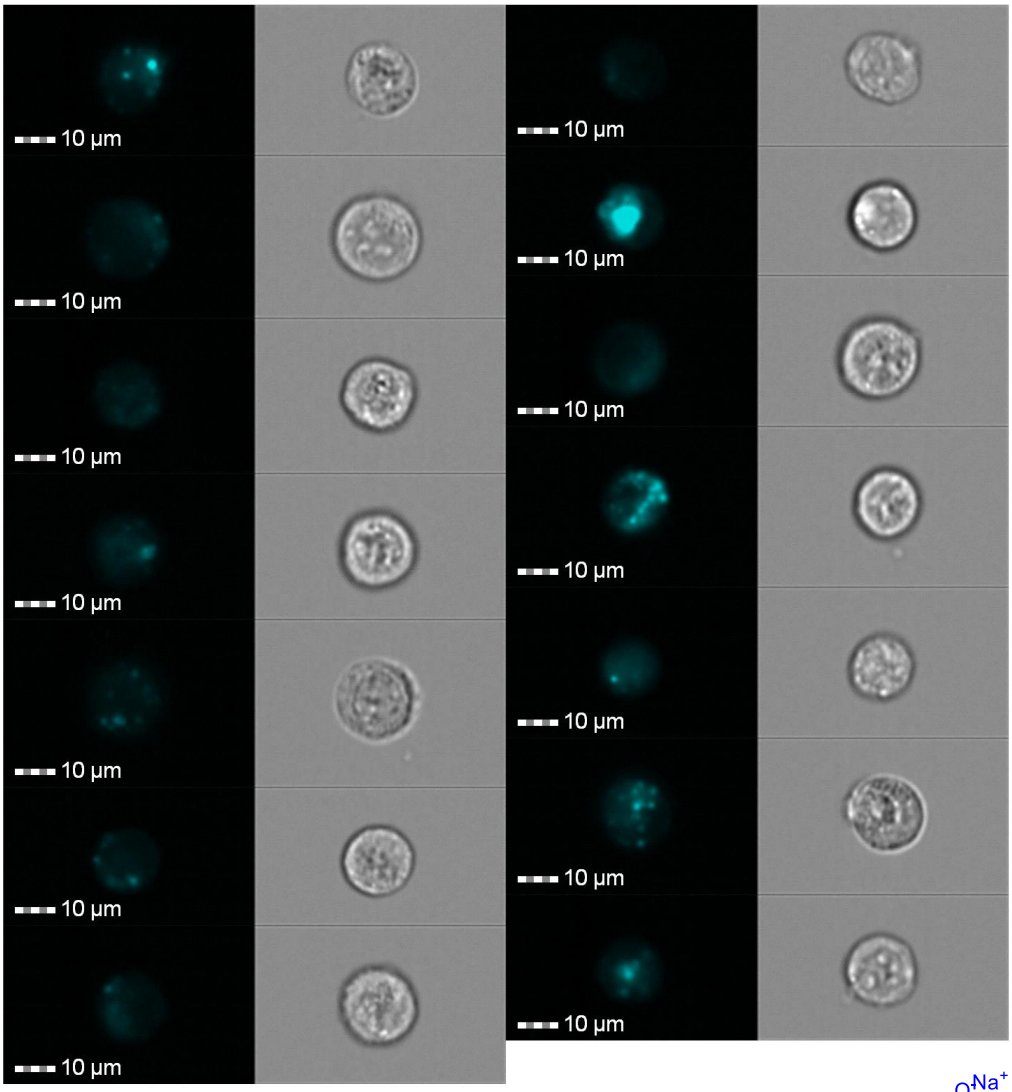


Figure 3.32 Flow cytometry images for Caco-2 cells treated with MalPyr Blue Chol-[(HEA)$_{100\%}$]$_{108}$, showing channel 03 (λ_{ex} = 377 nm and λ_{em} = 420 nm) and brightfield images.

Figure 3.32 illustrates the fluorescence distribution of MalPyr Blue Chol-[(HEA)$_{100\%}$]$_{108}$ in selected cells analysed by Flow Cytometry. The dye fluorescence

in these cells was not preferentially localised on the cell surface, and the observed fluorescence intensity is lower when compared with the shorter polymers. This reflects the lower MFI registered, and confirms the lower tendency for this polymer to interact with cell membranes.

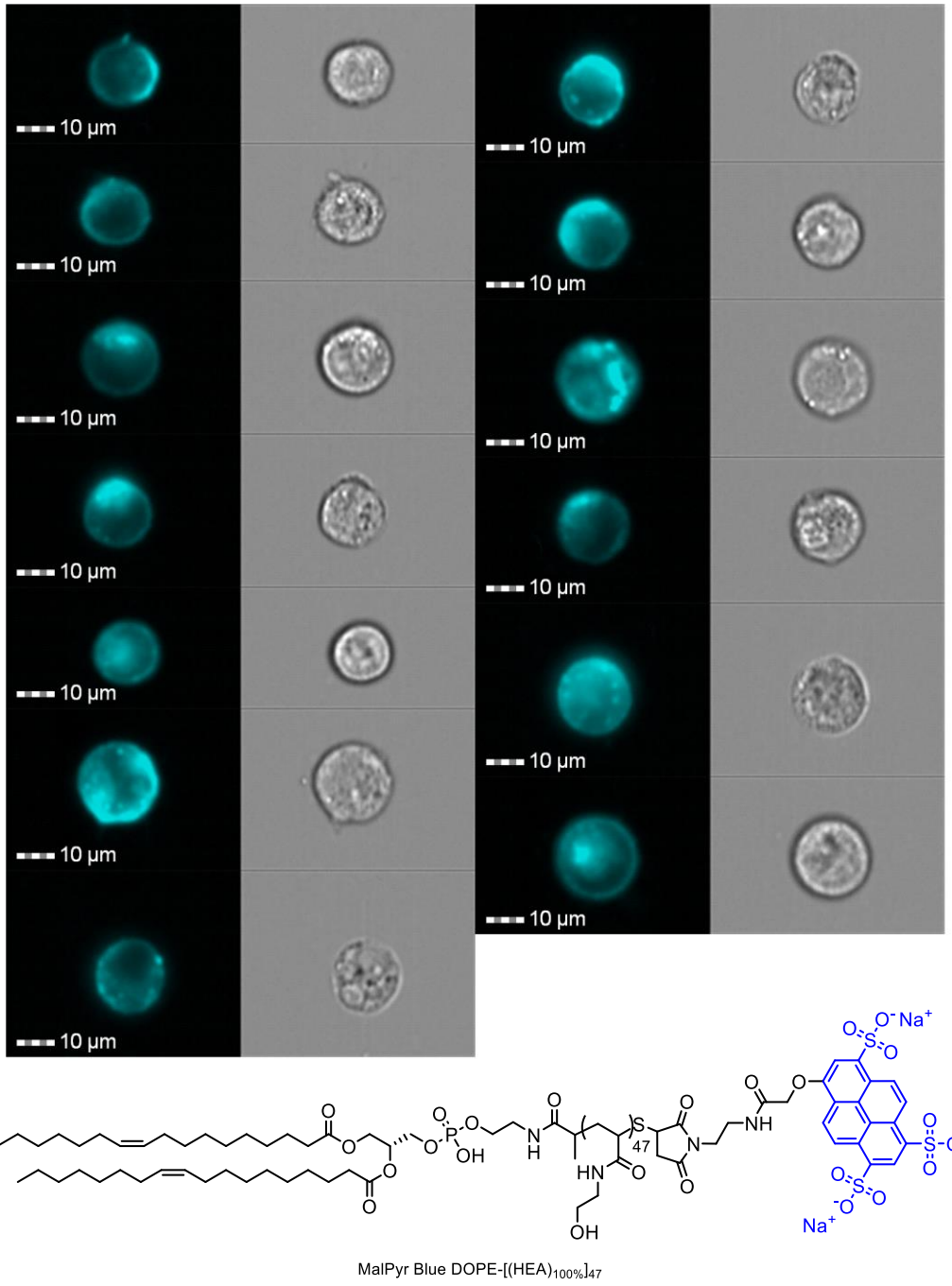


Figure 3.33 Flow cytometry images for Caco-2 cells treated with MalPyr Blue DOPE-$[(HEA)_{100\%}]_{47}$, showing channel 03 (λ_{ex} = 377 nm and λ_{em} = 420 nm) and brightfield images.

Figure 3.33 illustrates the fluorescence distribution of MalPyr Blue DOPE-$[(HEA)_{100\%}]_{47}$ in selected cells analysed by Flow Cytometry. The dye fluorescence in these cells showed similarity to what observed for the similar MalPyr Blue Chol-$[(HEA)_{100\%}]_{52}$, with the fluorescence localised on the cell surface and showing isolated pockets with a higher fluorescence intensity.

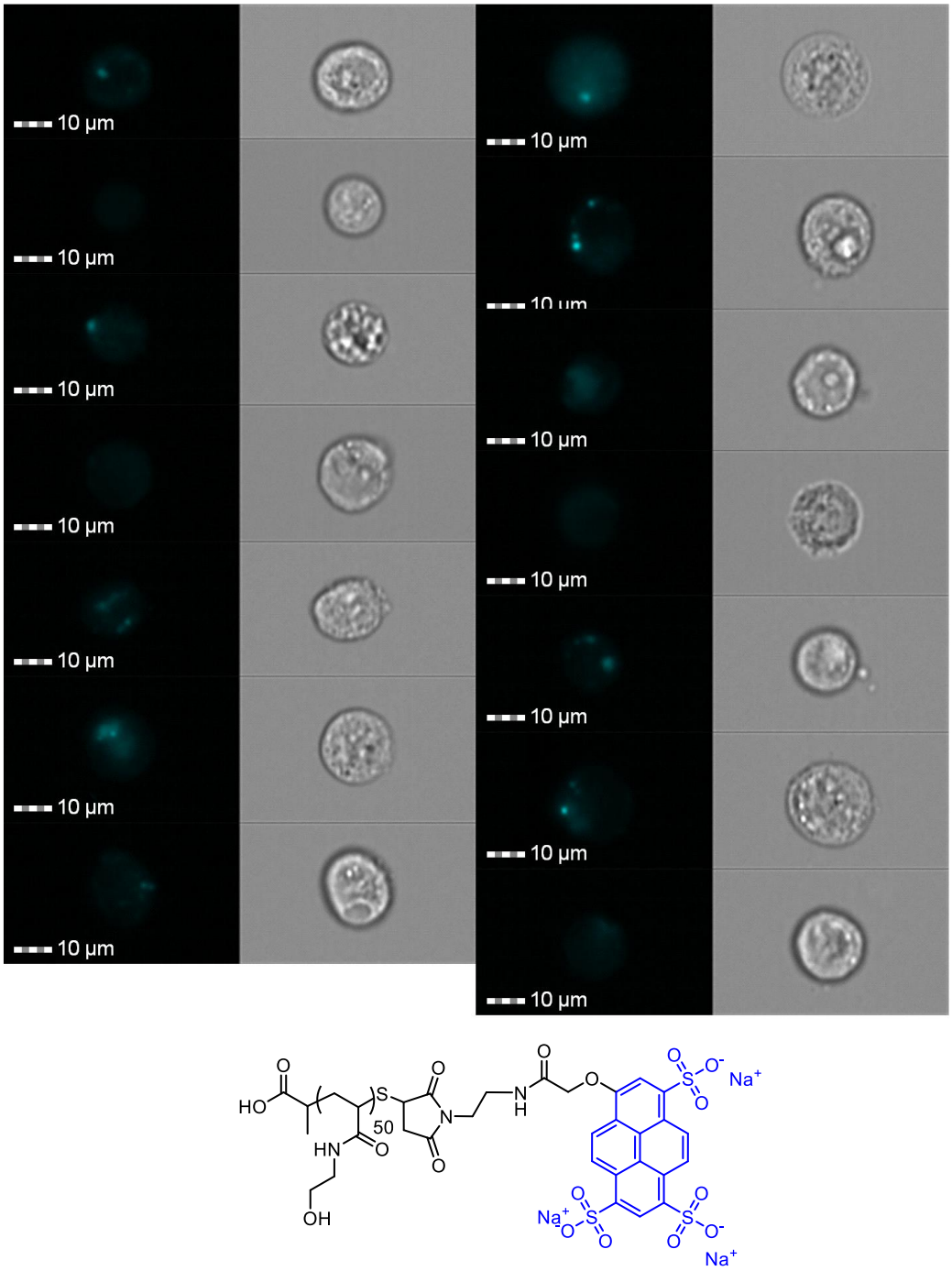


Figure 3.34 Flow cytometry images for Caco-2 cells treated with MalPyr Blue PABTC-[(HEA)$_{100\%}$]$_{50}$, showing channel 03 (λ_{ex} = 377 nm and λ_{em} = 420 nm) and brightfield images.

Figure 3.34 illustrates the fluorescence distribution of MalPyr Blue PABTC-[(HEA)$_{100\%}$]$_{50}$ in selected cells analysed by Flow Cytometry. The dye fluorescence in these cells showed similarity to what observed for the MalPyr Blue Chol-[(HEA)$_{100\%}$]$_{108}$, with a generally low fluorescence intensity and with the fluorescence not localised mainly on the cell surface. This is in line with what

observed in the MFI measurement, with the polymers interacting weakly with the cells and causing a lower accumulation of fluorescent polymers on Caco-2 cells.

These Flow Cytometry experiments confirmed that the membrane binding anchors increased the interaction of the polymers with cell membranes, and that longer membrane-binding polymers, which were causing less cell membrane fluidification, had lower association with cell membranes when compared with shorter polymers. The data observed for MalPyr Blue DOPE-$[(HEA)_{100\%}]_{47}$ confirmed that DOPE polymers tend to interact extensively with cell membranes, while not to the same degree observed for the analogue polymer MalPyr Blue Chol-$[(HEA)_{100\%}]_{52}$. This is in agreement with what observed in the Laurdan membrane fluidity evaluation, where DOPE polymers caused a lower degree of membrane fluidity increase when compared to cholesterol polymers with similar DP.

Hydrophilic control polymers behaved similarly to long membrane-binding polymers, showing a low degree of aMFI registered, and confirming that these polymers have little to no interaction with cell membranes.

3.4 Concluding remarks

In this chapter, we have investigated the ability of the polymers described in **Chapter 2** to interact with cell membranes. This part of this PhD study aimed at identifying a structure/function relationship for this family of materials.

Initial toxicity studies showed that the presence of the cholesterol at the polymer chain-ends influenced the cell metabolic activity and an increase in cell membrane damage, whilst the control polymers did not show similar behaviour at the same concentrations. Notably, recent studies[72,73] have shown that undifferentiated Caco-2 cells are more susceptible to cytotoxicity than their differentiated counterparts. This often causes an overestimation of the toxic effects of materials[5]. Further studies will aim at evaluating the interaction of the polymers with differentiated Caco-2 cells.

The cell membrane fluidity investigation corroborated the toxicity results, showing that cholesterol and DOPE-bearing polymers tended to increase cell membrane fluidity, whilst control polymers did not exert this effect on cells. Additionally, we observed that the cell membrane fluidification effect was concentration dependent; however, it was not influenced by the monomer composition but rather by the chain length. We observed that the shorter polymers (save for Chol-$[(HEA)_{100\%}]_{13}$) had a stronger effect on cell membrane fluidification than longer polymers, and we hypothesised that this was due to a lower number of polymers being able to interact with cell membranes. We also looked into the mechanism of interaction of the polymer with the Laurdan probe used for the cell membrane fluidity studies, showing that the treatment with membrane-interacting polymers also caused release of the dye that was previously embedded in the membrane.

Finally, we employed previously fluorescently-tagged polymers to visualise the localisation of these polymers within cell membranes, and compare different polymer for their relative ability of bind cell membranes. Using MalPyr Blue-tagged

polymers, we demonstrated that the shorter polymers inserted on cell membrane more than the longer ones. We were also able to visualise the interaction, showing that the polymers were accumulating on the cell membrane, rather than being internalised.

3.5 Bibliography

(1) Hooper, N. M. Glycosyl-Phosphatidylinositol Anchored Membrane Enzymes. *Clin. Chim. Acta* **1997**, *266* (1), 3–12. https://doi.org/10.1016/S0009-8981(97)00161-7.

(2) Ingels, F.; Deferme, S.; Destexhe, E.; Oth, M.; Van Den Mooter, G.; Augustijns, P. Simulated Intestinal Fluid as Transport Medium in the Caco-2 Cell Culture Model. *Int. J. Pharm.* **2002**, *232* (1–2), 183–192. https://doi.org/10.1016/S0378-5173(01)00897-3.

(3) Jumarie, C.; Malo, C. Caco-2 Cells Cultured in Serum-free Medium as a Model for the Study of Enterocytic Differentiation in Vitro. *J. Cell. Physiol.* **1991**, *149* (1), 24–33. https://doi.org/10.1002/jcp.1041490105.

(4) Pereira, C.; Costa, J.; Sarmento, B.; Araújo, F. Cell-Based in Vitro Models for Intestinal Permeability Studies. *Concepts Model. Drug Permeability Stud. Cell Tissue based Vitr. Cult. Model.* **2016**, 57–81. https://doi.org/10.1016/B978-0-08-100094-6.00005-5.

(5) Hempt, C.; Kaiser, J. P.; Scholder, O.; Buerki-Thurnherr, T.; Hofmann, H.; Rippl, A.; Schuster, T. B.; Wick, P.; Hirsch, C. The Impact of Synthetic Amorphous Silica (E 551) on Differentiated Caco-2 Cells, a Model for the Human Intestinal Epithelium. *Toxicol. Vitr.* **2020**, *67* (December 2019), 104903. https://doi.org/10.1016/j.tiv.2020.104903.

(6) Brown, M. F. Curvature Forces in Membrane Lipid-Protein Interactions. *Biochemistry* **2012**, *51* (49), 9782–9795. https://doi.org/10.1021/bi301332v.

(7) Marie, E.; Sagan, S.; Cribier, S.; Tribet, C. Amphiphilic Macromolecules on Cell Membranes: From Protective Layers to Controlled Permeabilization. *J. Membr. Biol.* **2014**, *247* (9–10), 861–881. https://doi.org/10.1007/s00232-014-9679-3.

(8) Heerklotz, H. H.; Binder, H.; Schmiedel, H. Excess Enthalpies of Mixing in Phospholipid-Additive Membranes. *J. Phys. Chem. B* **1998**, *102* (27), 5363–5368. https://doi.org/10.1021/jp980884x.

(9) Heerklotz, H. Interactions of Surfactants with Lipid Membranes. *Q. Rev. Biophys.* **2008**, *41* (3–4), 205–264. https://doi.org/10.1017/S0033583508004721.

(10) Heerklotz, H.; Binder, H.; Lantzsch, G.; Klose, G. Membrane/Water Partition of Oligo(Ethylene Oxide) Dodecyl Ethers and Its Relevance for Solubilization. *BBA - Biomembr.* **1994**, *1196* (2), 114–122. https://doi.org/10.1016/0005-2736(94)00222-3.

(11) Lafleur, M.; Bloom, M.; Eikenberry, E. F.; Gruner, S. M.; Han, Y.; Cullis, P. R. Correlation between Lipid Plane Curvature and Lipid Chain Order. *Biophys. J.* **1996**, *70* (6), 2747–2757. https://doi.org/10.1016/S0006-3495(96)79844-2.

(12) Nazari, M.; Kurdi, M.; Heerklotz, H. Classifying Surfactants with Respect to Their Effect on Lipid Membrane Order. *Biophys. J.* **2012**, *102* (3), 498–506. https://doi.org/10.1016/j.bpj.2011.12.029.

(13) Kragh-hansen, U.; Maire, M.; Møller, J. V. The Mechanism of Detergent Solubilization of Liposomes and Protein-Containing Membranes. *Biophys. J.* **1998**, *75* (August), 1–15.

(14) Kragh-Hansen, U.; Møller, J. V.; le Maire, M.; Gulik-Krzywicki, T.; Nöel, J. P. Transitional Steps in the Solubilization of Protein-Containing Membranes and Liposomes by Nonionic Detergent. *Biochemistry* **1993**, *32* (6), 1648–1656. https://doi.org/10.1021/bi00057a032.

(15) Fromherz, P.; Röcker, C.; Rüppel, D. From Discoid Micelles to Spherical Vesicles. The Concept of Edge Activity. *Faraday Discuss. Chem. Soc.* **1986**, *81*, 39–48. https://doi.org/10.1039/DC9868100039.

(16) Lasič, D. D. A Molecular Model for Vesicle Formation. *BBA - Biomembr.* **1982**, *692* (3), 501–502. https://doi.org/10.1016/0005-2736(82)90404-7.

(17) Brogden, K. A. Antimicrobial Peptides: Pore Formers or Metabolic Inhibitors in Bacteria? *Nat. Rev. Microbiol.* **2005**, *3* (3), 238–250. https://doi.org/10.1038/nrmicro1098.

(18) Ehrenstein, G.; Lecar, H. Electrically Gated Ionic Channels in Lipid Bilayers. *Q. Rev. Biophys.* **1977**, *10* (1), 1–34. https://doi.org/10.1017/S0033583500000123.

(19) Gazit, E.; Boman, A.; Boman, H. G.; Shai, Y. Interaction of the Mammalian Antibacterial Peptide Cecropin PI with Phospholipid Vesicles. *Biochemistry* **1995**, *34* (36), 11479–11488. https://doi.org/10.1021/bi00036a021.

(20) Bottega, R.; Epand, R. M. Inhibition of Protein Kinase C by Cationic Amphiphiles. *Biochemistry* **1992**, *31* (37), 9025–9030. https://doi.org/10.1021/bi00152a045.

(21) Chen, L.; Meng, Q.; Yu, X.; Li, C.; Zhang, C.; Cui, C.; Luo, D. Possible Mechanisms Underlying the Biphasic Regulatory Effects of Arachidonic Acid on Ca2+ Signaling in HEK293 Cells. *Cell. Signal.* **2012**, *24* (8), 1565–1572. https://doi.org/10.1016/j.cellsig.2012.03.016.

(22) Chen, L.; Meng, Q.; Jing, X.; Xu, P.; Luo, D. A Role for Protein Kinase C in the Regulation of Membrane Fluidity and Ca2+ Flux at the Endoplasmic Reticulum and Plasma Membranes of HEK293 and Jurkat Cells. *Cell. Signal.* **2011**, *23* (2), 497–505. https://doi.org/10.1016/j.cellsig.2010.11.005.

(23) Gleason, M. M.; Medow, M. S.; Tulenko, T. N. Excess Membrane Cholesterol Alters Calcium Movements, Cytosolic Calcium Levels, and Membrane Fluidity in Arterial Smooth Muscle Cells. *Circ. Res.* **1991**, *69* (1), 216–227. https://doi.org/10.1161/01.RES.69.1.216.

(24) Watanabe, H.; Kobayashi, A.; Yamamoto, T.; Suzuki, S.; Hayashi, H.; Yamazaki, N. Alterations of Human Erythrocyte Membrane Fluidity by Oxygen-Derived Free Radicals and Calcium. *Free Radic. Biol. Med.* **1990**, *8* (6), 507–514. https://doi.org/10.1016/0891-5849(90)90150-H.

(25) Cavanagh, R. J.; Smith, P. A.; Stolnik, S. Exposure to a Nonionic Surfactant Induces a Response Akin to Heat-Shock Apoptosis in Intestinal Epithelial Cells: Implications for Excipients Safety. *Mol. Pharm.* **2019**, *16* (2), 618–631. https://doi.org/10.1021/acs.molpharmaceut.8b00934.

(26) Burt, S. M.; Carter, T. J. N.; Kricka, L. J. Thermal Characteristics of Microtitre Plates Used in Immunological Assays. *J. Immunol. Methods* **1979**, *31* (3–4), 231–236. https://doi.org/10.1016/0022-1759(79)90135-2.

(27) Kricka, L. J.; Carter, T. J. N.; Burt, S. M.; Kennedy, J. H.; Holder, R. L.; Halliday, M. I.; Telford, M. E.; Wisdom, G. B. Variability in the Adsorption

Properties of Microtitre Plates Used as Solid Supports in Enzyme Immunoassay. *Clin. Chem.* **1980**. https://doi.org/10.1093/clinchem/26.6.741.

(28) Lundholt, B. K.; Scudder, K. M.; Pagliaro, L. A Simple Technique for Reducing Edge Effect in Cell-Based Assays. *J. Biomol. Screen.* **2003**, *8* (5), 566–570. https://doi.org/10.1177/1087057103256465.

(29) Invitrogen. Lipophilic Tracers–DiI, DiO, DiD, DiA, and DiR. *Tech. Inf.* **2008**.

(30) Griffin, W. C. Classification of Surface-Active Agents by "HLB." *J. Soc. Cosmet. Chem.* **1949**, 311–326. https://doi.org/10.1155/2012/187421.

(31) Griffin, W. C. Calculation of HLB Values of Non-Ionic Surfactants. *J. Soc. Cosmet. Chem.* **1954**, 249–256. https://doi.org/10.1002/jps.2600581203.

(32) Invitrogen. PrestoBlue ™ Reagent Product Overview. *Tech. Inf.* **2012**, No. 800, 1–13.

(33) Decker, T.; Lohmann-Matthes, M. L. A Quick and Simple Method for the Quantitation of Lactate Dehydrogenase Release in Measurements of Cellular Cytotoxicity and Tumor Necrosis Factor (TNF) Activity. *J. Immunol. Methods* **1988**. https://doi.org/10.1016/0022-1759(88)90310-9.

(34) Dukes, L. D.; McIntyre, M. S.; Mertz, R. J.; Philipson, L. H.; Roe, M. W.; Spencer, B.; Worley, J. F. Dependence on NADH Produced during Glycolysis for β-Cell Glucose Signaling. *J. Biol. Chem.* **1994**, *269* (15), 10979–10982. https://doi.org/10.1016/s0021-9258(19)78078-8.

(35) Bolaños, J. P.; Almeida, A.; Moncada, S. Glycolysis: A Bioenergetic or a Survival Pathway? *Trends Biochem. Sci.* **2010**, *35* (3), 145–149. https://doi.org/10.1016/j.tibs.2009.10.006.

(36) Plesofsky, N.; Brambl, R. Glucose Metabolism in Neurospora Is Altered by Heat Shock and by Disruption of HSP30. *Biochim. Biophys. Acta - Mol. Cell Res.* **1999**, *1449* (1), 73–82. https://doi.org/10.1016/S0167-4889(98)00172-4.

(37) Plesofsky, N.; Higgins, L. A.; Markowski, T.; Brambl, R. Glucose Starvation Alters Heat Shock Response, Leading to Death of Wild Type Cells and Survival of MAP Kinase Signaling Mutant. *PLoS One* **2016**, *11* (11), 1–31. https://doi.org/10.1371/journal.pone.0165980.

(38) Fulda, S.; Gorman, A. M.; Hori, O.; Samali, A. Cellular Stress Responses: Cell Survival and Cell Death. *Int. J. Cell Biol.* **2010**, *2010*. https://doi.org/10.1155/2010/214074.

(39) Mercado, S. A.; Slater, N. K. H. The Functional and Structural Effects of an Amphipathic PH Responsive Biopolymer: A Comprehensive Study in Osteosarcoma Cells. *Eur. Polym. J.* **2016**, *74*, 158–167. https://doi.org/10.1016/j.eurpolymj.2015.11.026.

(40) Rajan, R.; Hayashi, F.; Nagashima, T.; Matsumura, K. Toward a Molecular Understanding of the Mechanism of Cryopreservation by Polyampholytes: Cell Membrane Interactions and Hydrophobicity. *Biomacromolecules* **2016**, *17* (5), 1882–1893. https://doi.org/10.1021/acs.biomac.6b00343.

(41) Mosmann, T. Rapid Colorimetric Assay for Cellular Growth and Survival: Application to Proliferation and Cytotoxicity Assays. *J. Immunol. Methods* **1983**, *65* (1–2), 55–63. https://doi.org/10.1016/0022-1759(83)90303-4.

(42) Endres, T. K.; Beck-Broichsitter, M.; Samsonova, O.; Renette, T.; Kissel, T.

H. Self-Assembled Biodegradable Amphiphilic PEG-PCL-LPEI Triblock Copolymers at the Borderline between Micelles and Nanoparticles Designed for Drug and Gene Delivery. *Biomaterials* **2011**, *32* (30), 7721–7731. https://doi.org/10.1016/j.biomaterials.2011.06.064.

(43) Noi, I.; Schlachet, I.; Kumarasamy, M.; Sosnik, A. Permeability of Novel Chitosan-g-Poly(Methyl Methacrylate) Amphiphilic Nanoparticles in a Model of Small Intestine in Vitro. *Polymers (Basel).* **2018**, *10* (5). https://doi.org/10.3390/polym10050478.

(44) Davoodi, P.; Srinivasan, M. P.; Wang, C. H. Synthesis of Intracellular Reduction-Sensitive Amphiphilic Polyethyleneimine and Poly(ε-Caprolactone) Graft Copolymer for on-Demand Release of Doxorubicin and P53 Plasmid DNA. *Acta Biomater.* **2016**, *39*, 79–93. https://doi.org/10.1016/j.actbio.2016.05.003.

(45) Rotem, R.; Micale, A.; Rizzuto, M. A.; Migliavacca, M.; Giustra, M.; Salvioni, L.; Tasin, F.; Prosperi, D.; Colombo, M. Modeling the Interaction of Amphiphilic Polymer Nanoparticles with Biomembranes to Guide Rational Design of Drug Delivery Systems. *Colloids Surfaces B Biointerfaces* **2020**, *196* (September), 111366. https://doi.org/10.1016/j.colsurfb.2020.111366.

(46) Sovadinova, I.; Palermo, E. F.; Huang, R.; Thoma, L. M.; Kuroda, K. Mechanism of Polymer-Induced Hemolysis: Nanosized Pore Formation and Osmotic Lysis. *Biomacromolecules* **2011**, *12* (1), 260–268. https://doi.org/10.1021/bm1011739.

(47) Nunes Alves, E.; De Farias Presgrave, R.; França Presgrave, O. A.; Peres Sabagh, F.; Rolim De Freitas, J. C. B.; Pinto Corrado, A. A Reassessment of the in Vitro RBC Haemolysis Assay with Defibrinated Sheep Blood for the Determination of the Ocular Irritation Potential of Cosmetic Products: Comparison with the in Vivo Draize Rabbit Test. *ATLA Altern. to Lab. Anim.* **2008**, *36* (3), 275–284. https://doi.org/10.1177/026119290803600305.

(48) Dobrovolskaia, M. A.; Clogston, J. D.; Neun, B. W.; Hall, J. B.; Patri, A. K.; McNeil, S. E. Method for Analysis of Nanoparticle Hemolytic Properties in Vitro. *Nano Lett.* **2008**, *8* (8), 2180–2187. https://doi.org/10.1021/nl0805615.

(49) Liu, P.; Zhu, Z.; Zeng, C.; Nie, G. Specific Absorption Spectra of Hemoglobin at Different PO2 Levels: Potential Noninvasive Method to Detect PO2 in Tissues. *J. Biomed. Opt.* **2012**, *17* (12), 125002. https://doi.org/10.1117/1.JBO.17.12.125002.

(50) Clare, H.; Lin, P. K. T.; Tetley, L.; Cheng, W. P. The Use of Nano Polymeric Self-Assemblies Based on Novel Amphiphilic Polymers for Oral Hydrophobic Drug Delivery. *Pharm. Res.* **2012**, *29* (3), 782–794. https://doi.org/10.1007/s11095-011-0602-7.

(51) Zhai, J.; Suryadinata, R.; Luan, B.; Tran, N.; Hinton, T. M.; Ratcliffe, J.; Hao, X.; Drummond, C. J. Amphiphilic Brush Polymers Produced Using the RAFT Polymerisation Method Stabilise and Reduce the Cell Cytotoxicity of Lipid Lyotropic Liquid Crystalline Nanoparticles. *Faraday Discuss.* **2016**, *191*, 545–563. https://doi.org/10.1039/c6fd00039h.

(52) Sánchez, A. Laurdan Generalized Polarization. *FORMATEX* **2007**, 1007–1014.

(53) Parasassi, T.; Gratton, E. Membrane Lipid Domains and Dynamics as Detected by Laurdan Fluorescence. *J. Fluoresc.* **1995**, *5* (1), 59–69.

(54) Jay, A. G.; Hamilton, J. A. Disorder Amidst Membrane Order: Standardizing Laurdan Generalized Polarization and Membrane Fluidity Terms. *J. Fluoresc.* **2017**, *27* (1), 243–249. https://doi.org/10.1007/s10895-016-1951-8.

(55) Maskarinec, S. A.; Hannig, J.; Lee, R. C.; Lee, K. Y. C. Direct Observation of Poloxamer 188 Insertion into Lipid Monolayers. *Biophys. J.* **2002**, *82* (3), 1453–1459. https://doi.org/10.1016/S0006-3495(02)75499-4.

(56) Wang, J.-Y.; Marks, J. D.; Lee, K. Y. C. Nature of Interactions between PEO-PPO-PEO Triblock Copolymers and Lipid Membranes. *Biomacromolecules* **2013**, *13* (9), 2616–2623. https://doi.org/10.1021/bm300847x.Nature.

(57) Redhead, M.; Mantovani, G.; Nawaz, S.; Carbone, P.; Gorecki, D. C.; Alexander, C.; Bosquillon, C. Relationship between the Affinity of PEO-PPO-PEO Block Copolymers for Biological Membranes and Their Cellular Effects. *Pharm. Res.* **2012**, *29* (7), 1908–1918. https://doi.org/10.1007/s11095-012-0716-6.

(58) Wang, J. Y.; Chen, W.; Nagao, M.; Shelat, P.; Hammer, B. A. G.; Tietjen, G. T.; Cao, K. D.; Henderson, J. M.; He, L.; Lin, B.; Akgun, B.; Meron, M.; Qian, S.; Ward, S.; Marks, J. D.; Emrick, T.; Lee, K. Y. C. Tailoring Biomimetic Phosphorylcholine-Containing Block Copolymers as Membrane-Targeting Cellular Rescue Agents. *Biomacromolecules* **2019**, *20* (9), 3385–3391. https://doi.org/10.1021/acs.biomac.9b00621.

(59) Ercole, F.; Whittaker, M. R.; Quinn, J. F.; Davis, T. P. Cholesterol Modified Self-Assemblies and Their Application to Nanomedicine. *Biomacromolecules* **2015**, *16* (7), 1886–1914. https://doi.org/10.1021/acs.biomac.5b00550.

(60) Titova, T. Y.; Morozova, J. P.; Korolev, B. V. Fluorescence of Laurdan in Homogeneous Solvents and Water-Micellar Solutions. *Russ. Phys. J.* **2020**, *62* (12), 2330–2339. https://doi.org/10.1007/s11182-020-01985-w.

(61) Pramanik, P.; Ray, D.; Aswal, V. K.; Ghosh, S. Supramolecularly Engineered Amphiphilic Macromolecules: Molecular Interaction Overrules Packing Parameters. *Angew. Chemie* **2017**, *129* (13), 3570–3574. https://doi.org/10.1002/ange.201611715.

(62) Kurniasih, I. N.; Liang, H.; Mohr, P. C.; Khot, G.; Rabe, J. P.; Mohr, A. Nile Red Dye in Aqueous Surfactant and Micellar Solution. *Langmuir* **2015**, *31* (9), 2639–2648. https://doi.org/10.1021/la504378m.

(63) Moad, G.; Rizzardo, E.; Thang, S. H. End-Functional Polymers, Thiocarbonylthio Group Removal/Transformation and Reversible Addition-Fragmentation-Chain Transfer (RAFT) Polymerization. *Polym. Int.* **2011**, *60* (1), 9–25. https://doi.org/10.1002/pi.2988.

(64) Rieseberg, M.; Kasper, C.; Reardon, K. F.; Scheper, T. Flow Cytometry in Biotechnology. *Appl. Microbiol. Biotechnol.* **2001**, *56* (3–4), 350–360. https://doi.org/10.1007/s002530100673.

(65) Luminex. Amnis Imaging Flow Cytometers - Microscopy in Flow. 2020, p 15.

(66) Schulz, O.; Hanč, P.; Böttcher, J. P.; Hoogeboom, R.; Diebold, S. S.; Tolar, P.; Reis e Sousa, C. Myosin II Synergizes with F-Actin to Promote DNGR-1-Dependent Cross-Presentation of Dead Cell-Associated Antigens. *Cell Rep.* **2018**, *24* (2), 419–428. https://doi.org/10.1016/j.celrep.2018.06.038.

(67) Inui, O.; Teramura, Y.; Iwata, H. Retention Dynamics of Amphiphilic Polymers PEG-Lipids and PVA-Alkyl on the Cell Surface. *ACS Appl. Mater. Interfaces* **2010**, *2* (5), 1514–1520. https://doi.org/10.1021/am100134v.

(68) Taresco, V.; Abelha, T. F.; Cavanagh, R. J.; Vasey, C. E.; Anane-Adjei, A. B.; Pearce, A. K.; Monteiro, P. F.; Spriggs, K. A.; Clarke, P.; Ritchie, A.; Martin, S.; Rahman, R.; Grabowska, A. M.; Ashford, M. B.; Alexander, C. Functionalized Block Co-Polymer Pro-Drug Nanoparticles with Anti-Cancer Efficacy in 3D Spheroids and in an Orthotopic Triple Negative Breast Cancer Model. *Adv. Ther.* **2021**, *4* (1), 1–15. https://doi.org/10.1002/adtp.202000103.

(69) Teramura, Y.; Kaneda, Y.; Totani, T.; Iwata, H. Behavior of Synthetic Polymers Immobilized on a Cell Membrane. *Biomaterials* **2008**, *29* (10), 1345–1355. https://doi.org/10.1016/j.biomaterials.2007.11.048.

(70) Aubin, J. E. Autofluorescence of Viable Cultured Mammalian Cells. *J. Histochem. Cytochem.* **1979**, *27* (1), 36–43. https://doi.org/10.1177/27.1.220325.

(71) Wang, J. Y.; Marks, J.; Lee, K. Y. C. Nature of Interactions between PEO-PPO-PEO Triblock Copolymers and Lipid Membranes: (I) Effect of Polymer Hydrophobicity on Its Ability to Protect Liposomes from Peroxidation. *Biomacromolecules* **2012**, *13* (9), 2616–2623. https://doi.org/10.1021/bm300847x.

(72) Pietroiusti, A.; Bergamaschi, E.; Campagna, M.; Campagnolo, L.; De Palma, G.; Iavicoli, S.; Leso, V.; Magrini, A.; Miragoli, M.; Pedata, P.; Palombi, L.; Iavicoli, I. The Unrecognized Occupational Relevance of the Interaction between Engineered Nanomaterials and the Gastro-Intestinal Tract: A Consensus Paper from a Multidisciplinary Working Group. *Part. Fibre Toxicol.* **2017**, *14* (1). https://doi.org/10.1186/s12989-017-0226-0.

(73) Gerloff, K.; Pereira, D. I. A.; Faria, N.; Boots, A. W.; Kolling, J.; Förster, I.; Albrecht, C.; Powell, J. J.; Schins, R. P. F. Influence of Simulated Gastrointestinal Conditions on Particle-Induced Cytotoxicity and Interleukin-8 Regulation in Differentiated and Undifferentiated Caco-2 Cells. *Nanotoxicology* **2013**. https://doi.org/10.3109/17435390.2012.662249.

Chapter 4

Effect of polymers on model lipid bilayer membranes

This chapter will describe the experiments employed to further characterise the interaction between the synthesised polymers and membranes. The focus will be on model bilayer membranes such as liposomes, and on molecular modelling of cell membranes. Characterisation of lipid bilayers on gold surfaces was performed by Atomic Force Microscopy (AFM) in collaboration with Dr Long Jiang. Investigation in the kinetics of polymer-lipid bilayer interactions was performed by Surface Plasmon Resonance (SPR) in collaboration with Dr Gokhan Yilmaz. Confirmation of membrane embedding was conducted by Solid-State NMR (SSNMR) in collaboration with Dr Vivien Yeh. Finally, Molecular Modelling simulations were performed in collaboration with Dr Charlie Laughton, to simulate key timepoints in the polymer-bilayer interaction.

4.1 Introduction

In **Chapter 3**, we described the effect that membrane-binding amphiphilic polymers synthesised in this work have on the plasma membrane of Caco-2 cells. After confirming the interaction through different methods such as flow cytometry and confocal microscopy, as well as assessing the effect of such interaction on membrane fluidity by Laurdan assay, we decided to investigate further in the mechanism of interaction. Therefore, we decided to employ synthetic membrane models to study in depth the nature of the polymer-membrane interaction. Biological membranes are complex, multi-component systems[1] (complex lipid mixtures, proteins and carbohydrates amongst the main components[2], with further supramolecular organisation[3,4]) which are not yet fully understood and characterised[4]. Although synthetic lipid bilayer (from single phospholipid to phospholipid mixture + cholesterol) membranes are extremely simple when compared with the complexity of the cell membrane, they are easier to analyse and manipulate[5]. This allows for investigation of membrane properties under controlled conditions, complementing the data obtained with *in vitro* cell experiments[6].

The investigation detailed within this chapter focused first on assessing the suitability of the selected synthetic bilayer system based on dioctadecyl phosphatidylcholine and distearoyl phosphatidylcholine (DOPC:DSPC:cholesterol 2:1:1 mol:mol ratio) as a model for the interactions described in **Chapter 3**. Initial Laurdan membrane fluidity evaluation for this lipid bilayer system confirmed that interaction with polymers induced membrane fluidity increase, similar to what observed for *in vitro* cell experiments. Therefore, Surface Plasmon Resonance (SPR) was employed to detail the kinetics of interaction between this lipid bilayer model and select polymers, based on different characteristics (nature/absence of the lipophilic α-chain end, DP). Then, investigations based on Solid State NMR (SSNMR) were conducted to confirm embedding of membrane-interacting

polymers within simple (DSPC) and more representative (DSPC + cholesterol) lipid bilayer models. Finally, molecular modelling experiments were conducted to simulate the interactions between a simple bilayer membrane model (DPPC) and two model Cholesterol-based HEA homopolymers (Chol-$[(HEA)_{100\%}]_{58}$ and Chol-$[(HEA)_{100\%}]_{120}$). These computational simulations were employed to produce a model for the fluidification of bilayer membranes caused by the amphiphilic polymers.

4.2 Materials and Methods

4.2.1 Materials

Laurdan dye (6-dodecanoyl-2-dimethylaminonaphthalene), solvents and cell culture media were purchased from Thermo Fisher Scientific (Loughborough, UK).

Phospholipids were purchased from Avanti Polar Lipids Inc (Alabaster, Alabama). Biacore Series S L1 chip was purchased from Cytiva Life Sciences (Sheffield, UK).

4.2.2 Liposome preparation

Unilamellar liposomes were prepared following gentle hydration method[7,8], followed by membrane extrusion[9].

Briefly, the phospholipid stock solutions (2.5 mg/mL in CH_2Cl_2) were used to solubilise solid cholesterol in a round-bottomed flask (DOPC:DSPC:cholesterol 2:1:1 mol:mol ratio); if required, Laurdan stock solution (2.5 mg/mL in CH_2Cl_2, to result in 99:1 lipid:Laurdan mol:mol) was added during this step. The resulting organic solution was diluted with a CH_2Cl_2:MeOH 2:1 solution to reach a final 10 mg/mL lipid concentration. The organic solution was dried under reduced pressure using a rotary evaporator, protected from light if a Laurdan was employed during the preparation. The dried lipid film was heated to 55 °C and an aliquot of pre-heated (55 °C) PBS or HBSS was added dropwise while stirring, to achieve a 0.02 mg/mL lipid concentration. The solution was stirred gently (100 rpm) until it became clear, and was subject to 21 successive extrusions through a polycarbonate membrane (0.2 μM pore size). The resulting liposome suspension was analysed by DLS for particle size analysis.

4.2.3 Laurdan assay

Liposomes loaded with Laurdan were prepared as described in 4.2.2. 75 μL of liposome suspension (0.02 mg/mL lipid concentration) in HBSS and 75 μL of the

selected polymer solution (0.2 μM) in HBSS were transferred were added to each well of a 96-well plate. After 30 minutes of incubation at 37 °C, samples were excited at λ_{ex} = 360 nm and fluorescence was recorded at λ_{em} = 440 nm and at λ_{em} = 500 nm. The Generalised Polarisation (GP) of Laurdan was calculated by using the equation, where I_{460} and I_{500} are the fluorescence intensities recorded at λ_{em} = 460 nm and λ_{em} = 500 nm:

$$GP = \frac{(I_{460} - I_{500})}{(I_{460} + I_{500})}$$

The 96-well plates were analysed with a Spark 10M Plate Reader (Tecan), and data was processed with SparkControl 2.1 software, then further elaborated with Prism 8.4.2 (GraphPad).

4.2.4 Gold sputtering on glass coverslips

Round coverslips (22Dia, thickness 0.16 - 0.19 mm, Fischer Scientific) were cleaned by Piranha cleaning to remove any contaminants[10]. The cleaned coverslips were subject to deposition of a 10 nm of Indium/Tin oxide (ITO) layer, followed by deposition of a (47 ± 5%) nm gold thin film. The gold sputtering was performed at the Nanoscale and Microscale Research Centre (nMRC) Nottingham.

4.2.5 Phosphatidylcholine/1,2-dipalmitoyl-sn-glycero-3- phosphothioethanol liposomes preparation and adhesion

The liposomes were prepared as described in literature[11]. Briefly, egg PC (Avanti Lipids) and 1,2-dipalmitoyl-sn-glycero-3- phosphothioethanol (DPPTE, Avanti Lipids) were solubilised separately in chloroform (2.5 mg/mL). Aliquots of these stock solutions (99:1 PC:DPPTE mol:mol) were transferred in a round bottom flask and the solvent was removed flushing the flask with a N_2 stream while manually rotating the flask. The dried lipid film thus formed was rehydrated with PBS (0.01

M) to obtain a 0.02 mg/mL lipid concentration. The solution was stirred gently until it became clear, and was subject to 21 successive extrusions through a polycarbonate membrane (0.1 μM pore size). The resulting liposome suspension was analysed by DLS for particle size analysis.

Liposome suspensions were stored at 4 °C for a maximum of 24 hours before use.

4.2.6 AFM analysis of lipid bilayers on gold

The liposome suspensions described in 4.2.5 were loaded on the gold-coated coverslips. The surface was imaged using a Dimension Icon (Bruker) using Peak Force Tapping or Tapping mode in liquid, using ScanAsyst Fluid+ tips.

4.2.7 Surface plasmon resonance (SPR) – immobilisation of liposomes on chips on L1 chips

The extent of interaction between the Cholesterol and phospholipid DOPE-containing polymers and immobilised lipid bilayers was performed on a BIAcore T200 system (GE Healthcare). The SPR measurements were carried out after loading liposomes on a BiaCore L1 chip (Cytiva Life Sciences, Sheffield, UK). Throughout this process, two aqueous media were employed:

I. **Surface priming solution:** 20 mM 3-((3-cholamidopropyl)-dimethylammonio)-1- propane sulfonate (CHAPS)
II. **Buffer:** 10 mM HBSS

The loading process was conducted in three successive steps:

1. **Surface wash:** the L1 chip surface was cleaned with repeated (at least 2) injections of 10 μL of 20 mM CHAPS detergent solution.

2. **Liposome loading:** The liposome suspension (prepared as described in 4.2.2) was injected at a low flow rate (5 µL/min) at 0.5 mM lipid concentration. Adsorption was monitored by following an increase in Response index Units (RiU), which plateaued as the surface coverage approached completion. In terms of response, we targeted 5000 (RiU), which is generally accepted as an indication that lipid bilayer was immobilised on the L1 chip[12]. Bilayer immobilisation was found to be complete within a few minutes.

3. **Liposomal surface cleaning:** Regeneration of the sensor chip surface was performed using a long pulse of the buffer solution (10 mM HBSS) at high flow rate (50 µL/min, 420 sec).

Solutions of selected polymers (**Table 4.1**) were prepared at different concentrations (24 nM to 1.5 nM) in HBSS buffer solution. Sensorgrams for each polymer concentration were recorded with a 240 sec injection of polymer solution (ON period) followed by 120 sec of buffer alone (OFF period). Kinetic data was processed using a single set of sites (1:1 Langmuir binding) model in the BIAevalulation 3.1 software.

Table 4.1 Polymers selected for the surface plasmon resonance evaluation of polymer-bilayer interactions

Polymer
Chol-$[(HEA)_{100\%}]_{13}$
Chol-$[(HEA)_{100\%}]_{58}$
Chol-$[(HEA)_{100\%}]_{70}$
Chol-$[(HEA)_{100\%}]_{108}$
DOPE-$[(HEA)_{100\%}]_{80}$
PABTC-$[(HEA)_{100\%}]_{63}$

4.2.9 Solid-state NMR analysis of multilamellar lipid vesicles

The selected polymers (**Table 4.2**) were solubilised or suspended in the minimum amount of deionised water and added to solid dimyristoyl phosphatidylcholine (DMPC:polymer 10:1 molar ratio); the mixture was stirred until an almost clear suspension was obtained. The solution was subject to 8 freeze-thaw cycles to produce multilamellar vesicles; the solution was centrifuged for 20 minutes at 1500 rpm. The supernatant was removed, and the pellet collected and transferred to the solid-state NMR probe.

Table 4.2 Polymers selected for the solid-state NMR evaluation of polymer-bilayer interactions

Polymer
Chol-$[(HEA)_{100\%}]_{13}$
Chol-$[(HEA)_{100\%}]_{52}$
Chol-$[(HEA)_{100\%}]_{58}$
DOPE-$[(HEA)_{100\%}]_{47}$
PABTC-$[(HEA)_{100\%}]_{63}$
PABTC-$[(HEA)_{100\%}]_{80}$

All solid-state NMR experiments were performed with a Varian 400 MHz VNMRS spectrometer equipped with a 4 mm magic angle spinning (MAS) NMR probe. All ^{31}P and ^{13}C NMR spectra were referenced externally with 10% H_3PO_4 and adamantane, respectively.

^{31}P wideline NMR was performed at 28 °C using Hahn echo sequence with 100 kHz π/2 pulse and 12 μs delays. Spectra were acquired with 20 ms acquisition time with a recycle delay of 5 s and 2048 transients averaged.

^{13}C Magic Angle Spinning (MAS) NMR was performed at MAS frequency of 5 kHz and at 32 °C, for both cross polarisation and direct excitation experiments. Direct excitation experiments were done with a single 100 kHz π/2 before

acquisition, followed by 125 ms acquisition under 60 kHz SPINAL-64 to remove heteronuclear dipolar couplings. The recycle delay was 5 s, and spectra were obtained after average of 2048 transients.

Cross polarisation was performed with an initial 120 kHz π/2 ^{1}H excitation pulse, followed by 3.5 ms of 45 kHz Harmann-Hahn contact time for magnetisation transfer to ^{13}C. Spectra were recorded under 60 kHz SPINAL-64 scheme over 125 ms of acquisition time. The recycle delay was 3.5 s, and spectra were obtained by averaging 2048 transients.

4.2.11 Molecular Modelling of Cholesterol-HEA homopolymer interactions with a simulated DPPC bilayer membrane

All simulations were performed using AMBER 20[13–16]. For atomistic modelling purposes, Chol-[(HEA)]$_n$ polymers were divided into cholesterol, linker, HEA monomer (both enantiomers) and terminal units, with appropriate capping groups (**Scheme 4.1**). Models for each were built using Chimera[17], and then unit parameter files generated using AMBER's Antechamber module[18].

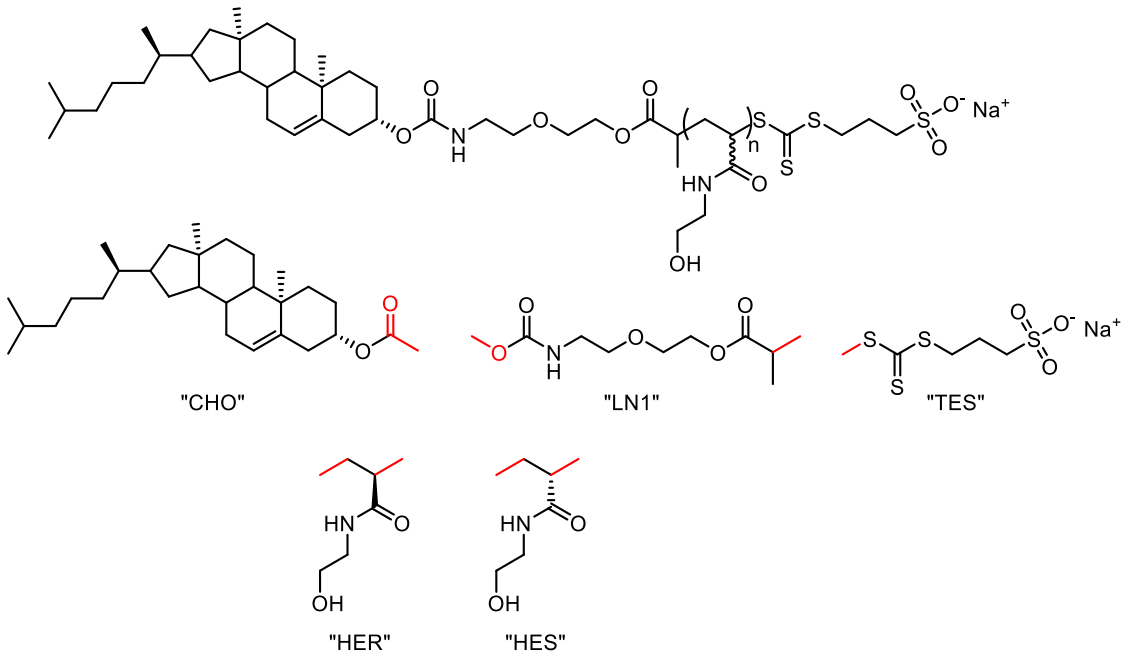


Figure 4.1 Division of Chol-[(HEA)]$_n$ (top) into fragments for modelling. Capping groups shown in red

Development of a coarse-grained model for Chol-[(HEA)]$_n$

An atomistic model for atactic Chol-[(HEA)]$_{10}$ was generated using LEAP, each HEA monomer being chosen as the R- or S-enantiomer to generate an "RRSSRRSSRR" oligomer. The models were relaxed using energy minimisation and a short (5ps) molecular dynamics (MD) simulation in implicit solvent, then the final structures for the polymer were used to build a solvated system (TIP3P water model[19], 1 sodium counterion, truncated octahedral unit cell with 63 Angstrom cell vectors). After energy minimisation and a 10ns MD NPT equilibration, a 100ns production simulation was run, saving coordinates every 100ps. Data from this run was used to parameterise a 2-bead Coarse Grained (CG) model for HEA. The backbone is modelled as a P1 bead, and the sidechain as a P2 bead (**Figure 4.2**). The model retains the distinction between the two HEA monomer enantiomers, as the data shows the CG inter-monomer torsion angle distributions are sensitive to this (**Figure 4.2**). Tabulated dihedral potentials were used for these terms, generated by Boltzmann inversion of the dihedral angle distributions. No CG model

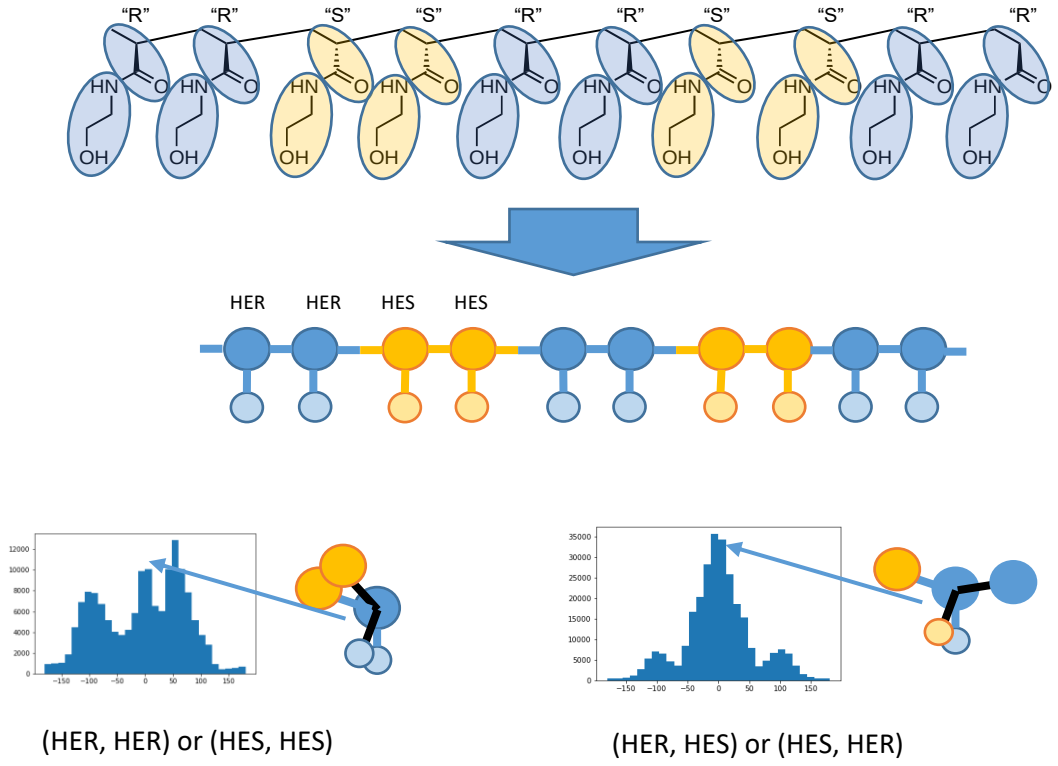


Figure 4.2 Coarse graining scheme for [(HEA)]$_n$ and details of polymer backbone dihedral distributions inferred from atomistic simulations

was built for the terminal unit, and the linker unit was modelled implicitly as a flat-bottomed distance restraint between the first HEA unit and an embedded CG cholesterol molecule, with length and force constant calculated again from the atomistic simulation data.

Atomistic simulations of Chol-[(HEA)]$_{50}$ and a DPPC bilayer

An atomistic model of Chol-[(HEA)]$_{50}$ was built as described for the 10-mer above. After the implicit then explicit solvent energy minimisation and MD equilibration process, the final structure was appropriately oriented, then embedded in a DPPC bilayer using PACKMOL-Memgen[20] so the cholesterol moiety lay within the top membrane leaflet but the attached HEA polymer was solvent exposed. The generated system contained one molecule of the polymer, 1 sodium ion, 195 DPPC lipids and 19293 TIP3P water molecules in a rectangular periodic box 89.4 x 89.4 x 136.6 Angstroms. The system was energy minimised then relaxed with isothermal-isobaric (NPT) MD simulations at 50K (100 ps) then 300K (100ps) before the 500ns production run, snapshots being saved every 100 ps. Using the MDTraj Python package[21], sub-trajectories were created from this data selecting the closest 20 lipids to the embedded cholesteryl moiety, then the next closest 30, and finally all remaining lipids. These trajectories were then analysed using the cpptraj lipdorder tool to obtain predicted deuterium order parameters for lipids within certain distance ranges of the cholesterol group. A control system containing a single cholesterol molecule, but no polymer, embedded in a dipalmitoyl phosphatidylcholine (DPPC) bilayer was generated, simulated and analysed using the same methodology.

Generation and validation of Martini CG models of $[(HEA)]_{58}$ and $[(HEA)]_{120}$

Using local Python scripts, a coarse-grained model for atactic $[HEA]_{58}$ in a globular conformation was generated using the backbone trace of the crystal structure of bovine pancreatic trypsin inhibitor (BPTI)[22] as a guide. The HEA P1 beads were placed at the carbonyl C atom positions, the P2 beads along the C=O vectors, and bond lengths then scaled as required. To check the CG parameterization, the CG $[_{HEA}]_{58}$ polymer was solvated in a cubic box of Martini water (7nm box edge), energy minimized and then subjected to 200,000 steps of NPT MD (timestep 30 fs), saving a snapshot every 1000 steps. Polymer chain torsion angle distributions were then compared with those from the original atomistic simulations. Using a similar approach, a CG model for atactic $[HEA]_{120}$ was created from the backbone trace of 2RSC[23].

Martini CG simulations of Chol-$[(HEA)]_{58}$ and Chol-$[(HEA)]_{120}$ in a plasma membrane

Using locally generated Python scripts, a copy of the plasma membrane model of Ingolfsson *et al.* was cut down to a 21 nm square patch, and sixteen molecules of either $[(HEA)]_{58}$ or -$[(HEA)]_{120}$ placed at the surface on a 5nm-spaced square grid, removing clashing water molecules. The cholesterol molecule in the membrane patch closest to the first HEA monomer in each of the 16 polymers was then identified and used to define a distance restraint that mimics the atomistic linker group (see above). After energy minimisation, MD simulations were performed using the same parameters as Ingolfsson *et al.*, wherever appropriate. Simulations were run for 800 ns in total (20 fs timestep), saving coordinates every 500 ps. Polymer-polymer radial distribution functions (in the xy plane) were calculated using local Python scripts.

4.3 Results and Discussion

4.3.1 Suitability of liposomes as bilayer membrane models for cell membrane-polymer interaction

Thanks to the structural and geometric similarity between cell membranes and unilamellar liposomal bilayer membranes, these have been extensively used as membrane models[24–26]. Liposomes are highly tuneable, and it is possible to tailor their composition and properties for specific investigations, such as lipid peroxidation[27], membrane integrity[24] or drug-membrane interactions[25] amongst others. The research idea behind this thesis was based on GPI anchored proteins[28] (see **Chapter 1**) and these structures are postulated to be involved in the formation of lipid rafts[29–31]. Therefore, we decided to employ a liposome composition (**Table 4.3**) that has been shown to produce phase partitioning between lipid ordered and disordered phases[32]. For this investigation, liposomal bilayers were prepared with embedded Laurdan dye[33], to investigate the effect that interaction with polymers had on the liposomal bilayer membrane fluidity.

Table 4.3 Composition of the liposomes employed as a model membrane for fluidity studies.

Liposome composition (mol %)	
DOPC	50%
DSPC	25%
Cholesterol	24.9%
Laurdan	0.1%

Studies that employ liposomal membranes as models for cell membranes often employ giant unilamellar vesicles (GUVs), with diameters reaching up to 100 μm to visualise phase separation and formation of lipid rafts[32,34]. However, assembly of giant GUVs and subsequent optimisation of composition to observe liquid-ordered and liquid-disordered domains often requires lengthy optimisation of lipid

composition and manufacturing conditions, thus for time constraints in this part of our study the (co)polymers produced in **Chapter 2** were tested on smaller liposomes and their effect on lipid membrane fluidity was estimated by Laurdan assay. The particle sizing analysis, performed through dynamic light scattering (DLS) confirmed that, following extrusion, liposomes had low polydispersity (0.143) and hydrodynamic diameter of 196 nm with a negligible subpopulation in the µm range (**Figure 4.3**) .

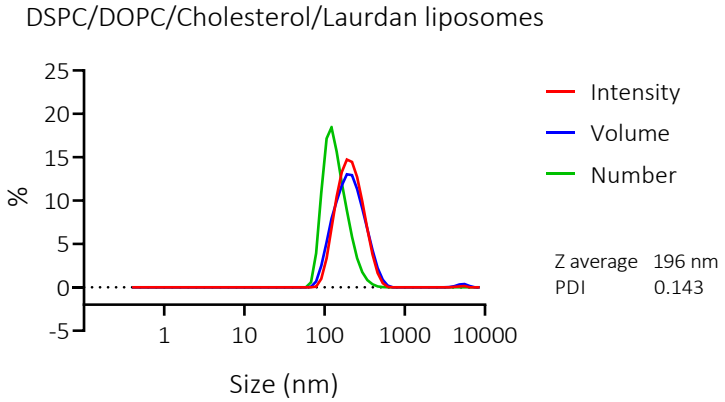


Figure 4.3 DLS particle size analysis of the Laurdan-loaded liposomes employed for membrane fluidity studies. Data are shown as intensity, volume and number distributons (%).

Laurdan-loaded liposomes were incubated with different polymer solutions (0.1 µM in HBSS, replicating the *in vitro* cell exposure to polymers), to observe their effect on the Laurdan fluorescence profile and therefore on liposomes membrane fluidity. The results were expressed as ΔGP, defined as the difference in GP of polymer-liposome samples, compared to untreated Laurdan-loaded liposomes (**Figure 4.4**). To assess the kinetics of polymer-membrane interaction, that is, the rate at which our materials interacted with the liposomal membrane, fluorescence was recorded over the course of 30 minutes. Data showed a similar trend to what observed on Caco-2 cells. . The cholesterol-containing polymers Chol-$[(HEA)_{100\%}]_{108}$ and Chol-$[(HEA)_{100\%}]_{52}$ still increased the membrane fluidity, but the observed ΔGP values for liposomes were lower than what measured for

cells (-0.1 average for liposomal membranes vs -0.3 average for cell membranes). The DOPE-based polymer DOPE-[(HEA)$_{100\%}$]$_{47}$ increased the liposomal membrane fluidity compared to untreated liposomes, although the effect was not statistically significant. Similarly, the effect of control polymers PABTC-[(HEA)$_{100\%}$]$_{80}$ and PABTC-[(HEA)$_{100\%}$]$_{50}$ on liposome membrane fluidity was not statistically significant. The cholesterol and DOPE polymers affected the bilayer fluidity rapidly (within 2-4 minutes), and the effect became statistically significant after 6 minutes exposure for Chol-[(HEA)$_{100\%}$]$_{108}$ and Chol-[(HEA)$_{100\%}$]$_{52}$. In **Chapter 3**, cells exposed to analogous conditions showed statistically significant increase in membrane fluidity within the first minute of exposure, suggesting that the liposomal bilayer:polymer interaction could follow a slower kinetic.

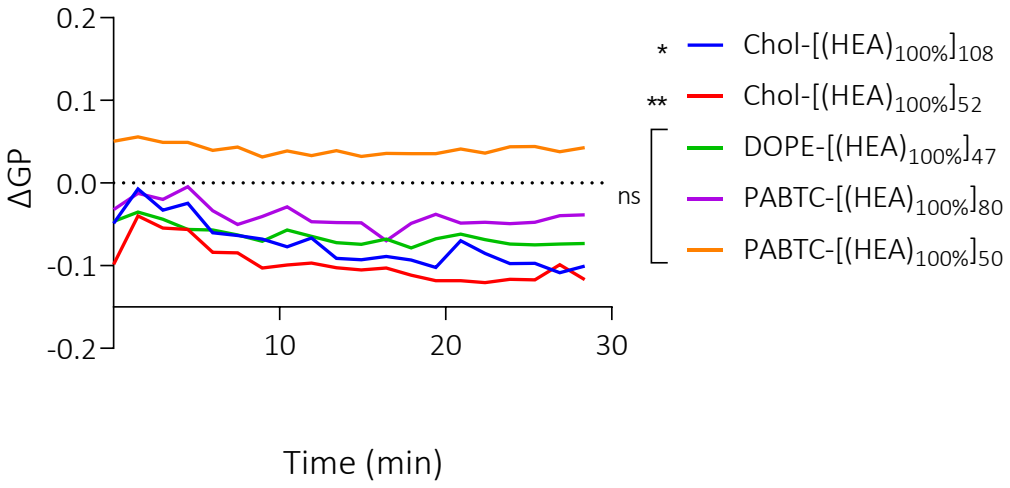


Figure 4.4 Kinetic Laurdan fluorescence measurement for Laurdan-loaded liposomes interacting with different types of polymers. Results are expressed as delta generalised polarisation (ΔGP): a positive value represents an increase in membrane rigidity, while a negative value an increase in membrane fluidity, compared to untreated liposomes. Statistical significance of the results was investigated through a one-way ANOVA test, comparing the fluidity values obtained with the values measured for untreated liposomes at the same timepoint (* $P<0.1$, ** $P<0.01$; n=3).

These initial results that showed results in line with what observed for Caco-2 cells, providing an initial indication that these liposomes could be used for membrane fluidity experiments.

4.3.2 Surface Plasmon Resonance (SPR)

Surface plasmon resonance is a label-free technique employed to evaluate the interaction of a ligand with a substrate. SPR has been previously employed to understand the dynamics of various species (drugs, proteins) interacting with membrane models[35–37]. This technique is based on changes in refractive index of a gold surface when ligands interact with any functionality attached to the gold surface. As exemplified in **Figure 4.5**, polarised light is shone through a prism on a gold sensor, and the light is then reflected by the gold surface. At a specific angle of incidence (SPR-dip angle), the light excites the metal surface plasmons to induce surface plasmon resonance and therefore causing a decrease in the intensity of reflected light. The angle where SPR happens is directly correlated to the gold surface refractive properties, which are dependent on the presence of material deposited on the other side of the gold chip. Therefore, by measuring the change in SPR-dip angle, it is possible to directly quantify the amount and calculate the kinetics for a species interacting with the gold chip[37–39].

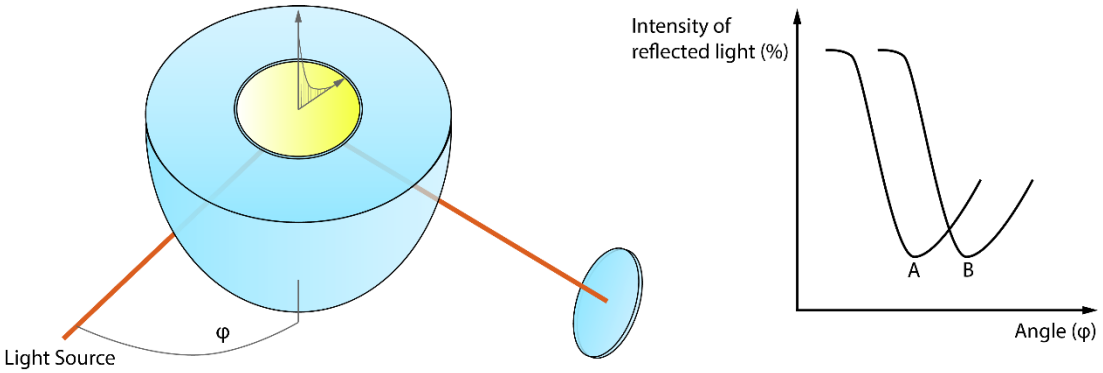


Figure 4.5 Representation of an SPR system: a gold chip is loaded on a prism; polarised light is generated from a source and the light intensity is measured by a detector. The surface plasmons excitation is achieved at a specific angle of incidence (φ), causing a dip in the light intensity. If any material is interacting with the chip surface there is a change in the angle of incidence, which is then recorded by the detector.

In a typical SPR experiment, the substrate is loaded on the chip and the analysis is carried out in four main phases[38], highlighted in the representative sensorgram shown in **Figure 4.6**:

1. Baseline phase: firstly, the baseline buffer is flowed on the surface to establish the baseline.
2. Association phase: a solution (10 mM HBSS in our experiments) of the analyte is flowed on the surface, and if the tested compound interacts with the immobilised substrate a change in refractive index is registered, allowing for measurement of the association kinetics.
3. Dissociation phase: the baseline solution is injected, and the analytes will start dissociating from the immobilised substrate, allowing for evaluation of the dissociation kinetics.
4. Regeneration phase: the regeneration solution is injected to completely remove the bound analytes. After restoring the baseline with the baseline buffer, a new analysis can begin.

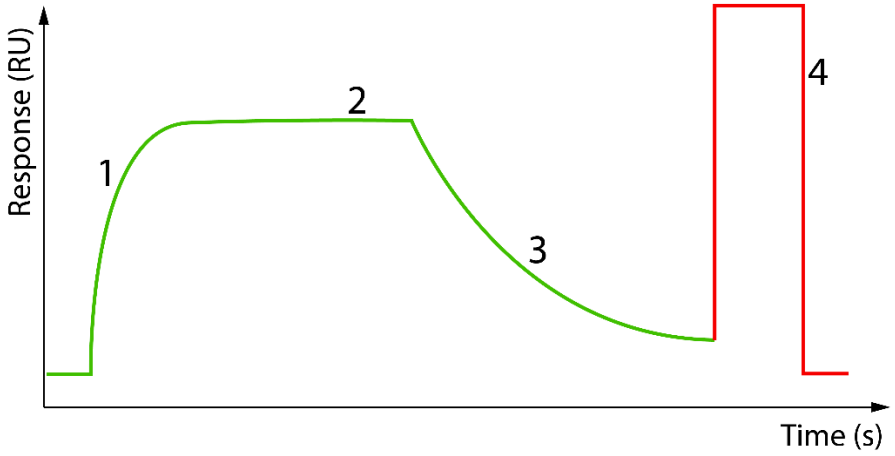


Figure 4.6 Example sensorgram highlighting the main phases in an SPR analysis: 1) baseline, 2) association, 3) dissociation and 4) regeneration.

The sensorgram shape and size (**Figure 4.7**) are dependent on the immobilised substrate and the ligand. When the analyte solution is injected and the analyte is

flowed over the sensor surface, an increase in response is registered due to binding between the immobilised substrate and the ligand. This increase is not linear, and is dependent mainly on the analyte concentration and the association constant between ligand and substrate.

After association of analytes, it is possible to reach a state of equilibrium (steady state), where the response is stable and does not increase with time. This is a dynamic equilibrium, where the dissociation of bound analytes and association of continuously injected analytes are balanced.

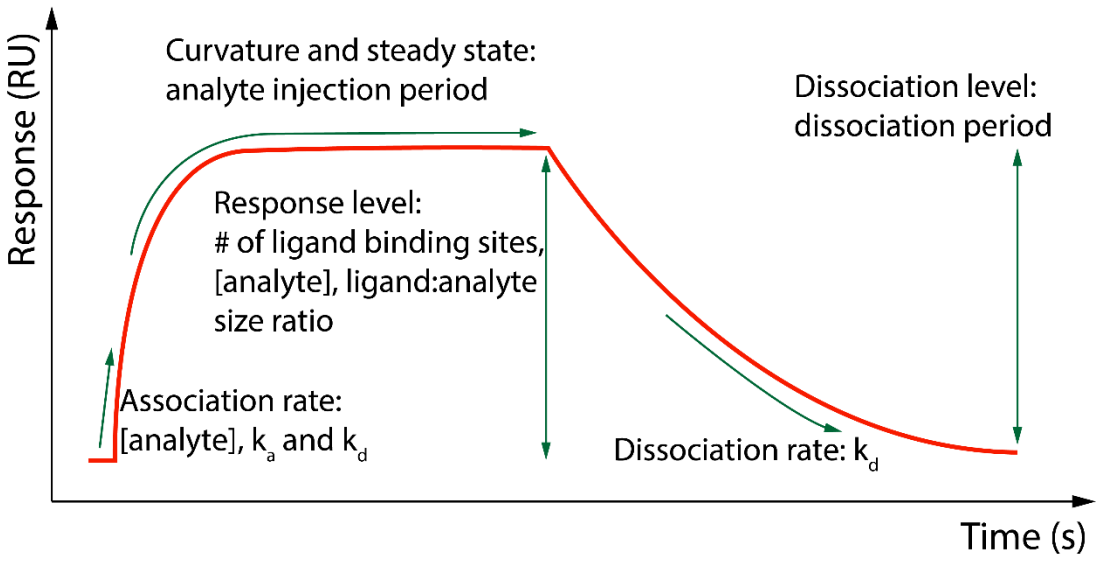


Figure 4.7 Example sensorgram, highlighting the parameters influencing each phase.

If the analyte concentration is sufficient to occupy all binding sites, saturation of the sensor (R_{max}) is reached. The response level is dependent on the availability of binding sites at the surface and on the relative effect that a specific ligand has on the response intensity. This is important to consider when comparing different species, as a single unit of a larger analyte (a longer polymer in our case) will elicit a different response than a smaller analyte (shorter polymer). R_{max} is therefore entirely analyte-dependent, and must be determined experimentally for each single analyte:immobilised substrate system.

The dissociation phase is dependent on the rate constant of dissociation k_d, and the dissociation period is highly dependent on the degree of ligand:substrate interaction. After the dissociation phase, it is possible that the response does not reach baseline levels due to some residual interactions between the ligand and the substrate. Should this happen, the baseline is regenerated by injecting a regeneration solution compatible with the immobilised substrate.

4.3.2.1 In-house assembly of SPR sensor chips

Initially, we aimed at in-house preparation of gold chips onto which we could deposit a lipid bilayer, which would act here as our immobilised substrate during SPR analysis. This approach has been previously employed to deposit a bilayer of phospholipids on a gold surface[11,40] and the uniformity of the resulting bilayer was tested by Atomic Force Microscopy (AFM). For this process a multi-step procedure was followed (**Figure 4.8**):

1. The glass coverslips (0.22 μm diameter, thickness 0.16 - 0.19 mm) were cleaned with Piranha solution[41] to remove any impurities from the surface.
2. A 10 nm layer of Indium-Tin oxide (ITO), employed to increase the surface conductivity[42], was deposited on the cleaned surface, followed by deposition of a 47±5% nm gold thin film[43,44].
3. After deposition of the gold film, liposomes based on phosphatidylcholine and 1,2-dipalmitoyl-sn-glycero-3-phosphothioethanol (DPPTE) (99:1, 9:1 or 8:2 mol:mol) were prepared and added to the gold surfaces. These specific compositions were chosen based on previous literature[11], as DPPTE possesses a thiol in its headgroup. Liposomes with thiolated phospholipids readily interact with gold surfaces to form a phospholipid bilayer[11], due to the rapid gold surface-thiol bond formation[45].
4. AFM in tapping mode was used to verify the formation of a uniform phospholipid bilayer.

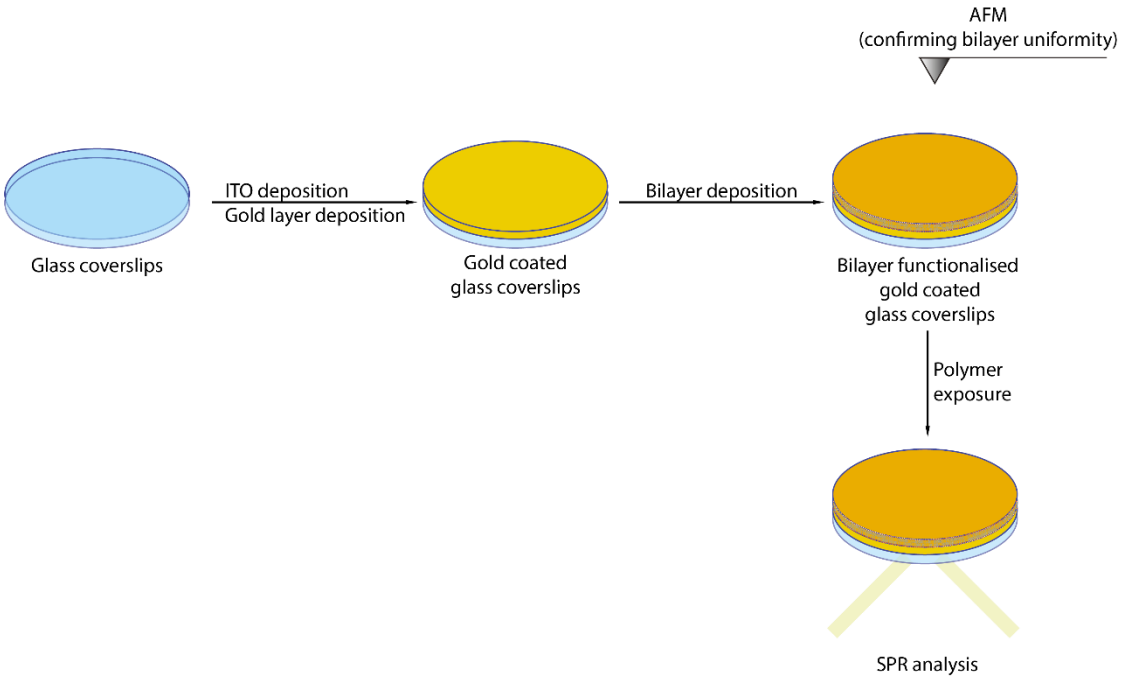


Figure 4.8 Glass coverslips functionalisation procedure to prepare surfaces for SPR. The coverslips were cleaned by Piranha cleaning, then a layer of ITO and a layer of gold were deposited on the glass surface. Afterwards, DPPTE-based liposomes were added to the gold surface, and AFM in tapping mode was used to verify the formation of a uniform phospholipid bilayer.

The cleaning of the coverslips and deposition of indium-tin oxide and gold on the surface was successful in producing a surface with morphological characteristics and coating height (20-25 nm) similar to what described in literature, as confirmed by AFM analysis in peak force tapping mode (**Figure 4.9 A**).

After addition of the liposomal suspension (0.02 or 0.2 mg/mL lipid concentration), the surface was imaged again by AFM in tapping mode, showing an increase in the registered surface height (**Figure 4.9 B**), and suggesting the presence of additional material deposited on the gold.

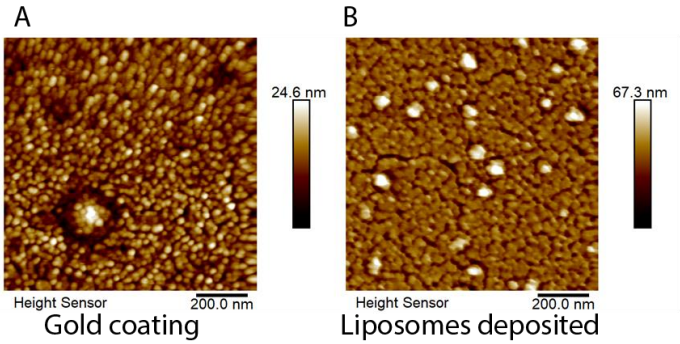


Figure 4.9 AFM images in peak force tapping mode showing the ITO + gold deposition layer (A) and the surface after deposition of liposomes (0.02 mg/mL in 10 mM HBSS, 30 minutes incubation at room temperature) (B).

However, a closer examination of the surface showed a dishomogeneous distribution of the bilayer on the surface (**Figure 4.10**). An additional range of conditions (9:1 PC:DPPTE molar ratio, shorter/longer incubation times, 0.2 mg/mL, 0.1 mM HBSS) were explored, without producing an improvement of the bilayer distribution. Thus, we decided to employ a pre-functionalised commercially available L1 chip

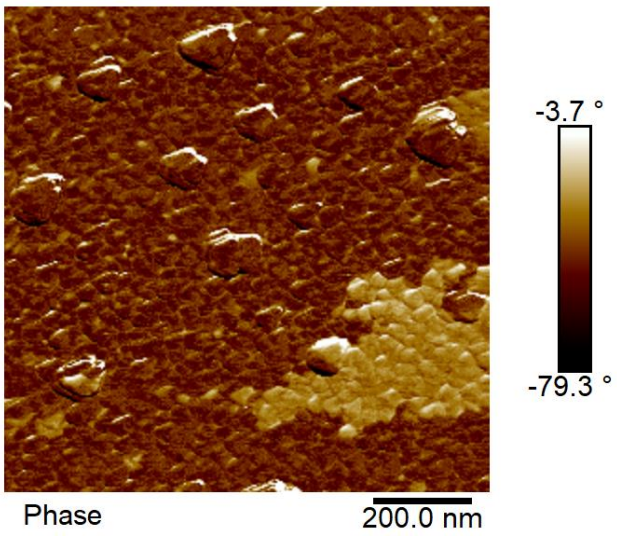


Figure 4.10 AFM image in tapping mode showing a dishomogeneous distribution of lipid bilayers (yellow areas) deposited following incubation of gold surface with liposomes (0. 2 mg/mL in 10 mM HBSS) deposited on the gold surface after 30 minutes incubation at room temperature.

4.3.2.2 Adhesion cholesterol- and DOPE-containing polymers to immobilised lipid bilayers: SPR analysis using a L1 chip.

Previous studies described the use of two commercially available sensor chips, HPA[46,47] and L1[37,48,49], to immobilise phospholipids for SPR analysis model (**Figure 4.11**).

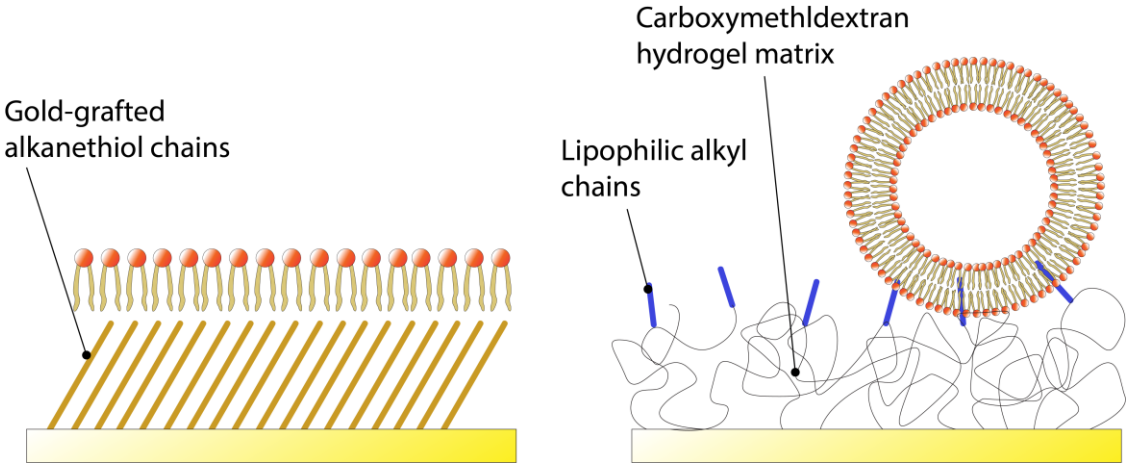


Figure 4.11 Diagrams depicting the two types of SPR sensor chips considered for this study. HPA chip (left) forming a hybrid grafted bilayer with injected phospholipids, and L1 (right) capturing liposomes on its surface.

Both types of sensor chips can be employed to form immobilised membrane models, albeit with different characteristics and structure. The HPA chip consists of a gold surface coated with a flat alkanethiol layer that can provide support for phospholipid deposition. This results in the formation of a hybrid bilayer membrane consisting of a gold-grafted alkanethiol layer coated by a phospholipid monolayer [12] (**Figure 4.11**, left). This approach is no longer widely used, as the hydrophobic chip surface is not easy to work with and detergents used for chip cleaning can be embedded into the grafted monolayer[36]. The L1 sensor chip was developed more recently, and employs lipophilic groups grafted on a carboxymethylated dextran matrix, which is in turn anchored to the gold surface[12]. This chip allows for capture of injected liposomes, which can also fuse into a

supported bilayer that can partially or fully cover the sensor surface[12,47,49] (**Figure 4.12**), based on liposome characteristics such as surface charge and analysis parameters such as flow rate[50].

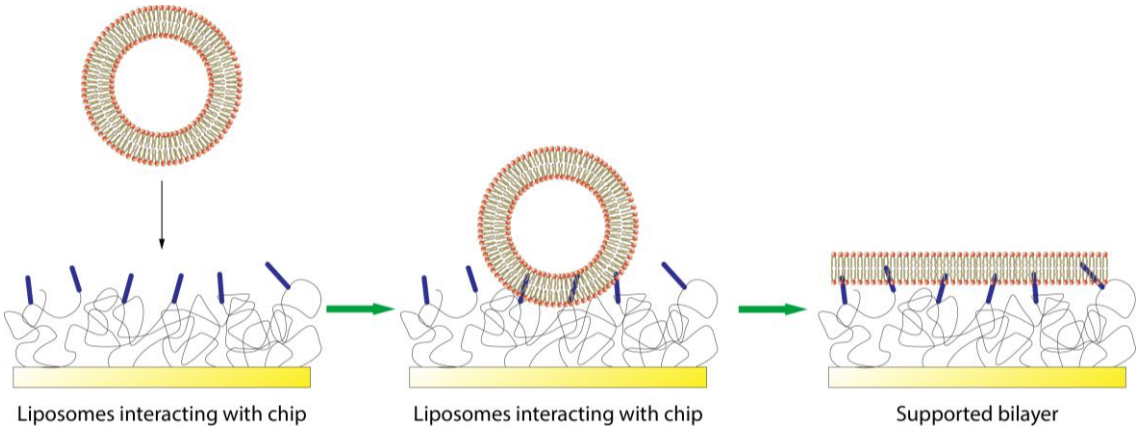


Figure 4.12 Immobilisation of phosholipid lipid bilayer on an SPR L1 sensor chip.

Due to the suitability to capture a wide variety of liposomes without extensive method development and their ability to generate immobilised bilayers, L1 sensor chips were chosen for this part of this study. To deposit the required phospholipid membrane, liposomes were prepared with a composition (DOPC/DSPC/cholesterol 2:1:1 molar ratio) that has been shown to produce phase partitioning between lipid ordered and disordered phases[32]. Liposomes were first extruded through 0.2 µm membrane filter as described in previous studies[47–49] to get a final vesicle size of 214 nm with and low PDI(0.184, **Figure 4.13**).

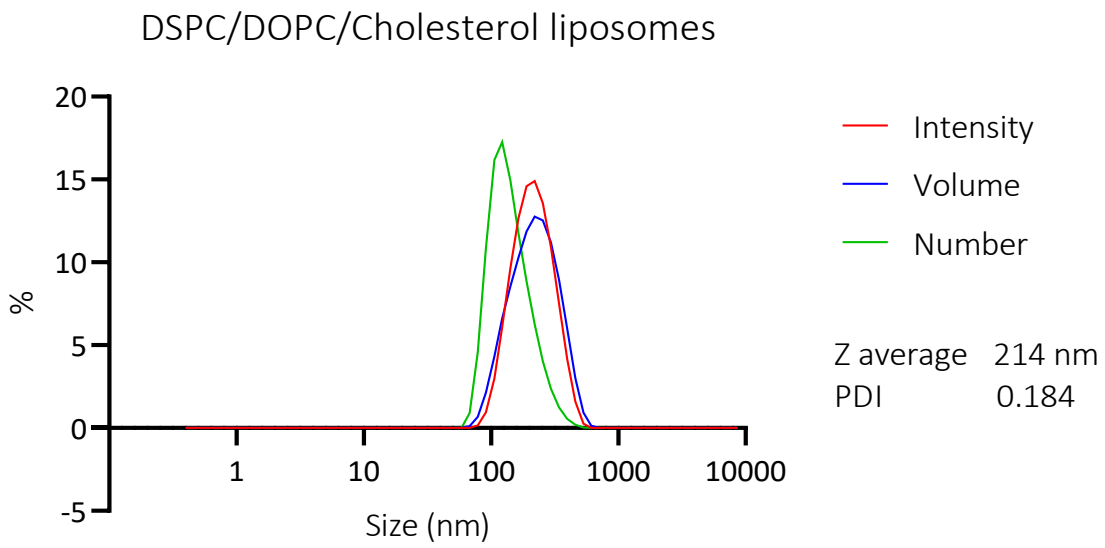


Figure 4.13 Dynamic light scattering (DLS) particle size analysis of liposomes (DOPC/DSPC/cholesterol 2:1:1 mol:mol ratio) employed to form immobilisied bilayers for the SPR studies. Data are shown as intensity, volume and number distributons (%).

The liposome suspension (0.02 mg/mL in 10 mM HBSS) was then injected on the L1 chip at 5 µL/min, until a stable baseline at 5600 RiU was reached. Previous studies by Karlsson[51] *et al.* and Kamimori *et al.*[52] suggest that values around 5000 RiU are indicative of formation of a supported bilayer on the sensor surface[12]. After the baseline was stabilised, polymer suspensions were injected at different concentrations (24 nM to 1.5 nM) to assess the ability of the membrane-inserting polymers with the immobilised phospholipid bilayer.

The sensorgrams for the cholesterol-polyHEA polymers, showed that the shortest polymer (Chol-$[(HEA)_{100\%}]_{13}$) elicited a low response and needed longer injection time to reach saturation, when comparing with longer Chol-polyHEA polymers (**Figure 4.14**). Chol-$[(HEA)_{100\%}]_{13}$ did not cause an increase in membrane fluidity in the previously described Laurdan studies, showing a low level of interaction with bilayers, reflected in the low response registered by SPR. Cell membrane binding studies – Laurdan membrane fluidity and Flow Cytometry - shown in **Chapter 3**, using Caco-2 cells showed that Chol-$[(HEA)_{100\%}]_{58}$, when compared

to the longer Chol-[(HEA)$_{100\%}$]$_{108}$, had the strongest effect in terms of increasing the fluidity of cell membranes and also in the number of polymer chains bound to cell plasma membrane.

In these SPR experiments, Chol-[(HEA)$_{100\%}$]$_{58}$ gave a rapid initial interaction with the immobilised phospholipid bilayer and maintained saturation of the bilayer for the remainder of the injection. Additionally, a very slow dissociation rate was observed, indicating that following insertion of its cholesterol chain-end, Chol-[(HEA)$_{100\%}$]$_{58}$ showed a strong tendency to remain bound to the immobilised bilayer.

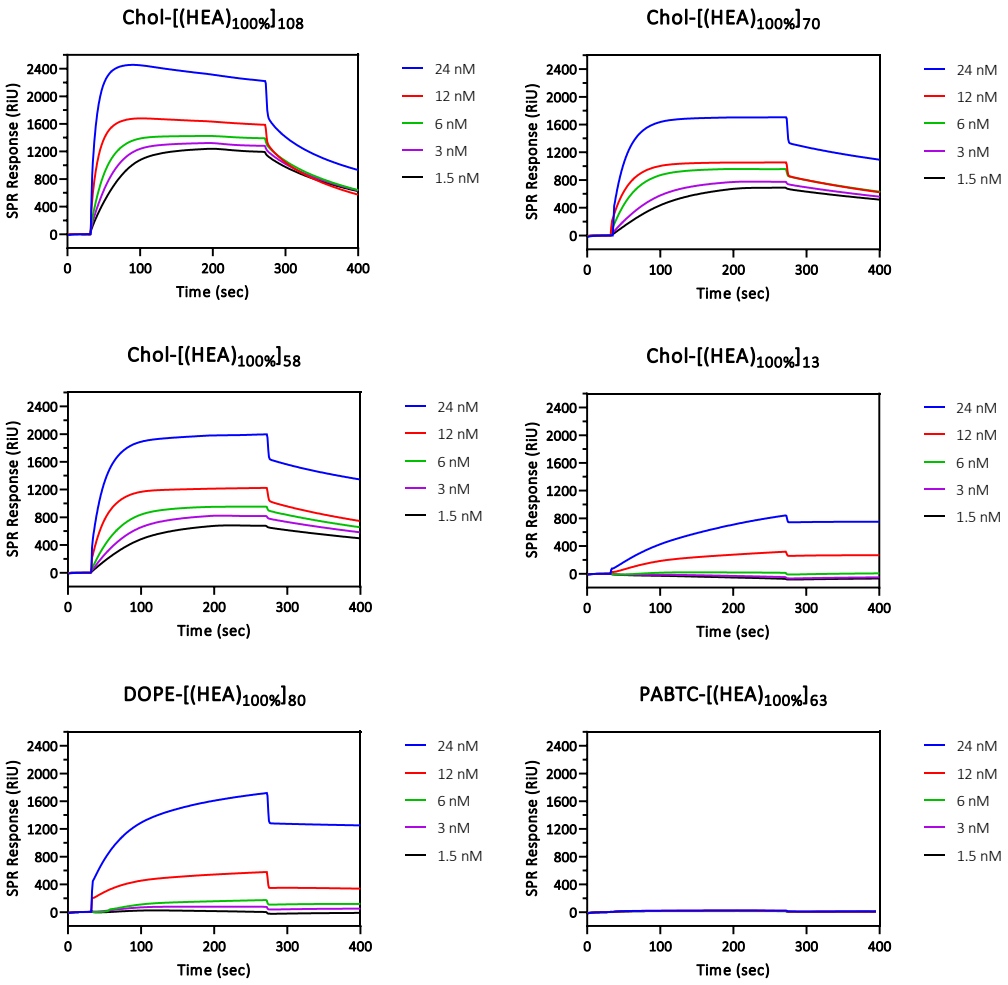


Figure 4.14 SPR sensorgrams for the cholesterol-and DOPE-containing polymers, and control PABTC polymer, using a L1 chip coated with a DOPC/DSPC/cholesterol (2:1:1 mol:mol ratio)bilayer. Results are expressed as SPR response, with higher values indicating the presence of more material deposited on the surface.

The longest polymer, Chol-[(HEA)$_{100\%}$]$_{108}$, showed a higher initial response when compared with the other cholesterol-containing polymers. This is likely due to the size of this polymer, as the SPR response is dependent on the amount of material deposited on the chip surface[38]. In this sensorgram, we also observed a progressive decline in response as soon as the maximum RiU value (R_{max}) was reached; this could have been caused by an initial saturation of the sensor with polymers. However, the hydrophilicity of the polymer was likely responsible for the steady decline of the RiU. The sensorgram for DOPE-[(HEA)$_{100\%}$]$_{80}$ showed similar results to what observed for cholesterol-containing polymers with a similar DP. The control polymer PABTC-[(HEA)$_{100\%}$]$_{63}$ showed no interaction between the polymers and the cell membrane models. This corroborated the results described in **Chapter 3** for interaction with cell bilayer membranes, where PABTC polymers showed little interaction in membrane fluidity studies and Flow Cytometry employing fluorescent PABTC-[(HEA)$_{100\%}$]$_{63}$ showed limited accumulation on cells.

Finally, kinetic and thermodynamic constants (**Table 4.4**) were analysed to derive a structure activity relationship for this sub-family of membrane-inserting polymers. DOPE-[(HEA)$_{100\%}$]$_{80}$ showed a lower k_a for interaction with bilayer membranes when compared with the cholesterol-HEA polymers with a similar chain length. This is in line with what observed previously in cell culture by flow cytometry experiments, where fewer fluorescently tagged DOPE-[(HEA)$_{100\%}$]$_{47}$ molecules interacted with cell membranes. As already discussed, the control polymer PABTC-[(HEA)$_{100\%}$]$_{63}$ did not interact with the immobilised bilayer, so the kinetic parameters could not be calculated. As expected, the comparatively less hydrophilic Chol-[(HEA)$_{100\%}$]$_{13}$ showed a significantly lower k_a when compared with the other cholesterol-HEA based polymers. The other cholesterol-based polymers had similar levels for their dissociation rate constant (k_d), therefore these polymers had a similar tendency to remain associated to the lipid bilayer,

once bound. The dissociation equilibrium thermodynamic constant K_D, which refers to the equilibrium between membrane-associated and dissociated polymers, was likewise very similar between these three cholesterol-containing polymers being all in the sub-nanomolar range for all these materials. This is indicative of a very strong interaction between these polymers and the immobilised DOPC/DSPC/cholesterol (2:1:1 mol:mol ratio) lipid bilayer. The main difference was in the kinetic of association and dissociation rate constants k_a, and K_d, respectively. The longest polymer (Chol-[$(HEA)_{100\%}$]$_{108}$) showed a 4-fold kinetic association constant k_a value when compared with the two shorter polymers. However, a significantly higher dissociation rate constant (k_d) was also observed for Chol-[$(HEA)_{100\%}$]$_{108}$ with the bilayer, which means it detached from the bilayer at a faster rate than other cholesterol-HEA based polymers. This translated in a lower equilibrium constant K_D, which confirmed that fewer Chol-[$(HEA)_{100\%}$]$_{108}$ are present on the bilayer at the equilibrium when compared with shorter cholesterol polymers. The K_D values for Chol-[$(HEA)_{100\%}$]$_{13}$ confirmed that there was comparatively little material deposited on the surface, explaining the lack of membrane fluidity changes observed in **Chapter 3** when this polymer was added administered to Caco-2 cells.

Table 4.4 Kinetic parameters obtained from SPR analysis for the interaction between the tested polymers and L1-immobilised bilayers.

Polymer	**k_a (M^{-1} s^{-1})[a]**	**k_d (s^{-1})[b]**	**K_D (M)[c]**	**R_{max} (RiU)[d]**
Chol-[$(HEA)_{100\%}$]$_{13}$	1.96×10^{3}	2.44×10^{-4}	1.24×10^{-7}	843
Chol-[$(HEA)_{100\%}$]$_{58}$	3.71×10^{6}	3.16×10^{-3}	8.50×10^{-10}	1996
Chol-[$(HEA)_{100\%}$]$_{70}$	3.51×10^{6}	3.12×10^{-3}	8.88×10^{-10}	1706
Chol-[$(HEA)_{100\%}$]$_{108}$	1.64×10^{7}	5.33×10^{-3}	3.26×10^{-10}	2456
DOPE-[$(HEA)_{100\%}$]$_{80}$	2.19×10^{3}	3.31×10^{-5}	1.51×10^{-8}	1718
PABTC-[$(HEA)_{100\%}$]$_{63}$	-	-	-	-

[a] association rate constant, [b] dissociation rate constant, [c] equilibrium dissociation constant and [d] maximum response.

DOPE-[(HEA)$_{100\%}$]$_{80}$ showed a lower K_D than comparable cholesterol polymers (Chol-[(HEA)$_{100\%}$]$_{58}$ and Chol-[(HEA)$_{100\%}$]$_{70}$), confirming that the lower effect on cell membrane fluidity described in **Chapter 3** was potentially due to less polymer being deposited on the cell membranes.

The SPR results have therefore confirmed that the cholesterol- and DOPE-containing polymers were directly interacting with membranes, while the control polymer PABTC-[(HEA)$_{100\%}$]$_{63}$ did not. Additionally, these experiments confirmed that the DOPE-based polymers have lower ka and K_D for membrane interaction when compared with the cholesterol counterparts. Finally, kinetic and thermodynamic results for the cholesterol polymers interacting with the bilayer showed that, although Chol-[(HEA)$_{100\%}$]$_{108}$ interacted at a faster rate than shorter polymers (DP 70 and 58), less material was present at the equilibrium. This confirmed the results reported in **Chapter 3**, where we observed the maximum amount of cell membrane interaction for DP 50 cholesterol polymers.

4.3.3 Solid-state NMR (SSNMR)

Next, the interaction between model lipid bilayers and the polymers synthesised in this work to was investigated by solid-state NMR (SSNMR) which is a non-destructive and non-intrusive technique[53,54] that can be used to investigate membrane dynamics[55,56]. SSNMR is a technique employed for analysis of solid and semisolid samples loaded in a rotor rapidly spinning[57,58] at the specific angle of 54° 44′ ("magic angle") respectively to the applied magnetic field[59]. This allows to overcome the issues encountered when analysing by NMR solid and semisolid samples, namely compensating for the low mobility of nuclei when compared with liquid samples[60].

4.3.3.1 ^{31}P NMR of polymers and DMPC multilamellar vesicles

The interaction between the previously described polymers and model lipid bilayer membranes was initially investigated by wideline ^{31}P SSNMR, which can reveal perturbations in model membranes caused by membrane-inserting (macro)molecules[55,61]. ^{31}P SSNMR is particularly suited to investigate changes in phase behaviour (liquid ordered, liquid disordered, membrane shedding) of phospholipid species when interacting with membrane-binding species[55]. First, the polymers were solubilised in the minimum amount of deionised water, which was then added to solid DMPC (DMPC:polymer 10:1 mol:mol ratio) to produce multilamellar vesicles (MLVs) by mechanical stirring and repeated freeze-thaw cycles. The rotor spinning causes fast axial rotation of the lipid molecules in the MLVs, forming the large chemical shift anisotropy shown in **Figure 4.15**[62]. Any perturbation in the membrane model would cause the appearance of secondary peaks (caused by shedding of smaller vesicles from the MLVs, rotating at different speeds) or a change in the shape of the large peak (caused by modification of the MLVs by membrane-interacting species).

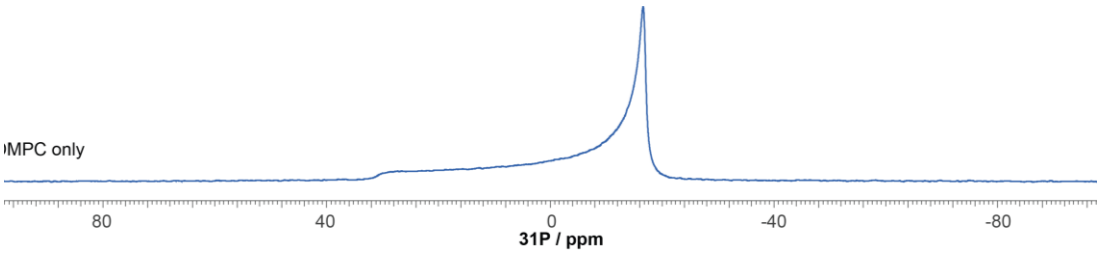


Figure 4.15 ^{31}P SSNMR spectrum of 1,2-dimyristoyl-sn-glycero-3-phosphocholine (DMPC) MLVs.

For this set experiments we employed a model membrane made from 1,2-dimyristoyl-sn-glycero-3-phosphocholine (DMPC), a synthetic phospholipid often included in liposomes and lipid bilayers as a simple model for biological membranes with SSNMR[55,56,61,63]. **Figure 4.16** shows different wideline spectra obtained by MAS ^{31}P NMR of DMPC multilamellar vesicles (MLV) after incubation with a polymer from each class of materials produced (Chol-[(HEA)$_{100\%}$]$_{52}$, DOPE-[(HEA)$_{100\%}$]$_{47}$, PABTC-[(HEA)$_{100\%}$]$_{50}$). These polymers were chosen here because they have a very similar number of HEA repeating units, but different membrane-inserting, or control, chain-ends. When compared to the spectrum of untreated DMPC MLV (**Figure 4.16 D**), the membrane-interacting polymers showed an additional isotropic peak around 0 ppm (**Figure 4.16 A, B**). This additional signal indicated the presence of non-bilayer structures, in the form of smaller and faster tumbling DMPC aggregates shed from the "main" bilayer structure. This suggested that membrane-interacting polymers at this concentration can disrupt DMPC bilayers to form smaller, secondary DMPC aggregates that tumble more quickly in the rotor. This is in line with what is shown in recent literature, where embedding of membrane-interacting species in a DMPC model membrane decreased the stability of bilayers and resulted in membrane shedding, as confirmed by SSNMR.[56]

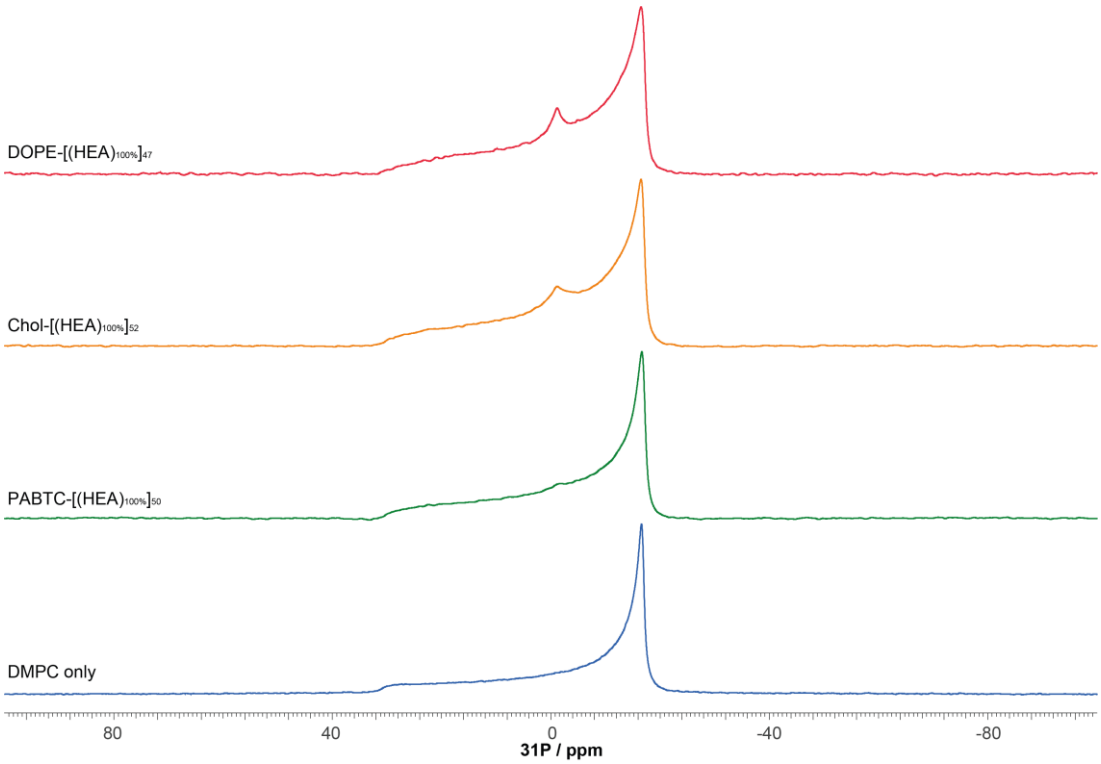


Figure 4.16 ^{31}P MAS wideline spectra of DMPC MLVs treated with polymers. A) DOPE-$[(HEA)_{100\%}]_{47}$B) Chol-$[(HEA)_{100\%}]_{52}$; C) PABTC-$[(HEA)_{100\%}]_{50}$; D) DMPC MLVs. The additional isotropic peak around 0 ppm indicates presence of non-bilayer structures, therefore that the polymer interaction with the bilayer is causing intrinsic instability and membrane shedding.

4.3.3.2 Solid-state NMR to confirm presence of polymers within model DMPC:cholesterol bilayer membranes

The initial results with ^{31}P NMR showed an interaction between the membrane-binding polymers and a simple DMPC model membrane. Therefore, we decided to investigate by employing a more relevant membrane model (DMPC:cholesterol 1:1 mol:mol ratio) and with techniques suitable for a more thorough investigation of polymer:bilayer interactions.

The two common methods for creating observable magnetisation in high resolution ^{13}C solid state NMR under magic angle spinning (MAS) are direct excitation and cross polarisation (CP). An exemplification of their pulse sequences is shown in **Figure 4.17**. Direct excitation relies on a single 90° pulse at the carbon Larmor frequency on the carbon channel to generate polarisation, followed by acquiring the signal under ^{1}H decoupling[64]. Cross polarisation, on the other hand, relies on polarisation transfer from neighbouring protons. In CP, nuclei with high gyromagnetic ratios such as ^{1}H, are polarised first, before the polarisation is transferred via Hartmann-Hahn condition by strong dipolar coupling to bounded weaker nuclei[65,66]. This results in an enhancement of ^{13}C signal, reflecting the higher proton polarisation (of up to 4-fold). In addition, the ^{13}C signal of CP is further improved compared to direct excitation as ^{13}C in CP have shorter proton T_1 instead of the longer ^{13}C T_1, leading to a reduction in interpulse delays and thus experimental time.

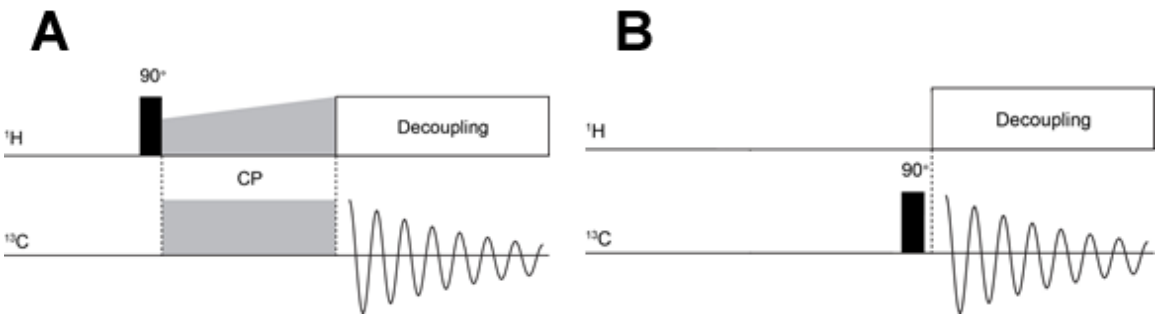


Figure 4.17 Solid state NMR pulse sequence of (**A**) cross polarisation and (**B**) direct excitation.

CP is particularly useful in membrane studies, as it can act as a motion filter to probe molecules interaction with membrane. The polarisation transfer from ^{1}H to ^{13}C relies on dipolar coupling. Dipolar coupling is an anisotropic interaction that is averaged to zero in molecular systems with fast molecular motions, for example in solution. This property of CP can be utilised to probe interactions of soluble membrane-active compounds with the membrane[67], as only molecules in a rigid system, in our case only polymers interacting with the DMPC:cholesterol MLVs can be detected in CP.

Direct excitation ^{13}C MAS NMR spectra of polymer mixed with lipid bilayer.

To first observe all components in the DMPC:cholesterol:polymer mixture, spectra were recorded by polarisation of ^{13}C nuclei via a direct 90° pulse, thus all ^{13}C nuclei in the system could be observable. **Figure 4.18** show the ^{13}C direct excitation NMR spectra of MLVs containing DMPC alone, DMPC:cholesterol 1:1

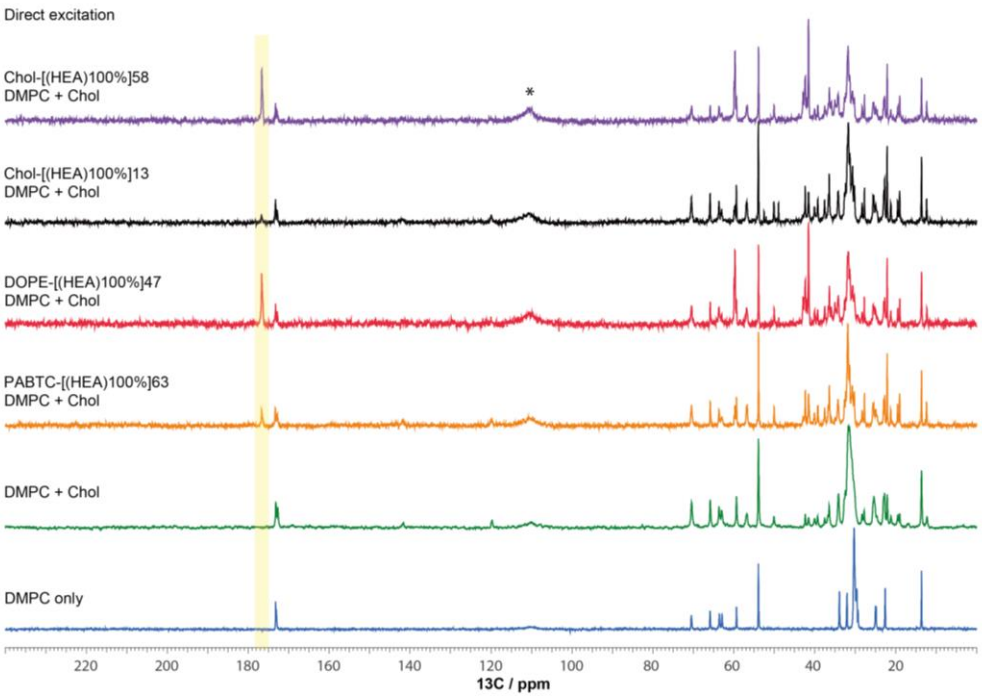


Figure 4. 18 ^{13}C MAS NMR spectra with direct excitation of (blue) DMPC lipid bilayer, (green) DMPC with cholesterol (1:1 mol:mol ratio), (orange) PABTC-$[(HEA)_{100\%}]_{63}$, (red) DOPE-$[(HEA)_{100\%}]_{47}$, (black) Chol-$[(HEA)_{100\%}]_{13}$ and (purple) Chol-$[(HEA)_{100\%}]_{58}$ prepared with DMPC and cholesterol membrane. The polymer:DMPC:cholesterol molar ratio is roughly 1:10:10. The (*) indicates a broad artefact signal from NMR rotor. Yellow panel highlights resonances from polymer that is absent in lipid-only samples.

mol:mol, and DMPC:cholesterol:polymer 1:1:0.1 mol:mol, recorded under MAS. The broad artefact signal at around 110 ppm (labelled with *) is typical in these experiments and is due to Teflon in the NMR rotor. The cholesterol resonances could be clearly observed in comparison to DMPC alone in the 60-20 ppm region.

The polymers selected for this part of the study were: a control polymer PABTC-[(HEA)$_{100\%}$]$_{63}$, DOPE-[(HEA)$_{100\%}$]$_{47}$, as well as two polymers with cholesterol chain-end - the Chol-[(HEA)$_{100\%}$]$_{13}$ and Chol-[(HEA)$_{100\%}$]$_{58}$. The addition of polymer introduced additional resonances. In particular, a peak around 176 ppm (corresponding to carbonyl groups of the polymers), highlighted in yellow in **Figure 4.18**, and 60 ppm (corresponding to CH_2OH in the HEA monomer), highlighted in yellow in **Figure 4.20**. Other minor polymer resonances shown in **Figure 4.20** included peaks around 43 ppm, 36 ppm and 35 ppm (**Figure 4.19**). Additional polymer contribution from different samples could be observed, and they were resulting from the differences in polymer headgroups.

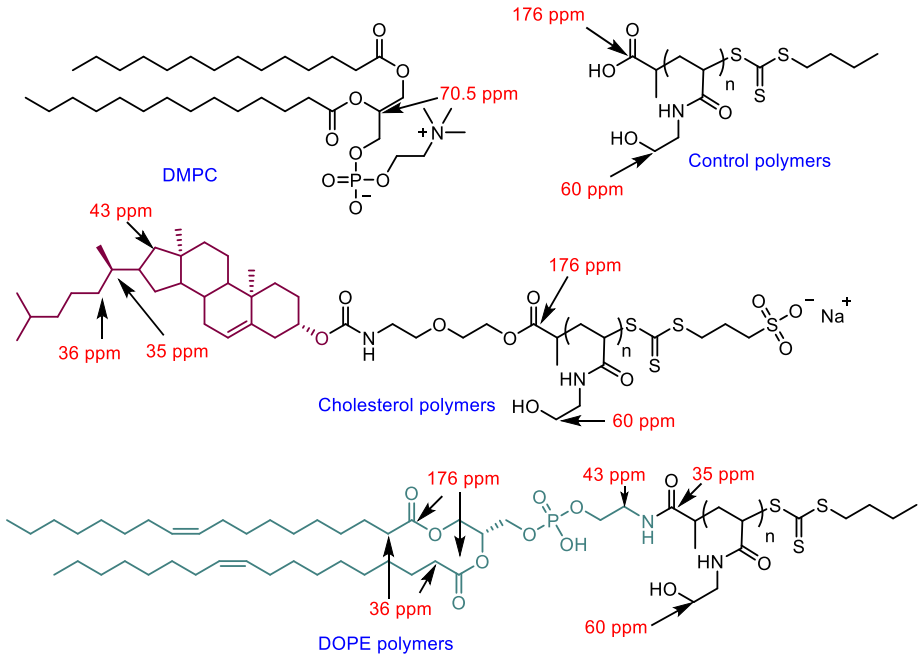


Figure 4.19 Assignments for the key peaks observed by SSNMR for the analysed HEA homopolymers and for DMPC.

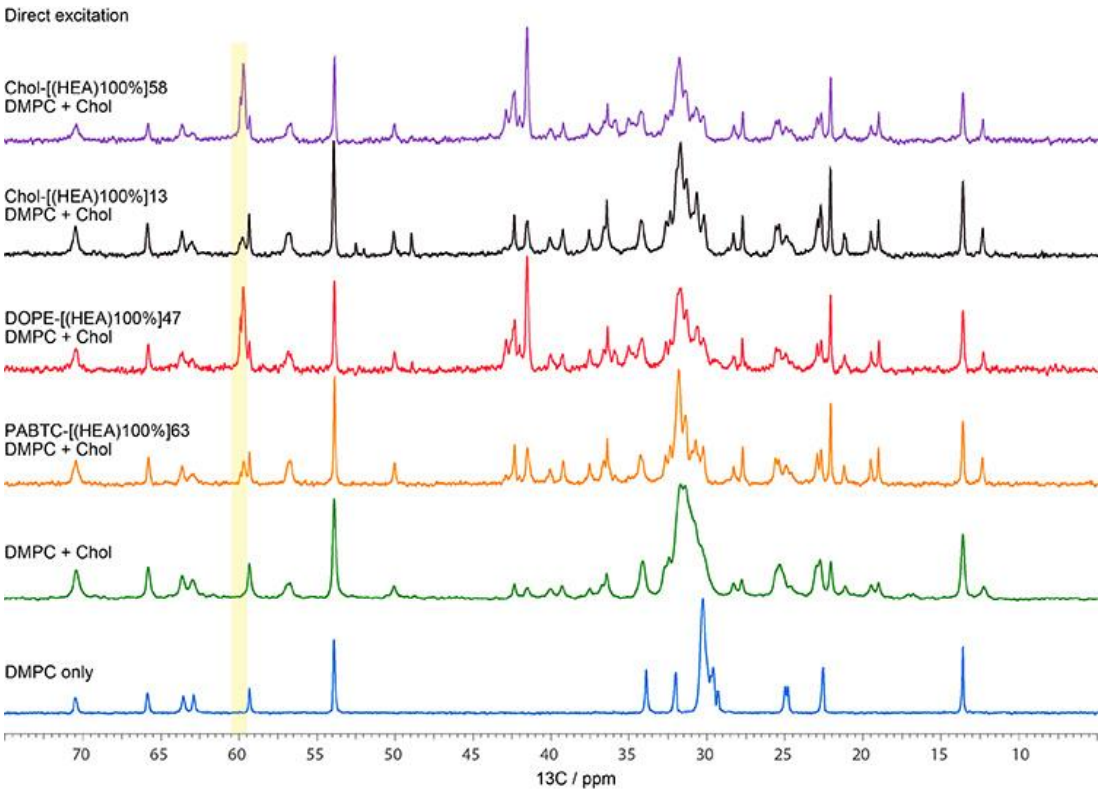


Figure 4.20 ^{13}C MAS NMR spectra, zoomed in between 5 to 75 ppm, with direct excitation of (blue) DMPC lipid bilayer, (green) DMPC with cholesterol (1:1 ratio mol:mol), (orange) PABTC-$[(HEA)_{100\%}]_{63}$, (red) DOPE-$[(HEA)_{100\%}]_{47}$, (black) Chol-$[(HEA)_{100\%}]_{13}$ and (purple) Chol-$[(HEA)_{100\%}]_{58}$ prepared with DMPC and cholesterol membrane. Yellow panel highlights resonances from polymer that is absent in lipid only samples.

Cross polarisation ^{13}C MAS NMR spectra of polymer mixed with lipid bilayer. Unlike direct excitation, where all ^{13}C nuclei are polarised and provide signal, cross polarisation relies on the polarisation of the proton population. The polarisation is then transferred to nearby ^{13}C nuclei by Hartmann-Hahn condition, and the polarisation is transferred via dipolar coupling to relatively immobile nuclei only. Therefore, CP not only enhances resolution of ^{13}C spectra, but also behaves as a motion filter to membrane active soluble compounds[53,65,67].

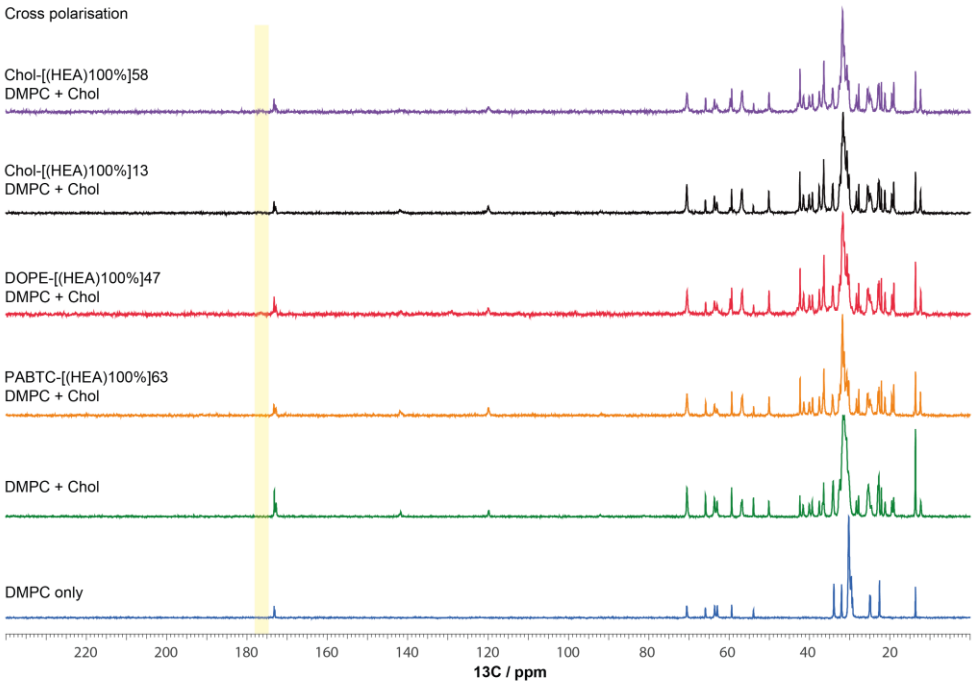


Figure 4.21 ^{13}C CP MAS NMR of (blue) DMPC lipid bilayer, (green) DMPC with cholesterol (1:1 mol:mol ratio), (orange) PABTC-$[(HEA)_{100\%}]_{63}$, (red) DOPE-$[(HEA)_{100\%}]_{47}$, (black) Chol-$[(HEA)_{100\%}]_{13}$ and (purple) Chol-$[(HEA)_{100\%}]_{58}$ prepared with DMPC and cholesterol membrane. Yellow panel highlights resonances from polymer that was identified in direct excitation experiment shown in **Figure 4.18**.

The lipid resonances belonging to DMPC and cholesterol were clearly observed in CP spectra. All resonances were observed, with some resonances displaying changes in relative intensity due to differences in CP transfer efficiencies. On the other hand, as shown in **Figure 4.21**, the polymer resonance at 176 ppm from all polymer samples observed in direct excitation was absent in the cross polarisation, due to the fact the carbonyl carbon does not have a directly bonded proton for polarisation transfer. The polymer contribution at 60 ppm, previously shown in **Figure 4.20**, could be observed for DOPE-$[(HEA)_{100\%}]_{47}$, and both Chol-$[(HEA)_{100\%}]_{13}$ and Chol-$[(HEA)_{100\%}]_{58}$. As the peak at 60 ppm (belonging to CH_2OH from the polymerised HEA) was absent in the DMPC only and DMPC/cholesterol sample, the presence of the 60 ppm signal in the polymer/lipid sample in CP spectra could be interpreted as polymer being immobilised within the membrane.

This peak was not observed in the control PABTC-[(HEA)$_{100\%}$]$_{63}$ polymer. As this signal was detectable via direct excitation in all polymer/lipid sample in **Figure 4.20**, we confirmed the presence of polymer in the sample, including the butyl polymer; the lack of 60 ppm peak in **Figure 4.22** for PABTC-[(HEA)$_{100\%}$]$_{63}$ suggested that polymers with butyl trithiocarbonate chain-end behaved differently to those with DOPE or cholesterol headgroups, not embedding within the MLVs.

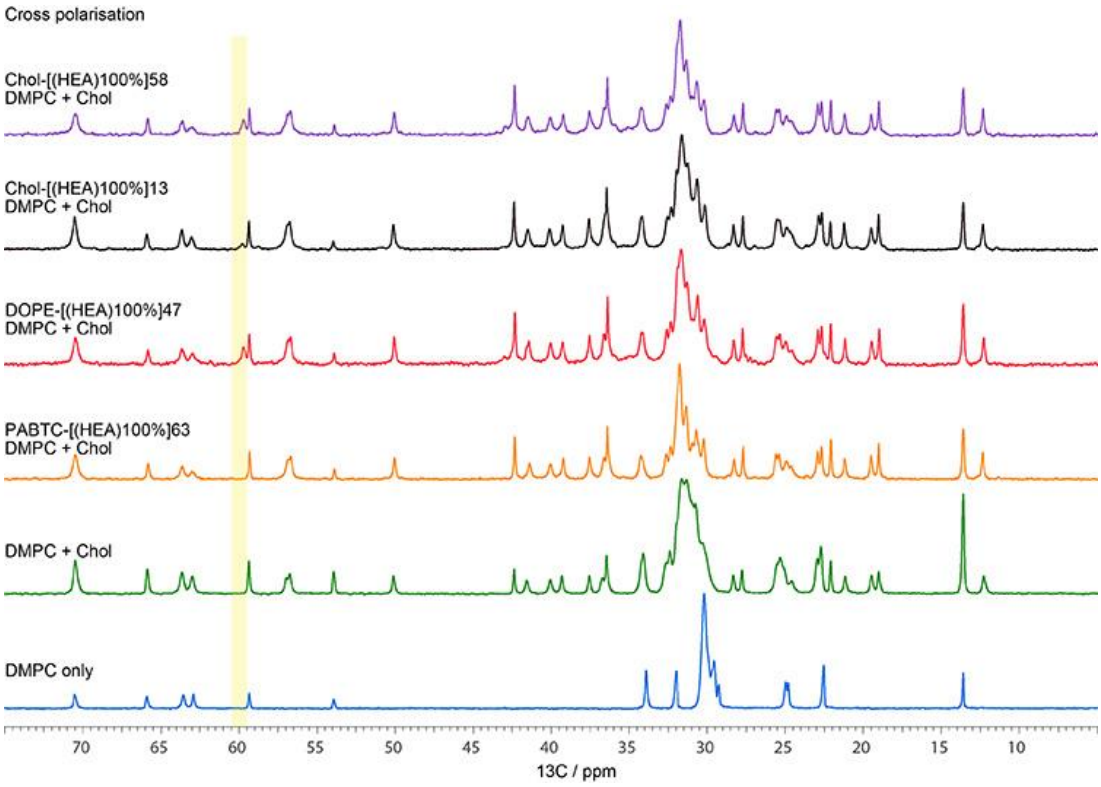


Figure 4.22 ^{13}C CP MAS NMR of (blue) DMPC lipid bilayer, (green) DMPC with cholesterol (1:1 mol:mol ratio), (orange) PABTC-[(HEA)$_{100\%}$]$_{63}$, (red) DOPE-[(HEA)$_{100\%}$]$_{47}$, (black) Chol-[(HEA)$_{100\%}$]$_{13}$ and (purple) Chol-[(HEA)$_{100\%}$]$_{58}$ prepared with DMPC and cholesterol membrane. Yellow panel highlights resonances from polymer that was identified in direct excitation experiment shown in **Figure 4.18**.

Figure 4.23 shows the overlay spectra of direct excitation (**Figure 4.20**) compared with CP spectra (**Figure 4.22**). The dotted lines represent spectra obtained from direct excitation. The spectra were normalised to the resonance intensity at 70.5 ppm, which corresponds to the glycerol CH on DMPC. The overlay of spectra clearly indicated the absence of 60 ppm polymer signal in the CP spectra for MLV samples and for PABTC-[(HEA)$_{100\%}$]$_{63}$. An additional polymer peak could

be detected around 43 ppm, which was present in all polymer with lipid samples except for the control polymer.

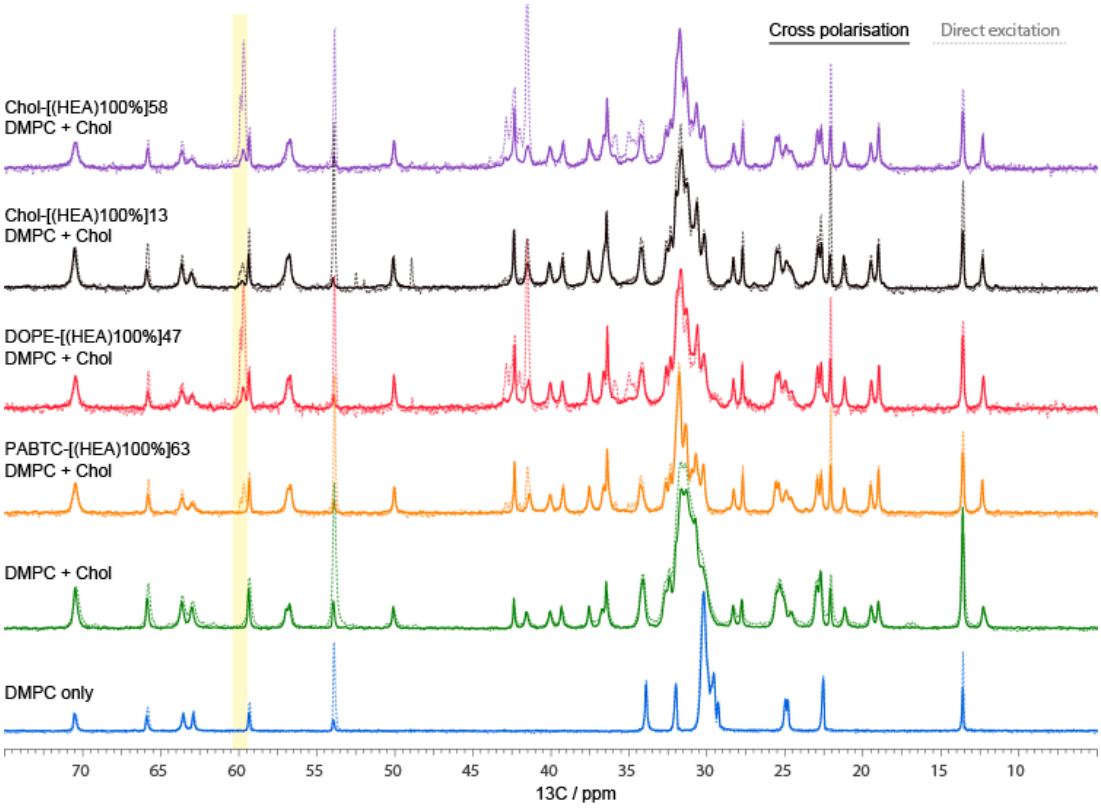


Figure 4.23 ^{13}C MAS NMR of (blue) DMPC lipid bilayer, (green) DMPC with cholesterol (2-to-1 ratio), ((orange) PABTC-$[(HEA)_{100\%}]_{63}$, (red) DOPE-$[(HEA)_{100\%}]_{47}$, (black) Chol-$[(HEA)_{100\%}]_{13}$ and (purple) Chol-$[(HEA)_{100\%}]_{58}$ prepared with DMPC and cholesterol membrane, comparing CP and direct excitation. Solid lines are spectra performed with cross polarisation, and dotted lines are spectra performed with direct excitation. The spectra intensities are normalised to the peak at 70.5 ppm, corresponding to the glycerol CH resonance of DMPC.

The results suggested that DOPE-$[(HEA)_{100\%}]_{47}$ and both Chol-$[(HEA)_{100\%}]_{13}$ and Chol-$[(HEA)_{100\%}]_{58}$ polymers have intercalated into a model DMPC/cholesterol membrane. Conversely, control polymer PABTC-$[(HEA)_{100\%}]_{63}$, did not show membrane interaction, as no immobilised polymer resonances were observed in the CP spectrum.

These results corroborated the evidence we previously showed (**Chapter 3** and **4.3.2**) for the model of interaction between the membrane-intercalating polymers and cells/model membranes. We demonstrated through direct observation of the model membrane NMR spectra that the cholesterol and DOPE-based polymers

were embedded into DMPC/cholesterol membranes, while the control PABTC polymer was not interacting.

4.3.4 Molecular Modelling

After confirmation of embedding of membrane-binding polymers within a model bilayer membrane, molecular modelling experiments were conducted to simulate the interactions between a simple bilayer membrane model (DPPC) and two model Cholesterol-based HEA homopolymers (Chol-$[(HEA)_{100\%}]_{58}$ and Chol-$[(HEA)_{100\%}]_{120}$). These computational simulations focused first on the production of coarse grained (CG) models for these polymers. This step was necessary, as large molecules need a degree of simplification to run complex simulations. Then, a model membrane bilayer based on DPPC was simulated. Finally, the simulated polymers and the membrane were employed to produce a model for the fluidification of bilayer membranes caused by the amphiphilic polymers.

4.3.4.1 Development of a coarse-grained model for Chol-$[(HEA)]_n$

The 100 ns trajectory of atomistic Chol-$[(HEA)]_{10}$ in water (see methods) was converted to an equivalent coarse-grained trajectory using the bead mappings shown in **Figure 4.24** the CG beads being placed at the centre of mass of the appropriate atoms. CG bond length, angle, and dihedral distributions were

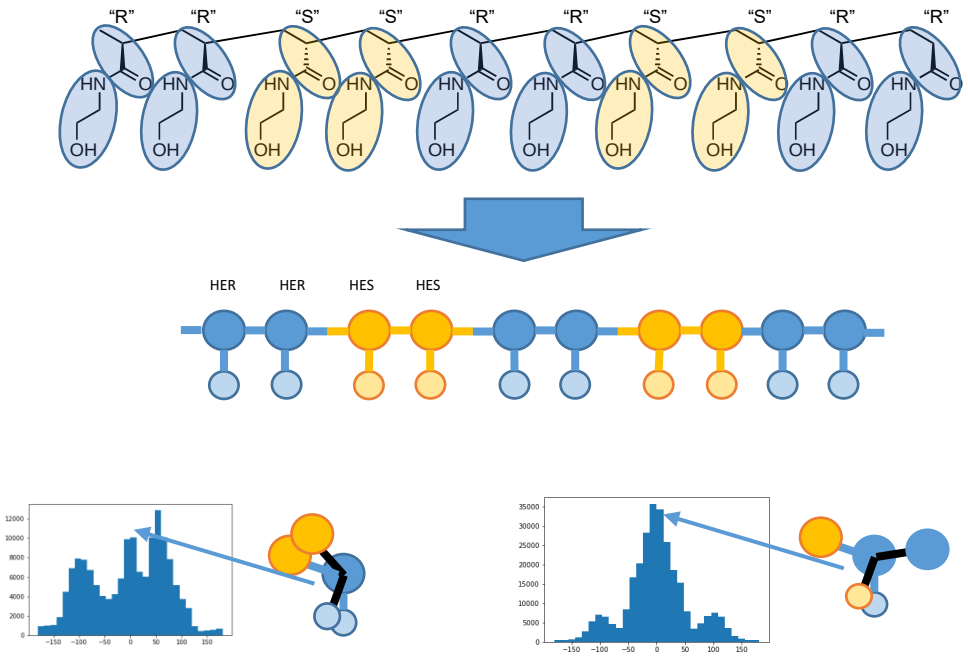


Figure 4.24 Coarse graining scheme for $[(HEA)]_n$ and details of polymer backbone dihedral distributions inferred from atomistic simulations

analysed to obtain the required parameters. We noticed that the P2-P1-P1-P2 dihedral angle distributions differ significantly according to whether the two HEA monomers have the same or opposite chirality (**Figure 4.24**). We attribute this to favourable hydrogen-bonding interactions between the sidechains in successive monomer units which are promoted when these units have opposing chirality because this permits a staggered backbone conformation; in contrast they are inhibited if the units have the same chirality as in this case it would require an eclipsed backbone conformation (**Figure 4.24**). In the CG model these torsion angle terms were modelled using tabulated potentials, while all other bonded parameters could be introduced in standard harmonic form.

In simulations of CG $[(HEA)]_{58}$ in water (see experimental section) the polymer shows "molten globule" behaviour, remaining relatively compact yet dynamic. The root square mean deviation (RMSD) from the initial structure shows a continuous increase, while the radius of gyration remains fairly constant at about 1.2 nm, with occasional peaks due to short-lived partial unfolding events. Compared to the initial structure, the mean distance matrix (i.e., mean of the distance matrices for each snapshot) shows little long-range order (**Figure 4.25**).

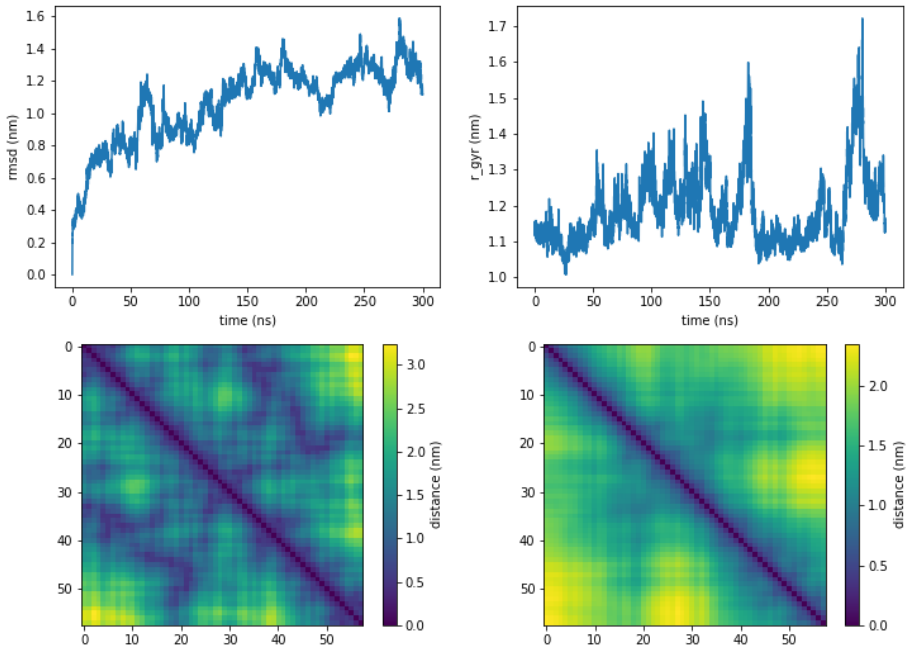


Figure 4.25 Analysis of 300 ns CG simulations of atactic $[(HEA)]_{58}$ in water. Top left: RMSD from initial structure; top right: radius of gyration; bottom left: distance matrix for initial structure; bottom right: mean distance matrix.

4.3.4.2 Atomistic simulations of Chol-$[(HEA)]_{50}$ and a DPPC bilayer

Throughout the 500ns production phase of the simulation (see experimental section for details) the cholesterol moiety remains firmly embedded in the lipid bilayer, while the -$[(HEA)]_{50}$ chain retains a relatively compact globular conformation above the lipid surface (**Figure 4.26**), in agreement with the observations from the CG simulations of $[(HEA)]_{58}$ (above). The system is quite fluid however, the orientation of the cholesterol in the bilayer is quite variable, and at times the linker moiety and first few HEA units bury significantly into the bilayer surface (**Figure 4.26**). The disruption to the lipid packing that results from this was evaluated by calculating the lipid deuterium order parameters (SCD_xy) along the lipid tails, separating the lipids into first the 20 closest to the embedded cholesterol group, then the next 30 closest, and finally all the rest.

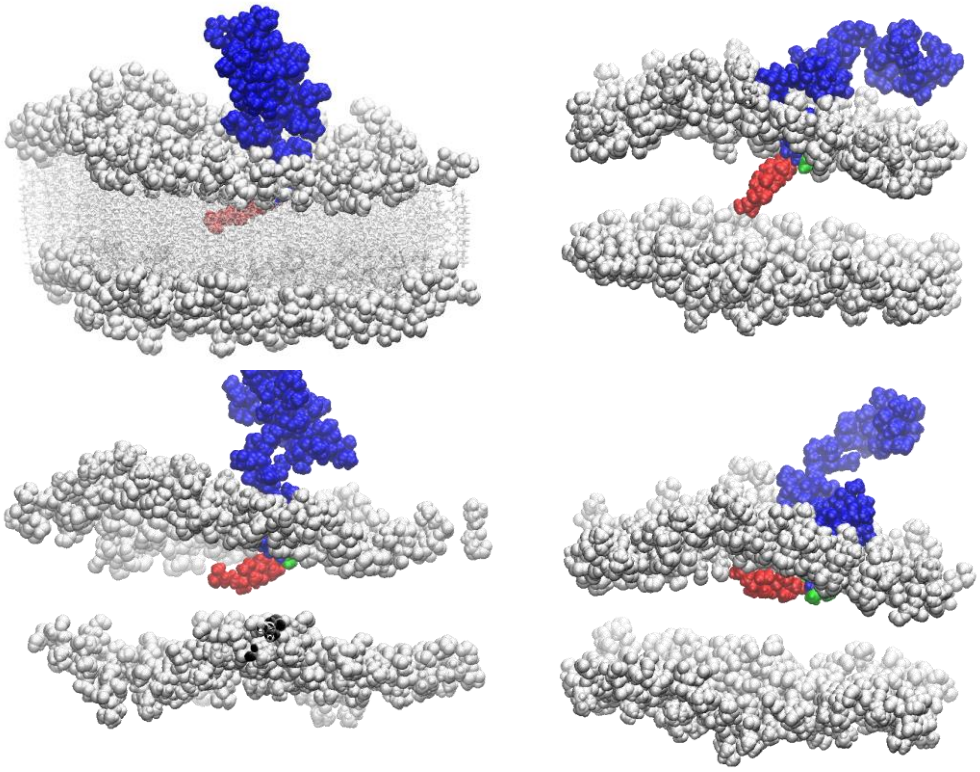


Figure 4.26 Snapshots from the 500 ns atomistic simulation of Chol-$[(HEA)]_{50}$ in a DPPC bilayer. Blue: HEA, red: cholesterol: green: linker; grey: lipid with head groups shown space-filling and tails (left panel only) as rods.

The same analysis was performed for the control simulation, featuring a single cholesterol molecule within the DPPC bilayer. The results show (**Figure 4.27**) that on average those lipid chains closest to the cholesterol anchor in the Chol-$[(HEA)]_{50}$ system are significantly less ordered than those further away, and that this effect is not seen for the control system (if anything, the cholesterol molecule alone seems to increase lipid order, particularly towards the centre of the bilayer).

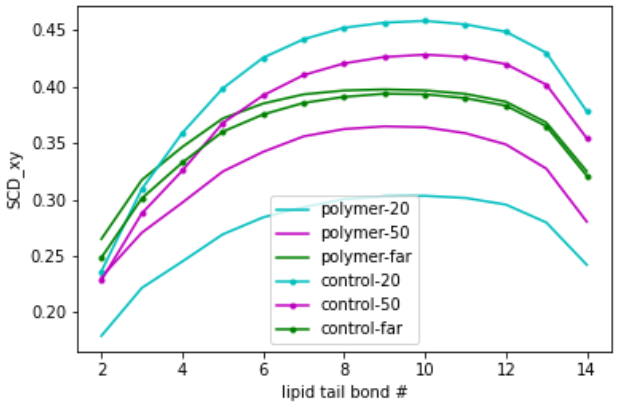


Figure 4.27 Deuterium order parameters calculated along lipid chains within radial shells a) within 2 nm, b) between 2 and 5 nm, and c) beyond 5 nm of the embedded cholesterol group. Data for control simulations (embedded cholesterol, no polymer) is also shown.

4.3.4.3 Martini CG simulations of Chol-[(HEA)]$_{58}$ and Chol-[(HEA)]$_{120}$ in a plasma membrane.

The CG simulations of sixteen independent Chol-[(HEA)]$_n$ polymers absorbed onto a patch of plasma membrane show, individually, behaviour that is fully consistent with the atomistic simulations. The cholesterol moieties remain firmly embedded within the bilayer, and the HEA "tails" retain their molten globule characteristics, appearing to be neither strongly attracted to, or repulsed from, the membrane surface. There are however significant attractive interactions between HEA chains, so that the anchored polymers diffuse across the membrane surface from their initial positions to form aggregates (**Figure 4.28**). Polymer-polymer radial distribution functions show a clear nearest-neighbour peak at 2.1 nm for the 58mer, and 3.2 nm for the 120-mer. In the case of the 58mer, comparing this value with the predicted radius of gyration of the polymer in aqueous solution (1.2 nm, see above), it seems that the aggregation is accompanied by slight compaction of the polymer structure. On going from the 58mer to the 120mer we would expect the polymer volume to double, and so the polymer radius to increase by the cube root of this (1.26) if it was spherical. Since the ratio of the nearest-neighbour distances in the two aggregates is 1.52, this suggests that, when close

to the membrane surface, the polymer globules are better regarded as oblate spheroids.

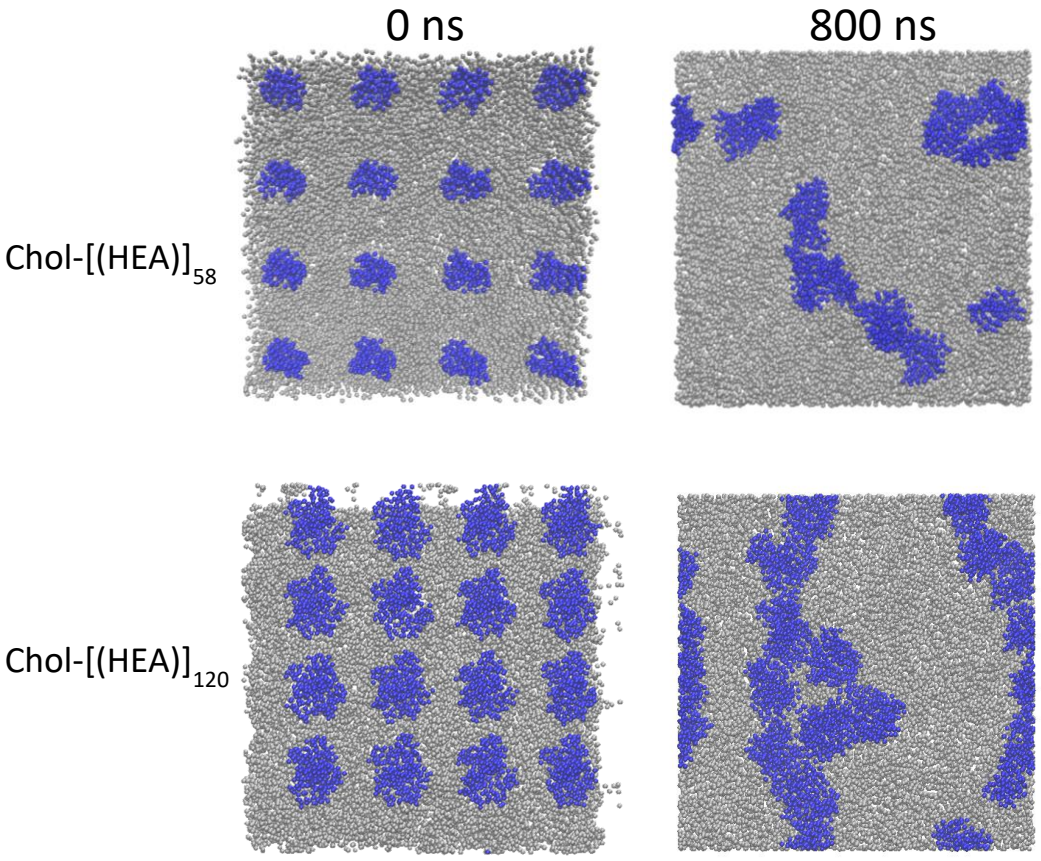


Figure 4.28 Aggregation simulations for Chol-$[(HEA)]_n$ (blue) on a plasma membrane surface (grey)

4.3.4.4 Interpretation of the experimental data in the light of the simulation results.

The simulations predict that Chol-$[(HEA)]_n$ polymers firmly absorb onto membrane surfaces through their anchoring cholesterol groups. They predict that the $[(HEA)]_n$ chain protrudes above the surface and adopts a dynamic "molten globule" form. They predict that the polymer is neither particularly attracted or repelled from the membrane surface. They predict that close to the point of insertion of the cholesterol anchor into the membrane, there is significant disruption of the lipid organisation, but that this effect decreases rapidly further

away from this point. They predict that Chol-$[(HEA)]_n$ polymers will tend to aggregate on the surface, but retain an oblate spheroid shape.

On the basis of these results we can put forward a coherent hypothesis to explain the experimental observation that shorter Chol-$[(HEA)]_n$ polymers induce greater membrane fluidity, as assessed by Laurdan fluorescence, than longer ones. As the polymers self-assemble on the membrane surface, a "puddle" of fluid membrane will form beneath each, close to the point of insertion of the cholesterol anchoring group. The longer the polymer chains, the larger the surface area each will occupy, and the wider spaced the points of insertion will be. As a result, on the macroscopic scale, the less fluid the membrane will appear to be.

4.4 Concluding Remarks

This chapter investigated artificial membrane models to further characterise the interaction between our membrane-inserting polymers and bilayers. Firstly, model bilayer membranes (DOPC:DSPC:cholesterol liposomes) were employed in membrane fluidity studies to establish whether these synthetic systems could be a representative model for cell bilayer membranes. As our results showed that the fluidity was affected by the interaction with polymers, we confirmed that synthetic bilayer membranes were a suitable model for the polymer-bilayer interaction. Therefore, we employed SPR to characterise kinetic and thermodynamic parameters within the interaction of different polymer classes with a model DOPC:DSPC:cholesterol bilayer. This study confirmed that the membrane-interacting polymers were depositing on immobilised bilayers if their structures included a membrane-interacting moiety, while control polymers did not interact with the model bilayer membrane. Additionally, the length of the hydrophilic chain in cholesterol-HEA homopolymers affected the kinetic and thermodynamic constants for the interaction process with the same trends observed in cell culture studies.

Additionally, solid-state NMR studies confirmed that the cholesterol and DOPE-based polymers were localised within simple DMPC:cholesterol MLVs, providing further evidence of the ability of these polymers directly interact with membranes. Finally, molecular modelling simulations offered a mechanistic confirmation of the trend described in **Chapter 3** for *in vitro* cell experiments, where shorter polymers (except for Chol-[(HEA)$_{100\%}$]$_{13}$, as expected from *in vitro* cell interaction results) were impacting the cell membrane fluidity more than longer polymers.

4.5 Bibliography

(1) Yeagle, P. L. *The Structure of Biological Membranes*, 3rd ed.; Yeagle, P. L., Ed.; CRC Press, 2012; Vol. 148.

(2) Guidotti, G. The Composition of Biological Membranes. *Arch. Intern. Med.* **1972**, *129* (2), 194. https://doi.org/10.1001/archinte.1972.00320020038003.

(3) Levental, I.; Levental, K. R.; Heberle, F. A. Lipid Rafts: Controversies Resolved, Mysteries Remain. *Trends Cell Biol.* **2020**, 1–13. https://doi.org/10.1016/j.tcb.2020.01.009.

(4) Levental, I.; Veatch, S. L. The Continuing Mystery of Lipid Rafts. *J. Mol. Biol.* **2016**, *428* (24), 4749–4764. https://doi.org/10.1016/j.jmb.2016.08.022.

(5) Chan, Y.-H. M.; Boxer, S. G. Model Membrane Systems and Their Applications State of the Field. *Curr. Opin. Chem. Biol.* **2007**, *11* (6), 581–587.

(6) Rascol, E.; Devoisselle, J. M.; Chopineau, J. The Relevance of Membrane Models to Understand Nanoparticles-Cell Membrane Interactions. *Nanoscale* **2016**, *8* (9), 4780–4798. https://doi.org/10.1039/c5nr07954c.

(7) Vemuri, S.; Rhodes, C. T. Preparation and Characterization of Liposomes as Therapeutic Delivery Systems: A Review. *Pharm. Acta Helv.* **1995**, *70* (2), 95–111. https://doi.org/10.1016/0031-6865(95)00010-7.

(8) Akashi, K.; Miyata, H.; Itoh, H.; Kinosita, K. Preparation of Giant Liposomes in Physiological Conditions and Their Characterization under an Optical Microscope. *Biophys. J.* **1996**, *71* (6), 3242–3250. https://doi.org/10.1016/S0006-3495(96)79517-6.

(9) Olson, F.; Hunt, C. A.; Szoka, F. C.; Vail, W. J.; Papahadjopoulos, D. Preparation of Liposomes of Defined Size Distribution by Extrusion through Polycarbonate Membranes. *BBA - Biomembr.* **1979**, *557* (1), 9–23. https://doi.org/10.1016/0005-2736(79)90085-3.

(10) Hu, J.; Li, W.; Chen, J.; Zhang, X.; Zhao, X. Novel Plating Solution for Electroless Deposition of Gold Film onto Glass Surface. *Surf. Coatings Technol.* **2008**, *202* (13), 2922–2926. https://doi.org/10.1016/j.surfcoat.2007.10.026.

(11) Kılıç, A.; Fazeli Jadidi, M.; Özer, H. Ö.; Kök, F. N. The Effect of Thiolated Phospholipids on Formation of Supported Lipid Bilayers on Gold Substrates Investigated by Surface-Sensitive Methods. *Colloids Surfaces B Biointerfaces* **2017**, *160*, 117–125. https://doi.org/10.1016/j.colsurfb.2017.09.016.

(12) Biacore. Sensor Surface Handbook. *GE Healthc.* **2008**, *BR-1005-71*, 8–10.

(13) Cordomí, A.; Caltabiano, G.; Pardo, L. Membrane Protein Simulations Using AMBER Force Field and Berger Lipid Parameters. *J. Chem. Theory Comput.* **2012**, *8* (3), 948–958. https://doi.org/10.1021/ct200491c.

(14) Weiner, P. K.; Kollman, P. A. AMBER: Assisted Model Building with Energy Refinement. A General Program for Modeling Molecules and Their Interactions. *J. Comput. Chem.* **1981**, *2* (3), 287–303. https://doi.org/10.1002/jcc.540020311.

(15) Jójárt, B.; Martinek, T. A. Performance of the General Amber Force Field in Modeling Aqueous POPC Membrane Bilayers. *J. Comput. Chem.* **2007**, *28* (12), 2051–2058. https://doi.org/10.1002/jcc.20748.

(16) Salomon-Ferrer, R.; Case, D. A.; Walker, R. C. An Overview of the Amber Biomolecular Simulation Package. *Wiley Interdiscip. Rev. Comput. Mol. Sci.* **2013**, *3* (2), 198–210. https://doi.org/10.1002/wcms.1121.

(17) Pettersen, E. F.; Goddard, T. D.; Huang, C. C.; Couch, G. S.; Greenblatt, D. M.; Meng, E. C.; Ferrin, T. E. UCSF Chimera - A Visualization System for Exploratory Research and Analysis. *J. Comput. Chem.* **2004**, *25* (13), 1605–1612. https://doi.org/10.1002/jcc.20084.

(18) Wang, J.; Wang, W.; Kollman, P. a; Case, D. a. Antechamber, An Accessory Software Package For Molecular Mechanical Calculations. *J. Am. Chem. Soc* **2001**, *222* (2), U403.

(19) Mark, P.; Nilsson, L. Structure and Dynamics of the TIP3P, SPC, and SPC/E Water Models at 298 K. *J. Phys. Chem. A* **2001**, *105* (43), 9954–9960. https://doi.org/10.1021/jp003020w.

(20) Schott-Verdugo, S.; Gohlke, H. PACKMOL-Memgen: A Simple-To-Use, Generalized Workflow for Membrane-Protein-Lipid-Bilayer System Building. *J. Chem. Inf. Model.* **2019**. https://doi.org/10.1021/acs.jcim.9b00269.

(21) McGibbon, R. T.; Beauchamp, K. A.; Harrigan, M. P.; Klein, C.; Swails, J. M.; Hernández, C. X.; Schwantes, C. R.; Wang, L. P.; Lane, T. J.; Pande, V. S. MDTraj: A Modern Open Library for the Analysis of Molecular Dynamics Trajectories. *Biophys. J.* **2015**, *109* (8), 1528–1532. https://doi.org/10.1016/j.bpj.2015.08.015.

(22) Karplus, M.; McCammon, J. A. Molecular Dynamics Simulations of Biomolecules. *Nat. Struct. Biol.* **2002**, *9* (9), 646–652. https://doi.org/10.1038/nsb0902-646.

(23) Sato, M.; Tochio, N.; Aizawa, T. *Solution Structure of the Bombyx Mori Lysozyme*; 2020.

(24) Routledge, S. J.; Linney, J. A.; Goddard, A. D. Liposomes as Models for Membrane Integrity. *Biochem. Soc. Trans.* **2019**, *47* (3), 919–932. https://doi.org/10.1042/BST20190123.

(25) Andrade, S.; Ramalho, M. J.; Loureiro, J. A.; Pereira, M. C. Liposomes as Biomembrane Models: Biophysical Techniques for Drug-Membrane Interaction Studies. *J. Mol. Liq.* **2021**, *334*. https://doi.org/10.1016/j.molliq.2021.116141.

(26) Matos, C.; Moutinho, C.; Lobão, P. Liposomes as a Model for the Biological Membrane: Studies on Daunorubicin Bilayer Interaction. *J. Membr. Biol.* **2012**, *245* (2), 69–75. https://doi.org/10.1007/s00232-011-9414-2.

(27) Chatterjee, S. N.; Agarwal, S. Liposomes as Membrane Model for Study of Lipid Peroxidation. *Free Radic. Biol. Med.* **1988**, *4* (1), 51–72. https://doi.org/10.1016/0891-5849(88)90011-1.

(28) Hooper, N. M. Glycosyl-Phosphatidylinositol Anchored Membrane Enzymes. *Clin. Chim. Acta* **1997**, *266* (1), 3–12. https://doi.org/10.1016/S0009-8981(97)00161-7.

(29) Paulick, M. G.; Bertozzi, C. R. The Glycosylphosphatidylinositol Anchor: A Complex Membrane-Anchoring Structure for Proteins. *Biochemistry* **2008**, *47* (27), 6991–7000. https://doi.org/10.1021/bi8006324.

(30) Baumgart, T.; Hammond, A. T.; Sengupta, P.; Hess, S. T.; Holowka, D. A.; Baird, B. A.; Webb, W. W. Large-Scale Fluid/Fluid Phase Separation of Proteins and Lipids in Giant Plasma Membrane Vesicles. *Proc. Natl. Acad. Sci. U. S. A.* **2007**, *104* (9), 3165–3170. https://doi.org/10.1073/pnas.0611357104.

(31) Paulick, M. G.; Wise, A. R.; Forstner, M. B.; Groves, J. T.; Bertozzi, C. R. Synthetic Analogues of Glycosylphosphatidylinositol-Anchored Proteins and Their Behavior in Supported Lipid Bilayers. *J. Am. Chem. Soc.* **2007**, *129* (37), 11543–11550. https://doi.org/10.1021/ja073271j.

(32) Zhao, J.; Wu, J.; Heberle, F. A.; Mills, T. T.; Klawitter, P.; Huang, G.; Costanza, G.; Feigenson, G. W. Phase Studies of Model Biomembranes : Complex Behavior of DSPC / DOPC / Cholesterol. *Biochim Biophys Acta* **2007**, *1768*, 2764–2776. https://doi.org/10.1016/j.bbamem.2007.07.008.

(33) Sánchez, A. Laurdan Generalized Polarization. *FORMATEX* **2007**, 1007–1014.

(34) Wesołowska, O.; Michalak, K.; Maniewska, J.; Hendrich, A. B. Giant Unilamellar Vesicles - a Perfect Tool to Visualize Phase Separation and Lipid Rafts in Model Systems. *Acta Biochim. Pol.* **2009**, *56* (1), 33–39. https://doi.org/10.18388/abp.2009_2514.

(35) Abdiche, Y. N.; Myszka, D. G. Probing the Mechanism of Drug/Lipid Membrane Interactions Using Biacore. *Anal. Biochem.* **2004**, *328* (2), 233–243. https://doi.org/10.1016/j.ab.2004.01.018.

(36) Beseničar, M.; Maček, P.; Lakey, J. H.; Anderluh, G. Surface Plasmon Resonance in Protein-Membrane Interactions. *Chem. Phys. Lipids* **2006**, *141* (1–2), 169–178. https://doi.org/10.1016/j.chemphyslip.2006.02.010.

(37) Kim, K.; Cho, S.; Park, J. H.; Byun, Y.; Chung, H.; Kwon, I. C.; Jeong, S. Y. Surface Plasmon Resonance Studies of the Direct Interaction between a Drug/Intestinal Brush Border Membrane. *Pharm. Res.* **2004**, *21* (7), 1233–1238. https://doi.org/10.1023/B:PHAM.0000033011.56536.c3.

(38) Myszka, D. G.; Abdiche, Y. N. *Handbook of Surface Plasmon Resonance*, 2nd ed.; Shasfoort, R., Ed.; CPI Group, 2017.

(39) de Mol, N. J.; Fischer, M. J. E. *Surface Plasmon Resonance: Methods and Protocols*; 2010. https://doi.org/10.1007/978-1-60761-670-2.

(40) Kilic, A.; Kok, F. N. Peptide-Functionalized Supported Lipid Bilayers to Construct Cell Membrane Mimicking Interfaces. *Colloids Surfaces B Biointerfaces* **2019**, *176* (October 2018), 18–26. https://doi.org/10.1016/j.colsurfb.2018.12.052.

(41) Cras, J. J.; Rowe-Taitt, C. A.; Nivens, D. A.; Ligler, F. S. Comparison of Chemical Cleaning Methods of Glass in Preparation for Silanization. *Biosens. Bioelectron.* **1999**, *14* (8–9), 683–688. https://doi.org/10.1016/S0956-5663(99)00043-3.

(42) Büschges, M. I.; Hoffmann, R. C.; Regoutz, A.; Schlueter, C.; Schneider, J. J. Atomic Layer Deposition of Ternary Indium/Tin/Aluminum Oxide Thin Films, Their Characterization and Transistor Performance under Illumination. *Chem. - A Eur. J.* **2021**, *27* (38), 9791–9800. https://doi.org/10.1002/chem.202101126.

(43) Howe, C. L.; Webb, K. F.; Abayzeed, S. A.; Anderson, D. J.; Denning, C.;

Russell, N. A. Surface Plasmon Resonance Imaging of Excitable Cells. *J. Phys. D. Appl. Phys.* **2019**, *52* (10), aaf849. https://doi.org/10.1088/1361-6463/aaf849.

(44) Ding, L.; Gao, Y.; Di, J. A Sensitive Plasmonic Copper(II) Sensor Based on Gold Nanoparticles Deposited on ITO Glass Substrate. *Biosens. Bioelectron.* **2016**, *83*, 9–14. https://doi.org/10.1016/j.bios.2016.04.002.

(45) Xue, Y.; Li, X.; Li, H.; Zhang, W. Quantifying Thiol-Gold Interactions towards the Efficient Strength Control. *Nat. Commun.* **2014**, *5*. https://doi.org/10.1038/ncomms5348.

(46) Sakanovic, A.; Hodnik, V.; Anderluh, G. *Lipid-Protein Interactions*, Second.; John M. Walker, Kleinschmidt, J., Eds.; Humana Press, 2019.

(47) Erb, E. M.; Chen, X.; Allen, S.; Roberts, C. J.; Tendler, S. J. B.; Davies, M. C.; Forsén, S. Characterization of the Surfaces Generated by Liposome Binding to the Modified Dextran Matrix of a Surface Plasmon Resonance Sensor Chip. *Anal. Biochem.* **2000**, *280* (1), 29–35. https://doi.org/10.1006/abio.1999.4469.

(48) Baird, C. L.; Courtenay, E. S.; Myszka, D. G. Surface Plasmon Resonance Characterization of Drug/Liposome Interactions. *Anal. Biochem.* **2002**, *310* (1), 93–99. https://doi.org/10.1016/S0003-2697(02)00278-6.

(49) Olaru, A.; Gheorghiu, M.; David, S.; Polonschii, C.; Gheorghiu, E. Quality Assessment of SPR Sensor Chips; Case Study on L1 Chips. *Biosens. Bioelectron.* **2013**, *45* (1), 77–81. https://doi.org/10.1016/j.bios.2013.01.045.

(50) Anderluh, G.; Beseničar, M.; Kladnik, A.; Lakey, J. H.; Maček, P. Properties of Nonfused Liposomes Immobilized on an L1 Biacore Chip and Their Permeabilization by a Eukaryotic Pore-Forming Toxin. *Anal. Biochem.* **2005**, *344* (1), 43–52. https://doi.org/10.1016/j.ab.2005.06.013.

(51) Karlsson, O. P.; Löfås, S. Flow-Mediated on-Surface Reconstitution of G-Protein Coupled Receptors for Applications in Surface Plasmon Resonance Biosensors. *Anal. Biochem.* **2002**, *300* (2), 132–138. https://doi.org/10.1006/abio.2001.5428.

(52) Kamimori, H.; Blazyk, J.; Aguilar, M. I. Lipid Membrane-Binding Properties of Tryptophan Analogues of Linear Amphipathic β-Sheet Cationic Antimicrobial Peptides Using Surface Plasmon Resonance. *Biol. Pharm. Bull.* **2005**, *28* (1), 148–150. https://doi.org/10.1248/bpb.28.148.

(53) Ciesielski, F.; Griffin, D. C.; Rittig, M.; Bonev, B. B. High-Resolution J-Coupled 13C MAS NMR Spectroscopy of Lipid Membranes. *Chem. Phys. Lipids* **2009**, *161* (2), 77–85. https://doi.org/10.1016/j.chemphyslip.2009.07.001.

(54) Lindblom, G.; Orädd, G. Order and Disorder in a Liquid Crystalline Bilayer: Pulsed Field Gradient NMR Studies of Lateral Phase Separation. *J. Dispers. Sci. Technol.* **2007**, *28* (1), 55–61. https://doi.org/10.1080/01932690600992522.

(55) Bonev, B.; Watts, A.; Bokvistb, M.; Gröbner, G. Electrostatic Peptide Lipid Interactions of Amyloid-β Peptide and Pentalysine with Membrane Surfaces Monitored by 31P MAS NMR. *Phys. Chem. Chem. Phys.* **2001**, *3* (14), 2904–2910. https://doi.org/10.1039/b103352m.

(56) Yeh, V.; Goode, A.; Eastham, G.; Rambo, R. P.; Inoue, K.; Doutch, J.;

Bonev, B. B. Membrane Stability in the Presence of Methacrylate Esters. *Langmuir* **2020**. https://doi.org/10.1021/acs.langmuir.9b03759.

(57) Andrew, E. R.; Bradbury, A.; Eades, R. G. NMR Spectra Recorded from a Crystal Rotated at High Speed. *Nature* **1958**, *182* (4650), 4650.

(58) Lowe, I. J. Free Induction Decays of Rotating Solids. *Phys. Rev. Lett.* **1959**, *2* (7), 285–287. https://doi.org/10.1103/PhysRevLett.2.285.

(59) Andrew, E. R. Magic Angle Spinning in Solid State n.m.r. Spectroscopy. *Philos. Trans. R. Soc. London. Ser. A, Math. Phys. Sci.* **1981**, *299* (1452), 505–520. https://doi.org/10.1098/rsta.1981.0032.

(60) Polenova, T.; Gupta, R.; Goldbourt, A. Magic Angle Spinning NMR Spectroscopy: A Versatile Technique for Structural and Dynamic Analysis of Solid-Phase Systems. *Anal. Chem.* **2015**, *87* (11), 5458–5469. https://doi.org/10.1021/ac504288u.

(61) Holland, G. P.; McIntyre, S. K.; Alam, T. M. Distinguishing Individual Lipid Headgroup Mobility and Phase Transitions in Raft-Forming Lipid Mixtures with 31P MAS NMR. *Biophys. J.* **2006**, *90* (11), 4248–4260. https://doi.org/10.1529/biophysj.105.077289.

(62) Seelig, J. 31P Nuclear Magnetic Resonance and the Head Group. *Biochim. Biophys. Acta, 515 105-140* **1978**, *515*, 105–140.

(63) Ladizhansky, V. Applications of Solid-State NMR to Membrane Proteins. *Biochim. Biophys. Acta - Proteins Proteomics* **2017**, *1865* (11), 1577–1586. https://doi.org/10.1016/j.bbapap.2017.07.004.

(64) Haber, S.; Leskes, M. What Can We Learn from Solid State NMR on the Electrode–Electrolyte Interface? *Adv. Mater.* **2018**, *30* (41). https://doi.org/10.1002/adma.201706496.

(65) Kolodziejski, W.; Klinowski, J. Kinetics of Cross-Polarization in Solid-State NMR: A Guide for Chemists. *Chem. Rev.* **2002**, *102* (3), 613–628. https://doi.org/10.1021/cr000060n.

(66) Lilly Thankamony, A. S.; Wittmann, J. J.; Kaushik, M.; Corzilius, B. Dynamic Nuclear Polarization for Sensitivity Enhancement in Modern Solid-State NMR. *Prog. Nucl. Magn. Reson. Spectrosc.* **2017**, *102–103*, 120–195. https://doi.org/10.1016/j.pnmrs.2017.06.002.

(67) Mani, R.; Buffy, J. J.; Waring, A. J.; Lehrer, R. I.; Hong, M. Solid-State NMR Investigation of the Selective Disruption of Lipid Membranes by Protegrin-1. *Biochemistry* **2004**, *43* (43), 13839–13848. https://doi.org/10.1021/bi048650t.

Chapter 5

Drug encapsulation

This chapter will describe the two approaches that were employed for encapsulation of the chosen drugs within polymers designed as previously described. We explored the possibility to encapsulate drugs containing basic groups, e.g. nitrofurantoin, by forming an acid-base (ionomeric) interaction between the basic drug and the acid-bearing polymers. A proof-of concept drug-polymer conjugation study was conducted using mesalazine as a model drug, by synthesising an acrylamide-based mesalazine monomer, which was then polymerised to produce a conjugated polymer library. The physicochemical properties of the polymers were characterised, as well as the interaction with relevant cell models (Caco-2) and drug release profiles under different conditions.

5.1 Introduction

In **Chapters 3-4** we investigated the interaction of our polymers with artificial and cell lipid bilayer membranes, both *in vitro* and *in silico.* In this part of the work, described here in Chapter 5, we investigated the potential for these materials for the delivery of model drugs. For this purpose, we investigated both non-covalent and covalent modalities of encapsulation, as proof-of-concept for future application of these polymers in therapy.

Accordingly, we first employed the ionomeric encapsulation[1–3] of model antibiotic nitrofurantoin, which involves the formation of an acid-base pair between the polymer and the drug. The ionomeric encapsulation employs the formation of acid-base pairs between the drug and the encapsulating species, resulting in drug conjugates that do not require covalent binding the drug to the polymer chain[4]. Furthermore, a single type of polymer (in our case, an acrylic acid containing copolymer) could be employed to encapsulate to a wide variety of drugs, as long as these possess the correct functionality (basic).Release of the drug is normally achieved by displacement of the non-covalent conjugate by ions present in physiological medium, or a pH-dependent relase[5]. This approach has already been successfully employed in previous studies within our group[6,7], which have shown that non-covalent polymer drug conjugation yielded stable adducts and avoided burst release, thanks to multivalent interactions between the polymer and the protein payloads. As in our case, we would be conjugating monovalent drugs to multivalent polymers, efficient and stable conjugation will need to be tested. In this study we used nitrofurantoin (**Figure 5.1**) due to its non-ideal dosing regimen (4 administrations per day[8]) and the presence of a mildly basic nitrogen atom (pK_{aH} 7.2[9]).

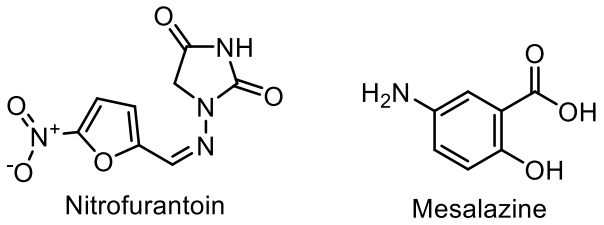


Figure 5. 1 Chemical structure of the model drugs chosen for encapsulation, nitrofurantoin and mesalazine.

In this PhD work a covalent conjugation approach was tested using mesalazine (**Figure 5.1**), an aminosalicylate drug used to treat ulcerative colitis and Crohn's disease and other types of inflammatory bowel disease. This drug was already previously conjugated with an acrylamide to produce a mesalazine-based monomer[10] and then employed for the synthesis of a polymer covalently conjugated with the drug. Additionally, as mesalazine its action locally in the intestine[11] and is currently used in therapy as a covalent co-drug, therefore we selected this drug as the model for covalent encapsulation and future candidate for release within the GI tract. Forming polymer-drug conjugates often allowed for higher dose loading, as well as additional stability of the conjugate[4], which avoided unwanted initial burst release[12].

5.2 Materials and Methods

5.2.1 Materials

The polymers employed were synthesised as described in **Chapter 2**. Reagents and solvents were purchased from Sigma-Aldrich (Dorset, UK) and from Fischer Scientific (Loughborough, UK).

Human epithelial colorectal adenocarcinoma cells (Caco-2, American Type Culture Collection ATCC; Manassas, Virginia, passage 45-52) were used for this study. EMEM, HBSS, streptomycin/amphotericin solution, FBS, L-glutamine, PBS and trypsin/EDTA solution were purchased from Sigma (UK).

PrestoBlue™ cell toxicity reagent, LDH cytotoxicity assay kit (Pierce™) and Laurdan dye (6-Dodecanoyl-2-Dimethylaminonaphthalene) were purchased from ThermoFisher Scientific (USA).

Esterase from porcine liver (lyophilized powder, ≥15 units/mg) was purchased from Sigma-Aldrich (Dorset, UK).

5.2.2 Nanoprecipitation

Encapsulation of nitrofurantoin with the selected polymers was performed via nanoprecipitation. Briefly, the selected polymer was solubilised or suspended in water (2.5 mg/mL, above CAC) and kept stirring at room temperature. Using a NE-1000 Single Syringe Pump (Scientific Instrument Services), a stock solution of nitrofurantoin (acetone, 0.5 mg/mL; THF, acetonitrile, 1-2 mg/mL) was added (1 ml/min ratio) to the stirring water-polymer solution. The mixture was then left stirring for 24-48 hours, until the organic solvent was fully evaporated. Acetonitrile was removed by evaporation under reduced pressure (200 mbar, 40 °C).

5.2.3 Solid drug encapsulation

The selected polymer was solubilised or suspended in water (2.5 mg/mL, above CAC, **Chapter 2**) and kept stirring. The weighed amount of nitrofurantoin was

then added to the stirring water-polymer solution. The mixture was then left stirring for 24 hours.

5.2.3 Dialysis of formulations

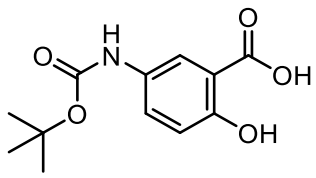
The formulation suspensions were transferred in a dialysis membrane with an appropriate MWCO (7 kDa), as to allow only the drug to cross the membrane. The dialysis was carried out in 1L beakers filled with a 1:1 water:acetone mixture.

5.2.4 PD10 on formulations

Before use, the columns were flushed with deionised water to remove any methanol used for column storage. The formulation suspension was loaded on the column in the minimum amount of medium possible. After loading of the formulation, deionised water was added, starting the chromatographic separation. 1 mL aliquots were collected, until the colouring in the column (yellow from nitrofurantoin) disappeared. After the separation, the columns were washed with 20 mL water:methanol (3:7), sealed and stored with a slight excess of the solution used to wash the columns.

5.2.5 Synthesis of mesalazine monomer

*5.2.5.1 Synthesis of **14***



Mesalazine (6.00 g, 38.2 mmol, 1 eq) was solubilised in a dioxane:H_2O mixture (260 ml, 2:1 vol:vol) in a round-bottomed flask. Aqueous 1M NaOH (85 mL) was added dropwise to the stirring solution, then di-*tert*-butyl decarbonate (9.19 g, 42.0 mmol, 1.1 eq) was added to the stirring solution. After 3 hours, the reaction mixture was acidified to pH 2.3 with a 5M HCl solution, and the product was

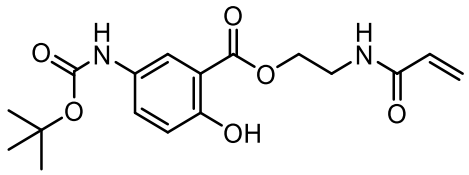
extracted with ethyl acetate (3x100 mL). The organic layers were collected and washed with brine, then dried with $MgSO_4$ and concentrated under reduced pressure, resulting in a light brown solid (**14**, 8.35 g, 86.3% yield).

ESI-MS (expected m/z $[M+H]^+$ 252.0877, found 252.0870).

^{1}H NMR (400 MHz, DMSO-d6) δ 9.23 (s, 1H, NH), 8.00 (s, 1H, aromatic CH), 7.50 (dd, J = 8.9, 2.7 Hz, 1H, aromatic CH), 6.86 (d, J = 8.9 Hz, 1H, aromatic CH), 1.46 (s, 9H, CH_3 from Boc).

^{13}C NMR (101 MHz, DMSO-d_6) δ 172.26 (COOH), 156.84 (aromatic C-OH), 153.42 (carbamate C), 131.67 (aromatic CNH), 127.08 (aromatic CH), 119.68 (aromatic CH), 117.57 (aromatic CH), 112.84 (aromatic C-C), 79.42 (C from Boc), 28.61 (CH_3 from Boc).

*5.2.5.2 Synthesis of **15***



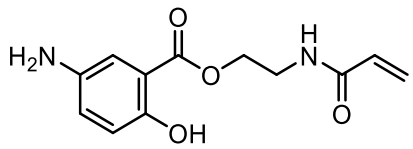
The Boc-protected mesalazine (**14**, 7.00 g, 25.6 mmol, 1eq) was solubilised in acetonitrile (50 mL) in a round-bottomed flask, and 2-hydroxyethyl acrylamide (4.43 g, 38.5 mmol, 1.5 eq) was added to the stirring solution. Dicyclohexylcarbodiimide (6.88 g, 33.3 mmol, 1.3 eq) and 4-(dimethylamino) pyridine (0.157 g, 1.28 mmol, 0.05 eq) were each solubilised in a small amount of acetonitrile and added to the stirring solution. After 24 hours, thin layer chromatography (EtOAc:MeOH 9:1). confirmed that starting material **(14)** was no longer present, and the reaction mixture was extracted using ethyl acetate:water (3x50 mL). The organic fractions were pooled, and the solvent was removed under reduced pressure. The resulting brown residue was purified by

column chromatography, using as eluent a solvent mixture with increasing polarity (EtOAc:MeOH 1:0 → 9:1). The main fraction was collected, and solvent was removed under reduced pressure, resulting in a pale orange solid (**15**, 3.25 g, 36.1% yield).

ESI-MS (expected m/z $[M+Na]^+$ 373.1370, found 373.1362).

^{1}H NMR (400 MHz, DMSO-d6) δ 9.26 (s, 1H, carbamate NH), 8.34 (t, J = 5.6 Hz, 1H, aromatic CH), 7.96 (d, J = 2.7 Hz, 1H, monomer NH), 7.57 – 7.48 (m, 1H, aromatic CH), 6.91 (d, J = 8.9 Hz, 1H, aromatic CH), 6.23 (dd, J = 17.1, 10.0 Hz, 1H, vinylic CH), 6.15 – 6.01 (m, 1H, vinylic CH_2), 5.65 – 5.52 (m, 1H, vinylic CH_2), 4.38 (t, J = 5.6 Hz, 2H, CH_2O ethanolamine), 3.52 (q, J = 5.7 Hz, 2H, CH_2N ethanolamine), 1.48 (d, J = 14.2 Hz, 15H, CH_3 from Boc, residual EtOAc).

*5.2.5.3 Synthesis of **16***



The Boc-protected mesalazine monomer (**15**, 2.00 g, 6.11 mmol, 1 eq) was solubilised in anhydrous dichloromethane (10 mL) in a 2-neck round-bottomed flask, which was sealed with a rubber septum and fitted with a sealed dropping funnel. The solution was degassed with Argon for 15 minutes, then trifluoroacetic acid (9.35 mL, 122 mmol, 20 eq) was added dropwise to the stirring solution. Completion of the reaction was checked at regular intervals by thin layer chromatography (EtOAc:MeOH 9:1). After the reaction was completed, the solvent was removed under reduced pressure. After having confirmed that TFA was still present by ^{19}F NMR analysis, the semi-solid was solubilised in methanol and Amberlite™ IRA402 was added to the stirring solution. After 2 hours, the

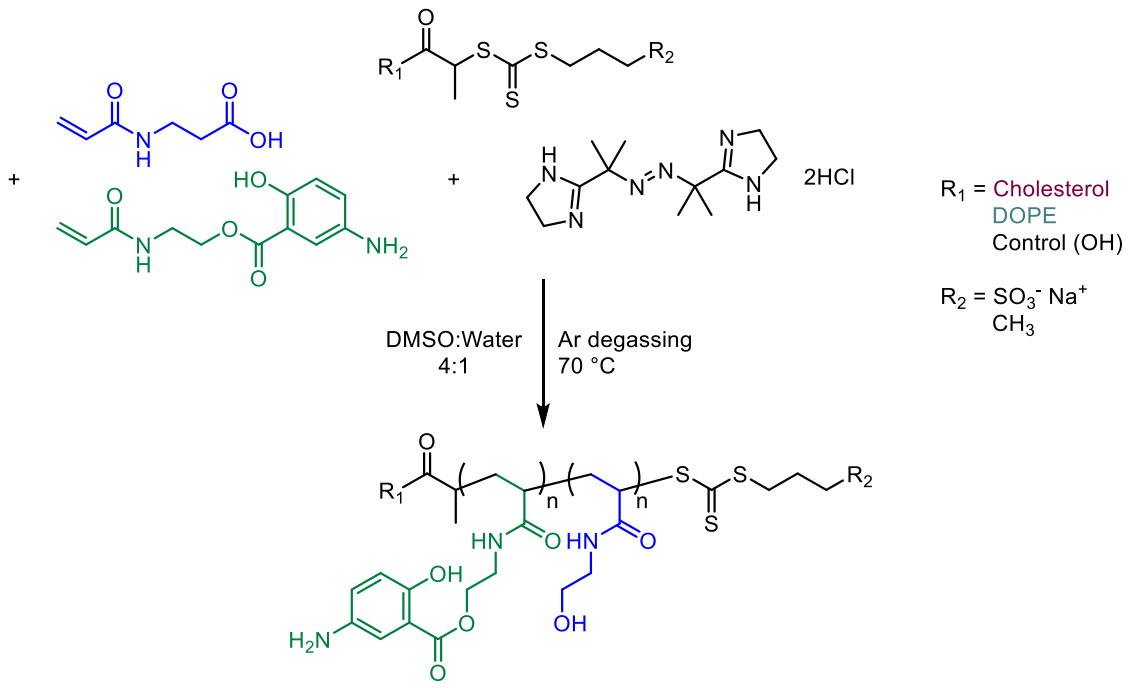
suspension was filtered and the collected organic phase was dried under reduced pressure, resulting in a dark brown semi-solid (**16**, 1.89 g, 88.3% yield).

ESI-MS (expected m/z $[M+H]^+$ 251.1026, found 251.1025).

^{1}H NMR (400 MHz, Acetone-d6) δ 8.29 (d, J = 2.7 Hz, 1H, aromatic CH), 7.64 (dd, J = 8.9, 2.7 Hz, 1H, aromatic CH), 7.12 (d, J = 8.9 Hz, 1H, aromatic CH), 6.39 (dd, J = 17.1, 10.2 Hz, 1H, vinylic CH), 6.20 (dd, J = 17.0, 2.2 Hz, 1H, vinylic CH_2), 5.56 (dd, J = 10.1, 2.2 Hz, 1H, vinylic CH_2), 4.50 – 4.41 (m, 2H, CH_2O ethanolamine), 4.03 (s, 2H, NH_2), 3.70 (t, J = 5.1 Hz, 2H, CH_2N ethanolamine).

^{13}C NMR (101 MHz, DMSO-d6) δ 167.26 (COO), 165.23 (CONH), 159.19 (aromatic COH), 131.57 (aromatic CNH_2), 130.37 (vinylic CH), 125.62 (vinylic CH_2) , 124.60 (aromatic CH), 123.04 (aromatic CH), 119.00 (aromatic CH), 114.26 (aromatic C-C), 64.20 (CH_2O ethanolamine), 37.81 (CH_2N ethanolamine).

5.2.6 Synthesis of mesalazine-containing polymers



In a typical polymerisation reaction, the RAFT agent was solubilised in DMSO in the reaction vessel (Schlenk tube, or scintillation vial), then the chosen monomers were solubilised in deionised water (2.0 M monomer concentration) and added to the DMSO solution (DMSO:water 4:1 vol:vol). The exact initial co-monomer ratio was determined by ^{1}H NMR analysis of an aliquot taken from the reaction mixture, then the initiator (VA-044, 1:0.025 CTA:initiator ratio mol:mol) 20 mg/mL aqueous stock solution was added. Exact conditions for all polymerisation reactions are shown in **Table 5.1** in the supporting information. The vessel was then closed using a rubber seal and degassed by N_2 bubbling for 15 minutes. The Schlenk tube was immersed in a 70 °C oil bath, under stirring. After 2 hours, the reaction was stopped by rapid cooling (ice bath) and exposure to air. Finally, the reaction solution was analysed by ^{1}H NMR to determine the final monomer conversion.

Table 5.1 Synthesis of mesalazine monomer **(16)**-containing copolymers: reaction conditions and targeted composition of final polymers.

Code	Chol-[(HEA)$_{80\%}$-*r*-(MES)$_{20\%}$]$_{80}$	Chol-[(HEA)$_{75\%}$-*r*-(MES)$_{25\%}$]$_{46}$	Chol-[(HEA)$_{90\%}$-*r*-(MES)$_{10\%}$]$_{44}$	PABTC-[(HEA)$_{90\%}$-*r*-(MES)$_{10\%}$]$_{38}$	DOPE-[(HEA)$_{90\%}$-*r*-(MES)$_{10\%}$]$_{44}$
$DP_{targeted}$[a]	100	75	50	50	50
Monomers (mg)	HEA (762) MES (710)	HEA (163) MES (178)	HEA (97) MES (53)	HEA (194) MES (105)	HEA (148) MES (80)
CTA (mg)	99	30	22	10	31
VA-044 (mg)	0.76	0.23	0.17	0.34	0.26
DMSO (mL)	3.78	0.85	0.42	0.84	0.64
H_2O (mL)	0.94	0.21	0.10	0.21	0.16
CTA:HEA:MES:Initiator (molar ratios in initial reaction feed)	1:70:30:0.025	1:50:25:0.025	1:40:10:0.025	1:40:10:0.025	1:40:10:0.025

[a] Degree of polymerisation (DP) at 100% monomer conversion.

The resulting polymers were purified as previously described in **Chapter 2**. The viscous or semi-solid reaction mixture was solubilised in the minimum amount of

CH_2Cl_2:MeOH 6:5 vol:vol, and precipitated (in acetone, or *tert*-butyl methyl ether for DOPE-based polymers) in a falcon tube. The suspension was centrifuged (4500 rpm, 10 min), the supernatant was removed, and the solid residue was dried under reduced pressure, then suspended in water, and purified by dialysis against a 1:1 water:acetonitrile mixture, changing the solvent every 12-24 h. The dialysis was carried out using dialysis bags with appropriate MWCO membrane (1, 2, 5 or 7 kDa) and finally the polymer solutions were freeze-dried. The mixture was then placed under reduced pressure (maximum 30 °C) to remove acetonitrile and then freeze-dried. The dry polymers were characterised by SEC, using DMF + 0.1 LiBr as the mobile phase (**Chapter 2**) and ^{1}H NMR.

5.2.7 Dynamic Light Scattering

Particle size analyses were carried out at 25 °C by Dynamic Light Scattering (DLS) using a Zetasizer Nano ZS spectrometer (Malvern Instruments Ltd) equipped with a 633 nm laser at a fixed angle of 173°, while maintaining a constant temperature (25 °C).

5.2.8 RP-HPLC quantitation of drugs

Characterisation of solutions with unknown concentration of nitrofurantoin or mesalazine were performed on a Shimadzu UFLC HPLC, equipped with: LC-20AD (liquid chromatograph), SIL-20A HT (autosampler), CTO-20A (column oven), SPD-M20A Diode array detector (Deuterium and Wolframium). A C18 column (Phenomenex Jupiter C18 300Å) was used as stationary phase. The mobile phase was selected based on the drug analysed: phosphate buffer(1%):methanol 60:40 was employed for mesalazine[13] with a 0.5 mg/mL flow rate, while water:acetonitrile:acetic acid (79:20:1) was employed for Nitrofurantoin at a 1 mg/mL flow rate. The wavelengths chosen for analysis were λ = 235 nm for mesalazine and λ = 389 nm for nitrofurantoin.

Nitrofurantoin concentration was determined by RP-HPLC after production of a calibration curve for relevant nitrofurantoin concentrations (**Figure 5.2**). As the drug was ionomerically bound to the polymer, we employed TFA in the mobile phase. This ensured full removal of the nitrofurantoin from the polymers, as TFA is a stronger acid (pKa 0.3) than polymerised acrylic acid (4.3-6.8)[14]. Therefore, the polymer-nitrofurantoin interaction was displaced by the H^+ groups generated by TFA.

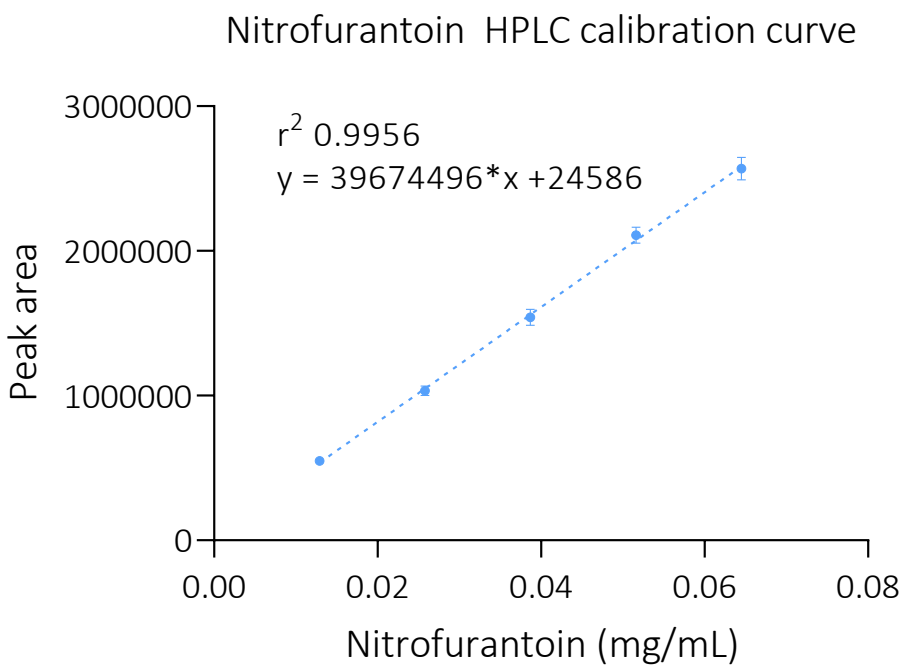


Figure 5. 2 Nitrofurantoin HPLC-UV calibration curve. Stock solutions of nitrofurantoin were prepared by dissolving nitrofurantoin in water:acetonitrile:acetic acid (79:20:1) at different concentrations in the 0.100-0.0100 mg/mL range. The samples were analysed in triplicates by RP -HPLC with UV detection (λ = 389 nm), using water:acetonitrile:acetic acid (79:20:1) as the mobile phase in isocratic elution.

The quantitation of mesalazine was carried out by RP-HPLC, using a previously described method[13]. As it can be observed from its UV-vis specrum (**Figure 5.3**), mesalazine showed two main absorbance peaks in water (11.1 μg/mL): λ = 235 nm and λ = 302 nm.

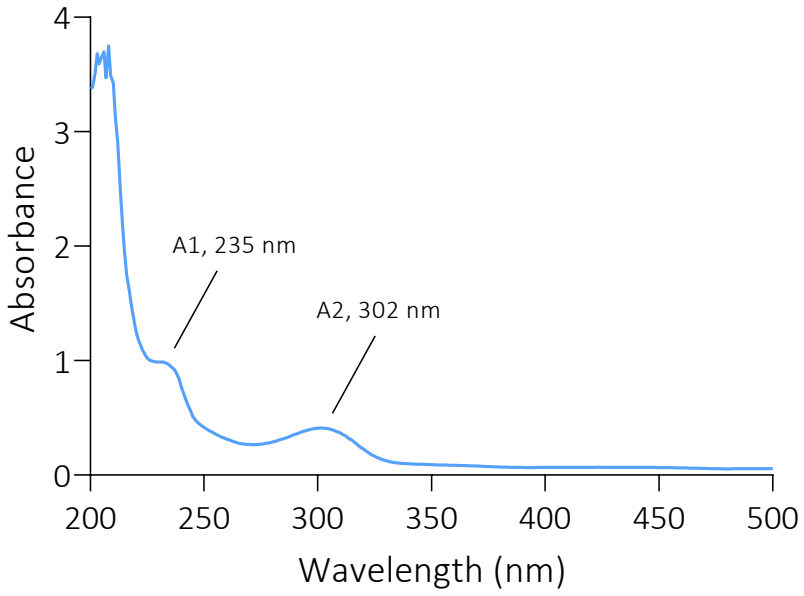


Figure 5.3 UV-vis spectrum of mesalazine in water (11.1 µg/mL), showing two major peaks at λ = 302 nm (A1) and λ = 235 nm (A2).

Since we needed to analyse relatively small amounts of mesalazine (0.1 mg/mL total concentration in the samples), we decided to use the more intense peak at λ =235 nm for quantitation using RP-HPLC.

The calibration curve (**Figure 5.4**) was produced employing appropriate known concentrations of mesalazine in FaSSIF, with 5 analytical repeats per concentration point (r^2 = 0.9944).

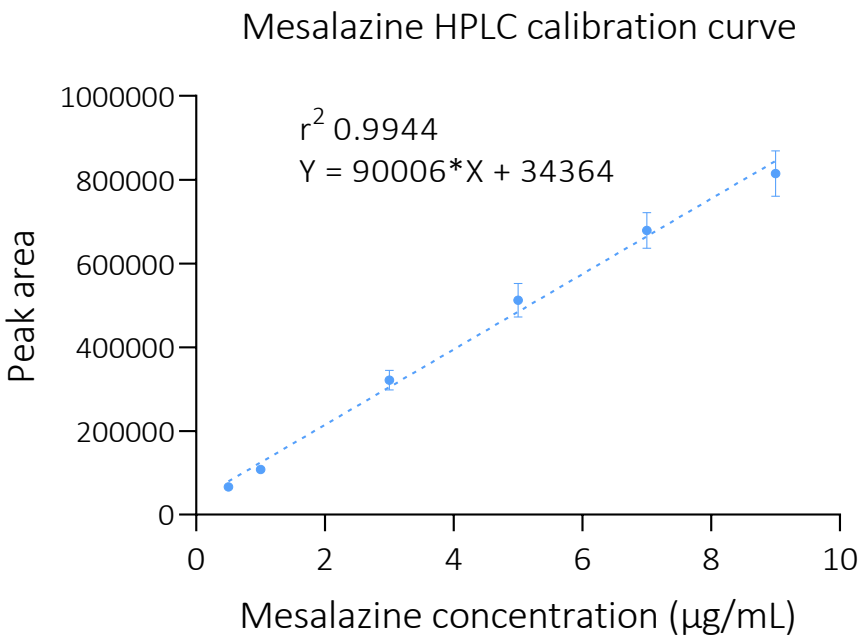


Figure 5.4 Mesalazine HPLC-UV calibration curve. Stock solutions of mesalazine were prepared by dissolving mesalazine in FaSSIF at different concentrations in the 0.500-9.00 µg/mL range. The samples were analysed in triplicates by RP- HPLC using UV detection (λ = 235 nm), using phosphate buffer (1%):methanol 60:40 as the mobile phase in isocratic elution.

5.2.9 Encapsulation efficiency of nitrofurantoin

We evaluated the different approaches to drug encapsulation by their encapsulation efficiency and loading capacity. Encapsulation efficiency (**Equation 5.1**) was used to understand how much of the free drug added at the beginning of the encapsulation was retained in the formulation. This parameter is fundamental to understand and choose the optimal encapsulation conditions, and was calculated as follows:

$$Encapsulation\ efficiency = \frac{[encapsulated\ drug]}{[starting\ drug]} \times 100$$

Equation 5.1 Encapsulation efficiency calculation, employed to estimate the percentage of starting drug that is encapsulated in the purified formulation.

The loading capacity (**Equation 5.2**) parameter is more relevant for potential therapeutic use of the formulation. This value was used to understand how much of the finished formulation was comprised of drug, and was calculated as follows:

$$Dose\ loading = \frac{encapsulated\ drug\ (weight)}{formulation\ total\ weight} \times 100$$

Equation 5.2 Dose loading calculation, employed to quantify the amount of drug contained in the completed formulation.

5.2.10 Mesalazine release from polymers

Mesalazine-based polymers were dispersed in FaSSIF buffer medium (pH 6.5) at concentrations above their CAC. When testing the effect of enzymatic release, porcine esterase was employed at a 20 IU/mL concentration in FaSSIF to disperse the polymers. The polymeric solutions were transferred in Slide-A-Lyzer MINI Dialysis Devices (3.5 kDa MWCO), which acted as a donor chamber. The donor chambers were sealed with an appropriate cap and then inserted in 2 mL Eppendorf Tubes® (acceptor chamber) pre-filled with 1.5 mL of FaSSIF medium. The assembled release device was then placed in a rocking water bath, heated at 37 °C. Samples were taken at regular time intervals, withdrawing 1.5 mL and replacing with 1.5 mL of fresh FaSSIF medium.

5.3 Results and Discussion

5.3.1 Nitrofurantoin ionotropic encapsulation

Since nitrofurantoin is poorly soluble in water (190 µg/mL in distilled water, 154 µg/mL in acidic pH)[15,16] and the polymers tested form supramolecular aggregates in water above 1-2 mg/mL (as described in **Chapter 2**), we employed two different approaches to encapsulate the drug.

Nanoprecipitation is routinely employed to produce drug-loaded polymer nanopartilces[17–19]. This technique is relatively easy to perform, does not employ high temperatures or extreme conditions. Nitrofurantoin is moderately soluble in acetone[15], which is in turn miscible with water and readily evaporates. Therefore, this solvent was selected for the nanoprecipitation process. Alternatively, we employed other solvents such as DMSO and acetonitrile; however, these needed to be removed by dialysis or evaporation under reduced pressure. The first approach caused unwanted release of encapsulated drug when purifying the formulations by dialysis. The second approach employs rotary evaporation under reduced pressure and increased temperature (30 °C maximum) for removal of the solvent by.

We also adopted an alternative approach that employed solid nitrofurantoin, directly added to an aqueous polymer suspension for encapsulation of the drug within the polymer aggregates. However, due to the poor solubility of the drug in water, encapsulation efficiencies were lower than what obtained when employing an organic solvent, likely due to a smaller percentage of nitrofurantoin being available to interact with the polymers in solution.

After encapsulation of the drug, unbound nitrofurantoin was removed to quantify drug loading and encapsulation efficiency. The separation of bound/unbound drug was performed via different methods:

i. Dialysis of the formulation, carried out with an appropriate MWCO membrane in a large vessel, to compensate for the low solubility of nitrofurantoin in water. This method was only employed for encapsulation using DMSO as solvent for nitrofurantoin, because it was not possible to remove this solvent by evaporation. The main issue with this separation was that some of the encapsulated drug could potentially be released from the formulation, with kinetics potentially dependent on the dialysis bag volume. This approach was applied in early studies and did not show successful encapsulation, likely due to nitrofurantoin release during dialysis.

ii. Separation with PD10 desalting columns (Sephadex™ G-25)[20,21]. These separating columns work on size exclusion principles, as different species will elute through the column at different speeds based on their hydrodynamic radius. This approach was used for most of the nanoprecipitation experiments described here.

Random copolymers of acid and hydrophilic monomers copolymers would have nitrofurantoin ionomerically interacting with acid repeating units randomly distributed along the polymer chain. Previous initial experiments conducted with the acid (co)polymers described in **Chapter 2** yielded low degrees of encapsulation of nitrofurantoin and poorly reproducible results. In an attempt to increase the encapsulation efficiency and dose loading, we produced block copolymers approachable to produce supramolecular aggregates with a core-shell architecture known as Block Ionomer Complexes (BICs)[1,22] (**Figure 5.5**). BICs have shown potential for delivery of a wide range of therapeutics, from imaging agents to cancer drugs[2]; this approach combines electrostatic, hydrogen bonding and hydrophobic interactions to produce a stable aggregate[23].

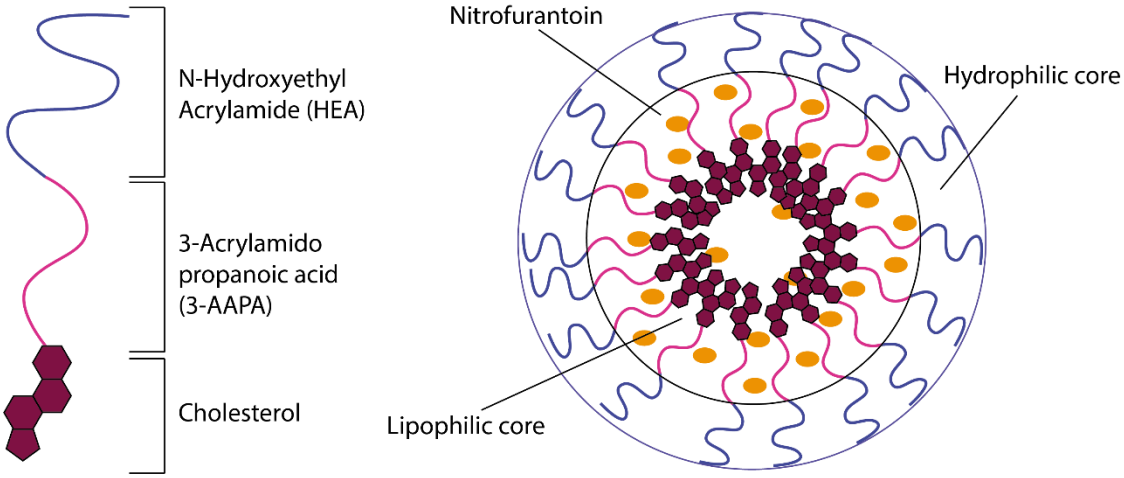
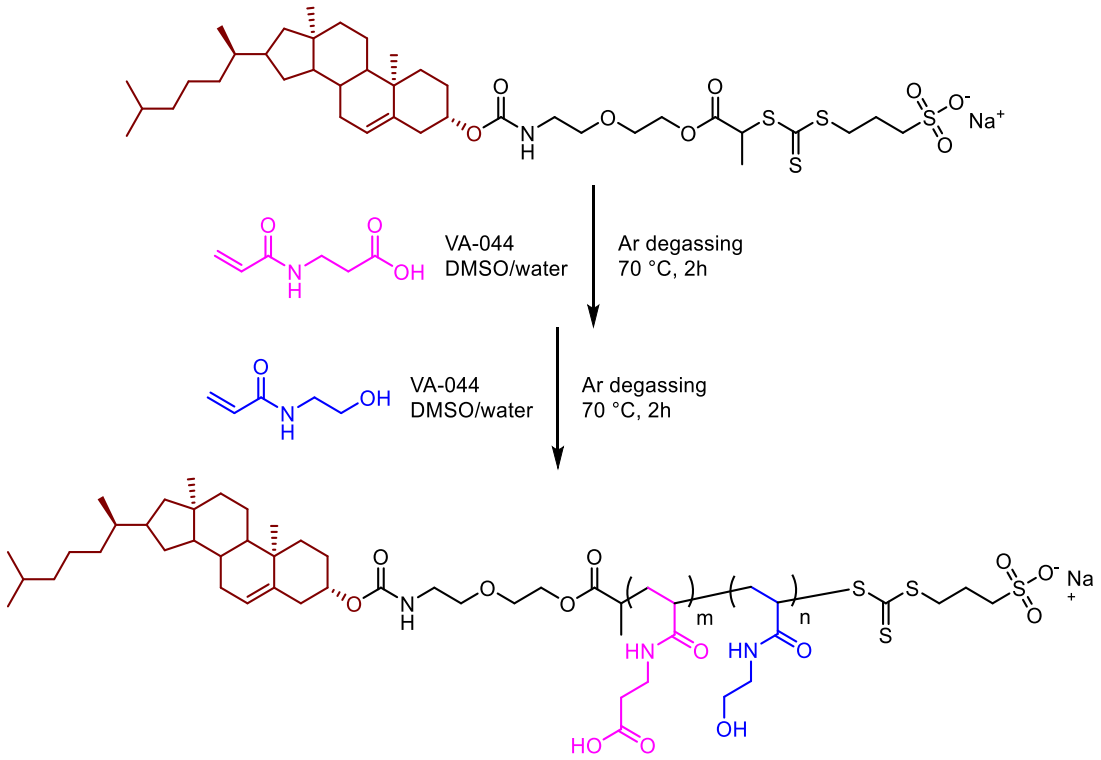


Figure 5.5 Schematic for the block copolymer approach to Nitrofurantoin ionomeric encapsulation. A) example of an alternating block 3-AAPA/HEA Cholesterol block copolymer; B) representation of the proposed supramolecular aggregation of these block copolymers with Nitrofurantoin.

For the synthesis, we employed the previously described cholesterol RAFT agent (**1**), adopting a modified version of the single-phase DMSO:water polymerisation (**Scheme 5.2**) described in **Chapter 2**. Accordingly, a poly 3-AAPA (**4**) was initially synthesised, and the reaction progress was monitored until >95% monomer conversion was achieved. At this point, a second, neutral hydrophilic monomer (HEA) was added to the reaction mixture, together with more VA-044 radical initiator. This one-pot block copolymerisation[24–26] increases the reaction yield, as it requires fewer purification steps. The block copolymers were designed to possess a similar acid:hydrophilic monomer ratio to what described by Ramasamy *et al.* and the shorter Chol-$[(AAPA)_{50\%}\text{-}(HEA)_{50\%}]_{99}$ was designed to have a similar size to what described in the same paper[2]. The longer Chol-$[(AAPA)_{50\%}\text{-}(HEA)_{50\%}]_{151}$ was designed to investigate whether a longer copolymer with the same composition would have the same encapsulation properties as Chol-$[(AAPA)_{50\%}\text{-}(HEA)_{50\%}]_{99}$.



Scheme 5.1 One-pot block copolymerisation for AAPA-HEA Cholesterol based polymers.

The polymers were characterised by ^{1}H NMR and SEC, which showed acceptable molecular weight dispersity (**Table 5.2**). This was an important parameter to characterise, as successive block copolymerisation reactions tend to increase the dispersity of polymers[27].

Table 5.2 Cholesterol HEA-AAPA block copolymers

Code	DP[a]	HEA[b]	AAPA[b]	Đ[c]	$M_{n\ (NMR)}$ (kDa)
Chol-[(AAPA)$_{50\%}$-(HEA)$_{50\%}$]$_{99}$	99	63	36	1.13	13.4
Chol-[(AAPA)$_{50\%}$-(HEA)$_{50\%}$]$_{151}$	151	90	61	1.33	20.1

[a] Degree of polymerisation (DP), calculated by ^{1}H NMR (see materials and methods). [b] HEA = hydroxyethyl acrylamide, AAPA 3-acrylamido propanoic acid. [c] Molecular weight dispersity (M_w/M_n, Đ) was determined by SEC (see materials and methods).

The synthesised block copolymers were employed in nitrofurantoin encapsulation via nanoprecipitation, employing acetone as the solvent for nitrofurantoin, and separating polymer-drug complexes from unbound drug by size-exclusion chromatography, using PD10 columns. We also decided to explore whether different charge ratios ([nitrofurantoin]:[polymer COOH groups]) had any effect on the encapsulation efficiency. These charge ratios were calculated based on the average number of acid groups present on each polymer (as determined by ^{1}H NMR). This value was multiplied by the molarity of the polymer suspension utilised for a given experiment, and an appropriate amount of nitrofurantoin was added to the polymer suspension.

As it can be observed from in **Figure 5.6**, the encapsulation had generally a better encapsulation efficiency and drug loading for the nitrofurantoin in solution when compared with the solid nitrofurantoin. This was expected, as solid nitrofurantoin needed to be solubilised before interacting with polymer suspensions. Regarding the polymer length, we observed better results for encapsulation for the shorter polymer (Chol[(AAPA)$_{50\%}$-(HEA)$_{50\%}$]$_{99}$). This could be explained by the lower hindrance that a shorter polymer chain would have offered for the polymer:drug interaction. Within the short polymer-acetone solution subset, the best result for dose loading (0.18:1 drug:polymer w:w ratio) was obtained for the 1:1 charge ratio experimental setting. Although the encapsulation efficiency here was lower than for the 1:3 charge ratio, we obtained the best dose loading result with this specific subset in the experiment.

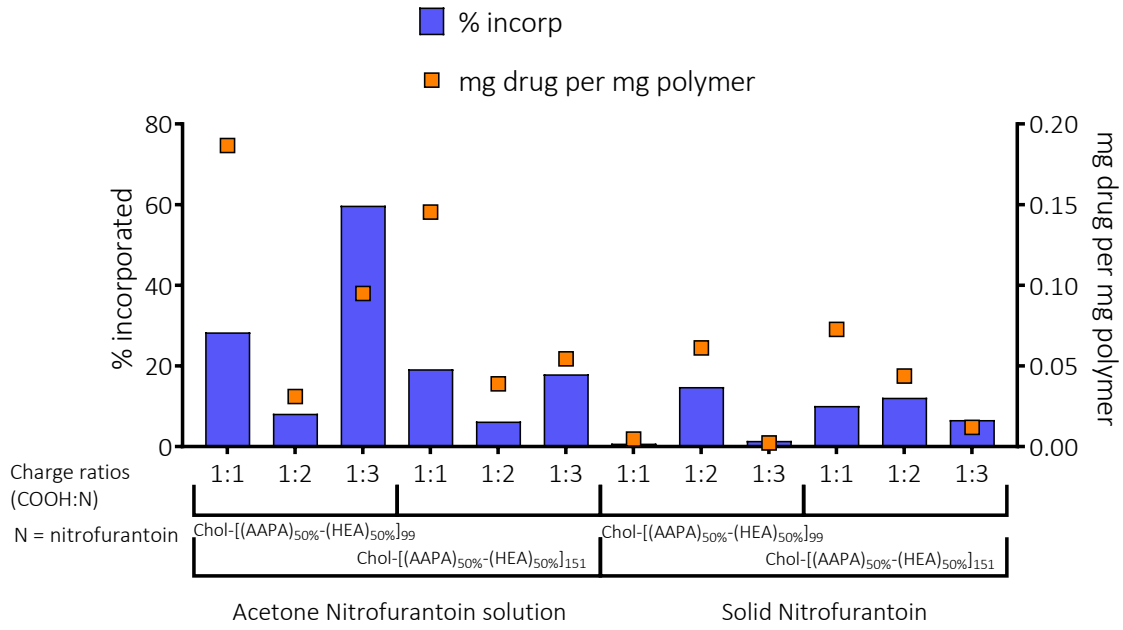


Figure 5.6 Encapsulation efficiency (left Y bar, % of starting nitrofurantoin incorporated) and dose loading (right Y bar, drug:polymer w:w ratio) for different approaches of nitrofurantoin encapsulation, comparing : two different DP block copolymers (Chol-[(AAPA)$_{50\%}$-(HEA)$_{50\%}$]$_{99}$ and Chol-[(AAPA)$_{50\%}$-(HEA)$_{50\%}$]$_{151}$), charge rations between polymers and nitrofurantoin (1:1, 1:2 and 1:3), and nitrofurantoin loading protocol (solid vs in solubilised in acetone, 0.5 mg/mL).

Based on these results, the most promising dose loading was 0.20 mg drug per mg polymer. Hence, a formulation of these two species would consist of 83% polymer and 17% nitrofurantoin. As the nitrofurantoin dosage is between 200-400 mg per day[28], a single dosage for a full day would require 1.2-2.4 g of the finished formulation.

Within this section, we demonstrated the feasibility of the ionomeric encapsulation approach to form polymer-nitrofurantoin complexes. However, further studies will be necessary to confirm the stability of this conjugation.

5.3.2 Polymer-drug conjugates – drug selection

As an alternative strategy to formation of BICs, we explored encapsulation by covalent bonding of the drug to the polymers. Since the project was in its final stages and time was limited we had two main options: i) covalently binding a drug to an already synthesised polymer, or ii) synthesise a drug-containing monomer with structure analogous to that of the monomers employed previously in this work. Each approach had its advantages and disadvantages:

i) Binding to a previously synthesised polymer: we would have needed to select drugs capable of covalently binding alcohols (HEA) or carboxylic acids (AA, 3-AAPA), forming a sufficiently labile bond that would grant drug release (e.g. anhydrides, esters, and potentially amides). However, most of the approaches in literature[29–31] focus on conjugating a single molecule of drug per polymer. This is feasible for very potent actives, but for an API that requires a large dose such as mesalazine (1.5 to 2.4 g daily)[32] this approach is not ideal. Moreover, efficient formation of anhydride or ester groups under aqueous conditions – the polymers prepared in this work are mostly hydrophilic – can be challenging

ii) Synthesising a drug-containing monomer and use it to produce new polymers: this approach offered a more streamlined synthetic pathway, as small molecules are easier to modify than large molecules such as polymers. However, a new monomer might not have reacted as well as the synthetic block it was generated from. The bond formed would need to be sufficiently labile to enable subsequent drug release, but stable enough in the polymerisation reaction conditions (2 h, 70 °C, DMSO:H_2O 8:2).

We also decided to select the potential drug from successful examples of polymer-drug conjugates previously described in literature, and with the potential for an improvement on their current application in the clinic.

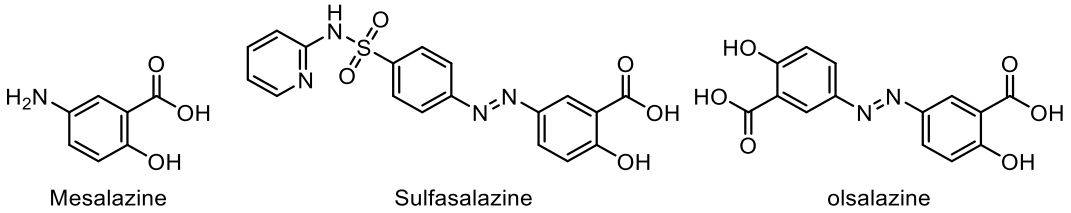
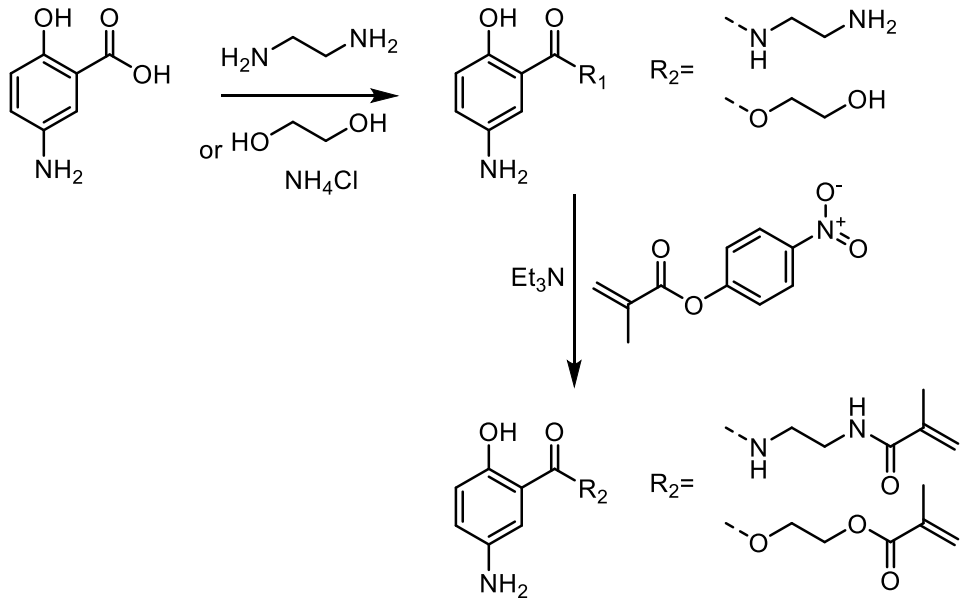


Figure 5.7 Chemical structures of mesalazine (left), and sulfasalazine (right), a clinically approved mesalazine co-drug.

Mesalazine (also known as mesalamine or 5-aminosalicylic acid, **Figure 5.7**) is a salicylate that exploits its action through modulation of the immune response[8], used to treat ulcerative colitis and Crohn's disease and other types of inflammatory bowel disease. It can also be administered as a prodrug - or more specifically a codrug, as following in vivo cleavage they can release two different drugs - covalently bound through an azo bond to form sulfapyridine (a sulfanilamide topical antibacterial[33], with potential free radical scavenger function[34]) to form sulfasalazine, or through an azo bond to a second molecule of mesalazine, to form olsalazine[35]. Importantly for this work, mesalazine has been previously employed to produce mesalazine-based monomers (**Scheme 5.2**) and successfully polymerised[10,36].



Scheme 5.2 Examples of synthesis of two different mesalazine-based monomers, methacryloyloxyethyl 5-amino salicylate (MOES) and N-methacryloylaminoethyl 5-amino salicylamide (MAES) described in the literature[10].

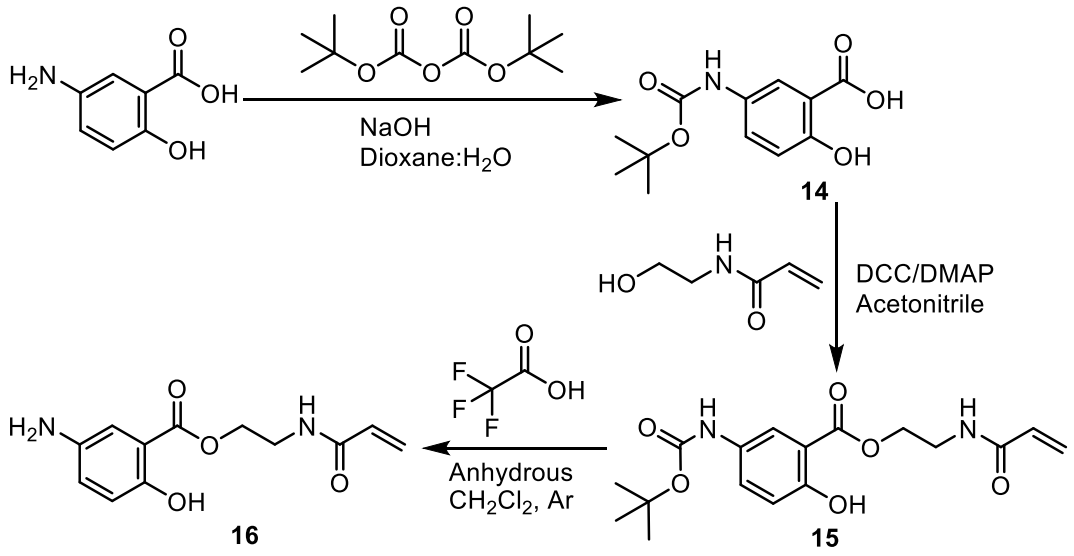
Here mesalazine was chosen as a model drug as ultimately our formulations aimed at intestinal drug delivery. Localised intestinal release of mesalazine from formulations has shown promise for the treatment of ulcerative colitis[37], and polymer-bound mesalazine could represent a new modality of achieving this topical approach. Additionally, mesalazine is often administered in very large doses (800 mg multiple times per day[8]) and the increase in weight caused by the polymer would not cause a marked decrease in compliance. The increase in overall formulation weight by introduction of a polymer could be potentially also be mitigated by an increased efficacy of this mesalazine formulation when compared to the sulfasalazine approach, thus requiring a smaller amount of mesalazine to achieve its therapeutic effect.

Here mesalazine was connected to the polymer backbone of the synthesised materials through ester bonds, as this would allow to synthesise the required monomers by simply adapting known literature protocols[10,36], and because ester bonds are relatively stable and are widely used in drug delivery as a prodrug approach[38]. Esters are mildly stable in neutral aqueous medium and are labile to

hydrolysis in acid and basic environments. Additionally, esters are susceptible to the effect of esterase enzymes, which are naturally present in the human gastrointestinal tract[39].

5.3.3 Mesalazine-based polymer-drug conjugates

The synthesis of the mesalazine monomer (**16**) was carried out starting from 2-hydroxyethyl acrylamide (HEA) as described in **Scheme 5.3**, by adapting a literature method for the synthesis of methacryloyloxyethyl 5-amino salicylate (MOES)[10]. This was done to synthesise an N-alkylsubstitutes acrylamide monomer that could be copolymerised using the reaction conditions already optimised in this work.



Scheme 5.3 Synthesis of mesalazine-based acrylamide monomer **(16)**.

Mesalazine has multiple potential reactive centres - a carboxylic acid, and a hydroxyl and amino groups. These groups can react with each other under coupling conditions (i.e. those used for the formation of an ester bond), resulting in unwanted side-products. To prevent this, during the first step the aromatic amino group was protected using di-tert-butyl-dicarbonate, leading to the

formation of a tert-butyl carbamate. This tert-butoxycarbonyl (Boc) protecting group is relatively unstable in acid aqueous solutions and can be easily removed under these conditions[40].

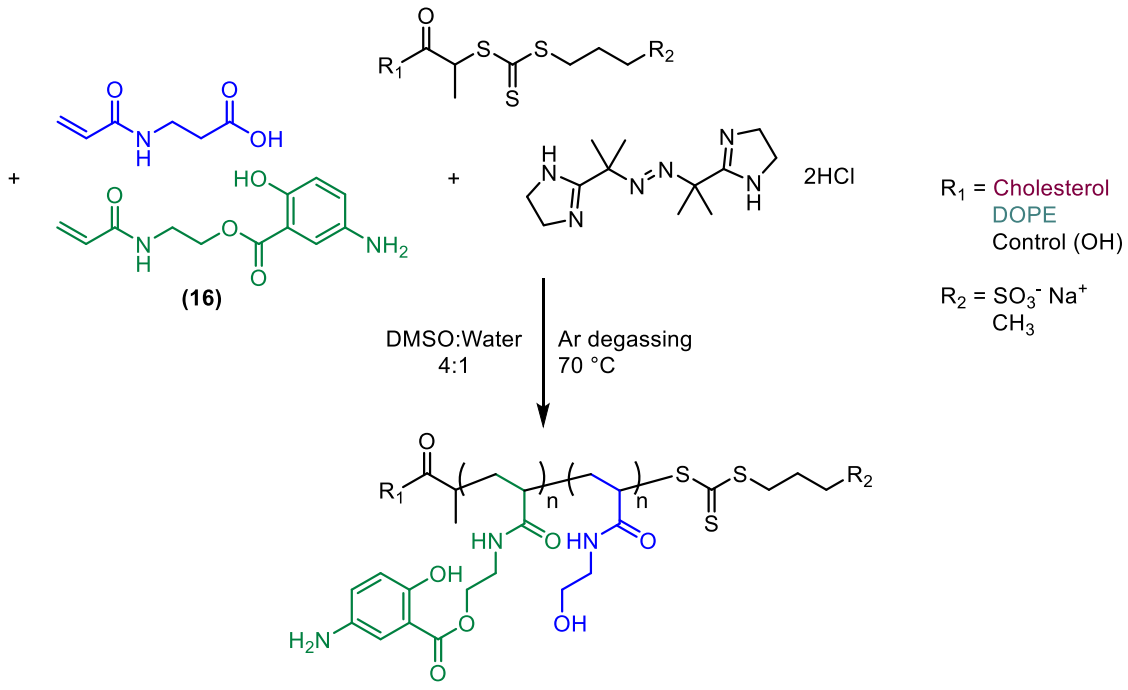
Boc-protected mesalazine **(14)** was synthesised by Steglich esterification[41], using DCC as the coupling agent and DMAP as the organocatalyst. The presence of DCC and DMAP promotes the esterification reaction, even with less reactive carboxylic acids and alcohols[42,43]. As amines can also participate in this reaction, it was necessary to protect with Boc in the previous step.

In this step, an excess (1.5 equivalents) of HEA was utilised to minimise the formation of an ester between two mesalazine molecules – as mesalazine also possess a hydroxyl group, albeit less reactive and more sterically hindered than that of HEA. Boc-protected mesalazine acrylamide **(15)** was purified by flash silica chromatography in 36.1 % yield.

Finally, the removal of the Boc protecting group was performed using trifluoroacetic acid. Carbamates are especially sensitive to acids, as when protonated they release CO_2 and, in the case of Boc-protected acyl amines, t-butyl cation. This cation is extremely unstable, and is rapidly deprotonated to form isobutylene, which is a gas at room temperature[44]. Both these volatile reaction co-products push the reaction to completion and can be fully removed by evaporation under reduced pressure during the reaction purification steps. The remaining traces of TFA were removed using a basic ion exchange resin (AmberLite™ IRA402 Cl). This step was particularly important, as incomplete removal of this strong acid may have caused unwanted cleaving of the ester bond during the polymerisation reaction. The dried product resulted in the final mesalazine monomer **(16)** in 88.3 % yield.

5.3.3.1 Synthesis of mesalazine-containing polymers

Mesalazine monomer **(16)** was copolymerised with hydrophilic monomer HEA to produce polymer-drug conjugated with good solubility in water. Additionally, HEA is also a *N*-alkyl acrylamide monomer, thus has a high rate of propagation (k_p) under the radical polymerisation conditions[45] already optimised in this PhD work for our RAFT agents. To produce these materials, all three RAFT agents described in **Chapter 2** were utilised, resulting in polymers with potential for membrane binding moieties, together with non-membrane inserting control PABTC polymers. To produce materials with structural analogies to those described in **Chapter 2**, DP ~ 50- and ~ 100 units were also synthesised. The conditions used (highlighted in **Scheme 5.4**) are the same single-phase polymerisation conditions described in **Chapter 2**, as these were successful with a wide variety of monomers.



Scheme 5.4 Scheme for the single-phase RAFT copolymerisation of HEA and **16** with the different RAFT agents - cholesterol, DOPE and PABTC (control).

As it can be observed in **Table 5.3**, the mesalazine-based polymers were synthesised with narrow dispersity, and we were able to maintain a good control over the monomer ratios and relatively low dispersity.

Table 5.3 Mesalazine **(16)**-HEA copolymers synthesised in this work

Code	DP[a]	HEA[b]	MES[b]	$Đ$[c]	$M_{n\ (NMR)}$ (kDa)
Chol-[(HEA)$_{80\%}$-*r*-(MES)$_{20\%}$]$_{80}$	80	64	16	1.15	13.1
Chol-[(HEA)$_{75\%}$-*r*-(MES)$_{25\%}$]$_{46}$	46	35	11	1.32	7.83
Chol-[(HEA)$_{90\%}$-*r*-(MES)$_{10\%}$]$_{44}$	44	40	4	1.17	6.66
DOPE-[(HEA)$_{90\%}$-*r*-(MES)$_{10\%}$]$_{44}$	44	40	4	1.16	6.57
PABTC-[(HEA)$_{90\%}$-*r*-(MES)$_{10\%}$]$_{38}$	38	34	4	1.08	5.61

[a] Degree of polymerisation (DP), calculated by ^{1}H NMR (see materials and methods). [b] HEA = hydroxyethyl acrylamide, MES = mesalazine-based monomer **(16)**. [c] Molecular weight dispersity ($M_{w/Mn}$, Đ) was determined by SEC (see materials and methods).

To compare the physicochemical characteristic of the mesalazine copolymers to the previously described polymers (**Chapter 2**), we measured the CAC of the mesalazine-based polymers. This showed that the CAC for the mesalazine-based copolymers was similar to the previously analysed analogous HEA-based homopolymers (**Figure 5.8**). Therefore, for the amphiphilic polymers, the introduction of mesalazine did not affect the polymer aggregation properties. Notably, unlike the PABTC control polymers described in **Chapter 2** (CAC > μM 2 for PABTC-[(HEA)$_{100\%}$]$_{50}$), PABTC-[(HEA)$_{90\%}$-*r*-(MES)$_{10\%}$]$_{38}$ showed a CAC of 0.29 μM showing that the introduction of a 10% of mesalazine repeating units made the resulting polymer sufficiently hydrophobic to induce polymer aggregation.

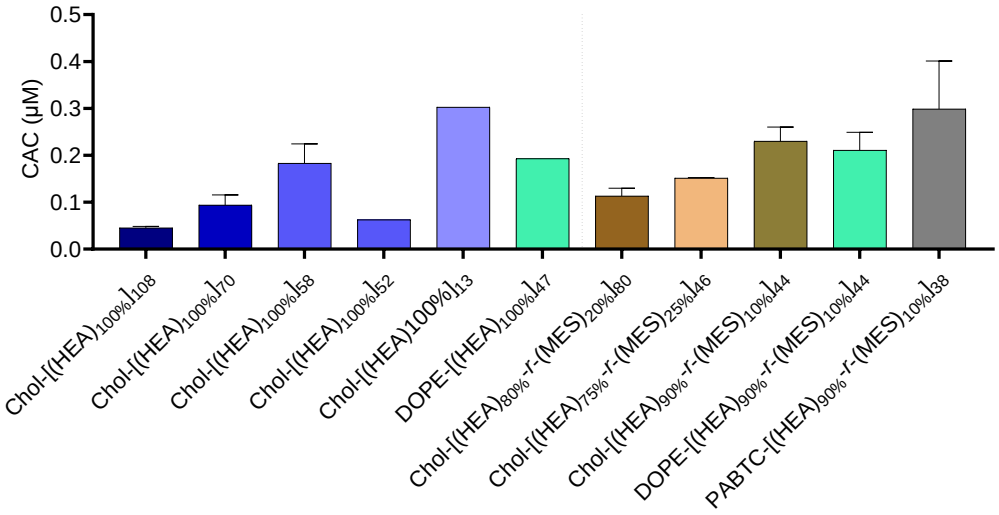


Figure 5.8 Comparison of critical aggregation concentration (CAC) in aqueous solution between the HEA-based polymers and the mesalazine-based copolymers.

To potentially cross the mucus layer, supramolecular polymer aggregates need to have an average diameter <100 nm[46]. Therefore, the average particle size and polidispersity of these polymers at concentrations above their respective CAC was investigated. The polymer suspensions were prepared in HBSS and filtered through a 0.4 μm filter to remove larger particles and precipitates.

Table 5.4 Particle size measurement results for aggregates of the mesalazine-based polymers, reporting the Z-average diameter (nm) and Pdi values.

Code	Z-average (d, nm)	Pdi
Chol-[(HEA)$_{80\%}$-*r*-(MES)$_{20\%}$]$_{80}$	52 ±1.7	0.478
Chol-[(HEA)$_{75\%}$-*r*-(MES)$_{25\%}$]$_{46}$	60 ±0.70	0.530
Chol-[(HEA)$_{90\%}$-*r*-(MES)$_{10\%}$]$_{44}$	67 ±0.78	0.469
PABTC-[(HEA)$_{90\%}$-*r*-(MES)$_{10\%}$]$_{38}$	46 ±2.4	0.650
DOPE-[(HEA)$_{90\%}$-*r*-(MES)$_{10\%}$]$_{44}$	72 ±0.47	0.440

The results showed that the average particle size was consistently smaller than what observed for the cholesterol polymer-nitrofurantoin aggregates (50 nm compared to 100-200 nm) (**Table 5.4**). However, the average polydispersity of the mesalazine-based polymer aggregates tended to be higher (0.5 compared to 0.2). This was caused by the presence of a numerically smaller population of larger aggregates. As it can be observed in the size distribution graphs, the mesalazine-based polymers were divided in two main populations: i) particles around 15-20 nm diameter that made up most of the aggregates in solution by number and volume; and ii) larger particles (around 100-200 nm diameter) which scattered light more intensely but made up a very small portion of the particles by number and volume (**Figure 5.9**).

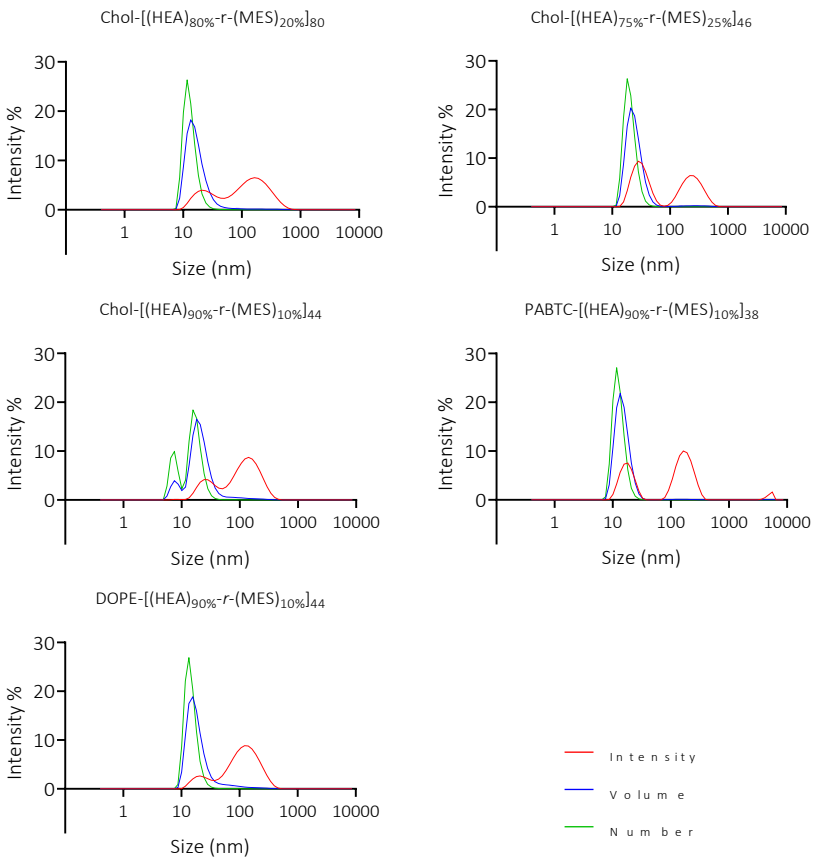


Figure 5.9 Particle size results obtained by DLS for the mesalazine-based polymers (10 mg/mL), comparing the intensity (red), volume (blue) and number (green) particle size distribution.

5.3.3.2 Effect of mesalazine-based polymers on Caco-2 cells

In **Chapter 3**, we investigated the nature of the interaction between our amphiphilic polymers and cell/artificial membranes. However, the introduction of the mesalazine repeating units could affect the interaction of the polymers with such lipid bilayers. In this part of this study Caco-2 cells were used, for consistency with the previous experiments and because mesalazine-bearing polymers would ideally be investigated for intestinal drug delivery.

Firstly, a PrestoBlue™ assay was carried out to assess the impact of these polymers on cell viability, and compare their IC_{50} with that of the structurally analogous non mesalazine-containing analogues. The cells were seeded at 10^4 cells/mL concentration in 96-well plates and cultured for 24 hours. Then, the cells were exposed for 24 hours to HBSS polymer solutions at different concentrations; after exposure, the polymer solutions were removed, and the cell metabolic activity was assessed. The activity was compared to a negative control (0% viability, cells treated with Triton X-100) and a positive control (100% viability, untreated Caco2 cells). Mesalazine itself can cause cytotoxicity, although at significantly higher concentrations than the ones employed within our studies (mM instead of μM)[47]. Therefore, the toxicity levels estimated with these experiments likely reflected the toxicity generated by the polymer-mesalazine-containing polymers as a whole, without effects from the potentially released mesalazine.

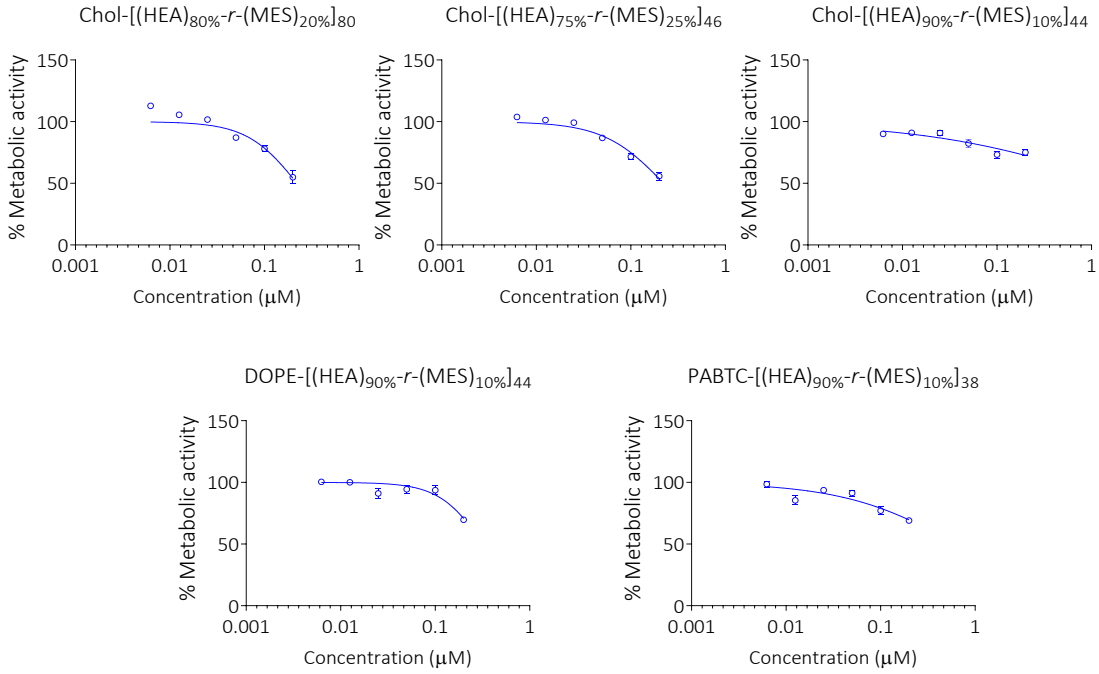


Figure 5.10 Metabolic activity of Caco2 cells incubated with mesalazine-containing polymers using PrestoBlue™ assay. Cells were incubated for 24 hours with polymer solutions at different concentrations. 0% metabolic activity is that of cells lysed with a 1% Triton X-100 solution and 100% metabolic activity was taken from that of untreated cells (n = 9, error bars expressed as SD).

The data (**Figure 5.10**) showed a slight decline in metabolic activity starting from 0.05 μM polymer concentrations, with the effect increasing for higher concentrations. The IC_{50} values (**Table 5.5**) were extrapolated using a nonlinear fit [inhibitor] *vs.* normalised response (variable slope) model. The impact on Caco-2 cell metabolic activity was similar to what observed for polymers that did not contain mesalazine, showing that the inclusion of this active did not radically change the toxicity profiles of the polymers. The most toxic polymers were the high % mesalazine-cholesterol based polymers Chol-[(HEA)$_{80\%}$-*r*-(MES)$_{20\%}$]$_{80}$ (IC_{50} 0.22 μM), Chol-[(HEA)$_{75\%}$-*r*-(MES)$_{25\%}$]$_{46}$ (IC_{50} 0.22 μM) and the DOPE-[(HEA)$_{90\%}$-*r*-(MES)$_{10\%}$]$_{44}$ (IC_{50} 0.32 μM) polymer. This is in agreement with the toxicity profiles illustrated in **Chapter 3**, where polymers with membrane-interacting moiety were shown to decrease cell viability at higher concentrations. PABTC-[(HEA)$_{90\%}$-*r*-(MES)$_{10\%}$]$_{38}$ also showed a similar IC_{50} (0.63 μM), therefore

the introduction of the hydrophobic mesalazine caused an increase in toxicity for this polymer.

Table 5.5 Cell metabolic activity - IC_{50} values for the mesalazine-based polymers. The values were calculated using an [inhibitor] versus normalised response nonlinear regression curve fitting.

Code	IC_{50} (μM)
Chol-[(HEA)$_{80\%}$-*r*-(MES)$_{20\%}$]$_{80}$	0.22
Chol-[(HEA)$_{75\%}$-*r*-(MES)$_{25\%}$]$_{46}$	0.22
Chol-[(HEA)$_{90\%}$-*r*-(MES)$_{10\%}$]$_{44}$	1.86
PABTC-[(HEA)$_{90\%}$-*r*-(MES)$_{10\%}$]$_{38}$	0.63
DOPE-[(HEA)$_{90\%}$-*r*-(MES)$_{10\%}$]$_{44}$	0.32

After establishing safe polymer concentrations to employ on Caco-2 cells, we investigated the effect of mesalazine-containing polymers on the membrane fluidity of Caco-2 cells, using a Laurdan assay (under the same conditions described in **Chapter 3**). Since these tests were run at different cell passage numbers than what described previously, in these experiments non mesalazine-containing polymers were also tested, for comparison. These polymers showed effects on membrane fluidity analogous to those observed previously, confirming that the number of cell passages did not have an effect on the outcome of these cell fluidity experiments

As it can be observed in **Figure 5.11 A**, both cholesterol-based polymers Chol-[(HEA)$_{80\%}$-*r*-(MES)$_{20\%}$]$_{80}$ and Chol-[(HEA)$_{75\%}$-*r*-(MES)$_{25\%}$]$_{46}$ markedly increased the cell membrane fluidity in a concentration-dependent fashion, with the effect persisting after replacing the polymer solutions with fresh medium (**Figure 5.11 B**). The trend observed previously and described in **Chapter 3** was confirmed,

where the shorter polymers with a cholesterol chain-end had a larger effect on cell membrane fluidity.

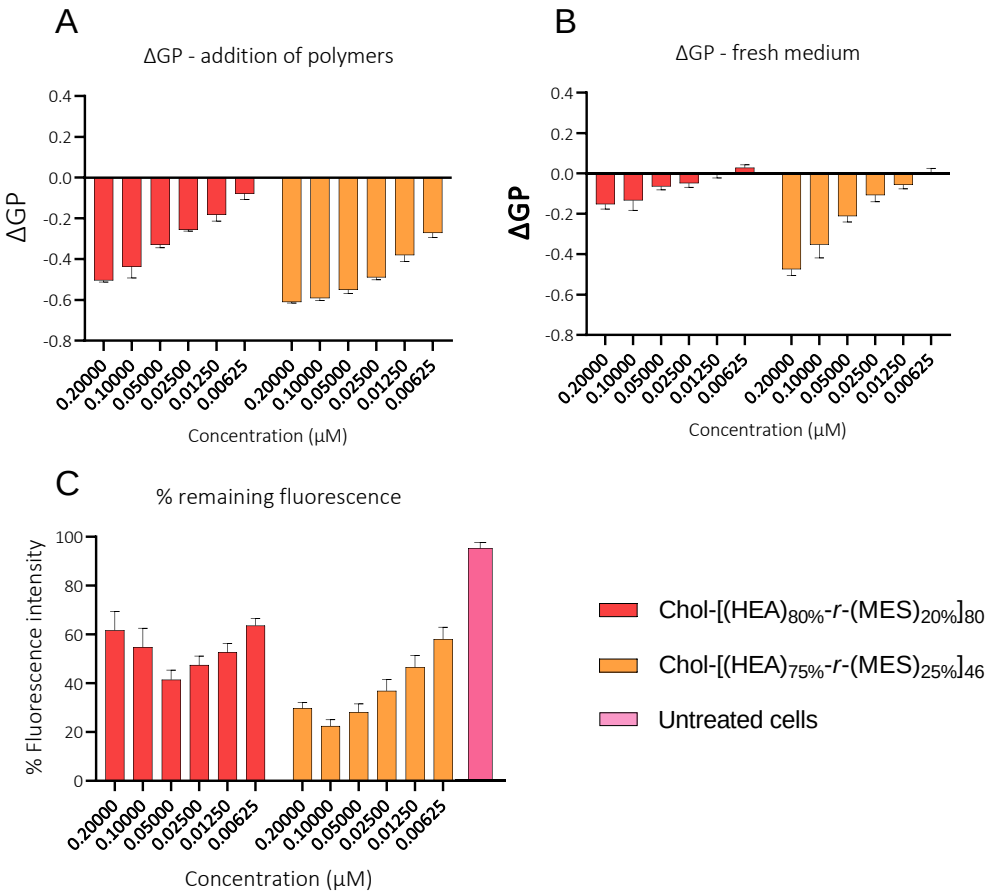


Figure 5.11 Change of membrane fluidity results for the different polymer solutions (Chol-[(HEA)$_{80\%}$-r-(MES)$_{20\%}$]$_{80}$ and Chol-[(HEA)$_{75\%}$-r-(MES)$_{25\%}$]$_{46}$) and Caco-2 cells (n = 6, error bars expressed as SD) analysed to identify the polymer-Laurdan interaction involving cells, with results expressed as ΔGP. **A** refers to the values obtained for cells treated with Laurdan and polymers, then analysed for fluorescence to calculate the ΔGP. **B** refers to samples prepared as in point A, where the supernatant was then removed and replaced with fresh supernatant **C** Fluorescence intensity (%) of Laurdan dye (λ_{em} = 440 and 490 nm) for cells with fresh medium. The values were calculated on a well-to-well basis, using the starting fluorescence intensity (cells+bound Laurdan+polymers) as 100%.

As previously described (**Chapter 3**), analysis of the Laurdan fluorescence intensity of samples with Caco2 cells treated with Laurdan and the test polymers was carried out before and after replacing the polymer-containing cell supernatant with fresh medium. This allowed us to evaluate the extent to which the polymers interacting with cell membranes were extracting the membrane-bound Laurdan

dye. For this calculation, the starting fluorescence intensity (averaged between λ_{em} = 440 and 490 nm and set as 100%) was measured when the polymer solutions were added to the Laurdan-loaded cells. In **Figure 5.11 C**, the observed fluorescence intensity % values decreased after removing the polymer supernatant and replacing with fresh medium. This effect is in line with what observed previously, where membrane-binding polymers were shown to extract a proportion of the Laurdan dye from the cell membranes. We could also observe that the longer polymer (Chol-[(HEA)$_{80\%}$-*r*-(MES)$_{20\%}$]$_{80}$, red bars) caused a lower extent of Laurdan dye removal from cell membranes, confirming the trend of the longer polymers tending to interact less with the cell membranes.

The effect on cell membrane fluidity was also tested for the other mesalazine-based polymers, namely a cholesterol-based polymer with a smaller proportion of mesalazine (Chol-[(HEA)$_{90\%}$-*r*-(MES)$_{10\%}$]$_{44}$), a DOPE-containing mesalazine polymer (DOPE-[(HEA)$_{90\%}$-*r*-(MES)$_{10\%}$]$_{44}$) and a control mesalazine polymer (PABTC-[(HEA)$_{90\%}$-*r*-(MES)$_{10\%}$]$_{38}$). As it can be observed in **Figure 5.12 A**, the effect was similar to what described previously for the analogous non mesalazine-containing materials, except for the control polymer. The latter, despite the absence of membrane-inserting chain ends was found to increase the cell membrane fluidity. This effect was present also after the removal of the supernatant and replacement with fresh medium (**Figure 5.12 B**) and was ascribed to the presence of lipophilic mesalazine repeating units that granted this polymer amphiphilic membrane-interacting capabilities. Statistical analysed of the data (two-way ANOVA, with Tukey's multiple comparisons test) showed no statistically significant difference between polymers with different alpha-chain ends (cholesterol, DOPE and PABTC) at the same molar concentration.

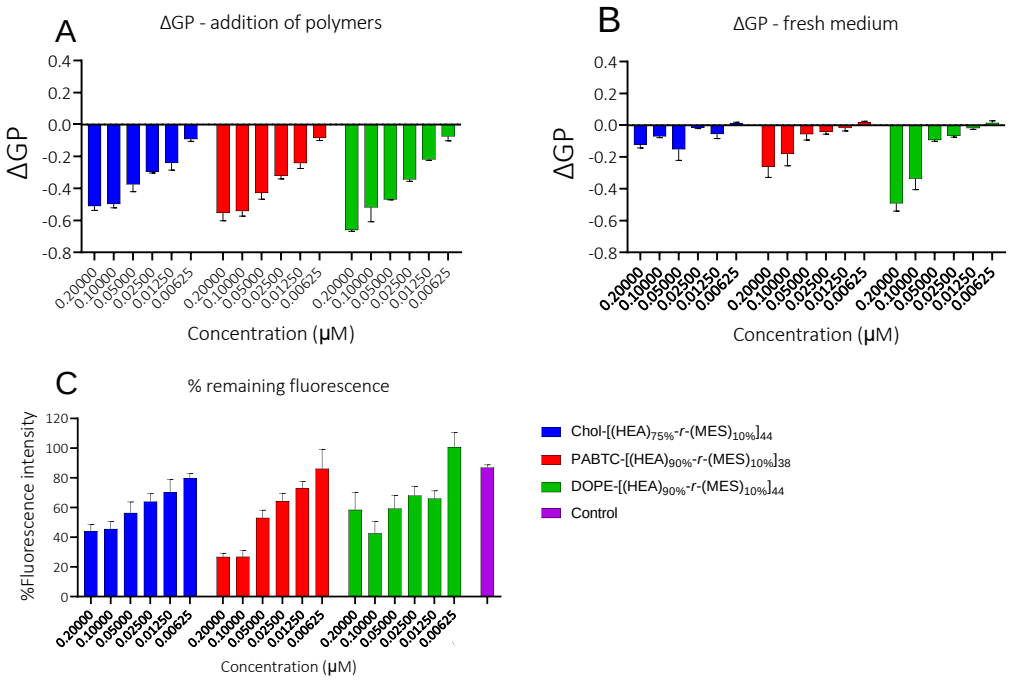


Figure 5.12 Change of membrane fluidity results for the different polymer solutions (Chol-[(HEA)$_{90\%}$-r-(MES)$_{10\%}$]$_{44}$, PABTC-[(HEA)$_{90\%}$-r-(MES)$_{10\%}$]$_{38}$ and DOPE-[(HEA)$_{90\%}$-r-(MES)$_{10\%}$]$_{44}$) and Caco-2 cells (n = 6, error bars expressed as SD) analysed to identify the polymer-Laurdan interaction involving cells, with results expressed as ΔGP. **A** refers to the values obtained for cells treated with Laurdan and polymers, then analysed for fluorescence to calculate the ΔGP. **B** refers to samples prepared as in point A, where the supernatant was then removed and replaced with fresh supernatant **C** Fluorescence intensity (%) of Laurdan dye (λ_{em} = 440 and 490 nm) for cells with fresh medium. The values were calculated on a well-to-well basis, using the starting fluorescence intensity (cells+bound Laurdan+polymers) as 100%

We also tested these three polymers for the Laurdan fluorescence intensity % to evaluate removal of membrane-bound dye caused by the polymers. The results (**Figure 5.12C**) showed that, similarly to previously described membrane-interacting polymers, these mesalazine-bearing polymers appeared to extract some of the membrane-bound Laurdan dye. The results obtained for the control polymer (red bars) confirmed what observed in the cell membrane fluidity assay, as this control polymer with the addition of mesalazine was capable of interaction with the cell membranes. The effect was concentration-dependent for all polymers, as previously observed for the non mesalazine-containing membrane-inserting polymers described in **Chapter 3**.

Similarly to what described in **Chapter 3**, we evaluated changes in cell membrane fluidity over time - 50 minutes – when Caco-2 cells were exposed to polymers (**Figure 5.13**). As previously described for the cholesterol-based polymers, we observed a sharp decrease in cell membrane fluidity as soon as the treatments were added (t0). The effect was concentration dependent, and it appeared more stable than what observed previously for non mesalazine-bearing polymers (**Chapter 3**). The more stable membrane fluidity increase caused by Chol-[(HEA)$_{80\%}$-*r*-(MES)$_{20\%}$]$_{80}$ when compared with Chol-HEA homopolymers could be explained by a stronger polymer membrane interaction caused by the presence of the hydrophobic mesalazine monomers.

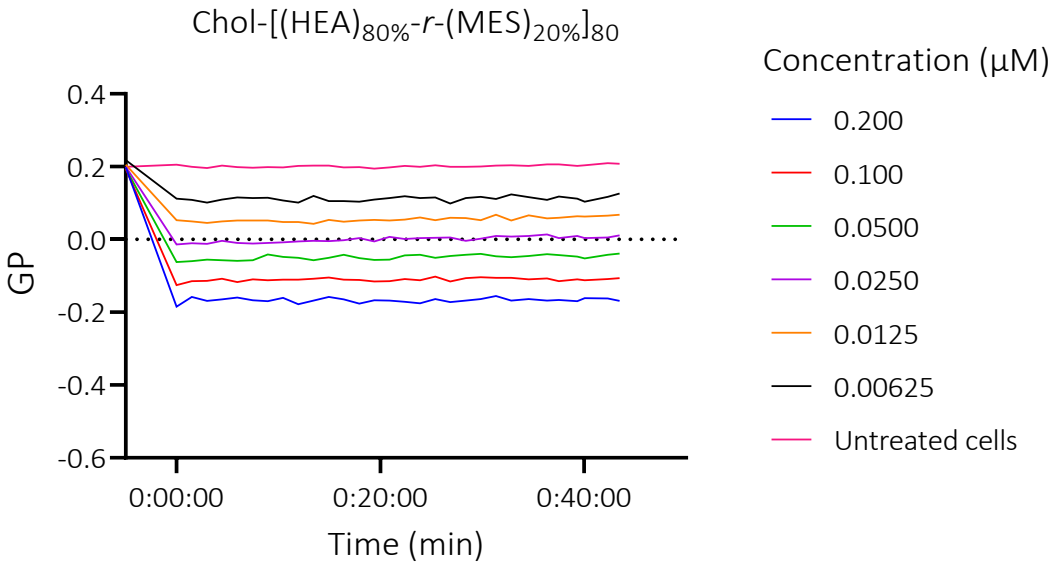


Figure 5.13 Membrane fluidity kinetic assay (Laurdan on Caco2 cells, different µM concentrations incubation for 50 minutes) for the Chol-[(HEA)$_{80\%}$-r-(MES)$_{20\%}$]$_{80}$.

5.3.3.3 Mesalazine release from polymers

The release of mesalazine from the mesalazine-loaded polymers was evaluated using a medium that simulates the intestinal environment. Fasted State Simulated Intestinal Fluid (FaSSIF) was prepared as previously described in literature[48]. This medium contains taurocholate and lecithin micelles[49] to produce a model of the

intestinal luminal fluid in the fasted state[50]. For this investigation, we employed Slide-a-Lyzer™ Mini dialysis devices, which allow for drug release experiments to be carried out[51] using small quantities of mesalazine-containing polymers[51].

To simulate the intestinal environment throughout the release assay, we needed to ensure that sink conditions were established. As defined by the European Pharmacopoeia, a drug is considered to be in sink conditions when it is in a volume of dissolution 3 to 10 times higher than the drug's maximum solubility[52]. These conditions are designed to ensure correlation between the *in vitro* data obtained and the *in vivo* observations[53]. This is due to the fact that in more complex systems, there is continuous removal of drug as it is released, and the drug concentration never reaches saturation.

Since mesalazine release was assessed at different pH values, sink conditions were established against the pH where mesalazine has the lowest solubility at 37 °C (pH 3, 1.5 mg/mL)[54]. The mesalazine-bearing polymer with the highest w/w mesalazine percentage is Chol-[$(HEA)_{75\%}$-*r*-$(MES)_{25\%}$]$_{46}$, 23% w/w mesalazine. At the highest tested concentration of the polymer (3 mg/mL), there would be a maximum of 0.69 mg/mL mesalazine in the donor compartment. Since the donor compartment was loaded with 0.3 mL donor solution, the maximum amount of mesalazine releasable in each mini dialysis device was 0.23 mg. This equated to 0.15 mg/mL in the 1.5 mL acceptor compartment. This value is 10% of the maximum solubility of mesalazine at the lowest known solubility registered for aqueous medium (between pH 1 and pH 6.7), confirming the sink conditions of these assays.

These experiments were designed to investigate the release kinetics of the drug from Chol-[$(HEA)_{75\%}$-*r*-$(MES)_{25\%}$]$_{46}$ polymer. The first experiment was conducted to ascertain whether the presence of esterase enzymes – porcine esterase in this case - could influence the drug release. Porcine esterase was employed at a 20

IU/mL concentration, as previously described in literature for release of methotrexate from a polyglycerol adipate polymer[55].

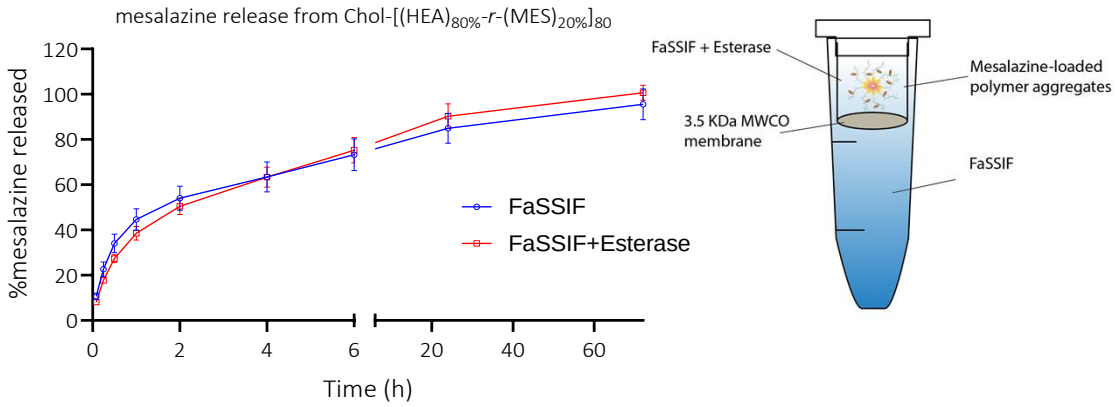


Figure 5.14 Mesalazine release (left) over the course of 3 days (n = 4, error bars expressed as SD), from Chol-[(HEA)$_{80\%}$-r-(MES)$_{20\%}$]$_{80}$ polymer, with and without the presence of porcine esterase enzyme. Scheme of the setup for the Slide-a-lyzer™ mini dialysis device release assay (right), showing the donor and acceptor compartments. The example shown represents the approach employed with the introduction of porcine esterase in the donor compartment.

The results of this comparison are illustrated in **Figure 5.14** and showed that most of the mesalazine (70%) was released over the course of the first six hours, while the remaining 30% was fully released within 72 hours. As it can be observed, the presence of esterase has little to no impact on the release of the drug. Although the effects were not statistically significant (two-way ANOVA, Šídák's multiple comparisons test), we could observe a slightly slower release in the first 2 hours and then a faster and more complete release in the presence of esterase. The difference between presence/absence of porcine esterase was non-statistically significant because two large molecules such as a polymer and an enzyme tended to not interact easily due to the steric hindrance caused by two large molecules. Previous studies[56,57] have shown esterase breakdown of methacrylate polymers; however, this effect was not observed for this mesalazine-based polymer as it is based on amide chemistry.

Since we observed that esterase was not significantly impacting the release of mesalazine, we ran the successive tests in FaSSIF (without esterase) and different types of medium.

A second series of experiments with buffers medium at pH levels was then run: A) acetate buffer 0.1 M (pH 4.0); B) FaSSIF 0.1 M buffer (pH 6.5) and C) phosphate buffer 0.1 M (pH 7.4). These different buffers were selected to observe changes in the release kinetics of mesalazine based on the acidity of the medium.

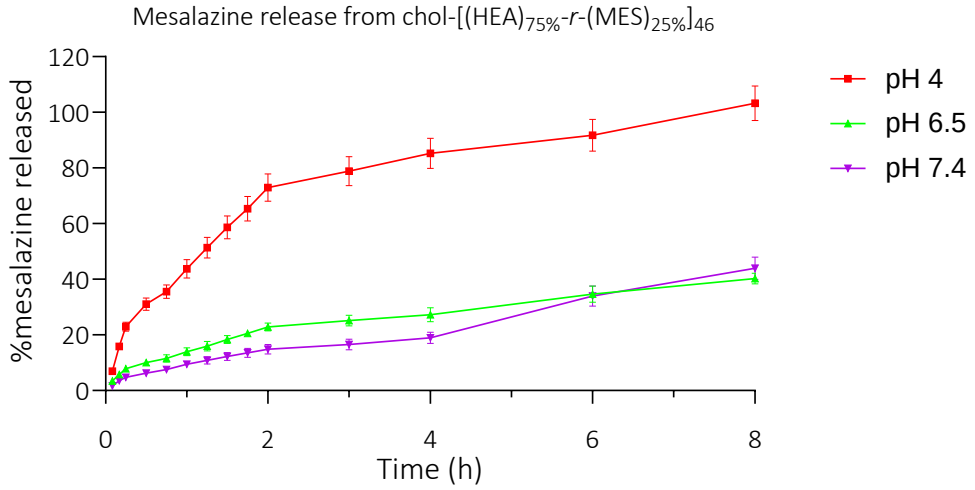
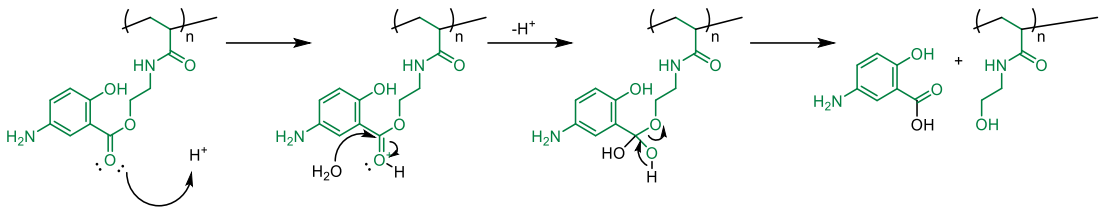


Figure 5.15 Release of Mesalazine from Chol-[(HEA)$_{75\%}$-r-(MES)$_{25\%}$]$_{46}$ (n = 4, error bars expressed as SD) comparing different pH conditions, focusing on the first 8 hours of release.

The results (**Figure 5.15**) showed that there was a marked increase in release when the polymer was in acidified aqueous medium. We could observe the mesalazine being fully released in 8 hours in acidic medium. When the polymers were exposed to more neutral aqueous solutions, the mesalazine release was statistically significantly slower, reaching only 30-40% release over the course of 8 hours. Therefore, the main mechanism of release appeared to be an acid-catalysed cleaving of the ester bond between mesalazine and HEA (**Scheme 5.5**). It is possible that protonation of mesalazine amine group which occurs under

increasingly more acidic conditions (pK_{aH} ~ 2) could also affect the rate of hydrolysis of the mesalazine ester group.



Scheme 5.5 Mechanism of acid-catalysed hydrolysis for mesalazine release from the polymers.

The remaining polymers were then tested under analogous conditions, to understand whether polymers with a different membrane-inserting groups at the polymer chain-ends and mesalazine content would result in different kinetics of drug release. When comparing Chol-[(HEA)$_{75\%}$-*r*-(MES)$_{25\%}$]$_{46}$ and Chol-[(HEA)$_{90\%}$-*r*-(MES)$_{10\%}$]$_{44}$, with very similar chain length but different mesalazine content, the one with the smaller percentage of mesalazine (10%) resulted in the faster release (**Figure 5.16**). This may be ascribed to the lower lipophilicity of Chol-[(HEA)$_{90\%}$-*r*-(MES)$_{10\%}$]$_{44}$, which would increase the exposure of the ester groups of the incorporated mesalazine to water, causing a faster release of the drug.

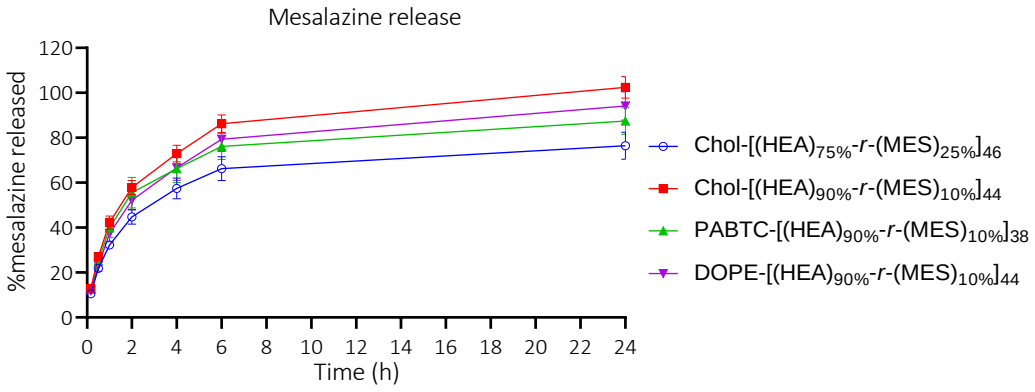


Figure 5.16 Release of mesalazine from Chol-[(HEA)$_{75\%}$-r-(MES)$_{25\%}$]$_{46}$, Chol-[(HEA)$_{90\%}$-r-(MES)$_{10\%}$]$_{44}$, PABTC-[(HEA)$_{90\%}$-r-(MES)$_{10\%}$]$_{38}$ and DOPE-[(HEA)$_{90\%}$-r-(MES)$_{10\%}$]$_{44}$ in FaSSIF over the course of 24 hours (n = 4, error bars expressed as SD).

5.4 Concluding Remarks

In summary in this part of our work we successfully encapsulated two different drugs with our polymers, using two different approaches:

I. Nitrofurantoin was ionomerically encapsulated, with different degrees of success. However, earlier experiments (not reported) showed a low degree of reproducibility for these processes.

II. Mesalazine was successfully incorporated by producing a mesalazine-based monomer and co-polymerising it to synthesise a small library of 5 polymers, with different structural characteristics (chain length, mesalazine content, membrane anchoring chain-end moiety).

The mesalazine-based polymers showed interactions with cells similar to what found for the non drug-conjugated polymers in **Chapter 3**, confirming that the introduction of this new mesalazine monomer did not alter the membrane-interaction properties of the polymers. The cell membrane fluidification increase described in **Chapter 3** and attributed to amphiphilic polymers was enhanced by the introduction of mesalazine in the polymer structure. Additionally, control polymers, which in **Chapter 3** did not show effects on the cell membrane fluidity, caused cell membrane fluidity increase as mesalazine copolymers.

The kinetics of mesalazine release from these polymers was investigated, showing that complete release could be achieved withing 24 hours in FaSSIF and PBS buffer, and faster complete release could be achieved in acid medium at pH 4.0 (8 hours). Although minimal hydrolysis was observed under neutral conditions during the release studies and the mesalazine content in the purified polymers were in line to those expected based on initial monomer feed composition one could not completely rule out that a small proportion of mesalazine was not cleaved from the monomer and polymers during the polymerisation reactions (2 h at 70 °C) and purification by dialysis. This point will be investigated in future

studies, as well as potential application of mesalazine copolymers formulated for *in vivo* applications, to evaluate the potential of these formulations in more complex models.

5.5 Bibliography

(1) Oh, K. T.; Bronich, T. K.; Bromberg, L.; Hatton, T. A.; Kabanov, A. V. Block Ionomer Complexes as Prospective Nanocontainers for Drug Delivery. *J. Control. Release* **2006**, *115* (1), 9–17. https://doi.org/10.1016/j.jconrel.2006.06.030.

(2) Ramasamy, T.; Kim, J.; Choi, H. G.; Yong, C. S.; Kim, J. O. Novel Dual Drug-Loaded Block Ionomer Complex Micelles for Enhancing the Efficacy of Chemotherapy Treatments. *J. Biomed. Nanotechnol.* **2014**, *10* (7), 1304–1312. https://doi.org/10.1166/jbn.2014.1821.

(3) Li, M.; Song, W.; Tang, Z.; Lv, S.; Lin, L.; Sun, H.; Li, Q.; Yang, Y.; Hong, H.; Chen, X. Nanoscaled Poly(l-Glutamic Acid)/Doxorubicin-Amphiphile Complex as PH-Responsive Drug Delivery System for Effective Treatment of Nonsmall Cell Lung Cancer. *ACS Appl. Mater. Interfaces* **2013**, *5* (5), 1781–1792. https://doi.org/10.1021/am303073u.

(4) Elvira, C.; Gallardo, A.; San Roman, J.; Cifuentes, A. Covalent Polymer-Drug Conjugates. *Molecules* **2005**, *10* (1), 114–125. https://doi.org/10.3390/10010114.

(5) Mastrotto, F.; Salmaso, S.; Alexander, C.; Mantovani, G.; Caliceti, P. Novel PH-Responsive Nanovectors for Controlled Release of Ionisable Drugs. *J. Mater. Chem. B* **2013**, *1* (39), 5335. https://doi.org/10.1039/c3tb20360c.

(6) Nieto-Orellana, A.; Di Antonio, M.; Conte, C.; Falcone, F. H.; Bosquillon, C.; Childerhouse, N.; Mantovani, G.; Stolnik, S. Effect of Polymer Topology on Non-Covalent Polymer–Protein Complexation: Miktoarm versus Linear MPEG-Poly(Glutamic Acid) Copolymers. *Polym. Chem.* **2017**, *8* (14), 2210–2220. https://doi.org/10.1039/C7PY00169J.

(7) Nieto-Orellana, A.; Li, H.; Rosiere, R.; Wauthoz, N.; Williams, H.; Monteiro, C. J.; Bosquillon, C.; Childerhouse, N.; Keegan, G.; Coghlan, D.; Mantovani, G.; Stolnik, S. Targeted PEG-Poly(Glutamic Acid) Complexes for Inhalation Protein Delivery to the Lung. *J. Control. Release* **2019**, *316* (June), 250–262. https://doi.org/10.1016/j.jconrel.2019.10.012.

(8) Brunton, L.; Chabner, B.; Knollman, B. *Goodman & Gilman's The Pharmacological Basis of Therapeutics*; 2013; Vol. 53. https://doi.org/10.1017/CBO9781107415324.004.

(9) Bates, T. R.; Young, J. M.; Wu, C. M.; Rosenberg, H. A. PH-dependent Dissolution Rate of Nitrofurantoin from Commercial Suspensions, Tablets, and Capsules. *J. Pharm. Sci.* **1974**, *63* (4), 643–645. https://doi.org/10.1002/jps.2600630441.

(10) Davaran, S.; Hanaee, J.; Khosravi, A. Release of 5-Amino Salicylic Acid from Acrylic Type Polymeric Prodrugs Designed for Colon-Specific Drug Delivery. *J. Control. Release* **1999**, *58* (3), 279–287. https://doi.org/10.1016/S0168-3659(98)00167-9.

(11) Abinusawa, A.; Tenjarla, S. Release of 5-Aminosalicylic Acid (5-ASA) from Mesalamine Formulations at Various PH Levels. *Adv. Ther.* **2015**, *32* (5), 477–484. https://doi.org/10.1007/s12325-015-0206-4.

(12) Fasiku, V.; Amuhaya, E. K.; Rajab, K. M.; Omolo, C. A. Nano/Microparticles Encapsulation Via Covalent Drug Conjugation. *Intechopen* **2020**, No. Cell Interaction-Regulation of Immune Responses, Disease Development and

Management Strategies, 1–15.

(13) Moharana, A. K.; Banerjee, M.; Panda, S.; Muduli, J. N. Development and Validation of UV Spectrophotometric Method for the Determination of Mesalamine in Bulk and Tablet Formulation. *Int. J. Pharm. Pharm. Sci.* **2011**, *3* (2), 19–21.

(14) Charman, W. N.; Christy, D. P.; Geunin, E. P.; Monkhouse, D. C. Interaction between Calcium, a Model Divalent Cation, and a Range of Poly (Acrylic Acid) Resins as a Function of Solution Ph. *Drug Dev. Ind. Pharm.* **1991**, *17* (2), 271–280. https://doi.org/10.3109/03639049109043824.

(15) Sigma-Aldrich. Nitrofurantoin. *Sigma Product Information*.

(16) Chen, L. -K; Cadwallader, D. E.; Jun, H. W. Nitrofurantoin Solubility in Aqueous Urea and Creatinine Solutions. *J. Pharm. Sci.* **1976**, *65* (6), 868–872. https://doi.org/10.1002/jps.2600650617.

(17) Hornig, S.; Heinze, T.; Becer, C. R.; Schubert, U. S. Synthetic Polymeric Nanoparticles by Nanoprecipitation. *J. Mater. Chem.* **2009**, *19* (23), 3838–3840. https://doi.org/10.1039/b906556n.

(18) Schubert, S.; Delaney, J. T.; Schubert, U. S. Nanoprecipitation and Nanoformulation of Polymers: From History to Powerful Possibilities beyond Poly(Lactic Acid). *Soft Matter* **2011**, *7* (5), 1581–1588. https://doi.org/10.1039/c0sm00862a.

(19) Liu, Y.; Yang, G.; Baby, T.; Tengjisi; Chen, D.; Weitz, D. A.; Zhao, C. Stable Polymer Nanoparticles with Exceptionally High Drug Loading by Sequential Nanoprecipitation. *Angew. Chemie* **2020**, *132* (12), 4750–4758. https://doi.org/10.1002/ange.201913539.

(20) GE Healthcare. PD10 Desalting Column - Product Booklet. *GE Healthc. Bio-Sciences* **2007**, 1–12.

(21) Xu, X.; Khan, M. A.; Burgess, D. J. A Quality by Design (QbD) Case Study on Liposomes Containing Hydrophilic API: I. Formulation, Processing Design and Risk Assessment. *Int. J. Pharm.* **2011**, *419* (1–2), 52–59. https://doi.org/10.1016/j.ijpharm.2011.07.012.

(22) Torchilin, V. P. Structure and Design of Polymeric Surfactant-Based Drug Delivery Systems. *J. Control. Release* **2001**, *73* (2–3), 137–172. https://doi.org/10.1016/S0168-3659(01)00299-1.

(23) Li, Y.; Bronich, T. K.; Chelushkin, P. S.; Kabanov, A. V. Dynamic Properties of Block Ionomer Complexes with Polyion Complex Cores. *Macromolecules* **2008**, *41* (15), 5863–5868. https://doi.org/10.1021/ma702671w.

(24) Mastrotto, F.; Breen, A. F.; Sicilia, G.; Murdan, S.; Johnstone, A. D.; Marsh, G. E.; Grainger-Boultby, C.; Russell, N. A.; Alexander, C.; Mantovani, G. One-Pot RAFT and Fast Polymersomes Assembly: A "beeline" from Monomers to Drug-Loaded Nanovectors. *Polym. Chem.* **2016**, *7* (44), 6414–6424. https://doi.org/10.1039/c6py01292b.

(25) Martin, L.; Gody, G.; Perrier, S. Preparation of Complex Multiblock Copolymers via Aqueous RAFT Polymerization at Room Temperature. *Polym. Chem.* **2015**, *6* (27), 4875–4886. https://doi.org/10.1039/c5py00478k.

(26) Gody, G.; Maschmeyer, T.; Zetterlund, P. B.; Perrier, S. Pushing the Limit of the RAFT Process: Multiblock Copolymers by One-Pot Rapid Multiple Chain Extensions at Full Monomer Conversion. *Macromolecules* **2014**, *47*

(10), 3451–3460. https://doi.org/10.1021/ma402435n.

(27) Gody, G.; Barbey, R.; Danial, M.; Perrier, S. Ultrafast RAFT Polymerization: Multiblock Copolymers within Minutes. *Polym. Chem.* **2015**, *6* (9), 1502–1511. https://doi.org/10.1039/c4py01251h.

(28) Wijma, R. A.; Fransen, F.; Muller, A. E.; Mouton, J. W. Optimizing Dosing of Nitrofurantoin from a PK/PD Point of View: What Do We Need to Know? *Drug Resist. Updat.* **2019**, *43* (November 2018), 1–9. https://doi.org/10.1016/j.drup.2019.03.001.

(29) Singer, J. W.; Bhatt, R.; Tulinsky, J.; Buhler, K. R.; Heasley, E.; Klein, P.; De Vries, P. Water-Soluble Poly-(L-Glutamic Acid)-Gly-Camptothecin Conjugates Enhance Camptothecin Stability and Efficacy in Vivo. *J. Control. Release* **2001**, *74* (1–3), 243–247. https://doi.org/10.1016/S0168-3659(01)00323-6.

(30) Singer, J. W.; Vries, P. D. E.; Bhatt, R.; Tulinsky, J.; Wallace, S. Conjugation of Camptothecins to Poly- (L -Glutamic Acid). *Ann. New York Acad. Sci.* **2006**, *922* (1), 136–150.

(31) Lele, B. S.; Hoffman, A. S. Mucoadhesive Drug Carriers Based on Complexes of Poly(Acrylic Acid) and PEGylated Drugs Having Hydrolysable PEG-Anhydride-Drug Linkages. *J. Control. Release* **2000**, *69* (2), 237–248. https://doi.org/10.1016/S0168-3659(00)00303-5.

(32) Brogden, R. N.; Sorkin, E. M. Mesalazine: A Review of Its Pharmacodynamic and Pharmacokinetic Properties, and Therapeutic Potential in Chronic Inflammatory Bowel Disease. *Drugs* **1989**, *38* (4), 500–523. https://doi.org/10.2165/00003495-198938040-00003.

(33) McIlwain, H. The Biochemical Specificity of Sulfanilamide and of Other Antibacterial Agents. *Science (80-.).* **1942**, *95* (2472), 509–511. https://doi.org/10.1126/science.95.2472.509.

(34) Joshi, R.; Kumar, S.; Unnikrishnan, M.; Mukherjee, T. Free Radical Scavenging Reactions of Sulfasalazine, 5-Aminosalicylic Acid and Sulfapyridine: Mechanistic Aspects and Antioxidant Activity. *Free Radic. Res.* **2005**, *39* (11), 1163–1172. https://doi.org/10.1080/10715760500177880.

(35) Wadworth, A. N.; Fitton, A. Olsalazine. *Drugs* **1991**, *41* (4), 647–664. https://doi.org/10.2165/00003495-199141040-00009.

(36) Babazadeh, M.; Edjlali, L.; Rashidian, L. Application of 2-Hydroxyethyl Methacrylate Polymers in Controlled Release of 5-Aminosalicylic Acid as a Colon-Specific Drug. *J. Polym. Res.* **2007**, *14* (3), 207–213. https://doi.org/10.1007/s10965-007-9099-5.

(37) Seibold, F.; Fournier, N.; Beglinger, C.; Mottet, C.; Pittet, V.; Rogler, G. Topical Therapy Is Underused in Patients with Ulcerative Colitis. *J. Crohn's Colitis* **2014**, *8* (1), 56–63. https://doi.org/10.1016/j.crohns.2013.03.005.

(38) Rautio, J.; Kumpulainen, H.; Heimbach, T.; Oliyai, R.; Oh, D.; Järvinen, T.; Savolainen, J. Prodrugs: Design and Clinical Applications. *Nat. Rev. Drug Discov.* **2008**, *7* (3), 255–270. https://doi.org/10.1038/nrd2468.

(39) Fukami, T.; Yokoi, T. The Emerging Role of Human Esterases. *Drug Metab. Pharmacokinet.* **2012**, *27* (5), 466–477. https://doi.org/10.2133/dmpk.DMPK-12-RV-042.

(40) Clayden, J.; Greeves, N.; Warren, S. *Organic Chemistry*, 2nd ed.; Oxford

University Press, 2012; Vol. 85. https://doi.org/10.1021/ja00892a048.

(41) Bernhard, N.; Wolfgang, S. Simple Method for the Esterification of Carboxylic Acids. *Angew. Chemie Int. Ed. English* **1978**, *17* (7), 522–524.

(42) Kvasnica, M. Dicyclohexylcarbodiimide (DCC). *Synlett* **2007**, No. 14, 2306–2307. https://doi.org/10.1055/s-2007-985575.

(43) Xu, S.; Held, I.; Kempf, B.; Mayr, H.; Steglich, W.; Zipse, H. The DMAP-Catalyzed Acetylation of Alcohols - A Mechanistic Study (DMAP = 4-(Dimethylamino)Pyridine). *Chem. - A Eur. J.* **2005**, *11* (16), 4751–4757. https://doi.org/10.1002/chem.200500398.

(44) Gibson, S.; Bergmeier, S. C.; Rapoport, H. Selective Removal of an N-BOC Protecting Group in the Presence of a Tert-Butyl Ester and Other Acid-Sensitive Groups. *J Org Chem* **1994**, *59*, 3216–3218.

(45) Valdebenito, A.; Encinas, M. V. Effect of Solvent on the Free Radical Polymerization of N,N-Dimethylacrylamide. *Polym. Int.* **2010**, *59* (9), 1246–1251. https://doi.org/10.1002/pi.2856.

(46) Bajka, B. H.; Rigby, N. M.; Cross, K. L.; Macierzanka, A.; Mackie, A. R. The Influence of Small Intestinal Mucus Structure on Particle Transport Ex Vivo. *Colloids Surfaces B Biointerfaces* **2015**, *135*, 73–80. https://doi.org/10.1016/j.colsurfb.2015.07.038.

(47) Noble, E.; Janssen, L.; Dierickx, P. J. Comparative Cytotoxicity of 5-Aminosalicylic Acid (Mesalazine) and Related Compounds in Different Cell Lines. *Cell Biol. Toxicol.* **1997**, *13* (6), 445–451. https://doi.org/10.1023/A:1007423911613.

(48) Marques, M. Dissolution Media Simulating Fasted and Fed States. *Dissolution Technol.* **2004**, *11* (2), 16. https://doi.org/10.14227/DT110204P16.

(49) Wuyts, B.; Riethorst, D.; Brouwers, J.; Tack, J.; Annaert, P.; Augustijns, P. Evaluation of Fasted State Human Intestinal Fluid as Apical Solvent System in the Caco-2 Absorption Model and Comparison with FaSSIF. *Eur. J. Pharm. Sci.* **2015**, *67*, 126–135. https://doi.org/10.1016/j.ejps.2014.11.010.

(50) Galia, E.; Nicolaides, E.; Hörter, D.; Löbenberg, R.; Reppas, C.; Dressman, J. B. Evaluation of Various Dissolution Media for Predicting In Vivo Performance of Class I and II Drugs. *Pharm. Res.* **1998**, *15* (5), 698–705. https://doi.org/10.1023/A:1011910801212.

(51) Zhang, L.; Chan, J. M.; Gu, F. X.; Rhee, J. W.; Wang, A. Z.; Radovic-Moreno, A. F.; Alexis, F.; Langer, R.; Farokhzad, O. C. Self-Assembled Lipid-Polymer Hybrid Nanoparticles: A Robust Drug Delivery Platform. *ACS Nano* **2008**, *2* (8), 1696–1702. https://doi.org/10.1021/nn800275r.

(52) Liu, P.; De Wulf, O.; Laru, J.; Heikkilä, T.; Van Veen, B.; Kiesvaara, J.; Hirvonen, J.; Peltonen, L.; Laaksonen, T. Dissolution Studies of Poorly Soluble Drug Nanosuspensions in Non-Sink Conditions. *AAPS PharmSciTech* **2013**, *14* (2), 748–756. https://doi.org/10.1208/s12249-013-9960-2.

(53) Gibaldi, M.; Feldman, S. Establishment of Sink Conditions in Dissolution Rate Determinations. *J. Pharm. Sci.* **1964**, *56* (10), 1238–1242.

(54) French, D. L.; Mauger, J. W. Evaluation of the Physicochemical Properties and Dissolution Characteristics of Mesalamine: Relevance to Controlled Intestinal Drug Delivery. *Pharm. Res. An Off. J. Am. Assoc. Pharm. Sci.* **1993**, *10* (9), 1285–1290. https://doi.org/10.1023/A:1018909527659.

(55) Suksiriworapong, J.; Taresco, V.; Ivanov, D. P.; Styliari, I. D.; Sakchaisri, K.; Junyaprasert, V. B.; Garnett, M. C. Synthesis and Properties of a Biodegradable Polymer-Drug Conjugate: Methotrexate-Poly(Glycerol Adipate). *Colloids Surfaces B Biointerfaces* **2018**, *167*, 115–125. https://doi.org/10.1016/j.colsurfb.2018.03.048.

(56) Bean, T. A.; Zhuang, W. C.; Tong, P. Y.; Eick, J. D.; Yourtee, D. M. Effect of Esterase on Methacrylates and Methacrylate Polymers in an Enzyme Simulator for Biodurability and Biocompatibility Testing. *J. Biomed. Mater. Res.* **1994**, *28* (1), 59–63. https://doi.org/10.1002/jbm.820280108.

(57) MUNKSGAARD, E. C.; FREUND, M. Enzymatic Hydrolysis of (Di)Methacrylates and Their Polymers. *Eur. J. Oral Sci.* **1990**, *98* (3), 261–267. https://doi.org/10.1111/j.1600-0722.1990.tb00971.x.

Chapter 6

Conclusions and future directions

This chapter will discuss the understanding of the polymer-cell membrane interaction gained throughout the PhD research described within this thesis, as well as conveying the key results produced within this study.

6.1 Conclusions

Polymers are extensively employed in drug delivery for a wide variety of purposes Specifically, bioadhesive polymers have been proposed as drug delivery systems for decades[1–3], with recent examples of cell membrane adhesive cholesterol-based polymers in hybrid liposomes for drug delivery[4]. Membrane-inserting polymers are emerging as very useful tools to investigate and dissect complex biologic phenomena. For example, Bertozzi and co-workers use them to elucidate the role of integrins[5] and glycocalyx[6,7] in cancer development. The same group utilised phospholipid-terminated glycopolymers to demonstrate that cancer cell hypersialylation is a key mechanism for their immunoevasion and subsequent cancer spreading[8]. The Godula group use glycocalyx engineering to influence complex cell-based processes as neuromuscular junction formation[9] or fine investigations in the orientation of surface-bound macromolecules[10]. As a further example, Katayama and co-workers employed polymers based on short peptide moieties[11] to and design artificial receptors[12]. However, whilst these (excellent) studies focus mostly on the added function – e.g. introduction of sugar-encoded information or a physical barrier at the cell-extracellular space interphase - to the best of our knowledge no study has yet addressed the impact that the insertion of these materials in biological membrane has on the physico-chemical properties of these lipid bilayers.

An important aspect of this PhD work is that, although its overall aim was to design formulations for prolonged release of drugs in the GI tract, it allowed for a thorough investigation of the interactions between membrane-inserting polymers and lipid bilayers. To understand and characterise the interaction between amphiphilic polymers and membranes, we synthesised three main classes of polymers: i) cholesterol-; ii) DOPE phospholipid- and iii) PABTC-containing control polymers (**Figure 6.1**). Based on these considerations, we worked on the

production of these polymer libraries with different structural and functional characteristics:

i) Nature of the membrane-inserting polymer chain end (or lack of it);

ii) Chemical composition of the polymers, with hydrophilic and acid monomers in different proportions;

iii) Chain length of the polymers.

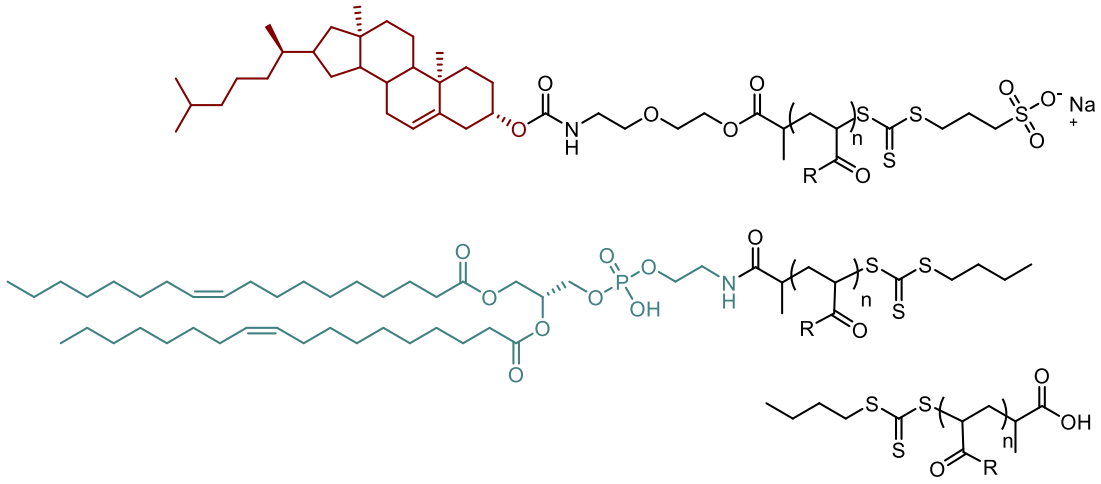


Figure 6.1 General structure of polymers employed in this study: cholesterol-, DOPE- and PABTC-containing control polymers (from top to bottom, respectively).

We have demonstrated that the synthesised amphiphilic polymers containing cell membrane lipids at their polymer chain-end readily interacted with lipid bilayer membranes, as confirmed by *in vitro* and *in silico* experiments. Conversely, analogous hydrophilic control polymers missing those functional chain-ends showed a negligible degree of interaction with these membranes. The degree of polymer-membrane interaction has been investigated *in vitro* by different techniques, such as Laurdan assay to assess the effect of polymers on cell membrane fluidity, cell membrane damage and association of structurally analogous fluorescently labelled polymers. Further elucidation of the polymer-membrane interaction was conducted on synthetic membrane models by SPR to characterise the kinetics (K_a and k_d) and thermodynamics (K_D) of polymer-

membrane association (SPR), by molecular modelling simulations to provide a model for the effect of amphiphilic polymers on membrane order and by solid-state NMR to confirm embedding of polymers in model membranes. The results showed that, for the cholesterol- and DOPE-containing polymers, the levels of polymer-membrane association, as well as kinetic and thermodynamic parameters for the membrane interaction were dependent on: i) the nature of the membrane-binding anchor, with cholesterol showing a faster and more extensive process of membrane association than DOPE, and ii) length of the hydrophilic chain, with the shorter polymers showing a higher level of polymer association with membranes.

The results obtained with these different investigations provided an initial understanding of these polymer-membrane interactions and suggests a structure-function relationship for the membrane-inserting materials synthesised in terms of effect of polymers on membrane fluidity (**Figure 6.2**), kinetics and thermodynamics of membrane association and dissociation, and modelling of such interactions.

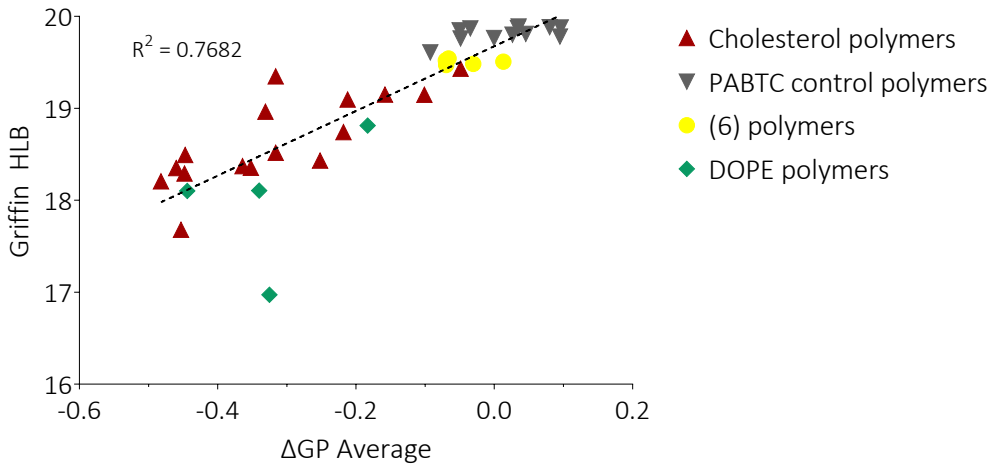


Figure 6.2 Correlation analysis between Griffin hydrophilic-lipophilic balance (HLB) of the polymers and average cell fluidity measurement (ΔGP) obtained for Caco-2 cells treated with a range of polymers at the same molar concentration (0.1 μM).

Finally, in **Chapter 5** we focused on potential applications for membrane-interacting polymers with two different approaches to drug incorporation. As membrane-binding polymers could help retention of the formulation in the targeted delivery area (small intestine), we worked on two potential delivery systems. We first focused on nitrofurantoin, an antibiotic used to treat infections in the urinary tract[13,14] with a fast intestinal absorption and fast elimination. The encapsulation experiments for this drug were based on the formation of an ionic interaction between the acid-bearing polymers and the basic drug. This approach yielded promising initial results, but poor reproducibility prompted the adoption of covalent drug encapsulation. For this purpose, we used mesalazine, an immunomodulatory drug employed in the treatment of inflammatory bowel diseases. We synthesised a mesalazine-bearing monomer and employed this novel monomer to produce mesalazine-conjugated polymers. The membrane-interacting polymers loaded with mesalazine were still able to interact with membranes. The polymers showed a pH-dependant mesalazine release and were able to fully release the encapsulated drug. These results showed that the membrane-inserting properties of the amphiphilic polymers were not influenced by the introduction of a covalently bound drug payload, constituting a proof-of-principle for potential applications of these amphiphilic polymers in further studies on drug delivery.

6.2 Future Directions

Further studies will be required to improve, expand and apply on more complex systems the work presented in this thesis, and in particular:

i. Synthesis and testing of additional cholesterol/DOPE/control-HEA polymers, with different DP ranges (20-40, 120-200) to expand the understanding of structure-activity relationship built within this work

ii. Application of the different polymers (cholesterol, phospholipid, control) on more relevant *in vitro* systems, such as polarised Caco-2 cells and Caco-2 cells co-cultured with HT-29 cells to mimic the mucus lining

iii. Application of the polymers in mucus diffusion studies, with models developed through microfluidics[15]

iv. Application of the different polymers on *ex vivo* models, such as porcine intestine to study interaction and drug release in Ussing chambers

v. Employing the understanding gained from this thesis, design more complex polymers: with more than one membrane binding anchor or polymers with the exact lipophilic/hydrophilic MW ratio to have an optimal membrane-binding capability.

vi. *In vivo* studies on relevant models for inflammatory bowel diseases, as well as models studying toxicity of the polymers and PD/PK of Mesalazine when administered as a drug-polymer conjugate

6.3 Bibliography

(1) Park, K.; Robinson, J. R. Bioadhesive Polymers as Platforms for Oral-Controlled Drug Delivery: Method to Study Bioadhesion. *Int. J. Pharm.* **1984**, *19* (2), 107–127. https://doi.org/10.1016/0378-5173(84)90154-6.

(2) Kumar, K.; Dhawan, N.; Sharma, H.; Vaidya, S.; Vaidya, B. Bioadhesive Polymers: Novel Tool for Drug Delivery. *Artif. Cells, Nanomedicine Biotechnol.* **2014**, *42* (4), 274–283. https://doi.org/10.3109/21691401.2013.815194.

(3) Kriwet, B.; Kissel, T. Interactions between Bioadhesive Poly(Acrylic Acid) and Calcium Ions. *Int. J. Pharm.* **1996**, *127* (2), 135–145. https://doi.org/10.1016/0378-5173(95)04098-6.

(4) Essi Taipaleenmäki, A.; Gustav Christensen, a# Edit Brodszkij, A.; Sidsel A. Mouritzen, A.; Noga Gal, A.; Sidsel; Madsen, B.; Mette Skou Hedemann, b Tine Ahrendt Knudsen, C.; Henrik Max Jensen, C.; Laage, S.; Christiansen, c Flemming Vang Sparsø, c and B. S. Mucopenetrating Polymer – Lipid Hybrid Nanovesicles as Subunits in Alginate Beads as an Oral Formulation. *J. Control. Release* **2020**. https://doi.org/10.1016/j.aquaculture.2020.734967.

(5) Paszek, M. J.; Dufort, C. C.; Rossier, O.; Bainer, R.; Mouw, J. K.; Godula, K.; Hudak, J. E.; Lakins, J. N.; Wijekoon, A. C.; Cassereau, L.; Rubashkin, M. G.; Magbanua, M. J.; Thorn, K. S.; Davidson, M. W.; Rugo, H. S.; Park, J. W.; Hammer, D. A.; Giannone, G.; Bertozzi, C. R.; Weaver, V. M. The Cancer Glycocalyx Mechanically Primes Integrin-Mediated Growth and Survival. *Nature* **2014**, *511* (7509), 319–325. https://doi.org/10.1038/nature13535.

(6) Woods, E.; Yee, N.; Shen, J.; Bertozzi, C. R. Glycocalyx Engineering with a

Recycling Glycopolymer That Increases Cell Survival in Vivo. *Angew Chem Int Ed Engl.* **2015**, *54* (52), 15782–15788. https://doi.org/10.1586/14737175.2015.1028369.Focused.

(7) Woods, E. C.; Kai, F.; Barnes, J. M.; Pedram, K.; Pickup, M. W.; Hollander, M. J.; Weaver, V. M.; Bertozzi, C. R. A Bulky Glycocalyx Fosters Metastasis Formation by Promoting G1 Cell Cycle Progression. *Elife* **2017**, *6*, 1–15. https://doi.org/10.7554/eLife.25752.

(8) Hudak, J. E.; Canham, S. M.; Bertozzi, C. R. Glycocalyx Engineering Reveals a Siglec-Based Mechanism for NK Cell Immunoevasion. *Nat. Chem. Biol.* **2014**, *10* (1), 69–75. https://doi.org/10.1038/nchembio.1388.

(9) Huang, M. L.; Tota, E. M.; Lucas, T. M.; Godula, K. Influencing Early Stages of Neuromuscular Junction Formation through Glycocalyx Engineering. *ACS Chem. Neurosci.* **2018**, *9* (12), 3086–3093. https://doi.org/10.1021/acschemneuro.8b00295.

(10) Godula, K.; Umbel, M. L.; Rabuka, D.; Botyanszki, Z.; Bertozzi, C. R.; Parthasarathy, R. Control of the Molecular Orientation of Membrane-Anchored Biomimetic Glycopolymers. *J. Am. Chem. Soc.* **2009**, *131* (29), 10263–10268. https://doi.org/10.1021/ja903114g.

(11) Matsuda, M.; Hatanaka, W.; Takeo, M.; Kim, C. W.; Niidome, T.; Yamamoto, T.; Kishimura, A.; Mori, T.; Katayama, Y. Short Peptide Motifs for Long-Lasting Anchoring to the Cell Surface. *Bioconjug. Chem.* **2014**, *25* (12), 2134–2143. https://doi.org/10.1021/bc500465j.

(12) Hatanaka, W.; Kawaguchi, M.; Sun, X.; Nagao, Y.; Ohshima, H.; Hashida, M.; Higuchi, Y.; Kishimura, A.; Katayama, Y.; Mori, T. Use of Membrane Potential to Achieve Transmembrane Modification with an Artificial Receptor. *Bioconjug. Chem.* **2017**, *28* (2), 296–301. https://doi.org/10.1021/acs.bioconjchem.6b00449.

(13) Brunton, L.; Chabner, B.; Knollman, B. *Goodman & Gilman's The Pharmacological Basis of Therapeutics*; 2013; Vol. 53. https://doi.org/10.1017/CBO9781107415324.004.

(14) Cunha, B. A.; Schoch, P. E.; Hage, J. R. Nitrofurantoin: Preferred Empiric Therapy for Community-Acquired Lower Urinary Tract Infections. *Mayo Clin. Proc.* **2011**, *86* (12), 1243–1244. https://doi.org/10.4065/mcp.2011.0411.

(15) Taipaleenmäki, E. M.; Mouritzen, S. A.; Schattling, P. S.; Zhang, Y.; Städler, B. Mucopenetrating Micelles with a PEG Corona. *Nanoscale* **2017**, *9* (46), 18438–18448. https://doi.org/10.1039/c7nr06821b.

Appendix

A1 Supporting information for Chapter 2

A1 Supporting information for Chapter 2 – NMR spectra

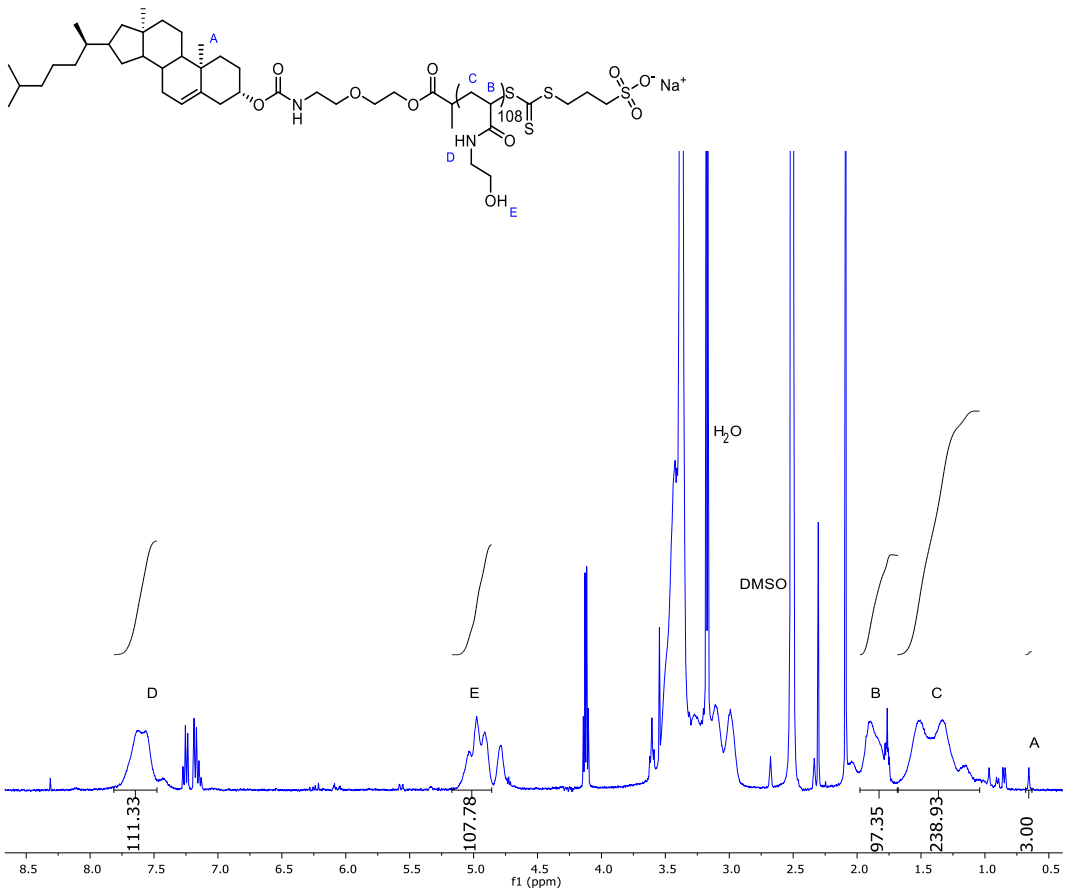


Figure A1.1 ^{1}H NMR spectrum of Chol-[(HEA)$_{100\%}$]$_{108}$ in DMSO-d$_6$

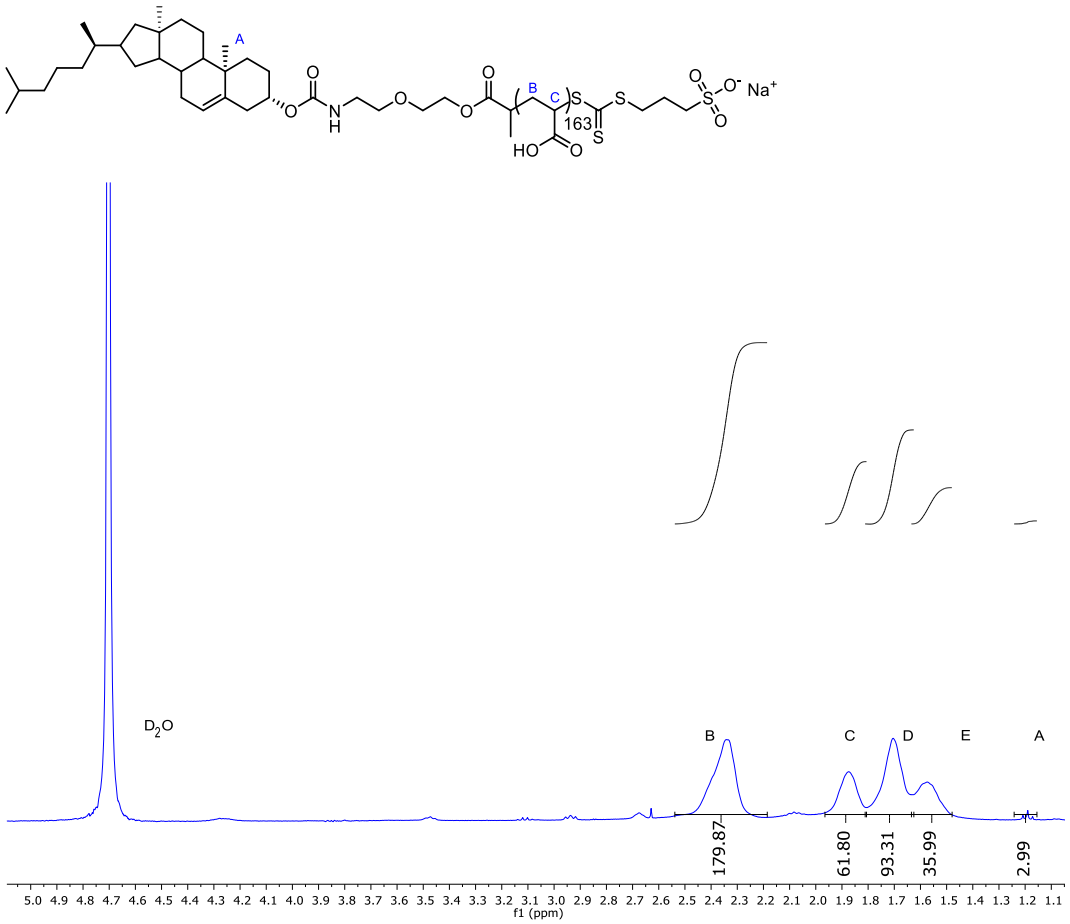


Figure A1.2 ^{1}H NMR spectrum of Chol-$[(AA)_{100\%}]_{163}$ in D_2O

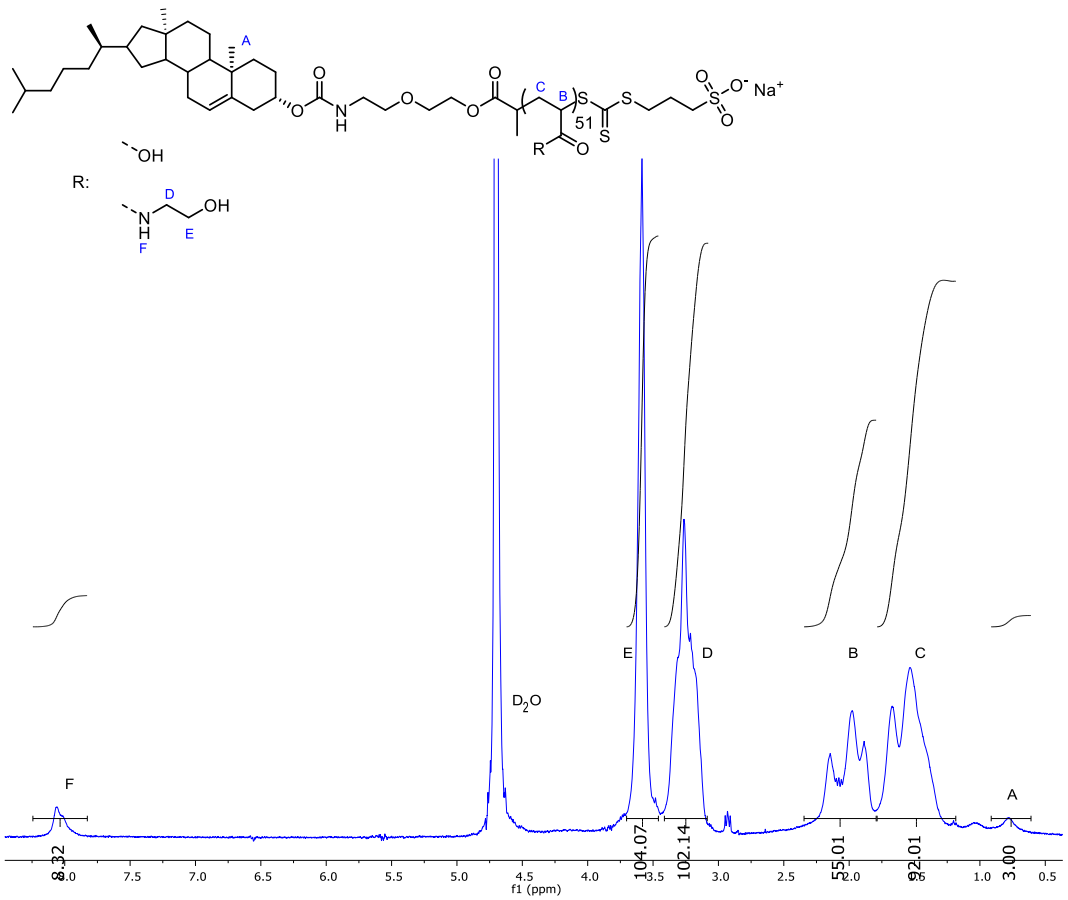


Figure A1.3 ^{1}H NMR spectrum of Chol-[(HEA)$_{90\%}$-*r*-(AA)$_{10\%}$]$_{51}$ in D_2O

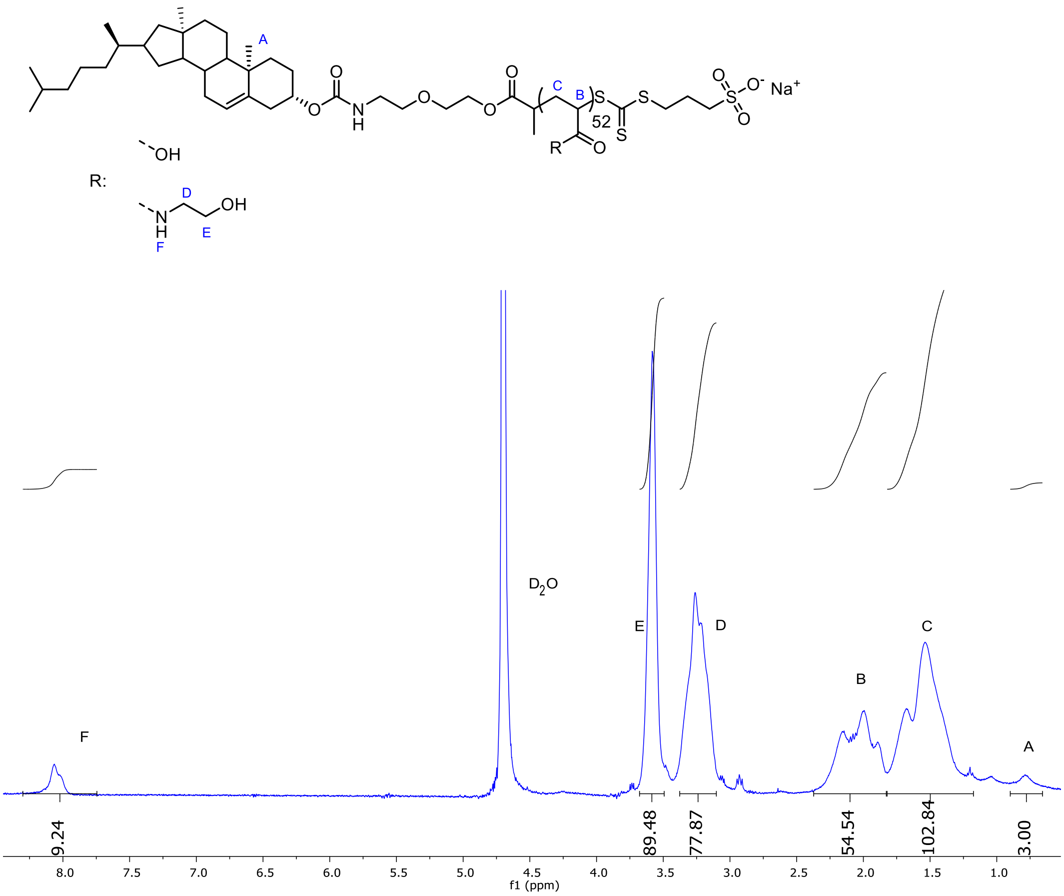


Figure A1.4 ^{1}H NMR spectrum of Chol-[$(HEA)_{70\%}$-*r*-$(AA)_{30\%}$]$_{52}$ in D_2O

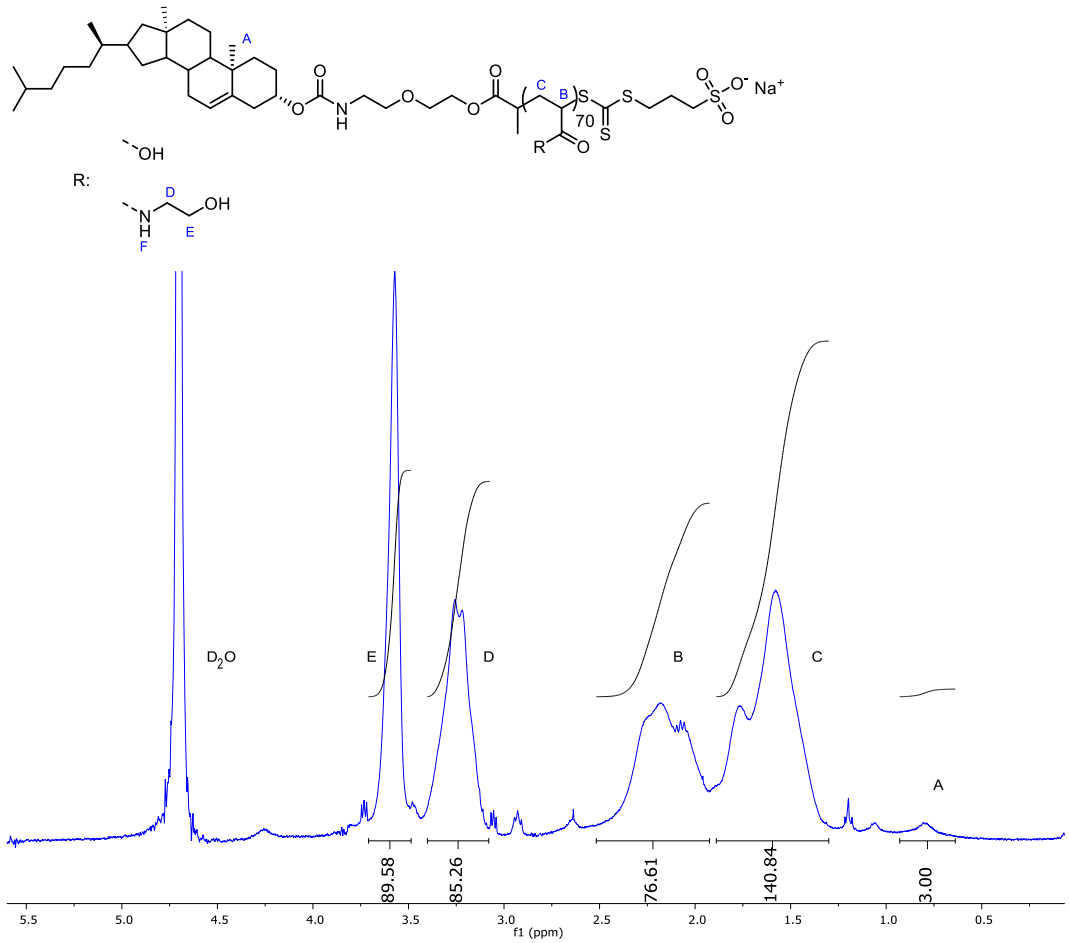


Figure A1.5 ^{1}H NMR spectrum of Chol-[(HEA)$_{50\%}$-*r*-(AA)$_{50\%}$]$_{70}$ in D_2O

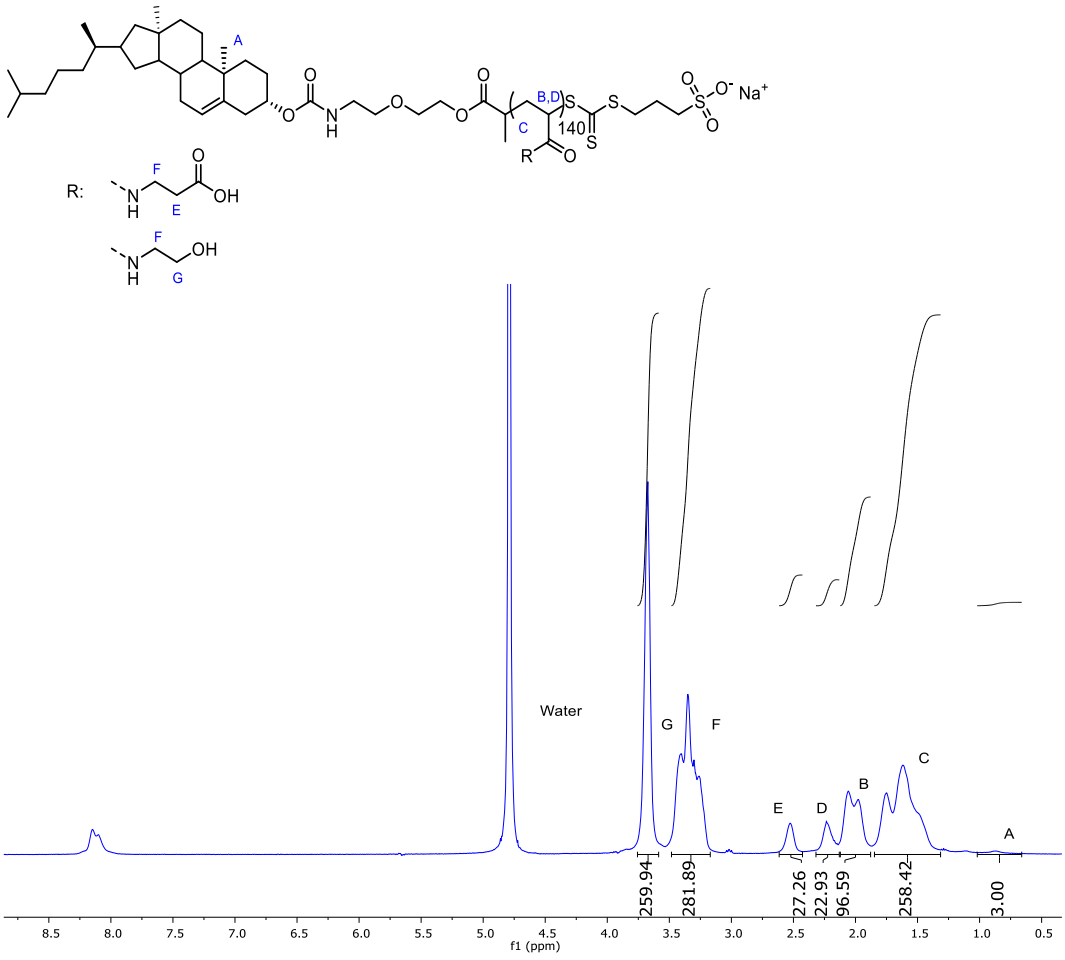


Figure A1.6 ^{1}H NMR spectrum of Chol-$[(HEA)_{90\%}$-*r*-$(AAPA)_{10\%}]_{140}$ in D_2O

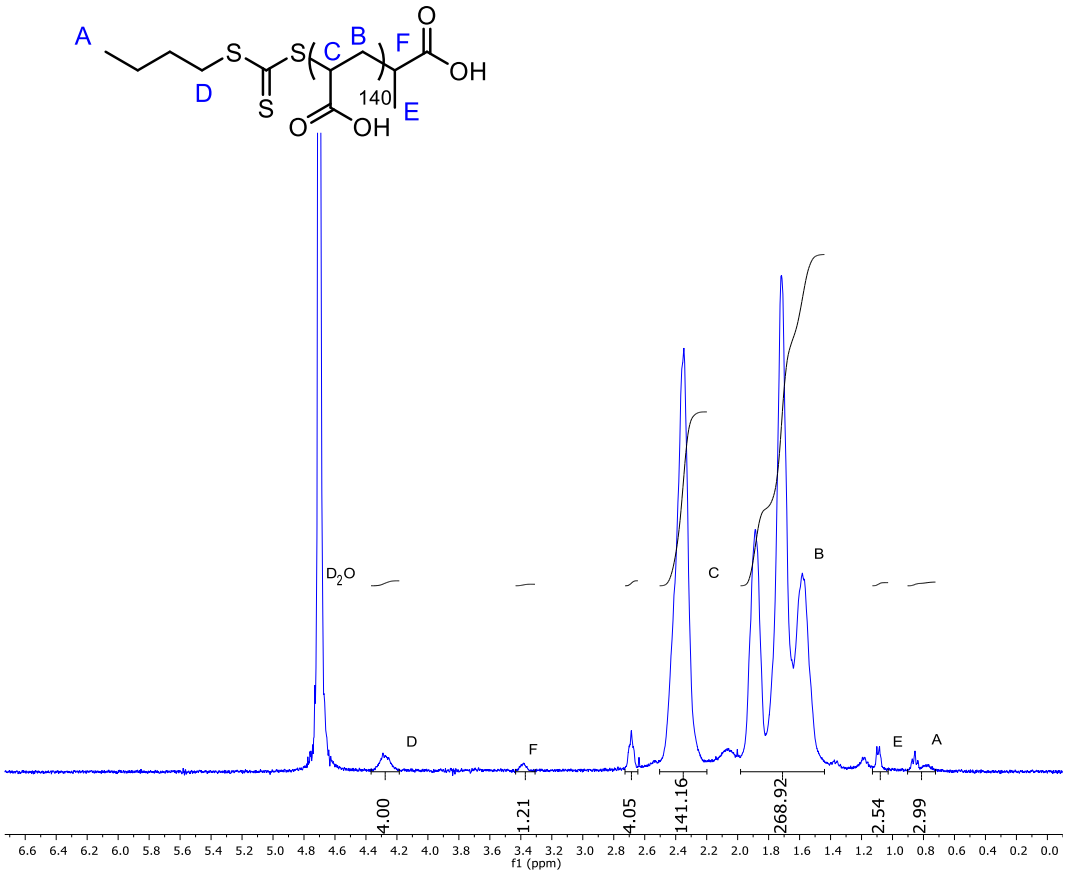


Figure A1.7 ^{1}H NMR spectrum of PABTC-$[(AA)_{100\%}]_{140}$ in D_2O

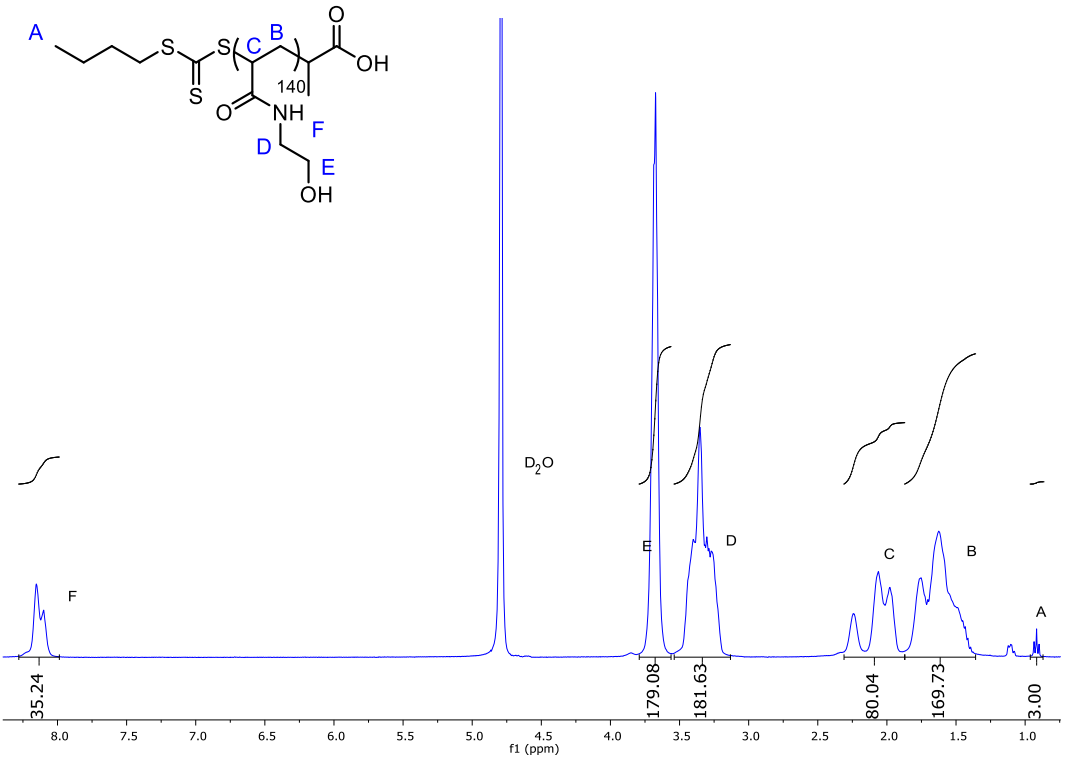


Figure A1.8 ^{1}H NMR spectrum of PABTC-[(HEA)$_{100\%}$]$_{80}$ in D_2O

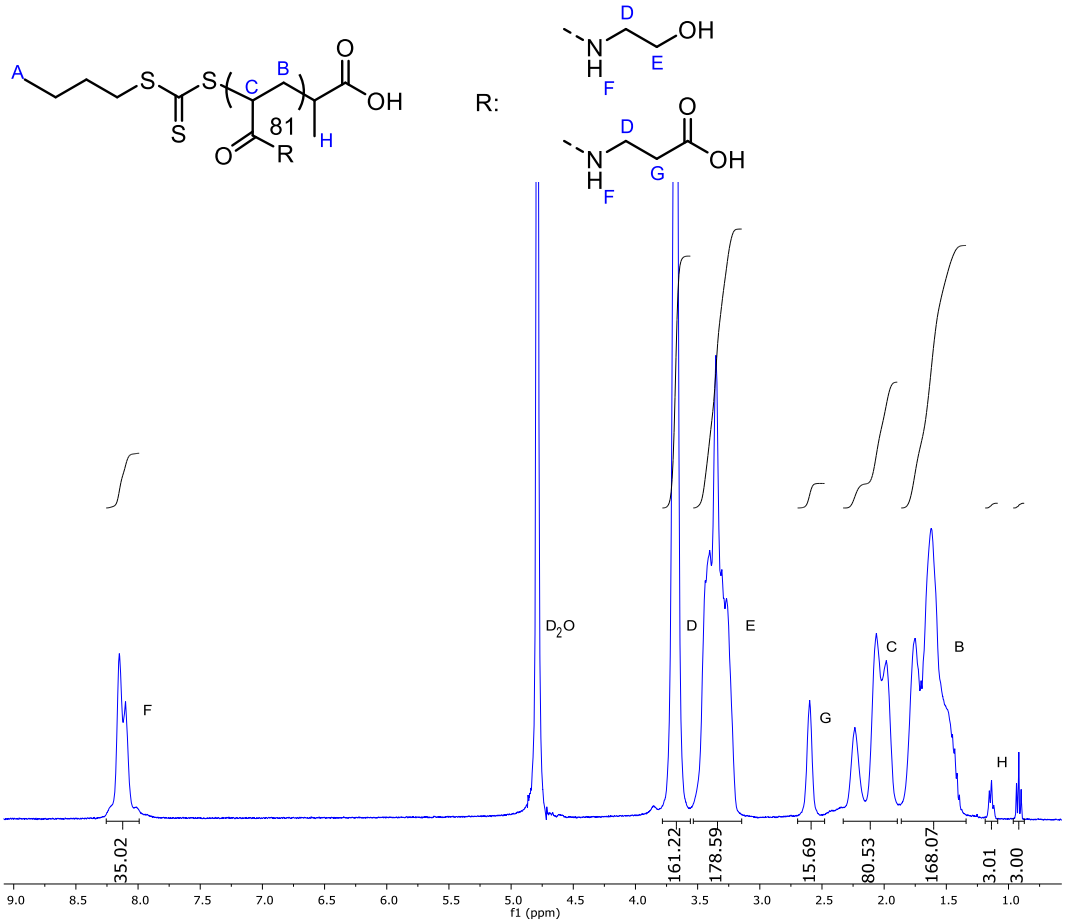


Figure A1.9 ^{1}H NMR spectrum of PABTC-[(HEA)$_{90\%}$-*r*-(AAPA)$_{10\%}$]$_{81}$ in D_2O

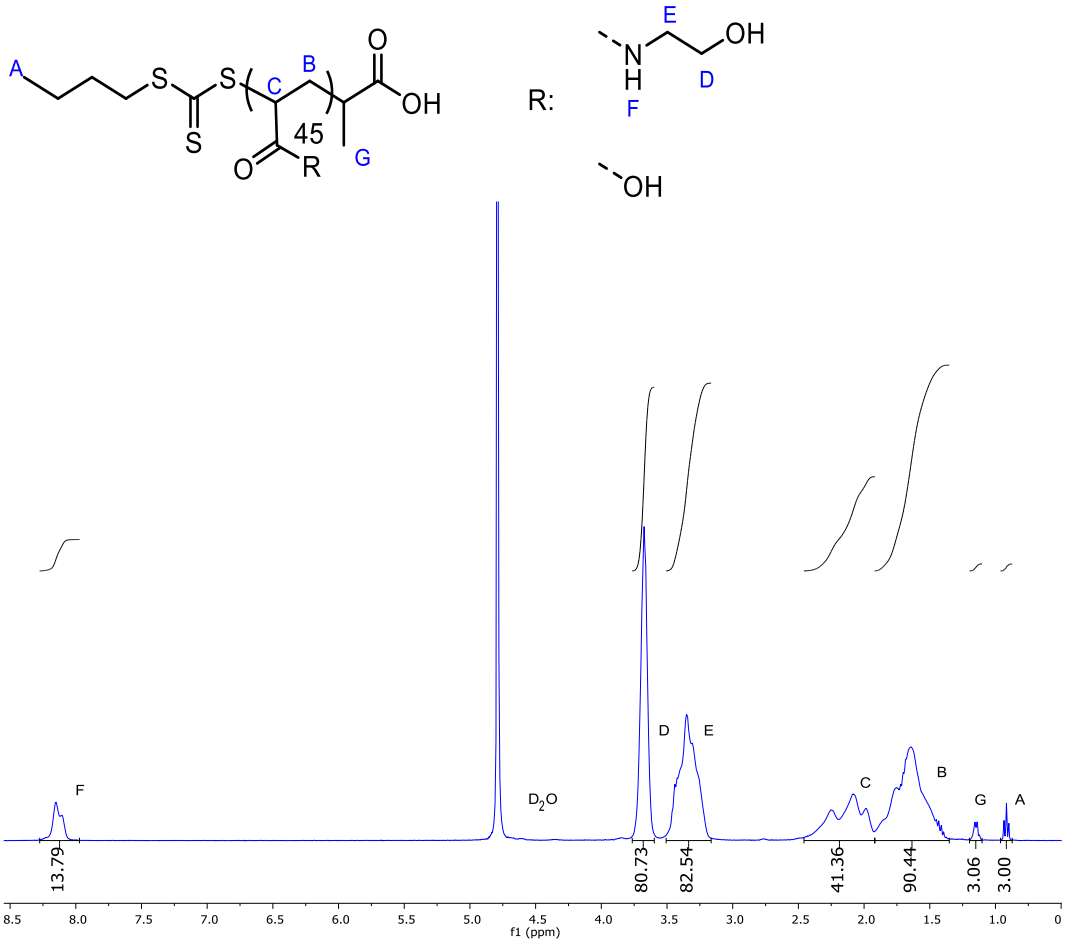


Figure A1.10 ^{1}H NMR spectrum of PABTC-[(HEA)$_{90\%}$-*r*-(AA)$_{10\%}$]$_{45}$ in D_2O

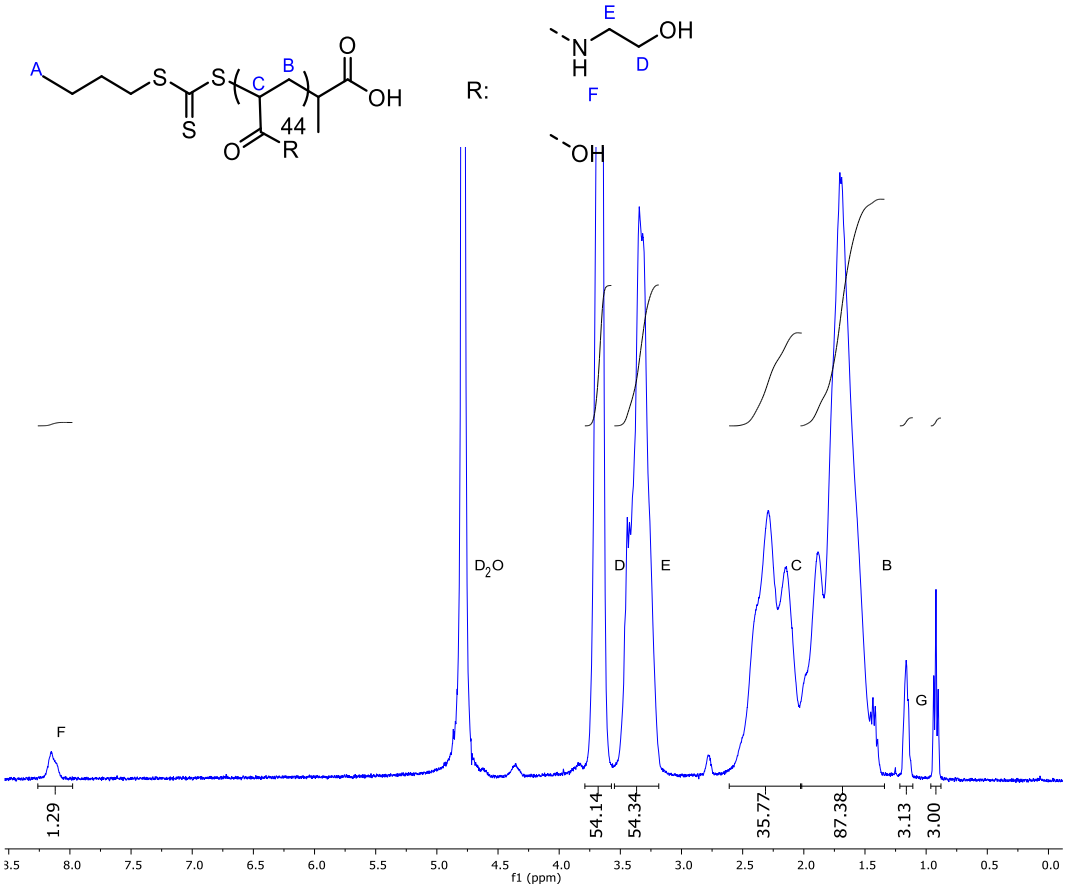


Figure A1.11 ^{1}H NMR spectrum of PABTC-[(HEA)$_{70\%}$-*r*-(AA)$_{30\%}$]$_{44}$ in D_2O

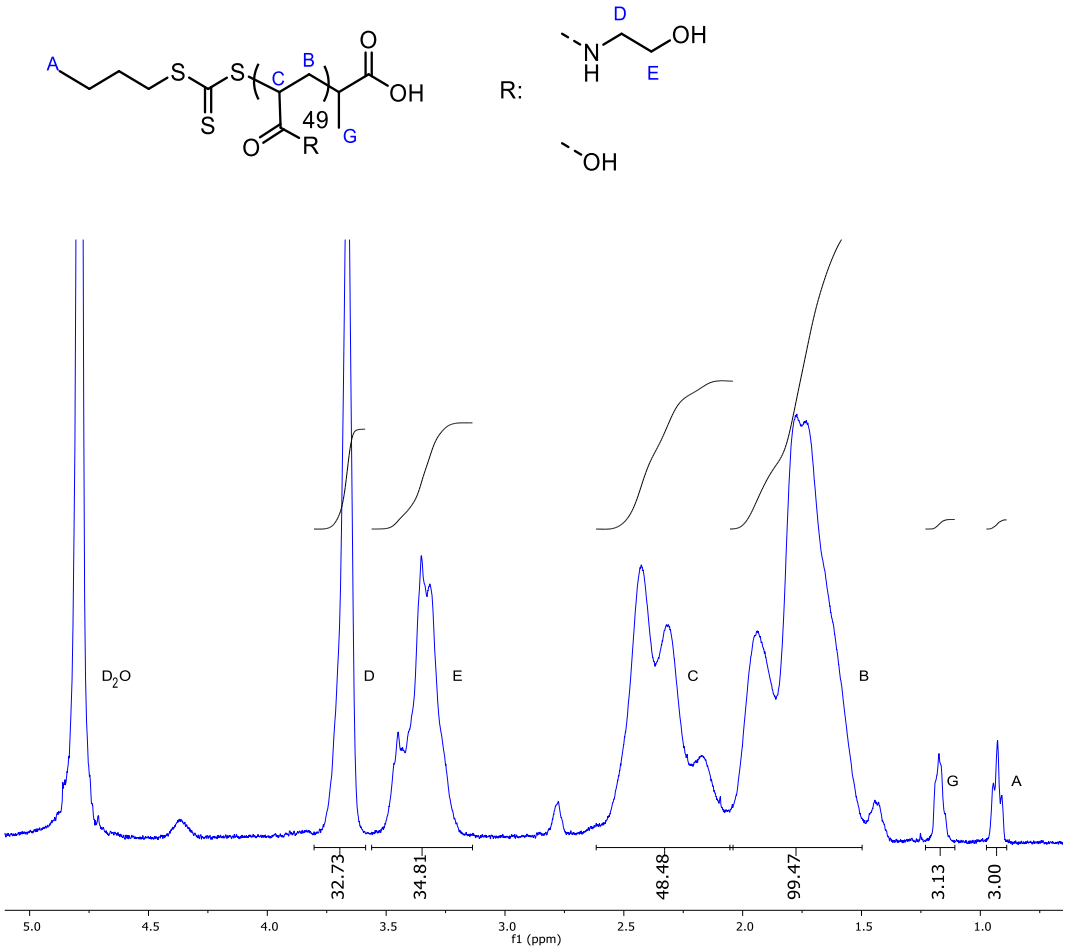


Figure A1.12 ^{1}H NMR spectrum of PABTC-[(HEA)$_{50\%}$-*r*-(AA)$_{50\%}$]$_{49}$ in D_2O

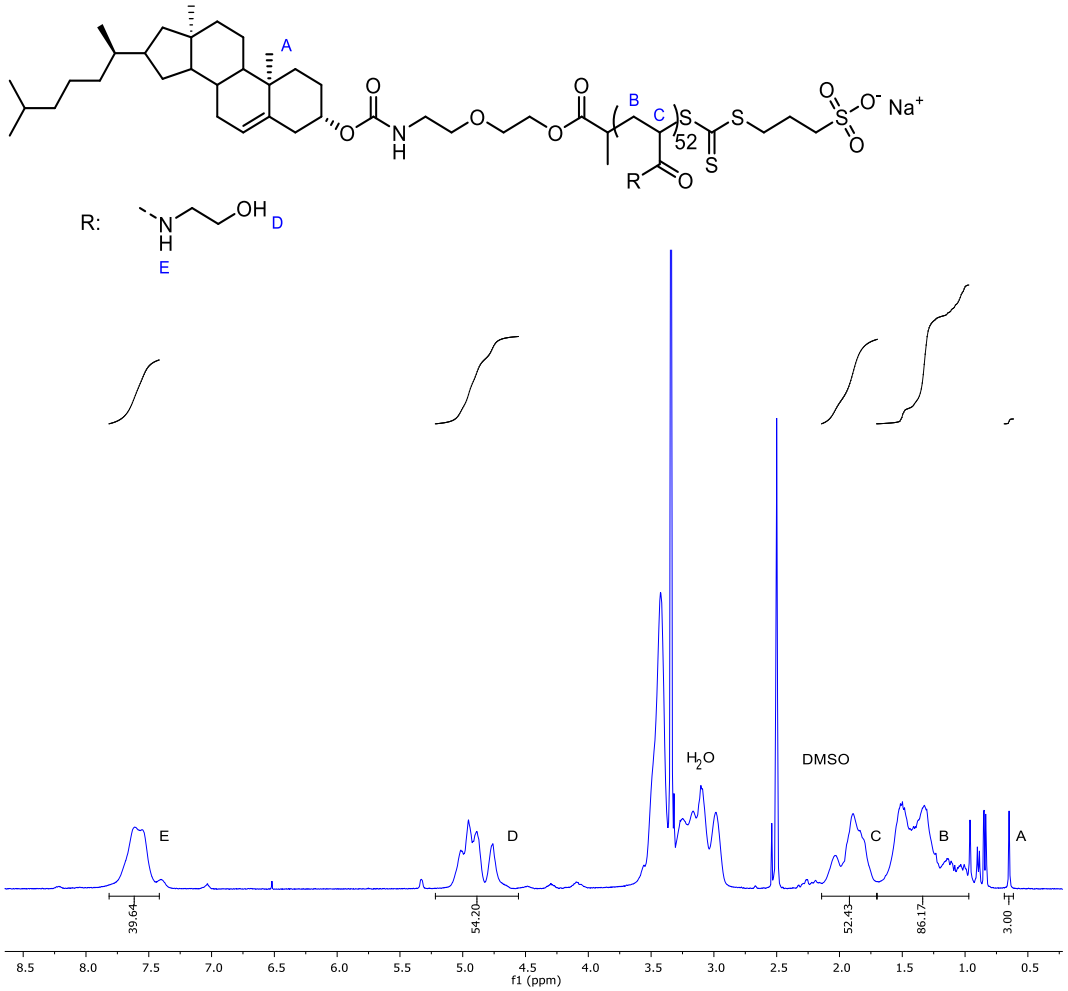


Figure A1.13 ^{1}H NMR spectrum of Chol-[(HEA)$_{100\%}$]$_{52}$ in DMSO-d$_6$

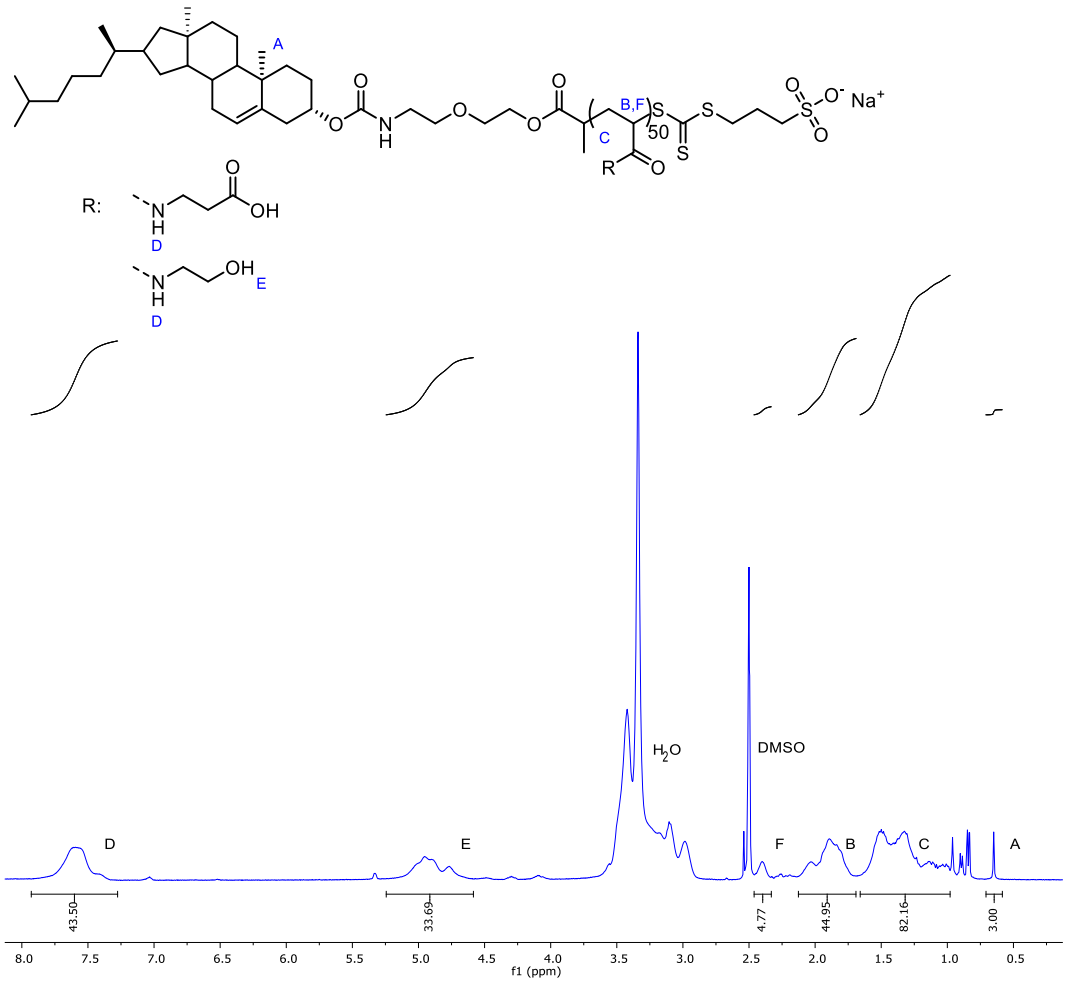


Figure A1.14 ^{1}H NMR spectrum of Chol-[(HEA)$_{90\%}$-*r*-(AAPA)$_{10\%}$]$_{50}$ in DMSO-d$_6$

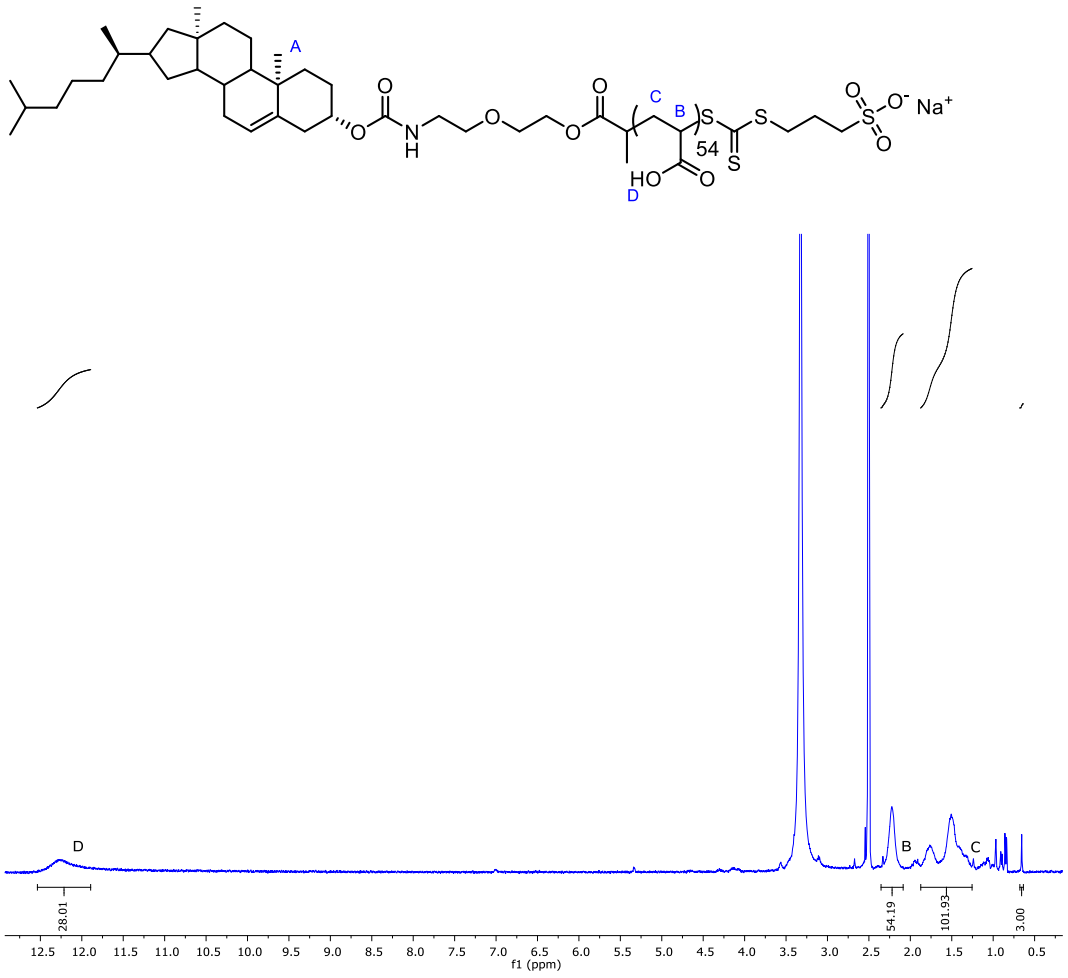


Figure A1.15 ^{1}H NMR spectrum of Chol-[(AA)$_{100\%}$]$_{54}$ in DMSO-d$_6$

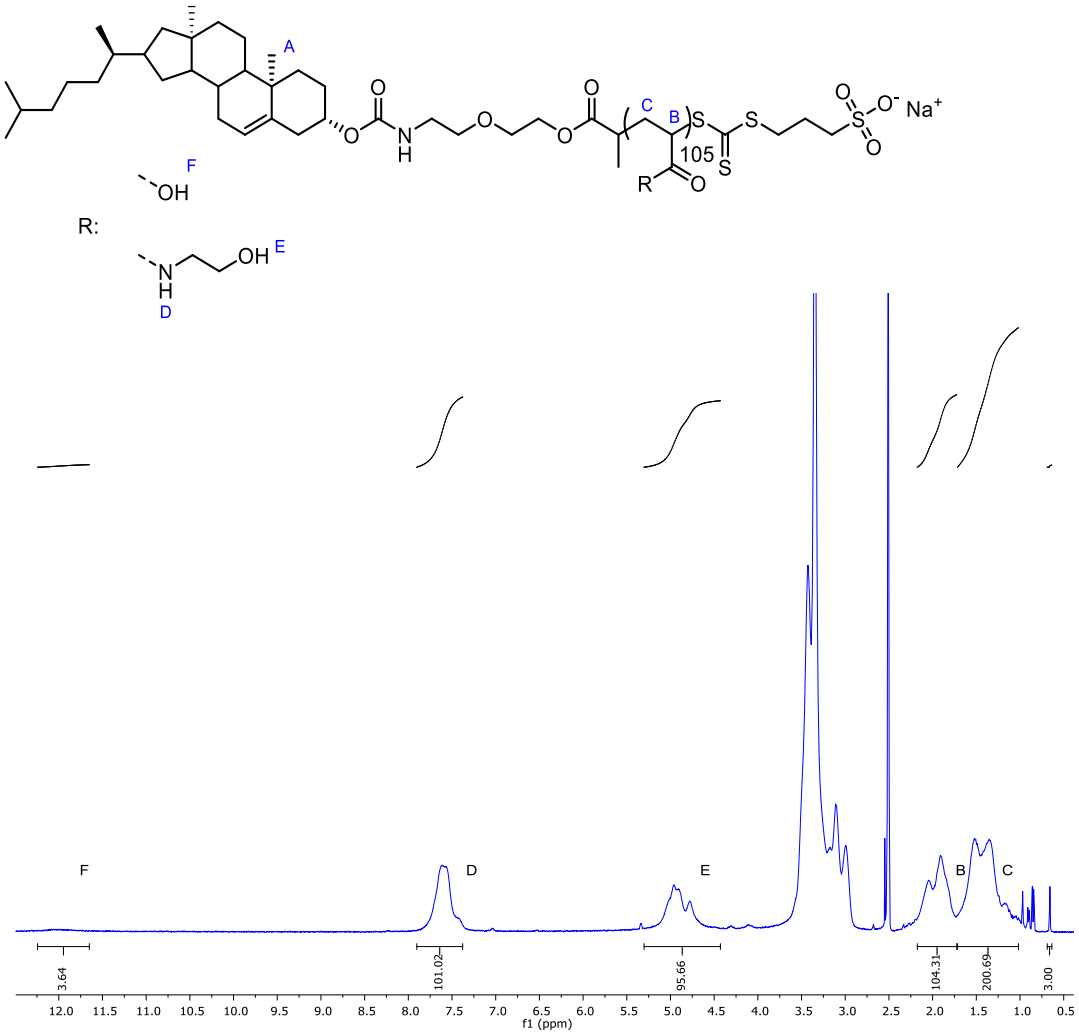


Figure A1.16 ^{1}H NMR spectrum of Chol-[(HEA)$_{90\%}$-*r*-(AA)$_{10\%}$]$_{54}$ in DMSO-d$_6$

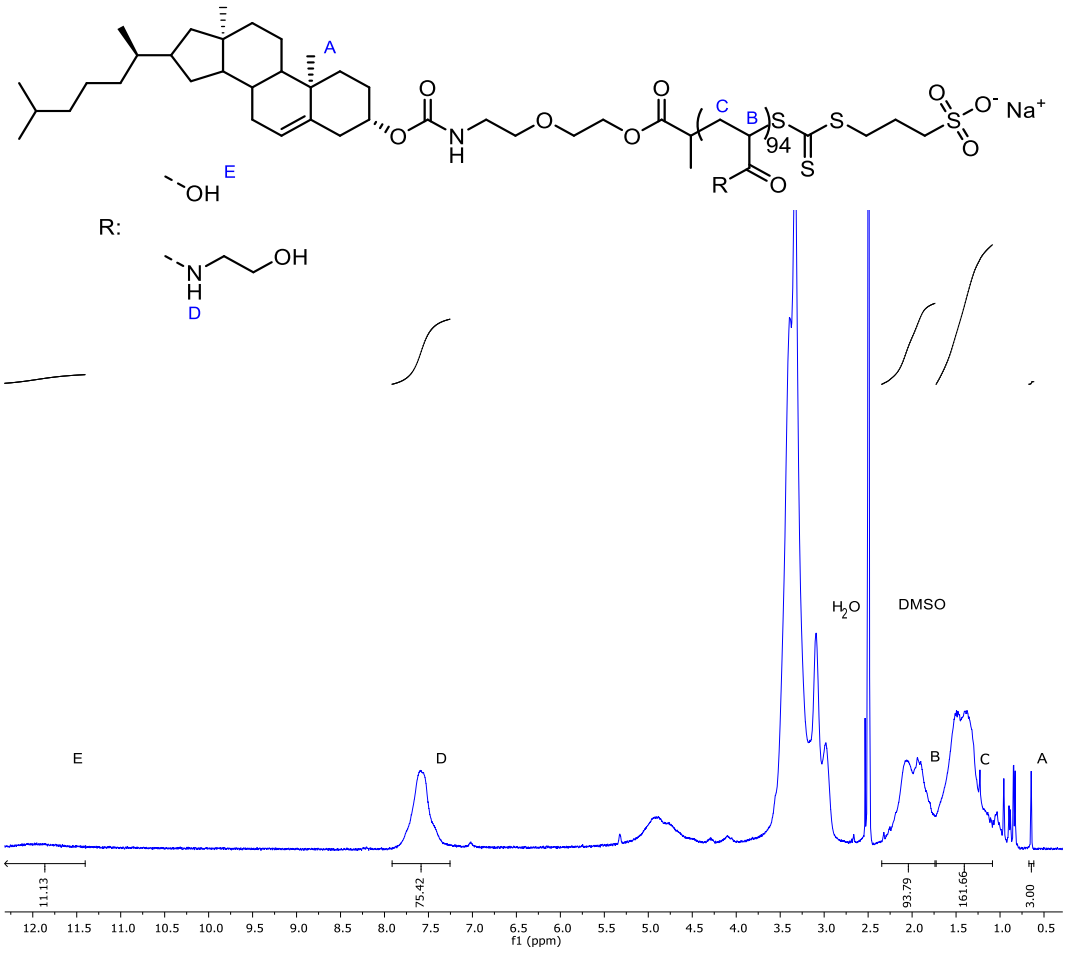


Figure A1.17 ^{1}H NMR spectrum of Chol-[(HEA)$_{70\%}$-*r*-(AA)$_{30\%}$]$_{94}$ in DMSO-d$_6$

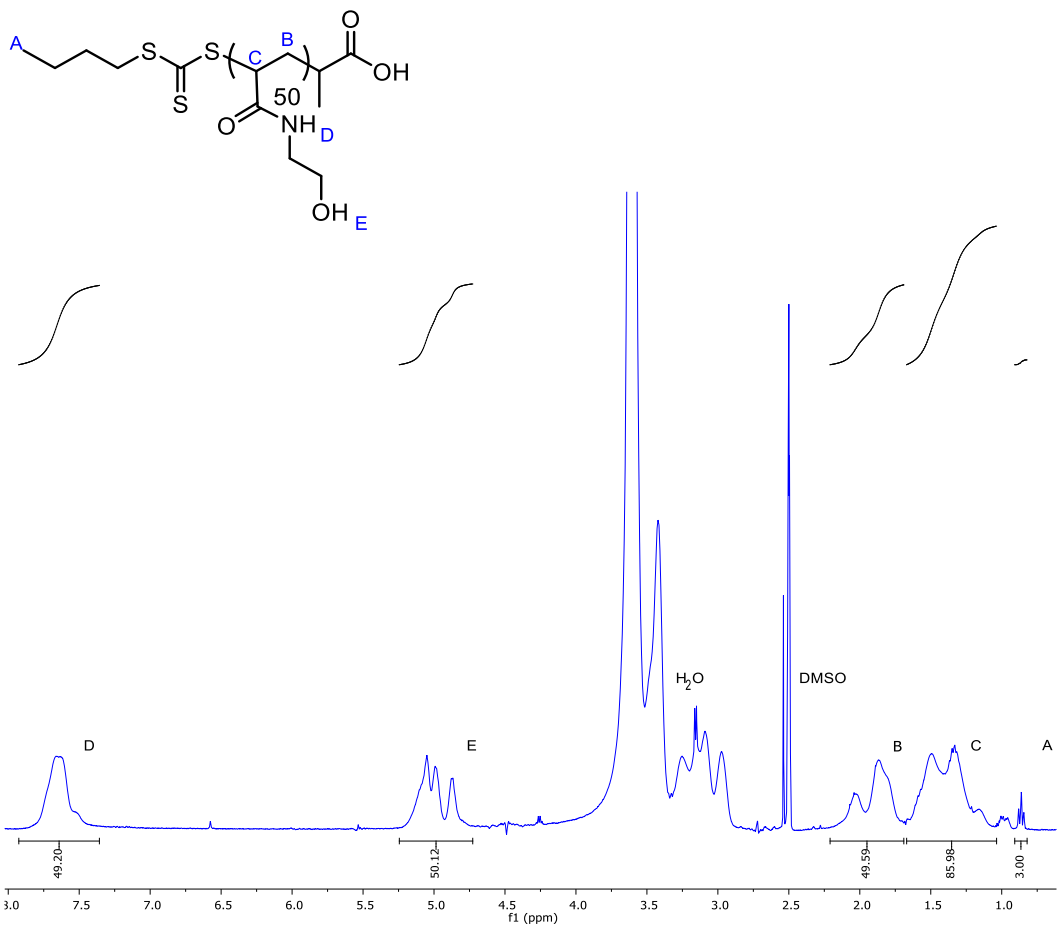


Figure A1.18 ^{1}H NMR spectrum of PABTC-[(HEA)$_{100\%}$]$_{50}$in DMSO-d$_6$

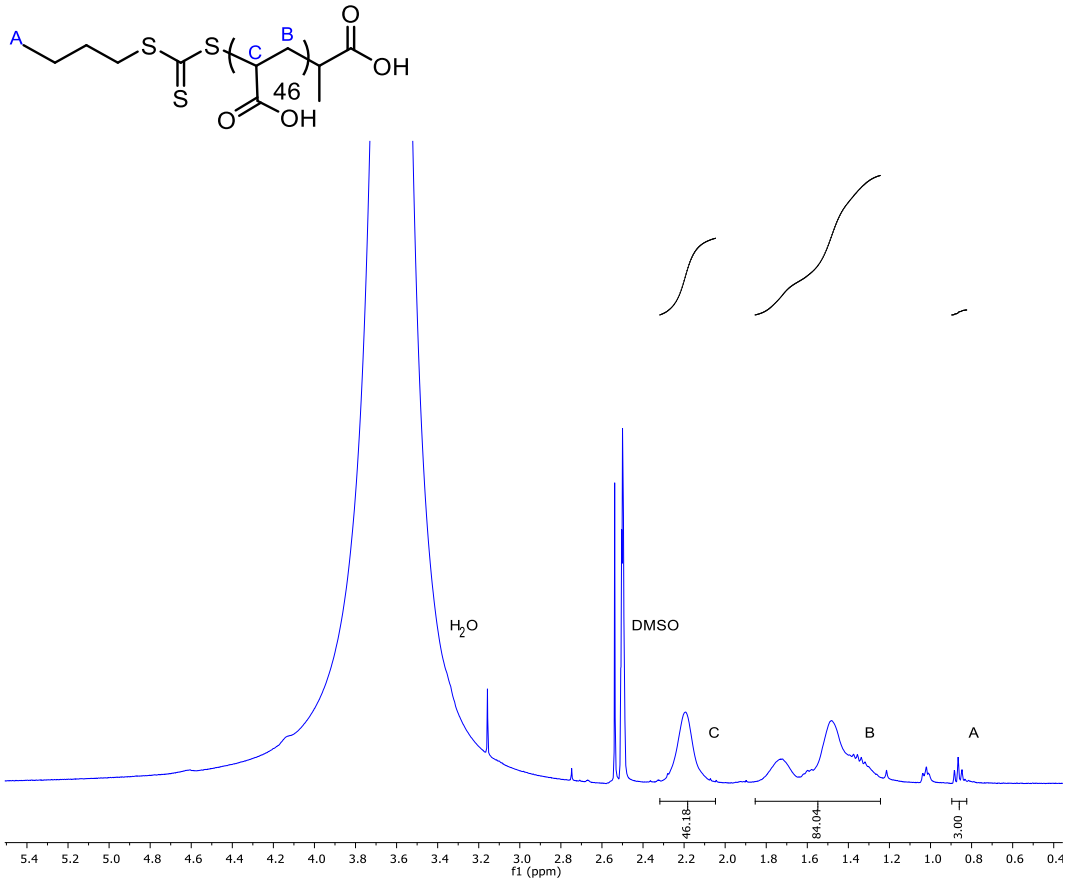


Figure A1.19 ^{1}H NMR spectrum of PABTC-[$(AA)_{100\%}]_{46}$ in DMSO-d_6

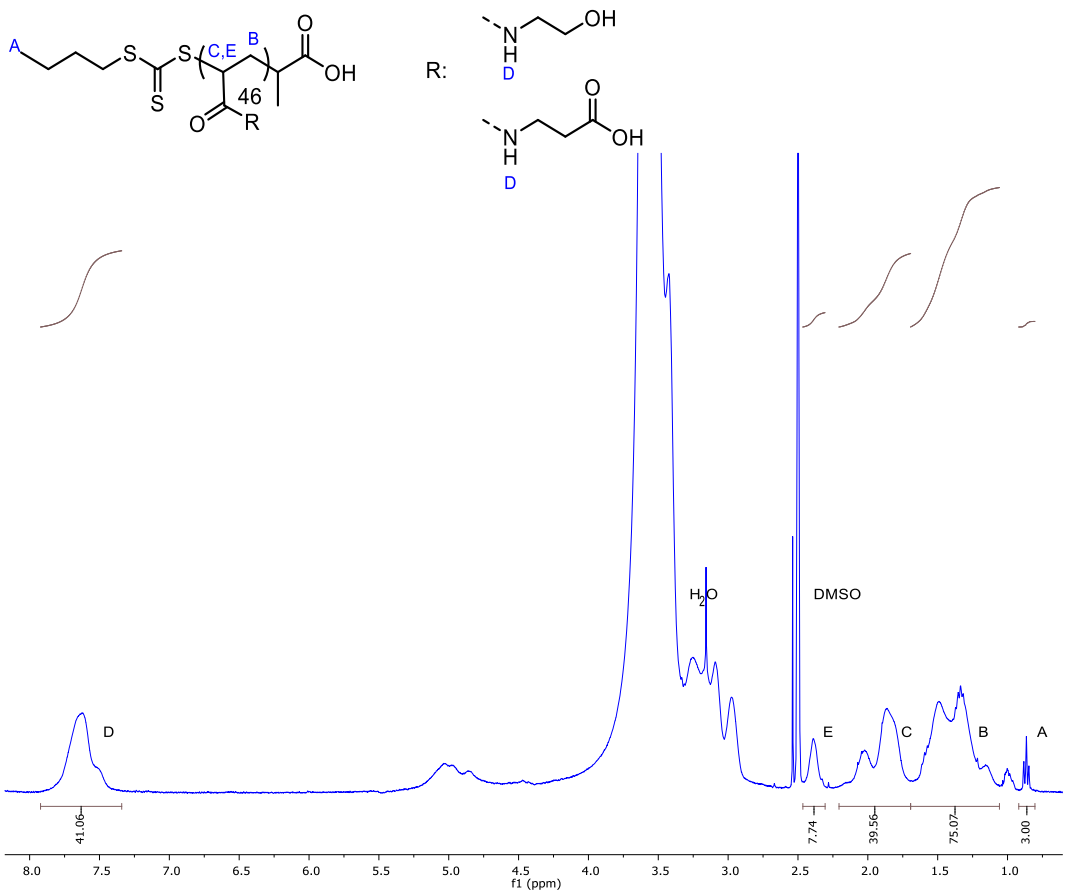


Figure A1.20 ^{1}H NMR spectrum of PABTC-[(HEA)$_{90\%}$-*r*-(AAPA)$_{10\%}$]$_{46}$ in DMSO-d$_6$

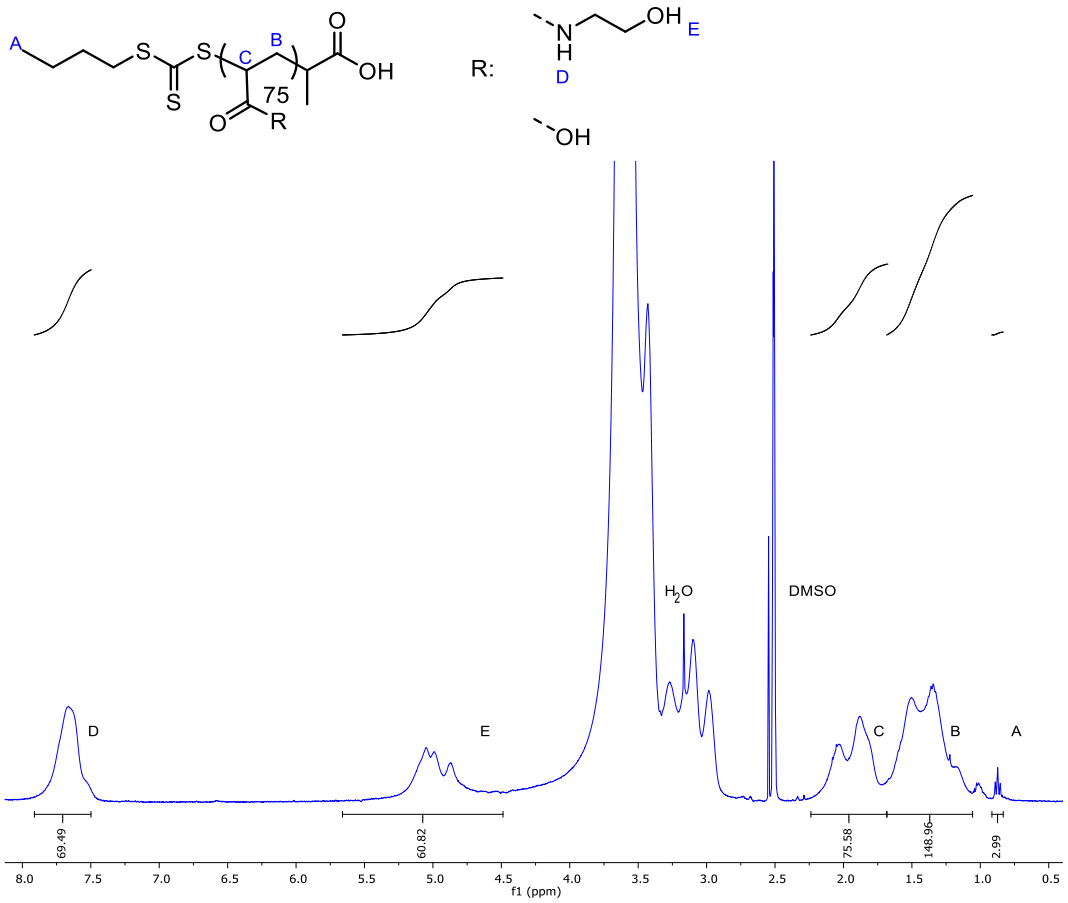


Figure A1.21 ^{1}H NMR spectrum of PABTC-[(HEA)$_{90\%}$-*r*-(AA)$_{10\%}$]$_{75}$ in DMSO-d$_6$

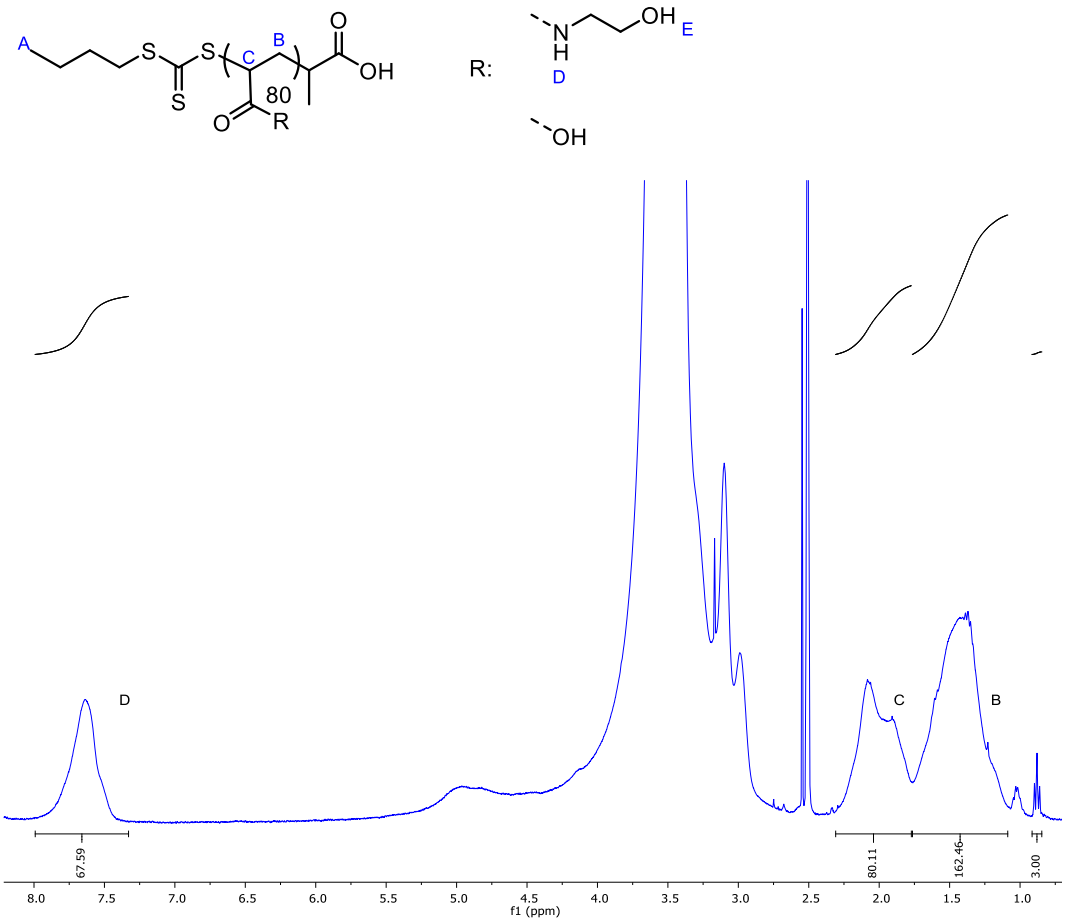


Figure A1.22 ^{1}H NMR spectrum of PABTC-[(HEA)$_{70\%}$-*r*-(AA)$_{30\%}$]$_{80}$ in DMSO-d$_6$

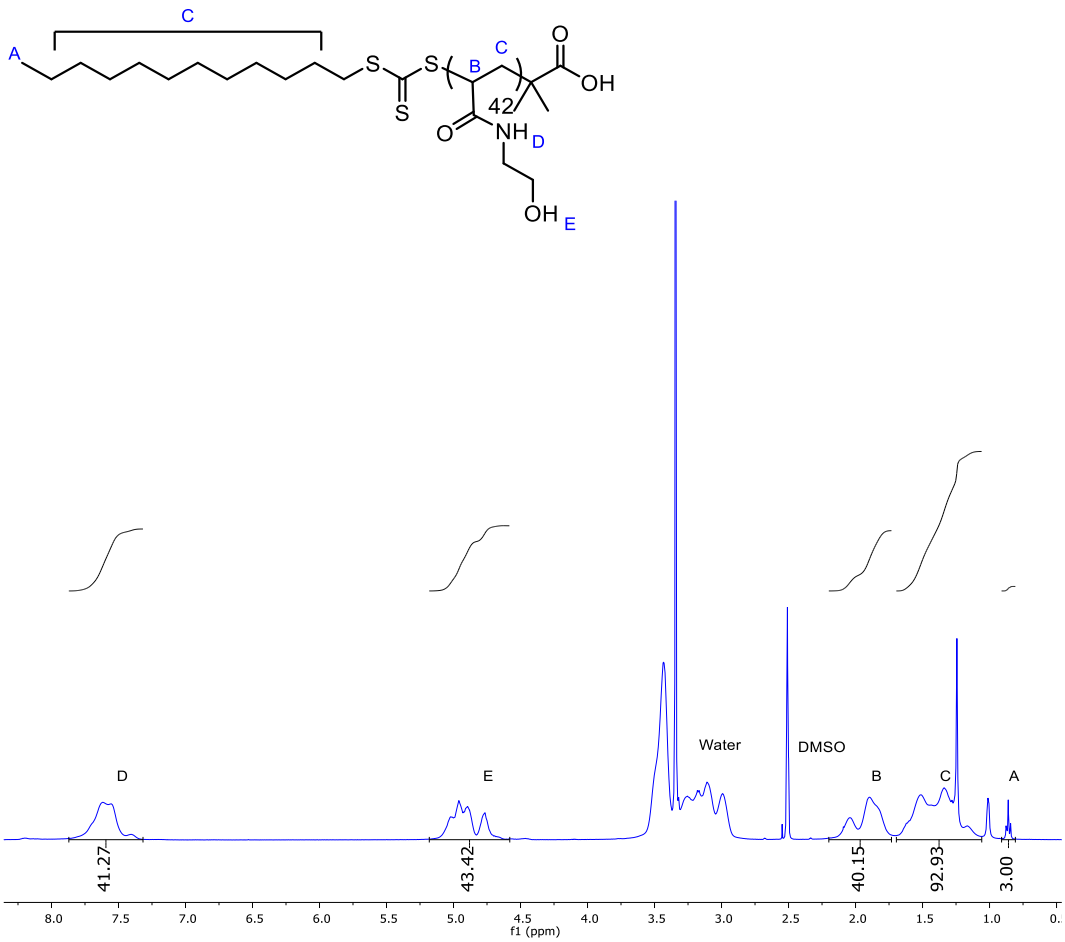


Figure A1.23 ^{1}H NMR spectrum of DDMAT-[(HEA)$_{100\%}$]$_{42}$ in DMSO-d$_6$

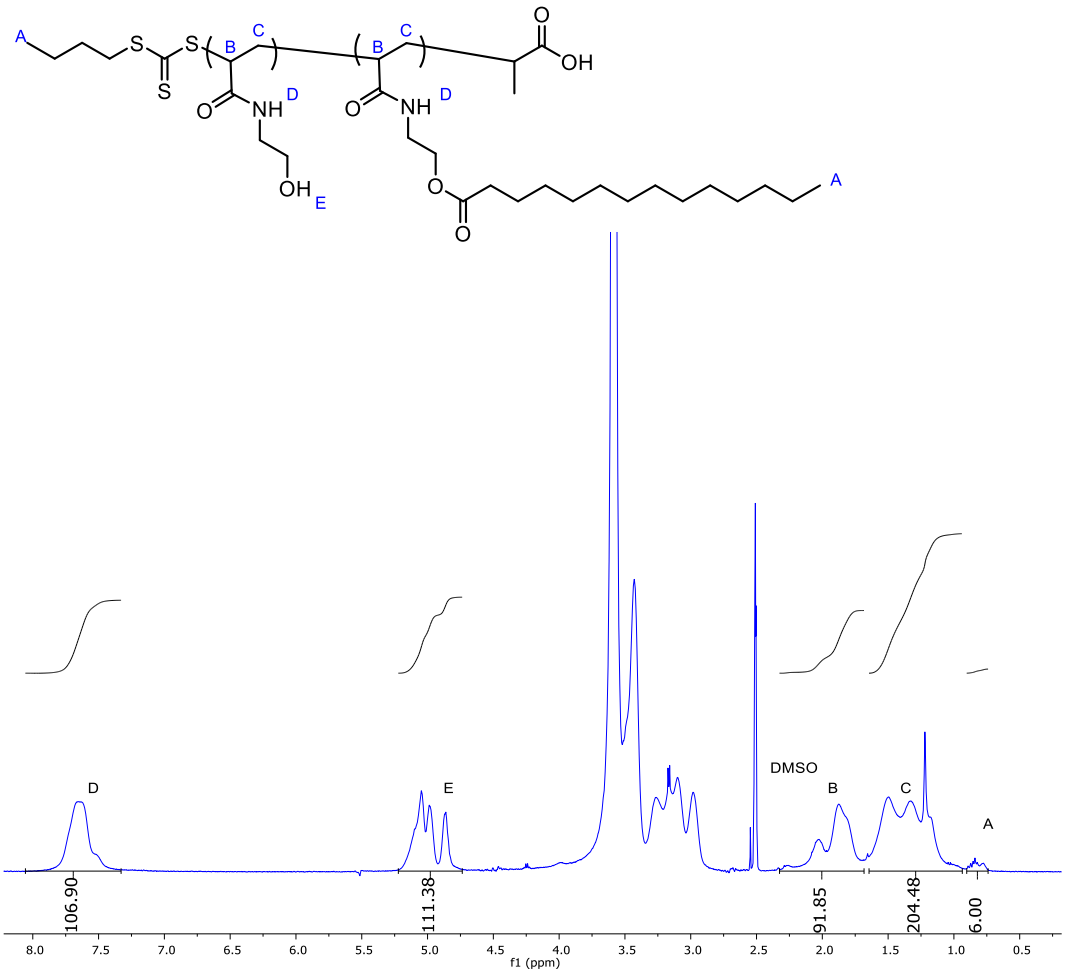


Figure A1.24 ^{1}H NMR spectrum of **(6)**-$[(HEA)_{100\%}]_{102}$ in DMSO-d_6

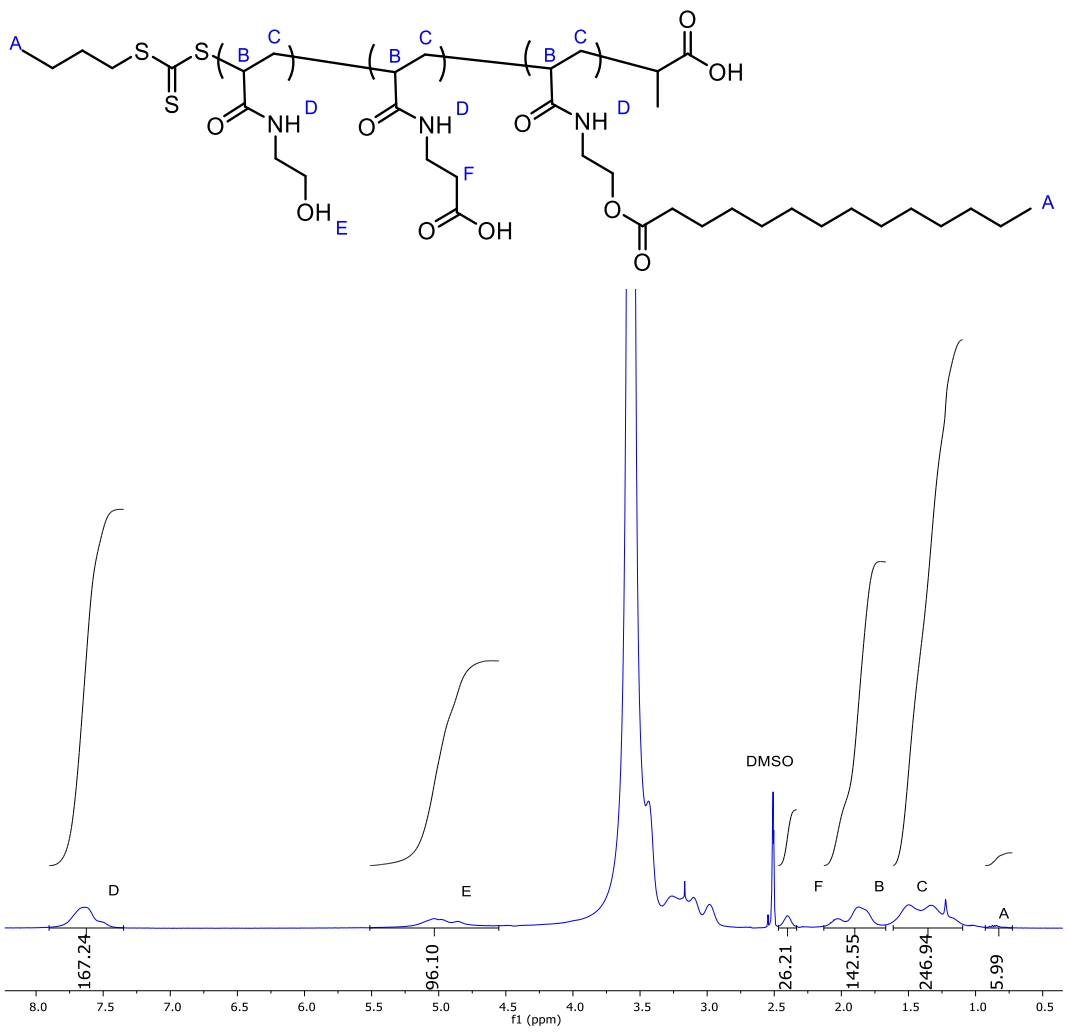


Figure A1.25 ^{1}H NMR spectrum of **(6)**-[(HEA)$_{90\%}$-*r*-(AAPA)$_{10\%}$]$_{167}$ in DMSO-d$_6$

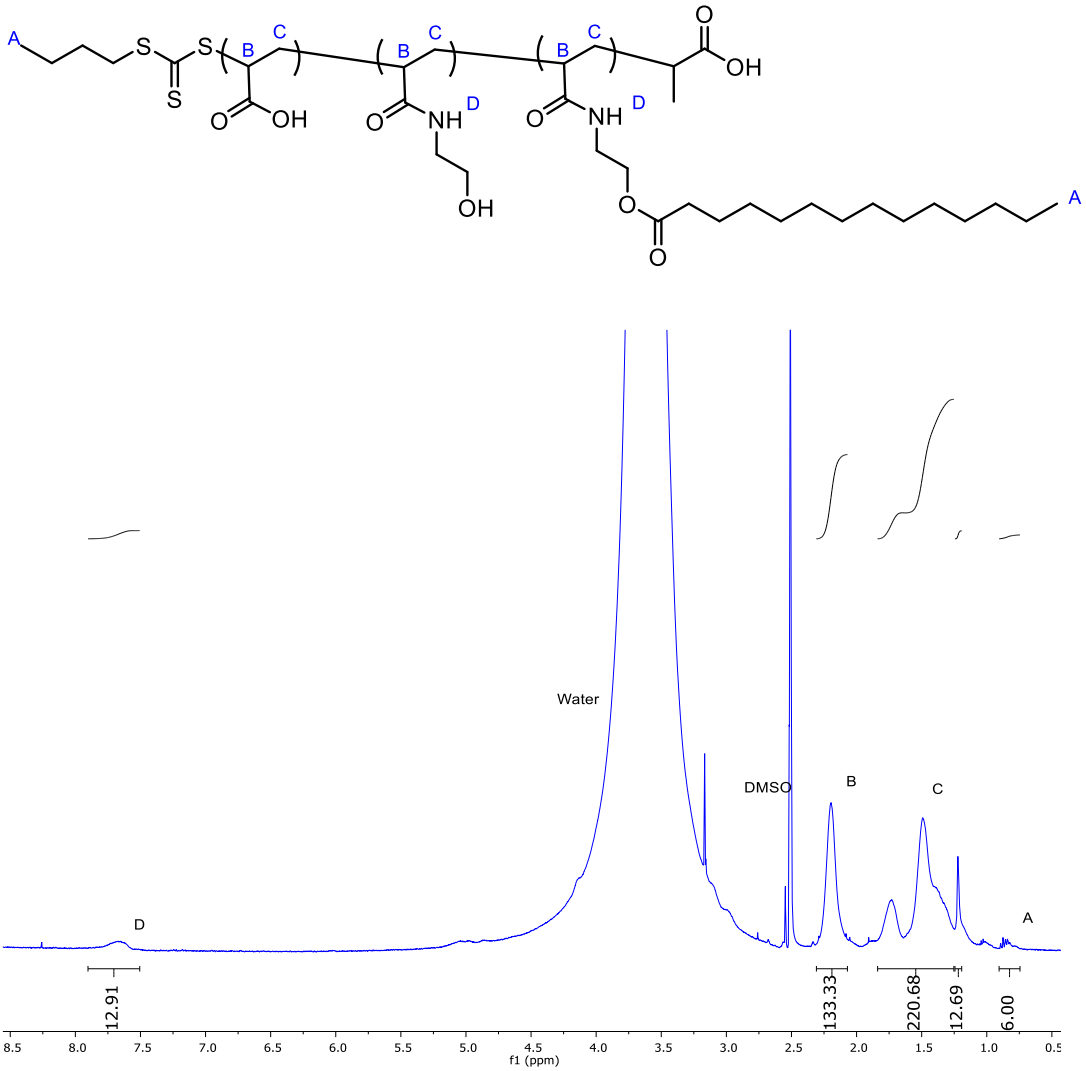


Figure A1.26 ^{1}H NMR spectrum of **(6)**-$[(AA)_{100\%}]_{120}$ in DMSO-d_6

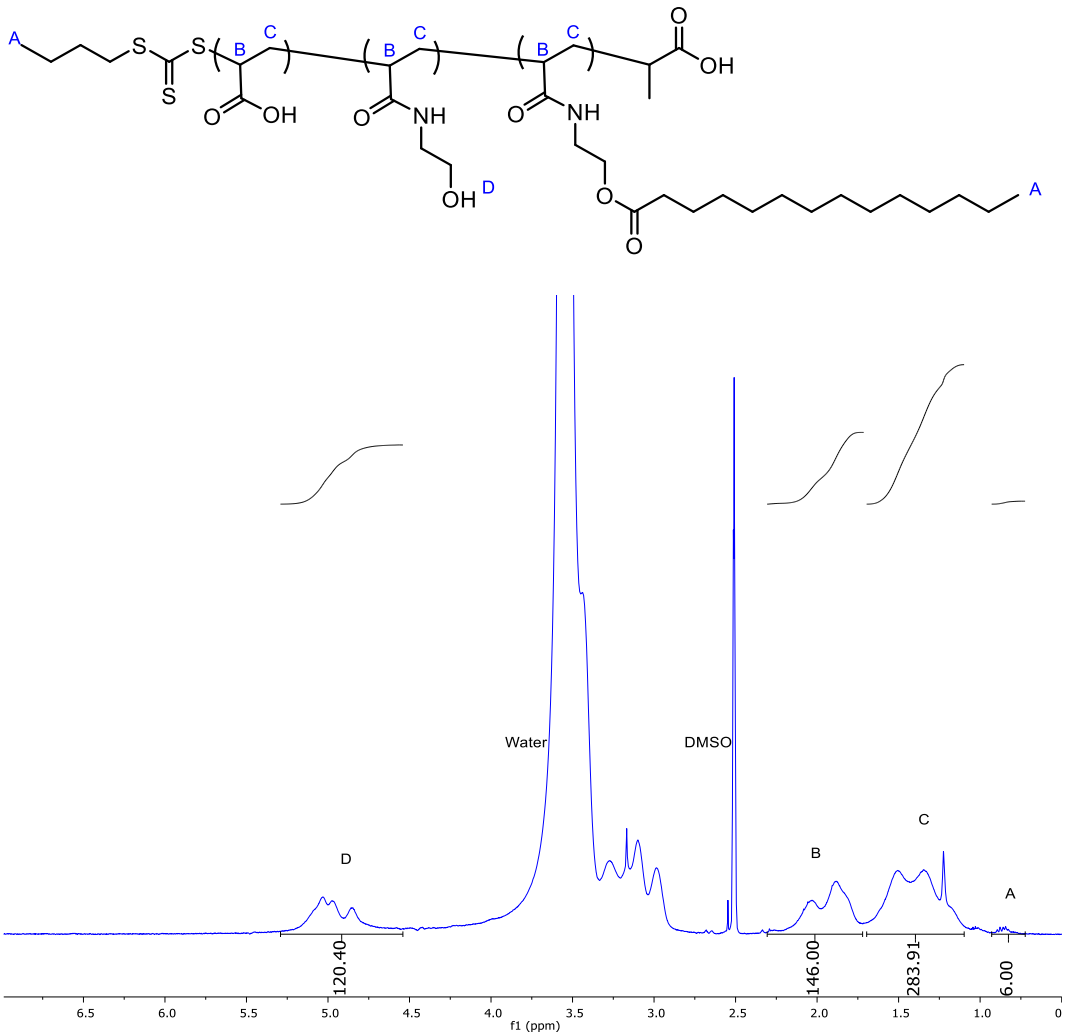


Figure A1.27 ^{1}H NMR spectrum of **(6)**-[(HEA)$_{90\%}$-*r*-(AA)$_{10\%}$]$_{146}$ in DMSO-d$_6$

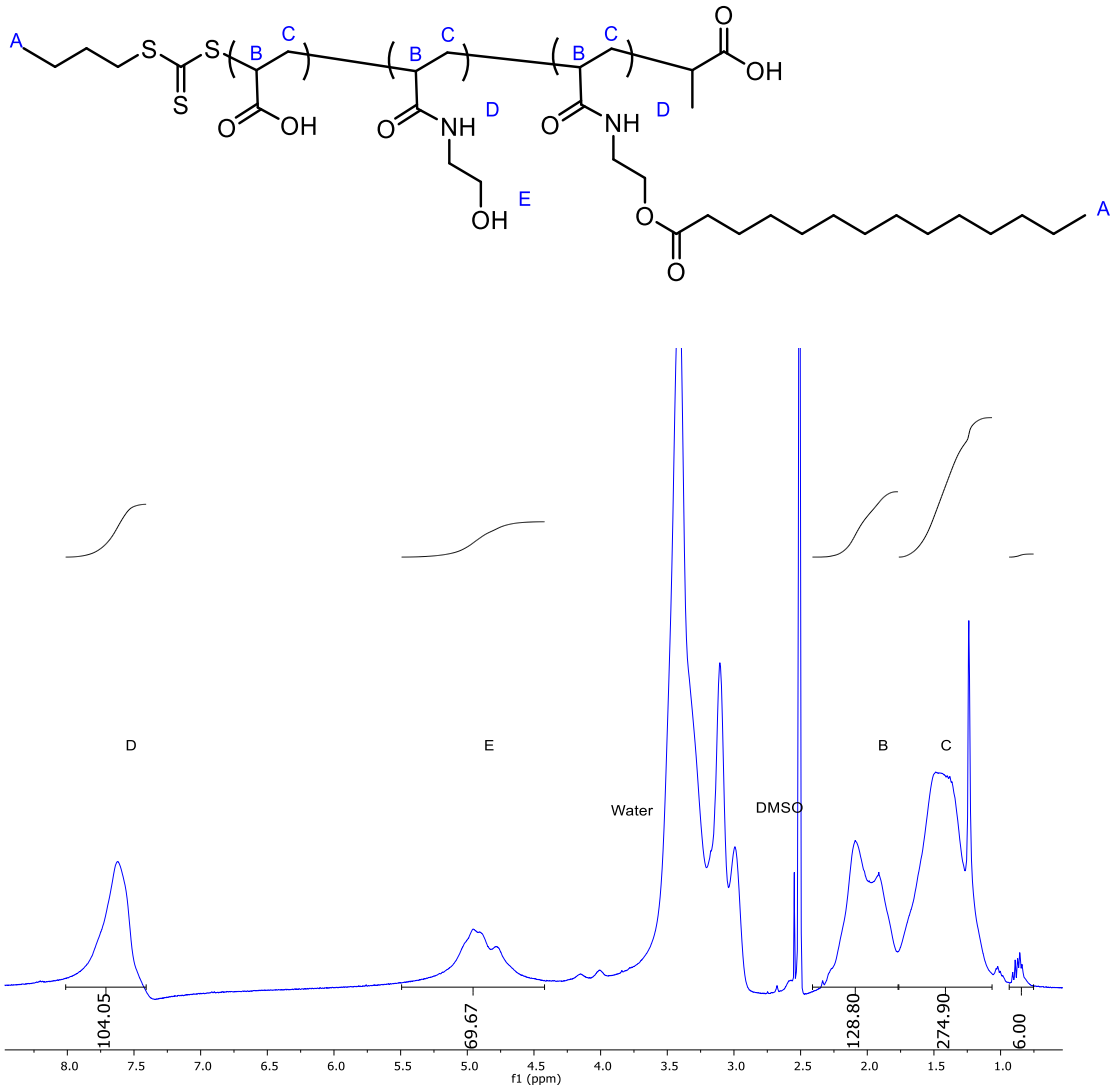


Figure A1.28 ^{1}H NMR spectrum of **(6)**-[(HEA)$_{70\%}$-*r*-(AA)$_{30\%}$]$_{130}$ in DMSO-d$_6$

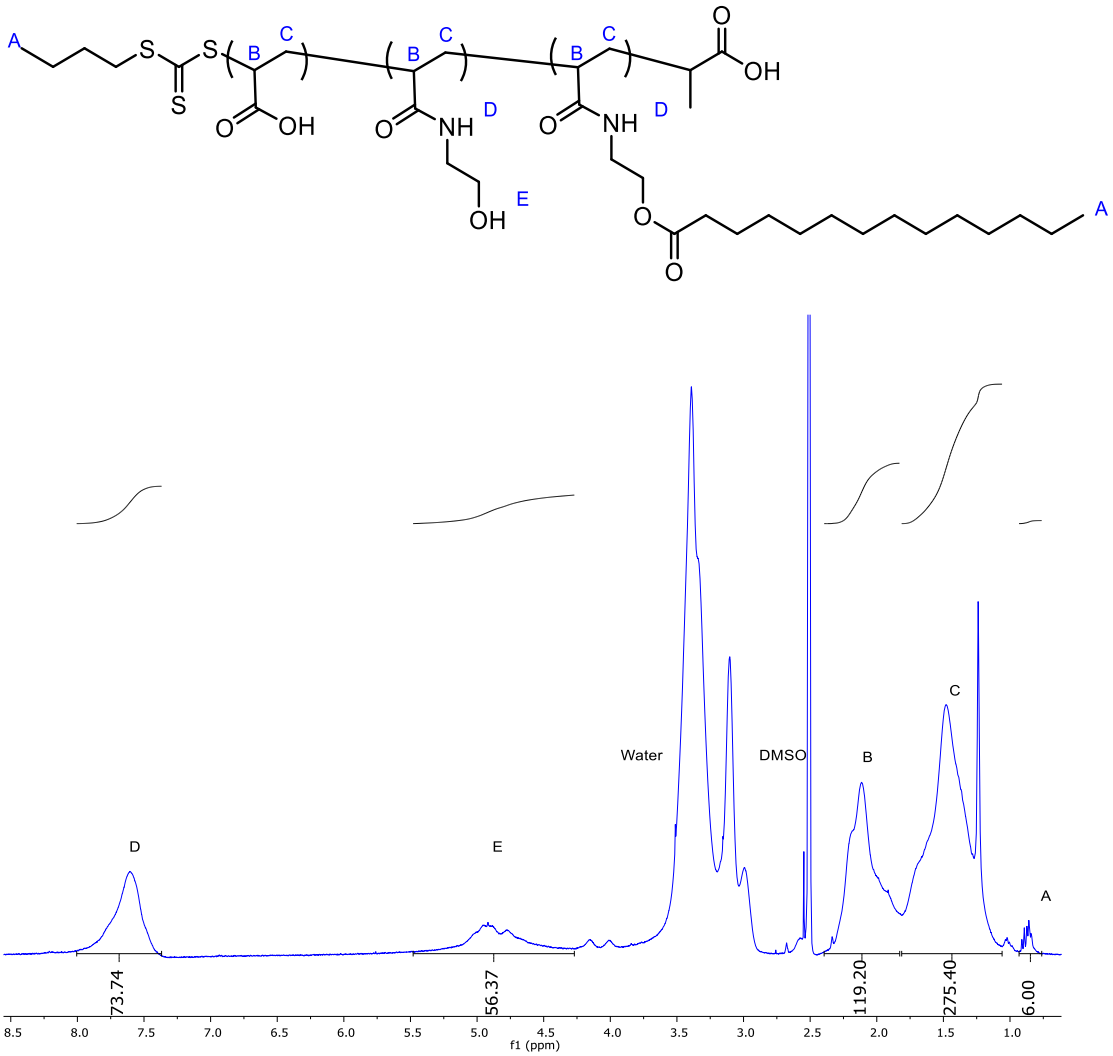


Figure A1.29 ^{1}H NMR spectrum of **(6)**-[(HEA)$_{50\%}$-*r*-(AA)$_{50\%}$]$_{120}$ in DMSO-d$_6$

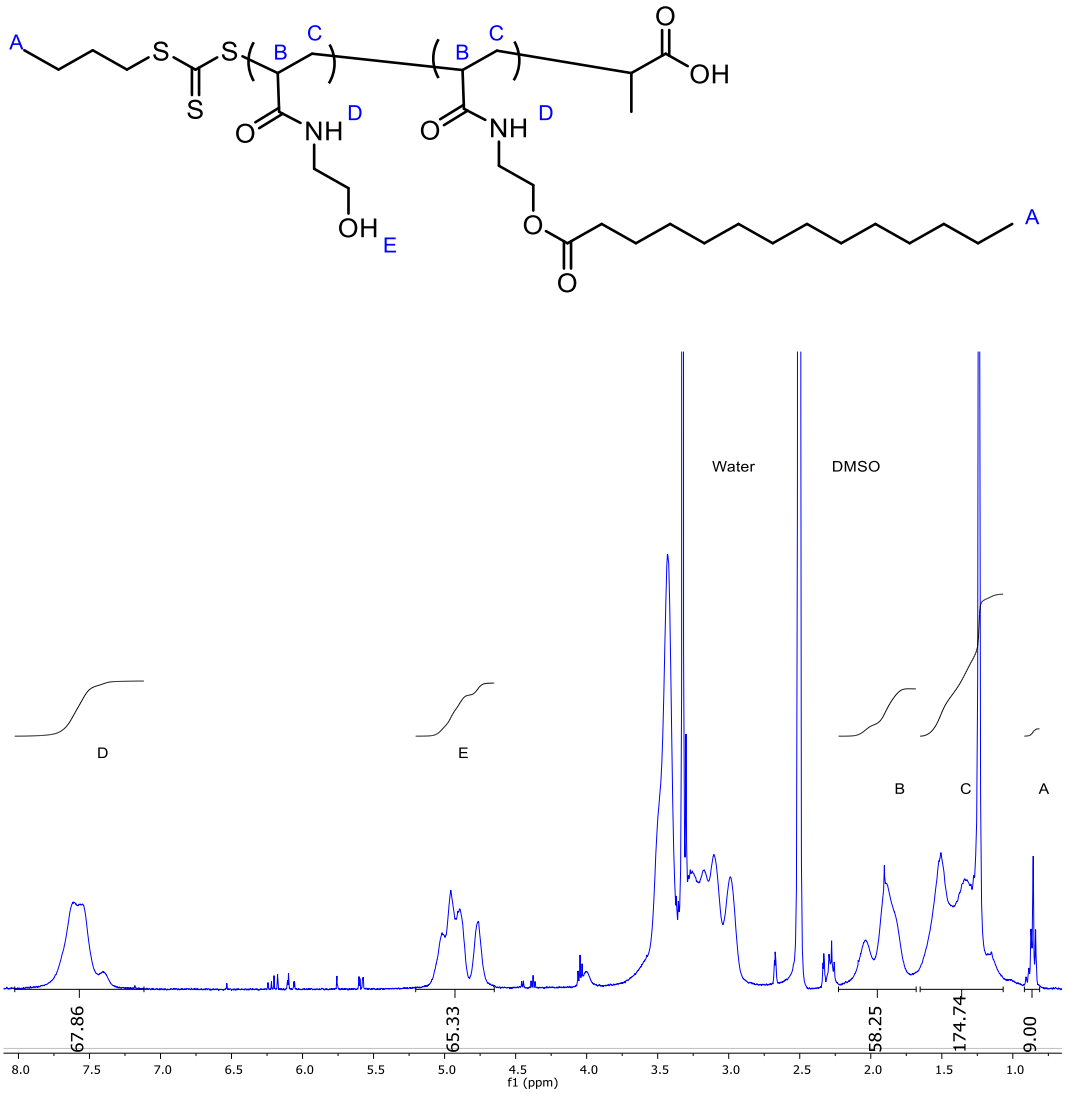


Figure A1.30 ^{1}H NMR spectrum of [**(5)**$_{30\%}$-*r*-(HEA)$_{70\%}$]$_{10}$-b-[(HEA)$_{100\%}$]$_{65}$ in DMSO-d$_6$

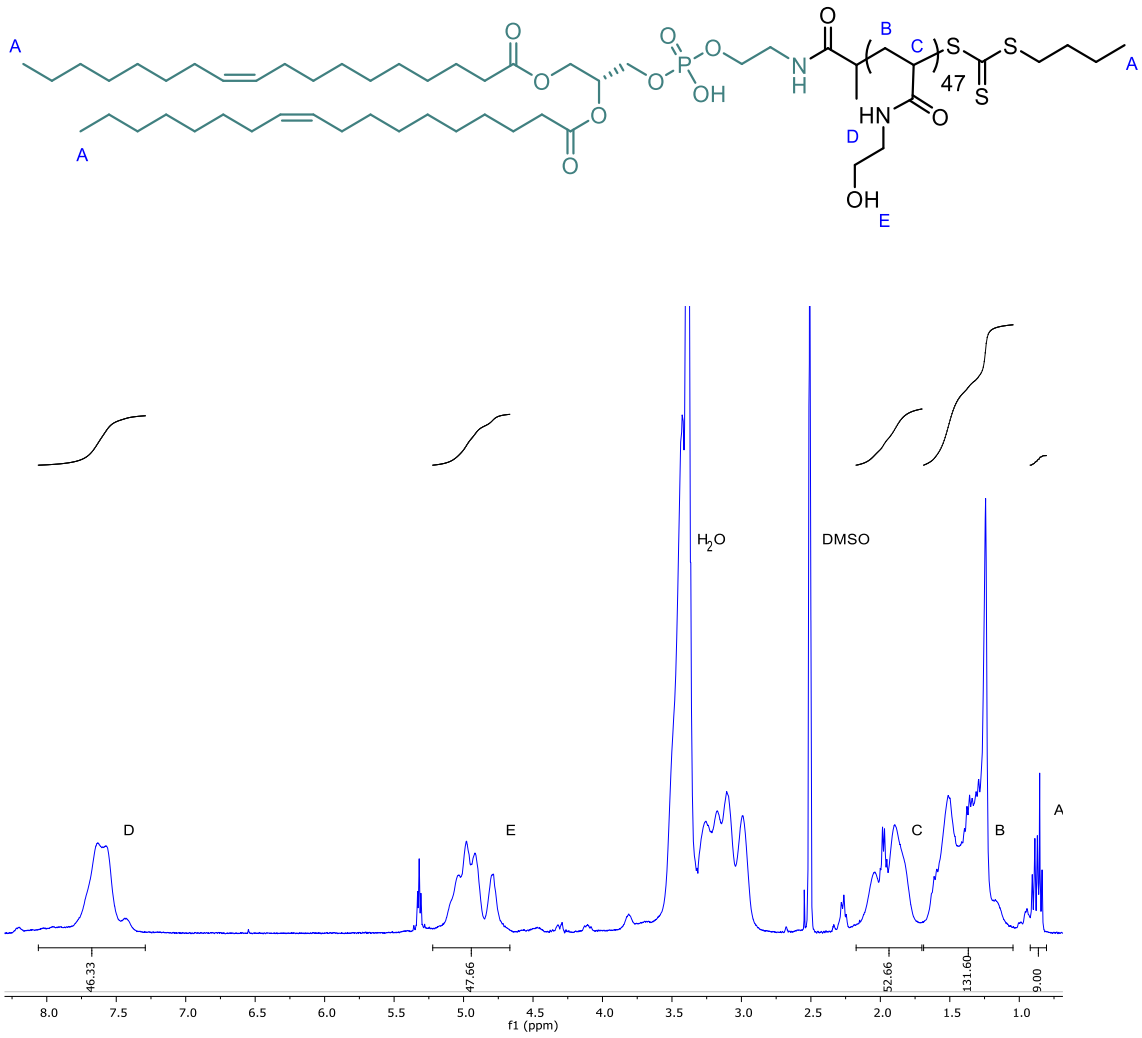


Figure A1.31 ^{1}H NMR spectrum of DOPE-$[(HEA)_{100\%}]_{47}$ in DMSO-d_6

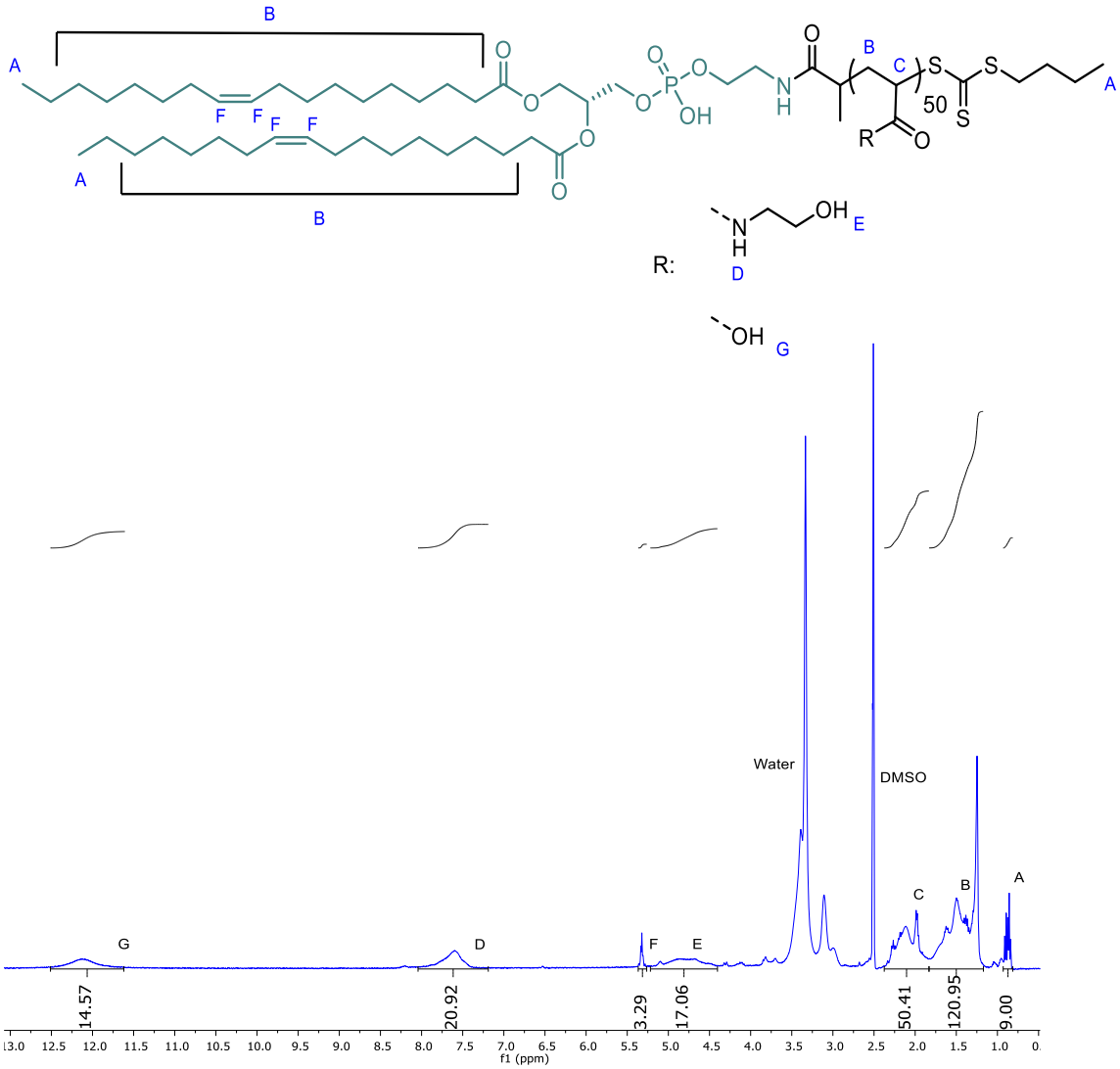


Figure A1.32 ^{1}H NMR spectrum of DOPE-[(HEA)$_{50\%}$-*r*-(AA)$_{50\%}$]$_{50}$ in DMSO-d$_6$

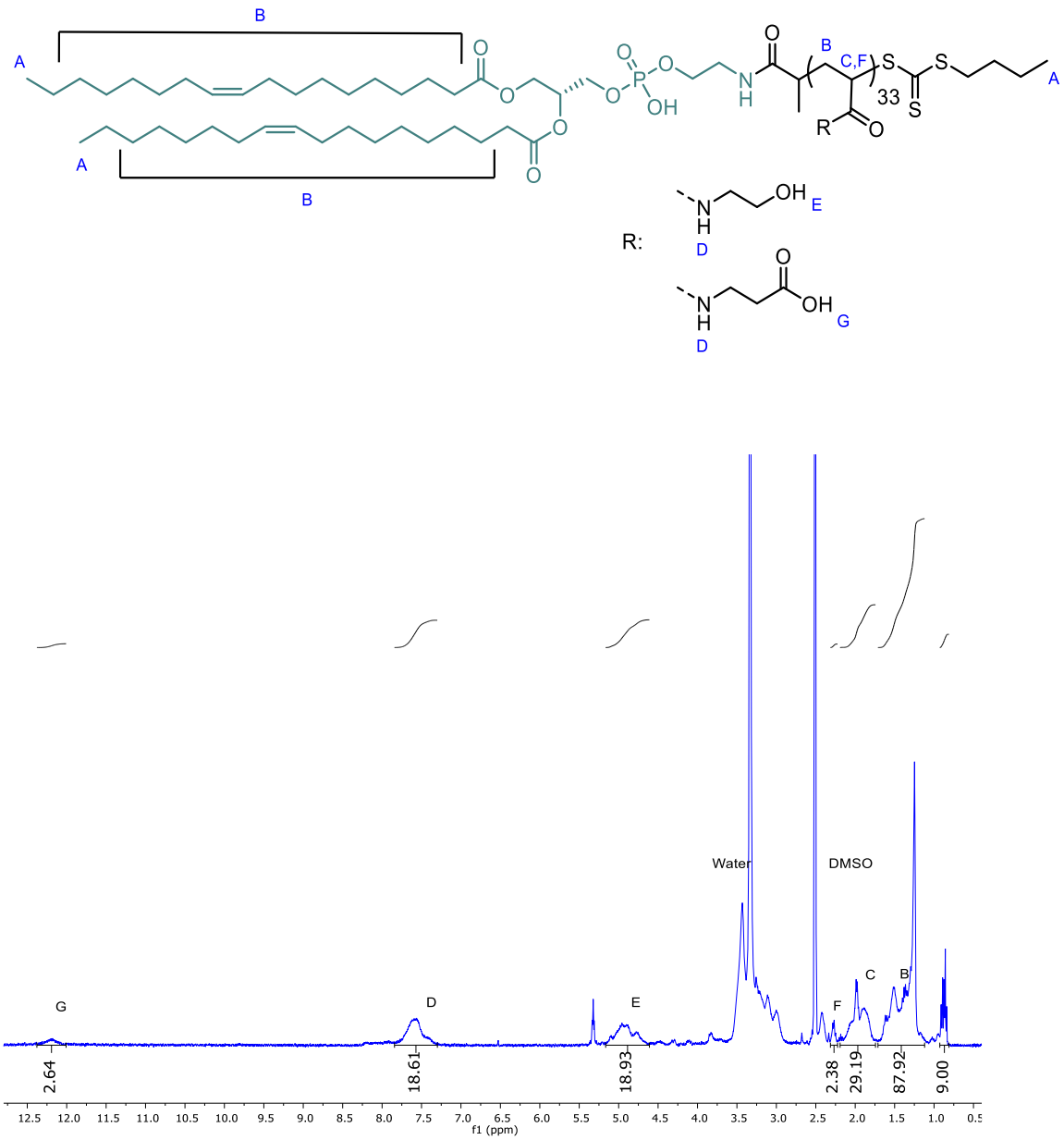
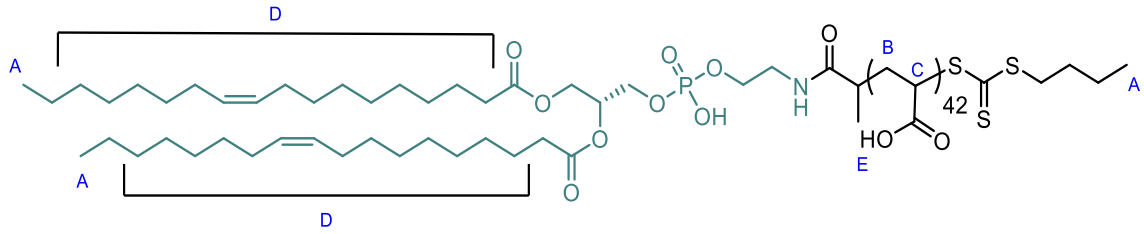


Figure A1.33 ^{1}H NMR spectrum of DOPE-[(HEA)$_{90\%}$-*r*-(AAPA)$_{10\%}$]$_{33}$ in DMSO-d$_6$



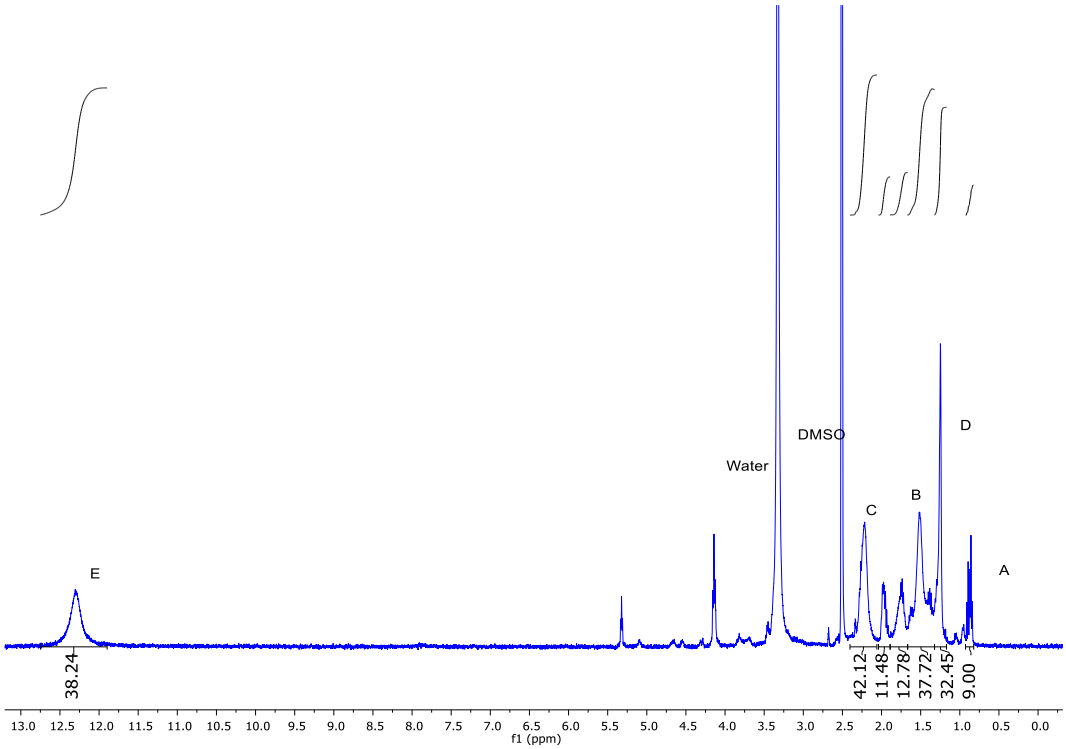


Figure A1.34 ^{1}H NMR spectrum of DOPE-$[(AA)_{100\%}]_{42}$ in DMSO-d_6

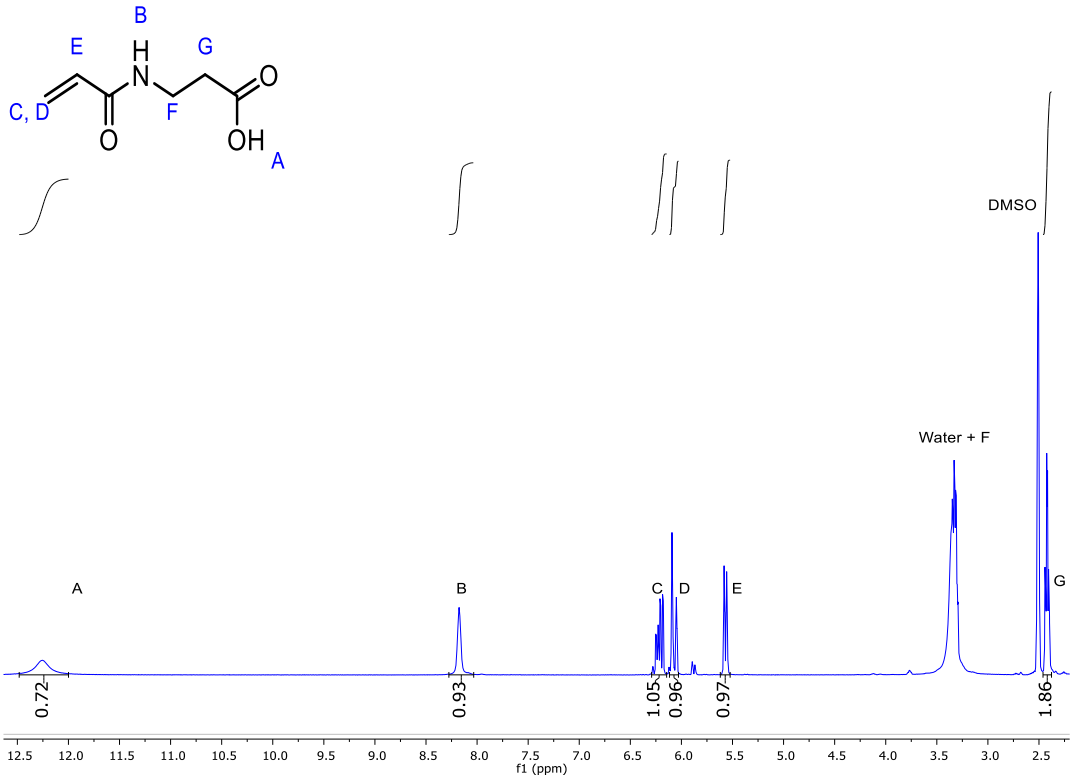


Figure A1.35 ^{1}H NMR spectrum of 3-AAPA, **(4)** in DMSO-d_6

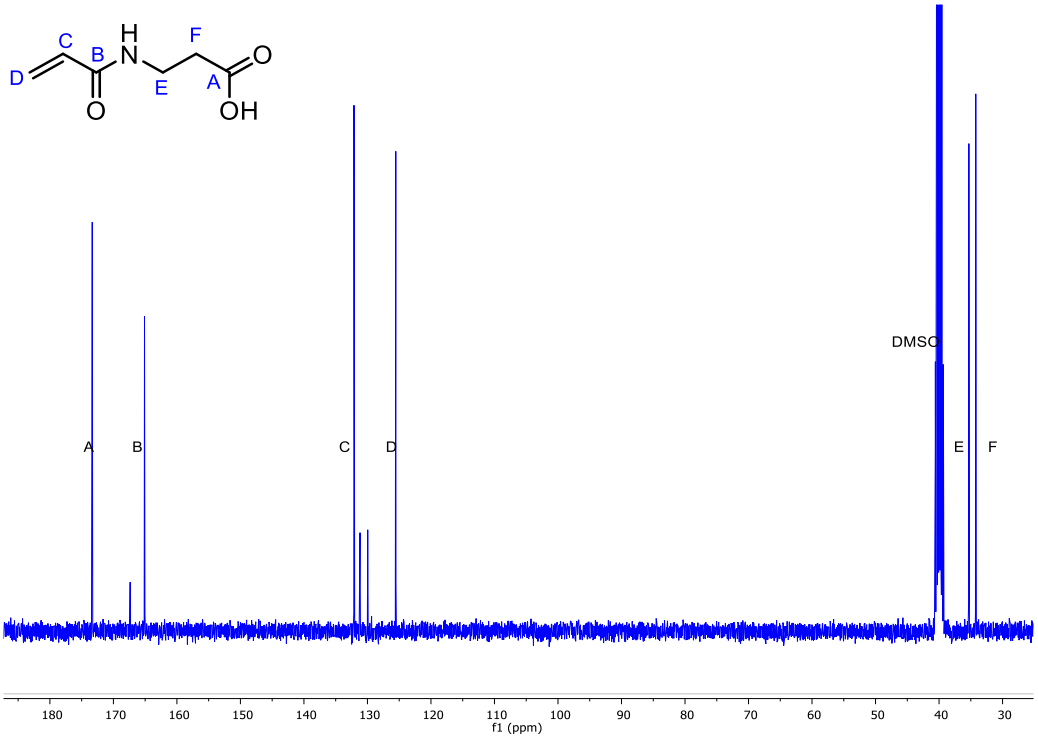


Figure A1.36 ^{13}C NMR spectrum of spectrum of 3-AAPA, **(4)** in DMSO-d_6

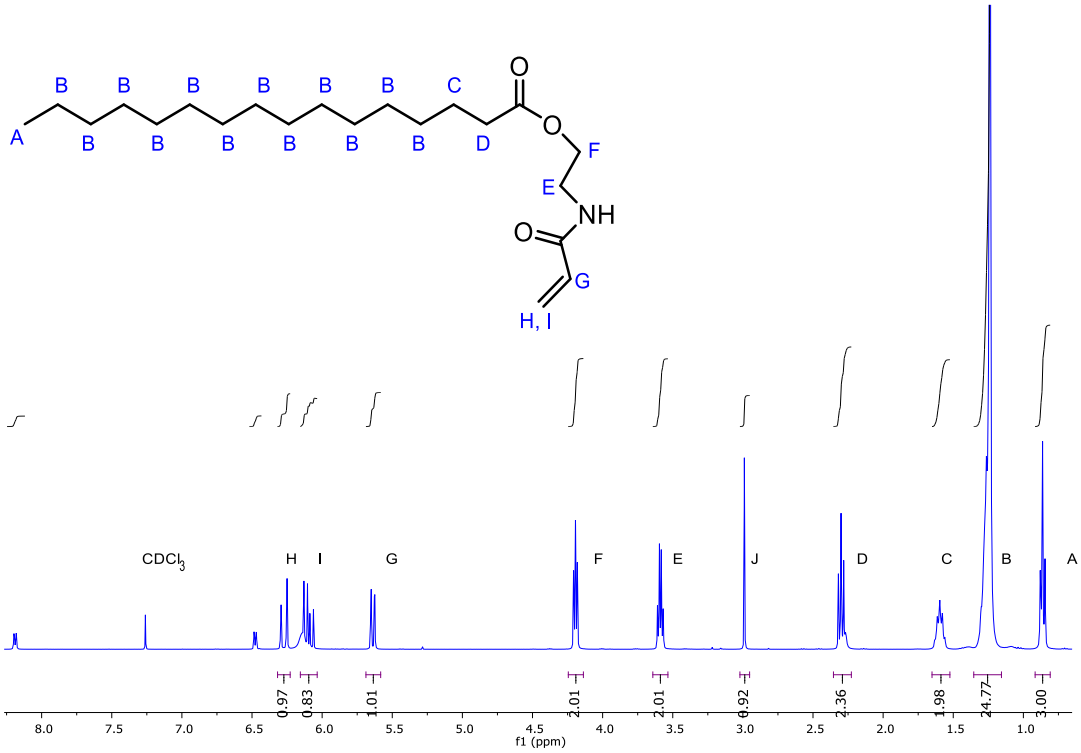


Figure A1.37 ^{1}H NMR spectrum of 2-AP, **(5)** in $CDCl_3$

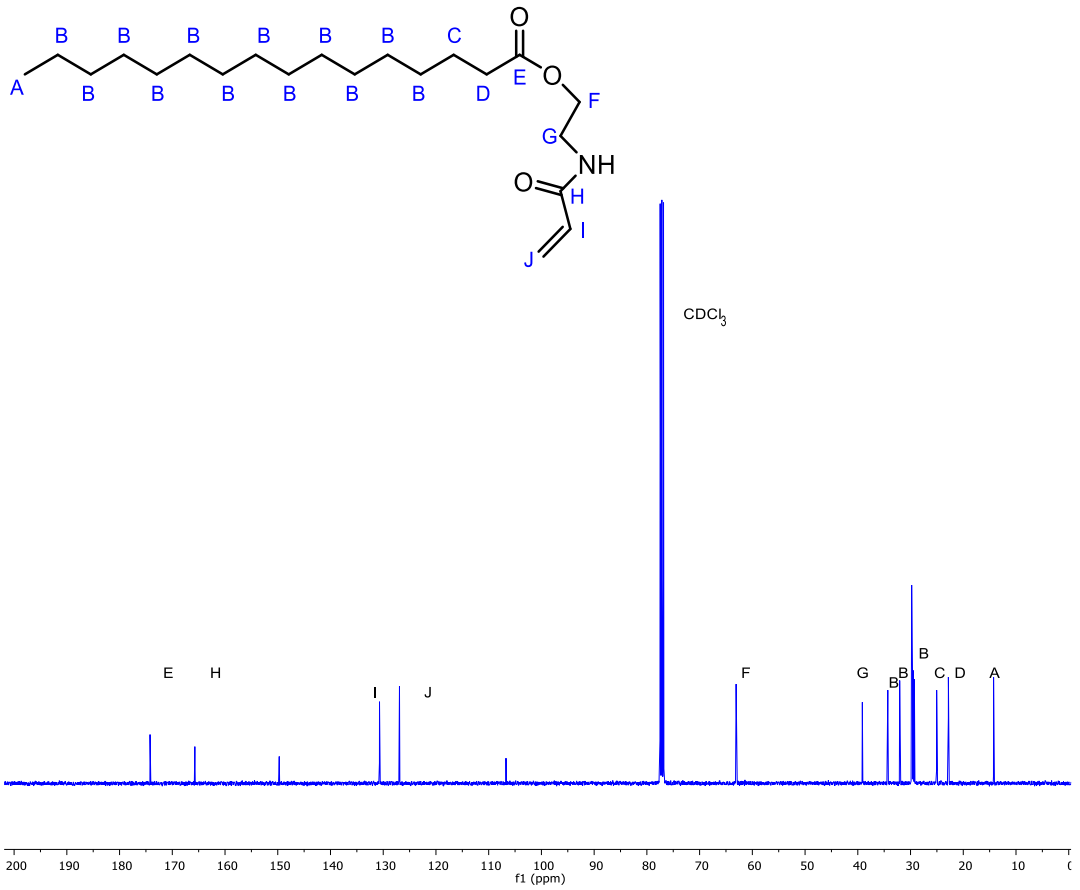


Figure A1.38 ^{13}C NMR spectrum of 2-AP, **(5)** in $CDCl_3$

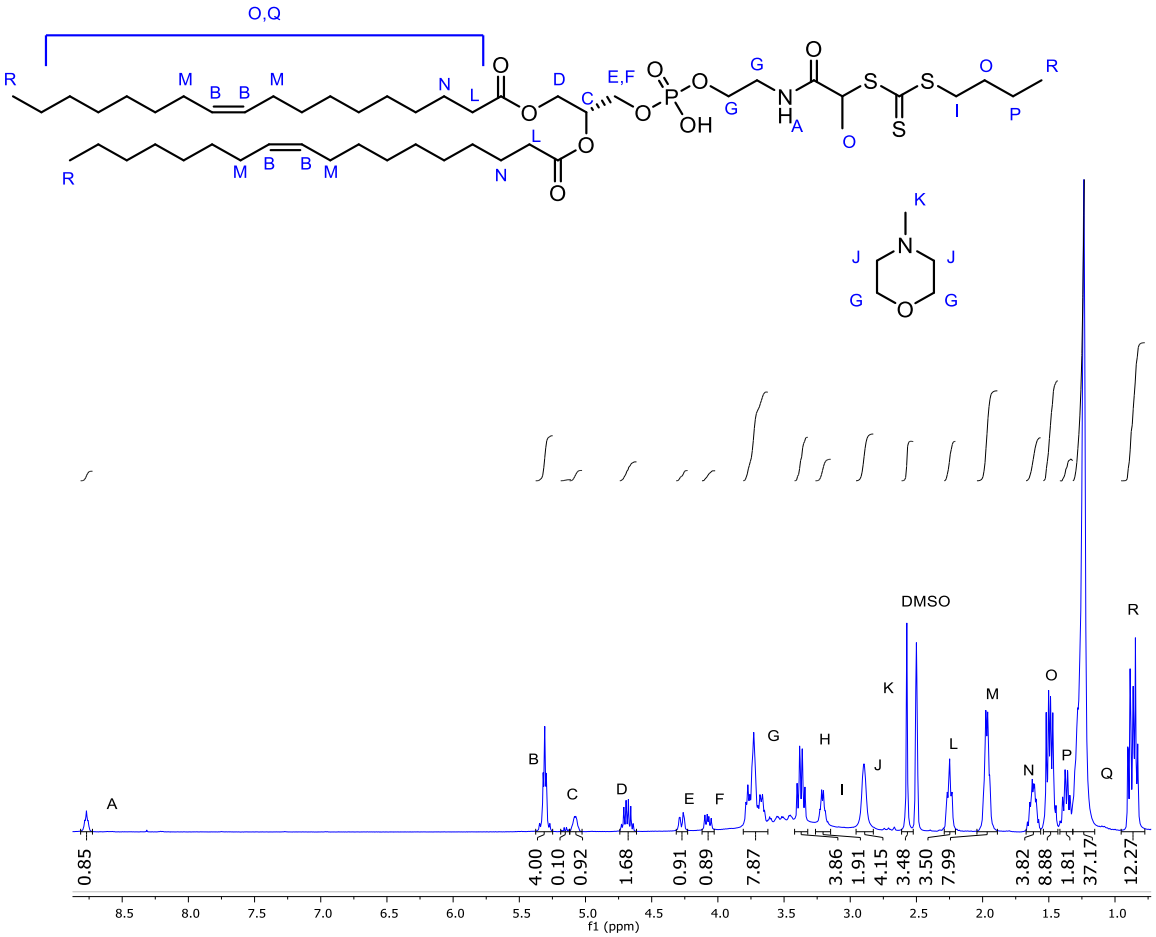


Figure A1.39 ^{1}H NMR spectrum of DOPE RAFT agent **(2)** in DMSO-d_6

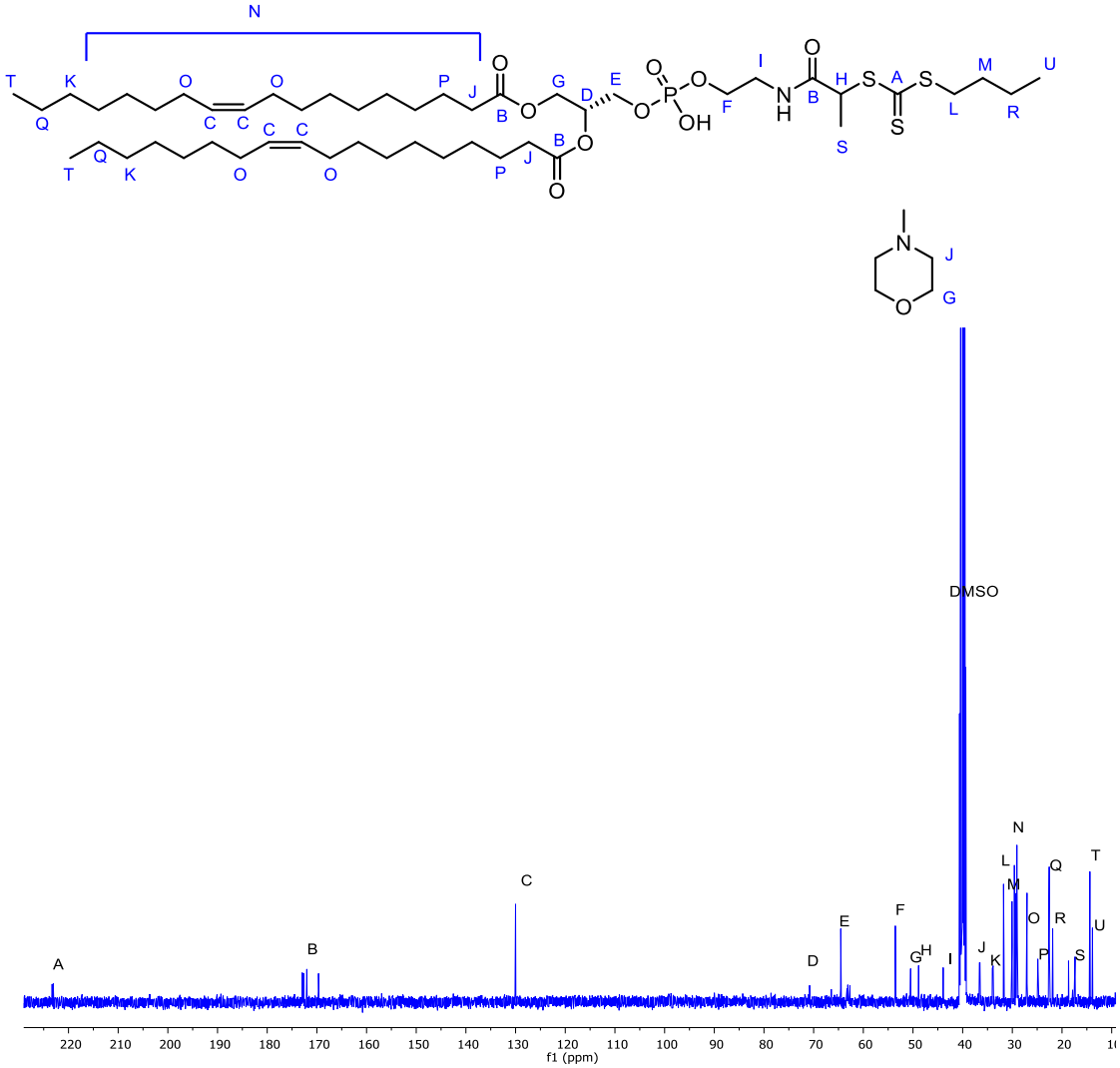


Figure A1.40 ^{13}C NMR spectrum of DOPE RAFT agent **(2)** in DMSO-d_6

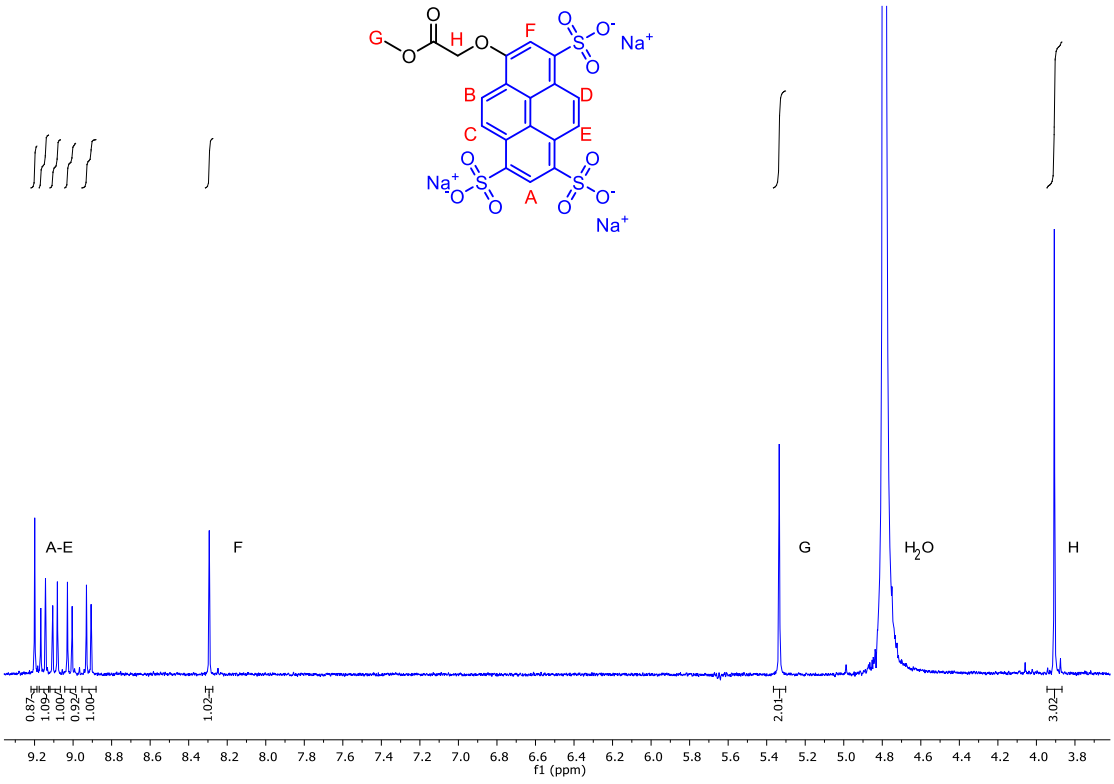


Figure A1.41 ^{1}H NMR spectrum of Pyranine methyl ester **(7)** in D_2O

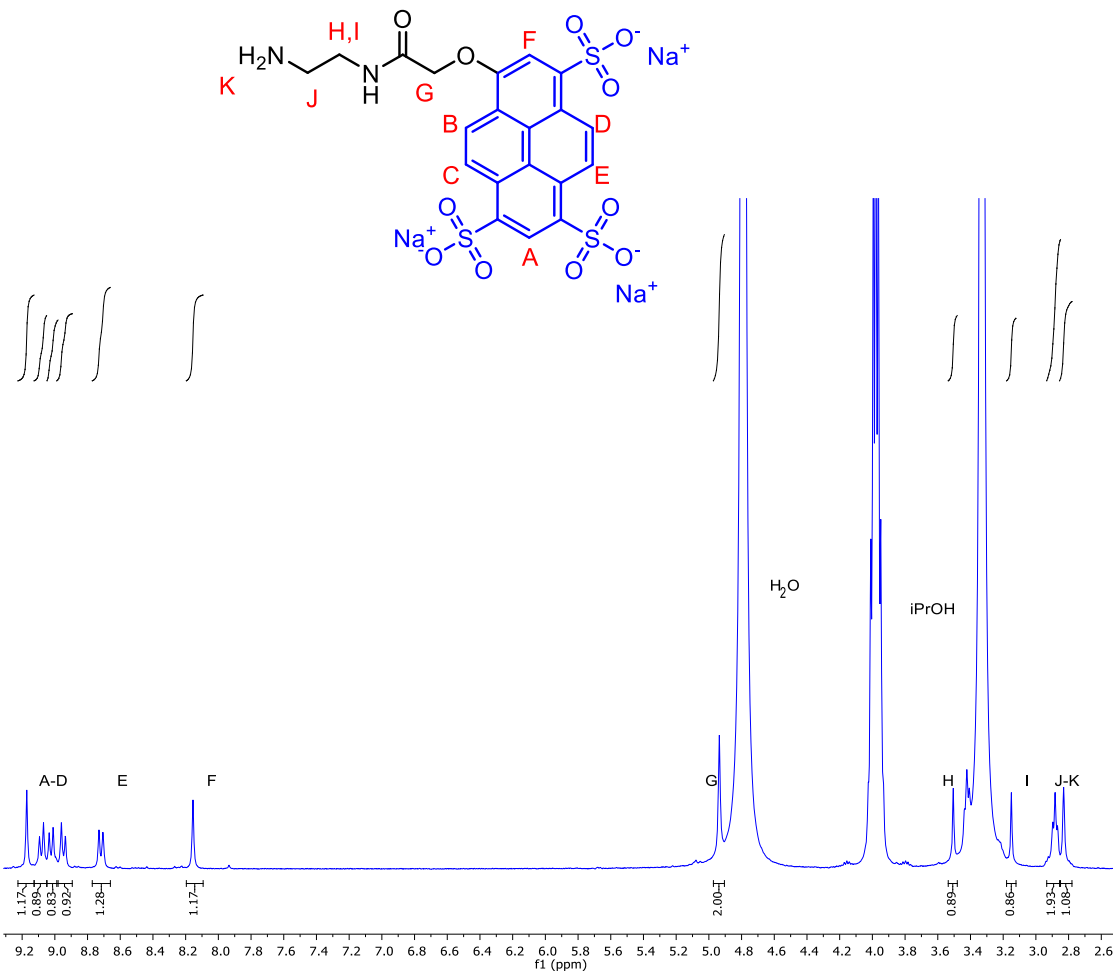


Figure A1.42 ^{1}H NMR spectrum of Pyranine ethylenediamine **(8)** in D_2O

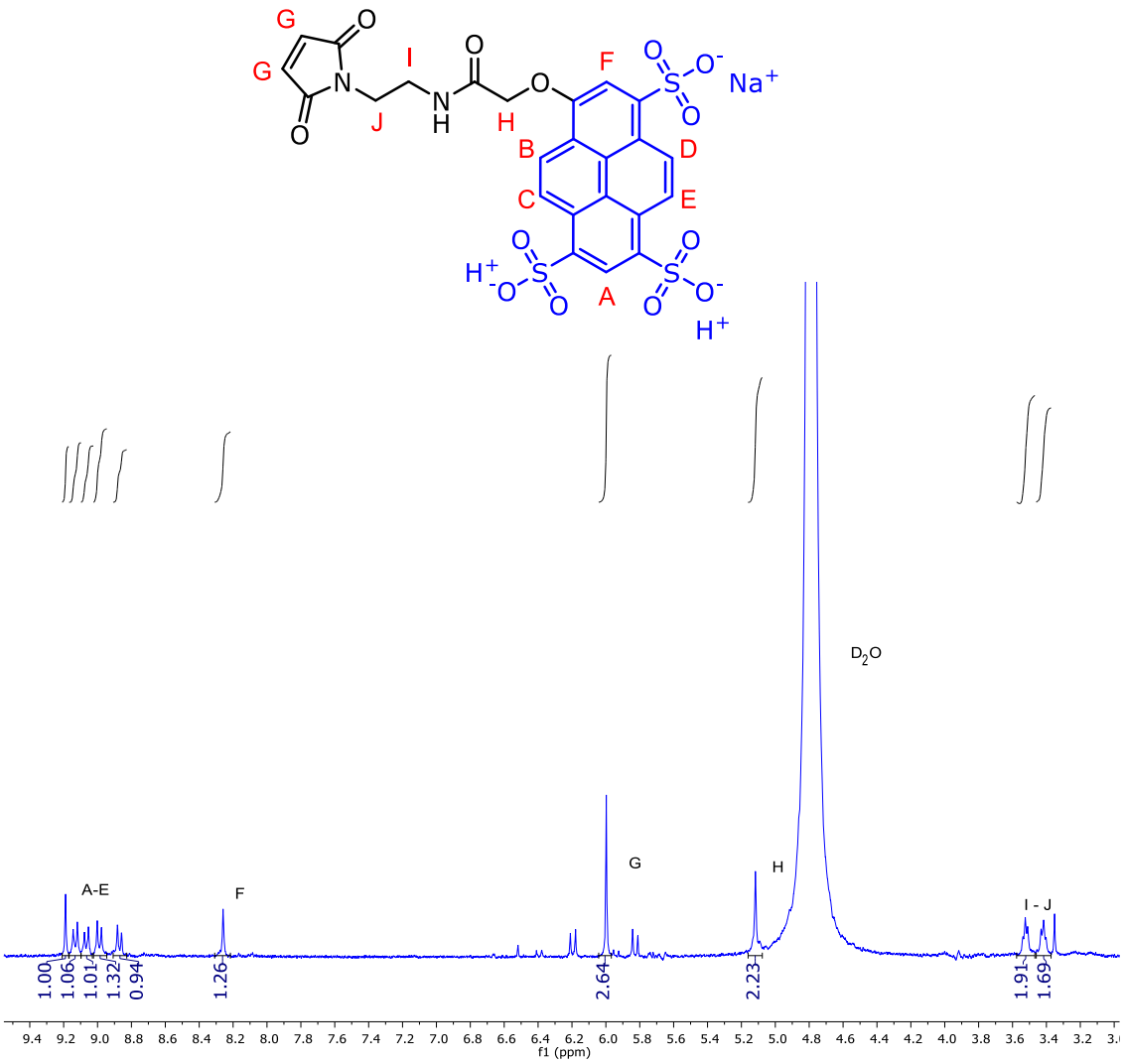


Figure A1.43 ^{1}H NMR spectrum of MalPyr Blue **(9)** in D_2O

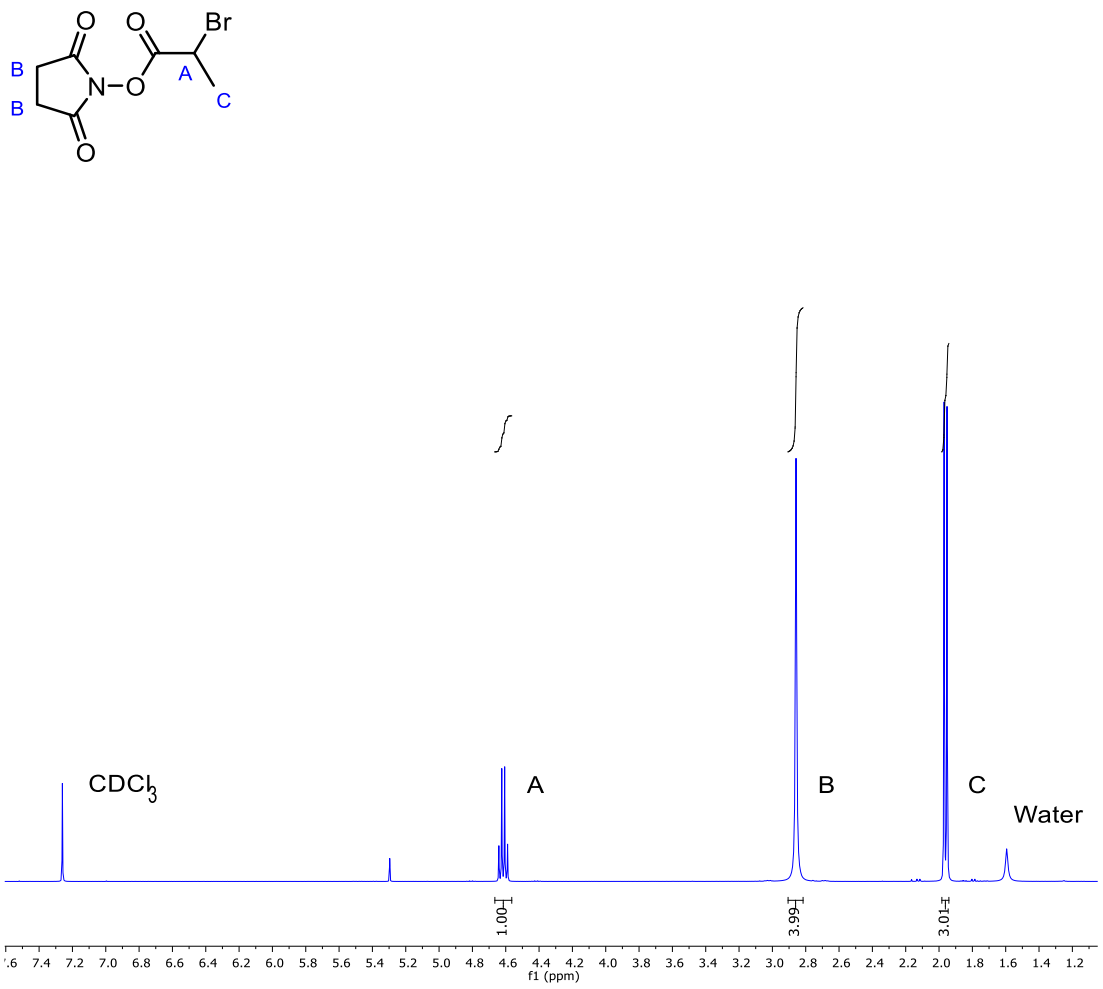


Figure A1.44 ^{1}H NMR spectrum of bromopropyonyl O-succinimide **(10)** in $CDCl_3$

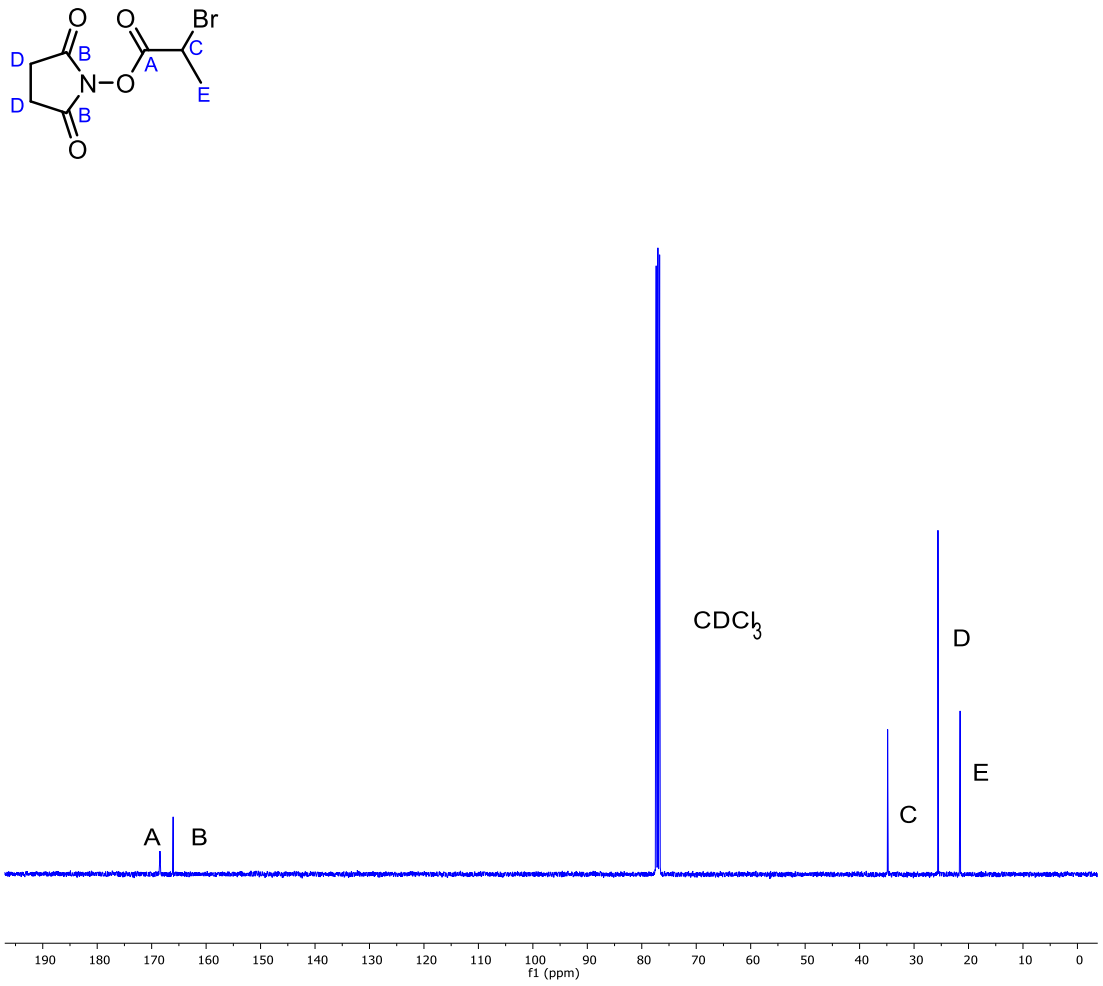


Figure A1.45 ^{13}C NMR spectrum of bromopropyonyl O-succinimide **(10)** in $CDCl_3$

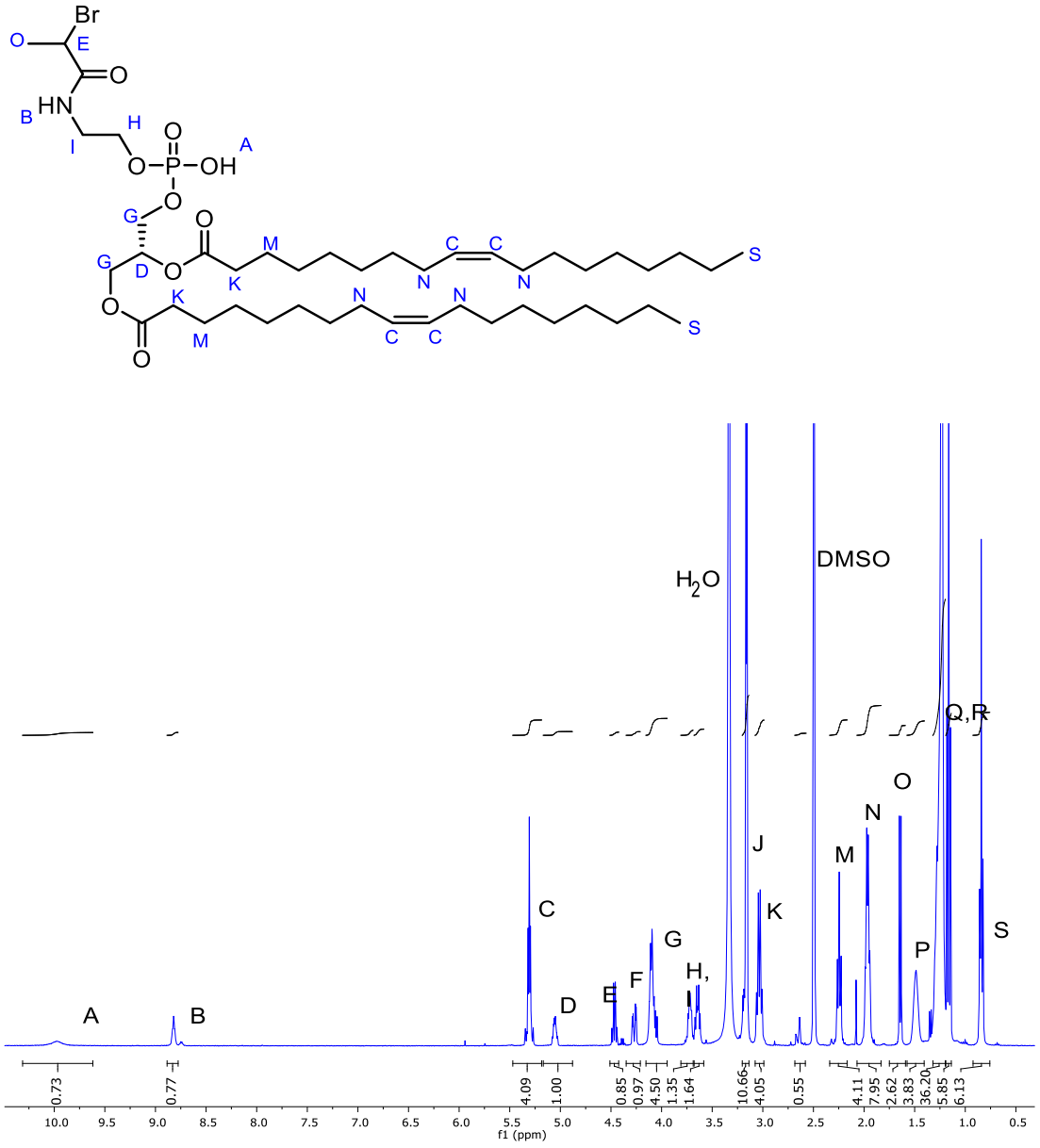


Figure A1.46 ^{1}H NMR spectrum of bromo-phosphatidylethanolamide **(11)** in DMSO-d_6

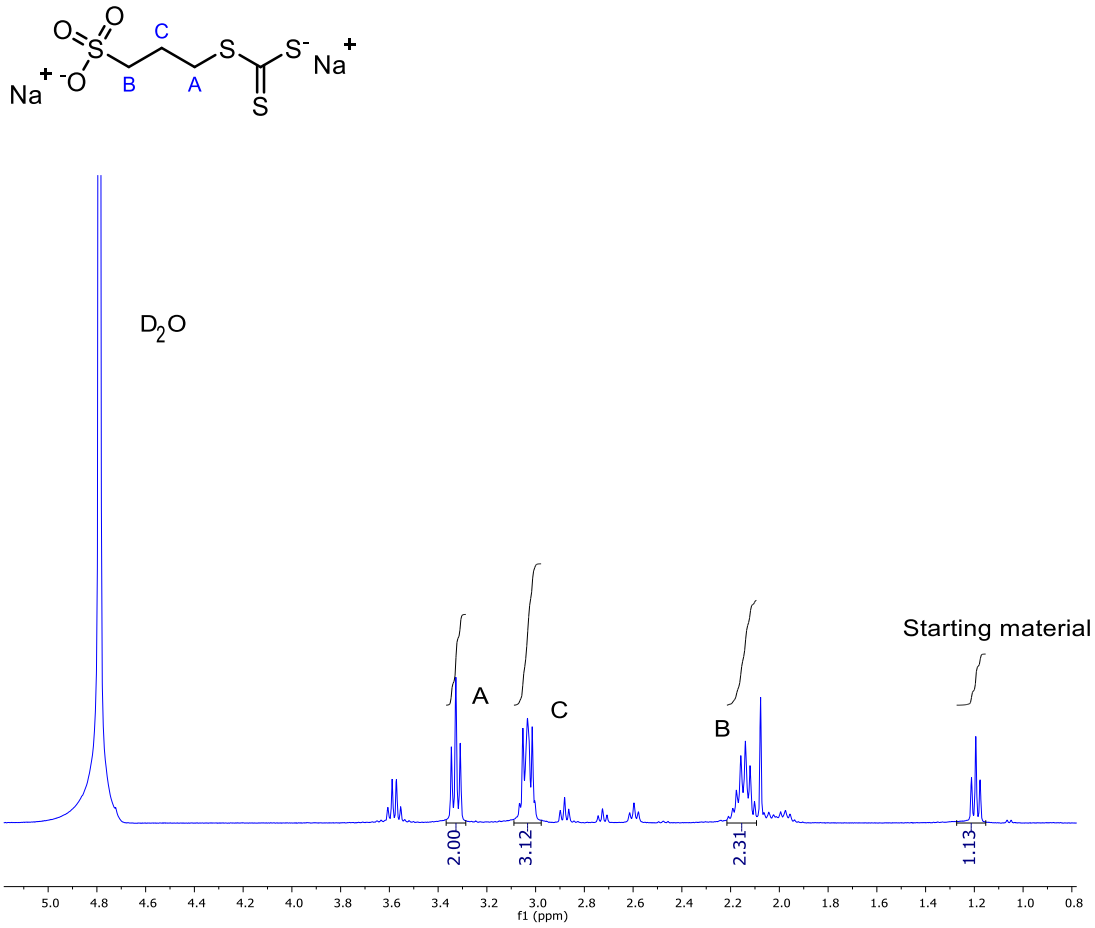


Figure A1.47 ^{1}H NMR spectrum of 3-(trithiocarboxyl)propane-1-sulfonate **(12)** in D_2O

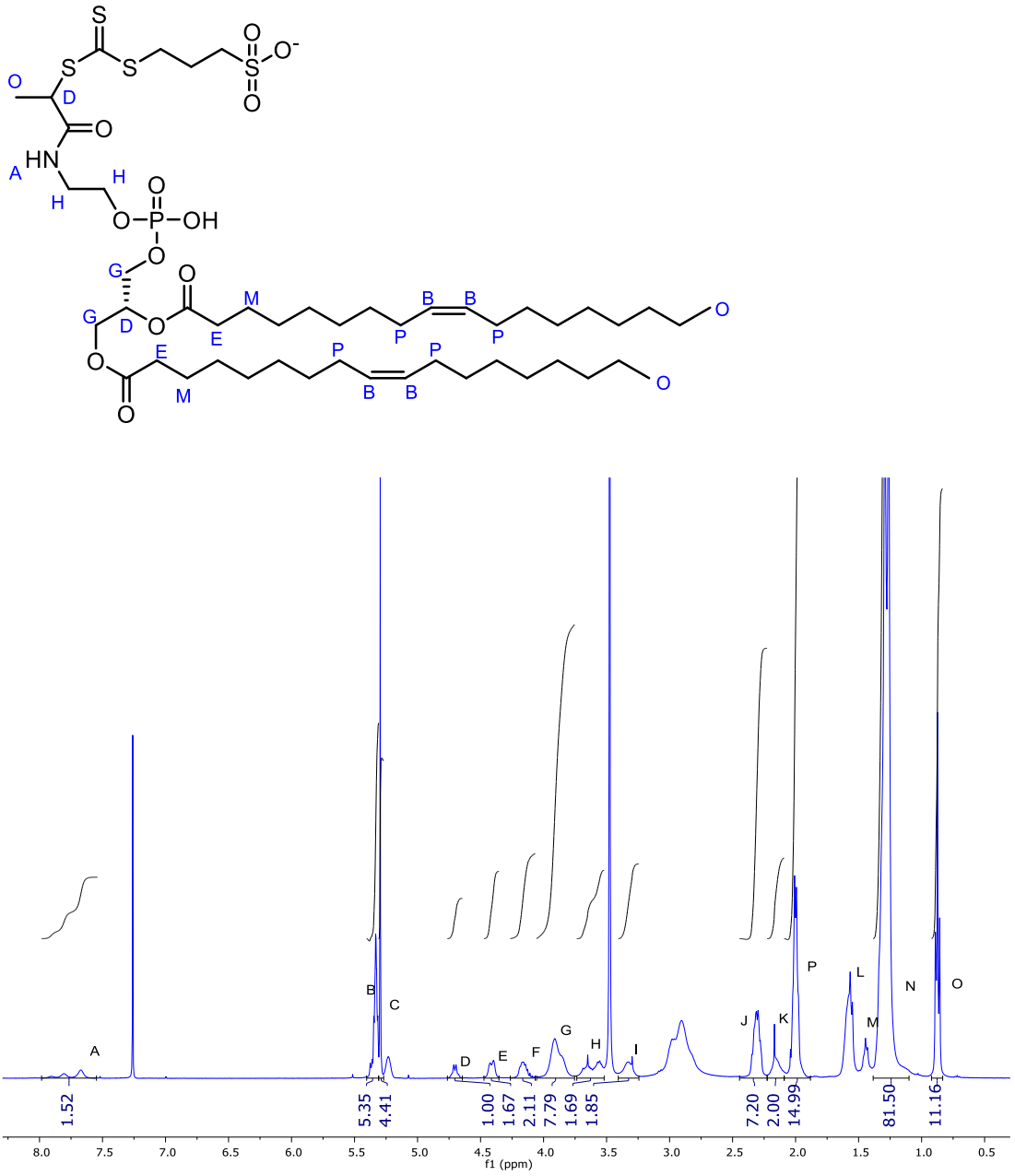


Figure A1.48 ^{1}H NMR spectrum of first DOPE-based RAFT agent **(13)** in $CDCl_3$

A1 Supporting information for Chapter 2 – Mass spectra

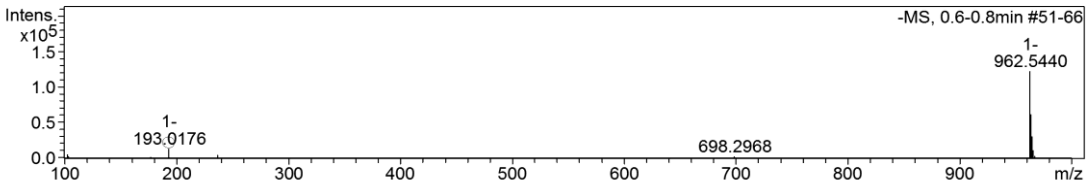


Figure A1.49 ESI-MS analysis of DOPE RAFT agent (**2**)

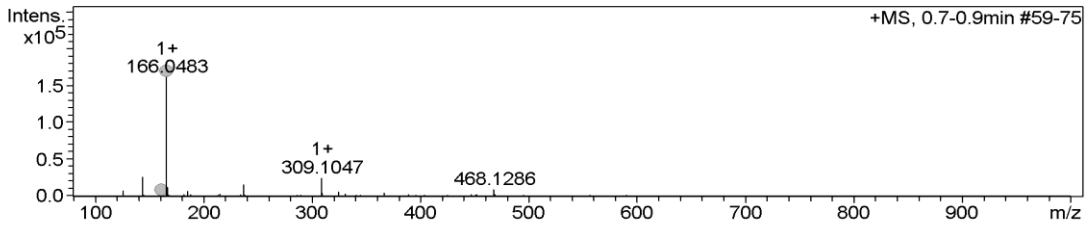


Figure A1 50 ESI-MS analysis of 3-AAPA (**4**)

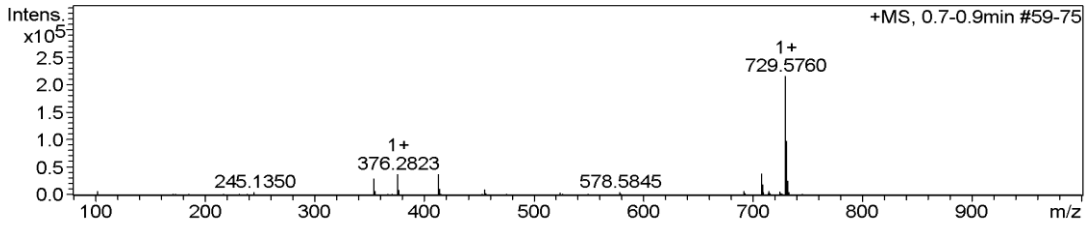


Figure A1.51 ESI-MS analysis of 2-AP (**5**)

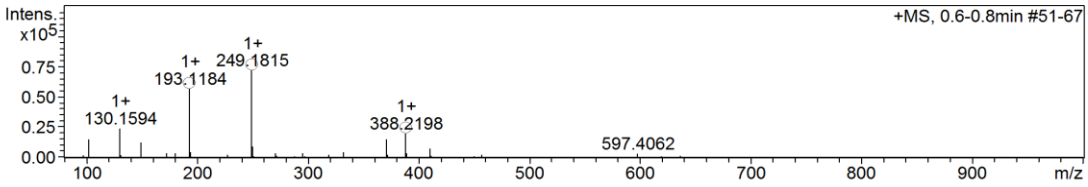


Figure A1.52 ESI-MS analysis of Pyranine methyl ester **(7)**

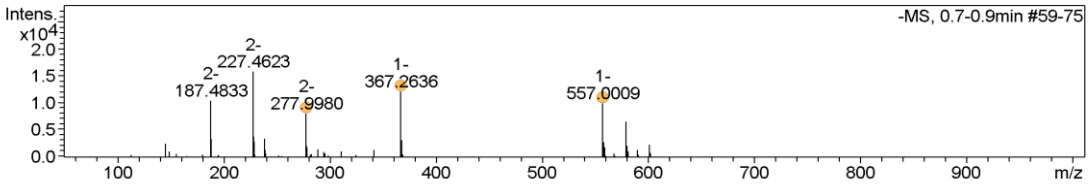


Figure A1.53 ESI-MS analysis of Pyranine ethylenediamine **(8)**

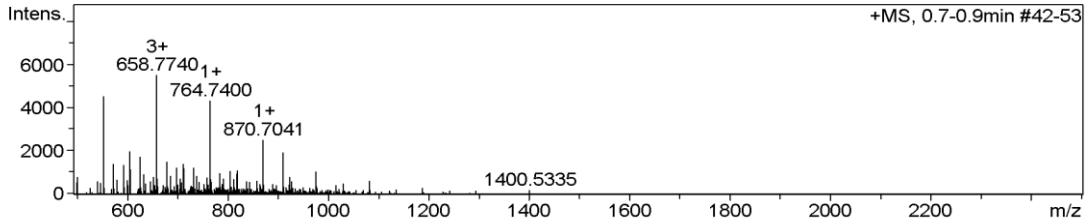


Figure A1.54 ESI-MS analysis of MalPyr Blue **(9)**

A1 Supporting information for Chapter 2 – FT-IR spectra

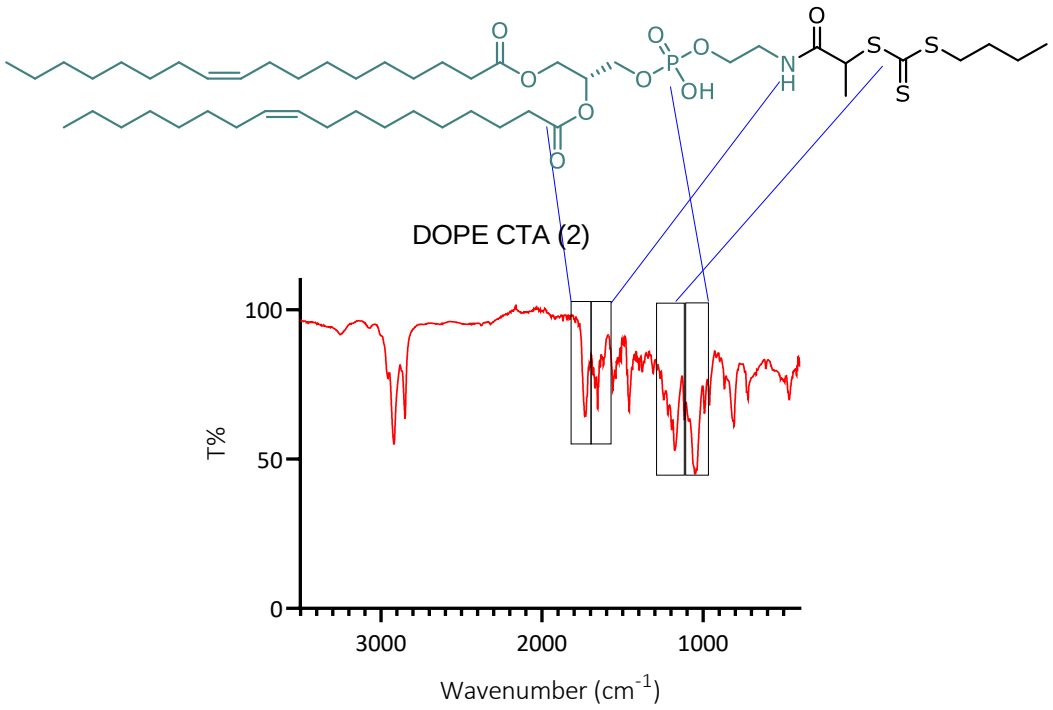


Figure A1.55 FT-IR spectrum of DOPE RAFT agent **(2)**

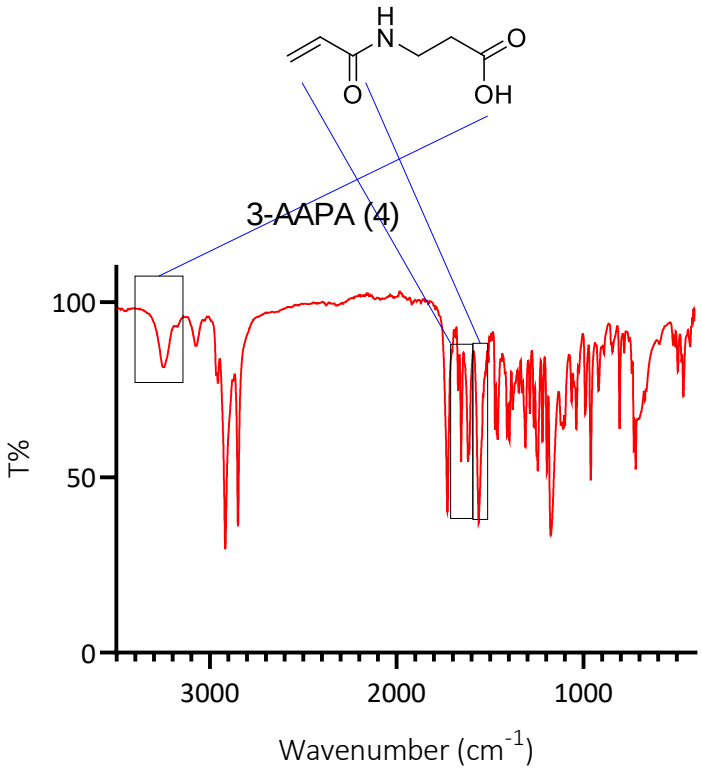


Figure A1. 56FT-IR spectrum of 3-acrylamido propanoic acid monomer **(4)**

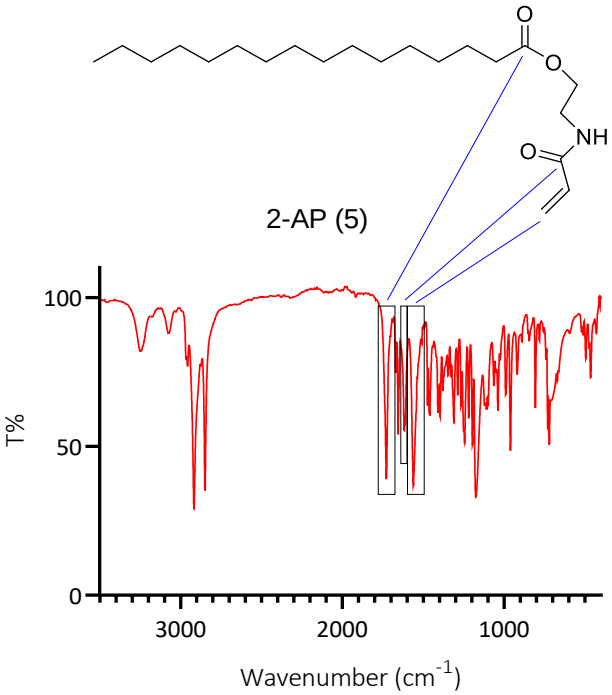


Figure A1. 57 FT-IR spectrum of 2-acrylamido palmitate monomer **(5)**

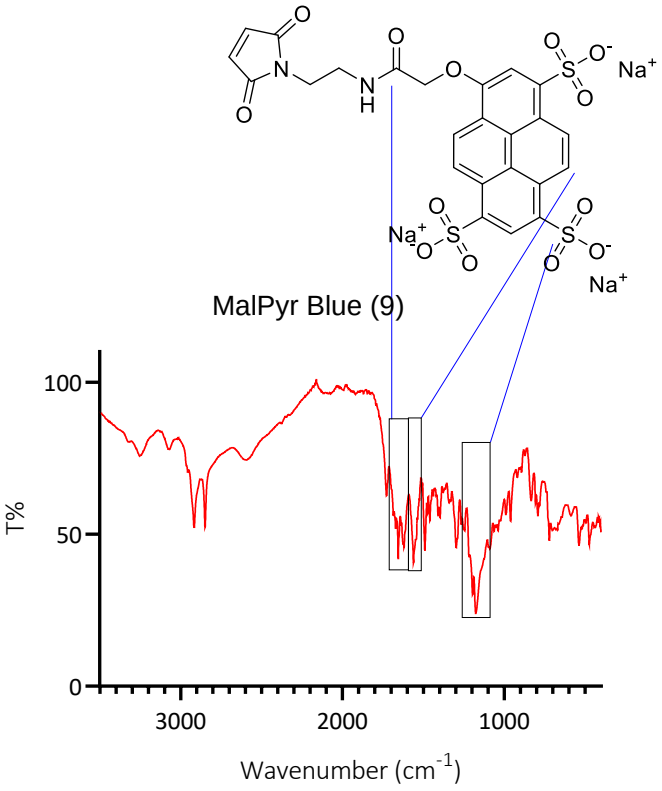


Figure A1. 58 FT-IR spectrum of MalPyr Blue fluorescent tagging agent **(9)**

A1 Supporting information for Chapter 2 – GPC Chromatograms

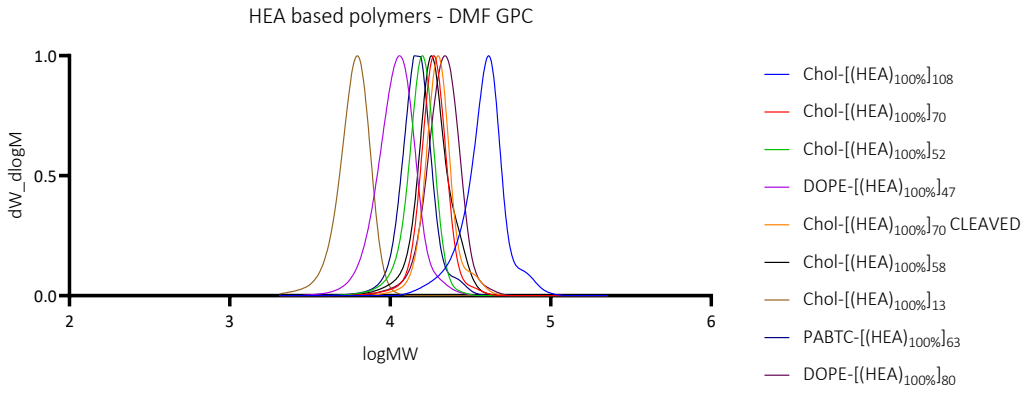


Figure A1. 59 Normalised SEC traces of HEA homopolymers. Analyses were performed in DMF + 0.1 % LiBr (PMMA standards)

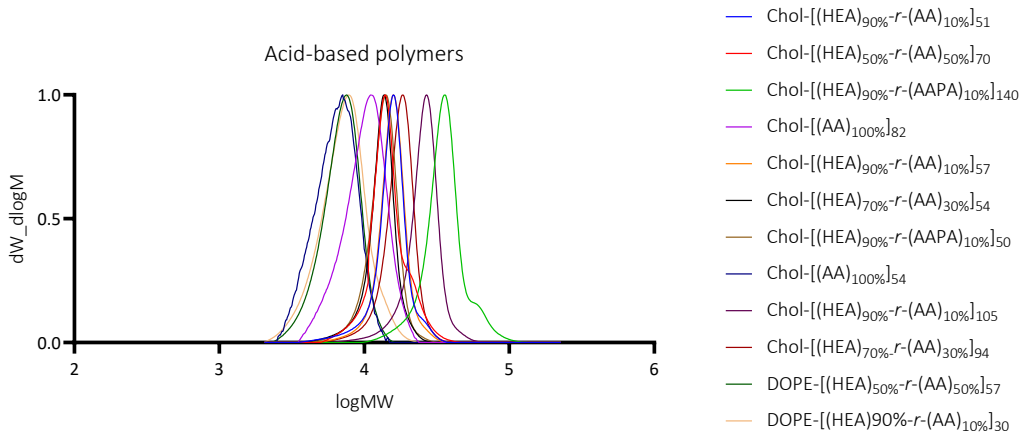


Figure A1. 60 Normalised SEC traces of HEA, AA and 3-AAPA (co)polymers. Analyses were performed in DMF + 0.1 % LiBr (PMMA standards)

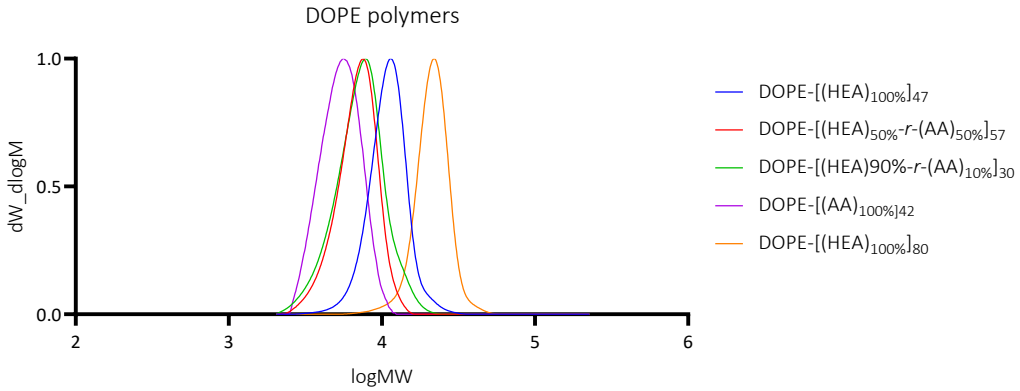


Figure A1.61 Normalised SEC traces of DOPE HEA, AA and 3-AAPA (co)polymers. Analyses were performed in DMF + 0.1 % LiBr (PMMA standards)

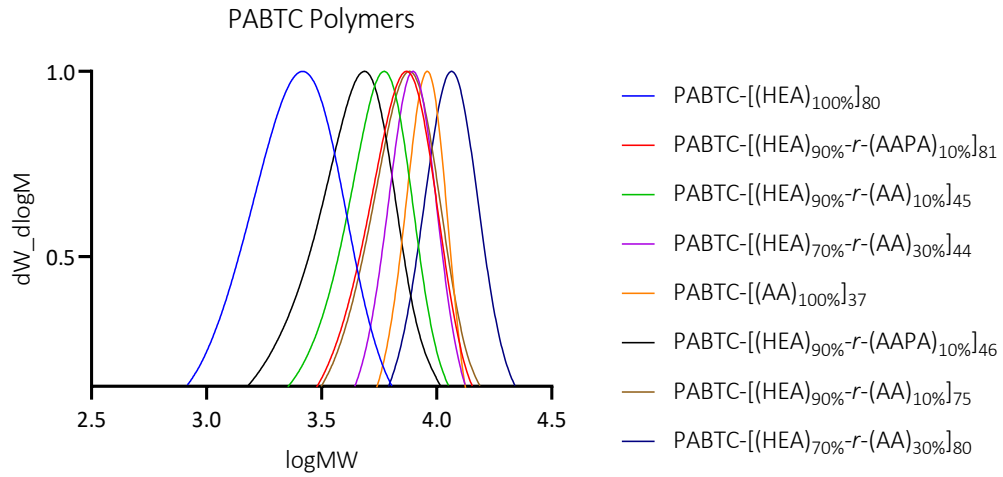


Figure A1.62 Normalised SEC traces of PABTC HEA, AA and 3-AAPA (co)polymers. Analyses were performed in HPLC water + 0.1 M $NaNO_3$ (PEO/PEG standards)

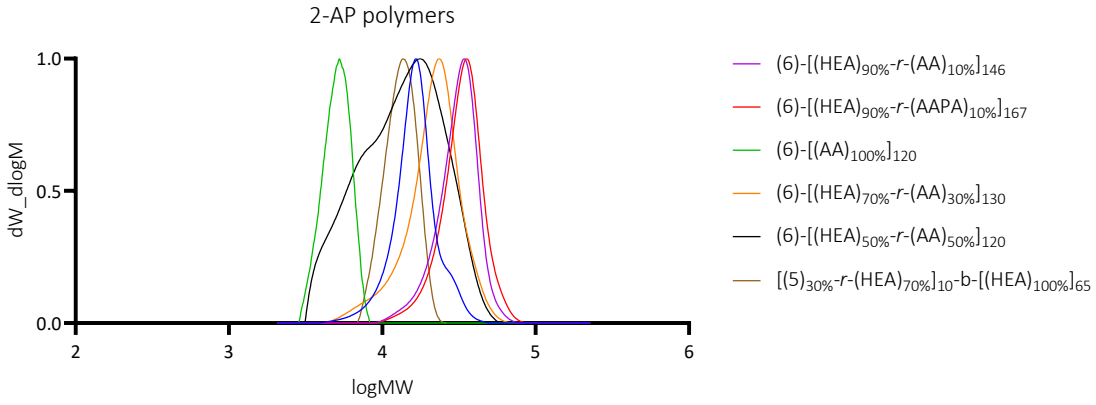


Figure A1.63 Normalised SEC traces of **(6)**-based HEA, AA and 3-AAPA (co)polymers. Analyses were performed in DMF + 0.1 % LiBr (PMMA standards)

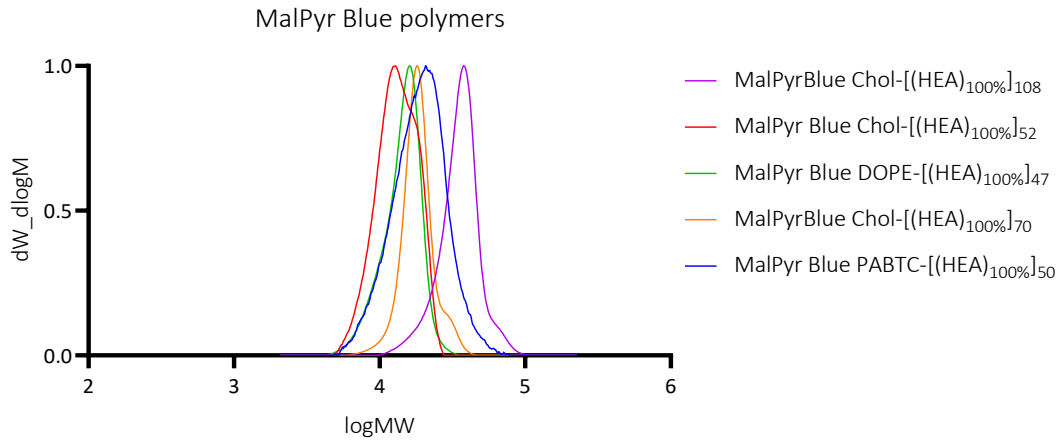


Figure A1.64 Normalised SEC traces of fluorescently tagged HEA homopolymers. Analyses were performed in DMF + 0.1 % LiBr (PMMA standards)

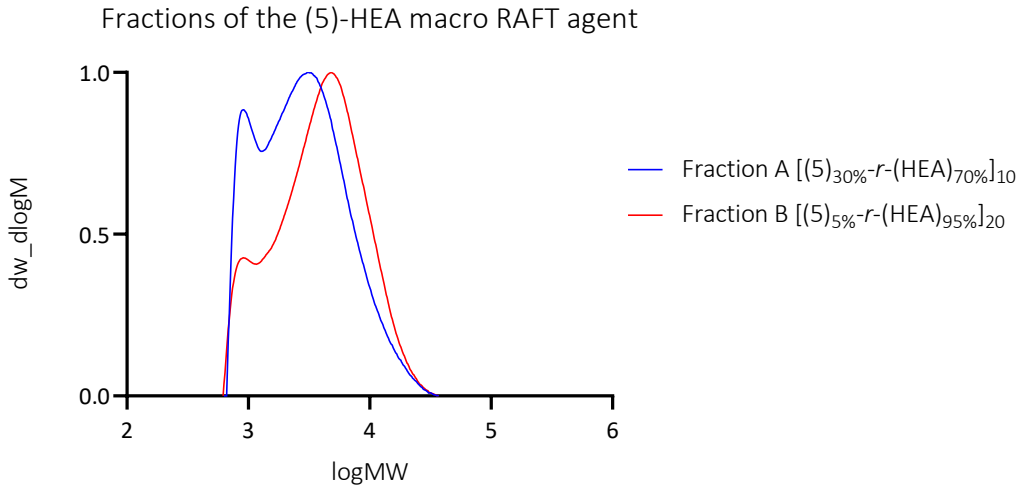


Figure A1.65 Normalised SEC traces for the fractions of the **(5)**-HEA macro RAFT agent purified by SiO_2 flash chromatography. Analyses were performed in DMF + 0.1 % LiBr (PMMA standards)

A2 Supporting information for Chapter 3

A2 Supporting information for Chapter 3 - Toxicity graphs

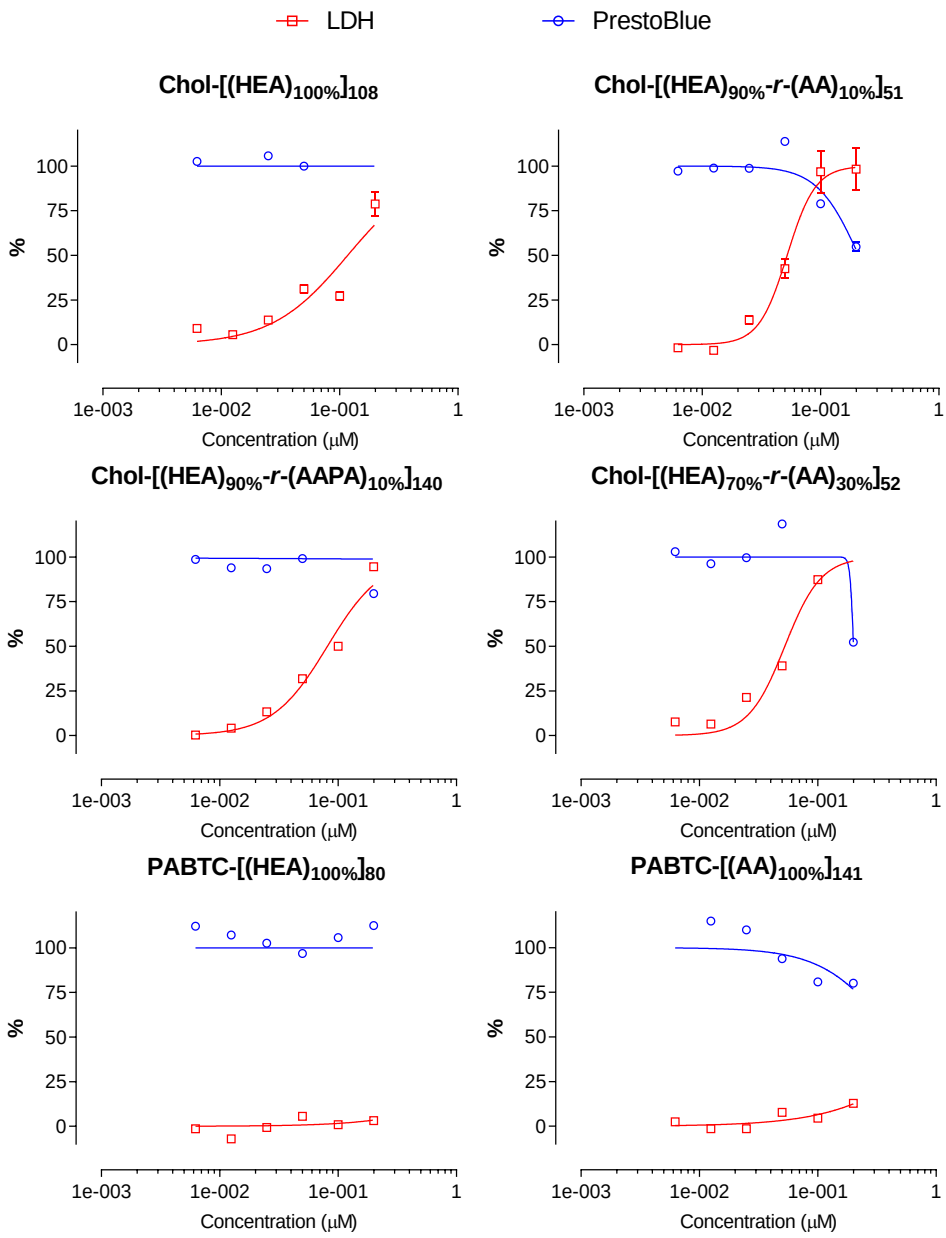


Figure A2.1 Cell toxicity results for select cholesterol and control polymers. The assays were performed on Caco2 cells, after 24 hours exposition to the polymer suspensions at different concentrations. The graph shows LDH release, indicative of membrane damage, in red and PrestoBlue™ results, which indicate cell viability, in blue. IC_{50} values were calculated using an [inhibitor] versus normalised response nonlinear regression curve fitting. 100% membrane damage was assumed for cells treated with a 1% Triton X-100 solution and 0% membrane damage was assumed for untreated cells. 0% metabolic activity was assumed for cells treated with a 1% Triton X-100 solution and 100% metabolic activity was assumed for untreated cells.

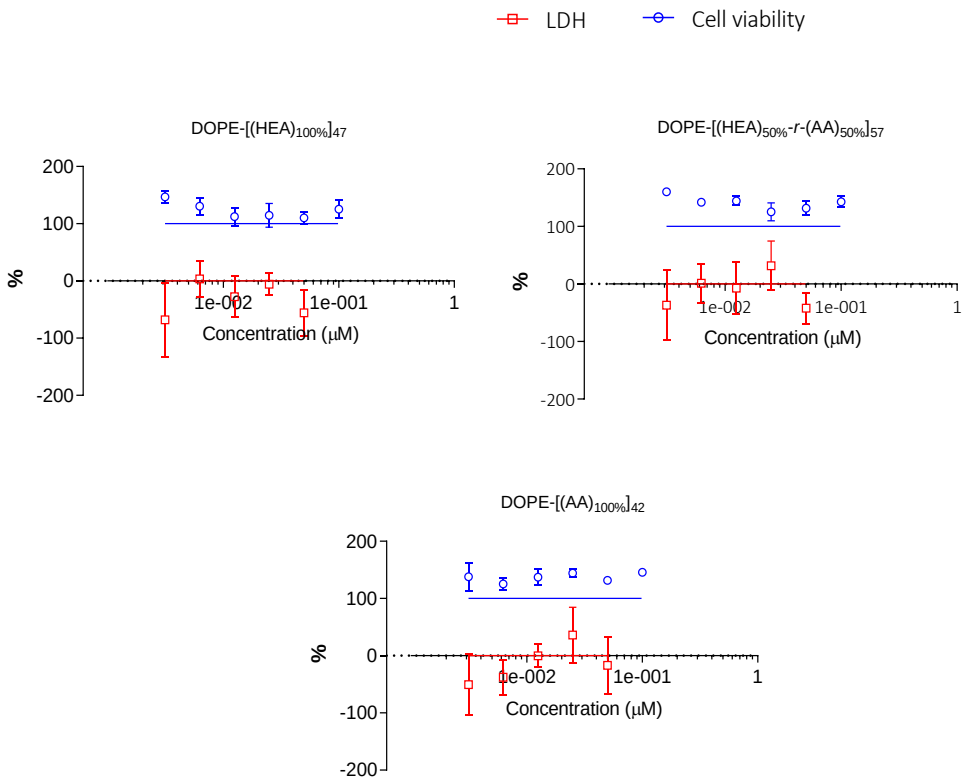


Figure A2.2 Cell toxicity results for select DOPE-based polymers. The assays were performed on Caco2 cells, after 24 hours exposition to the polymer suspensions at different concentrations. The graph shows LDH release, indicative of membrane damage, in red and PrestoBlue™ results, which indicate cell viability, in blue. IC_{50} values were calculated using an [inhibitor] versus normalised response nonlinear regression curve fitting. 100% membrane damage was assumed for cells treated with a 1% Triton X-100 solution and 0% membrane damage was assumed for untreated cells. 0% metabolic activity was assumed for cells treated with a 1% Triton X-100 solution and 100% metabolic activity was assumed for untreated cells.

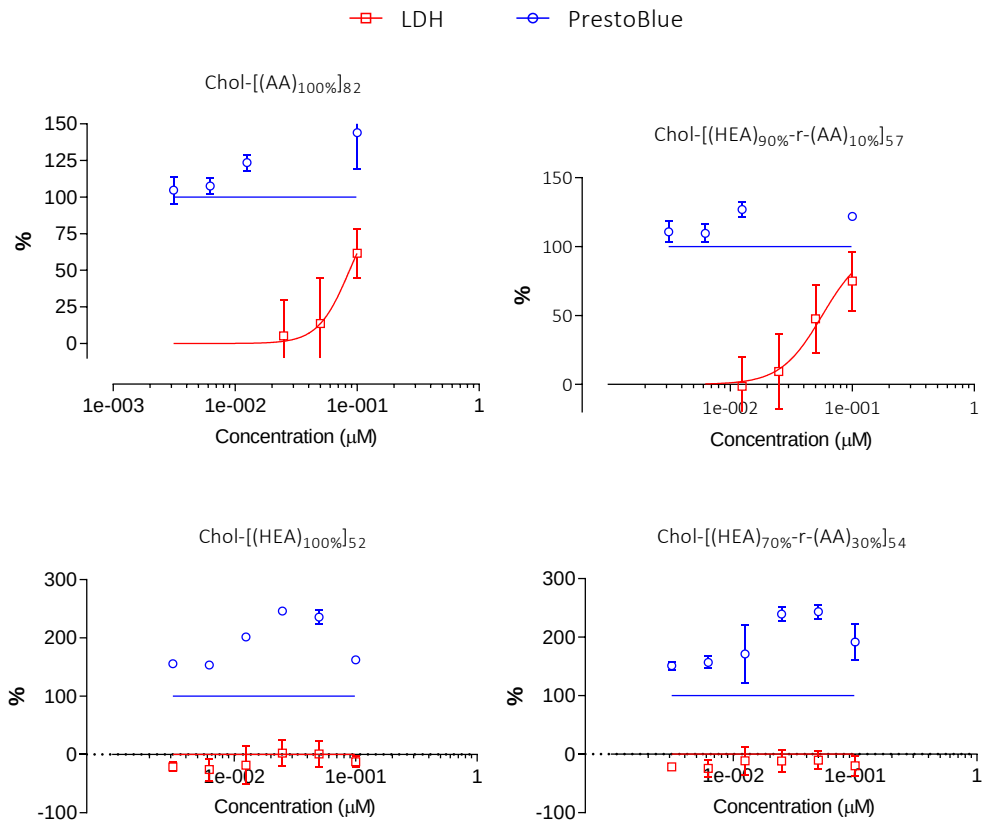


Figure A2.3 Cell toxicity results for select cholesterol-based polymers. The assays were performed on Caco2 cells, after 24 hours exposition to the polymer suspensions at different concentrations. The graph shows LDH release, indicative of membrane damage, in red and PrestoBlue™ results, which indicate cell viability, in blue. IC_{50} values were calculated using an [inhibitor] versus normalised response nonlinear regression curve fitting. 100% membrane damage was assumed for cells treated with a 1% Triton X-100 solution and 0% membrane damage was assumed for untreated cells. 0% metabolic activity was assumed for cells treated with a 1% Triton X-100 solution and 100% metabolic activity was assumed for untreated cells.

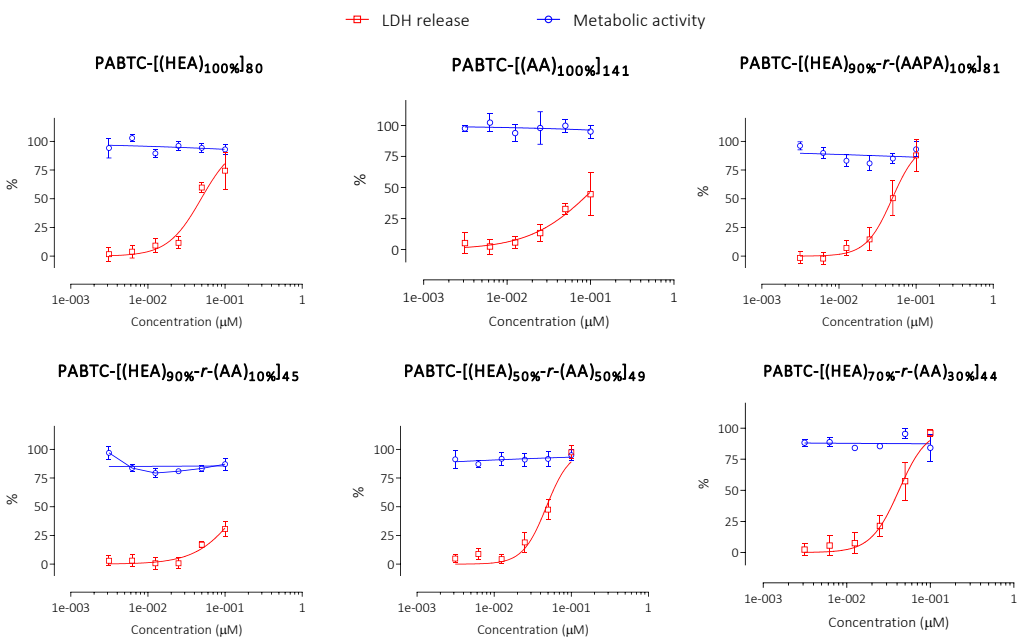


Figure A2.4 Cell toxicity results for select PABTC-based control polymers. The assays were performed on Caco2 cells, after 24 hours exposition to the polymer suspensions at different concentrations. The graph shows LDH release, indicative of membrane damage, in red and PrestoBlue™ results, which indicate cell viability, in blue. IC_{50} values were calculated using an [inhibitor] versus normalised response nonlinear regression curve fitting. 100% membrane damage was assumed for cells treated with a 1% Triton X-100 solution and 0% membrane damage was assumed for untreated cells. 0% metabolic activity was assumed for cells treated with a 1% Triton X-100 solution and 100% metabolic activity was assumed for untreated cells.

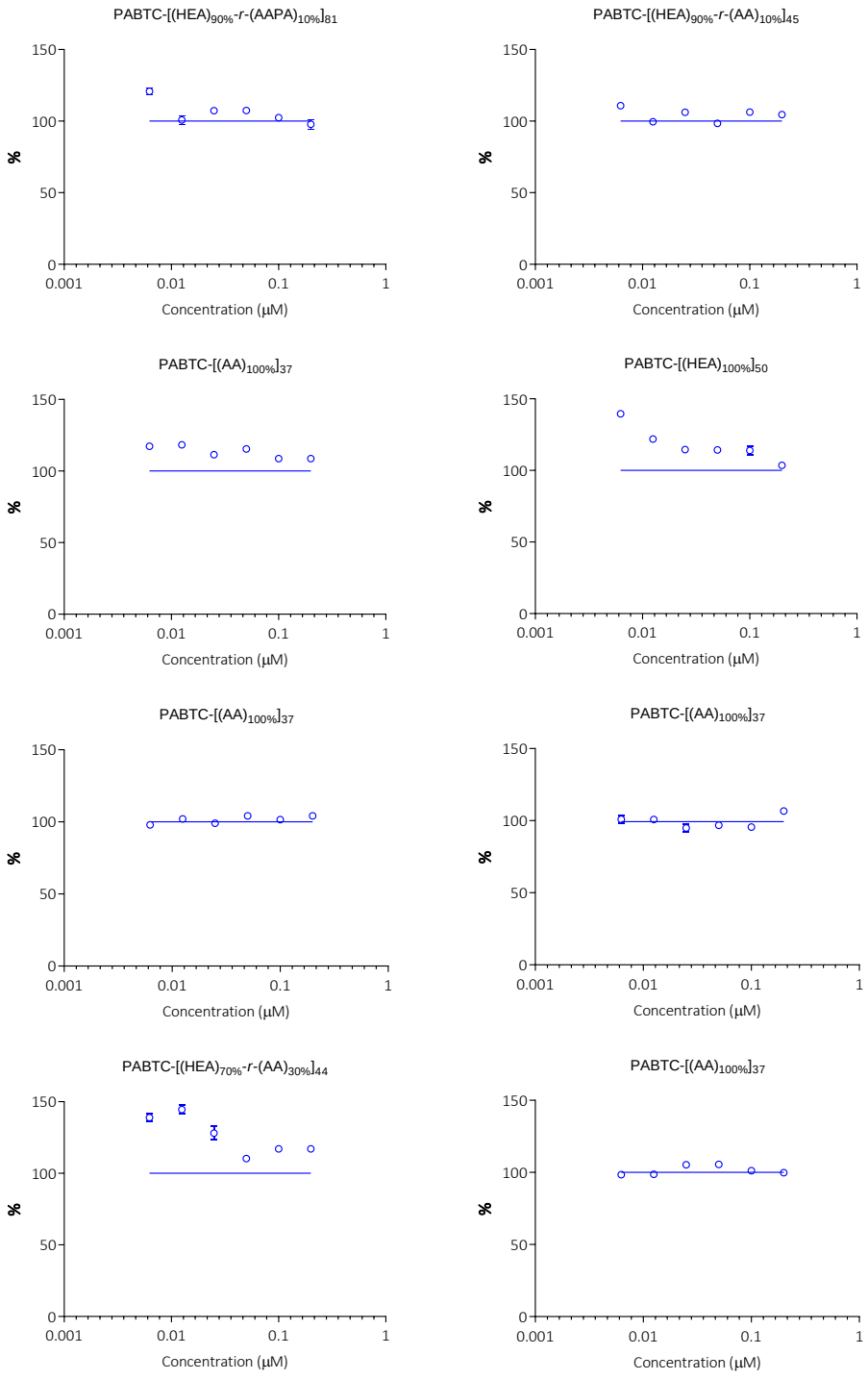


Figure A2. 5 Cell toxicity results for select PABTC-based control polymers. The assays were performed on Caco2 cells, after 24 hours exposition to the polymer suspensions at different concentrations. The graph shows PrestoBlue™ results, which indicate cell viability, in blue. IC_{50} values were calculated using an [inhibitor] versus normalised response nonlinear regression curve fitting. 0% metabolic activity was assumed for cells treated with a 1% Triton X-100 solution and 100% metabolic activity was assumed for untreated cells.

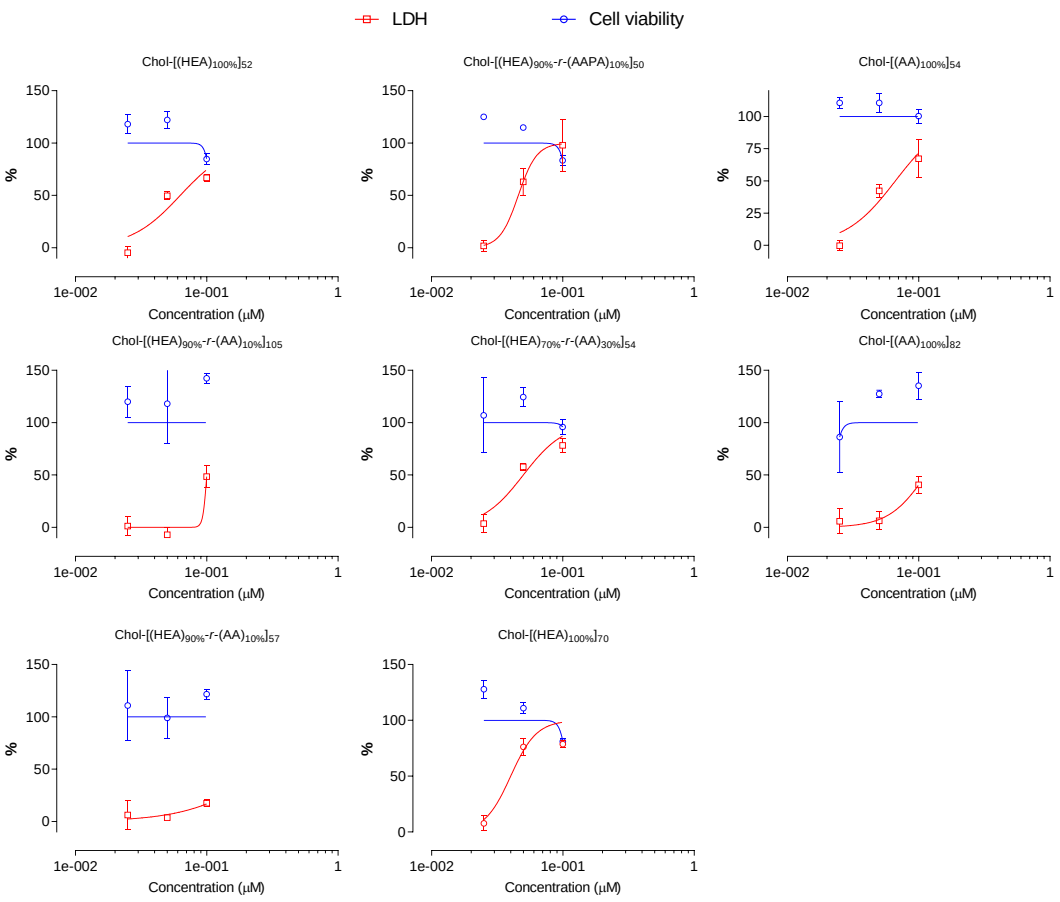


Figure A2.6 Cell toxicity results for select cholesterol-based polymers. The assays were performed on Caco2 cells, after 24 hours exposition to the polymer suspensions at different concentrations. The graph shows LDH release, indicative of membrane damage, in red and PrestoBlue™ results, which indicate cell viability, in blue. IC_{50} values were calculated using an [inhibitor] versus normalised response nonlinear regression curve fitting. 100% membrane damage was assumed for cells treated with a 1% Triton X-100 solution and 0% membrane damage was assumed for untreated cells. 0% metabolic activity was assumed for cells treated with a 1% Triton X-100 solution and 100% metabolic activity was assumed for untreated cells.

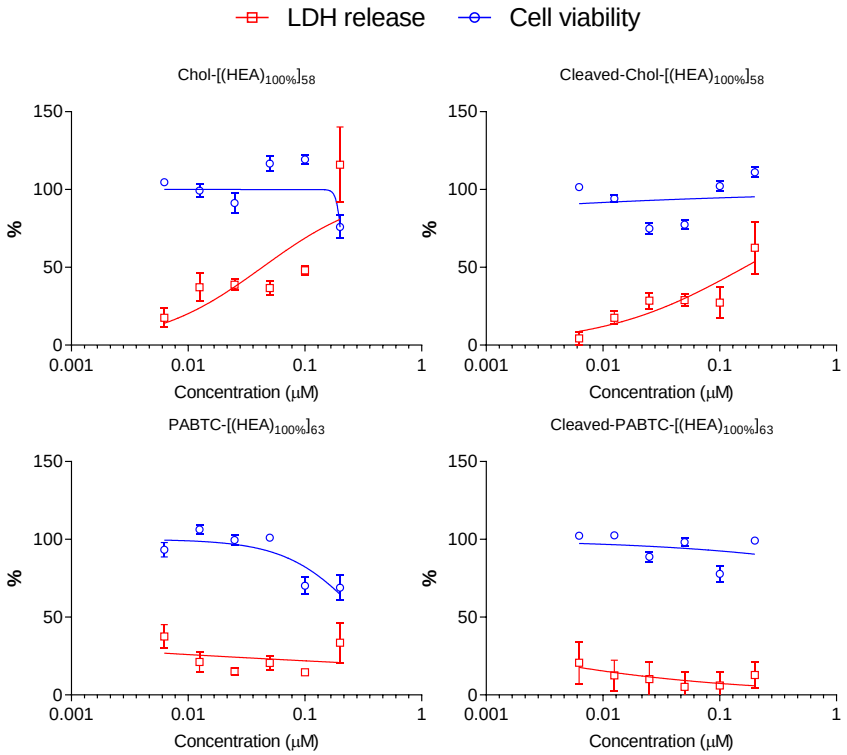


Figure A2.7 Cell toxicity results for select cholesterol and control polymers, comparing the polymers where trithiocarbonate is present as an omega chain end versus the polymers where this group was substituted with a H group (Cleaved). The assays were performed on Caco2 cells, after 24 hours exposition to the polymer suspensions at different concentrations. The graph shows LDH release, indicative of membrane damage, in red and PrestoBlue™ results, which indicate cell viability, in blue. IC_{50} values were calculated using an [inhibitor] versus normalised response nonlinear regression curve fitting. 100% membrane damage was assumed for cells treated with a 1% Triton X-100 solution and 0% membrane damage was assumed for untreated cells. 0% metabolic activity was assumed for cells treated with a 1% Triton X-100 solution and 100% metabolic activity was assumed for untreated cells.

A3 Supporting information for Chapter 5

A3 Supporting information for Chapter 5 – NMR spectra

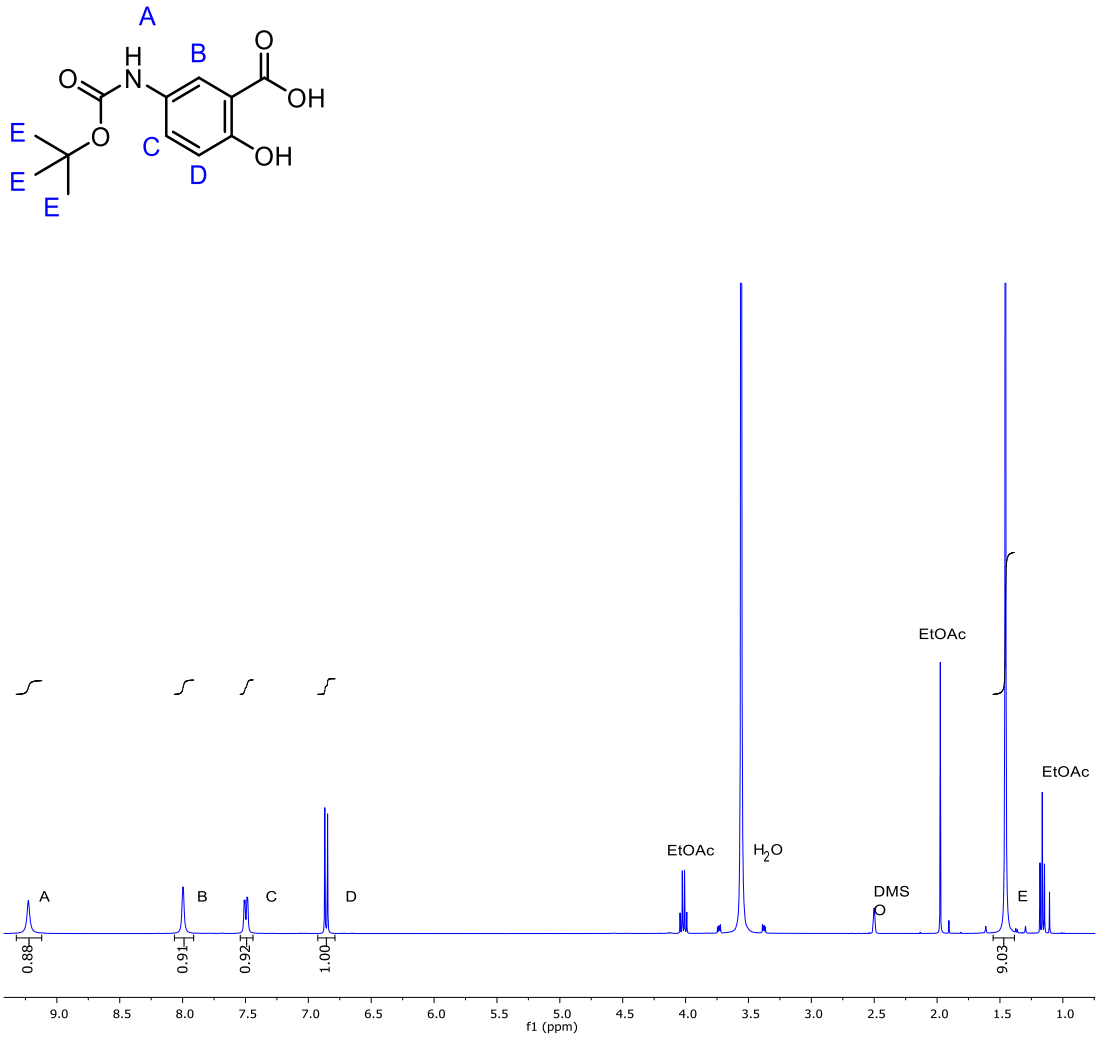


Figure A3.1 ^{1}H NMR spectrum of Boc-protected mesalazine **(14)** in DMSO-d_6

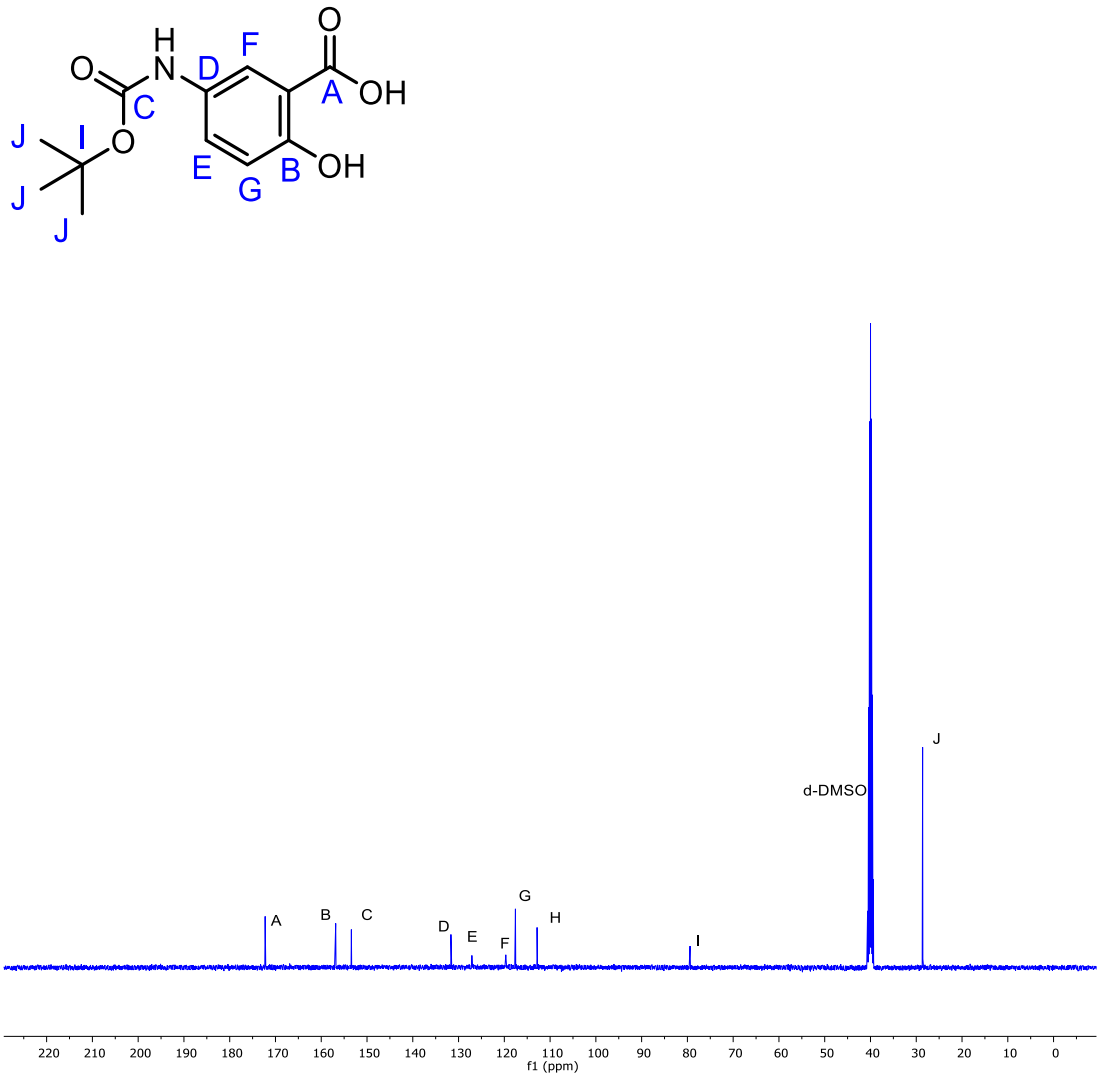


Figure A3.2 ^{13}C NMR spectrum of Boc-protected mesalazine **(14)** in DMSO-d_6

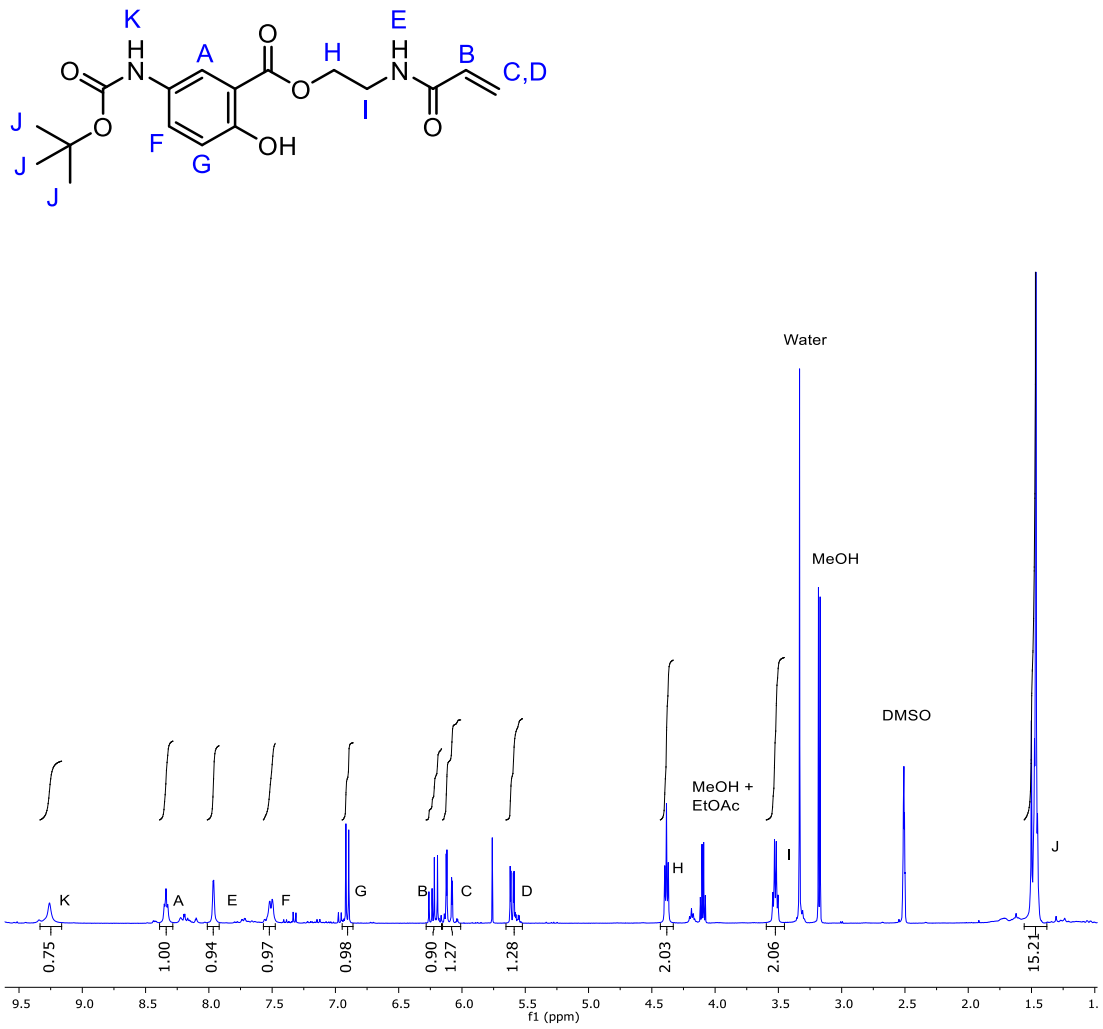


Figure A3.3 ^{1}H NMR spectrum of Boc-protected mesalazine monomer **(15)** in DMSO-d_6

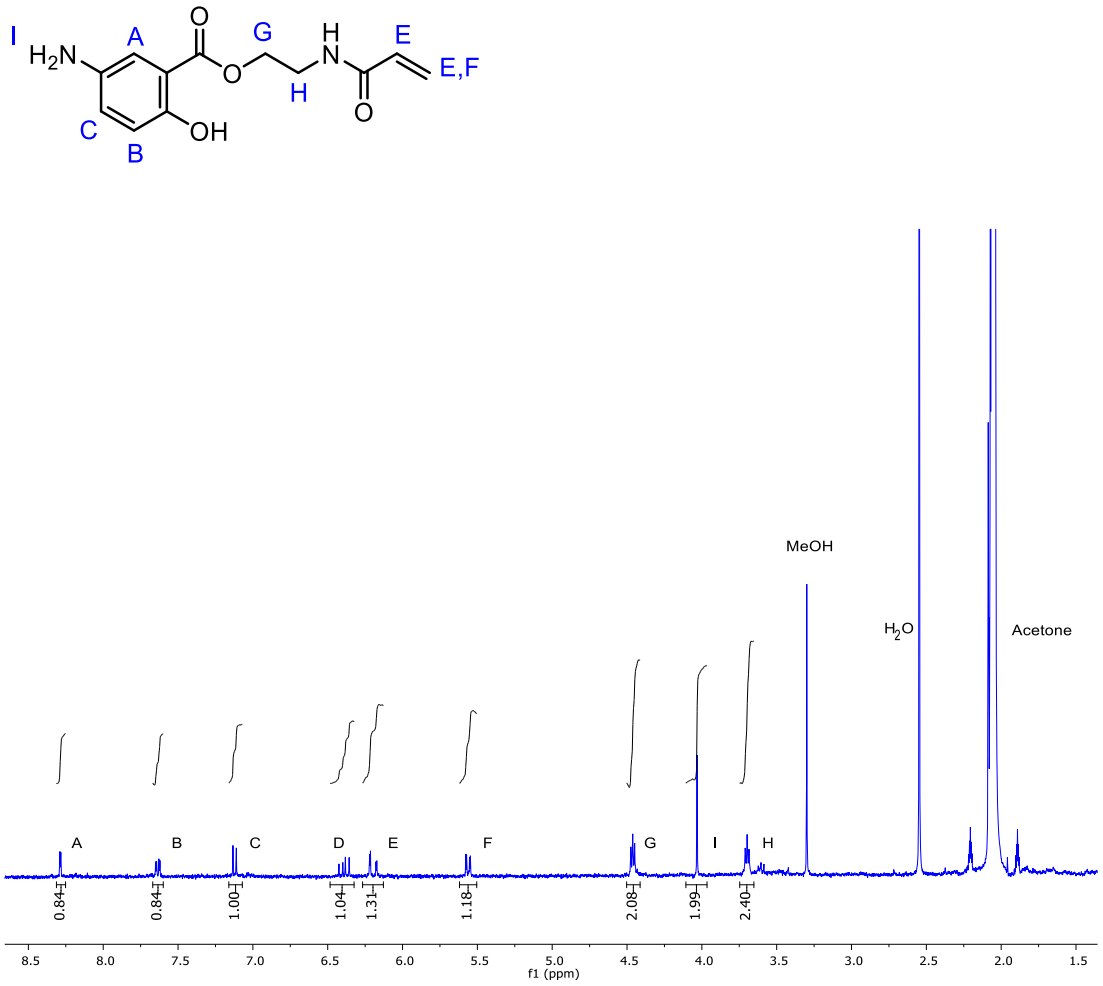


Figure A3.4 ^{1}H NMR spectrum of mesalazine monomer **(16)** in DMSO-d_6

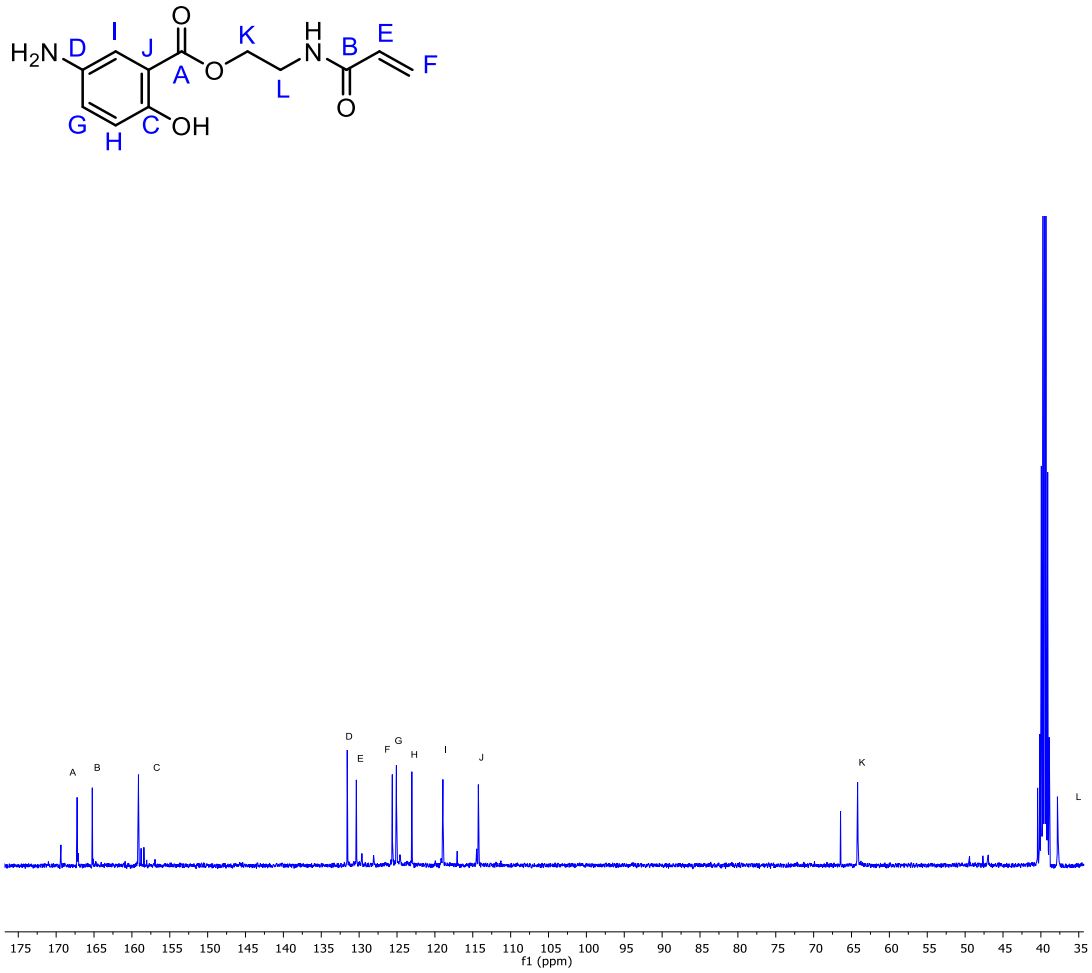


Figure A3.5 ^{13}C NMR spectrum of mesalazine monomer **(16)** in DMSO-d_6

A3 Supporting Information for Chapter 5 – Mass spectra

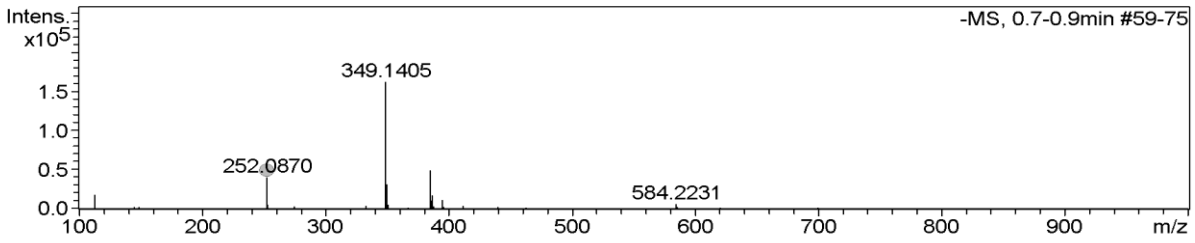


Figure A3.6 ESI-MS analysis of Boc-protected mesalazine **(14)**

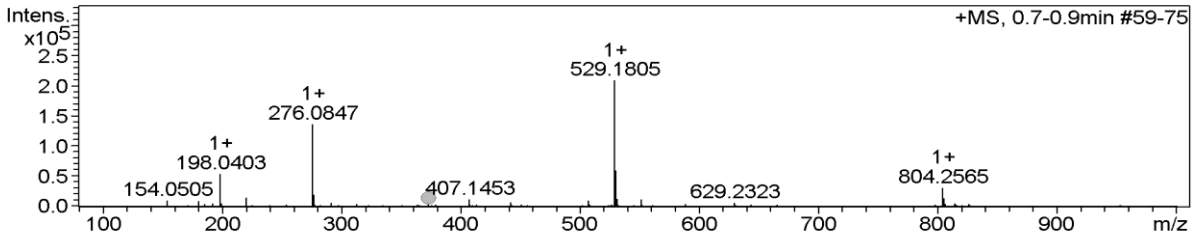


Figure A3. 7 ESI-MS analysis of Boc-protected mesalazine monomer **(15)**

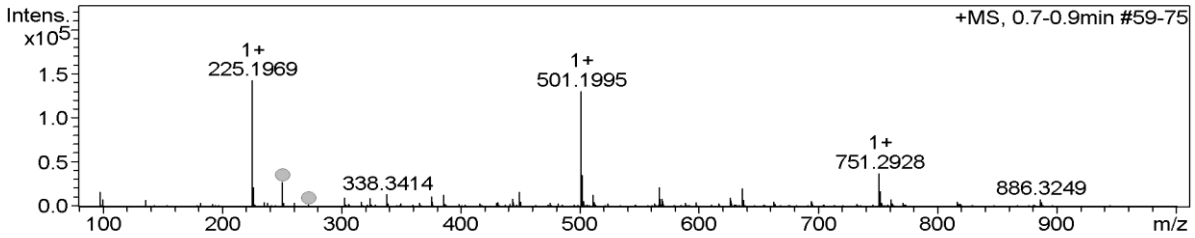


Figure A3. 8 ESI-MS analysis of mesalazine monomer **(16)**

A3 Supporting information for Chapter 5 – GPC Chromatograms

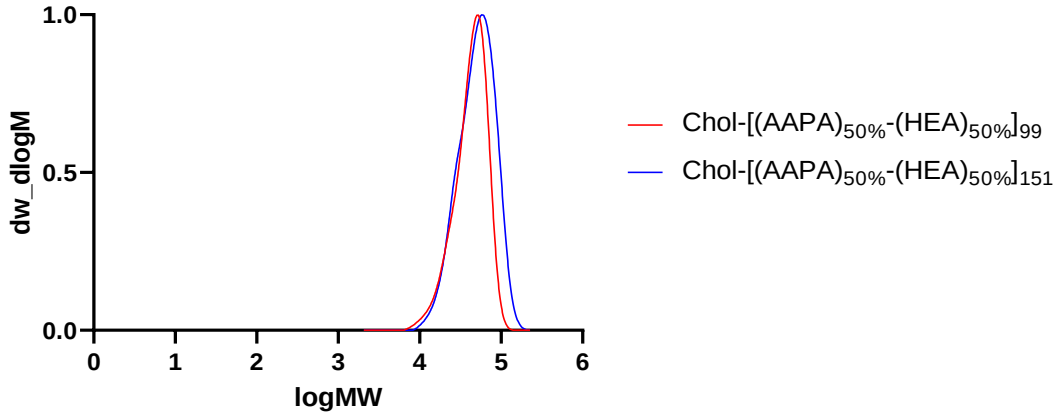


Figure A3. 9 Figure A1.66 Normalised SEC traces of cholesterol HEA:3-AAPA block copolymers. Analyses were performed in DMF + 0.1 % LiBr (PMMA standards)

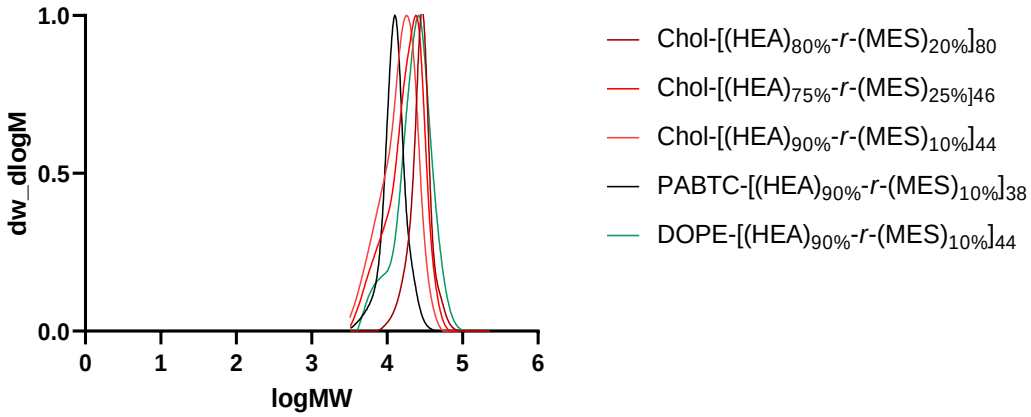


Figure A3. 10 Figure A1.67 Normalised SEC traces of HEA:**(16)** copolymers. Analyses were performed in DMF + 0.1 % LiBr (PMMA standards)